Analysis of BMP and NAD Signalling during Zebrafish Embryogenesis

Dissertation

der Mathematisch-Naturwissenschaftlichen Fakultät

der Eberhard Karls Universität Tübingen

zur Erlangung des Grades eines

Doktors der Naturwissenschaften

(Dr. rer. nat.)

vorgelegt von

Autumn Penecilla Pomreinke, M.Sc.

San Fernando (Pampanga)

Philippinen

Tübingen

2023

Gedruckt mit Genehmigung der Mathematisch-Naturwissenschaftlichen Fakultät der Eberhard Karls Universität Tübingen.

Tag der mündlichen Qualifikation:	05.12.2023
Dekan:	Prof. Dr. Thilo Stehle
1. Berichterstatter:	Prof. Dr. Ulrich Rothbauer
2. Berichterstatter:	Prof. Dr. Patrick Müller

Abstract

Embryogenesis is a dynamic process during which a single fertilized cell develops into a multicellular organism, often with functional organs spatially arranged within the body. Across the animal kingdom, a conserved repertoire of signalling pathways orchestrates embryogenesis. How the molecular players of the signalling pathways function in a species-specific manner is yet to be investigated. Tackling this question involves a concerted effort of many developmental biologists. My part in this effort is to investigate the Bone Morphogenetic Protein (BMP) signalling dynamics during dorsal-ventral patterning and how Nicotinamide Adenine Dinucleotide (NAD) salvage pathway fine-tunes haematopoiesis during zebrafish embryonic development.

First, a BMP signalling gradient is involved in organising the dorsal-ventral axis of the zebrafish. There are five disparate models with different assumptions about how the BMP signalling gradient is established by a BMP-Chordin activator/inhibitor system with additional accessory proteins, namely, Tolloid, Sizzled, and Anti-dorsalizing morphogenetic protein (ADMP). In Chapter 1, I will discuss how we tested these models by quantifying the BMP signalling gradient upon loss-of-function of individual components and by measuring the biophysical properties of BMP, Chordin, and Sizzled fluorescent fusion constructs. Together, our data suggest that a graded source-sink mechanism underlies the BMP-Chordin system to shape the BMP signalling gradient during zebrafish gastrulation. Furthermore, Tolloid amplifies BMP signalling throughout the dorsal-ventral axis, while Sizzled restricts BMP signalling ventrally. In addition, *admp* overexpression affects BMP signalling in a concentration-dependent manner in zebrafish embryos: high levels of ADMP attenuate BMP signalling, whereas low levels of ADMP enhance BMP signalling. Thus, these extracellular components may refine the shape of the BMP signalling gradient, in addition to BMP inhibition by Chordin.

Second, it is currently unclear how the BMP-mediated body axis evolved in bilaterally symmetric organisms. Our collaborators found that in the anthozoa cnidarian, *Nematostella vectensis*, knockdown of a previously uncharacterised zinc finger protein with a SWIM domain (Zswim4-6) caused flattening of the BMP signalling gradient and incorrect endoderm compartmentalisation. Whether the zebrafish homologue Zswim5 has a conserved role in the axis formation of bilaterians such as

the zebrafish is yet to be investigated. In Chapter 2, I present how Zswim5 may have a role in the development of distal structures along the dorsal-ventral axis, for example, eyes, blood, and tail. Similar to findings in *Nematostella*, overexpression of *zswim5* in zebrafish embryos can flatten the BMP signalling gradient slope. This shallower BMP signalling gradient may have caused the developmental defects. Since homologous Zswims in *Nematostella* and zebrafish have a conserved role in BMP-mediated axis formation, this further supports that bilaterians and cnidarians could have a bilaterally symmetric common ancestor.

Finally, the ventral-most mesodermal cells that receive the highest BMP signalling will differentiate into blood cells. Recycling of NAD by the zebrafish nicotinamide phosphoribosyltransferase-a (Nampta) is essential for haematopoiesis and the viability of the embryo. However, there is a discrepancy in the reported phenotypes upon *nampta* loss-of-function. Therefore, in Chapter 3, I re-examine the role of Nampta during blood development by comparing two loss-of-function approaches: stable mutant knockout line using CRISPR/Cas9 and transient gene knockdown using morpholino. My findings suggest that the *nampta* morpholino has off-target effects and that Nampta provides robustness by supplying additional NAD to increase blood cell markers, but *nampta* loss-of-function does not affect zebrafish viability or abolish haematopoiesis.

Overall, this dissertation deepens our understanding of how key signalling pathways have evolved in a species-specific manner to fine-tune cellular differentiation during zebrafish embryogenesis. This is accomplished by first demonstrating how Chordin, Sizzled, Tolloid, and ADMP make up an extracellular network to shape the BMP signalling gradient for dorsal-ventral patterning. Second, an intracellular protein Zswim5 is likely a modulator of the BMP signalling gradient and is conserved in bilaterally symmetric organisms. Third, in later stages, NAD recycled by Nampta redundantly supports blood cell specification. I hope that these novel findings improve our understanding of zebrafish as an animal model for vertebrate development and highlight potential mechanisms to consider during animal embryogenesis.

Zusammenfassung

Im gesamten Tierreich reguliert ein konserviertes Repertoire an Signalwegen die Embryogenese. Noch ist unklar, wie dieses Repertoire auf molekularer Ebene seine speziesspezifischen Funktionen erfüllt. Um diesen Prozess zu verstehen, bedarf es der konzertierten Anstrengung vieler Entwicklungsbiologen. Mein Teil dieser Bemühungen besteht darin, die Signaldynamik von Bone Morphogenetic Protein (BMP) während der dorsal-ventralen Strukturierung und außerdem die Feinabstimmung der Hämatopoese durch den Nicotinamid-Adenin-Dinukleotid (NAD)-salvage-pathway während der Embryonalentwicklung des Zebrafisches zu untersuchen.

Erstens analysiere ich den BMP-Signalgradienten, der die dorsal-ventrale Achse des Zebrafisches organisiert. Derzeit gibt es fünf unterschiedliche Modelle mit verschiedenen Annahmen über die biophysikalischen Eigenschaften des Aktivators BMP und seines Inhibitors Chordin die erklären wie der BMP Signalgradient, unter Mitwirkung der extrazellulären Proteine, nämlich – Sizzled, Tolloid und Anti-dorsalizing Morphogenetic Protein (ADMP), erzeugt wird. In Kapitel 1 werde ich diskutieren, wie wir diese Modelle getestet haben, indem wir den BMP Signalgradienten nach Ausschaltung/Funktionsverlust individueller Komponenten quantifiziert haben und die biophysikalischen Eigenschaften von BMP, Chordin und Sizzled gemessen haben. Insgesamt deuten unsere Daten darauf hin, dass dem BMP-Chordin-System ein *graded source-sink* Mechanismus zugrunde liegt, um den BMP-Signalgradienten während der Zebrafischgastrulation zu formen. Zusätzlich verstärkt Tolloid das BMP-Signal entlang der dorsal-ventralen Achse, während Sizzled das BMP-Signal ventral begrenzt. Darüber hinaus beeinflusst die Überexpression von ADMP die BMP-Signalübertragung in Zebrafischembryonen konzentrationsabhängig: Hohe ADMP-Werte dämpfen die BMP-Signalübertragung, während niedrige ADMP-Werte das BMP-Signal verstärken. Somit können diese extrazellulären Komponenten die Form des BMP-Signalgradienten zusätzlich zur BMP-Hemmung durch Chordin verfeinern.

Zweitens ist derzeit unklar, wie sich die durch BMP-vermittelte Körperachse in bilateral symmetrischen Organismen entwickelt hat. Unsere Kollegen fanden heraus, dass beim Nesseltier Nematostella vectensis die gedämpfte Expression eines bisher nicht charakterisierten Zinkfingerproteins mit einer SWIM-Domäne (Zswim4-6) zu

einer Abflachung des BMP-Signalgradienten und einer falschen Endoderm-Kompartimentierung führte. Ob das Zebrafisch-Homolog Zswim5 eine konservierte Rolle bei der Achsenbildung von Bilateria wie dem Zebrafisch spielt, muss noch untersucht werden. In Kapitel 2 erkläre ich, wie Zswim5 eine Rolle bei der Entwicklung distaler Strukturen entlang der dorsal-ventralen Achse spielen könnte. Ähnlich wie bei Nematostella kann eine Überexpression von Zswim5 in Zebrafischembryonen die Steigung des BMP-Signalgradienten abflachen. Meine Daten legen nahe, dass dieser flachere BMP-Signalgradient zu Entwicklungsstörungen führen könnte. Da homologe Zswims in Nematostella und Zebrafischen eine konservierte Rolle bei der BMP-vermittelten Achsenbildung spielen, unterstützt dies die Annahme, dass Bilateria und Cnidaria einen bilateral symmetrischen gemeinsamen Vorfahren gehabt haben könnten.

Schließlich untersuche ich die ventralsten mesodermalen Zellen, die das höchste BMP-Signal empfangen und sich zu Blutzellen differenzieren. Das Recycling von NAD durch die Zebrafisch-Nikotinamid-Phosphoribosyltransferase-a (Nampta) ist für die Hämatopoese und die Lebensfähigkeit des Embryos von wesentlicher Bedeutung. Es besteht jedoch eine Diskrepanz in den publizierten Phänotypen bei einem Funktionsverlust von Nampta. Daher untersuche ich in Kapitel 3 erneut die Rolle von Nampta während der Blutentwicklung, indem ich zwei Ansätze zum Funktionsverlust vergleiche: eine stabile Mutanten-Knockout-Linie mit CRISPR/Cas9 und einen transienten Gen-Knockdown mit Morpholino. Meine Ergebnisse deuten darauf hin, dass *nampta*-Morpholino hat Off-Target-Effekte und dass Nampta die Robustheit der Entwicklung fördert, indem es zusätzliches NAD zur Erhöhung von Blutzellmarkern bereitstellt, der Funktionsverlust von Nampta jedoch weder die Lebensfähigkeit von Zebrafischen beeinträchtigt noch die Hämatopoese unterbindet.

Insgesamt vertieft diese Dissertation unser Verständnis darüber, wie sich wichtige Signalwege auf speziesspezifische Weise entwickelt haben, um die Zelldifferenzierung während der Embryogenese von Zebrafischen zu verfeinern. Zunächst wird gezeigt, wie Chordin, Sizzled, Tolloid und ADMP ein extrazelluläres Netzwerk bilden, um den BMP-Signalgradienten für die dorsal-ventrale Musterbildung zu formen. Zweitens erläutere ich, dass ein intrazelluläres Protein – Zswim5 – wahrscheinlich ein Modulator des BMP-Signalgradienten ist und in evolutionär weit entfernten, bilateral symmetrischen Organismen konserviert ist. Drittens wird gezeigt,

dass das von Nampta recycelte NAD in späteren Phasen redundant die Blutzellspezifikation unterstützt. Ich hoffe, dass diese neuen Erkenntnisse unser Verständnis des Zebrafisches als Tiermodell für die Entwicklung von Wirbeltieren verbessern und mögliche Mechanismen, die bei der Embryogenese von Tieren zu berücksichtigen sind, aufzeigen.

Acknowledgements

My heartfelt thanks…

To Prof. Dr. Patrick Müller, for the opportunity to do a PhD in your lab. You have set a high standard for the lab and have given me the space to grow intellectually.

To my TAC, Prof. Dr. Christian Mosimann and Prof. Dr. Ulrich Rothbauer, for your valuable input and encouragement.

To the Christiane Nüsslein-Volhard-Foundation, for choosing me as an award recipient.

To Dr. Katherine W. Rogers, for being reliable and always willing to help in every way and for setting the ideal scientist we should strive for.

To Dr. Gary H. Soh, for being the best friend a budding scientist can have and for working together as an assembly line to push our projects out. Those were the best and worst of times. Thanks for taking the night shift.

To Dr. Daniel Čapek, for inspiring me by saying 'I don't know how', thus giving a perfect example of someone willing to learn. Thanks for all the laughter and the help, such as giving me a crash course on statistics and translating the abstract of my thesis.

To Dr. Anna Kögler, for helping me throughout the thesis-writing process and for reminding me to take a break.

To the lab's former biochem wiz, Dr. David Mörsdorf, for always explaining concepts and reminding me to fight for what PhD students deserve because 'we're worth it'. Your PhD comics were an inspiration and a source of laughter.

To Maria Langegger, the perfect lab mom, for taking care of everyone in the lab.

To Prof. Dr. Andrei Lupas, for supporting me as a guest scientist at the institute during the writing process.

To the RST and BioOptics, for the support and the stimulating discussions over the years.

To everyone at the Max Planck Campus Tuebingen, for making an excellent environment for budding scientists.

To Sr. Man Coi, for the love and prayers since high school.

To my brother and sister-in-law, Jonathan and Rochelle Otchengco, for your support and reminding me why siblings are important.

To my parents, Israel and Dr. Yolanda Otchengco, who continuously provide me with the tools I need to overcome challenges. You are the loving and caring pillars that have kept me up from day 1.

To my son, Friedrich Pomreinke, being your mom is the best job in the world. This was all for you.

To my dear husband, Patrick Pomreinke, who shares this journey with me. From raising a family to our academic debates, comparing law and science, you have inspired me to be the best version of myself. Thank you for filling our home with love, laughter, and books.

And to God, who gave me the people mentioned here and for filling the gap between what I can and what I cannot.

Table of Contents

List of Figures

List of Tables

Publications of this thesis and author contributions

1. **Pomreinke, A. P.**, Soh, G. H., Rogers, K. W., Bergmann, J. K., Bläßle, A. J., & Müller, P. (2017). Dynamics of BMP signaling and distribution during zebrafish dorsal-ventral patterning. *eLife*, *6*.

   Patrick Müller conceived the study, performed the mathematical modelling, and wrote the manuscript. Katherine W. Rogers, Alexandre Bläßle, Gary H. Soh, and I edited the manuscript and performed the experiments with Jennifer Bergmann. Specifically, I performed the immunostaining and *in toto* imaging and subsequently generated the 2D maps and videos. I characterised the fluorescent constructs by scoring phenotypes and by Western blot. This published work is integrated and cited accordingly in Chapter 1 of this dissertation. The published manuscript was also previously included in two dissertations that were submitted to the Faculty of Science at the University of Tübingen: Alexander Bläßle's dissertation in 2018 for the Biology department and Gary H. Soh's dissertation in 2020 for the Biochemistry department.

2. Soh, G. H., **Pomreinke, A. P.**, & Müller, P. (2020). Integration of Nodal and BMP Signaling by Mutual Signaling Effector Antagonism. *Cell Rep*, *31*(1), 107487.

   Patrick Müller and Gary H. Soh initiated and planned the study and analysed the results together. Gary H. Soh wrote the manuscript, which was revised with the help of Patrick Müller. Gary H. Soh performed most of the experiments. I characterised the fluorescent constructs by scoring phenotypes and by Western blot. This published work is cited in this dissertation. The published manuscript was also included in Gary H. Soh's dissertation that was submitted to the Biochemistry department of the Faculty of Science at the University of Tübingen in 2020.

3. Knabl, P., Schauer, A., **Pomreinke, A. P.**, Zimmermann, B., Rogers, K. W., Müller, P., & Genikhovich, G. (2022). Analysis of SMAD1/5 target genes in a sea anemone reveals ZSWIM4-6 as a novel BMP signaling modulator. *bioRxiv*, 2022.2006.2003.494682.

   Grigory Genikhovich conceived the study. Paul Knabl, Alexandra Schauer, and Grigory Genikhovich performed the *Nematostella* experiments,

analysed the data, and wrote the paper. Patrick Müller and I planned the zebrafish experiments. Maximum likelihood phylogeny results were included with permission from Grigory Genikhovich. Katherine W. Rogers generated and analysed the data shown in Figure 7 (see Appendix C). All authors edited the paper. Specifically, I designed the primers and the protocol for cloning zebrafish *zswim5*. I performed the initial characterisation of *zswim5* overexpression phenotypes. This pre-print in bioRxiv is included and cited accordingly in Chapter 2 of this dissertation, and some of the *Nematostella* results of the manuscript were included in Alexandra Schauer's Master's Thesis for the 'Genetik und Entwicklungsbiologie' program of the University of Vienna in 2016.

Main Introduction

A fundamental question in developmental biology is how a single fertilized cell develops into a complex animal (Gilbert & Barresi, 2016; Rogers & Schier, 2011). A zygote goes through successive divisions and specifications to produce various cell types. These cells then form specialized tissues and organs all arranged in a consistent order along the body axis. Despite an animal's complexity, somatic cells hold the same genetic blueprint (Gilbert & Barresi, 2016). This was observed in Hans Driesch's recombination experiment in which the nuclei of a sea urchin embryo were reshuffled into different cells, and the cells still developed into a properly patterned sea urchin (Gilbert, 2003). Driesch concluded that the embryo acts as a 'harmonious equipotential system' in which… 'every cell, during development, carries the totality of all primordia' (Gilbert, 2003). It is then puzzling that these equipotent cells 'know' which developmental landscape to take and how to assemble into an animal. From a concerted effort by many generations of developmental biologists, it is clear that one key aspect that drives development is cell signalling.

Signalling pathways orchestrate several processes during embryonic development (Briscoe & Small, 2015; Gilbert, 2003). Drawing from the studies of many model organisms, from fruit flies to mice, cell signalling controls cell movement, cell division, and cell fate specification for assembling and synchronizing cells into one complex animal. This is accomplished by cells sending and receiving information via several signalling pathways that drive a sequence of changes in gene expression within each cell (Gorfinkiel & Martinez Arias, 2021). The changes in gene expression can be regulated at different levels: gene transcription, RNA processing, RNA translation, and protein post-translational modification (Gilbert & Barresi, 2016). Therefore, genes can be turned on or off, and proteins can be kept in an inactive or active state at different stages of development.

> *'Notably, even though universal organizational principles can be identified through comparative embryology, these principles coexist with particular solutions specific to each organism'* (Valet et al., 2022).

Despite the diversity in animal morphologies and different embryonic processes, the ancestral signalling pathways regulating embryogenesis are conserved and reiterated throughout development across the animal kingdom (Bier & De

Robertis, 2015; Gilbert & Barresi, 2016). It is then puzzling how a conserved set of molecular players can orchestrate embryogenesis and fine-tune cell transcriptional trajectories in a species-specific manner. Therefore, the focus of my dissertation is to delineate the molecular mechanisms underlying the signalling pathways specifically during zebrafish embryonic development. The following is a brief overview of the zebrafish embryo as the biological system and snapshots of the zebrafish embryo anatomy in the first 24 hours post-fertilization (hpf) that are assessed in this dissertation.

Zebrafish as a model organism for vertebrate embryogenesis

Prior to the zebrafish, a systematic screen for zygotically functioning genes for vertebrate embryogenesis has not been possible due to the 'difficulty of analysing and maintaining sufficiently large numbers of mutagenized animals' (Mullins et al., 1994). Owing to its high fecundity, easy manipulation of its embryos, and the fact that 70% of human genes have zebrafish orthologues (Howe et al., 2013), the zebrafish has become a prominent model organism for vertebrate development and human genetic diseases (Howe et al., 2013; Mullins et al., 1994; Parichy, 2015). It goes without saying that the success of large genetic screens using zebrafish to identify genes involved in early development has put the spotlight on the zebrafish (Parichy, 2015; Zebrafish Issue, 1996).

Above all, the zebrafish embryos are well suited for easy manipulation. The embryos are large and are fertilized externally, allowing for observations of developing organs such as the brain, notochord, and heart, to name a few (Haffter & Nusslein-Volhard, 1996; Mullins et al., 1994). Due to the embryo's inherent optical transparency and rapid development, time-lapse imaging of embryogenesis with light microscopy is possible in a relatively short amount of time (Keller et al., 2008; Mullins et al., 1994).

From one-cell stage to a fully patterned organism, critical embryonic stages can be readily observed in zebrafish embryos all within 24 hpf (Figure I. 1) (Karlstrom & Kane, 1996; Kimmel et al., 1995). Initially, a fertilized zygote rapidly divides to form a field of cells called a blastula. Then during gastrulation, the overall body plan of an organism is laid out. At this stage, the developing embryo is divided into a coordinate system of cranial (anterior) to caudal (posterior) and stomach (ventral) to back (dorsal). Cells are also organised into germ layers: endoderm (gut and blood), mesoderm

(blood, muscles, and bones), and ectoderm (brain and skin). During the segmentation stage, the dorsal-ventral and anterior-posterior axes become evident (Kimmel et al., 1995). Organs such as eyes and tail bud appear. Mesodermal tissue form somites sequentially, which are the precursor to muscles and vertebra. The lateral plate mesoderm along the yolk gives rise to presumptive cardiovascular cells. As the body plan comes into form, organogenesis begins, and cells become further specified. By 1-day post fertilization (dpf), the zebrafish has an elongated body axis with cranial structures, heart cavity, ventral and dorsal tail fins, and circulating blood cells.

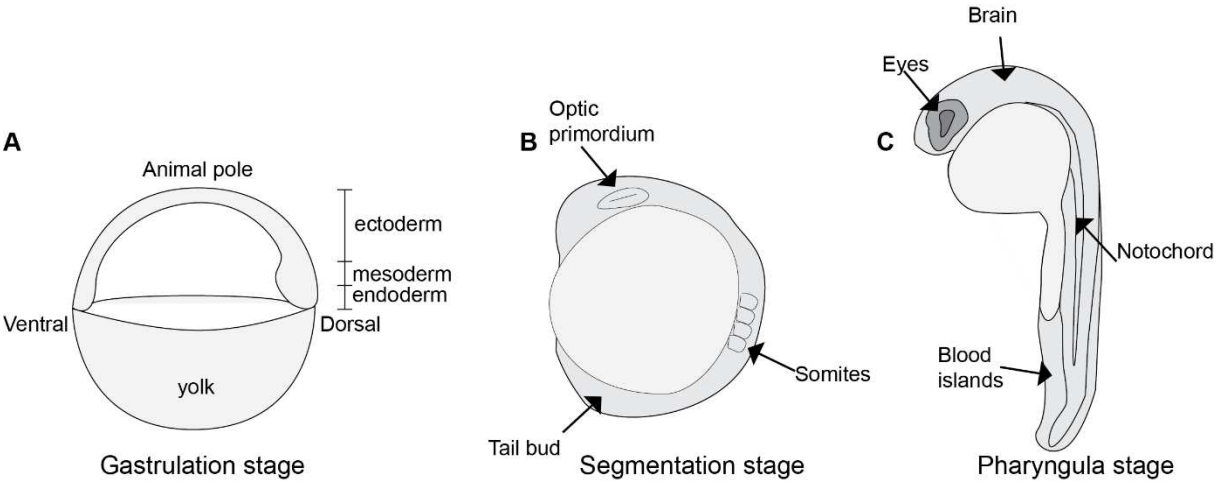

Figure I. 1 Anatomy of the zebrafish embryo.
A) During gastrulation, the zebrafish coordinate system consists of an animal-vegetal axis subdivided into the three germ layers and the dorsal-ventral axis. **B)** During the segmentation stage, rudimentary organs become evident. **C)** By the pharyngula stage at 1 dpf, the zebrafish lengthens, and a patterned body plan is evident.

Aims

Since embryogenesis consists of several tightly regulated processes – from fertilization to axis formation to organ formation, my approach is to deconstruct embryonic development into discrete developmental processes and investigate how two associated ancestral signalling pathways precisely control each process in the zebrafish. Therefore, there are three chapters in this thesis, and within each, I provide an overview of the fundamental concepts behind the specific developmental processes and then dive into the specific details of the associated signalling mechanisms.

First, the process of axis formation: How are cells instructed to follow a coordinate system such as the anterior to posterior and the ventral to dorsal axes (Gilbert & Barresi, 2016)? In particular, in Chapter 1, I focus on how the dorsal-ventral

axis is patterned under the control of the Bone Morphogenetic Protein (BMP) pathway. In Chapter 2, I took an evolutionary developmental approach in which I determine the role of a previously uncharacterised protein, Zswim5, as a potential intracellular modulator of the BMP signalling in zebrafish dorsal-ventral patterning.

Second, the process of differentiation: How do genetically equivalent cells become specialized to different types of cells (Gilbert & Barresi, 2016)? For example, humans, fish, and mice have muscle, blood, and neural cells that serve different functions such as movement, oxygen regulation, and physiological control. These functions are all vital for the viability of the organism. In Chapter 3, I focus on organogenesis, specifically, on how blood specification may depend on the NAD salvage pathway as an additional layer of gene regulation.

To address these questions, I combine gain-of-function and loss-of-function assays with cutting-edge tools such as CRISPR/Cas9 and *in toto* imaging with light sheet microscopy using zebrafish embryos. The findings in this dissertation have implications for improving our understanding of the molecular mechanisms orchestrating zebrafish embryogenesis, which consequently serves as a model system for understanding animal development.

Chapter 1 – An extracellular network shapes the BMP signalling gradient

In this chapter, the main aim is to understand the mechanisms underlying dorsal-ventral patterning during early zebrafish embryogenesis by investigating the BMP signalling gradient dynamics. This is accomplished by directly testing five mathematical models describing how the BMP signalling gradient may be established by a network of extracellular molecules. First, I will introduce the concepts of morphogen gradients for pattern formation and the BMP signalling pathway. Then I will present how we determined that (1) a graded source-sink mechanism with diffusible activator and inhibitor underlies the BMP-Chordin system to generate a steep BMP signalling gradient, (2) the gradient is further refined by Sizzled and Tolloid, and (3) Anti-dorsalizing morphogenetic protein (ADMP) is dispensable for dorsal-ventral patterning.

Introduction

The development of anatomical structures along the dorsal-ventral axis is achieved by a process called dorsal-ventral patterning (Anderson et al., 1992) (Figure 1.1). Dorsal-ventral patterning is a reproducible scale-invariant process. That is, individual animals belonging to the same species share the same body plans, albeit variations in body size (Bier & De Robertis, 2015; Inomata et al., 2013). This adaptive property of dorsal-ventral patterning is further demonstrated by the capacity of embryos from some species to regenerate and maintain wild-type proportions along the dorsal-ventral axis after experimental perturbations. For example, Spemann (1918) observed that when the ventral side of newt embryos is surgically removed, the dorsal half containing a blastopore lip can regenerate into a smaller but correctly proportioned embryo. Similarly, bisecting *Xenopus* embryos into two halves containing dorsal and ventral tissues produces two smaller correctly proportioned embryos (Inomata et al., 2013; Moriyama & De Robertis, 2018). Furthermore, Shih and Fraser (1996) observed that by transplanting the dorsal organizer of a donor zebrafish embryo to the ventral side of a host zebrafish embryo, a secondary axis develops, thus creating zebrafish Siamese twins. Together, these observations demonstrate the plasticity of dorsal-ventral patterning across species and are indicative of an adaptive mechanism. There are currently different models of how an extracellular network of molecules may

regulate dorsal-ventral patterning. Here, I focus on investigating which of the prominent mathematical models best fits the dynamics of the BMP signalling pathway during zebrafish embryonic development. The following is a brief overview of the concepts of pattern formation and then a brief review of BMP signalling during dorsal-ventral patterning in prominent model organisms.

Morphogen gradients during pattern formation

The question of morphological organization belongs to the concept of pattern formation. It stems from early observations that some animals have a stereotypical arrangement of their anatomical structures; for example, the organs are arranged in the coordinate system of anterior to posterior and ventral to dorsal axes. This spatial array of prospective organs can be fate-mapped to specific regions of a developing embryo (Figure 1.1). For example, zebrafish head and neural tissue arise from the animal and dorsal poles, while the blood and somites are arranged along the margin with blood arising from the ventral-most regions. So, then, what are the mechanisms involved in patterning embryonic cells?

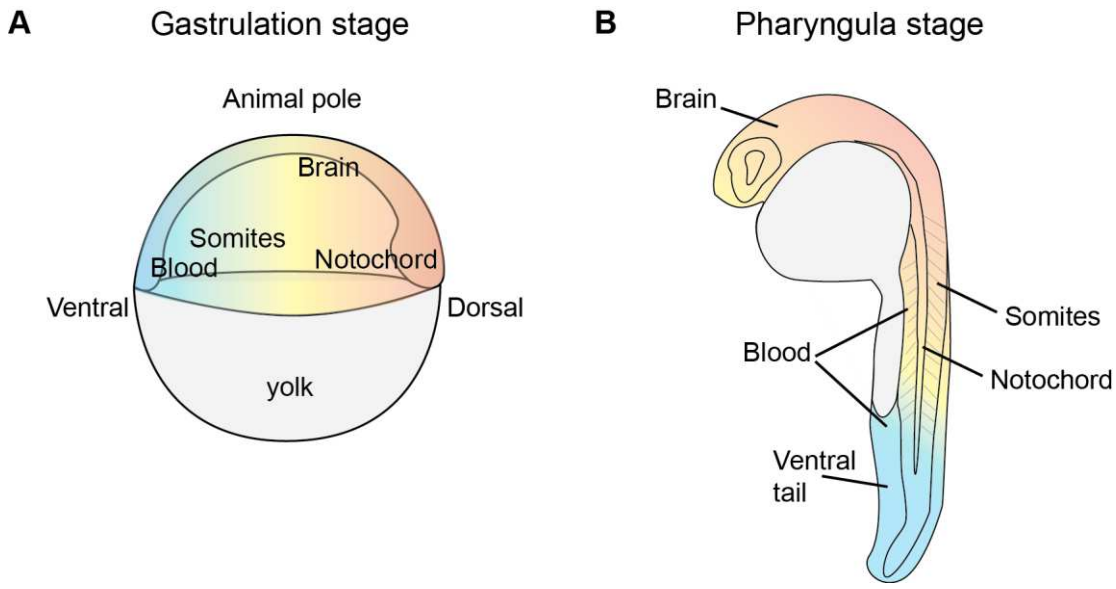

Figure 1.1 Prospective organs fate-mapped onto zebrafish embryo.
A) The animal-to-dorsal and ventral-lateral regions of a zebrafish gastrula develop into **B)** neural tissue (brain) and blood and somites, respectively, during the pharyngula stage.

Several theories were proposed regarding the chemical and biophysical basis of morphogenesis. One of which is the concept of gradients as the mechanism underlying tissue patterning (Figure 1.2) (Briscoe & Small, 2015). First, Thomas Hunt

Morgan (1898, 1904) observed that when both anterior and posterior regions of flatworms are removed, the remaining segment of the trunk can regenerate both head and tail regions (Gilbert & Barresi, 2016). Morgan proposed that there must be anterior- and/or posterior-producing materials that form a gradient to establish polarity in an organism (Figure 1.2, discussed below). Furthermore, it was thought that along this gradient, there are specific thresholds with defined concentration ranges to specify discrete regions of cell fates (Dalcq, 1938; Rogers & Schier, 2011; Sander, 1960). Specifically, differential gene activation may occur along the gradient (Rogers & Schier, 2011; von Ubisch, 1953). Then Alan Turing (1952) proposed that 'a system of chemical substances…reacting together and diffusing through a tissue' can account for morphogenesis. Turing coined the term 'morphogens' meaning form producer as the substances that could move by laws of diffusion, from high to low concentration.

Another theoretician, Lewis Wolpert, tackled the question of scale-invariance in tissue proportion; for example, the proportion of the endoderm and the ectoderm in a sea urchin embryo is constant, irrespective of the absolute size of the embryo (Wolpert, 1969). He referred to it as the French Flag problem. That is, tissue patterning resembles flags because, irrespective of the size of the flag, the proportion of blue, white, and red stripes is maintained (Wolpert, 1968, 1969) (Figure 1.2). Here, the colours represent developmental fate regions across a field of cells. Wolpert proposed the concept of positional information where the cells' location in the embryo determines their molecular differentiation. The cells interpret the positional information within a field; such that, some cells would interpret the information to either become blue, white, or red (Figure 1.2). Additionally, he posed the concept of pattern regulation in which the system can regenerate in a scale-invariant manner in that the distinct tissues are restored, and their relative sizes remain constant (Sharpe, 2019). Hence, Wolpert (1969) proposed that a mechanism to address the French Flag problem involves three basic elements (Figure 1.2): 1) mechanism for specifying polarity as reference points, 2) mechanism for differential response of the cells, such as thresholds, 3) at least one spontaneous self-limiting reaction.

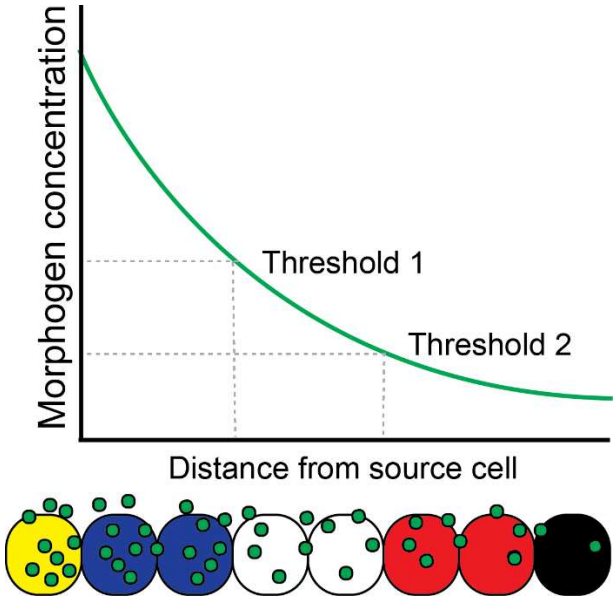

Figure 1.2 The gradient-based model for positional information established by a source-sink model mechanism.
To specify cells within a field, a source cell (yellow) produces a morphogen (green) that diffuses towards a 'sink' cell (black), where the morphogen is degraded. This establishes a morphogen gradient (green line) from high to low concentration. Certain ranges within the gradient make up a threshold such that the cells can then interpret the morphogen concentration at their respective position to differentiate into specific tissues type (blue, white, or red). Based on Rogers and Schier (2011).

There were several proposed mechanisms of how polarity and positional information are specified at the time (Wolpert, 1969). To name a few, one is the source-sink model (Figure 1.2) in which the substance (green) could be produced at one end (yellow) and be destroyed at the other end (black), so in these cells, the concentration of a substance is fixed to a specified value (green line) (Rogers & Schier, 2011; Stumpf, 1966; Wolpert, 1968, 1969). Therefore, the absolute value of the substance along the gradient would designate a cell's position in a system. Another mechanism proposed was 'the possibility of active transport in a direction opposite to that of the gradient's' (Lawrence, 1966; Wolpert, 1969). Morphogens could be pumped in one direction to establish a graded distribution (Gierer & Meinhardt, 1972; Lawrence, 1966). Additional mechanisms proposed specifically for dorsal-ventral patterning will be introduced below. However, since the genetic basis of pattern formation during animal embryogenesis remained unknown at the time (Wieschaus & Nusslein-Volhard, 2016; Wolpert, 1969), the models predicting how gradients form could not be tested.

Eventually, systematic screens on *Drosophila melanogaster* (fruit fly) (Anderson & Nusslein-Volhard, 1984; Nusslein-Volhard & Wieschaus, 1980) and subsequently on *Danio rerio* (zebrafish) (Mullins et al., 1994; Zebrafish Issue, 1996) led to the

identification of genes that act as graded signals for the spatial patterning of embryos. The earliest identified morphogens are maternally-deposited transcription factors that define the spatial coordinates of developing *Drosophila* embryos (Driever & Nusslein-Volhard, 1988; Nusslein-Volhard & Wieschaus, 1980). One of them is Dorsal, which is translocated to the nuclei in a gradient along the dorsal-ventral axis (Anderson & Nusslein-Volhard, 1984; Gilbert, 2000; Nusslein-Volhard & Wieschaus, 1980; Roth et al., 1989; Steward et al., 1988). The other is Bicoid, which diffuses in the *Drosophila* syncytium for patterning the anterior-posterior axis (Driever & Nusslein-Volhard, 1988). Both Bicoid and Dorsal are maternally-deposited RNAs that function as DNA-binding transcription factors and may not be representative of patterning across cellularized tissues (Nellen et al., 1996).

Further work was done to identify genes that can function across fields of cells to pattern developing embryos (Nusslein-Volhard, 2022; Wieschaus & Nusslein-Volhard, 2016). Together, studies from *Drosophila*, *Xenopus*, mouse, and zebrafish demonstrate that embryogenesis is mediated by extracellular signalling factors belonging to families such as Hedgehog, Fibroblast Growth Factor (FGF), Wnt, and the TGF-β superfamily (Bone Morphogenetic Proteins (BMP), Activin, Nodal) (Ferguson & Anderson, 1991; Irish & Gelbart, 1987; Niehrs, 2010; Nusslein-Volhard & Wieschaus, 1980; Schier & Shen, 2000; Schier & Talbot, 2005).

It is now well understood that these families of signalling pathways are involved in different processes during development across species (Bier & De Robertis, 2015; Genikhovich & Technau, 2017). For example, the Hedgehog pathway plays a role in the development of appendages in flies and mice and also functions in neuronal fate specification and axonal guidance (Lee et al., 2016). Another example is *Drosophila* BMP homologue, Decapentaplegic (Dpp), which functions to pattern the dorsal-ventral axis during early embryonic development and wing imaginal disc development in later stages (Irish & Gelbart, 1987). Additionally, BMP homologues are found to play a role in axis formation in fish, mice, *Xenopus*, and sea anemones, to name a few (Bier & De Robertis, 2015). Similar to the Hedgehog pathway, a BMP signalling gradient is also essential for neural tube patterning (Dutko & Mullins, 2011). Overall, the identification of these molecular players paved the way to finally dissect the mechanism underlying pattern formation.

BMP signalling during dorsal-ventral patterning

It is now well understood that the dorsal-ventral patterning of several model organisms is influenced by an ancestral signalling system called the BMP pathway (Figure 1.3) (Bier & De Robertis, 2015; Little & Mullins, 2006). A graded BMP signalling provides the spatiotemporal cues to pattern pluripotent embryonic cells. While the constituents of the BMP signalling network are found to be conserved among different species, the species-specific function of these components and their integrated function to shape the BMP signalling gradient are not well understood (Ben-Zvi et al., 2008; Bier & De Robertis, 2015). The following is a brief introduction to the BMP signalling gradient formation during dorsal-ventral patterning, with an emphasis on the zebrafish.

As previously mentioned, BMPs are part of the TGF-β family (Bier & De Robertis, 2015). BMP ligands consist of a prodomain and a mature domain. BMPs assemble into dimers in which the prodomain is cleaved off by Furin-type proteinases in the Golgi and by metalloproteinases in the extracellular space, thus releasing the mature domains as active ligands (Constam, 2014; Dutko & Mullins, 2011). Then these dimers bind to serine/threonine kinase receptors (Figure 1.3A) (Dutko & Mullins, 2011; Kondo, 2007). First, the BMP ligands bind to BMP type II receptors that then recruit and phosphorylate BMP type I receptors. The latter phosphorylate transcription effectors Smad1/5/9 (pSmad1/5/9). Two pSmad1/5/9 and one Smad4 form a heterotrimer, and then, this trimeric complex translocates to the nucleus to regulate BMP target genes by recruiting co-activators and co-repressors to mediate BMP signalling (Affolter et al., 2001; Dutko & Mullins, 2011).

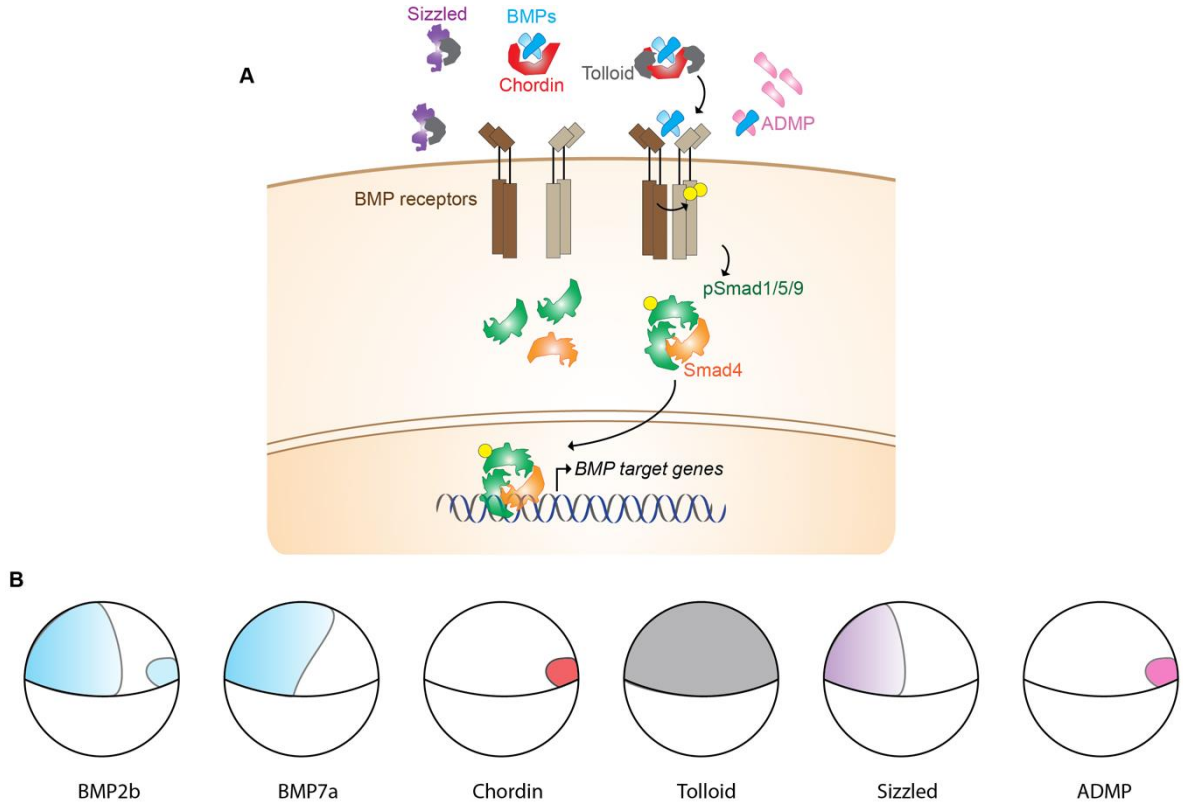

Figure 1.3 The components of the BMP signalling pathway and their respective expression domain in zebrafish embryos at shield stage.
A) A molecular regulatory network may determine the distribution of BMP ligands (blue) in the extracellular space. Chordin (red) acts as a BMP inhibitor and is cleaved by Tolloid metalloproteinases (grey) to release BMP ligands. Sizzled (purple) acts as a BMP negative feedback regulator by binding to Tolloid. BMP signalling is transduced intracellularly by the binding of BMP ligands to the BMP receptors (brown), which subsequently leads to phosphorylation of Smad1/5/9 (green). These form a heterotrimer including Smad4. The heterotrimer complex translocates to the nucleus and regulates BMP target genes. Anti-dorsalizing morphogenetic protein (ADMP) (pink) is a BMP homologue expressed in the zebrafish dorsal organizer and can modulate BMP signalling activity. **B)** Compilation of the expression domain of the constituents in (A) during zebrafish mid-gastrulation along the dorsal-ventral axis as a reference for the following subsections.

There are several lines of evidence that the BMP signalling gradient underlies dorsal-ventral patterning. First, BMP can elicit different genetic programs in a concentration-dependent manner – a conserved function in invertebrates and vertebrates (Holley & Ferguson, 1997). Injection of increasing amounts of *dpp* RNA, a *Drosophila* BMP homologue, induces progressively stronger dorsal phenotypes such as dorsal epidermis and amnioserosa, a structure required for dorsal closure in the larva, and this is complemented by the loss of ventrally-derived tissues (Ferguson & Anderson, 1992a; Scuderi & Letsou, 2005). Similarly, except with an inversion of the dorsal-ventral axis in vertebrates with respect to arthropods during evolution (De

Robertis & Sasai, 1996; Meinhardt, 2015), strong BMP signalling leads to ventral fates, and loss of BMP signalling leads to expansion of dorsal fates in vertebrates such as *Xenopus* and zebrafish (Dale et al., 1992; Hemmati-Brivanlou & Thomsen, 1995; Kishimoto et al., 1997). *Xenopus* and zebrafish embryos overexpressing either *Xenopus bmp4* or zebrafish *bmp2b* have expanded ventrally-derived tissues such as blood and have diminished dorsally-derived tissues such as the notochord (Dale et al., 1992; Kishimoto et al., 1997).

Second, a graded BMP signalling is detected in developing embryos, which is indicative of the polarity along an initially homogeneous tissue (Bier & De Robertis, 2015; Little & Mullins, 2006; Meinhardt, 2015; Ramel & Hill, 2012; Tucker et al., 2008). Phosphorylation of transcription effector Smad1/5/9, or Mad in *Drosophila*, a read-out of BMP signalling, is graded along the dorsal-ventral axis in *Drosophila*, *Xenopus*, and zebrafish. This signalling gradient can turn on distinct genetic programs to specify cells that then develop into tissues and organs in a specified order along the dorsal-ventral axis of the embryo.

Finally, to pattern across the embryonic field, BMP can act at a distance away from the BMP source. Clones expressing *dpp* in *Drosophila* wings induced expression of target genes that respond to different concentrations of Dpp at different distances from the clones (Nellen et al., 1996). This further supports BMP activation of different genetic programs in a concentration-dependent manner across tissues. Similarly, transplantation of *bmp2b*-expressing clones into host zebrafish showed that BMP activity is detected outside its source, thus zebrafish BMP ligands are expected to diffuse from its source forming a gradient (Xu et al., 2014). Note, however, not all BMP homologues are thought to diffuse away from their source. For example, *Xenopus* BMP4 induced expression of target genes ‘within the immediate environment of its synthesis’ (Jones et al., 1996).

Intriguingly, BMP signalling begins as a shallow gradient in vertebrates and invertebrates (Hemmati-Brivanlou & Thomsen, 1995; Kishimoto et al., 1997; Little & Mullins, 2006; Meinhardt & Roth, 2002). Hence, one of the essential factors shaping the BMP signalling gradient are the regulatory molecules in the extracellular space (Figure 1.3) (Bier, 2008; Rogers & Müller, 2019; Zinski et al., 2018). One prominent BMP regulator is the BMP antagonist, Chordin (Figure 1.3A). Chordin directly and specifically binds to BMP to block the ligands binding to receptors (Figure 1.3A) (Francois & Bier, 1995; Mullins, 1998; Piccolo et al., 1996; Schulte-Merker et al., 1997).

In contrast to the BMP gain-of-function effect, Chordin overexpression leads to dorsalization in *Xenopus* and zebrafish (Francois & Bier, 1995; Sasai et al., 1994; Schulte-Merker et al., 1997) and ventralization in *Drosophila* (Ferguson & Anderson, 1992b).

In prominent invertebrate model organisms, Chordin may also act as an agonist by mobilizing BMP ligands in the extracellular space and generating a signalling peak (Eldar et al., 2002; Meinhardt & Roth, 2002). First, in starlet sea anemone, *Nematostella vectensis*, the knockdown of Chordin leads to a loss of BMP signalling instead of an increase in BMP activity, supporting Chordin's function in generating and maintaining the BMP signalling gradient (Genikhovich et al., 2015). Second, in wild-type *Drosophila* embryos, there is high Dpp activity dorsally and low Dpp activity ventrally. However, in homozygous *sog*/*chordin* mutant embryos, the strong Dpp activity in the dorsal region is decreased, and surprisingly, the weak Dpp activity in the ventral region is increased (Ferguson & Anderson, 1991). This is supported by observations that in *sog* mutants, the pMad domain (the *Drosophila* pSmad1/5/9 homologue) was expanded in the dorsal region in contrast to the typical narrow stripe in the dorsal side of wild-type embryos (Eldar et al., 2002). Overall, in addition to inhibiting BMP ligands, Chordin facilitates the distribution of BMP ligands to shape the BMP signalling gradient for dorsal-ventral patterning in *Drosophila* and *Nematostella* (Eldar et al., 2002; Genikhovich et al., 2015; Leclere & Rentzsch, 2014). Then the next question was: is this two-component system sufficient to regulate dorsal-ventral patterning or do other components play essential roles in shaping the BMP signalling gradient (Eldar et al., 2002)?

Mathematical modelling and experimental evidence have revealed that a molecular network of proteins is essential for Dpp transport in *Drosophila* (Eldar et al., 2002; Ross et al., 2001; Shimmi & O'Connor, 2003). Dpp ligands are poorly diffusible; however, when Dpp ligands are coupled with Sog, they form a highly diffusible complex. In addition, the inhibition of Dpp by Sog is further enhanced by Twisted gastrulation (Tsg). In the absence of Tsg, pMad is detected only in cells overexpressing *dpp* and not in neighbouring cells. Furthermore, the Dpp-Sog complex is cleaved by metalloproteinase Tolloid (Figure 1.3A) to release Dpp from Sog to create a pool of Dpp at the dorsal-most region. This molecular network regulates Dpp distribution to create a sharp boundary of the BMP signalling (Shimmi & O'Connor, 2003). It is also

thought to provide robustness in BMP-mediated dorsal-ventral patterning by buffering against gene expression fluctuations and environmental perturbations (Eldar et al., 2002; Meinhardt & Roth, 2002).

Similarly, in vertebrate models, such as the zebrafish, the initially shallow BMP gradient peaks at and becomes restricted to the ventral side (Figure 1.4A) (Little & Mullins, 2006; Ramel & Hill, 2013; Tucker et al., 2008; Xue et al., 2014). However, there is some experimental evidence suggesting divergent functions of Chordin and Tolloid in vertebrates. For example, injection of *Drosophila sog* (Schmidt et al., 1995) and *Xenopus chordin* (Sasai et al., 1994) in the ventral side of *Xenopus* embryos can induce an ectopic axis. However, Decotto and Ferguson (2001) showed that when *Xenopus chordin* is injected into *Drosophila* embryos, Chordin blocks BMP signalling similar to Sog; however, *Xenopus* Chordin does not have the same capacity to elevate BMP signalling as Sog. Additionally, *Drosophila tolloid* is expressed only on the dorsal side, while zebrafish *tolloid* is uniformly expressed (Figure 1.3B) (Connors et al., 1999). Therefore, it is not fully elucidated how Chordin and other accessory proteins integrate functionally to generate a BMP signalling gradient and how the system can adapt and regulate the BMP signalling gradient to achieve a reproducible dorsal-ventral patterning in vertebrates. Currently, there are several prominent models with varying biophysical assumptions that describe how the BMP signalling gradient is established (Figure 1.4 B-F) (Ben-Zvi et al., 2008; Francois et al., 2009; Pomreinke et al., 2017; Ramel & Hill, 2013; Zinski et al., 2017). To analyse BMP signalling dynamics specifically in the zebrafish (Figure 1.4A), we compiled and tested these five prominent models. Their accompanying mathematical formulations are available in Pomreinke et al. (2017), Appendix A. For this dissertation, I adapted these models and made additional predictions qualitatively based on the descriptions for each model in the respective reports. These are described below (Figure 1.4B-F) and summarised in Table 1.1.

Table 1.1 Summary of model assumptions and predictions compared to experimental findings.
This is an extended version of the model assumption or prediction compared to experimental results table published in Pomreinke et al. (2017). Model assumptions and predictions that are consistent with the experimental findings are highlighted in green. Some findings are already published in Pomreinke et al. (2017)(*), while other findings are presented in this dissertation (**). NA: Not applicable, no model assumption or prediction to be tested.

Table 1.1 (Continued).

	Model 1: Graded source-sink (immobile BMP)	Model 2: Graded source-sink (mobile BMP)	Model 3: Shuttling	Model 4: Self-regulating reaction-diffusion system	Model 5: Long-range accumulation and feedback	Experimental findings
pSmad gradient formation kinetics	Progressive rise ventrally, always low dorsally	Progressive rise ventrally, always low dorsally	Progressive rise ventrally, always low dorsally	Progressive rise ventrally, always low dorsally	Initially high dorsally and ventrally	Progressive rise ventrally, always low dorsally*
Ventral pSmad peak decreased in *chordin*$^{-/-}$?	No	No	Yes	No	No	No*
pSmad expanded dorsolaterally in *chordin*$^{-/-}$?	Yes	Yes	Yes	No	No	Yes*
Ventral pSmad peak decreased in *tolloid*$^{-/-}$?	NA	NA	Yes	NA	Yes	Yes**
Ventral pSmad peak decreased in *sizzled*$^{-/-}$?	NA	NA	NA	No	No	No**
pSmad expanded dorsolaterally in *sizzled*$^{-/-}$?	NA	NA	NA	No	Yes	Yes, but minimally**
Free diffusion of BMP and Chordin	NA	NA	NA	NA	NA	D_f(BMP) ≤ D_f(Chd) (≈ 46 & 59 μm²/s)*
Effective diffusion of BMP and Chordin	D(BMP) ≈ 0 D(Chd) = high	D(BMP) > 0 D(BMP) < D(Chd)	D(BMP) << D(Chd)	D(BMP) ≈ D(Chd) Both low	D(BMP) ≈ D(Chd) Both high	D(BMP) ≤ D(Chd) (≈ 2 & 6 μm²/s)*
Half-life of BMP and Chordin	Unconstrained	τ(BMP) ≈ τ(Chd)	τ(BMP) > τ(Chd)	τ(BMP) ≈ τ(Chd)	τ(BMP) >> τ(Chd)	τ(BMP) ≈ τ(Chd) (130 & 120 min)*
Effect of Chordin on BMP diffusivity	No effect	No effect	Chordin increases BMP diffusion	No effect	No effect	No effect*
Diffusivity of Sizzled relative to BMP/Chordin	NA	NA	NA	D(ADMP) & D(Szl) >> D(BMP) & D(Chd)	D(ADMP) & D(Szl) ≈ D(BMP) & D(Chd)	D(Szl) ≈ D(BMP) & D(Chd) (≈ 10, 2, & 6 μm²/s)*

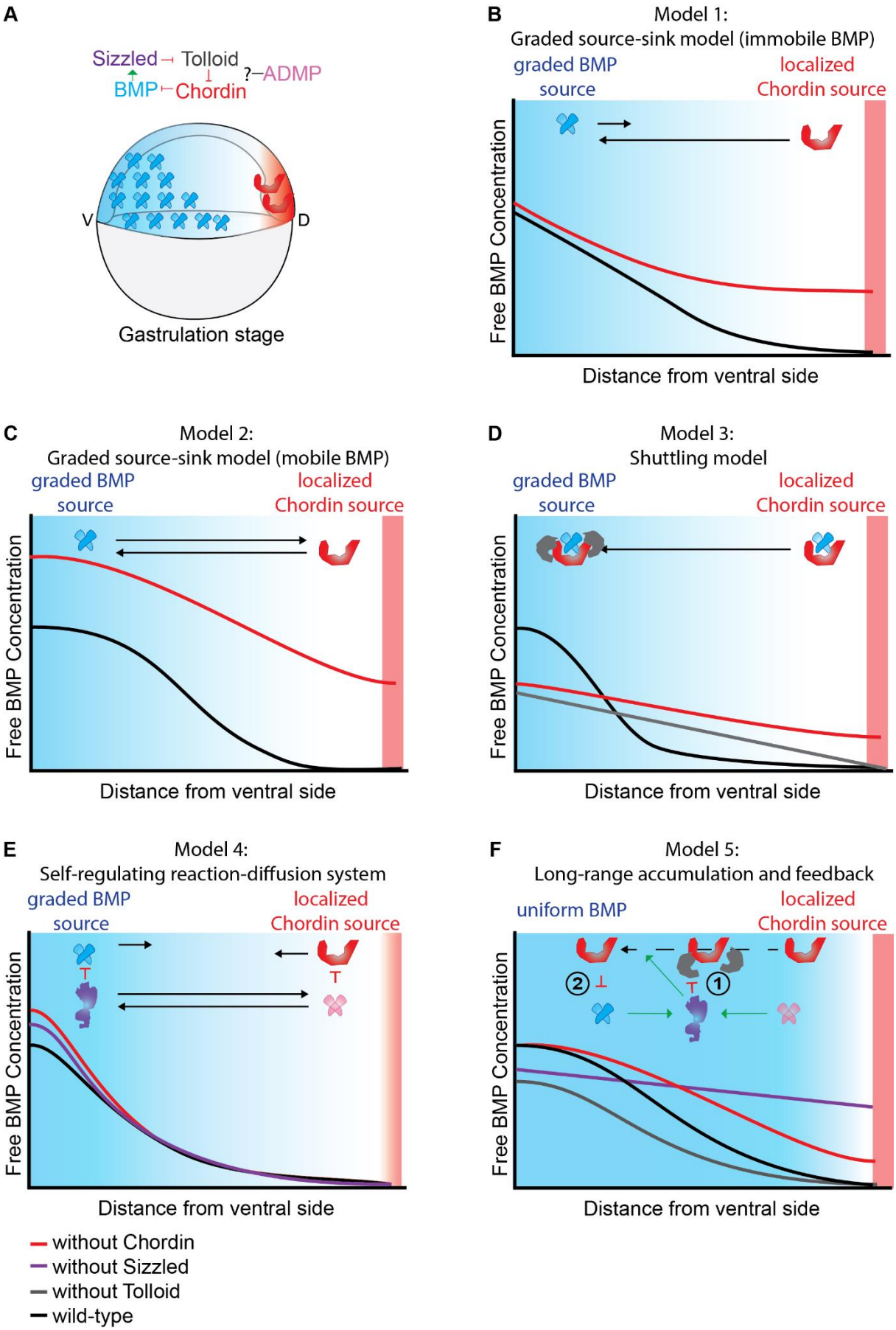
A
Sizzled
Tolloid
?
ADMP
BMP
Chordin
V
D
Gastrulation stage
B
Model 1:
Graded source-sink model (immobile BMP)
graded BMP source
localized Chordin source
Free BMP Concentration
Distance from ventral side
C
Model 2:
Graded source-sink model (mobile BMP)
graded BMP source
localized Chordin source
Free BMP Concentration
Distance from ventral side
D
Model 3:
Shuttling model
graded BMP source
localized Chordin source
Free BMP Concentration
Distance from ventral side
E
Model 4:
Self-regulating reaction-diffusion system
graded BMP source
localized Chordin source
Free BMP Concentration
Distance from ventral side
without Chordin
without Sizzled
without Tolloid
wild-type
F
Model 5:
Long-range accumulation and feedback
uniform BMP
localized Chordin source
Free BMP Concentration
Distance from ventral side

Figure 1.4 Theoretical predictions of the biophysical parameters of BMP, Chordin, Tolloid, Sizzled, and ADMP to regulate BMP ligand distribution.
A) Overview of the interplay between the components of the BMP signalling pathway in a zebrafish gastrula (V – ventral, D – dorsal). Chordin (red) acts to inhibit BMP ligands (blue). Tolloid (grey) inhibits Chordin. BMP signalling causes the expression of *sizzled* (purple) that blocks Tolloid. The contribution of ADMP (pink) is not well elucidated. **B-F)** Diagram of the mobility and the interaction of each molecule based on five mathematical models (Models 1-5) of the BMP-Chordin system, compiled in Pomreinke et al. (2017). BMP distribution is represented by the blue background on the left, and Chordin source is represented by the red bar on the right. The different slopes represent the predicted BMP signalling gradient in the presence of all components (black) and in the absence of individual components (Chordin (red), Tolloid (grey), Sizzled (purple)). **B)** The 'Graded source-sink with immobile BMP model', Model 1, assumes ventrally-localised BMP ligands minimally diffuse (short black arrow), and dorsally-localised Chordin readily diffuses (long black arrow) to the opposite pole (Ramel & Hill, 2013). **C)** The 'Graded source-sink with mobile BMP model', Model 2, assumes ventrally-localised BMP ligands and dorsally-localised Chordin readily diffuse to the opposite pole (long black arrow) (Pomreinke et al., 2017; Zinski et al., 2017). **D)** The 'Shuttling model', Model 3, assumes Chordin transports BMP ligands to the ventral side, and Tolloid cleaves Chordin to free BMP ligands (Ben-Zvi et al., 2008). **E)** The 'Self-regulating reaction-diffusion system model', Model 4, assumes a low diffusion rate (short black arrow) for BMP and Chordin with an initial ventral or dorsal bias in the system. The regulation of the BMP signalling gradient relies on highly diffusible molecules, Sizzled and ADMP, inhibiting BMP and Chordin, respectively (blunt red line) (Francois et al., 2009). **F)** The 'Long-range accumulation and feedback model', Model 5, assumes that (1) free BMP and ADMP ligands cause Sizzled upregulation, which then blocks Tolloid (blunt red line) to allow (green arrows) (2) Chordin expansion towards the ventral pole, which then blocks BMP ligands (Inomata et al., 2013). This model was developed to explain how uniform BMP signalling can become graded.

Five models of the BMP gradient formation mechanism in zebrafish embryos

Model 1

The transcriptional determination or 'Graded source-sink with immobile BMP model' (Figure 1.4B, Table 1.1) postulates that a BMP transcript gradient is central to generating a BMP signalling gradient instead of diffusion or facilitated transport of BMP ligands, and that BMP diffusion is negligible (Pomreinke et al., 2017; Ramel & Hill, 2013; Rogers & Müller, 2019). This model also postulates that Chordin acts as a diffusible sink, which is partially reminiscent of Wolpert's source-sink model described above. This is supported by *in situ* hybridization results that show a ventrally-biased *bmp* expression (Dick et al., 2000; Kishimoto et al., 1997; Ramel & Hill, 2013) and dorsally-localised *chordin* expression in zebrafish (Miller-Bertoglio et al., 1997) (Figure 1.3B).

However, it is important to consider the changes in BMP2b protein and mRNA domains at different developmental time points of the zebrafish. First, at 40% epiboly, BMP2b protein and mRNA are absent in the dorsal organizer of the zebrafish (Ramel & Hill, 2013; Xue et al., 2014), and that BMP2b protein, *bmp2b* mRNA, pSmad1/5/9, and expression of BMP responsive elements have overlapping domains (Ramel & Hill, 2013), thus supporting the hypothesis that BMP diffusion is negligible (Pomreinke et al., 2017; Ramel & Hill, 2013). Then, by shield stage and 60% epiboly, other reports have shown that BMP2b protein and *bmp2b* mRNA are present in the dorsal organizer (Kishimoto et al., 1997; Xue et al., 2014), and that BMP2b protein is detected outside the *bmp2b* expression domain (Xue et al., 2014). Indeed, specifically blocking dorsally-expressed BMP2b dorsalizes zebrafish embryos and causes a ventral expansion of *chordin* expression and a decrease in the expression of ventrally-expressed BMP target gene *eve1* (Xue et al., 2014). Therefore, ventral and dorsal expression of *bmp2b* are essential for dorsal-ventral patterning (Figure 1.3B), in which dorsally-expressed BMP2b may be mobilized towards the ventral-lateral region. One caveat is that the BMP2b protein gradient was assayed using an antibody raised against the prodomain of the zebrafish BMP2b (Ramel & Hill, 2013; Xue et al., 2014), which, therefore, may not account for the differential diffusivity of the BMP2b mature domain since, in *Xenopus*, differential post-translational cleavage of BMP4 alters the BMP4 signalling activity range (Cui et al., 2001). Conversely, a recombination assay using *Xenopus* embryos in which two animal caps are combined with one uninjected and the other injected with *bmp4* RNA demonstrated that BMP4 target genes were only detected within the injected animal cap; therefore, BMP4 may not diffuse in *Xenopus* (Jones et al., 1996).

Model 2

The ‘Graded source-sink with mobile BMP model’ (Figure 1.4C, Table 1.1) postulates that the BMP signalling gradient is the result of both BMP and Chordin diffusing from their respective sources in addition to an initial ventrally-biased graded *bmp* expression, as proposed by Model 1 (Pomreinke et al., 2017; Rogers & Müller, 2019; Zinski et al., 2017). This is inferred from experimental evidence in zebrafish in which *bmp*-expressing clone induces BMP target gene expression outside the clone, suggesting that BMP can diffuse from its source and can signal onto neighbouring cells (Xu et al., 2014). Additionally, in *Xenopus*, fluorescently-tagged BMP2 was detected

outside its local source using immunostaining (Plouhinec et al., 2013). BMP2b and Chordin are also found beyond their expression domains in zebrafish embryos (Xue et al., 2014). Furthermore, Model 2 postulates that the diffusible BMP ligands are bound by diffusible Chordin inhibitor as a graded 'sink' (Miller-Bertoglio et al., 1997; Plouhinec et al., 2013).

Note, however, that these first two models do not account for the presence of other BMP regulators and their role in the scale-invariant, reproducible property of dorsal-ventral patterning (Pomreinke et al., 2017), hence the question: Do additional extracellular BMP regulators play a role in BMP ligand distribution during dorsal-ventral patterning in zebrafish, similar to *Drosophila*? For example, zebrafish *sizzled* and *tolloid* mutants have tail defects (Connors et al., 1999; Hammerschmidt et al., 1996; Wagner & Mullins, 2002). Expression of BMP target genes such as blood-related gene *eve1* is expanded in *sizzled* mutants (Hammerschmidt et al., 1996) and reduced in *tolloid* mutants (Connors et al., 1999). Additionally, ADMP is another extracellular component that has been reported to play a central role in *Xenopus* embryo regeneration (Ben-Zvi et al., 2008). How do these molecules integrate into the BMP-Chordin system to regulate BMP signalling in zebrafish dorsal-ventral patterning? Therefore, the following are additional mathematical models to be considered (Ben-Zvi et al., 2008; Francois et al., 2009; Inomata et al., 2013).

Model 3

The 'Shuttling model' (Figure 1.4D, Table 1.1) postulates that Chordin acts not only as an inhibitor, but Chordin may also bind to and transport BMP ligands to generate a signalling gradient, similar to the BMP-Chordin system in *Drosophila* (Ben-Zvi et al., 2008; Pomreinke et al., 2017). In *Drosophila*, BMP ligands have low diffusivity and require a highly diffusible Chordin to 'shuttle' BMP to the dorsal side to reach maximum pMad levels (Eldar et al., 2002). In addition, a dorsally-expressed Tolloid metalloproteinase is the third component that cleaves Chordin to release BMP in the dorsal pole of *Drosophila* embryos (Figure 1.3) (Eldar et al., 2002; Meinhardt & Roth, 2002; Mullins, 1998). Therefore, this model also assumes BMP is more stable than Chordin.

Model 3 could also account for experimental observations in *Xenopus* and in zebrafish. One example is that the ectopic expression of Chordin in the ventral pole

leads to *sizzled* expression between the ventral and dorsal poles, instead of a ventrally-biased *sizzled* expression (Ben-Zvi et al., 2008). Additionally, injection of *chordin* mRNA into a ventrovegetal blastomere at 8-cell stage induced a secondary axis in *Xenopus* (Sasai et al., 1994). Moreover, transplantation of dorsal tissue of *Xenopus* embryos injected with *chordin*-morpholino did not induce the formation of a secondary axis on the ventral side (Oelgeschlager et al., 2003), which suggests that, without Chordin, BMP ligands are not transported laterally from the ventral side (Ben-Zvi et al., 2008). In that sense, since a secondary axis is also induced in the zebrafish upon transplantation of the dorsal organizer (Shih & Fraser, 1996) where *bmp2b* and chordin are expressed (Figure 1.3B) (Kishimoto et al., 1997; Miller-Bertoglio et al., 1997), and BMP2b proteins are found beyond *bmp2b* expression domain (Xue et al., 2014), it could be that a second BMP signalling gradient is generated by facilitated diffusion.

However, as previously mentioned, overexpression of *Xenopus chordin* could not generate a signalling peak at a distance from the injection site in *Drosophila* (Decotto & Ferguson, 2001), and *tolloid* is uniformly expressed in the zebrafish (Connors et al., 1999) in contrast to *Drosophila tolloid* (Ferguson & Anderson, 1992b). Furthermore, *Xenopus* Chordin has a higher affinity to shuttle ADMP, a dorsally-expressed BMP ligand in *Xenopus* and zebrafish (Figure 1.3B), which is absent in *Drosophila* (Ben-Zvi et al., 2008; Lele, Nowak, et al., 2001). These observations suggest divergent functions of Chordin and Tolloid in vertebrates. Therefore, the following models must be considered.

Model 4

The ‘Self-regulating reaction-diffusion system model’ (Figure 1.4E, Table 1.1) (Francois et al., 2009; Pomreinke et al., 2017) postulates that ordinary diffusion can account for the experimental observations on which the Shuttling model (Model 3) is based on. The Self-regulating reaction-diffusion system model postulates two self-organizing reaction-diffusion systems at opposing poles. The first system containing BMP is suppressed by the second system containing Chordin. Based on this model, a biological system requires an initial bias that generates a single ventral signalling peak. This is consistent with the biased expression of BMP and Chordin in their respective poles in *Xenopus* and in zebrafish (Bier & De Robertis, 2015; Holley & Ferguson, 1997). In addition, Model 4 assumes that these two molecules have equal protein stabilities – hence similar degradation rate – in contrast to the Shuttling model’s (Model

3) assumption of BMP being more stable than Chordin because Chordin is degraded by Tolloid to liberate BMP ligands. Moreover, Model 4 postulates that BMP and Chordin have low diffusivities and are instead coupled to highly diffusible molecules Sizzled and ADMP, respectively. In the zebrafish, *sizzled* is ventrally expressed and is part of the BMP system, while *admp* is dorsally expressed and is part of the Chordin system (Figure 1.3B, Figure 1.4E). ADMP and Sizzled are predicted to be 25x more diffusible than BMP and Chordin, thereby Sizzled diffuses to repress BMP activity, and ADMP diffuses to repress Chordin activity (Francois et al., 2009). This dual coupling system allows regulation of each system even with initially noisy conditions (Pomreinke et al., 2017). The role of ADMP in buffering against gene expression fluctuations for robust dorsal-ventral patterning is consistent with recent findings by Itoh et al. (2021). In contrast to Model 3, Model 4 assumes that Chordin's diffusion from ventral and dorsal poles without shuttling BMP ligands can generate two BMP signalling gradients for secondary axis formation in *Xenopus* (Francois et al., 2009).

Model 5

Finally, the 'Long-range accumulation and feedback model' postulates that BMP and Chordin are both equally diffusible, and that the difference in activator/inhibitor protein stability establishes a gradient (Figure 1.4F, Table 1.1) (Inomata et al., 2013; Pomreinke et al., 2017). The system relies on a feedback mechanism that dynamically regulates Chordin stability and, ultimately, its distribution. In the first part of the feedback mechanism, BMP ligands, including ADMP, activate BMP signalling, causing the production of Sizzled in the ventral-lateral domains (Figure 1.3B, Figure 1.4A, F). Then Sizzled competitively inhibits Tolloid from degrading Chordin (Figure 1.3A, Figure 1.4A), thus promoting Chordin diffusion and accumulation in the ventral side (Figure 1.4F). Consequently, the presence of Chordin on the ventral side will inhibit BMP signalling and reduce *sizzled* expression as the other part of the feedback loop. Hence, this model assumes BMP is more stable than Chordin. This model was proposed based on the assumption that surgically removing the ventral half of *Xenopus* embryos consequently removes the ventrally-located Sizzled source (Inomata et al., 2013). Without competitive inhibition by Sizzled from the ventral side, there is a feedback mechanism involving available Tolloid to degrade Chordin and release BMP ligands, so the BMP signalling gradient is re-established in the smaller regenerating embryos.

Overall, the Long-range accumulation and feedback model postulates an embryo-wide feedback mechanism to allow for scale-invariant dorsal-ventral patterning.

Overall, these five models have arisen from indirect observations of the BMP ligand distribution in different species (Ben-Zvi et al., 2008; Eldar et al., 2002; Francois et al., 2009; Inomata et al., 2013) and developmental contexts such as those inferred from: BMP protein domain assayed by an antibody that recognizes pre-processed BMP, changes in expression of BMP target genes, or changes in BMP responsive elements during zebrafish gastrulation (Ramel & Hill, 2013). Therefore, we aim to test the predictions of Models 1-5 by first determining how each extracellular molecular component contributes to shaping the BMP gradient in zebrafish embryos (Figure 1.4A) (Pomreinke et al., 2017). First, under the assumption that unbound BMP or free BMP ligand is correlated to the pSmad1/5/9 signalling (Francois et al., 2009; Pomreinke et al., 2017), we determined how BMP signalling is affected in the absence of either Chordin, Sizzled, or Tolloid by measuring pSmad1/5/9 in the mutant lines using *in toto* imaging with light sheet microscopy (Figure 1.5). We found that the BMP signalling gradient was altered in all three mutant lines but to varying degrees (Figure 1.6-1.7). Next, zebrafish ADMP is poorly characterised; therefore, we performed loss-of-function and gain-of-function analyses (Figure 1.8-1.11) and transplantation experiments (Figure 1.12). We determined that ADMP has a biphasic effect on the BMP signalling, and that this is perhaps independent of Chordin and BMP2b (Figure 1.11-1.12). Finally, prior to this study, the ligand distribution has not been directly measured, and the most direct measurement is by assaying pSmad1/5/9 intensity (Francois et al., 2009); therefore, we aimed to determine the biophysical properties of BMP, Chordin, Sizzled, and ADMP. To do this, we directly visualised these proteins by designing and characterising fluorescent fusion constructs (Figure 1.13-1.17) and then quantified protein diffusivity and stability *in vivo* (Figure 1.18). Overall, we found that the basic mechanism to pattern the dorsal-ventral axis in the zebrafish is best defined by the Graded source-sink model with diffusible BMP and Chordin (Pomreinke et al., 2017) and with fine-tuning by Sizzled and Tolloid (Figure 1.19). This is also supported by a parallel study reported by Zinski et al. (2017).

Results

Each mathematical model (Models 1-5) predicts different trajectories of how the BMP signalling is shaped over time to establish a signalling gradient (Pomreinke et al.,

2017). The mathematical formulation of each model and the predicted gradient formation kinetics can be found in Pomreinke et al. (2017), Appendix A. The following recounts our approach to test which model reflects the BMP signalling dynamics *in vivo*.

We measured pSmad1/5/9 as a means to measure free BMP ligands in the extracellular space (Pomreinke et al., 2017). This is under the assumption that the pSmad1/5/9 signal is a read-out of ligand-receptor binding and, therefore, a read-out of free BMP ligand distribution. Previously, the BMP signalling gradient was empirically quantified in the zebrafish embryo (Tucker et al., 2008). They immunostained for pSmad1/5/9 and imaged the embryos from two angles – animal and lateral view. They found that, from the blastula stage (4 h) to the late gastrula stage (9 h), the BMP signalling gradient becomes progressively restricted to the ventral side, and that the BMP signalling increases in the ventral-most region of the embryos.

However, subsequent studies highlighted the caveats in the current methods to measure BMP signalling gradients embryo-wide in zebrafish embryos (Zinski et al., 2019). There are two challenges: the inherent morphology and biology of the zebrafish embryos. First, BMP signalling is detected in several layers, and second, BMP signalling has also been shown to orchestrate both anterior-posterior and dorsal-ventral axes (Hashiguchi & Mullins, 2013). Their proposed solution is *in toto* imaging of zebrafish embryos to examine the signalling dynamics (Zinski et al., 2019). This then opens a third challenge – acquiring high-quality 3D images when applying current imaging approaches such as confocal microscopy because there are two caveats to using confocal microscopy. The first is the potential mismatch in the refractive index between the cells, the embedding media, the yolk, the immersion oil, and the coverslip. Therefore, Zinski et al. (2017, 2019) recommend yolk removal and sample clearing. They also developed additional tools to align embryos and quantify the BMP signalling gradient. However, there is one evident pitfall in their approach. That is, while they demonstrated how to image pSmad1/5/9 signal throughout the animal cap, the authors only quantified a 40 µm thick marginal band and excluded more anterior regions (Zinski et al., 2017). Hence, approximately 200 µm of the anterior region of the animal cap is excluded from the quantification, which is not embryo-wide quantification of the BMP signalling. The second caveat is that ‘conventional confocal imaging suffers from … depth-dependent degradation in scattering samples and volumetric bleaching’ (Wu et

al., 2021). This is evident in Zinski et al. (2019), Figure 3, in which, despite the yolk being scraped off during sample preparation, there is still nonuniformity in intensity along the XY axis (reported at 40% drop in Alexa 647 fluorophore sample) and along the Z-axis from the animal pole towards the margin in an embryo stained with Sytox Green.

Therefore, to quantify the BMP signalling gradient *in toto*, we followed up on their recommendation of 3D imaging of pSmad1/5/9 (Zinski et al., 2019). We used available light sheet microscopy that allows for less time-demanding sample preparation, overcomes the drawbacks of the current confocal imaging approach regarding refractive index mismatch, and reduces depth-dependent degradation (see Materials and Methods for additional details). In brief, the samples can be prepared and imaged within 24 hours with a washing robot to reduce hands-on work. Using the light sheet microscope, we matched the refractive index of the lens, the media (water), and the embedding medium (low melting agarose). This can be also done with confocal microscopy. Then pivot scanning by rapidly changing the illumination direction combined with multidirectional illumination allows homogeneous imaging spanning 5-cells deep from the enveloping layer to the yolk (Daetwyler & Huisken, 2016; Huisken & Stainier, 2009; Zeiss). Deeper tissues like the yolk are not relevant for quantification. Additionally, each embryo is illuminated and imaged uniformly from every angle since the sample can be rotated for multi-view imaging (Figure 1.5A) (Zeiss). We also developed a pipeline of the available method for the 3D reconstruction of multi-angle imaging (Schmid et al., 2013; Soh, 2020). Hence, the most time-demanding steps are the 3D-to-2D projection using Hugin software with Hammer-Aitoff projection function (Figure 1.5B) and the quantification along the dorsal-ventral axis using Fiji.

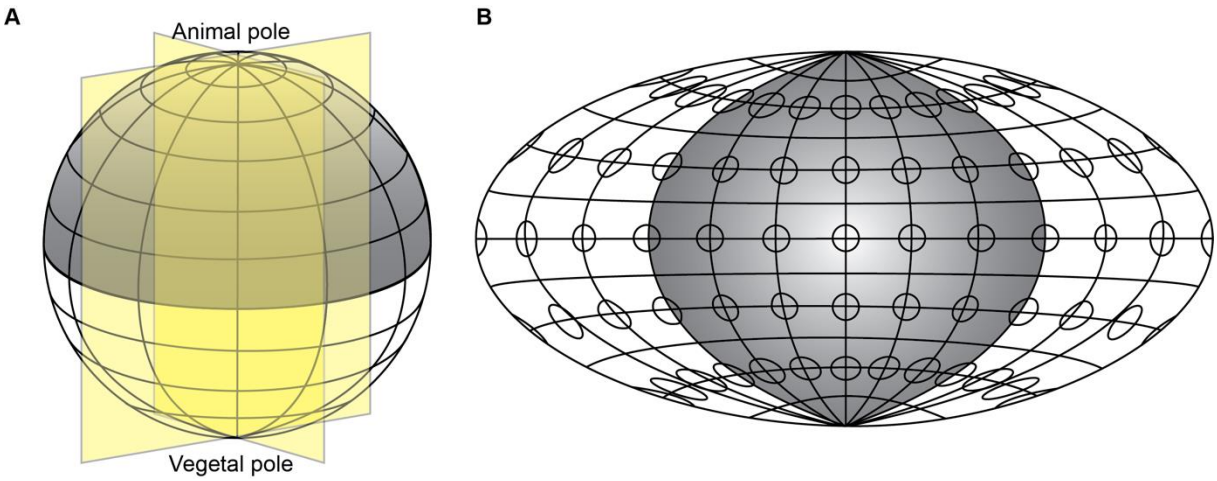

Figure 1.5 3D reconstruction of the zebrafish embryo.
A) The spherical globe represents a zebrafish embryo with the dark grey area as the animal pole and the white area as the yolk. Lines are regions of the globe that represent the 3D areas that are converted to 2D projections in (B). Zebrafish embryos are imaged from four angles (yellow panels) using selective plane illumination microscopy. The 3D image is projected into a two-dimensional image using the **B)** Hammer-Aitoff azimuthal equal area map projection (Xiao et al., 2018). Regions in the centre of the 2D projections have equal proportions (small black circles) with minimal distortions.

Using *in toto* imaging, we showed that by the late blastula stage, at the sphere stage, approximately 4 hpf, BMP signalling was weak and equally distributed throughout the blastoderm (Figure 1.6). By 30% epiboly (4.5 hpf), pSmad1/5/9 was restricted to the ventral side, with a peak in the ventral-most region. The pSmad1/5/9 levels increased steadily on the ventral side and remained low on the dorsal side as development progressed. Therefore, the gradient kinetics of BMP signalling are mostly consistent with Model 1-4, but not with Model 5 (Table 1.1) (Pomreinke et al., 2017).

Previous studies have shown that the pSmad1/5/9 gradient continues to increase at least up to 9 hpf (Tucker et al., 2008). At this stage, the ventral- and dorsal-most cells have migrated to the vegetal pole that the embryo is fully enveloped by migrating cells. We have yet to adapt our 2D projection for later stages in terms of how to orient the embryo when the ventral- and dorsal-most regions meet at the vegetal pole. Nevertheless, the results of *in toto* imaging and 2D maps are consistent with previous reports that the BMP signalling gradient progressively increases on the ventral side and remains low on the dorsal side (Tucker et al., 2008); therefore, we can use our 3D-to-2D protocol to quantify the BMP signalling gradient in mutants as presented below.

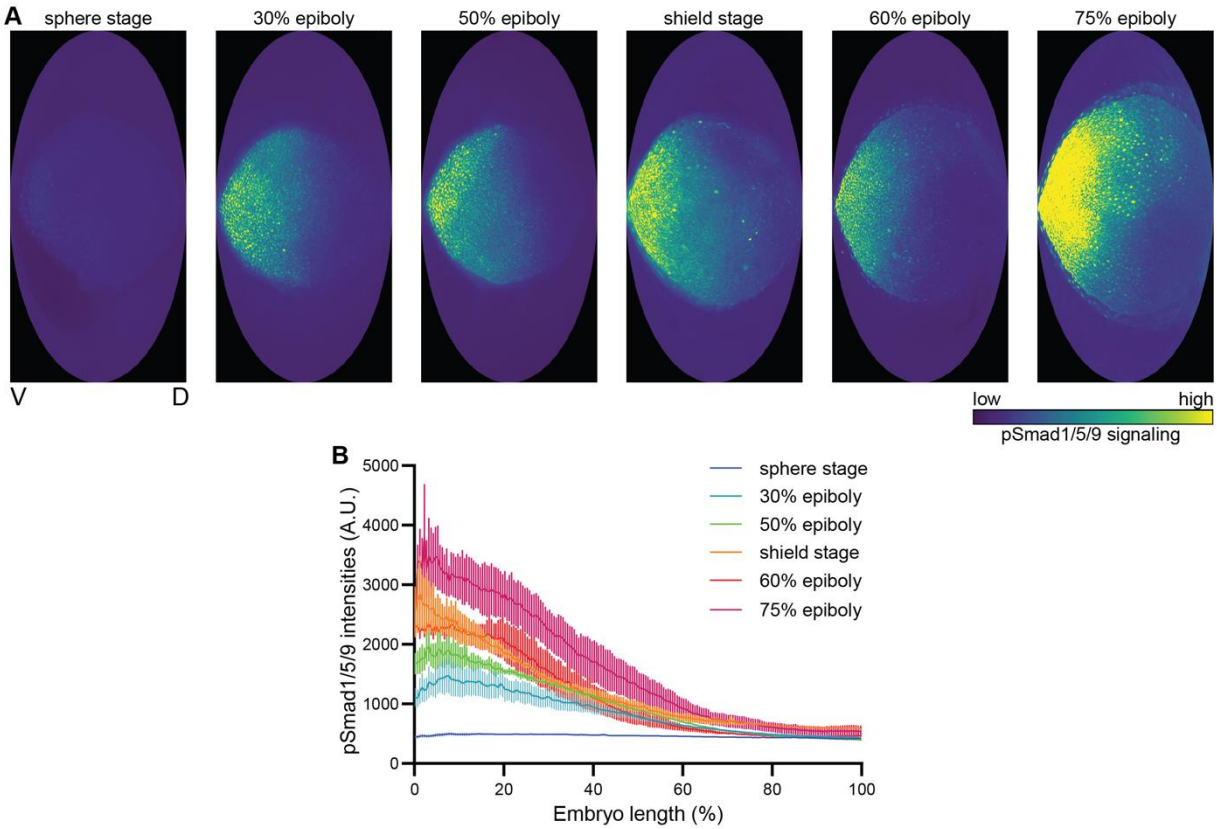

Figure 1.6 BMP signalling gradient steadily increases on the ventral side and remains consistently low on the dorsal side.
A) *In toto* imaging of BMP signalling in zebrafish embryos. Zebrafish embryos were fixed at different points between late blastula to mid-gastrulation and immunostained for pSmad1/5/9. The 3D images were acquired by a light sheet microscope and were projected into 2D images using Hammer-Aitoff projection, as described in Figure 1.5, with views from the animal pole. BMP signalling steadily increased on the ventral side (V) and consistently remained low on the dorsal side (D). **B)** pSmad1/5/9 intensities along the dorsal-ventral axis were quantified using Fiji. The results were plotted using Prism (GraphPad Software) with n = 3 for each time point. Bars represent the standard error of mean. Data from the sphere stage to 60% epiboly were previously published in Pomreinke *et al*. (2017).

Aberrant BMP signalling gradient in mutant lines

Large-scale mutagenesis in zebrafish helped identify a network of extracellular signalling molecules involved during dorsal-ventral patterning such as Chordin, Tolloid, and Sizzled (Hammerschmidt et al., 1996; Mullins et al., 1996; Zebrafish Issue, 1996). Upon loss-of-function of these three molecules, zebrafish embryos exhibited abnormal dorsal-ventral patterning, albeit to varying degrees (Figure 1.7A). The current model of their molecular interactions is that Chordin directly binds BMP ligands, and that this complex is cleaved by the metalloproteinase Tolloid, thus liberating BMP ligands (Figure 1.7B). BMP signalling leads to the expression of *sizzled* that can block

degradation of the BMP-Chordin complex by competing for Tolloid, so Sizzled acts as a BMP negative feedback regulator.

Each model (Models 1-5) accounts for and assigns different roles to individual extracellular constituents in shaping the BMP signalling gradient. To my knowledge, prior to the beginning of my PhD, how each molecule affects the BMP signalling gradient embryo-wide in these mutants was not known. Therefore, to test each model, we took a targeted approach by deconstructing the extracellular network and assaying how the BMP signalling gradient profile is affected upon the loss-of-function of each component. In Pomreinke et al. (2017), we tested Models 1-5 by quantifying how the BMP signalling gradient is affected upon *chordin* loss-of-function. Then, for this dissertation, I made qualitative predictions of the BMP gradient profile in *sizzled* and *tolloid* mutants and test these predictions experimentally.

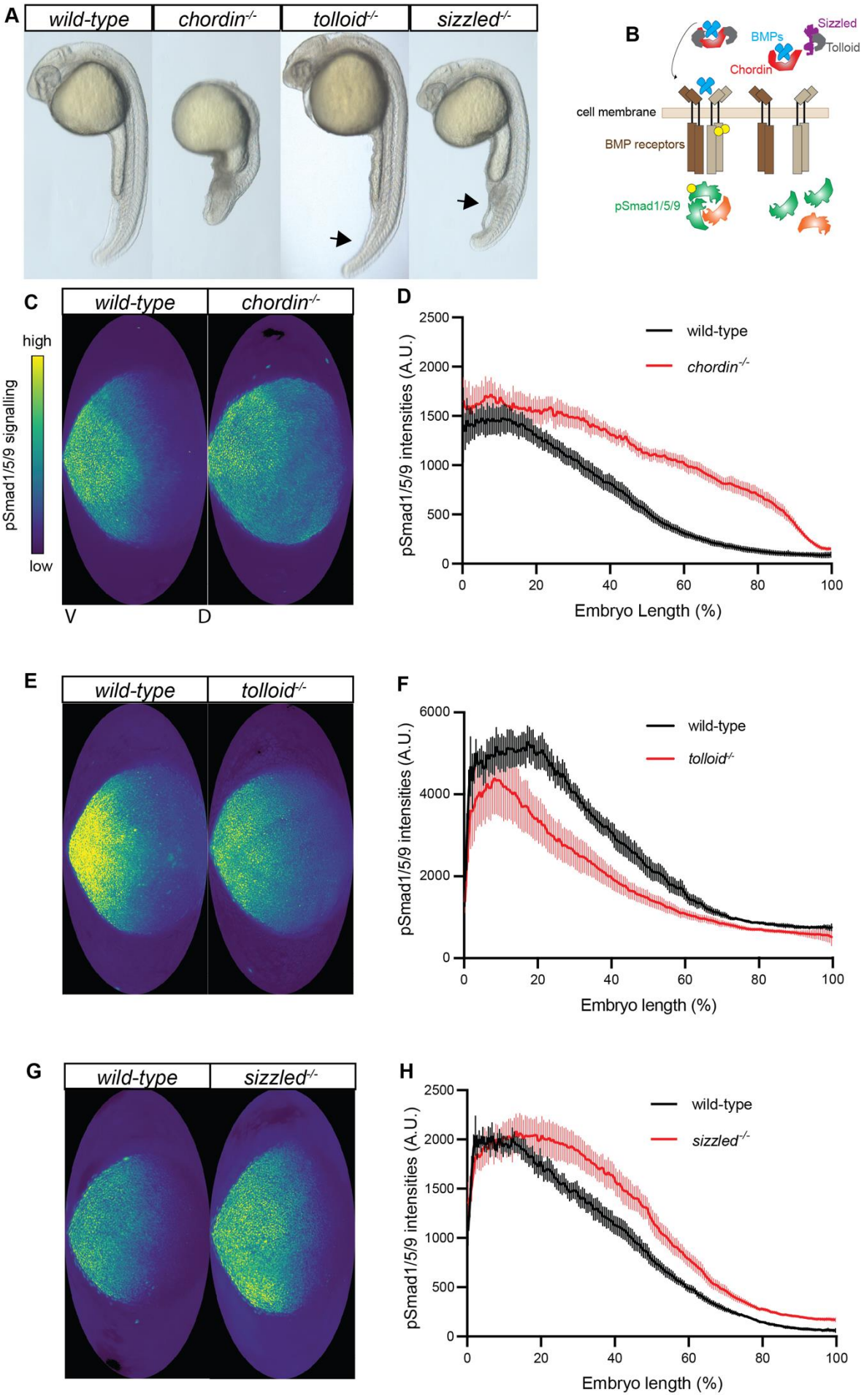
A
wild-type
chordin-/-
tolloid-/-
sizzled-/-
B
Sizzled
BMPs
Tolloid
Chordin
cell membrane
BMP receptors
pSmad1/5/9
C
wild-type
chordin-/-
high
low
pSmad1/5/9 signalling
V
D
D
wild-type
chordin-/-
pSmad1/5/9 intensities (A.U.)
Embryo Length (%)
E
wild-type
tolloid-/-
F
wild-type
tolloid-/-
pSmad1/5/9 intensities (A.U.)
Embryo length (%)
G
wild-type
sizzled-/-
H
wild-type
sizzled-/-
pSmad1/5/9 intensities (A.U.)
Embryo length (%)

Figure 1.7 BMP signalling gradient profiles are affected in *chordin*, *sizzled*, and *tolloid* mutants.
A) Phenotypic comparison of wild-type, *chordin* mutant, *sizzled* mutant, and *tolloid* mutant embryos at 24 hpf. Black arrows indicate abnormal tails. Images were adjusted to have comparable background signal and image contrast. **B)** Schematic of the BMP, Chordin, Tolloid, and Sizzled interaction in the extracellular space. **C-D)** Heterozygous *chordin*, **E-F)** *tolloid*, and **G-H)** *sizzled* adult fish were in-crossed, and the embryos were fixed at the shield stage and immunostained for pSmad1/5/9. Wild-type and homozygous mutant siblings were analysed. pSmad1/5/9 intensities along the dorsal-ventral axis were quantified using Fiji. Views are from the animal pole with ventral side (V) on the left and dorsal side (D) on the right. The results were plotted using Prism (GraphPad Software). Error bars represent standard error of mean. D) wild-type, n = 4; homozygous *chordin* mutant, n = 5. F) wild-type, n = 4; homozygous *tolloid* mutant, n = 4. H) wild-type, n = 4; homozygous *sizzled* mutant, n = 5. Chordin data were previously published in Pomreinke et al. (2017).

Chordin generates a steep BMP signalling slope without affecting the ventral-most region

In *chordin*^{tt250} mutants, dorsally-derived structures such as the head are lost, and ventrally-derived structures, such as the blood, are expanded (Figure 1.7A) (Hammerschmidt et al., 1996). To examine which model best describes how Chordin shapes the BMP signalling gradient dynamics, we first simulated the resulting BMP signalling gradient upon *chordin* loss-of-function based on each model's assumption (Figure 1.4B-F) (Pomreinke et al. (2017), Appendix A). Then we assessed the BMP signalling profile by comparing pSmad1/5/9 levels in wild-type and *chordin* mutants *chordin*^{tt250} (Figure 1.7C-D).

Model 1: Graded source-sink with immobile BMP predicts that BMP does not diffuse, and that Chordin diffuses to the ventral side to block BMP signalling (Figure 1.4B) (Pomreinke et al., 2017; Ramel & Hill, 2013). Upon *chordin* loss-of-function, there is an increase of free BMP ligands in the extracellular space, but this depends upon the BMP expression gradient (Figure 1.3B). Therefore, it is predicted that in *chordin* mutants, the BMP signalling is minimally increased at the ventral-most region where there is the least amount of Chordin and maximally increased towards the dorsal side containing the Chordin source.

In contrast, Model 2: Graded source-sink with mobile BMP predicts that since BMP ligands are diffusible, then there is an additional accumulation of free BMP ligands diffusing from high to low concentration in *chordin* mutants, thus the BMP signalling gradient is higher in the dorsal side and flatter overall (Figure 1.4C)

compared to Model 1's predicted slope (Figure 1.4B) (Pomreinke et al., 2017; Zinski et al., 2017).

Model 3: Shuttling predicts that Chordin transports BMP ligands to the ventral side to generate a BMP signalling peak (Ben-Zvi et al., 2008; Pomreinke et al., 2017). Therefore, in *chordin* mutants, the slope of the BMP signalling gradient remains relatively low and uniform throughout (Figure 1.4D).

Model 4: Self-regulating reaction-diffusion system postulates that there are ventral and dorsal systems (Francois et al., 2009; Pomreinke et al., 2017). With an initial bias in either side of the embryo and low BMP diffusivity, *chordin* mutants can autoregulate to generate a single peak and would have a slight increase in the BMP signalling on the ventral side where BMPs are expressed, but not on the dorsal side compared to wild-type embryos (Figure 1.4E).

Model 5: Long-range accumulation and feedback model postulates that BMP and Chordin are equally diffusible (Inomata et al., 2013; Pomreinke et al., 2017). Therefore, upon *chordin* loss-of-function, BMP ligands diffusing towards the dorsal side are not inhibited, thus resulting in an increase of BMP signalling on the dorsal side (Figure 1.4F) similar to Model 1 and Model 2.

To test these predictions, we assessed the BMP signalling profile by assaying the pSmad1/5/9 gradient in wild-type and *chordin* mutants *chordin*^{tt250} during gastrulation at the shield stage. We found that the BMP signalling gradient was expanded in c*hordin* mutants. Specifically, there was a significant increase of pSmad1/5/9 intensity in the 20% to 95% dorsal half of the embryo, but the pSmad1/5/9 levels in the ventral-most and dorsal-most regions did not significantly differ to the wild-type siblings (Figure 1.7C-D). An increase in the BMP signalling gradient in the lateral domains but not in the ventral/dorsal-most extremes suggests that Chordin plays a role in shaping the BMP signalling gradient, but it is not required to generate a BMP signalling peak ventrally or trough dorsally. Additionally, the finding suggests that Chordin is not essential to generate polarity. This is in line with the *chordin* mutant phenotype where anatomical structures are lost along the lateral domains, but the remaining organs are oriented properly (Figure 1.7A). Together, the experimental finding partially supports Models 1, 2, and 5, and not Models 3-4 (Table 1.1).

Tolloid and Sizzled further refine and steepen the BMP signalling gradient

The basic model of the molecular interactions between BMP, Chordin, and Tolloid is that BMP ligands are liberated from Chordin by the metalloproteinase Tolloid (Figure 1.7B) (Ferguson and Anderson, 1992, Mullins, 1998). In *Drosophila*, Tolloid is expressed dorsally and cleaves Sog to release BMP to generate a signalling peak, and as a result, *tolloid* mutants have a shallower BMP signalling gradient (Ferguson & Anderson, 1991). Hence, the *Drosophila* Tolloid function is best described by the Shuttling model (Model 3) (Eldar et al., 2002). This model was also used to assign Tolloid's role for scale-invariant patterning in *Xenopus* (Ben-Zvi et al., 2008). If Model 3 applies to the zebrafish BMP signalling dynamics, then in zebrafish *tolloid* mutants, BMP ligands remain bound to Chordin, and the resulting BMP signalling slope is predicted to decrease ventrally and increase dorsally (Figure 1.4E). However, in zebrafish, *tolloid* is expressed ubiquitously (Figure 1.3B) (Connors et al., 1999), while in *Xenopus*, *tolloid* is ventrally biased (Dale et al., 2002). Furthermore, our finding suggests that the generation of ventral BMP signalling peak does not dependent on Chordin (Pomreinke et al., 2017) – then the next question is what is Tolloid's function in shaping the BMP signalling gradient in the zebrafish?

Zebrafish *tolloid* mutants exhibit mild dorsalization with loss of ventral tail fin and reduction of caudal haematopoietic tissue (Connors et al., 1999) in contrast to the ventralized *chordin* mutants (Figure 1.7A). Interestingly, the adult *tolloid* mutant phenotype ranges from pigment abnormalities in the tail to complete tail loss. In severe cases, adult *tolloid* mutants produce viable gametes but cannot release gametes due to full loss of the tail fin and underdeveloped sex organs (Connors et al., 1999). During normal development, these organs develop from the ventral pole of the embryo with the highest BMP signalling. Overall, this suggests that *tolloid* mutants have deficient BMP signalling in the ventral pole. On the one hand, the Shuttling model (Model 3) predicts that *tolloid* loss-of-function would lead to a decrease in BMP signalling on the ventral pole and an increase on dorsal-lateral regions. On the other hand, at a later stage of my doctoral research, Tuazon et al. (2020) reported that the BMP signalling gradient was unaffected in *tolloid*^{tm124a} mutants due to genetic redundancy. Therefore, to test whether Tolloid has a function in shaping the BMP signalling gradient and further test Model 3, I examine the BMP signalling gradient profile upon *tolloid* loss-of-function in zebrafish by comparing the pSmad1/5/9 levels in wild-type and *tolloid* mutants

tolloid^{tm124a}. I found that *tolloid* mutants had a mild reduction in BMP signalling on the ventral most-region and, surprisingly, in the 20% to 40% ventral lateral region without affecting the dorsal-most side (Figure 1.7E-F). This is in line with the reduction of ventrally-derived organs such as the ventral tail and blood in *tolloid* mutant (Figure 1.7A). This suggests that Tolloid functions to liberate BMP to generate a steeper slope for specifying ventral-most cells, such as tail and blood island and, in some cases, laterally derived cells, such as the notochord as previously reported (Connors et al., 1999). This also suggests that Chordin is present in the ventral-most side of the embryo. The lower BMP signalling in the ventral half of *tolloid* mutants is indicative of Chordin's long-range diffusivity to bind BMP ligands, hence does not support Model 4's assumption of a slowly-diffusing Chordin. This partially supports Model 3's prediction of Tolloid's function in generating a BMP signalling peak (Figure 1.4D, Table 1.1). Nevertheless, this observation is more in line with Chordin as a graded sink in Model 1 and Model 2. Note, however, that since there is a range in *tolloid* phenotypes (Connors et al., 1999), it is possible that Tolloid is dispensable for dorsal-ventral patterning, but it is required to ensure reproducible patterning by buffering against signalling fluctuations.

So far, the BMP signalling dynamics in wild-type zebrafish dorsal-ventral patterning can be explained by a simple graded source-sink between BMP and Chordin as described by Model 1 and Model 2. However, dorsal-ventral patterning is a scale-invariant process; therefore, additional mechanisms have been proposed in which a complex interaction between BMP, Chordin, and other accessory proteins provides robustness against signalling fluctuations (Models 3-5). Above, we saw that in zebrafish embryos, Chordin acts as a graded sink, and Tolloid limits Chordin's inhibitory range. In turn, Tolloid's function can be limited by BMP negative regulator, Sizzled, in organisms such as zebrafish and *Xenopus* (Figure 1.7B) (Bijakowski et al., 2012; Lee et al., 2006; Mullins, 2006).

In the present models, only Models 4 and 5 assign a role for Sizzled. Both models assume Sizzled plays a role in limiting BMP signalling either by blocking Chordin or BMP activity range. In Model 4: Self-regulating reaction-diffusion system, there is a ventral system in which the BMP activity range is regulated by Sizzled and a dorsal system in which the Chordin activity range is regulated by ADMP (Francois et al., 2009; Pomreinke et al., 2017) (Figure 1.4E). Therefore, an initial bias with either

BMP or Chordin is sufficient to maintain the BMP signalling profile, and there would be minimal change in BMP signalling upon *sizzled* loss-of-function (Figure 1.4E). From a different perspective, Model 5: Long-range accumulation and feedback postulates that Sizzled blocks Tolloid to regulate Chordin stability and activity range thus providing a system-wide feedback loop to respond to gene-fluctuations and size variations (Figure 1.4F) (Inomata et al., 2013; Pomreinke et al., 2017). Model 5 assigns a more central role for Sizzled, and therefore, without Sizzled, the system cannot establish a steep BMP signalling gradient (Figure 1.4F).

In zebrafish, *sizzled* is ventrally expressed and overlaps with BMP signalling (Figure 1.3B) (Yabe et al., 2003). Zebrafish *sizzled* mutants have expanded blood islands and ventralized tails with normal heads and trunk structures (Figure 1.7A) (Hammerschmidt et al., 1996). This suggests that *sizzled* mutants have excess BMP signalling, and that Sizzled is required to pattern ventral and lateral domains by preventing ventralization of dorsal-lateral domains, which further suggests Sizzled's role in limiting BMP signalling. Notwithstanding, Tuazon et al. (2020) did not find a difference in BMP signalling between wild-type and *sizzled* mutants in early gastrula at 5.7 hpf, thus suggesting that Sizzled may be dispensable. To experimentally determine the BMP signalling profile upon *sizzled* loss-of-function, I assayed and compared the pSmad1/5/9 levels in wild-type and *sizzled* mutants *sizzled*^{tm305} at shield stage (appx. 6 hpf). Surprisingly, I found that *sizzled* mutants have higher BMP signalling from the 30% to 100% dorsal half of the embryos (Figure 1.7G-H). This is inconsistent with the findings of Tuazon et al. (2020) that the BMP signalling gradient in *sizzled* embryos was similar to wild-type embryos. This difference could be due to the time points analysed. Furthermore, the expanded BMP signalling is partially consistent with *sizzled* phenotype with enlarged blood islands; however, the dorsally-derived structures such as the head and trunk developed normally (Figure 1.7A). These results suggest that the ventral-lateral cells that would normally form somites were ventralized and differentiated to blood cells, but the ventral/dorsal-most cells were not affected. In addition, it is surprising that the BMP signalling in the ventral-most region is not affected in *sizzled* mutants even though *sizzled* is expressed throughout the ventral half of the embryo (Figure 1.3B) (Yabe et al., 2003), which suggests that Sizzled refines the BMP signalling gradient profile by blocking Tolloid and excessive cleavage of Chordin-BMP on the lateral domains in line with previous findings (Muraoka et al., 2006).

In terms of the models, the results contradict Model 4 since Model 4 postulates that the BMP signalling is unaffected upon *sizzled* loss-of-function. Together, the current finding supports Model 5, which postulates that Sizzled regulates Chordin inhibitory range, but does not contradict Chordin's role as a graded sink as in Model 1 and Model 2 (Table 1.1).

ADMP – a biphasic BMP modulator

Next, we further tested the self-regulating models (3-5), which posit that ADMP has a central role in scaling the BMP signalling gradient (Ben-Zvi et al., 2008; Francois et al., 2009; Reversade & De Robertis, 2005). The Shuttling model (Model 3) describes that, in *Drosophila*, a ventrally-expressed Sog shuttles dorsally-expressed BMP ligands Dpp and Screw (Figure 1.4D) (Eldar et al., 2002). A modified version of Model 3 is proposed in *Xenopus* in which Chordin has a higher affinity to shuttle another BMP ligand, ADMP, which is dorsally expressed in *Xenopus* and in zebrafish (Figure 1.3B) but absent in *Drosophila* (Ben-Zvi et al., 2008). This is based on the findings that bisected *Xenopus* embryos fail to regenerate dorsal-ventral patterning upon knockdown of *admp* (Reversade & De Robertis, 2005). One opposing explanation to the Shuttling model is the Self-regulating reaction-diffusion system (Model 4), which postulates that Chordin and ADMP are coupled, and that ADMP acts to limit Chordin's inhibitory range through simple diffusion (Figure 1.4E) (Francois et al., 2009). Finally, the Long-range accumulation and feedback system (Model 5) postulates that BMP activity, including ADMP, activates *sizzled* expression, which, in turn, blocks Tolloid and stabilizes Chordin to accumulate in the ventral side (Figure 1.4F) (Inomata et al., 2013).

In the zebrafish, however, there are varying reports of ADMP's role in dorsal-ventral patterning. Earlier reports suggest that ADMP regulates axial (notochord and neural tube) and anterior (head) structures by restricting organizer function in a distinct but also cooperative manner with other BMP ligands (Lele, Nowak, et al., 2001; Willot et al., 2002). Specifically, overexpression of *admp* did not fully rescue *bmp* mutants, but enhanced *chordin* mutant phenotype (Willot et al., 2002). However, these two studies reported different phenotypes upon *admp* loss-of-function and gain-of-function in wild-type embryos (Lele, Nowak, et al., 2001; Willot et al., 2002). Additionally, during my doctoral studies, Yan et al. (2019) have shown that *admp* mutants are phenotypically wild-type, and that the BMP signalling gradient in *admp* mutants is

similar to wild-type embryos. The authors proposed that ADMP cooperates with a different BMP ligand called Pinhead to buffer against BMP signalling fluctuations. Furthermore, they showed that only double mutants of *admp* and *pinhead* caused an increased proportion of dorsalized embryos. Therefore, to verify whether ADMP plays a secondary role, as inferred from Models 1-2, or a more central role in the dorsal-ventral patterning in zebrafish, as postulated by Models 3-5, we first performed loss-of-function (Figure 1.8) and gain-of-function experiments (Figure 1.9-1.10). Then we assayed whether ADMP can signal in the absence of Chordin (Figure 1.11) and BMP ligands such as BMP2b (Figure 1.12).

admp mutants were not isolated during the large-scale mutagenesis to identify genes involved in early zebrafish development (Zebrafish Issue, 1996). Therefore, for loss-of-function experiments, I first generated *admp* mutants using CRISPR/Cas9. Mutants have a 52 bp deletion and 5 bp insertion in exon-1 and can be genotyped by primers annealing to the 5' and 3' end of exon-1 (Figure 1.8A-B). The mutant protein is predicted to be truncated with only 87 residues compared to wild-type *admp* with 391 residues. However, the resulting mature transcript is yet to be determined in follow-up experiments. Nevertheless, homozygous *admp* mutants are phenotypically wild-type and viable (Figure 1.8C-D). This is consistent with the previous findings of Yan et al. (2019) but inconsistent with *admp* morphant studies (Lele, Nowak, et al., 2001; Willot et al., 2002). Furthermore, these homozygous *admp* mutants are fertile, and their progenies are also viable and fertile (data not shown). This suggests that maternally-deposited and zygotically-expressed *admp* are not essential for dorsal-ventral patterning in zebrafish. The BMP signalling profile in our *admp* mutants is yet to be assayed. Nevertheless, based on previous findings of Yan et al. (2019) and the *admp* mutant phenotype results shown here, ADMP may be dispensable for the normal development of zebrafish embryos in standard laboratory conditions.

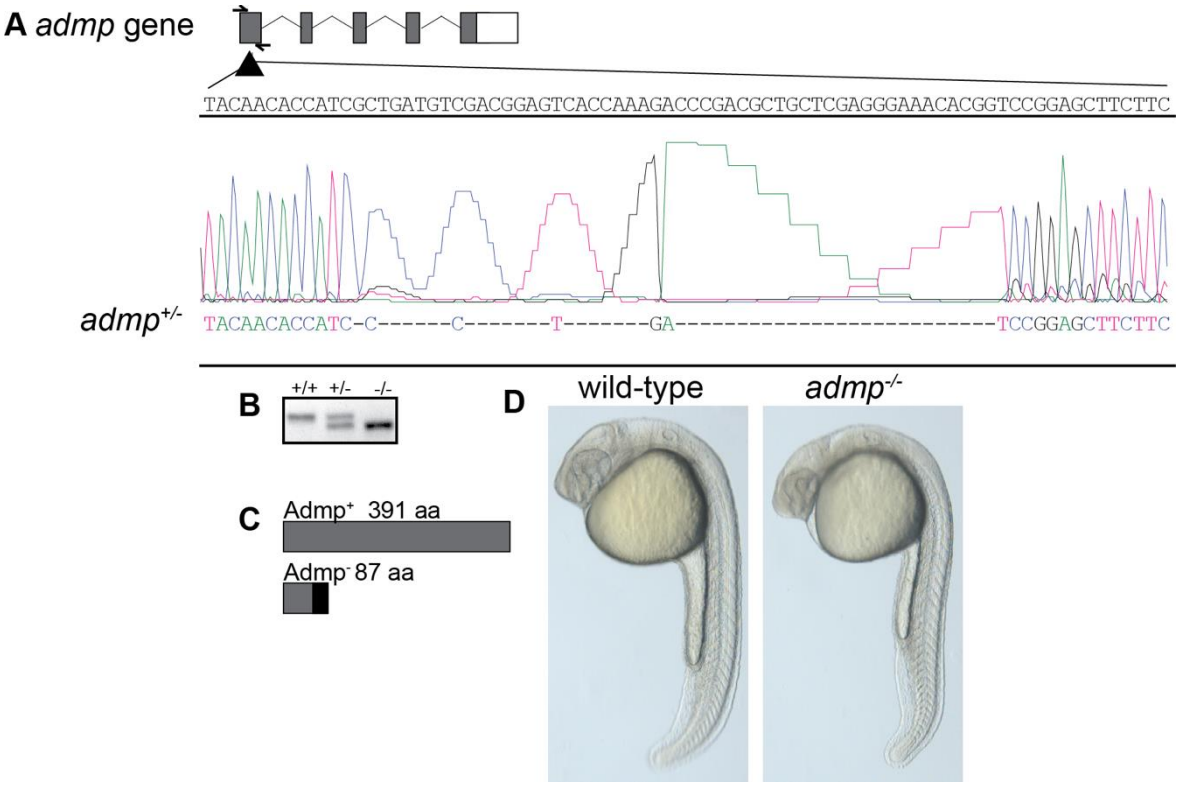

Figure 1.8 *admp* mutants are phenotypically wild-type.
A) Alignment of CRISPR/Cas9 generated *admp* mutant allele to wild-type *admp* gene illustrates a 52 bp indel. Half arrows indicate the primer annealing sites. Triangle represents CRISPR/Cas9 target site. **B)** PCR amplification of the *admp* locus using the primer set in (A) showed that a shorter PCR product is present in heterozygous (+/-) and homozygous (-/-) *admp* mutants compared to wild-type *admp* (+/+). **C)** *In silico* prediction of mutant ADMP protein compared to wild-type. *admp* mutants have 87 residues containing additional aberrant residues before a premature stop. **D)** Maternal zygotic *admp* homozygous embryos exhibit wild-type phenotype similar to wild-type embryos.

Next, I examined the effects of *admp* gain-of-function. In one report, overexpression of *admp* at 50 pg mRNA caused severe ventralization with expanded blood islands and complete loss of cranial structures (Lele, Nowak, et al., 2001). In another report, overexpression of *admp* at 600 pg mRNA caused moderate ventralization with smaller eyes, enlarged somites, and progressive loss of the notochord (Willot et al., 2002). Therefore, to characterise ADMP and address the discrepancy in gain-of-function phenotypes at different concentrations, I overexpressed ADMP by injecting 5, 50, and 250 pg of *admp* mRNA into zebrafish embryos and assessed their phenotypes at 1 dpf. At a low concentration of 5 pg *admp*, embryos were ventralized with enlarged somites and blood islands and loss of cranial structures (Figure 1.9A-B). This is consistent with phenotypes reported by Willot et al. (2002), albeit with different *admp* mRNA concentrations. In contrast, at a high

concentration of 250 pg *admp*, embryos were dorsalized with loss of tail structures and somites. The curled tail phenotype is reminiscent of the piggy tail phenotype of heterozygous *smad5* mutants (Mullins et al., 1996), suggesting a decrease in BMP signalling. This dorsalizing effect of ADMP is unexpected since, as a BMP ligand, ADMP is thought to have ventralizing effect (Lele, Nowak, et al., 2001). Overall, these findings suggest that ADMP has a biphasic effect on dorsal-ventral patterning.

To determine at which point ADMP switches from ventralizing to dorsalizing, I performed a more detailed titration analysis by injecting varying amounts of *admp* mRNA. Based on two experimental rounds, I observed that approximately 50 pg of *admp* mRNA could either dorsalize or ventralize (Figure 1.9C-D). This suggests that below 50 pg of *admp* mRNA, ADMP is ventralizing and can cause loss of dorsal structures. In contrast, above 50 pg of *admp* mRNA, ADMP is partially dorsalizing and can cause loss of ventral structures. This suggests that overexpression of ADMP can ventralized and dorsalized in a concentration-dependent manner.

Next, to determine whether *admp* overexpression affects the BMP signalling gradient, I injected embryos with either 5 pg (ventralizing) or 250 pg (dorsalizing) of *admp* mRNA and immunostained for pSmad1/5/9. I observed that at low concentrations of *admp*, the pSmad1/5/9 level was increased, while at high concentrations of *admp*, the pSmad1/5/9 level was decreased (Figure 1.10A-B), consistent with the ventralized/dorsalized phenotypes of embryos injected with *admp*, respectively (Figure 1.9). This suggests that ADMP can modulate BMP signalling in a concentration-dependent manner. Altogether, loss-of-function and gain-of-function analyses suggest that ADMP may modulate BMP signalling, but it is not an essential molecule for dorsal-ventral patterning.

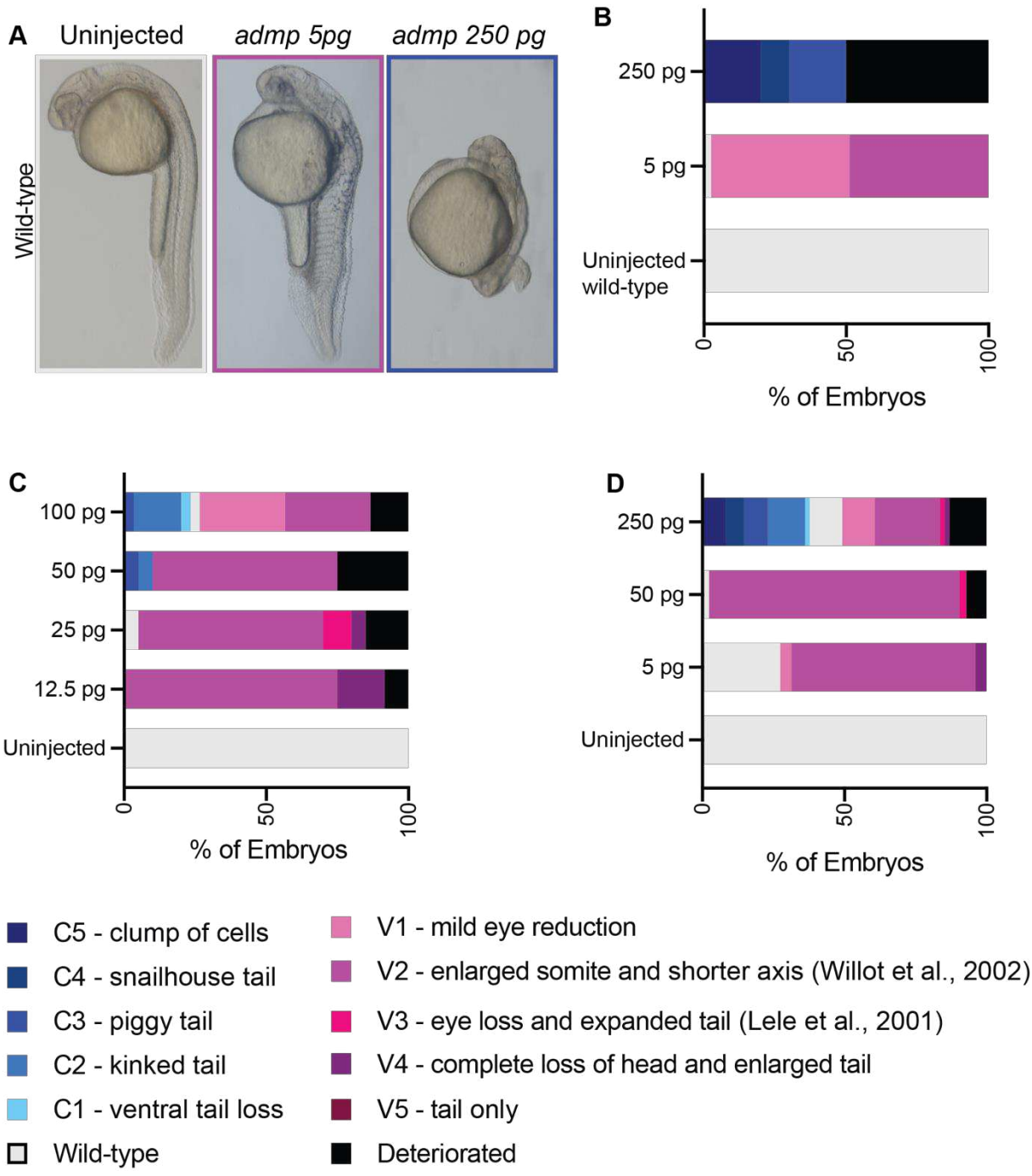

Figure 1.9 High and low concentrations of ADMP have opposing effects on dorsal-ventral patterning.
A) At 5pg *admp* mRNA, injected embryos were ventralized with loss of head structures and expanded tails. At 250 pg *admp*, some embryos were dorsalized with retracted tails. **B)** Distribution of phenotypes at 1 dpf. Uninjected embryos, n = 28; embryos injected with 5 pg *admp*, n = 39, and 250 pg *admp*, n = 20. **C-D)** Additional trials of *admp* gain-of-function experiment at varying concentrations using wild-type embryos were performed, and the phenotypes were scored at 1 dpf. C) First round of titration experiments: uninjected embryos, n = 9; injected with 12.5 pg *admp*, n = 12; 25 pg *admp*, n = 12; 50 pg *admp*, n = 20, and 100 pg *admp*, n = 30. D) Second round of titration: uninjected embryos, n = 20; injected with 5 pg *admp*, n = 51; 50 pg *admp*, n = 42, and 250 pg *admp*, n = 61.

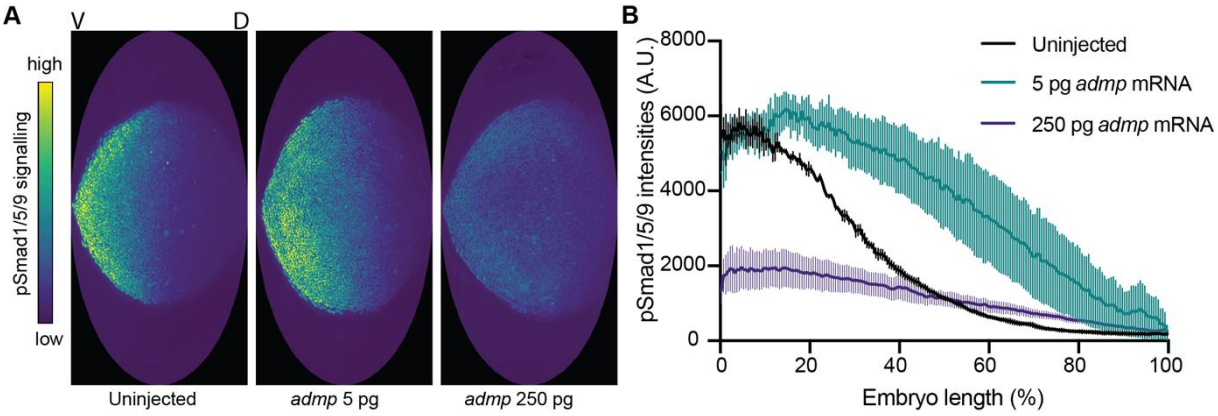

Figure 1.10 Different concentrations of *admp* have opposing effects on the BMP signalling gradient.
A) Injected with either 5 pg or 250 pg *admp* mRNA, embryos were fixed at the shield stage and were immunostained for pSmad1/5/9. **B)** Quantification of pSmad1/5/9 immunostaining: uninjected, n = 3; 5 pg *admp*, n = 3, and 250 pg *admp*, n = 4. The results are plotted using Prism (GraphPad Software). Error bars indicate standard error.

ADMP functions independently of Chordin and BMP2b

Models 4-5 postulate that ADMP's primary role is to regulate Chordin function. On one hand, Model 4 (Self-regulating reaction-diffusion system) postulates that Chordin and ADMP are coupled in which ADMP limits Chordin's activity range. On the other hand, Model 5 (Long-range accumulation and feedback) postulates that ADMP and BMP induce expression of *sizzled* to promote Chordin expansion towards the ventral side. Therefore, I wanted to test if ADMP can modulate BMP signalling as shown above in the absence of Chordin, such that ADMP can additionally ventralize *chordin* mutants at 5 pg of *admp* mRNA and can rescue dorsal structures at 250 pg of *admp* mRNA. Indeed, *chordin* mutants injected with 5 pg of *admp* caused the additional reduction of head and trunk regions with only the posterior tail remaining (Figure 1.11A-B). This is consistent with ADMP's ventralizing effect on wild-type embryos at low concentrations and with ADMP's ventralizing function as a BMP homologue. This is also consistent with the findings of Willot et al. (2002) that *admp* overexpression enhances *chordin* mutant phenotypes. Surprisingly, *chordin* mutants injected with 250 pg of *admp* have eyes, otoliths, and extended tails, but the typically enlarged blood islands are absent (Figure 1.11A-B). This is inconsistent with findings by Willot et al. (2002) that increasing amounts of ADMP did not cause severe defects in head and tail structures. Overall, the formation of cranial organs in the absence of Chordin, which are dorsally derived structures, suggests that ADMP has dorsalizing capacities

independent of Chordin. Additionally, the eyes are the first organs that are lost accompanied by the enlargement of blood islands upon *bmp2b* and *bmp7a* overexpression in zebrafish (Dick et al., 2000; Kishimoto et al., 1997). This finding suggests that ADMP has divergent functions from other BMP homologues.

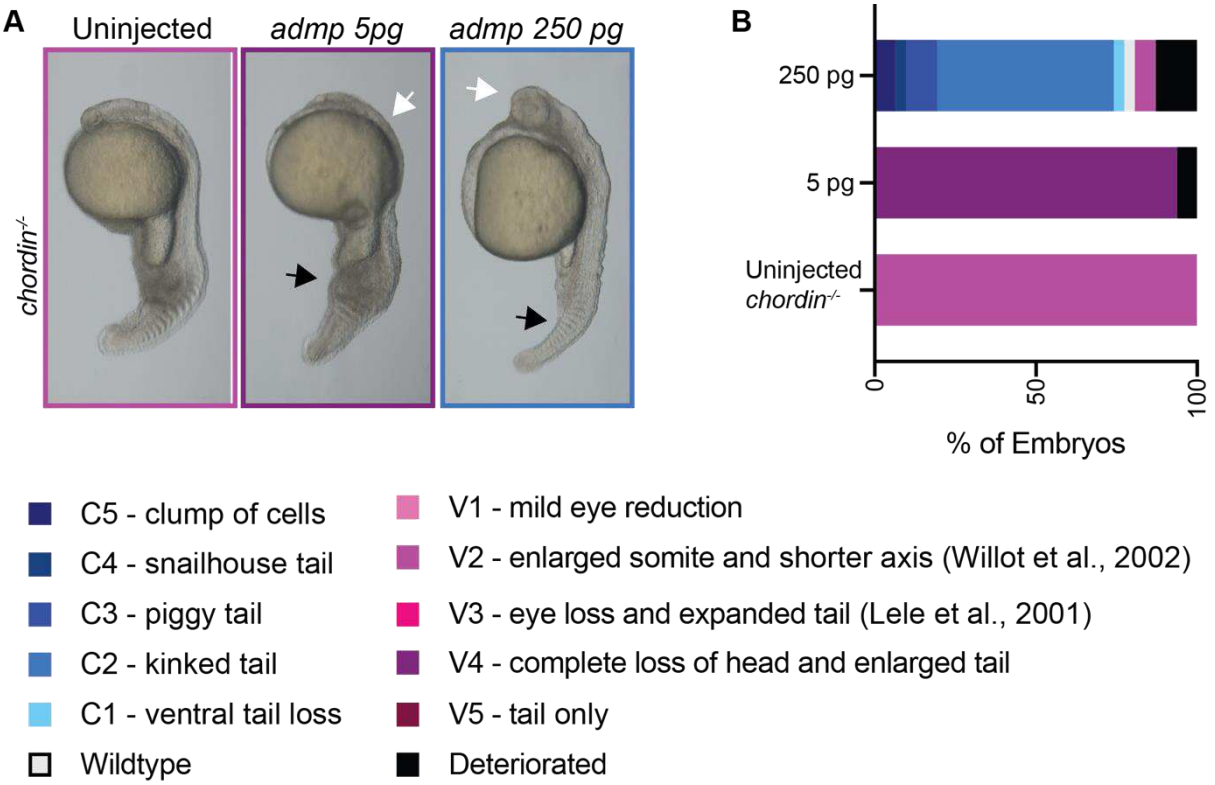

Figure 1.11 ADMP's biphasic effect is independent of Chordin.
A) Upon injection of 5pg of *admp* mRNA, *chordin*$^{-/-}$ mutant embryos were additionally ventralized with loss of head (white arrow) and further enlargement of the blood islands (black arrow). Injection of 250 pg of *admp* mRNA, *chordin*$^{-/-}$ mutants had extended tails (black arrow) and developed cranial structures such as eyes (white arrow). **B)** Distribution of phenotypes at 1 dpf of uninjected *chordin*$^{-/-}$ embryos, n = 14; embryos injected with 5 pg *admp*, n = 32, and 250 pg *admp*, n = 31.

However, whether ADMP can trigger BMP signalling autonomously and the extent of its signalling range are not known. Previous studies have shown that ADMP is a secreted and diffusible molecule that acts cooperatively with other BMPs, and that co-injection of *admp* and *bmp2b* has a stronger ventralizing effect (Willot et al., 2002). To determine whether ADMP can signal via BMP receptors in the absence of other BMP homologues, the BMP signalling gradient was quantified from clones overexpressing low and high *admp* concentration in embryos in which *bmp2b* was down-regulated, and this was compared to *bmp2b*-expressing clones (Figure 1.12). Briefly, at the sphere stage, a clone of cells from *h2a:GFP* donors injected at the one-cell stage with either 5 pg or 250 pg of *admp* or 5 pg of *bmp2b* were transplanted onto

host embryos injected at the one-cell stage with *bmp2b* morpholino (Figure 1.12A) and fixed at 30 min and 60 min after transplantation. Then the host embryos were immunostained for pSmad1/5/9. For negative control, I verified that pSmad1/5/9 was not detectable in uninjected and *bmp2b* morphants at the sphere stage (Figure 1.12B). I found that *bmp2b*-expressing clones had consistently higher pSmad1/5/9 signalling than *admp*-expressing clones; however, at 175 µm, the host cells surrounding the clone from embryos injected with 250 pg *admp* had higher pSmad1/5/9 level than 5 pg *bmp2b* (Figure 1.12C-E). It is not clear whether a higher concentration of *bmp2b* will also lead to Smad1/5/9 phosphorylation beyond 175 µm. Taken together, this suggests that ADMP is a weaker activator of BMP signalling compared to BMP2b, and that ADMP can diffuse and trigger BMP signalling away from its source.

Overall, my quantification of the BMP signalling profile in respective mutants supports the shared basis of Model 1 and 2 in which Chordin may act as a diffusible BMP inhibitor to shape the BMP signalling gradient; however, in contrast to Models 1-2, Chordin does not contribute to generating a signalling peak. While these simple models illustrate the central mechanism underlying BMP-Chordin system during wild-type zebrafish embryonic development, I propose an additional layer of feedback mechanism in which Sizzled and Tolloid refine the BMP signalling in the ventral-lateral regions. Furthermore, findings on *admp* mutants suggest that ADMP does not have a critical role in the normal development of zebrafish embryos in standard laboratory rearing conditions. Nevertheless, these results are indirect readouts of BMP distribution in the extracellular space. Therefore, in the following sections, we further tested the assumptions of the five models regarding the biophysical properties of the extracellular constituents during dorsal-ventral patterning in zebrafish.

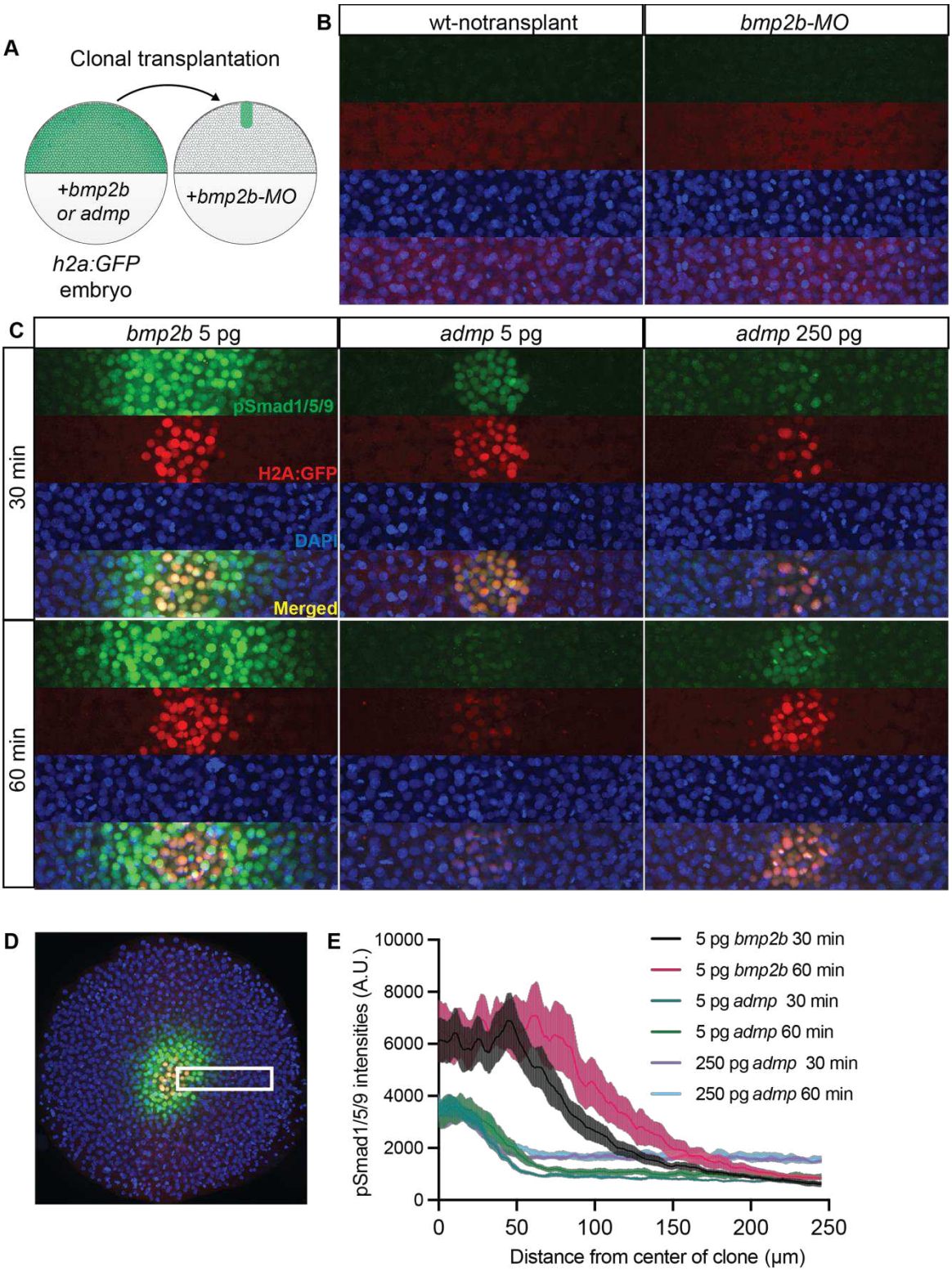

Figure 1.12 Comparison of the BMP2b and ADMP signalling range.
A) At sphere stage (4 hpf), cells were transplanted from donor *h2a:GFP* embryos injected with either *bmp2b* (5 pg) or *admp* (5 pg or 250 pg) into host embryos injected with *bmp2b* morpholino (*bmp2b-MO*). **B)** Control embryos without clonal transplant (left) and injected with *bmp2b-MO* (right). **C)** Host embryos were fixed 30 min or 60 min after transplantation and double immunostained for GFP and pSmad1/5/9. **D)** pSmad1/5/9 was quantified 250 µm outwards from the centre of the clone (inlet). **E)** pSmad1/5/9 intensity was measured using Fiji and plotted using Prism (GraphPad Software), n = 6 for all. Error bars indicate standard error.

Characterising fluorescent fusion constructs

Recall that Models 1-5 have conflicting assumptions: whether or not BMP and Chordin are diffusible molecules; whether or not Chordin facilitates BMP ligand mobility; and for Models 3-5, whether or not additional factors such as Sizzled, Tolloid, and/or ADMP can modulate the interaction between BMP and Chordin. To test these different assumptions, we performed several quantitative fluorescence assays (Pomreinke et al., 2017). To do so, we first designed and characterised fluorescent fusion constructs of each component, mainly, BMP2b, Chordin, Sizzled, and ADMP (Figure 1.13-1.17). BMP7a fluorescent fusion constructs were published in Soh et al. (2020) (see Appendix B). It is imperative to properly characterise fluorescently-tagged proteins since the tags may interfere with native protein function (Montecinos-Franjola et al., 2020). Therefore, I tested the activity of our fluorescent fusion constructs by scoring their phenotypes compared to untagged constructs. Then, to address concerns about fluorescent fusion constructs in terms of: (1) incorrect post-translational processing because the fluorescent tag hinders proper proteolytic processing, (2) the fluorescent construct remains covalently bonded to the prodomain instead of the mature domain, and (3) the effective translated amount of each different construct, the fluorescent constructs were fused to small FLAG tags and were subsequently analysed using Western blot. Once their activities are properly evaluated and confirmed to be comparable to untagged constructs, these fluorescently-tagged versions can be used to infer the biophysical parameters of untagged wild-type versions. The results of the quantitative fluorescence assays are presented in the Discussion section as they were performed by my colleagues (Figure 1.18, Table 1.1).

BMP2b

BMP ligands have two domains (Cui et al., 2001; Cui et al., 1998). The prodomain is 30 kDa, and the mature domain is 20 kDa. BMP is processed to release the functional mature domain located at the C-terminus, which then binds to transmembrane receptors (Constam, 2014; Cui et al., 1998; Dutko & Mullins, 2011). Therefore, to ensure that we are visualising and detecting the mature domain, the fluorescent tags were placed between the prodomain and the mature domain, downstream of the Furin proprotein convertases cleavage site RSSR (Cui et al., 1998), and flanked with linkers to allow flexibility between BMP2b and GFP or Dendra2 and

to avoid blocking the mature domain binding to receptors (Huang et al., 2013) (Figure 1.13A, Pomreinke et al. (2017)).

To assess if BMP2b-sfGFP/-Dendra2 have similar ventralizing activity as untagged constructs, embryos were injected with each construct at equimolar amounts, and their phenotypes were scored at 1 dpf (Pomreinke et al., 2017). We found that overexpression of each *bmp2b* fluorescent construct caused ventralization (Figure 1.13B). BMP2b-sfGFP had stronger ventralizing activity, and BMP2b-Dendra2 had a weaker ventralizing activity than untagged BMP2b. This suggests that the different tags may have different effects on BMP2b activity. This could be due to the fluorescent fusion constructs having different stability; for example, sfGFP was optimised to fold even when fused to poorly folded polypeptides (Evanko, 2006; Pedelacq et al., 2006). Nevertheless, injecting either fluorescent fusion construct restored normal development in *bmp2b/swr* mutants (Figure 1.13C) (Pomreinke et al., 2017). Moreover, using a Western blot assay, we found that BMP2b-FLAG had two prominent bands. The first band represented the unprocessed BMP2b at 50 kDa, and the second band represented the mature domain at 20 kDa (Figure 1.13D). Similarly, BMP2b-sfGFP/-Dendra2 lanes had the unprocessed protein at 75 kDa and the processed protein at 48 kDa. In all three constructs, the processed protein band was more prominent than the unprocessed protein in the extracellularly enriched fractions, suggesting that the BMP2b mature domain is covalently bonded to the protein tags, and for the purpose of our fluorescent assays, it suggests that we are visualising the tagged mature domain. Furthermore, the thickness of the bands for each construct corresponded to its ventralizing activity (Figure 1.13B), further suggesting that the fluorescent constructs have varying ventralizing capacities due to different protein levels. Altogether, these results suggest that, first, our fluorescent BMP2b constructs have similar biological activity as wild-type constructs, and second, the fluorescent proteins are cleaved from the prodomain and remain covalently linked to the mature domain.

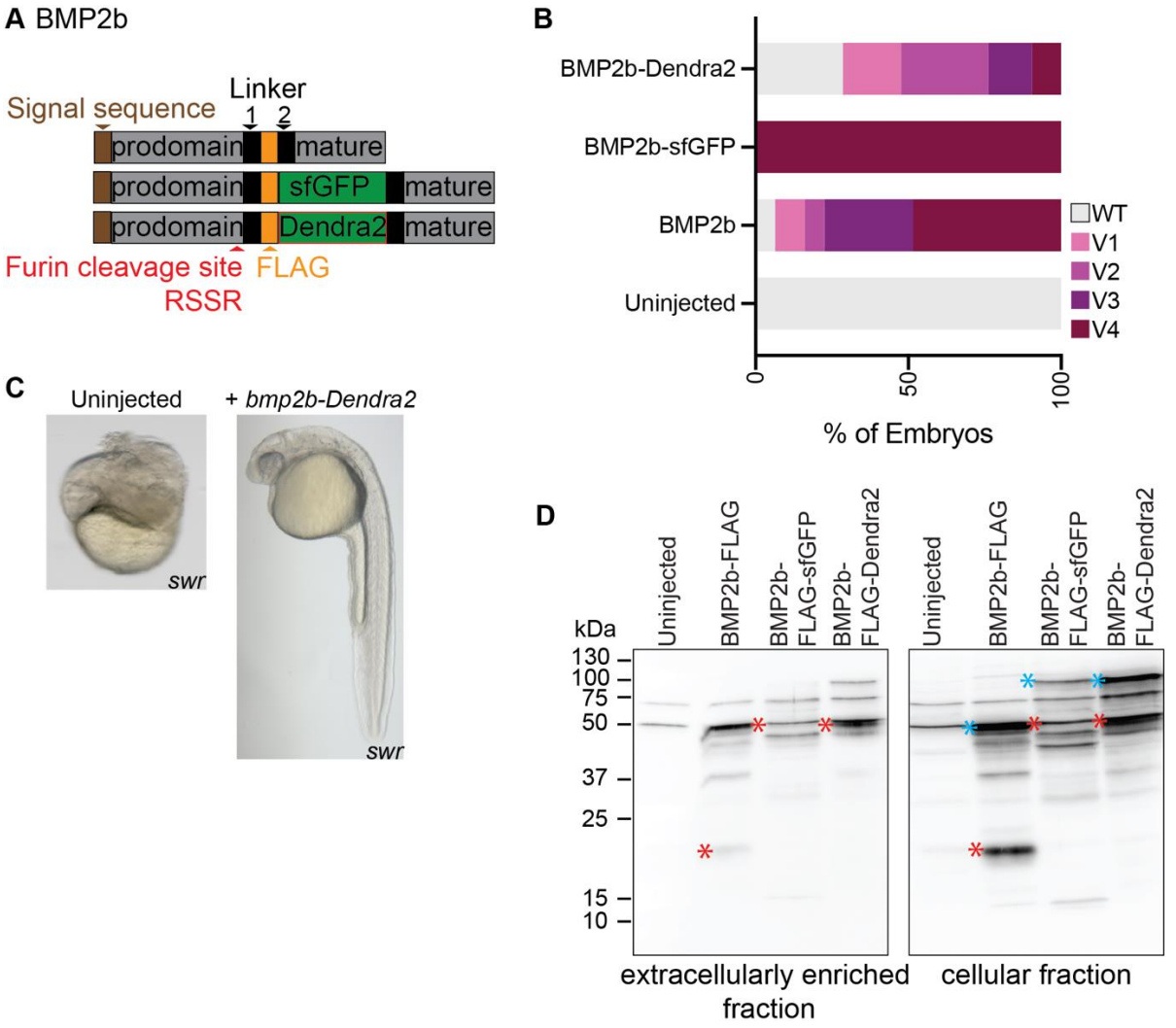

Figure 1.13 Zebrafish fluorescent BMP2b constructs are functional and processed similarly to expected wild-type constructs.
A) Schematic of BMP2b fluorescent fusion constructs, adapted from Pomreinke et al. (2017). **B)** Embryos were injected at equimolar amounts with *bmp2b* (1 pg), n = 31; *bmp2b-sfGFP* (1.47 pg), n = 32; *bmp2b-Dendra2* (1.48 pg), n = 11, or left uninjected, n = 30. Their phenotypes were scored at 1 dpf. **C)** *bmp2b*/*swr*$^{tc300-/-}$ (*swr*) was rescued by injecting *bmp2b-Dendra2* (2.47 pg). **D)** Cellular and extracellularly enriched fractions of embryos injected with FLAG-tagged *bmp2b* constructs were analysed using Western blot with anti-FLAG antibody. The full-length unprocessed proteins are indicated with blue asterisks, and the processed proteins are indicated with red asterisks.

Chordin

A similar approach was taken to design fluorescent Chordin constructs (Pomreinke et al., 2017). Recall that the full-length Chordin binds to BMP, and Chordin is cleaved in the extracellular space by Tolloid to release BMP ligands (Mullins, 1998; Piccolo et al., 1997; Shimmi & O'Connor, 2003). Therefore, to design Chordin fluorescent fusion constructs, the fluorescent proteins were inserted between the two

Tolloid cleavage sites of Chordin (Figure 1.14A). To assess if Chordin-FLAG-sfGFP/-Dendra2 have similar dorsalizing activity as untagged constructs, embryos were injected with each construct at equimolar concentrations, and their phenotypes were scored at 1 dpf. We found that overexpression of the fluorescent Chordin constructs caused dorsalization in embryos comparable to untagged Chordin (Figure 1.14B). This suggests that the fluorescent Chordin constructs are biologically active. Next, to investigate if the fluorescent Chordin constructs are processed in the embryo similar to constructs with a small FLAG tag, embryos were injected with FLAG-tagged fluorescent constructs and were subsequently analysed using Western blot. The Chordin-FLAG cellular fraction had a strong band at 130 kDa, which is the predicted side of the full-length Chordin (Figure 1.14C). In the extracellularly enriched fractions, cleaved Chordin-FLAG products were present as faint bands with the most abundant product at 100 kDa. In the Chordin-FLAG-sfGFP/-Dendra2, the full-length unprocessed product was at 150 kDa, which was more abundant in the cellular fractions, and the cleaved Chordin-FLAG-sfGFP/-Dendra2 products were more abundant in the extracellularly enriched fractions. This suggests that the fluorescent Chordin fusion constructs are cleaved in line with previous reports of Chordin processing (Piccolo et al., 1997). Altogether, the results suggest that our fluorescent Chordin constructs have similar biological activity as wild-type constructs, and that the fluorescent proteins are processed similarly to Chordin with a small FLAG tag.

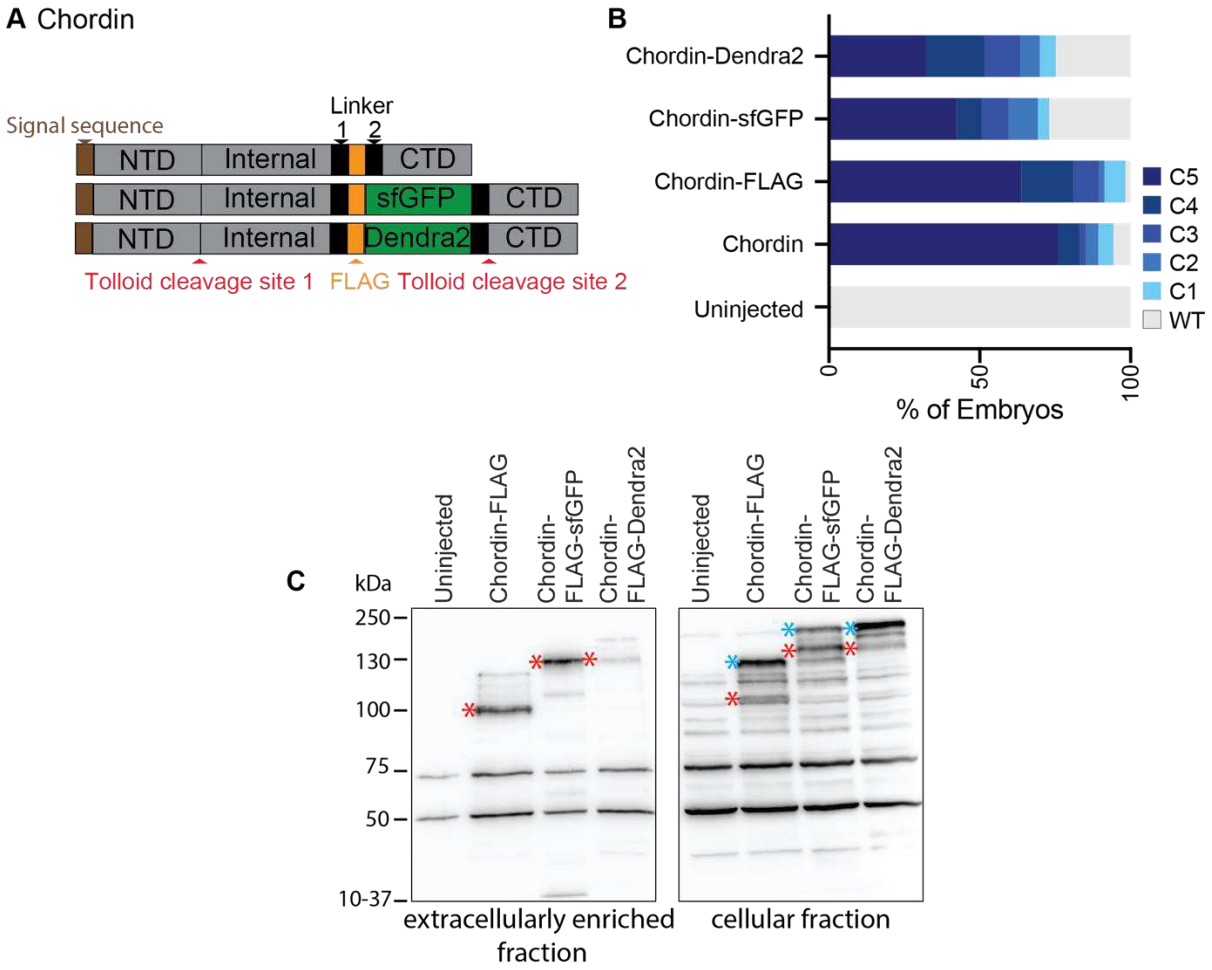

Figure 1.14 Zebrafish fluorescent Chordin constructs are functional and processed similarly to expected wild-type constructs.
A) Schematic of Chordin adapted from Pomreinke et al. (2017). **B)** Embryos were injected with *chordin* (30 pg), n = 159; *chordin-FLAG* (30 pg), n = 58; *chordin-sfGFP* (36.9 pg), n = 141; *chordin-Dendra2* (36.6 pg), n = 153, or left uninjected, n = 159. The phenotypes were scored at 1 dpf, and the graph was from a combination of four experimental trials, except for Chordin-FLAG that was from one experimental trial. **C)** Cellular and extracellularly enriched fractions of embryos injected with the FLAG-tagged Chordin constructs were analysed using Western blot with anti-FLAG antibody. The full-length unprocessed proteins are indicated with blue asterisks, and the processed proteins are indicated with red asterisks.

Sizzled

Next, Sizzled is a negative feedback regulator of BMP (Yabe et al., 2003). It inhibits Tolloid via competitive inhibition against Chordin. Since Sizzled does not have enzymatic functions nor is it enzymatically cleaved (Lee et al., 2006; Mullins, 1998), the fluorescent proteins were placed at the C-terminal end of Sizzled (Figure 1.15A) (Pomreinke et al., 2017). To assess whether Sizzled-FLAG/-sfGFP have similar dorsalizing activity as untagged constructs, embryos were injected with each construct at equimolar concentrations, and their phenotypes were scored at 1 dpf. We found that

overexpression of Sizzled-sfGFP constructs caused dorsalization in embryos comparable to untagged Sizzled (Figure 1.15B). This suggests that the Sizzled-sfGFP construct is biologically active. Next, to investigate if the Sizzled-sfGFP is processed in the embryo similar to constructs with a small FLAG tag, embryos were injected with FLAG-tagged fluorescent construct and were subsequently analysed using Western blot. Comparing cellular fractions and extracellularly enriched fractions, the results suggest that Sizzled-FLAG and Sizzled-FLAG-sfGFP were translated as full-length proteins without cleaved versions as predicted (Figure 1.15C). One exception was, in the Sizzled-sfGFP lane, there was a band at 37 kDa. Since this band was in the cellular fraction only, this was perhaps degraded Sizzled-sfGFP. Overall, the results suggest that Sizzled-sfGFP has similar biological activity as wild-type constructs and is processed similarly to Sizzled containing a small tag such as FLAG tag.

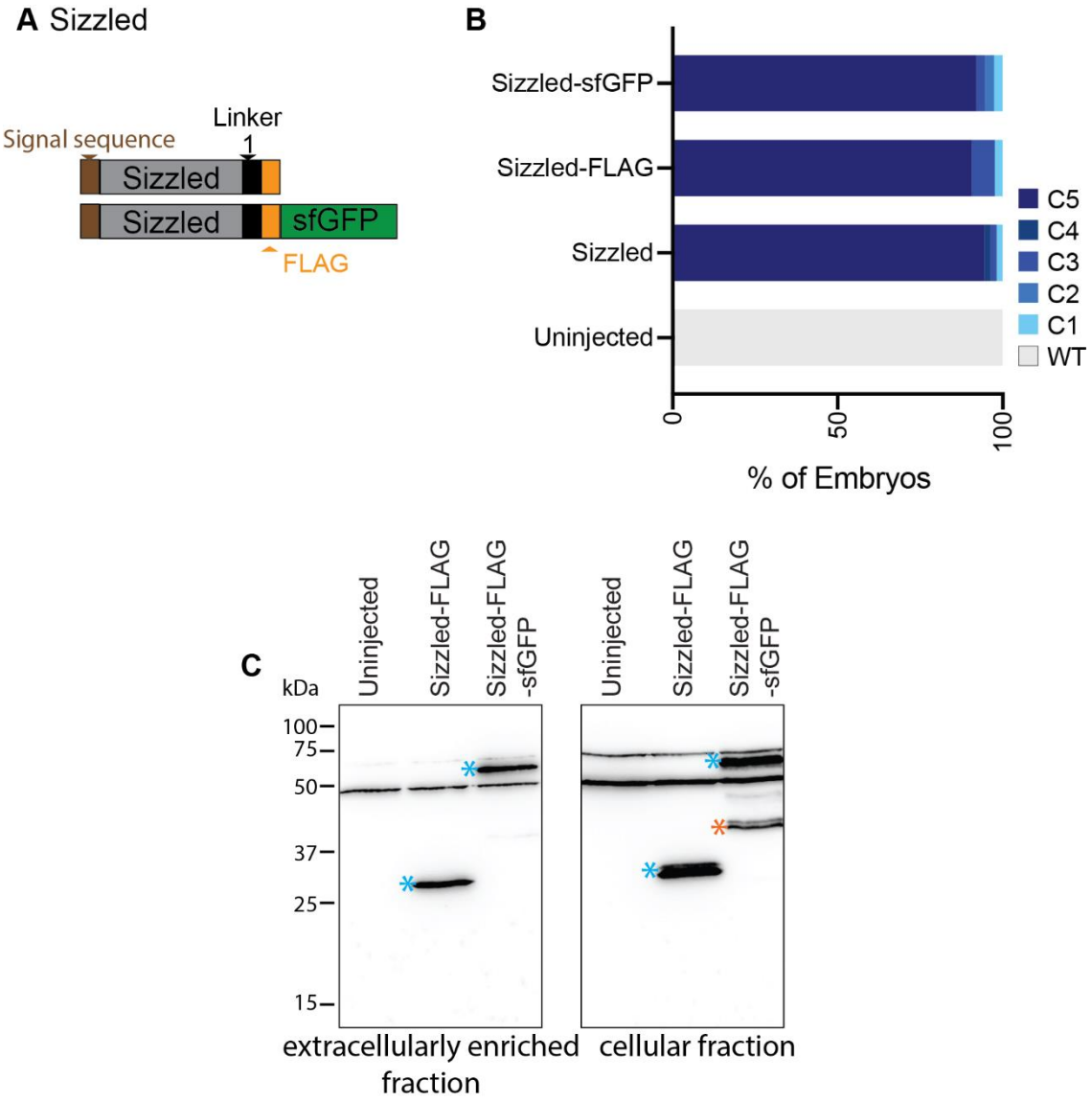

Figure 1.15 Zebrafish fluorescent Sizzled constructs are functional and processed similarly to expected wild-type constructs.
A) Schematic of Sizzled adapted from Pomreinke et al. (2017). **B)** Embryos were injected with *sizzled* (2.5 pg), n = 55; *sizzled-FLAG* (2.57 pg), n = 43; *sizzled-sfGFP* (4.07 pg), n = 38, or left uninjected, n = 13, and their phenotypes were scored at 1 dpf. **C)** Cellular and extracellularly enriched fractions of embryos injected with Sizzled constructs were analysed using Western blot with anti-FLAG antibody. The full-length proteins are indicated with blue asterisks, and the degraded protein is indicated with an orange asterisk.

ADMP

To define the biophysical properties of ADMP, we designed different fluorescently-tagged ADMPs and functionally characterised them. We initially based the positioning of the fluorescent tag in ADMP on Plouhinec et al. (2013) in which 11 amino acids SVDYDERGEKM were between the cleavage site RSSR and linker 1 (Figure 1.16A-B). There was one band for the unprocessed ADMP for all 11 aa

versions at 49 kDa and 70 kDa (blue asterisks). This suggests that the full-length ADMP is translated. However, in the extracellularly enriched fractions, the processed mature ADMP-FLAG and ADMP-sfGFP/-Dendra2 had at least two bands – indicative of two products present (red asterisks). This suggests that ADMP has 2 versions of the mature domain, or that the ADMP is sequentially processed. Additionally, ADMP-FLAG-sfGFP-11aa had multiple bands at 17, 25, 30, 35, 40, and 45 kDa, which suggests that ADMP-FLAG-sfGFP may be degraded. In a separate trial, multiple bands were also detected with anti-GFP antibody (Figure 1.16B). This further suggests that the ADMP-sfGFP-11-aa is being degraded with sfGFP detected at 25 kDa. Another possibility is that the ADMP-sfGFP-11aa had a greater amount of protein product than ADMP-FLAG and ADMP-Dendra2, and so the degraded products of ADMP-FLAG and ADMP-Dendra2 were below detection. This suggests that either ADMP is differently processed post-translationally compared to BMP2b in wild-type conditions, or the tag hinders the correct post-translational processing of ADMP. Furthermore, the phenotypes observed in ADMP-sfGFP and untagged ADMP were not consistently comparable in each experimental trial (Figure 1.16C-D). For example, in one trial, embryos injected with untagged *admp* were all ventralized, while those injected with tagged *admp* were either dorsalized or ventralized (Figure 1.16C). Then in a separate trial, embryos injected with *admp*, *admp-sfGFP*, and *admp-Dendra2* were ventralized and dorsalized, but those injected with *admp-FLAG* were only dorsalized (Figure 1.16D). Altogether, the fluorescently-tagged ADMP exhibited bipotential effects similar to untagged ADMP; however, we could not conclude whether these constructs are representative of untagged ADMP due to the differences in how the different fluorescent ADMP versions are post-translationally processed.

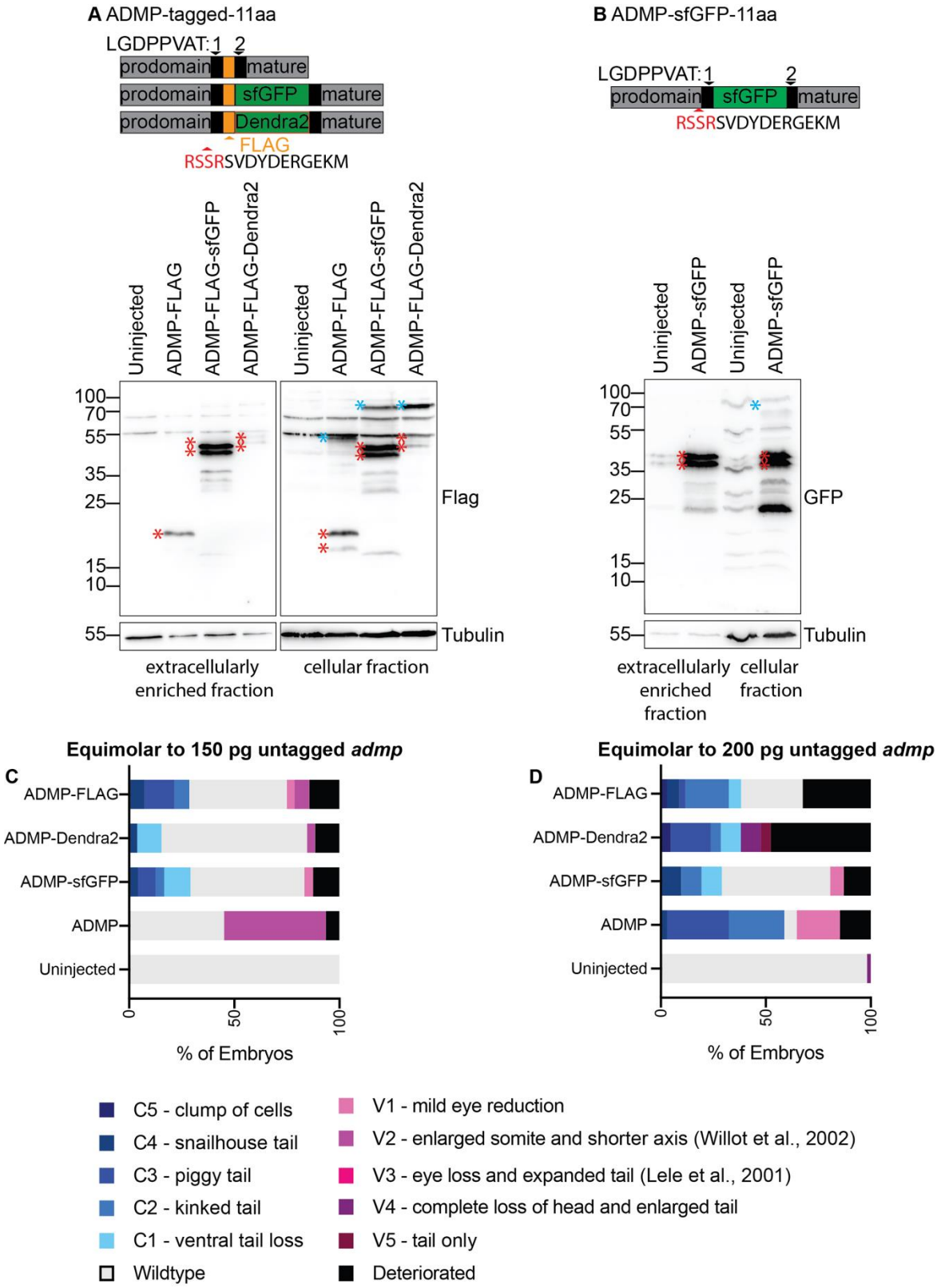

Figure 1.16 ADMP fluorescent constructs designed based on Plouhinec et al. (2013) did not have similar biological activity as untagged ADMP.

A) Embryos were injected at the one-cell stage with equimolar amounts of *admp* fluorescent fusion constructs mRNA and deyolked at the sphere stage. Animal caps were separated into cellular and extracellularly enriched fractions. Samples were analysed using Western blot and detected with anti-FLAG antibody. The full-length unprocessed proteins are indicated with blue asterisks, and the processed proteins are indicated with red asterisks. The membrane was stripped and probed with anti-tubulin

antibody as a loading control. **B)** Embryos were injected with *admp-sfGFP-11aa* in a similar procedure as (A) and probed with anti-GFP antibody. **C-D)** Phenotypic scores of the ADMP fluorescent constructs injected at equimolar concentrations to (C) 150 pg or (D) 200 pg of untagged *admp* mRNA. C) *admp,* n = 31; *admp-sfGFP*, n = 24; *admp-Dendra2*, n = 26; *admp-FLAG*, n = 28, or left uninjected, n = 16. D) *admp*, n = 56; *admp-sfGFP*, n = 31; *admp-Dendra2*, n = 21; *admp-FLAG*, n = 34, or left uninjected, n = 56.

Therefore, we tested additional constructs with the fluorescent protein inserted one amino acid downstream of RSSR (ADMP-sfGFP-1aa) and another construct based on the previously reported zebrafish MYC-tagged ADMP (Willot et al., 2002) in which the tag was placed 5 amino acids downstream of RSSR (ADMP-sfGFP-5aa) (Figure 1.17A). Compared to ADMP-sfGFP-11aa, which had 2 processed 'mature' bands (Figure 1.16A, Figure 1.17A) , there was one processed band for the 5aa and 1aa versions (Figure 1.17B). However, phenotypic scores of 1aa and 5aa indicate that the fluorescently-tagged construct did not recapitulate untagged ADMP activity (Figure 1.17C-D). Taken together, the results from the characterisation of fluorescent ADMP constructs are inconclusive, so we could not directly quantify the biophysical properties of fluorescent ADMP.

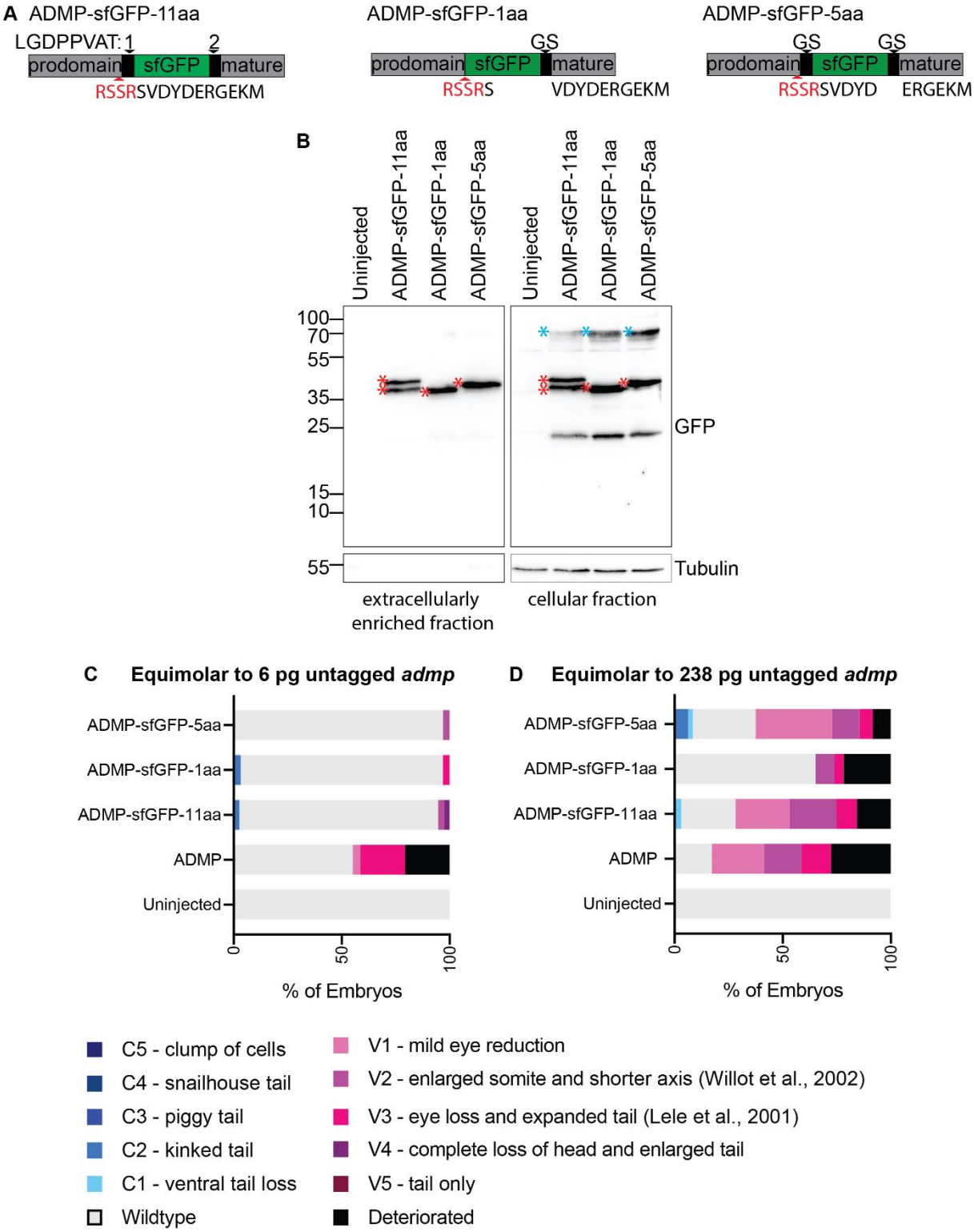

Figure 1.17 Redesigned ADMP fluorescent constructs did not have similar biological activity as untagged ADMP.

A) Two additional ADMP-sfGFP constructs were designed in which the linker was shortened to GS, and the number of residues between the prodomain and sfGFP was altered. **B)** Embryos were injected at the one-cell stage with equimolar amounts of fluorescent *admp-sfGFP* constructs and deyolked at the sphere stage. Animal caps were separated into cellular and extracellularly enriched fractions. Samples were analysed using Western blot and detected with anti-GFP antibody. The full-length unprocessed proteins are indicated with blue asterisks, and the processed proteins are indicated with red asterisks. The membrane was stripped and probed with anti-tubulin

antibody as a loading control. **C-D)** Phenotypic scores of the ADMP fluorescent constructs injected at equimolar concentration to (C) 6 pg or (D) 238 pg of untagged *admp*. C) *admp*, n = 29; *admp-sfGFP-11aa*, n = 38; *admp-sfGFP-1aa*, n = 31; *admp-sfGFP-5aa*, n = 32, or left uninjected, n = 25. D) *admp*, n = 29; *admp-sfGFP-11aa*, n = 32; *admp-sfGFP-1aa*, n = 23; *admp-sfGFP-5aa*, n = 48, or left uninjected, n = 12.

Discussion

Summary of the biophysical properties of fluorescently-tagged BMP2b, Chordin, and Sizzled

To sum up, Models 1-5 have conflicting assumptions about whether or not BMP and Chordin are diffusible molecules (poorly/highly diffusible, equally diffusible, differently diffusible); whether or not Chordin can modulate the distribution of BMP; whether or not Chordin and BMP have differences in degradation rates; and for Models 3-5, whether or not additional factors such as Sizzled, Tolloid, and/or ADMP can modulate the interaction between BMP and Chordin (Pomreinke et al., 2017). To test these different assumptions, my colleagues performed the following quantitative fluorescent assays (Figure 1.18) using the fluorescently-tagged BMP2b, Chordin, and Sizzled constructs that I characterised. I recapped their results from Pomreinke et al. (2017) below and in Table 1.1.

BMP- and Chordin-fluorescent constructs form a gradient in the extracellular space

First, to determine if BMP and Chordin are mobile in the extracellular space, we measured gradient formation kinetics from a local morphogen source by performing clonal transplantation and time-lapse imaging with light sheet microscopy (Pomreinke et al., 2017). Briefly, a set of donor wild-type embryos were injected with either *bmp2b-sfGFP* or *chordin-sfGFP* (Figure 1.18A). Then cells from donor embryos were transplanted into uninjected host embryos, which were subsequently imaged 20-70 min post-transplantation (Pomreinke et al., 2017). We found that both BMP2b-sfGFP and Chordin-sfGFP were secreted, diffused from the clone, and formed protein gradients within one hour (Table 1.1), which coincides with the BMP signalling dynamics necessary to generate a BMP signalling peak in wild-type embryos from 4 hpf to 5 hpf (Figure 1.6) (Pomreinke et al., 2017). This suggests that BMP ligands and inhibitor Chordin readily diffuse in the extracellular space for dorsal-ventral patterning. This finding that BMP2b-sfGFP is diffusible is in contrast with Model 1, which postulates that BMP ligands do not diffuse (Figure 1.4B) (Pomreinke et al., 2017;

Ramel & Hill, 2013), but the finding is more consistent with Model 2 (Figure 1.4C) (Pomreinke et al., 2017; Zinski et al., 2017). In addition, we found that the distance from the clone in which the signal drops to 50% was farther in Chordin-sfGFP (at 50-60 μm) than in BMP2b-sfGFP (at 30-40 μm); therefore, Chordin-sfGFP had a moderately longer range than BMP2b-sfGFP (Pomreinke et al., 2017). This suggests that Chordin-sfGFP is either more diffusible or more stable than BMP2b-sfGFP. To determine whether the difference in gradient formation kinetics is due to a difference in diffusion or stability, we performed the following experiments.

BMP- and Chordin-fluorescent constructs have moderate differences in local and global diffusivities

The models assume different diffusivities for BMP and Chordin, ranging from both with low diffusion (Model 4: Self-regulating reaction-diffusion system) to a large difference such that Chordin is required for facilitated diffusion of BMP (Model 3: Shuttling) (Pomreinke et al., 2017). To test these assumptions, we first determined the local diffusivities of BMP2b-sfGFP and Chordin-sfGFP using fluorescence correlation spectroscopy (FCS) (Pomreinke et al., 2017). In brief, FCS measures the local diffusion in small observation volumes such as the extracellular space at a distance from cells' surface (Müller et al., 2013; Ng et al., 2018) (Figure 1.18B i). It detects and records the inherent fluctuations in the fluorescent signal. From these fluctuation data, information about the transit time of fluorescent molecules through the observation volume can be extracted to determine the local diffusion rates of a given fluorescently-tagged protein. We found that the free diffusion coefficient for BMP2b-sfGFP was 46 ± 1 $\mu m^2/s$ and for Chordin-sfGFP was 59 ± 2 $\mu m^2/s$ (Figure 1.19, Table 1.1). These results suggest that, in small volumes away from the cell surface, BMP2b-sfGFP and Chordin-sfGFP have high diffusivities (Pomreinke et al., 2017).

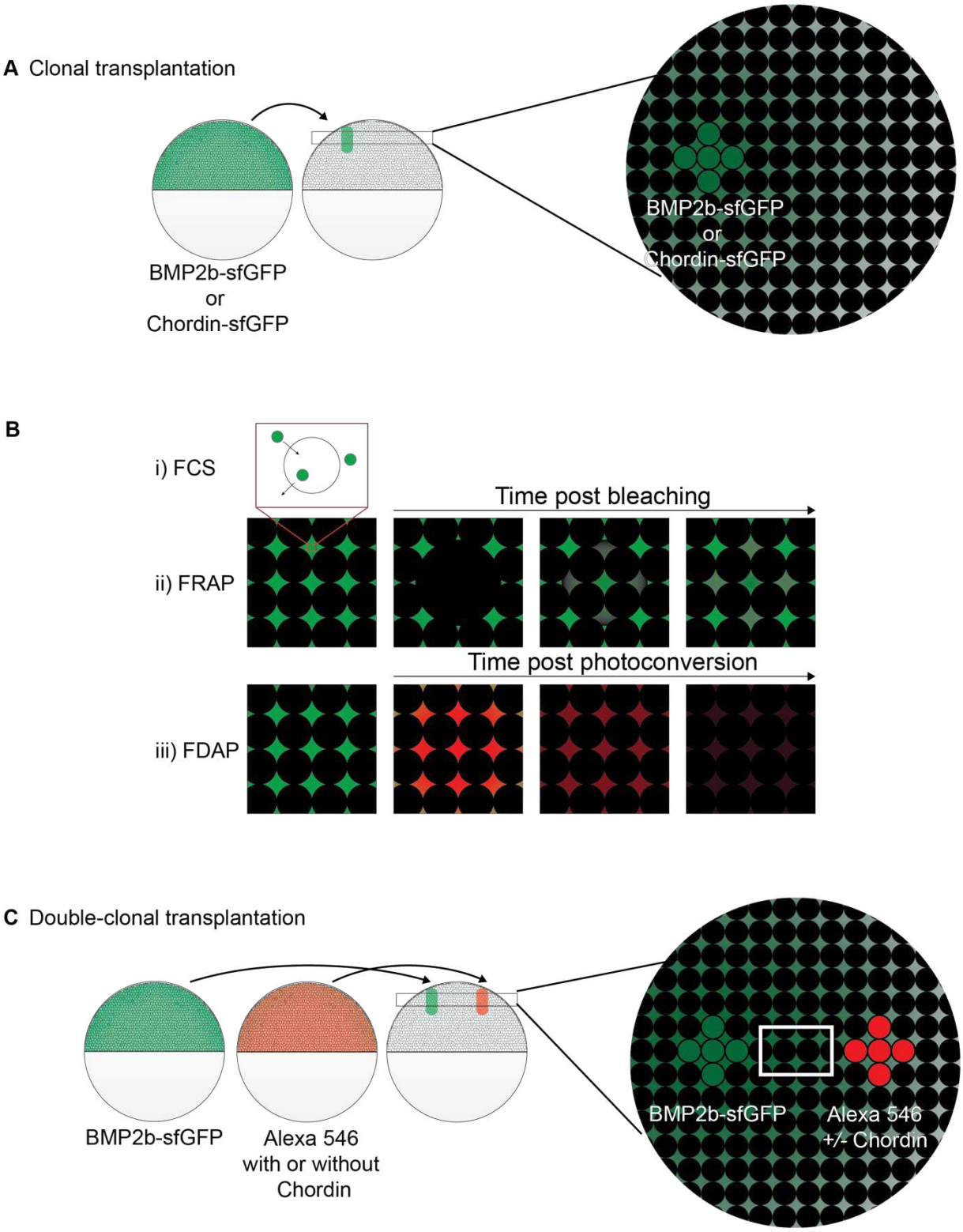

Figure 1.18 Schematics of clonal transplantations, FCS, FRAP, and FDAP experiments in Pomreinke et al. (2017) to measure the biophysical properties of fluorescent BMP2b, Chordin, and Sizzled in zebrafish embryos.
A) For clonal transplantation, cells from donor embryos injected with either *bmp2b-sfGFP* or *chordin-sfGFP* are transplanted to uninjected host embryos. Donor cells (green circles) express and secrete fluorescently-tagged proteins into the extracellular

space, which then diffuse to form a gradient in the extracellular space across host cells (black circles). **B) i**) Local diffusivities of fluorescently-tagged proteins away from cells can be measured in small observation volumes using FCS. **ii**) Embryo-wide diffusivities of fluorescently-tagged proteins can be measured using FRAP. Embryos expressing GFP-tagged proteins are bleached at the centre, and the recovery of the fluorescence in the centre is quantified. **iii**) The stability of BMP or Chordin can be inferred by measuring the degradation of Dendra2-tagged proteins using FDAP. Embryos expressing Dendra2-tagged proteins are photoconverted from green to red, and the decay of fluorescent signal is measured. **C)** For double-clonal transplantation, cells from donor embryos injected with *bmp2b-sfGFP* (green) and from those injected with Alexa 546 dextran (red) with or without *chordin* are transplanted into one host embryo. The gradient formation kinetics of BMP2b-sfGFP can be measured (white box) in the absence or presence of Chordin.

In terms of BMP and Chordin diffusion embryo-wide, other factors can modify the mobility of these molecules. For example, BMP and Chordin may interact with extracellular matrix proteins and membrane-bound proteins (Müller et al., 2013; Rogers & Schier, 2011). Therefore, to test how these local diffusion coefficients translate to embryo-wide diffusion, we determined the effective diffusivities of BMP2b-sfGFP and Chordin-sfGFP in zebrafish embryos using Fluorescence Recovery After Photobleaching (FRAP) (Müller et al., 2012; Pomreinke et al., 2017). In brief, FRAP is a method to measure the diffusion of fluorescently-tagged proteins (Figure 1.18B ii) (Carisey et al., 2011). A region-of-interest is irreversibly bleached in an embryo with a uniform expression of fluorescently-tagged proteins. Then the recovery of the fluorescence within the region-of-interest is measured (Carisey et al., 2011; Pomreinke et al., 2017). We found that the effective diffusion coefficient for BMP2b-Dendra2 was 2.0 ± 0.4 $\mu m^2/s$; BMP2b-sfGFP was 2.6 ± 0.7 $\mu m^2/s$; Chordin-Dendra2 was 6.0 ± 0.7 $\mu m^2/s$, and Chordin-sfGFP was 7.3 ± 3.9 $\mu m^2/s$ (Pomreinke et al., 2017) (Table 1.1). The observed difference between the local free diffusion and the global effective diffusion suggests that there are additional molecular players that hinder BMP2b and Chordin's mobility, such as extracellular matrix proteins (Rogers & Schier, 2011). In addition, these FRAP results suggest that there is a difference in the effective diffusion of BMP2b and Chordin. This is consistent with the moderate difference between their gradient formation kinetics from a local morphogen source (Figure 1.18A, Table 1.1). Together, these results are in line with the assumptions of Model 2: Graded-sink with mobile BMP since BMP is diffusible and with Model 4: Self-regulating reaction-diffusion system since BMP and Chordin have relatively low effective diffusion. This is in contrast to Model 3: Shuttling that assumes there is a large difference in the diffusion

coefficient between BMP and Chordin in that BMP ligands are poorly diffusible unless bound by Chordin.

BMP- and Chordin-fluorescent constructs have moderate differences in protein stability

Next, the models assume differences in protein stability between BMP and Chordin, ranging from equal protein stabilities (Model 4) to a more stable BMP than Chordin (Model 3 and Model 5) (Pomreinke et al., 2017). Therefore, to determine the protein stability *in vivo*, we applied fluorescence decay after photoconversion (FDAP) (Figure 1.18B iii) (Pomreinke et al., 2017). Recall that we developed BMP2b-Dendra2 and Chordin-Dendra2 constructs (Figure 1.13-1.14) because Dendra2 is a green-to-red photoconvertible fluorescent tag (Chudakov et al., 2007). In FDAP, a subset of Dendra2-tagged proteins can be photoconverted by short light exposure and, subsequently, the decay of these pulse-labelled proteins can be measured (Bläßle & Müller, 2015; Rogers et al., 2015) (Figure 1.18B iii). We found that BMP2b-Dendra2 and Chordin-Dendra2 had half-lives of 130 min and 120 min, respectively (Table 1.1) (Pomreinke et al., 2017). This suggests that BMP2b and Chordin have similar protein stabilities. Therefore, this suggests that the difference in BMP2b-sfGFP and Chordin-sfGFP protein distribution range can be attributed to the differences in their effective diffusion coefficients rather than differences in their stability. This result is in line with Model 4, but it does not support Model 3 and Model 5's assumption of BMP as a more stable protein than Chordin *in vivo*.

Chordin does not affect BMP diffusivity

As previously mentioned, Model 3 predicts that Chordin modulates BMP diffusion to shuttle BMP to the ventral side. Therefore, to determine whether the BMP diffusion rate increases in the presence of Chordin, we also measured the diffusion of fluorescently-tagged BMP2b in embryos overexpressing untagged Chordin using FRAP (Pomreinke et al., 2017). We found that the diffusion of BMP2b-Dendra2 was 2.2 ± 0.2 $\mu m^2/s$ and BMP2b-sfGFP was 2.8 ± 0.7 $\mu m^2/s$ in embryos overexpressing Chordin, which were not largely different from embryos without Chordin overexpression (Table 1.1) (Pomreinke et al., 2017). This suggests that Chordin does not enhance BMP2b diffusion.

To further test if Model 3's proposal of Chordin's role in shuttling BMP to establish a steeper BMP gradient, we used double-clone transplantations with the first clone producing BMP2b-sfGFP and the second clone producing untagged Chordin (Figure 1.18C) (Pomreinke et al., 2017). To quantify the BMP2b-sfGFP gradient formation kinetics between the two clones, we then performed time-lapse imaging using light sheet microscopy. We found that the BMP2b-sfGFP protein gradient was mildly steeper adjacent to Chordin-expressing clones; however, this minor difference could not account for the BMP signalling dynamics required for zebrafish dorsal-ventral patterning (Pomreinke et al., 2017). Together, these findings do not support Model 3's assumption that Chordin facilitates BMP2b diffusion.

Sizzled-fluorescent construct diffusivity is within the same order of magnitude as BMP2b and Chordin

Moreover, as previously mentioned, Model 4 and Model 5 postulate that ADMP and Sizzled have regulatory roles in modulating the BMP signalling gradient (Francois et al., 2009; Inomata et al., 2013; Pomreinke et al., 2017). ADMP and Sizzled are proposed to be essential for scale-invariant patterning (Inomata et al., 2013) and for adapting to fluctuations in the environment (Francois et al., 2009). Model 4 postulates ADMP and Sizzled diffusion coefficients are 25-fold greater than that of BMP and Chordin, while Model 5 postulates equal diffusivities for all four components. To determine the diffusion coefficients of ADMP and Sizzled, recall that we fused sfGFP to ADMP (Figure 1.16-1.17) and Sizzled (Figure 1.15A). We succeeded in developing Sizzled-sfGFP with activity comparable to untagged Sizzled, but the results for fluorescent ADMP fusion constructs were inconclusive (Pomreinke et al., 2017). Using FRAP, we found that the effective diffusivity of Sizzled-sfGFP was 9.7 ± 3.2 $\mu m^2/s$ (Table 1.1) (Pomreinke et al., 2017). This illustrates that the diffusion coefficients of BMP2b-sfGFP (2.6 ± 0.7 $\mu m^2/s$), Chordin-sfGFP (7.3 ± 3.9 $\mu m^2/s$), and Sizzled-sfGFP (9.7 ± 3.2 $\mu m^2/s$) were all within the same order of magnitude (Pomreinke et al., 2017). This finding is more in line with Model 5 that assumes equal diffusivities for all three components, but not Model 4 that assumes a 25-fold diffusion coefficient for Sizzled compared to BMP and Chordin. In addition, a relatively higher effective diffusion coefficient for Sizzled than Chordin corroborates with the current findings that in the *sizzled* mutants, there is a minor increase in BMP signalling in the dorsal side but not

in the ventral side (Figure 1.7E-F). This suggests that Sizzled can readily diffuse from the ventral-most to the dorsal-most regions.

A graded source-sink mechanism in zebrafish embryos and beyond

The main aim of this chapter was to investigate which of the current models best fit how the BMP signalling gradient is shaped to pattern the dorsal-ventral axis of the zebrafish embryo. To do so, we quantified BMP signalling upon loss-of-function of each component and also used quantitative fluorescence assays to measure the biophysical parameters of fluorescently-tagged versions of the BMP2b, Chordin, and one accessory protein, Sizzled (Pomreinke et al., 2017). First, we found that fluorescently-tagged BMP2b readily diffused in the extracellular space from transplanted clones, which does not support Model 1: Graded-source sink with immobile BMP (Table 1.1). Second, our finding that fluorescently-tagged BMP2b and Chordin both have comparably low diffusivity and similar protein stabilities does not support Model 3: Shuttling and Model 5: Long-range accumulation and feedback (Table 1.1). Third, our finding that the effective diffusion coefficient of Sizzled-sfGFP is within the same order of magnitude as BMP2b-sfGFP and Chordin-sfGFP does not support Model 4: Self-regulating reaction-diffusion system (Table 1.1). Fourth, our observation that in the absence of Chordin, the BMP signalling gradient expands to dorsal-lateral regions without affecting ventral/dorsal-most regions rules out Model 3 (Figure 1.7C, Table 1.1, Figure 1.19). Specifically, Chordin does not redistribute BMP to the ventral side of the embryo to generate a signalling peak. However, Tolloid enhances the BMP signalling peak up to the ventral-most region, which further suggests that Chordin acts as a long-range inhibitor (Figure 1.19). Finally, the BMP signalling gradient slope along the lateral regions is further refined by Sizzled (Figure 1.19). Therefore, our observations are mostly in line with Model 2, which describes the interaction between BMP and Chordin as a graded source-sink mechanism with both molecules diffusible (Pomreinke et al., 2017; Zinski et al., 2017). However, some of our results highlight how the Graded source-sink model with mobile BMP can be expanded to also account for the contribution of other accessory proteins, and how we have yet to define the role of diffusion for a reproducible, scale-invariant dorsal-ventral patterning.

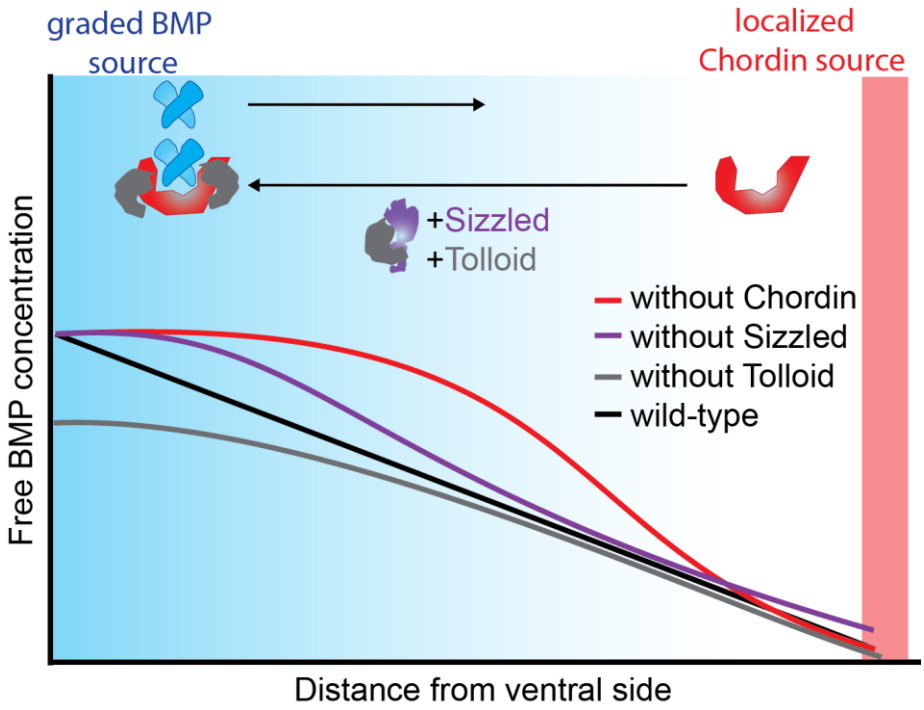

Figure 1.19 A graded source-sink model best fits experimental findings of the BMP ligand dynamics in zebrafish embryos.
This model describes a ventrally-biased graded expression of BMP (blue background) and dorsally-localised expression of its inhibitor Chordin (red bar). Both BMP and Chordin are diffusible. Chordin acts as a sink to bind BMP. The BMP signalling gradient is further refined by Sizzled and Tolloid. The lines show the resulting free BMP ligand distribution upon loss-of-function of the individual components.

First, our findings suggest that both Sizzled and Tolloid generate a steeper gradient in the ventral-lateral regions (Figure 1.7E-H). Our result is contrary to findings in Tuazon et al. (2020) that BMP signalling is not affected in either mutant. This difference may be due either to the developmental stage examined (before versus right at shield stage) or to the imaging techniques and quantified embryonic region – i.e. confocal imaging and average pSmad1/5/9 marginal intensities (Tuazon et al., 2020) versus light sheet microscopy and quantified pSmad1/5/9 throughout the whole animal cap. Future work would require additional experimental trials with a larger sample size of stage-matched embryos to compare the two imaging techniques. Nevertheless, the mutant phenotypes indicate that the additional refinement of the BMP signalling gradient by Sizzled and Tolloid may improve the accuracy of the positional information to instruct cells. This may be essential for reproducible and robust patterning by reducing misinterpretation of the signalling gradient. For example, in *sizzled*/*tolloid* double mutants, loss-of-function of both genes led to 63% of progeny exhibiting wild-type phenotype, and the remaining embryos were either dorsalized or ventralized (Wagner & Mullins, 2002). From an evolutionary perspective, the presence of Tolloid

and Sizzled may increase the evolutionary fitness of zebrafish. After all, with a substantial proportion of the progeny exhibiting abnormal development, the zebrafish would have poor reproductive success. In that sense, without Sizzled and/or Tolloid, the BMP-Chordin system may be sufficient for the proper patterning of zebrafish embryos, but the system is unstable. Therefore, the Graded source-sink model with mobile BMP can incorporate Model 5 in which Sizzled and Tolloid function as a feedback mechanism.

Second, I have shown that ADMP can potentially act as a biphasic modulator in which overexpression of ADMP can cause ventralization and dorsalization and has the potential for long-range signalling independent of Chordin and BMP2b (Figure 1.9-Figure 1.12). Similarly, upon overexpression of *admp*, *chordin* mutants developed cranial structures and did not have expanded blood islands (Figure 1.11). I have also shown that ADMP is a weaker activator of pSmad1/5/9 than BMP2b (Figure 1.12). Overall, the findings suggest that ADMP may function to pattern dorsal and lateral embryonic domains that give rise to somites and neural tissue, and that ADMP cannot activate sufficient pSmad1/5/9 for the development of ventrally-derived structures. This is in line with the findings of Willot et al. (2002) that ADMP has distinct functions from BMP2b and BMP7a. In the next steps, we can assess which target genes are regulated by ADMP at different concentrations.

Additionally, our results on ADMP fluorescent constructs are inconclusive since there were different ADMP mature products and since the fusions did not fully mimic untagged ADMP when injected at equimolar concentrations (Figure 1.16-1.17). While we currently do not know what these products are, previous studies have demonstrated that differential cleavage of *Xenopus* BMP4 at two Furin-cleavage sites causes differential activity and signalling range (Cui et al., 2001; Cui et al., 1998). Therefore, one possibility is that ADMP may be strictly processed post-translationally to regulate its signalling range. For example, ADMP and another ventrally-expressed BMP ligand Pinhead function in a see-saw-like manner to buffer fluctuations in BMP signalling in zebrafish (Yan et al., 2019), such that knockdown of *pinhead* caused a ventral expansion of *admp* expression. In that sense, different versions of ADMP could exist to function at short- and long-range distances. Future experiments could be to mutate the different Furin-cleavage sites in ADMP and assay the protein products and their activity range.

Furthermore, here, we have not found evidence for facilitated diffusion of BMP2b by Chordin, but we have yet to determine if Chordin shuttles ADMP as proposed by Ben-Zvi et al. (2008). By further understanding ADMP regulation, as well as Pinhead, and successfully designing fluorescent fusion constructs, we can determine the biophysical properties of ADMP and Pinhead and address questions such as: Do either ADMP or Pinhead diffuse or are there BMP regulators that shuttle ADMP ventrally and Pinhead dorsally to buffer against BMP signalling fluctuations?

Third, we have designed fluorescently-tagged BMP2b, Chordin, and Sizzled and determined that the fluorescent fusion constructs are mobile in the extracellular space. Additionally, we have shown that *bmp2b* mutants can be rescued with BMP2b-sfGFP and BMP2b-Dendra2 (Pomreinke et al., 2017), a similar finding to the rescue of mutants upon injection of untagged BMP2b (Kishimoto et al., 1997). These findings raise the following questions. First, how efficient are these mutant rescues? One future experiment is to rescue *bmp2b* mutant embryos from *bmp2b* mutant parent in-cross whose progenies are 100% *bmp2b* mutants. Second, how can homogenous expression of *bmp2b* and its tagged versions rescue mutants? A graded source-sink mechanism with Chordin may restore a BMP signalling gradient, but how can it support the progression of a dynamic BMP signalling gradient without an endogenous source of BMP2b? After all, it has been shown that BMP signalling is dynamic (Pomreinke et al., 2017; Tucker et al., 2008) and essential for proper patterning until 13 hpf (Hashiguchi & Mullins, 2013).

Leading to the final question: is diffusion essential for scale-invariant dorsal-ventral patterning? Our current measurements are based on the ectopic expression of each fluorescent construct, but these may not reflect the concentration of endogenous proteins. To that extent, knock-in lines can be used to address these questions. Recently, Dendra2 was knocked-in to the zebrafish *bmp2b* locus (He et al., 2020). The next step is to quantify BMP gradient formation throughout early development and assess whether the endogenous diffusion reflects our current measurements. Furthermore, to test the function of diffusion, membrane-tethered nanobodies (morphotraps) can be used to modulate the diffusion of fluorescent BMP and its regulators (Harmansa et al., 2017; Harmansa et al., 2015; Mörsdorf & Müller, 2019). In that way, we can also assess whether specific diffusion rates are essential for patterning by using nanobodies with varying binding affinities.

Similarly, it is yet to be determined how dorsal-ventral patterning is scaled in differently-sized embryos and how a graded source-sink BMP-Chordin system adjusts depending on the size of the embryos. Recent findings have shown that after reducing embryo size by 30%, germ layer patterning is preserved by the Nodal inhibitor, Lefty, which diffuses and regulates Nodal activity range (Almuedo-Castillo et al., 2018). However, scaling of tissue proportions failed in embryos in which the diffusion of Lefty is hindered. Hence, the diffusion of fluorescent BMP and its regulators could also be manipulated in smaller embryos using nanobodies to test whether diffusion is essential for scale-invariant dorsal-ventral patterning. Moreover, the role of each component in scaling the BMP signalling gradient can be tested by assaying whether dorsal-ventral patterning is restored in smaller embryos in different mutant backgrounds, such as *tolloid*, *sizzled*, *admp*, and *pinhead*.

To conclude, while the BMP-Chordin system in the zebrafish can be modelled as a graded source-sink in normal development (Figure 1.19), we have yet to consider the BMP signalling dynamics in different biological contexts, such as regeneration and secondary axis formation in the zebrafish and in other species. That is, we can envision that different models may be observed in different biological processes and species. Applications of gene-editing and *in toto* live-imaging can help unravel the BMP signalling dynamics in different biological contexts.

Chapter 2 – A Zswim homologue as a novel modulator of BMP signalling in Cnidaria and Bilateria

In the previous chapter, the focus was on how extracellular components of the BMP pathway contribute to robustly shape the BMP signalling gradient for dorsal-ventral patterning in the zebrafish. In this chapter, the focus is to provide insight into how the BMP-mediated body axis evolved. First, I will introduce the relationship between bilaterally symmetric organisms: bilaterians and anthozoa cnidarians. Then I will present how a previously uncharacterised zinc finger with SWIM domain 5 (Zswim5) may act as a potential intracellular modulator of the BMP signalling gradient in zebrafish embryos.

Introduction

BMP-mediated axis formation in Bilateria and Cnidaria

The majority of known animals are categorized into the clade Bilateria (Figure 2.1) (Finnerty, 2003; Genikhovich & Technau, 2017; Niehrs, 2010). Approximately 99% of the 2 million animals described so far are bilaterians (Ritchie, 2022). This includes prominent model organisms such as the fruit fly, zebrafish, mouse, and frog. Bilaterians share a general body plan in which organs are spatially arranged into a coordinate system consisting of two orthogonal body axes: the anterior-posterior axis and the dorsal-ventral axis (Figure 2.1) (Finnerty, 2003; Genikhovich & Technau, 2017; Niehrs, 2010). First, the anterior-posterior axis, also referred to as the primary axis, runs from cranial to caudal with through-gut or mouth-anus opening. Second, the dorsal-ventral axis or the secondary axis runs from back to belly. This spatial organization of tissues and organs along two defined body axes is not an inherent characteristic of all animals. For example, animals belonging to the phylum Porifera and Placozoa have specialized cells with a basic organization, but lack an evident body axis (Figure 2.1) (Musser et al., 2021; Schierwater & DeSalle, 2018), and animals belonging to the phylum Ctenophores are biradially symmetric with two planes of symmetry (Ryan & Baxevanis, 2007). Therefore, an outstanding evolutionary-developmental question is ‘How did the two axes arise?’. To address this question with a focus on BMP-mediated axis formation, I take a comparative molecular biology approach, in collaboration with the

lab of Dr. Grigory Genikhovich who studies the sister group of Bilateria called Cnidaria. The following is a brief comparison of the bilaterian and cnidarian basic body plan.

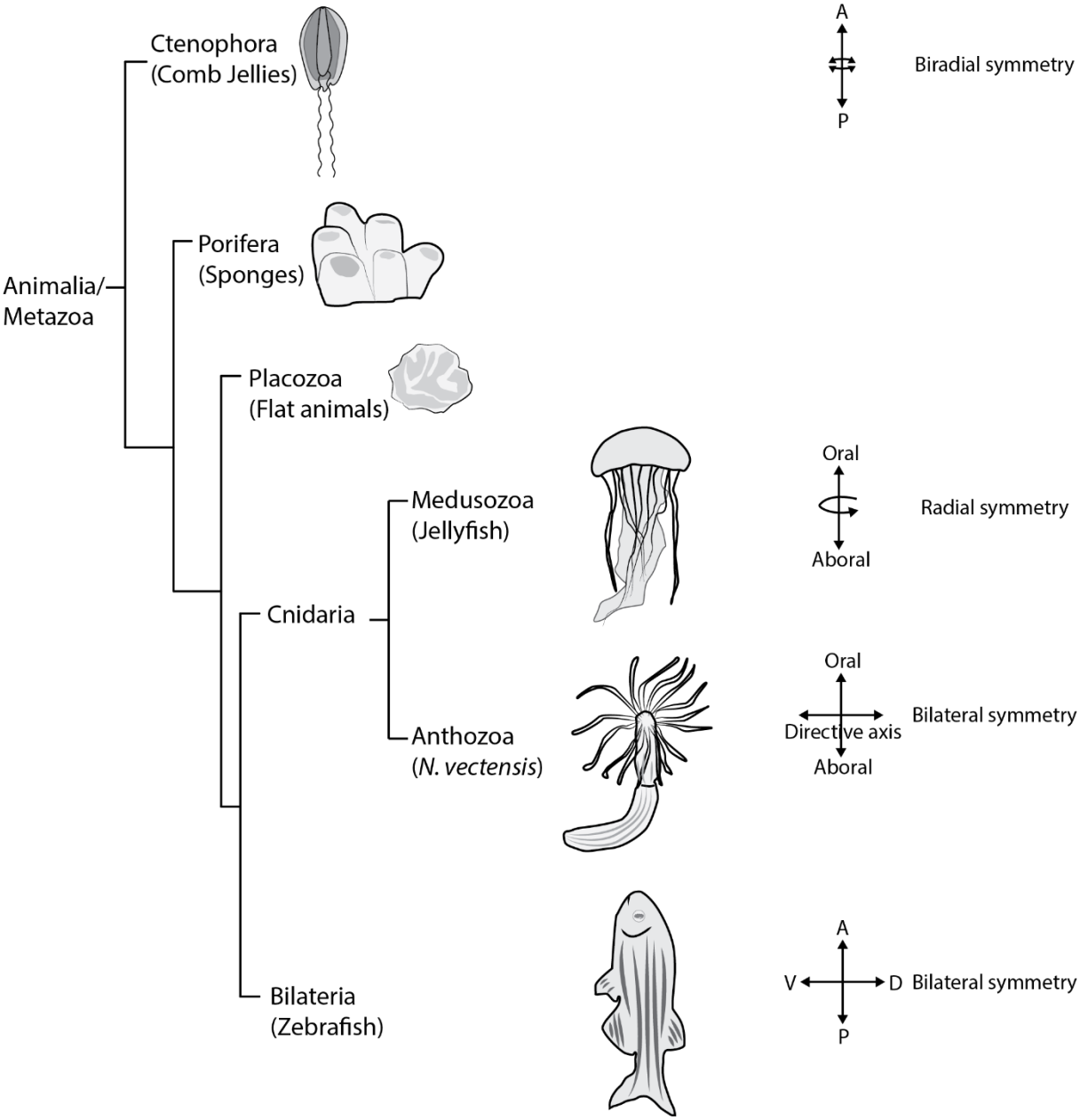

Figure 2.1 The phylogenetic tree of the animal kingdom with emphasis on Cnidaria and Bilateria and the corresponding coordinate system of their body axes.

Most animal body plans have distinguishable coordinate systems. Bilaterians, such as zebrafish, exhibit bilateral symmetry with two perpendicular body axes: anterior (A) to posterior (P) and dorsal (D) to ventral (V). These coordinates are often likened to the two orthogonal body axes of anthozoa cnidarians: the oral to aboral and the directive axis, such as those of the starlet sea anemone *Nematostella vectensis*. In contrast, medusozoa cnidarians, such as the jellyfish, are radially symmetric with only the oral to aboral axis. Other phyla such as Ctenophora have biradial symmetry, and others such as Porifera and Placozoa do not exhibit distinct body coordinates. This phylogenetic tree was designed based on Genikhovich and Technau (2017) and Whelan et al. (2017).

Bilateria and Cnidaria are considered phylogenetic sister groups that have evolved morphological differences (Figure 2.1) (Genikhovich and Technau, 2017). First, while all bilaterians are triploblastic with three germ layers, cnidarians are diploblastic with two germ layers, endoderm and ectoderm (Steinmetz et al., 2017). Second, most cnidarians only have one body axis – the oral-aboral axis. This axis is considered to be homologous to the bilaterian anterior-posterior axis (Genikhovich & Technau, 2017), as it is patterned by the staggered expression of *Hox* genes (Finnerty et al., 2004). Furthermore, instead of a second axis, most cnidarians exhibit radial symmetry (Genikhovich & Technau, 2017) that may appear as if the dorsal side wraps around the ventral side. Without a central nervous system, their neuronal-like cells are dispersed throughout their body (Nakanishi et al., 2012) around a columnar gut. Examples of these are hydras and jellyfish which belong to medusozoa cnidarians (Finnerty, 2003).

An exception is anthozoa cnidarians such as the sea anemones *Nematostella vectensis*, which are considered to have bilateral symmetry. Externally, they appear radially symmetric; however, internally, the gut cavity is asymmetric. This is evident by the orientation of a ciliated groove, called the siphonoglyph, that is only present on one side of the pharynx (Finnerty, 2003). Furthermore, the mesenteries, which are endodermal epithelium subdividing the gastric cavity, are also bilaterally oriented (Finnerty et al., 2004; Frank & Bleakney, 1976; Leclere & Rentzsch, 2014). Therefore, anthozoans have a secondary axis, called the directive axis, that is perpendicular to the primary oral-aboral axis.

Two main hypotheses that have been proposed regarding the emergence of the secondary body axis (Finnerty, 2003; Genikhovich & Technau, 2017). The first is that the common ancestor of Bilateria and Cnidaria had bilateral symmetry, and the cnidarians lost the secondary axis and evolved to have radial symmetry with the exception of anthozoa cnidarians. The second hypothesis is that the dorsal-ventral axis and the directive axis evolved independently through convergent evolution.

To gain insight into the emergence of a secondary body axis, one approach is to examine how evolutionarily conserved are the molecular mechanisms underlying the formation of the secondary axis in both animal phyla. Notably, orthogonal signalling gradients are the key developmental regulators involved in achieving bilateral symmetry in the sister groups (Niehrs, 2010). First, Wnt/β-catenin signalling is involved

in the formation of the primary axis: the oral-aboral axis in *Nematostella* and the anterior-posterior axis in bilaterians (Lebedeva et al., 2021). Second, for the secondary axis, BMP signalling via pSmad1/5/9 patterns the dorsal-ventral axis in bilaterians (Ramel & Hill, 2012) and the directive axis of *Nematostella* (Leclere & Rentzsch, 2014). Recall from Chapter 1 that BMP signalling peaks ventrally, and that *bmp* loss-of-function caused the loss of many organs except cranial structures in zebrafish embryos. Similarly, upon knockdown of *dpp*, *chordin*, *bmp5-8* (Saina et al., 2009), and another molecule called *Repulsive Guidance Molecule* (*rgm*) (Leclere & Rentzsch, 2014) with morpholinos, morphant *Nematostella* embryos fail to develop mesenteries and remained radially symmetric, thus demonstrating that BMP signalling is involved in patterning the endodermal layer and orienting the mesenteries. The conserved morphogen signalling between bilaterians and anthozoa cnidarians supports the hypothesis of a bilaterally symmetric common ancestor in which the BMP-mediated directive axis in anthozoa cnidarians and dorsal-ventral axis in bilaterians may be homologous. Therefore, the secondary axis may have been lost in radially symmetric medusozoa Cnidaria. However, to what extent the downstream BMP target genes directing the secondary axis formation in Bilateria and Cnidaria are conserved is yet to be examined. Do these phyla have conserved BMP target genes to establish a secondary axis?

The BMP target gene *zswim4-6* modulates the BMP signalling gradient in *Nematostella*

In search for evolutionarily conserved genes downstream of BMP signalling between bilaterian and cnidarian secondary axes, our collaborators performed a genome-wide search for direct BMP signalling targets via pSmad1/5 using *Nematostella* embryos. To do this, they performed chromatin immunoprecipitation sequencing (ChIP-seq) with an anti-pSmad1/5 antibody (see Knabl et al. (2022), Appendix C). Then the *Nematostella* pSmad1/5 targets were compared to available ChIP-seq data from bilaterian organisms: *Drosophila melanogaster* (Deignan et al., 2016) and *Xenopus laevis* (Stevens et al., 2017). They found that the majority of the shared genes are transcription factors and signalling molecules. Of these, there is a high ChIP enrichment of the gene *zswim4-6*, which encodes a previously uncharacterised zinc finger protein with a swim domain (nvZswim4-6). The *Xenopus* homologue *xzswim5* was also enriched in *Xenopus* ChIP-seq data (Stevens et al., 2017). Notably, SWIM domains contain SWI2/SNF2 and MuDR-type zinc fingers for

protein-protein and protein-DNA interactions in diverse organisms from archaea to eukaryotes (Makarova et al., 2002; Smith et al., 2014).

The relationship between nvZswim4-6 and BMP signalling was further analysed (Knabl et al., 2022). For example, expression analysis by *in situ* hybridization showed that *nvzswim4-6* expression domain overlaps with BMP signalling via pSmad1/5. In addition, loss of BMP signalling gradient by knockdown of either *bmp* or *chordin* abolished *nvzswim4-6* expression in the majority of the *Nematostella* embryos. Furthermore, in terms of nvZswim4-6 function, morpholino knockdown of *nvzswim4-6* caused the reduction of tentacles from 4 to 3 (Figure 2.2A, A') and the fusion of mesenteries (Figure 2.2B, B'). The morphant phenotype was linked to the flattened BMP signalling slope in the endoderm (Figure 2.2C, C', D). This, in turn, led to the misexpression of genes that are negatively regulated by BMP signalling, including the activator BMP2/4 and the inhibitor Chordin. Together, these results suggest that *nvzswim4-6* is a BMP target gene, which then acts as a BMP signalling modulator for tissue compartmentalisation in *Nematostella* by modulating the expression of BMP-repressed genes (Figure 2.3). Therefore, nvZswim4-6 may be contributing to the development of the directive axis in bilaterally symmetric anthozoa cnidarians. If the BMP-mediated secondary axis in bilaterians is homologous to the directive axis of cnidarians, then the next question is 'Do bilaterian Zswim4-6 homologues modulate BMP signalling for dorsal-ventral patterning in Bilateria?'.

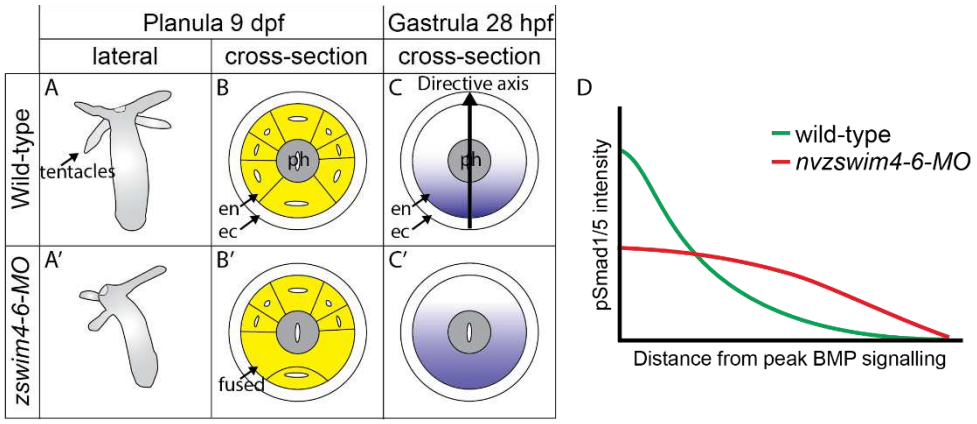

Figure 2.2 Knockdown of Zswim4-6 flattened the slope of the BMP signalling gradient in *Nematostella vectensis*.
A-A') Schematic of wild-type and *nvzswim4-6* morphants *Nematostella vectensis* at planula stage 9 dpf from the lateral view. A) Wild-type *N. vectensis* have 4 tentacles, but (A') *nvzswim4-6* morphants lose 1 tentacle (Knabl et al., in 2022). **B-B')** Schematic of a cross-section of the samples from (A-A') illustrate that (B) wild-type *N. vectensis* have 8 mesenteric compartments in the endoderm (en), but (B') *nvzswim4-6* morphants have 2 fused chambers. Ectoderm is depicted as the white outer layer. **C-C')** Schematic of BMP signalling gradient along the directive axis in (C) wild-type and (C') *nvzswim4-6* morphant *N. vectensis* at gastrula stage 28 hpf. Only the results of pSmad1/5/9 immunostaining (violet gradient) in the endoderm are depicted. **D)** Schematic of pSmad1/5 signalling gradient in (C-C'). BMP signalling was flattened upon the knockdown of *nvzswim4-6* compared to wild-type embryos. en - endoderm, ec - ectoderm, ph - pharyngeal ectoderm.

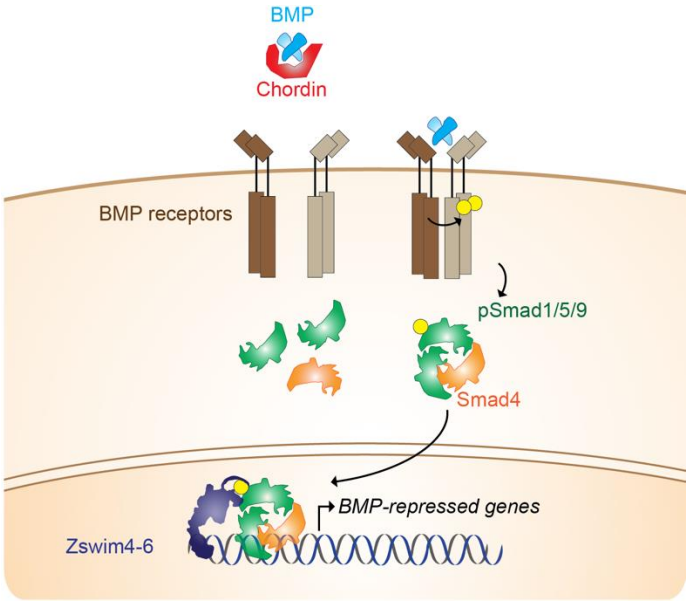

Figure 2.3 Proposed role of *Nematostella* Zswim4-6.
A recap of the BMP signalling pathway from Chapter 1. BMP ligands (blue) bind to the BMP receptors (brown), which subsequently phosphorylate Smad1/5/9 (green), which then binds to Smad4 to form a heterotrimer. The Smad complex translocates to the nucleus and regulates BMP target genes. Chordin (red) acts as a BMP inhibitor. *Nematostella* zinc finger with SWIM-type domain 4-6 (Zswim4-6) (dark violet) is predicted to be localised in the nucleus to modulate BMP signalling and, in particular, to support the silencing of BMP-repressed genes for patterning of the *Nematostella* directive axis.

Previously, the evolutionary conservation between zebrafish and *Nematostella* was demonstrated by Rentzsch et al. (2006) in which *Nematostella vectensis* Dpp and Chordin have been shown to induce ventralization and dorsalization, respectively, in zebrafish embryos. Therefore, in this chapter, my aim is to investigate if the bilaterian Zswim homologues, such as in the zebrafish, also have a modulatory role in BMP-mediated dorsal-ventral patterning. First, I assayed whether nvZswim4-6 can also modulate BMP signalling in bilaterians by microinjecting *nvzswim4-6* mRNA into zebrafish embryos. However, the slope of pSmad1/5/9 is flattened only at a high concentration of *nvzswim4-6* mRNA that may be due to RNA toxicity from a large amount of injected mRNA and unrelated to Zswim effects (Figure 2.4). Therefore, we assessed zebrafish Zswims' (zZswim) role in modulating BMP signalling. While there are several zZswims reported (Table 2.1) (ZFIN), we first took a directed approach by searching for closely related homologues in zebrafish (Figure 2.5). Our collaborators performed a phylogenetic analysis and have found that nvZswim4-6 clusters with zebrafish zZswim5 and zZswim6. Analysis of their expression using Expression Atlas (Papatheodorou et al., 2020) indicates that *zzswim5* expression is more dominant

during gastrulation compared to *zzswim6* (Figure 2.5). This is reflected by the successful cloning of *zzswim5* but not *zzswim6* from cDNA of zebrafish embryos at the gastrulation stage (Figure 2.6). Available *in situ* hybridization of *zzswim5* expression illustrates that *zzswim5* is predominantly expressed along the margin during gastrulation and becomes more localised in the central nervous system later in development (Figure 2.7). Moreover, overexpression of *zzswim5* causes loss of dorsally-derived structures such as head and ventrally-derived structures such as tail (Figure 2.8), and this may be due to the flattening of the slope of pSmad1/5/9 in zebrafish during gastrulation (Figure 2.9). However, there is currently no *zzswim5* loss-of-function data because the results from *zzswim5* morphants are inconclusive (Figure 2.10-2.12). In summary, I present preliminary work demonstrating that zebrafish and *Nematostella* have Zswim homologues that have conserved modulatory function in BMP-mediated patterning of the dorsal-ventral axis and directive axis, respectively (Figure 2.13). This provides further support that the Bilateria and Cnidaria sister groups may have evolved from a common bilateral symmetric ancestor.

Results

In *Nematostella vectensis*, gain-of-function experiments by microinjecting *nvzswim4*-6 mRNA caused a reduction in the BMP signalling gradient along the directive axis in the ectodermal layer (Knabl *et al*., 2022). To determine whether the function of nvZswim4-6 is evolutionarily conserved in dorsal-ventral axis formation in Bilateria, I performed gain-of-function analysis by microinjecting *nvzswim4*-6 mRNA into zebrafish embryos. Embryos injected with n*vzswim4-6* mRNA had curled tails, which are similar phenotypes to zebrafish embryos with low BMP signalling. However, these phenotypes were only observed at high amounts of 480 pg *nvzswim4-6* (Figure 2.4A-B). Therefore, to verify if the gain-of-function phenotypes are caused by changes in the BMP signalling gradient profile, I performed anti-pSmad1/5/9 immunostaining (Figure 2.4C-D) and found that embryos injected with 480 pg *nvzswim4-6* mRNA had significantly lower pSmad1/5/9 levels. Therefore, this suggests that nvZswim4-6 can also modulate the BMP signalling gradient along the dorsal-ventral axis of zebrafish, which is reminiscent of nvZswim4-6 modulatory effect in the BMP-mediated directive axis formation of *Nematostella vectensis*. However, it is important to note that this may be due to an off-target effect caused by a high concentration of *nvzswim4-6* mRNA. For example, embryos injected with mRNA of a “neutral” molecule such as GFP at 250

pg led to expansion of pSmad2/3 (Mörsdorf, 2019). It is currently unknown if GFP injected at high concentrations can affect the BMP signalling gradient similarly.

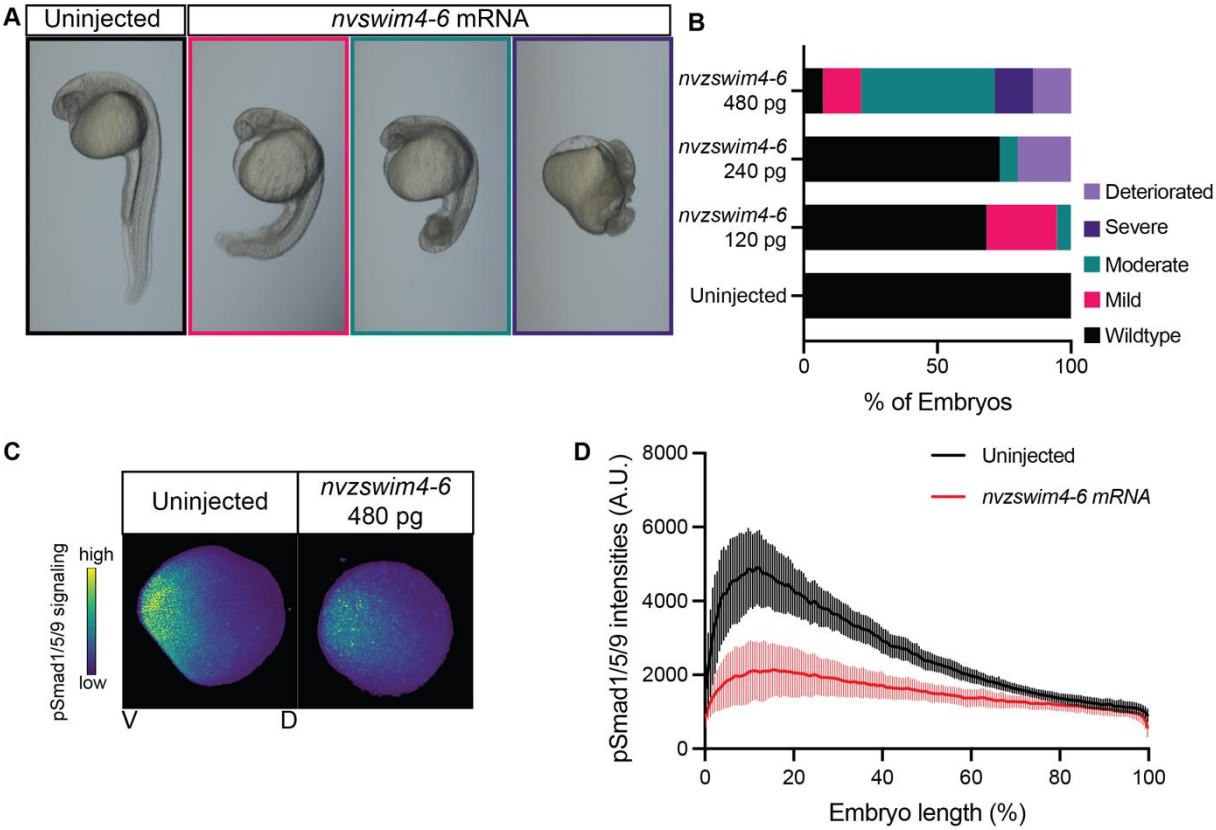

Figure 2.4 Gain-of-function experiment by injecting *Nematostella vectensis zswim4-6* into zebrafish embryos caused maldevelopment of organs and flattening of the BMP signalling gradient.
A) Representative images of embryos injected with *nvzswim4-6*. **B)** Distribution of phenotypes of embryos at 1 dpf: uninjected, n = 43; 120 pg *nvzswim4-6*, n = 19; 240 pg *nvzswim4-6*, n = 15, and 480 pg *nvzswim4-6*, n = 28. **C)** Embryos injected with 480 pg of *nvzswim4-6* were fixed at the shield stage and immunostained for pSmad1/5/9. Embryos were imaged from animal pole to margin with a light sheet microscope, and maximum intensity projection images are shown. **D)** Quantification of pSmad1/5/9 intensity in (C). Uninjected, n = 10 and *nvzswim4-6* mRNA, n = 8. The solid line represents the mean, and the error bars represent the 95% confidence interval, plotted using Prism (GraphPad Software). A.U. – arbitrary unit, V – ventral, D – dorsal.

An alternative is to test zebrafish Zswim homologues. There are 5 zZswims: zZswim2, zZswim5, zZswim6, zZswim7, and zZswim8 (Table 2.1, Figure 2.5A) (ZFIN). A summary of each homologue is compiled in Table 2.1 and their respective expressions in Figure 2.5A (Papatheodorou et al., 2020). Currently, there is a limited amount of research on all zZswims.

Multiple phylogenetic likelihood analysis showed that zebrafish Zswim5 and Zswim6 formed a cluster with anthozoa cnidarian homologues: *Nematostella* Zswim4-

6 and *Exaiptasia* Zswim5-like. Therefore, this suggests that these two zZswims are more closely related to nvZswim4-6 than the other zZswims (Figure 2.5B) (Knabl et al., 2022). Furthermore, *zzswim5* has a stronger expression than *zzswim6* and other *zzswims* during gastrulation when *bmp2b* is also strongly expressed (Figure 2.5A), which suggests that zZswim5 has a more central role for dorsal-ventral patterning during early zebrafish development.

Table 2.1 Summary of zebrafish Zswims.
There are 5 Zswims in zebrafish reported in ZFIN including the polypeptide length, predicted binding partners, and physiological functions. References for implicated diseases in human Zswim homologues are included.

Gene name	Length (aa)	Predicted molecular interaction	Predicted physiological function
zswim2	589	Ubiquitin protein ligase activity Zinc ion binding	Unknown
zswim5	1151	Cul2-RING ubiquitin ligase complex	Axonal guidance regulation
zswim6	1130	Proteasome Neuron restrictive silencer factor (Smith *et al*., 2014)	Implicated in acromelic frontonasal dysostosis (Smith *et al*., 2014)
zswim7	140	Shu complex Zinc ion binding activity	Double-strand break repair via homologous recombination Implicated in spermatogenesis (Alhathal *et al*., 2020, Li *et al*., 2021) Ovarian development (McGlacken-Byrne *et al*., 2022)
zswim8	1949	Cul2-RING ubiquitin ligase complex Zinc ion binding activity	Axonal guidance regulation

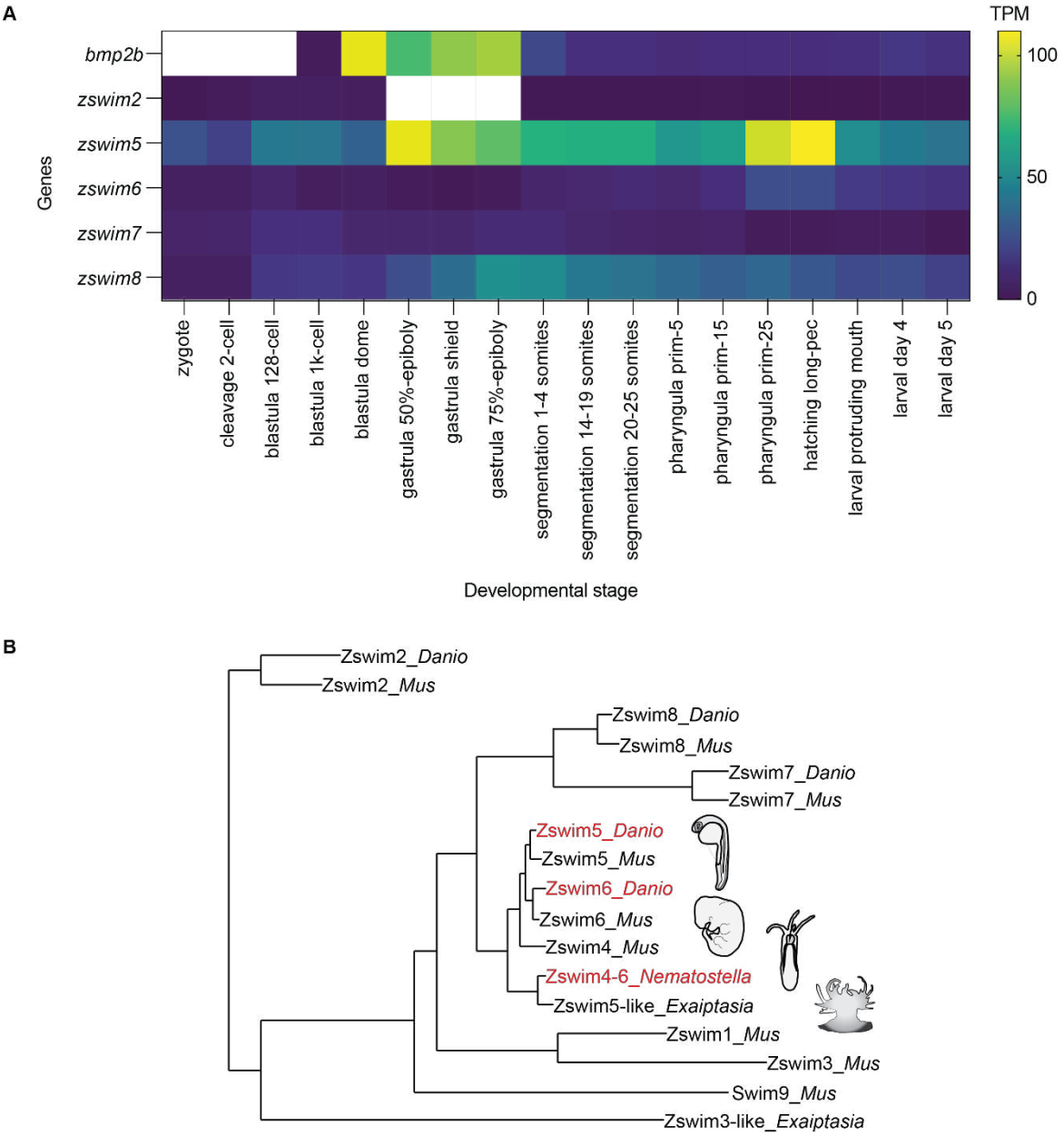

Figure 2.5 Zebrafish *zswim5* expression is stronger than other zebrafish *zswims* during gastrulation and clusters with zZswim6 and *Nematostella* Zswim4-6.
A) Comparison of zebrafish *bmp2b* to all *zzswims'* expressions (TPM: transcript per million) during embryonic stage (Papatheodorou et al., 2020). **B)** Maximum likelihood phylogeny shows the evolutionary relationship of zebrafish Zswim5 and Zswim6 zebrafish (in red) with Zswims of other organisms such as mouse and anthozoa cnidarians, *Nematostella* (in red) and *Exaiptasia*. This was adapted and modified from Knabl et al. (2022).

To perform gain-of-function experiments, *zzswim5* and *zzswim6* must first be cloned. Due to the long length of *zzswim5* (3456 bp) and *zzswim6* (3399 bp), the cloning procedure required troubleshooting the PCR protocol such as changing different factors including polymerases, melting temperature, and developmental time point of the embryos used for the cDNA. I chose Q5 DNA polymerase, which is

reported to have the highest amplification fidelity available since it is approximately 280 times higher than Taq with a maximum amplicon length of up to 20 kb depending on target sequence complexity, and KOD, which is reported to be 12 times higher fidelity than Taq polymerase with maximum length amplicon of up to 6 kb (Potapov & Ong, 2017). Then NEB calculator was used to determine the annealing temperature for Q5 at 72°C. Since KOD elongation temperature is 70°C, an annealing temp of at least 5°C below was recommended, and therefore, three temperatures were tested: 58°C, 62°C, and 65°C. Moreover, I chose two positive controls to amplify: *sizzled*, for gastrulation, and *namptb*, for all developmental time points (Papatheodorou et al., 2020). In addition, blank samples were included to account for any contamination in the reagents used.

In the first experimental trials, using cDNA from embryos at 50% epiboly, I found that *namptb* was amplified but not *sizzled*, and the *zzswim5* and *zzswim6* lanes had multiple short bands (Figure 2.6A). The PCR condition in Figure 2.6A failed several times at other annealing temperatures including optimisation steps such as touchdown PCR, which progresses from high to low annealing temperature to increase specificity (data not shown) (Korbie & Mattick, 2008). Then *zzswim5* was successfully amplified from cDNA from embryos at 75% epiboly with Q5 (Figure 2.6B) and KOD polymerases with notable improvement at higher annealing temperatures (Figure 2.6C). Although *zzswim5* is reported to be expressed until 2 dpf (Figure 2.5A), it was not amplified from cDNA samples of 1-day old embryos (Figure 2.6D). Perhaps this is due to the lower expression around 1 dpf (Figure 2.5A). In terms of the controls, *namptb* was amplified in all conditions (Figure 2.6A-D), and Sizzled was amplified only at 75% epiboly and not at 1 dpf as expected (Figure 2.6B-D) (Papatheodorou et al., 2020). However, the full-length *zzswim6* was not amplified in any of the conditions (Figure 2.6). There were fragmented PCR products observed for all conditions, but it is currently unknown if those are *zzswim6* related. This suggests that the full-length *zzswim5* mRNA but not *zzswim6* mRNA is present during gastrulation, which is in line with their expression levels (Figure 2.5A) (Papatheodorou et al., 2020). This further supports that zZswim5 may have a more critical role during dorsal-ventral axis formation, and zZswim6 has a role later in development.

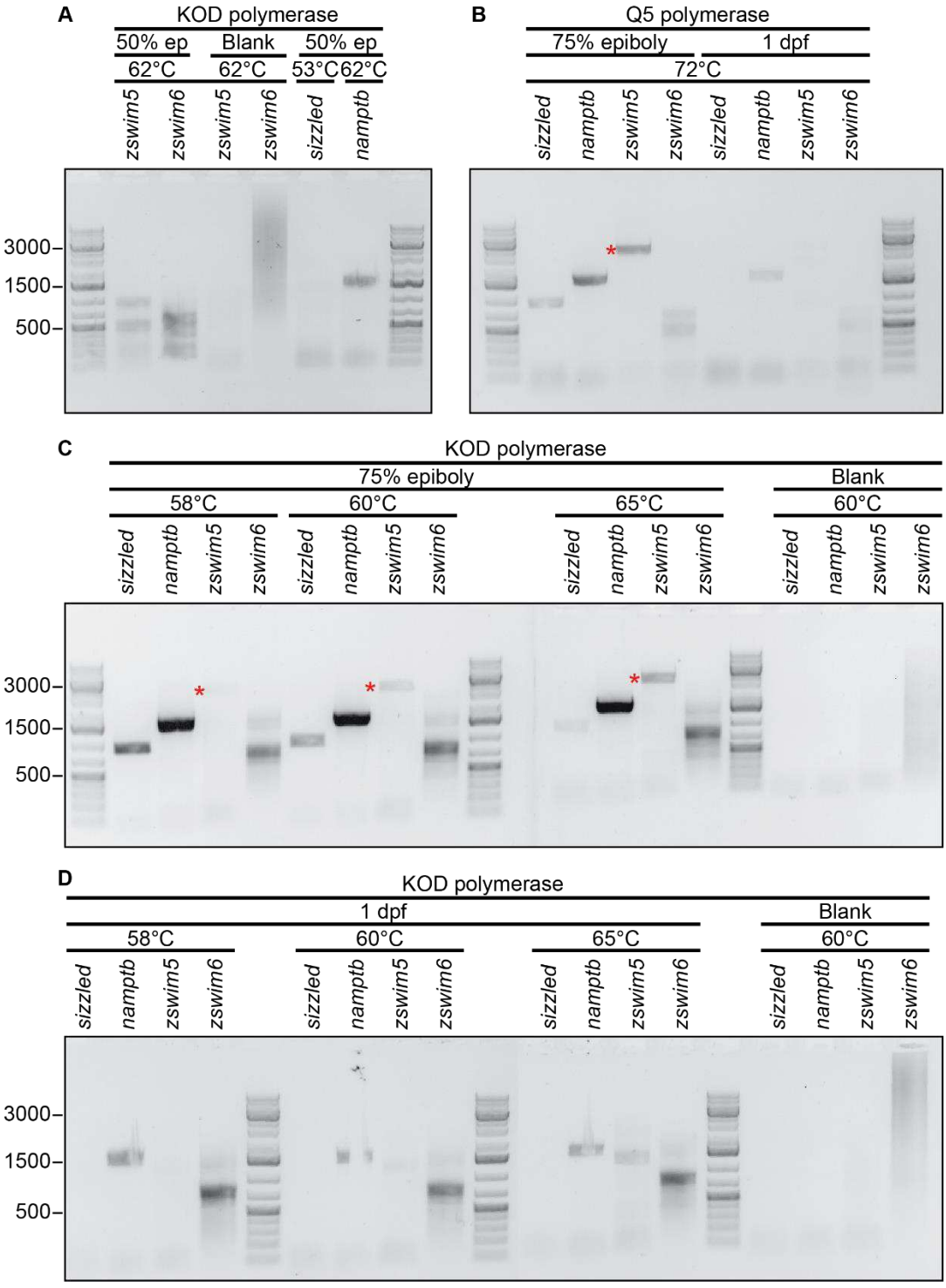

Figure 2.6 Zebrafish *zswim5* was cloned from the cDNA of embryos at 75% epiboly.
To clone *zzswim5* and *zzswim6*, KOD or Q5 polymerase was used using cDNA prepared from embryos at **(A)** 50% epiboly, **(B-D)** 75% epiboly, or 1 dpf. *sizzled* and *namptb* served as controls. ep – epiboly. The red asterisks indicate the correct band size for *zzswim5*.

Because zZswim5 clusters with nvZswim4-6 and the full-length was successfully cloned during gastrulation, zZswim5's role during dorsal-ventral patterning in zebrafish was further investigated.

Large-scale *in situ* hybridization screens revealed that the zebrafish *zswim5* expression pattern appears to overlap with the expression of gene markers for mesodermal and neuronal progenitors (Figure 2.7) (Thisse et al., 2001), and that *zzswim5* expression could be regulated by Nodal, BMP, and FGF signalling during early zebrafish embryogenesis. During gastrulation, the *zzswim5* expression domain is initially localised throughout the mesoderm along the margin and the anterior-to-posterior axis on the dorsal side (Figure 2.7A-A'). At this stage, *zzswim5* expression appears ring-like around the embryo's margin with a slight dorsal bias similar to the expression of *tbxta*, a well-established Nodal target gene (Thisse et al., 2001) and *sox3*, a gene responsive to FGF signalling (Dee et al., 2008; Rentzsch et al., 2004). This would be in line with previous findings in which *zzswim5* was detected using macroarray expression profiling in the search for Nodal-regulated genes (Bennett et al., 2007). Additionally, *zzswim5* expression partially overlaps with BMP target genes such as *eve1*, which is expressed along the margin during gastrulation, except in the dorsal organizer (Xue et al., 2014). However, by the segmentation stage, *zzswim5* is expressed in the central nervous system (CNS), ventral mesoderm, and tail bud (Figure 2.7B-B', C-C'), while *tbxta* expression would be localised to the notochord and tail bud, and *sox3* is expressed in the CNS and spinal cord (Thisse et al., 2001); therefore, *zzswim5* expression begins to diverge from *tbxta* and to overlap more with *sox3* expression. By 1 dpf, *zzswim5* expression is more localised in the CNS from the forebrain down to the caudal end of the spinal cord (Figure 2.7D-D'), and this expression domain is sustained at least up to 2 dpf (Thisse et al., 2001), overlapping with *sox3* expression. This suggests that in later stages zZswim5 is under FGF regulation. Overall, the *zzswim5* expression domain suggests that zZswim5 plays a role in mesodermal and neuronal tissue development and is regulated by BMP, FGF, and Nodal signalling.

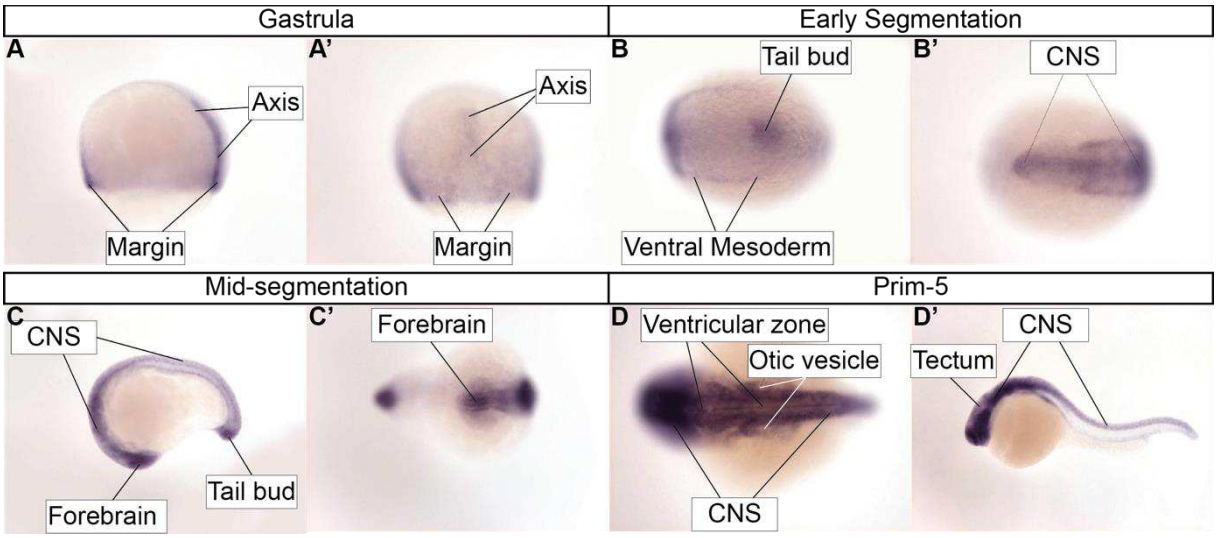

Figure 2.7 Zebrafish *zswim5* expression is localised in the mesoderm during gastrulation and progressively becomes localised to the central nervous system.
zzswim5 expression data is from the large-scale *in situ* hybridization screens for genes that are spatially regulated during zebrafish embryogenesis. This was directly submitted to ZFIN by Thisse et al. (2001). Their work was supported by grant RR15402-01 from the NIH. Anatomical structures are relabelled for clarity. **A-A')** During gastrulation, *zzswim5* expression spans the margin in the mesoderm and the anterior to posterior axis (A – lateral view, A' – dorsal view). **B-B')** Early segmentation around the 1-4 somite stage, *zzswim5* expression persists in the ventral mesoderm (B) and spans the anterior to posterior CNS (B-B'). **C-C')** At 14-19 somitogenesis, *zzswim5* expression spans the embryo from the anterior to posterior end (C – lateral view, C' ventral view). **D-D')** By 1 dpf, *zzswim5* expression becomes localised to the brain and the spinal cord (D – anterior view, D' – lateral view). CNS – central nervous system.

Moreover, it is yet to be determined whether zZswim5 has a conserved role in BMP-mediated dorsal-ventral patterning in bilaterians, similar to anthozoa cnidarians. Therefore, I performed a gain-of-function analysis by microinjecting *zzswim5* mRNA into zebrafish embryos. Overexpression of *zzswim5* in zebrafish embryos caused mild to severe developmental defects from head to tail (Figure 2.8A-B). Embryos with mild to moderate phenotypes had enlarged blood islands and underdeveloped eyes (Figure 2.8A-B), which is partially reminiscent of the ventralized phenotypes of *chordin* and *sizzled* mutant embryos (Figure 1.7) (Schulte-Merker et al., 1997) and in contrast with the phenotypes described in Appendix C. Nevertheless, embryos with severe phenotypes had a complete loss of head, curled tail, and disorganised somites. The curled tail is reminiscent of BMP loss-of-function, which are in line with phenotypes described in Appendix C. The eye buds failed to develop at the somite stage (Figure 2.8C) and remained underdeveloped at later stages (Figure 2.8D). Overall, the embryos lacked defined organs, with distal structures, such as blood and eyes,

severely affected. These phenotypes are in line with tentacle loss and poor mesenteric chamber compartmentalisation in *Nematostella nvzswim4-6* morphants (Figure 2.2A'-B'). This suggests that overexpression of *zzswim5* caused abnormal development of structures along the dorsal-ventral and anterior-posterior axes of the zebrafish.

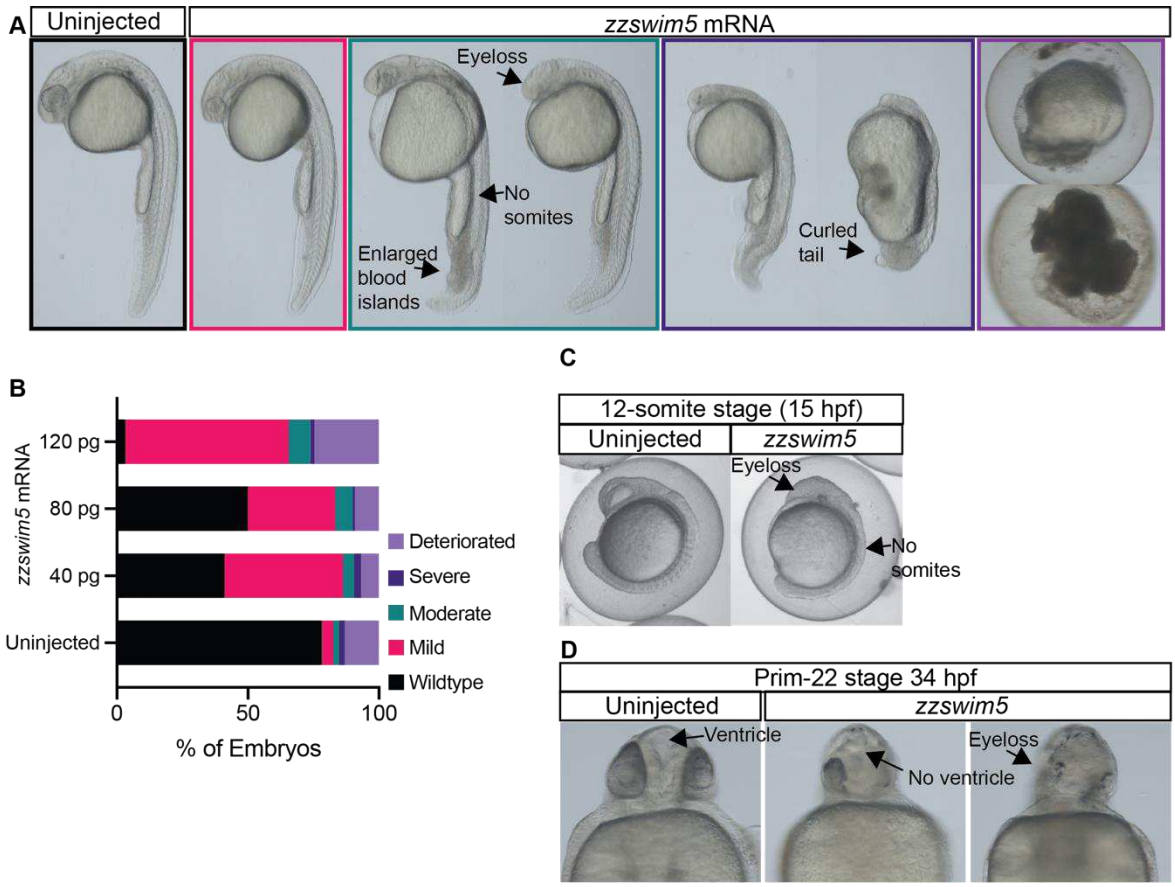

Figure 2.8 Overexpression of zebrafish *zswim5* caused patterning defects from head to tail.
A) Representative images of embryos injected with *zzswim5* mRNA. Embryos overexpressing *zzswim5* mRNA exhibit loss of eyes, smaller heads, no somites, enlarged blood islands, and/or curled tails. **B)** Distribution of phenotypes of 1 dpf embryos with varying concentrations of *zzswim5* mRNA: uninjected, n = 46; 40 pg *zzswim5*, n = 73; 80 pg *zzswim5*, n = 120, and 120 pg *zzswim5*, n = 61. **C)** Loss of eyes was noticeable during somitogenesis (lateral view), which persisted in embryos **D)** at 34 hpf (ventral view).

To corroborate whether these phenotypes are due to changes in the BMP signalling gradient, pSmad1/5/9 was immunostained and quantified in embryos microinjected with *zzswim5* mRNA (Figure 2.9A-B). The slope of the BMP signalling gradient in embryos injected with 80 pg *zzswim5* was flattened compared to wild-type embryos. This suggests that the exogenous expression of *zzswim5* reduces BMP signalling. This is in line with reduced BMP signalling in the ectoderm of *Nematostella vectensis* upon overexpression of *nvzswim4-6* and in the endoderm in *nvzswim4-6*

morphants (Figure 2.2C'-D) (Knabl et al., 2022). Additionally, since *zzswim5*-injected embryos are partially reminiscent of ventralized mutants such as *chordin* and *sizzled* (Chapter 1, Figure 1.7), the results suggest that the cells along the dorsal-ventral axis lack a strongly polarized BMP signalling gradient for proper development of organs (Briscoe & Small, 2015) especially those arising from the dorsal- and ventral-most embryonic regions.

Findings in *Nematostella vectensis* suggest that NvZswim4-6 interacts with pSmad1/5/9 for efficient BMP signalling-mediated gene repression (Knabl et al., 2022). In this regard, overexpression of *zzswim5* would cause a decrease in the expression of BMP-repressed genes and have no effect on the expression of BMP-activated genes. Here, I found that overexpression of *zzswim5* flattened the BMP signalling gradient (Figure 2.9A). In that sense, the expression of BMP-repressed genes are expected to increase, and the expression of BMP-activated genes are expected to decrease. Therefore, to investigate how the expression profiles of BMP target genes are altered in *zzswim5*-injected embryos, I performed fluorescent *in situ* hybridization for one BMP-repressed gene, *admp*, and one BMP-activated gene, *sizzled*, and imaged the embryos using confocal microscopy, which was the only available imaging equipment at the time of the experiment (Figure 2.9C-F). I found that, compared to uninjected embryos, *admp* expression was mildly decreased from 0% to 95% of the ventral to dorsal axis, but increased in the dorsal-most region at 95% to 100% along the embryo length in *zzswim5*-injected embryos (Figure 2.9C, C', E). This suggests that the presence of zZswim5 repressed *admp* expression, which is in line with the role of NvZswim4-6 as a mediator of BMP-repression of target genes (Knabl et al., 2022). However, this is in contrast to the lower pSmad1/5/9 levels in *zzswim5*-injected embryos, which should cause an increase in *admp* expression. Next, as expected, *sizzled* expression in *zzswim5*-injected embryos was similar to uninjected embryos, except for a mild decrease in the dorsal-most region (Figure 2.9D, D', F). Overall, this suggests that excess zZswim5 flattens BMP signalling, but has minimal effects on the expression of BMP target genes, *admp* and *sizzled*, in contrast to findings in *Nematostella nvZswim4-6* morphants that have expanded BMP-repressed genes (Knabl et al., 2022). How other BMP target genes are affected is yet to be determined. One caveat is that, in this trial, there was low signal-to-noise ratio since there was signal for both *admp* and *sizzled* samples outside their reported expression domains

even in the uninjected controls (Lele, Nowak, et al., 2001; Yabe et al., 2003); therefore, additional experimental trials should be done in the future.

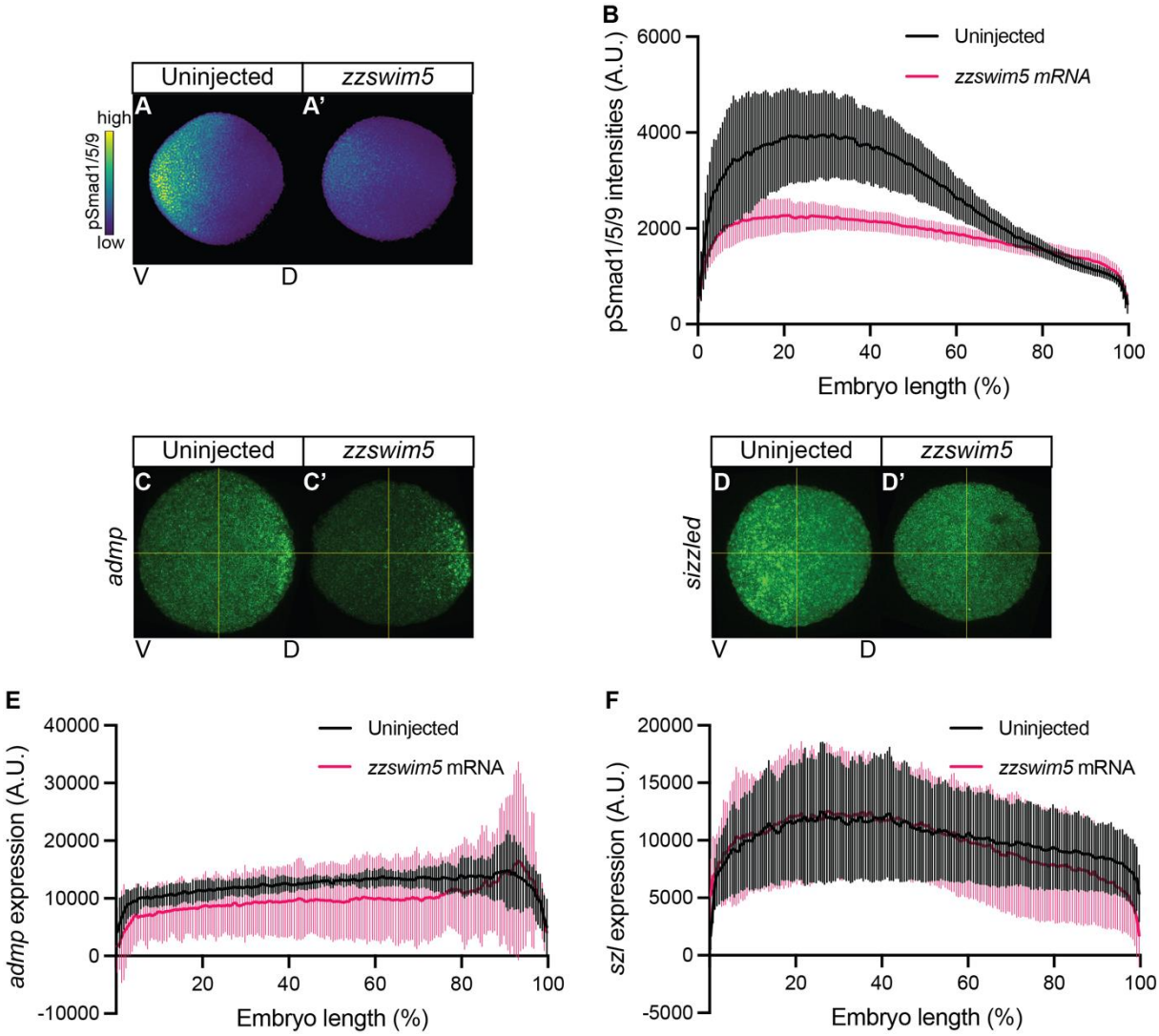

Figure 2.9 Overexpression of zebrafish *zswim5* flattened the slope of BMP signalling gradient.
Embryos were injected with 80 pg of zebrafish *zzswim5* mRNA or left uninjected and fixed at 50% epiboly. **A-B)** BMP signalling levels were assessed by immunofluorescence staining for pSmad1/5/9 and imaged with a light sheet microscope. Uninjected n = 10 (A), *zzswim5*-injected n = 10 (A'). **C-F)** Fluorescence *in situ* hybridization (FISH) of BMP target genes *admp* (uninjected n = 5 (C), *zzswim5*-injected n = 3 (C')) and *sizzled* (uninjected n = 5 (D), *zzswim5*-injected, n = 5 (D')) were imaged using a confocal microscope with views from the animal pole. Quantifications of immunofluorescence (B) and FISH of target genes (E-F) were performed by measuring the average column pixel intensity from ventral to dorsal side using Fiji with the background subtracted. The solid line represents the mean, and the error bars represent the 95% confidence interval, plotted using Prism (GraphPad Software). A.U. – arbitrary unit, V – ventral, D – dorsal.

Furthermore, in *Nematostella vectensis*, in addition to gain-of-function experiments, knockdown of *nvzswim4-6* flattened the slope of the BMP signalling

gradient in the endoderm during gastrulation, causing loss of tentacles and fused mesenteric chambers (Figure 2.2) (Knabl et al., 2022). To further assess the role of zZswim5 in dorsal-ventral patterning in bilaterians, I performed loss-of-function analysis by using morpholinos to knockdown *zzswim5*. I designed one translation blocking morpholino and two splice-site morpholinos (MO) (Figure 2.10A). I titrated the *zzswim5-MO* concentration and scored the phenotypes (Figure 2.10B-D). Surprisingly, at 50 µM, *zzswim5* morphants did not exhibit developmental defects, except that *zzswim5-MO-1* and *zzswim5-MO-2* had a few embryos with mild malformations such as expanded somites and smaller heads (Figure 2.10B-C). Triple morphants injected with all 3 *zzswim5-MO* exhibited necrosis. It is currently unclear whether this could be due to toxicity caused by the high concentration of morpholinos or if this is the required morpholino concentration to properly knockdown *zzswim5*. To test this, embryos were injected with *zzswim5-MO-1* and *zzswim-MO-2* at 150 µM separately or with all three morpholinos. Morphants injected with the start-site *zzswim5-MO-1* exhibited severe necrosis but not those injected with *zzswim5-MO-2-3* splice-site morpholinos (Figure 2.10D). The differences in phenotypes between morpholinos could be due to *zzswim5-MO-1* effectiveness to anneal to *zzswim5* transcript compared to the splice-site morpholinos.

However, morpholinos are reported to have toxic effects by activation of the p53 pathway, unrelated to the target gene function (Stainier *et al.*, 2017). Therefore, to determine whether the necrosis observed in *zzswim5-MO-1* injected embryos is zZswim5 specific or is caused by the activation of the p53 pathway, I co-injected *p53-MO* and *zzswim5-MO-1* with 2:1 ratio as previously reported (Robu et al., 2007). I found that knockdown of *p53* reduced necrosis in *zzswim5-MO-1* morphants (Figure 2.10E-F), except that some embryos co-injected with *p53-MO* and *zzswim5-MO-1* had smaller heads and kinked tails, which partially resembles *zzswim5* overexpression (Figure 2.8). This suggests that the necrotic tissue observed in morphants is due to morpholino toxicity and is not caused by knockdown of *zzswim5*.

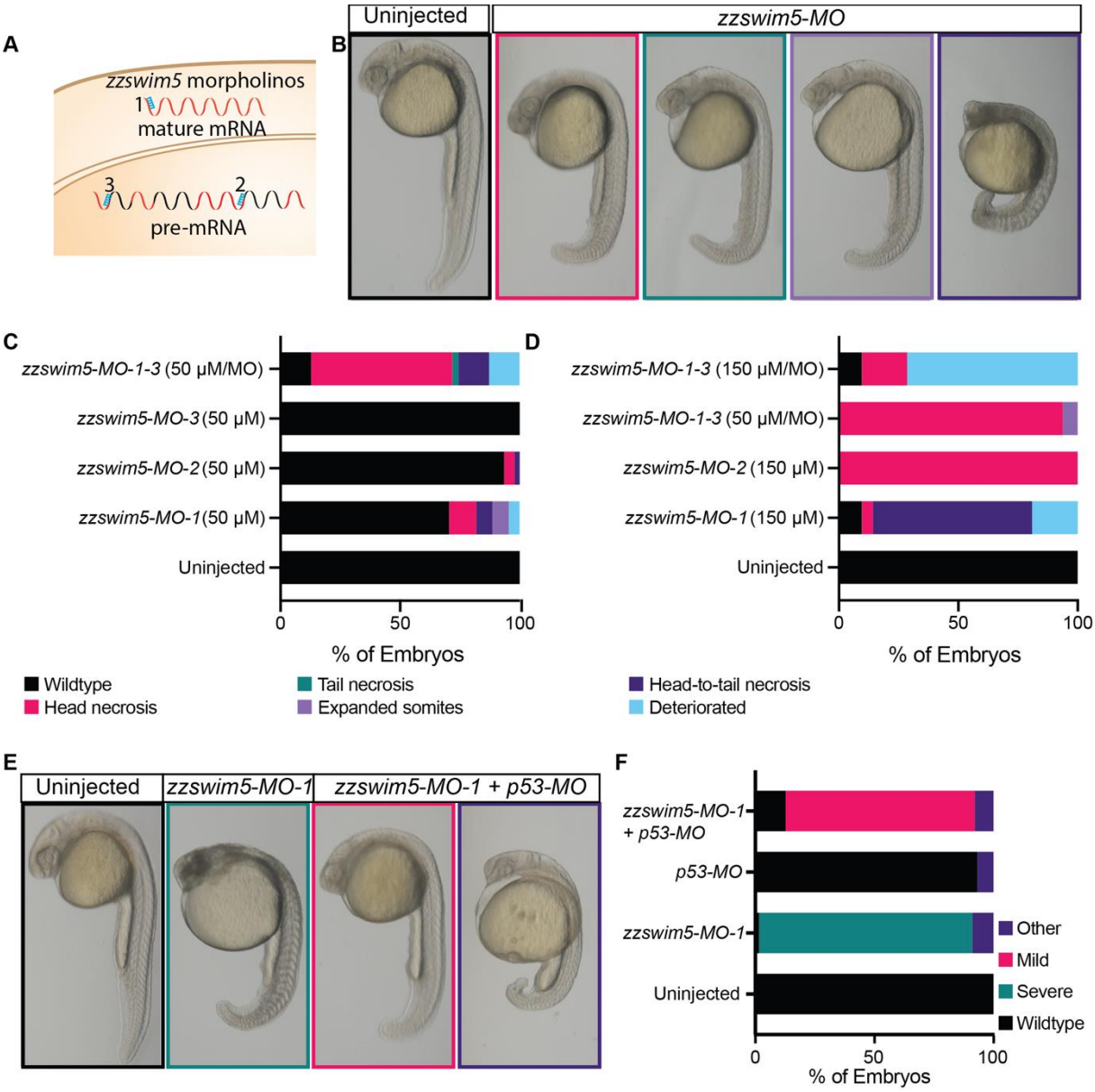

Figure 2.10 Zebrafish *zswim5* start-site morpholino caused mild underdevelopment of head structures in zebrafish embryos.
A) Schematic of the three *zzswim5* morpholinos (blue combs) were tested. *zzswim5-MO-1* anneals to the translation start site. *zzswim5-MO-2* and *zzswim5-MO-3* anneal to splice-site junctions. **B)** Representative images of 1 dpf embryos injected with *zzswim5-MOs* at the one-cell stage. **C-D)** Distribution of phenotypes following injections of morpholinos. C) Uninjected, n = 6; *zzswim5-MO-1*, n = 44; *zzswim5-MO-2*, n = 46; *zzswim5-MO-3*, n = 58, and *zzswim5-MO-1-3*, n = 39. D) uninjected, n = 23; *zzswim5-MO-1*, n = 21; *zzswim5-MO-2*, n = 20; 50 µM *zzswim5-MO-1-3*, n = 16, and 150 µM *zzswim5-MO-1-3*, n = 21. **E)** Co-injection of p53 morpholino reduced the severe necrosis effect of *zzswim5-MO-1*. Embryos injected with *zzswim5-MO-1* at 150 µM had severe necrosis with dense dark tissues throughout the head, and the somites were enlarged and surrounded by dark tissues. Upon co-injection with *p53-MO* at 300 µM, embryos had more normal somites and trunk structures but with smaller heads and dense tissues around the eyes compared to uninjected. **F)** Distribution of observed phenotypes upon injection of *zzswim5-MO-1*, n = 67; *p53-MO*, n = 74; *zzswim5-MO-1+p53-MO*, n = 63, or left uninjected, n = 28.

To determine whether the mild morphant phenotype is caused by alterations in the BMP signalling during gastrulation, I performed anti-pSmad1/5/9 immunostainings in zebrafish embryos fixed at the shield stage and imaged them using light sheet microscopy using two approaches. In the first experimental trial, embryos were imaged from the animal pole to the margin, and the pSmad1/5/9 intensities were quantified from the maximum intensity projections of the image slices (Figure 2.11A-D). Then the second trial was by *in toto* imaging and quantification as in Chapter 1 (Figure 2.11E-H). In both imaging approaches, the pSmad1/5/9 gradient profile was not affected in *zzswim5-MO-1* injected embryos, including those co-injected with *p53-MO* (Figure 2.11I-J). Similarly, this was reflected by similar *admp* expression in wild-type and *zzswim5* morphant embryos (Figure 2.12A-B).

Of note, the pSmad1/5/9 gradient was mildly decreased in *p53* morphants, suggesting that the knockdown of *p53* can dampen BMP signalling; however, there was no observable phenotype (Figure 2.10F). This finding was further supported by assaying *admp* expression using *in situ* hybridization in which uninjected and *p53* morphant embryos had similar *admp* expression domains (Figure 2.12A-B). Overall, the findings suggest that the mild phenotype in *zzswim5-MO-1+p53-MO* embryos is not due to an alteration in BMP signalling during gastrulation. Since there is currently no antibody against zZswim5 to verify the reduction in protein product in *zzswim5* morphants, it cannot be concluded how effective and specific the *zzswim5-MO-1* is. Stable mutant lines can be considered as an alternative loss-of-function approach.

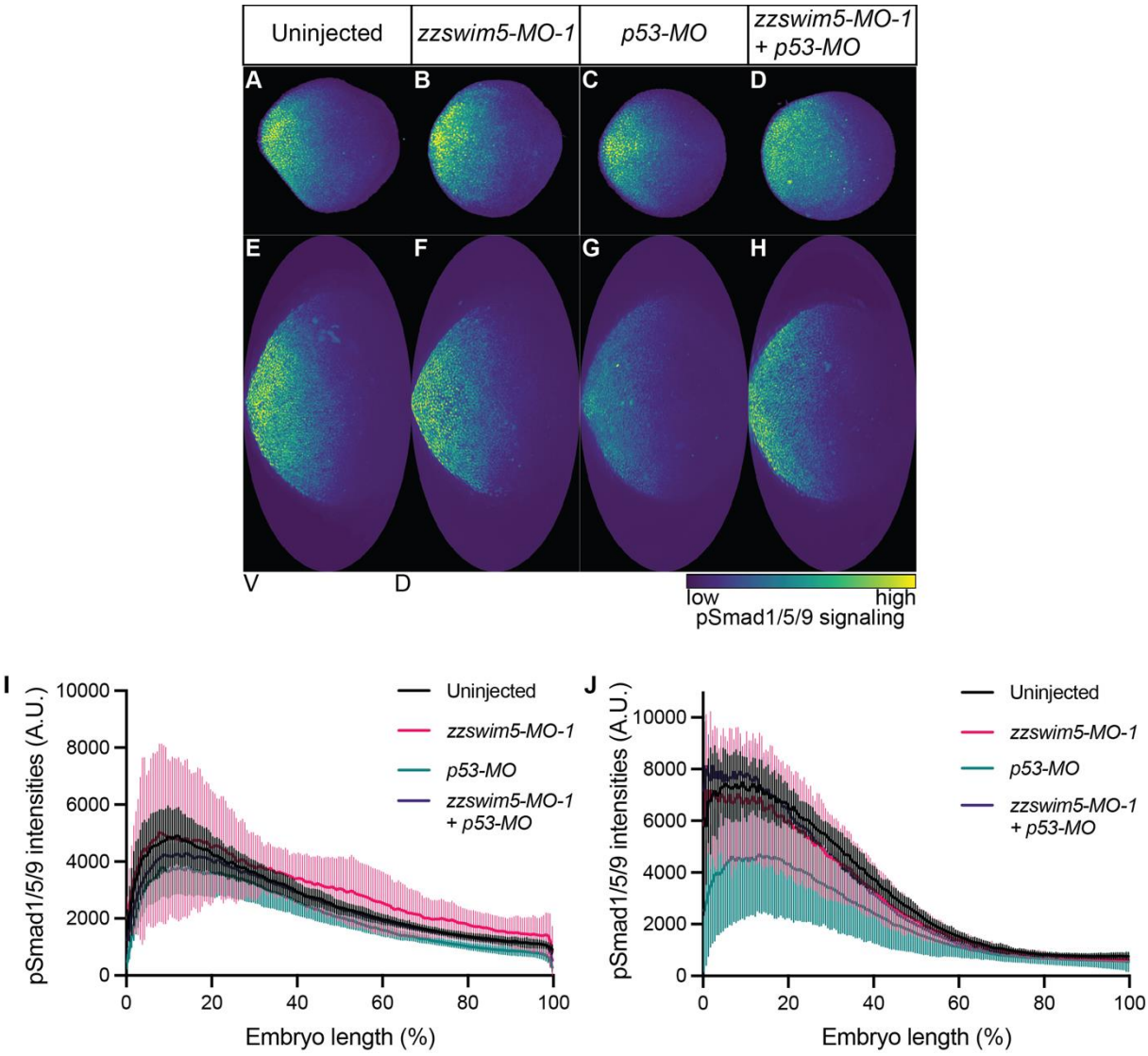

Figure 2.11 Zebrafish *zswim5-MO-1* has no effect on the BMP signalling gradient. Injected and uninjected embryos were fixed at the shield stage and immunostained for pSmad1/5/9 and imaged with light-sheet microscopy. **A-D)** Embryos were imaged from animal pole to margin, and the maximum intensity projections are shown. This experiment was performed simultaneously with Figure 2.4, hence the same control was used for quantification. **E-H)** In a separate experimental trial, embryos were imaged from angles 0°, 90°, 180°, and 270°. The raw imaging data were 3D reconstructed using Fiji and projected into 2D maps. Views are from the animal pole with ventral side (V) on the left and dorsal side (D) on the right. I) Quantification of pSmad1/5/9 immunostaining in A-D, n = 5 for each condition and (J) in E-H, uninjected, n = 10; *zzswim5-MO-1*, n = 4; *p53-MO*, n = 9, or *zzswim5-MO+p53-MO*, n = 10. The solid line represents the mean, and the error bars represent the 95% confidence interval and are plotted using Prism (GraphPad Software). A.U. – arbitrary unit.

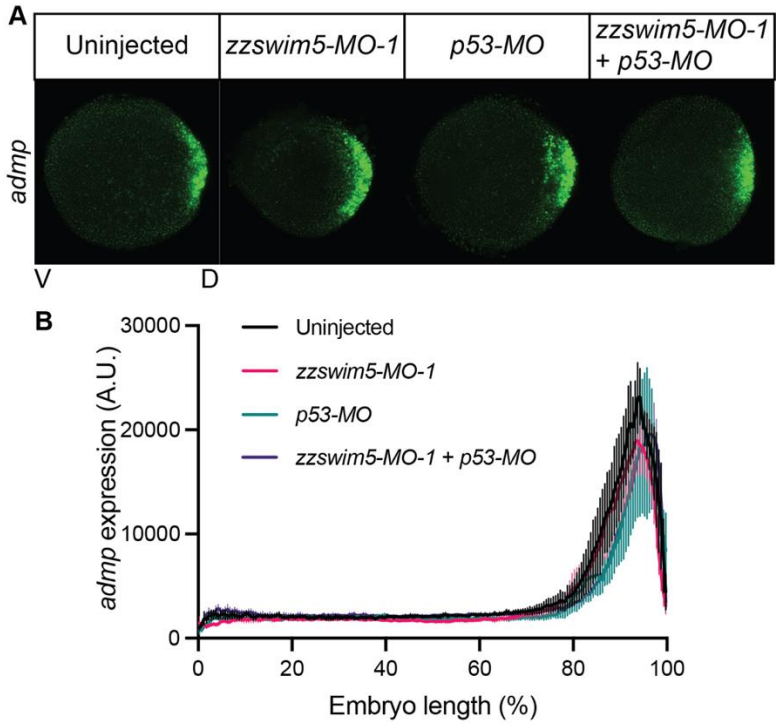

Figure 2.12 Zebrafish *zswim5-MO-1* has no effect on *admp* expression.
A) Embryos were injected with 150 µM *zzswim5-MO-1*, 300 µM *p53-MO*, or both morpholinos. Injected and uninjected embryos were fixed at the shield stage. Fluorescence *in situ* hybridization was performed against BMP-repressed gene *admp* and imaged with light sheet microscopy from animal pole to the margin, and the maximum intensity projections of the image slices are shown. **B)** The signal intensities in (A) were quantified from ventral to dorsal side using Fiji. Sample size: uninjected, n = 3; *zzswim5-MO-1*, n = 4; *p53-MO*, n = 3, and *zzswim5-MO+p53-MO*, n = 3. The solid lines represent the mean, and the error bars represent the standard error, plotted using Prism (GraphPad Software). A.U. – arbitrary unit, V – ventral, D – dorsal.

Discussion

Animals have their organs spatially arranged along distinct body axes by utilizing homologous signalling pathways (Genikhovich & Technau, 2017; Soh et al., 2020). This includes graded BMP signalling via pSmad1/5 for the formation of the dorsal-ventral axis in Bilateria (Ramel & Hill, 2012) and the directive axis in anthozoa Cnidaria (Leclere & Rentzsch, 2014). The extent of evolutionary conservation between the BMP-mediated axes from these two bilaterally symmetric sister groups is highlighted by the shared BMP target genes consisting of transcription factors and signalling molecules in bilaterians: *Xenopus laevis* (Stevens et al., 2017) and *Drosophila melanogaster* (Deignan et al., 2016) and in anthozoa cnidarian *Nematostella vectensis* (Knabl et al., 2022). One of the BMP target genes enriched in *Xenopus* and *Nematostella* is a previously uncharacterised *xzswim5* and *nvzswim4-6*, respectively (Knabl et al., 2022). Interestingly, in *Nematostella*, nvZswim4-6

contributes to tentacle development (Figure 2.13I A-A') and compartmentalisation of the mesenteric cavities (Figure 2.13I B-B') by potentially modulating the slope of the BMP signalling gradient (Figure 2.13I C-C', D). The next step is to investigate if the Zswim homologues in bilaterians may also play a role in BMP-mediated axis formation. Here, I have shown that overexpression of zebrafish *zswim5* caused maldevelopment of organs along the body axis, which may be caused by a flattened BMP signalling gradient. Hence, the findings indicate that zZswim5 and nvZswim4-6 have modulatory roles in BMP-mediated axis formation in zebrafish and in *Nematostella*, respectively.

Specifically, I have shown that upon *zzswim5* overexpression, organs derived from ventral-most and dorsal-most embryonic regions are poorly defined and not compartmentalised. The blood island is expanded, and the eyes and ventricles are lost (Figure 2.8, Figure 2.13II). This is reminiscent of the fused mesenteric chambers and tentacle loss in *nvzwim4-6 Nematostella* morphants (Figure 2.13I A-B'). Hence, this is indicative of zZswim5's role in axis patterning in the zebrafish. Note that there is a discrepancy between my findings and those reported in Appendix C in which the ventralized phenotypes such as underdeveloped eyes and smaller head phenotypes were not reported. One possibility is that *zzswim5* overexpression has a biphasic effect, but the dorsalized phenotypes are more prevalent in embryos overexpressing *zzswim5*. This binary effect is reminiscent of *admp* overexpression as presented in Chapter 1. In addition, this binary effect is in line with observations that knockdown of *bmp2/4* in *Nematostella*, embryos either had 0 or 8 mesenteries, but no intermediate phenotypes were observed (see Appendix C).

Moreover, the loss-of-function assay that was done for *Nematostella* was not recapitulated in zebrafish because the results of *zzswim5* morphants are currently inconclusive. One explanation is that all three *zzswim5* morpholinos were ineffective in knocking down *zzswim5*, but there are currently no antibodies available to measure zZswim5 protein levels in the morphants. Another possibility is that there are compensatory mechanisms upon *zzswim5* loss-of-function. For example, the result from the multiple likelihood phylogeny highlights that both zZswim5 and zZswim6 cluster with nvZswim4-6, thus suggesting that zZswim5 and zZswim6 may function redundantly (Figure 2.5B) (Knabl et al., 2022). This is supported by the similarities between the maldevelopment of distal organs in *zzswim5*-injected zebrafish embryos (Figure 2.8) and acromelic frontonasal dysostosis disease in humans with mutations

in the *zswim6* gene, the zebrafish *zswim6* homologue (Smith et al., 2014). With *zswim6* mutations, patients have severe facial asymmetry, underdeveloped airways, shortened or missing tibial bone, and polydactyl, which are all distal organs in humans, thus further supporting zZswim5 and zZswim6 redundant functions. Therefore, one solution is to test their redundancy, that is, whether *zzswim6* is compensating for *zzswim5*. This would entail examining whether the *zzswim6* expression is stronger in *zzswim5* morphants than in uninjected embryos by *in situ* hybridization or quantitative reverse transcription PCR (qRT-PCR). This can be followed up by co-injecting *zzswim5* and *zzswim6* morpholinos into zebrafish embryos.

Nevertheless, based on the Expression Atlas by Papatheodorou et al. (2020), *zzswim6* expression is approximately 5x less than *zzswim5* in wild-type embryos (Figure 2.5A). The difference in *zzswim5* and *zzswim6* expression levels is also observed in other pairs of paralogous genes. For example, Zinc Finger Protein 143 (Znf143), a transcriptional activator protein, has two paralogs in zebrafish: Znf143a and Znf143b (Huning & Kunkel, 2020). Both *znf143*s are strongly expressed in the brain, and knockdown of either gene leads to a similar degree of brain abnormalities. Interestingly, qRT-PCR analysis has revealed that *znf143a* expression is higher than *znf143b*. While overexpression of either paralog may be detrimental, the maintenance of both genes, with one paralog expression at a basal level, may confer some evolutionary advantage (Huning & Kunkel, 2020). Therefore, the low expression level of *zzswim6* could be due to genetic dosage adaptation (Basilicata & Keller Valsecchi, 2021) as a response to the genomic duplication in teleost fish (Postlethwait et al., 2000).

Furthermore, I have shown that the maldevelopment of *zzswim5*-overexpressing embryos may be caused by a lower BMP signalling gradient (Figure 2.9A-B), which is in line with the finding that misexpression of *nvZswim4-6* affected the pSmad1/5 gradient along the directive axis in *Nematostella* (Figure 2.13I C-D, Knabl et al. (2022), Appendix C). Together, these results suggest that these Zswim homologues may modulate BMP signalling gradient for dorsal-ventral and directive axis patterning.

However, the expressions of BMP-repressed gene *admp* and BMP-activated gene *sizzled* in *zzswim5*-injected embryos were minimally affected (Figure 2.9C-F). Note that these are preliminary results with a low sample size and low signal-to-noise

ratio. Nonetheless, in *Nematostella*, the knockdown and overexpression of *nvZswim4-6* specifically affected BMP-repressed gene expression domains such as Chordin (Knabl et al., 2022). It is proposed that nvZswim4-6 interacts with pSmad1/5 to promote BMP signalling-mediated gene repression in *Nematostella* (Figure 2.3). One explanation to the inconsistency between the effect of zZswim5 and nvZswim4-6 on their respective BMP target genes is that Zswim5 and nvZswim4-6 may differ in their roles and/or in the target genes in their respective organisms. For example, only high concentration of *nvZswim4-6* mRNA caused maldevelopment of zebrafish embryos (Figure 2.4), which suggests that *nvzwim4-6* overexpression has no effect in zebrafish embryos, except when injected at high concentration. Another explanation is that some genes such as *admp* have biphasic effects and may not be a precise read-out of the changes in BMP signalling gradient, as I have shown in Chapter 1. Hence, in the future, to determine if Smad5 can mediate down-regulation of BMP repressed genes in the absence or presence of zZswim5, one follow-up experiment is to use constitutively active Smad5 (Soh et al., 2020) upon knockdown or overexpression of *zzswim5* and measure the changes in gene expression of BMP target genes. Additionally, based on the expanded blood islands and loss of cranial structures in *zzswim5*-injected embryos (Figure 2.8, Figure 2.13II), future experiments would involve analysing the BMP-activated gene *gata1a* for blood development (Mullins et al., 1996) and Δ*Np63* for suppression of neural genes, in conjunction with neural-related genes such as *sox3* (Rentzsch et al., 2004) and *six3* (Inbal et al., 2007).

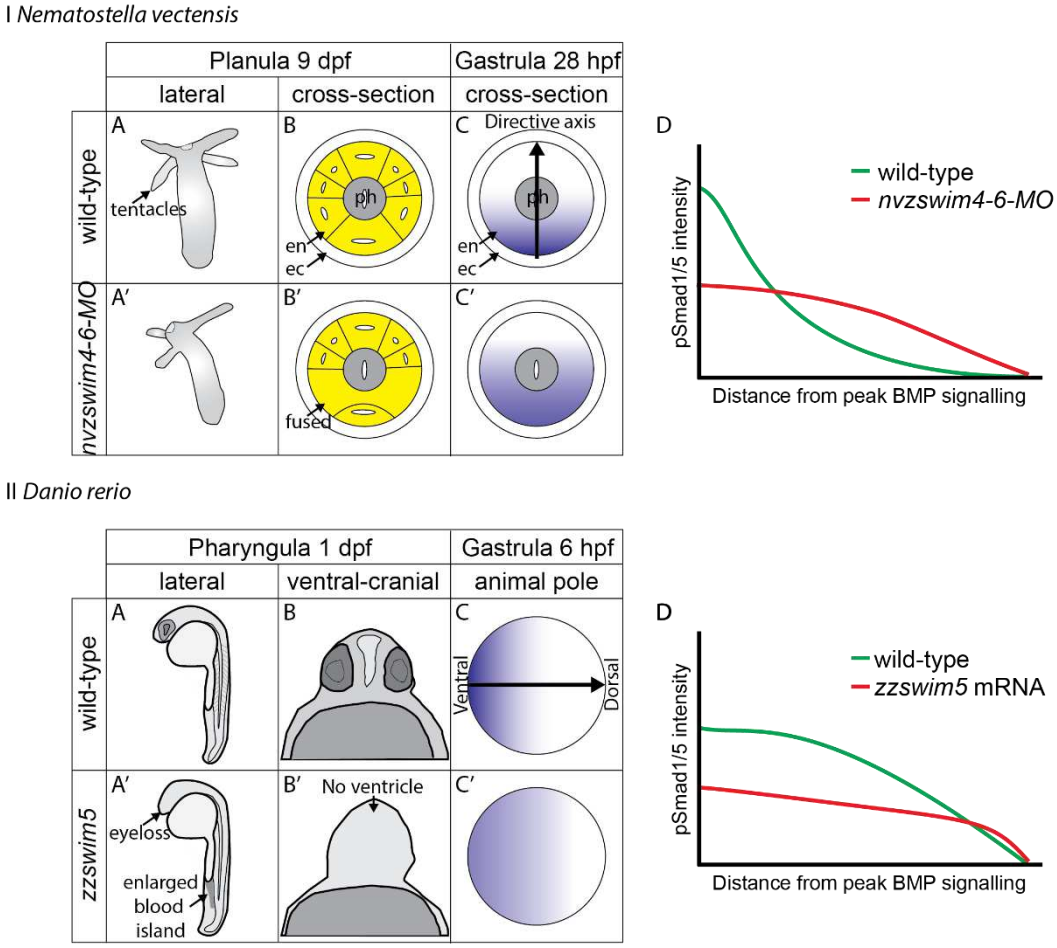

Figure 2.13 Misexpression of *zswim* homologues caused loss of structures and poor tissue regionalization perhaps due to the flattening of the BMP signalling gradient in cnidarians and bilaterians model organisms.
Comparison of the effects of Zswim homologues in **I)** *Nematostella vectensis* as an animal model for anthozoa Cnidaria (already shown in Figure 2.2) and in **II)** *Danio rerio*, zebrafish, as animal model for Bilateria. **A-B)** Schematic of wild-type, uninjected embryos. Overexpression of *zzswim5* in zebrafish embryos resulted in **(A'-B')** abnormal development of organs such as eyes, brain, and blood. **C-C')** Schematic of BMP signalling gradient (violet) at gastrula stage 6 hpf along the dorsal-ventral axis in (C) wild-type and (C') *zzswim5*-injected embryos. **D)** Schematic of pSmad1/5 signalling gradient in (C-C'). BMP signalling is flattened in embryos overexpressing *zzswim5* compared to wild-type embryos.

Several outstanding questions remain. First, what are the upstream signalling pathways regulating zZswim5? During gastrulation, *zzswim5* expression is along the zebrafish margin and dorsal axis, partially overlapping with BMP, Nodal, and FGF signalling (Figure 2.7) (Thisse et al., 2001). This suggests that endogenous zZswim5 may initially be under combinatorial control and has an initial role for mesendoderm development. However, as the embryo develops, *zzswim5* expression becomes localised to the presumptive central nervous system, suggesting a role for brain and spinal cord development. One possible mechanism is via activation of *zzswim5* by

Nodal, since *zzswim5* was among the genes identified using combined macroarray and *in situ* hybridization to screen for Nodal-regulated genes (Bennett et al., 2007). Another possible mechanism is via FGF signalling, which has been proposed to suppress BMP signalling by blocking at the level of Smad proteins and by inducing neural genes such as *sox3*, thus promoting neurogenesis (Pera et al., 2003; Rentzsch et al., 2004). Similarly, a previous report has shown that BMP inhibits FGF signalling to promote cardiogenesis (Tirosh-Finkel et al., 2010). Overall, this suggests a possible mutual antagonism between FGF and BMP signalling for regulating gene expression for tissue patterning similar to Nodal and BMP signalling mutual antagonism for body axis formation in zebrafish (Soh et al. (2020), Appendix B). Future experiments would include measuring *zzswim5* expression at different time points in the presence or absence of BMP, Nodal, and FGF signalling. Another possible assay would be ChIP-seq of the transcription effectors of these signalling pathways to directly test which transcription effector binds to *zzswim5* promoter region.

The second question is: what is the molecular mechanism underlying zZswim5's function to modulate BMP signalling intracellularly? As compiled in Table 2.1, zZswims have been implicated in multiple cellular processes (ZFIN), and SWIM domains are implicated in mediating protein-protein and protein-DNA interaction (Makarova et al., 2002; Smith et al., 2014). Therefore, on the one hand, zZswim5 may mediate FGF signalling inhibition of Smad1/5 (Rentzsch et al., 2004) or may interact with ubiquitin complex as its predicted binding protein partner (ZFIN). On the other hand, zZswim5 may also act as part of a complex to bind DNA similar to zZswim7 (Alhathal et al., 2020; Li et al., 2021; McGlacken-Byrne et al., 2022). These hypotheses are supported by findings in *Nematostella* in which nvZswim4-6:eGFP was found to localise in the nucleus, form puncta, and interact with pSmad1/5 at the regulatory region of *chordin*, a BMP-repressed gene (Knabl et al., 2022). To further compare zZswim5 and nvZswim4-6, we can consider ChIP-seq for a genome-wide search of zZswim5 and pSmad1/5/9 DNA binding sites in zebrafish. Then, to identify protein-protein interactions of zZswim5, we can consider co-immunoprecipitation of protein binding partners using a zZswim5 fused to a protein tag.

Finally, at the beginning of the chapter, I posed the question: how did the two body axes arise? Current evidence supports that there is a degree of evolutionary conservation between the genes involved in BMP-mediated axis formation in both

cnidarians and bilaterians (Genikhovich et al., 2015; Genikhovich & Technau, 2017; Knabl et al., 2022; Rentzsch et al., 2006). Furthermore, medusozoa cnidarians, such as jellyfish, are reported to have *bmp* expression localised to the anterior pole in the developing larva, overlapping Wnt signalling axis (Reber-Muller et al., 2006). Additionally, Hydras – also belonging to Medusozoa – have a Chordin-like molecule that functions to localise BMP signalling in the oral pole in Hydras and can dorsalize zebrafish embryos (Rentzsch et al., 2007). Overall, these earlier findings demonstrate that the BMP signalling is an ancestral system that functions to organize the oral-aboral axis of radially-symmetric medusozoa cnidarians (Rentzsch et al., 2007), the directive axis of anthozoa cnidarians (Genikhovich et al., 2015), and dorsal-ventral axis of bilaterians (Bier & De Robertis, 2015; Ramel & Hill, 2012). Hence, these findings suggest a bilaterally symmetric common ancestor for bilaterians and cnidarians and the divergent evolution of radial symmetry in other cnidarian classes.

However, we cannot fully exclude the possibility of convergent evolution in that bilaterians and cnidarians independently evolved to use BMP and Zswims for bilateral symmetry. For example, the expression pattern of *nvzswim4-6* overlaps with BMP signalling in *Nematostella* (Knabl et al., 2022), but zebrafish *zzswim5* expression may be regulated by multiple signalling pathways including Nodal (Bennett et al., 2007) (Figure 2.7). Furthermore, since cnidarian Wnt and BMP signalling axis are along the oral-aboral axis in medusozoa cnidarians, Rentzsch et al. (2007) proposed the evolutionary model that the two axes in bilaterians did not evolve by '"adding" an orthogonal axis to an already existing one, but rather by "splitting" one axis into two'. It is possible that BMP and Wnt signalling have been reiterated and re-oriented independently to evolve two orthogonal axes (Genikhovich & Technau, 2017). Therefore, we still cannot exclude that bilateral symmetry arose independently in anthozoa cnidarians and in bilaterians. One approach is to investigate what has happened to the extracellular constituents of BMP signalling and downstream targets, such as NvZswim4-6 homologues, in radially symmetric cnidarians, such as jellyfish and Hydra. In line with Chapter 1's question on BMP-Chordin system evolution, what is the difference between BMP-Chordin system in radially-symmetric and bilaterally-symmetric animals? Would ectopic expression of NvZwim4-6 induce a secondary axis in jellyfish and hydras?

To conclude, in Chapter 2, I investigated how BMP-mediated axis patterning has evolved in Cnidaria and Bilateria. The similar effect of zZswim5 and nvZswim4-6 on the BMP signalling gradient in their respective organisms further highlights an evolutionarily conserved molecular repertoire to pattern the secondary axes in bilaterally symmetric animals – anthozoa cnidarians and bilaterians. Future work would involve the analysis of the regulation and functional role of zZswim5 and nvZswim4-6 homologues in different branches of the animal kingdom to further understand the molecular evolution of axis formation.

Chapter 3 – Analysis of Nampta during zebrafish blood cell specification

In the previous chapters, the main focus was to understand how embryonic cells acquire positional information to develop into different organs, spatially oriented along the dorsal-ventral axis of the zebrafish. This was addressed by delineating how extracellular signalling molecules (Chapter 1) and intracellular modulators (Chapter 2) contribute to shaping the BMP signalling gradient, which provides spatiotemporal cues to embryonic cells during gastrulation. In this final chapter, we look at cell fate specification during organogenesis – a developmental time window after gastrulation and when cells become more committed and organs begin to form. Specifically, the focus is to investigate the role of the NAD salvage pathway during blood cell fate specification in zebrafish. I demonstrate how Nampta, a component of the NAD salvage pathway, may support erythrocyte maturation and endothelial cell population, but Nampta is dispensable for zebrafish viability and the progression of haematopoiesis.

Introduction

To support embryonic growth and development, the first functional unit in a vertebrate embryo is the blood-circulatory system (Gilbert and Barresi, 2016). The system constitutes circulating blood cells for tissue repair, oxygen delivery, and protection against pathogens (Hromas et al., 1992). These tasks are accomplished by specialized cells such as red blood cells (erythrocytes) and white blood cells (leukocytes), which are found in vertebrates such as humans, zebrafish, *Xenopus*, and mice (Davidson & Zon, 2004; Dzierzak & Bigas, 2018). The development of these cells is called haematopoiesis, a process closely conserved among vertebrates (Figure 3.1).

Haematopoiesis is a dynamic process (Hromas et al., 1992). Early during embryogenesis, pluripotent cells are instructed to establish prospective blood stem cell niches (Jagannathan-Bogdan & Zon, 2013). These niches then serve as reservoirs for all terminally committed blood cell types during the lifespan of an organism. Therefore, an organism's survival depends on persistent haematopoiesis for the constant replenishment of the blood cell population. This involves balancing between blood stem cell renewal and cell fate commitment under the control of signalling molecules

and transcription factors. Since haematopoiesis is closely conserved among vertebrates, the zebrafish has served as an applicable model organism to study blood development (Davidson & Zon, 2004; Dzierzak & Bigas, 2018). However, we do not fully understand how well-conserved is the molecular regulation of haematopoiesis across species. Here, the focus is to understand how an ancestral signalling pathway, the NAD salvage pathway, precisely regulates zebrafish haematopoiesis.

Zebrafish haematopoiesis

In the zebrafish, blood cell fate specification can be traced back to the onset of gastrulation. *draculin*-positive cells (green) in the mesodermal gastrula migrate to the lateral plate mesoderm during the segmentation stage (Figure 3.1, Figure 3.2A-B) (Mosimann et al., 2015). A subset of these lateral plate mesodermal cells, initially from the ventral-mesoderm with the highest BMP signalling, undergo haematopoiesis to become blood cells (Figure 3.1A-B) (Bertrand et al., 2007; Davidson & Zon, 2004; Vogeli et al., 2006). Other cells in the lateral plate mesoderm are fated to become vascular endothelial cells, kidney cells, and heart cells (Gering et al., 1998).

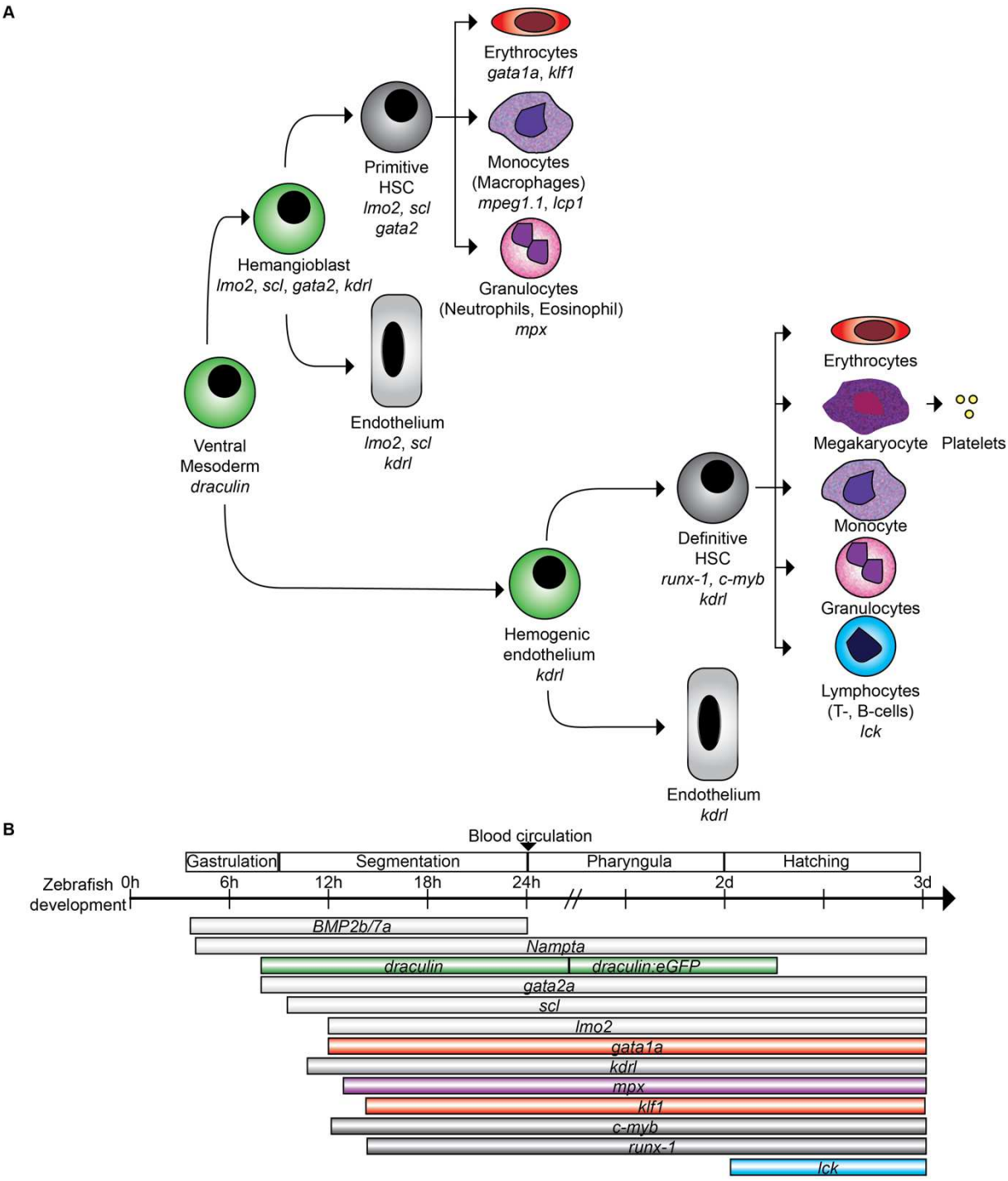

Figure 3.1 Zebrafish haematopoiesis.
A) The haematopoietic differentiation landscape. A subset of *draculin*-positive cells in the ventral mesoderm undergo one of two waves of haematopoiesis. First, during the primitive wave, primitive haematopoietic stem cells (HSCs) arise from bipotential hemangioblasts. These primitive HSCs differentiate into primitive erythrocytes and leukocytes. Second, during the definitive wave, HSCs arise from the hemogenic endothelium. These definitive HSCs differentiate into erythrocytes and specialized leukocytes in later stages of development. Primitive and definitive blood cells are identified by their respective gene markers (italicized). **B)** A summary of the temporal expression profiles of signal pathways components and transcription factors involved in the specification of cell types in (A). Markers and transcription factors have specific colour shading related to specific cell types in (A). Their respective expression onset is based on Expression Atlas by Papatheodorou et al. (2020). Highest BMP signalling

in the ventral-most region gives rise to hemangioblasts. These hemangioblasts differentiate into primitive HSCs through the down-regulation of endothelial marker *kdrl* and the assembly of haematopoietic transcription factors *gata1a/2a*, *scl*, and *lmo2*. Their assembly requires NAD, which is recycled by the enzyme Nampt of the NAD salvage pathway (see Figure 3.3). Additionally, definitive HSCs can be identified by *c-myb* and *runx-1* as expression markers.

Like in other vertebrates, there are two distinct waves of haematopoiesis in zebrafish embryos: the primitive wave and the definitive wave (Boatman et al., 2013; Davidson & Zon, 2004; Robertson et al., 2016). While the exact timing of these waves is currently under active investigation, each wave serves different purposes.

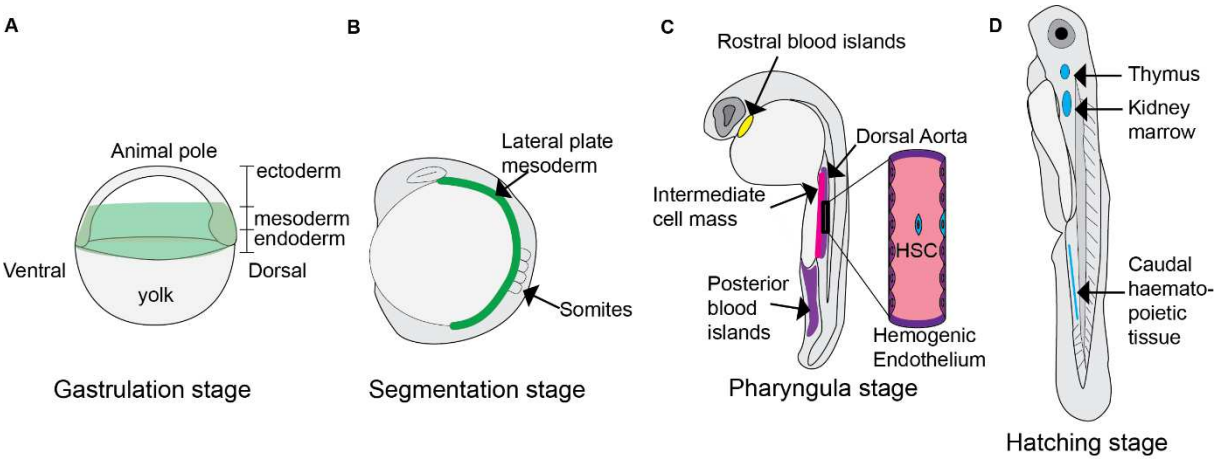

Figure 3.2 The migration of future blood cells during zebrafish embryonic development.
A) *draculin* (green) marks the prospective lateral plate mesoderm during gastrulation. **B)** During the segmentation stage, prospective blood cells migrate from the ventral mesoderm to the lateral plate mesoderm (green). Other mesodermal cells form cardiac cells and somites for muscular and vertebral development. **C)** By the pharyngula stage at 24 hpf, primitive erythrocytes arise from the intermediate cell mass (pink); primitive macrophages arise from the rostral blood islands (yellow). Definitive haematopoietic stem cells (HSCs) arise from the dorsal aorta (purple) and from the posterior blood islands (purple). HSCs (blue) bud out from the hemogenic endothelium (inlet) to migrate and colonize blood stem niches: **(D)** thymus, kidney marrow, and caudal haematopoietic tissue (blue). These niches act as reservoirs for blood cell supply throughout adulthood.

The purpose of the primitive wave is to provide primitive HSCs that differentiate into short-lived erythrocytes and innate immune cells such as monocytes and granulocytes (Figure 3.1A) (Davidson & Zon, 2004). These primitive blood cells help to sustain the rapidly developing embryo (Jagannathan-Bogdan & Zon, 2013) and to remodel the growing tissues of the embryo (Bertrand et al., 2007; Hume et al., 1995; Palis & Yoder, 2001; Wattrus & Zon, 2018). Primitive erythrocytes arise from the intermediate cell mass (Stachura & Traver, 2016; Zhu et al., 2005), and primitive

macrophages arise from the rostral blood islands (Bertrand et al., 2007) (Figure 3.2C). These primitive cells start to circulate in the zebrafish embryo at 24 hpf (Figure 3.1A), but they are short-lived and are fully replaced by blood cells from the definitive wave at the larval stage approximately 7 dpf (Belele et al., 2009).

It is reported that there are two sources of definitive blood cells. The first source consists of transient erythroid-myeloid progenitor cells arising from the posterior blood islands that colonized the caudal haematopoietic tissue in the first 2-3 days (Bertrand et al., 2007). These cells are eventually replaced by cells from the hemogenic endothelium as the second source (Figure 3.2C). The hemogenic endothelium is a specialized structure in the ventral dorsal aorta (Murayama et al., 2006) (Figure 3.2C). During the definitive wave, multilineage haematopoietic stem cells bud out of the hemogenic endothelium between 24 hpf and 48 hpf (Figure 3.2C, inlet) (Bertrand et al., 2010; Bonkhofer et al., 2019; Esain et al., 2016; Lacaud & Kouskoff, 2017; Soto et al., 2021), then migrate through the caudal haematopoietic tissue and eventually colonize the kidney marrow and the thymus (Figure 3.2D). These organs will serve as the blood stem cell niches for a continuous supply of all blood lineages in adult zebrafish (Bertrand et al., 2010; Davidson & Zon, 2004; Stachura & Traver, 2016; Wattrus & Zon, 2018). The blood cells that arise from these niches include (Figure 3.1A): (1) myeloid progenitors that differentiate into red blood cells and innate immune cells and (2) lymphoid progenitor cells that differentiate into adaptive immune cells such as T-cells and B-cells.

A gene regulatory network consisting of transcription factors specifies blood cell fate (Figure 3.1B) (Patterson et al., 2007). LIM domain only 2 (Lmo2), stem cell leukaemia/T-cell acute lymphoblastic leukaemia (Scl/Tal1) and GATA-binding-1/2 (Gata1/2) proteins are at the apex of the haematopoietic transcriptional hierarchy and are conserved among vertebrates (Davidson & Zon, 2004; El Omari et al., 2011; Gering et al., 1998). These are essential transcription factors that function synergistically to specify the blood cells (Figure 3.1) (Davidson & Zon, 2004; Gering et al., 2003; Mead et al., 2001; Patterson et al., 2007).

Note that, in zebrafish, there are two gene homologues for Gata1: *gata1a* and *gata1b* (Bradford, 2022), and Gata2: *gata2a* and *gata2b* (Dobrzycki et al., 2020). However, earlier zebrafish findings do not specify the homologues investigated and mainly present and discuss the general gene names '*gata1*' and '*gata2*' (Belele et al.,

2009; Detrich et al., 1995; Gering et al., 1998; Gering et al., 2003; Lyons et al., 2002; Patterson et al., 2007; Vogeli et al., 2006). 'Gata1' is most likely *gata1a* since it is expressed at the onset of haematopoiesis, while *gata1b* expression is only present at a low level at 75% epiboly (Papatheodorou et al., 2020). As for Gata2, *gata2a* is expressed starting at the blastula stage, while *gata2b* is expressed at 2-3 dpf. Therefore, since the main focus of this thesis is embryogenesis within 1 dpf, zebrafish Gata1a and Gata2a are the main players to consider.

Initially, Lmo2 acts as a scaffold and associate with the LIM-domain interacting protein (Ldb1), which then recruits Scl (Figure 3.3) (El Omari et al., 2011; Morishima et al., 2019). Together, Lmo2/Ldb1/Scl can associate with additional transcription factors to convert mesodermal cells to hemangioblast – the common precursor cell for blood and vascular endothelial cells (Figure 3.1A) (Gering et al., 1998; Gering et al., 2003; Patterson et al., 2007). The hemangioblasts also express blood transcription factor *gata2a* and vascular endothelial receptor *kinase insert domain receptor-like* (*kdrl*) also known as *vascular endothelial growth factor receptor-2* (*vegf2*) in addition to *lmo2* and *scl/tal* (Figure 3.1) (Detrich et al., 1995; Gering et al., 1998). The expression of both *kdrl* and *gata2a* in the hemangioblasts is indicative of their bipotential property (Liang et al., 2001).

To become terminally committed, blood cells require a combination of transcription factors. For example, during the primitive wave, a subset of *scl*$^{+}$/*kdrl*$^{+}$ cells within the intermediate cell mass stop expressing *kdrl* and instead, express *gata1a*, which then forms a complex with Lmo2 and Scl (Figure 3.1, Figure 3.3) (Davidson & Zon, 2004; Dooley et al., 2005; El Omari et al., 2011; Gering et al., 1998; Gering et al., 2003; Tripic et al., 2009). Gata1a is required for the commitment of hemangioblasts and HSCs to erythroid cell lineage (El Omari et al., 2011; Gering et al., 1998; Patterson et al., 2007; Sewell et al., 2014) and the survival of primitive and definitive erythrocytes (Lyons et al., 2002; Weiss & Orkin, 1995). In addition to erythroid commitment, Gata1 has a dual role in initiating and subsequently limiting transcription factor *myeloid-specific peroxidase* (*mpx*) expression in a subset of erythro-myeloid precursor cells (Glenn et al., 2014). Furthermore, Gata1a has a role in maintaining the expression of essential hemangioblast transcription factors. For example, the zebrafish *gata1a* mutant *bloodless* initially show normal expression of *lmo2*, *scl*, and *gata1a* up to 24

hpf, but, interestingly, *scl* expression disappears completely by 30 hpf (Lyons et al., 2002).

Concurrently, Gata2a/b are required for the maintenance and proliferation of HSCs (Dobrzycki et al., 2020; Moriguchi & Yamamoto, 2014) and cannot replace Gata1a for erythroid cell commitment in zebrafish (Gering et al., 2003). This is in line with their expression domains in which *Gata1a* is expressed at the 2-somite stage during which *scl*$^{+}$ cells commit to the erythroid fate (Gering et al., 1998), and *gata2a* expression is detected in zebrafish at 75% epiboly and has an additional role for neuronal development (Detrich et al., 1995). However, this is contradicted by zebrafish morpholino experiments in which the expression of either *gata1a* or *gata2a* is sufficient to maintain the basal expression of both genes, and only knockdown of both *gata1a/2a* will completely abolish the expression of both genes in zebrafish (Galloway et al., 2005). One explanation is that, in mice, Gata2 works with the Gata1 transcription factor for blood cell lineage, and together, they form the Gata switching factors for auto- and reciprocal regulation (Suzuki et al., 2013).

Then members of transcription factors belonging to the Krüppel-like factor (Klf) family, such as Klf1, function to turn on *β-globin* gene expression for the maturation of primitive erythrocytes (Oates et al., 2001; Siatecka & Bieker, 2011; Xue et al., 2015). Currently, the upstream regulation of Klfs is not well elucidated, but Klf4 is thought to be partially Gata-independent (Galloway et al., 2005).

Moreover, cells that express *mpx*, *Spi-1 proto-oncogene b* (*pu.1*), and *lymphocyte cytosolic protein 1 l-plastin* (*lcp1*), but not *gata1a*, eventually differentiate into primitive immune cells (Rhodes et al., 2005). The mutual antagonism of Gata1 and Pu.1 is achieved by directly out-competing each other for binding to their respective target genes (Gore et al., 2018; Graf, 2002; Nerlov et al., 2000; Rekhtman et al., 1999; Zhang et al., 1999; Zhang et al., 2000). Findings in zebrafish show that *gata1a* morphants have expanded *pu.1* expression at 20 hpf and expanded *mpx* and *lcp1* expression at 32 hpf, thus causing an increase in myeloid cells such as granulocytes and monocytes (Rhodes et al., 2005) and demonstrating the interdependent differentiation of myeloid and erythroid cells.

In the absence of *gata1* and *pu.1*, the remaining cells maintain *kdrl* expression and differentiate into endothelial cells to form the vasculature (Gering et al., 1998; Gering et al., 2003). While *kdrl* is often used as a marker of vascular endothelial cells in zebrafish (Gore et al., 2018; Liao et al., 1997), transgenic reporter lines for *kdrl*,

combined with other blood cell markers, are routinely used to identify definitive HSCs in zebrafish (Esain et al., 2016). Additionally, mice deficient in *kdrl* fail to develop blood and vasculature (Shalaby et al., 1995), and all blood cells in the mouse yolk sac and aorta are derived from *kdrl*$^{+}$ cells, thus indicating a dual function for *kdrl*.

Moreover, during the definitive wave, a subset of *scl*$^{+}$/*gata1a*$^{+}$ cells in the medial-lateral plate mesoderm migrate to the dorsal aorta (Figure 3.2B-C) (Bertrand et al., 2007; Murayama et al., 2006). These hemogenic endothelial cells undergo endothelial to haematopoietic transformation to become haematopoietic stem cells, which can be further specified to all blood cell types (Esain et al., 2016). These haematopoietic cells express *v-myb avian myeloblastosis viral oncogene homolog* (*c-myb*) and *RUNX family transcription factor 1* (*runx-1*) that are key transcription factors for the regenerative capacity of HSCs (Figure 3.1B) (Bertrand et al., 2007; Patterson et al., 2007). Together, variations in the components interacting with Lmo2 that make up an oligomeric complex control the genetic program for blood differentiation.

'Haematopoiesis is a risky business' (Hromas et al., 1992). It is a dynamic process that balances blood cell specification and stem cell renewal as it responds to physiological demands, for example, during injuries and infection. This balance is achieved by tightly regulating Lmo2/Scl/Gata1/2 activity (Visvader et al., 1997). In humans, oncogenic blood diseases, such as congenital or acquired leukaemia, are clinical representations of aberrant haematopoiesis. In these leukaemia cases, unhealthy stem cells fail to terminally commit and, instead, divide uncontrollably (Arnone et al., 2020). For example, Lmo2 and Scl were first discovered in human T-cell leukaemia caused by chromosomal translocation of either *LMO2* and *SCL* genes downstream of a lymphocyte promoter, thus arresting lymphocyte differentiation in a stem cell-like state in young patients (Hromas et al., 1992; Rabbitts, 1994; Yamada et al., 1998). This chromosomal translocation shifts the balance of cell fate toward a stem-cell stage and away from a terminally committed one (Morishima et al., 2019). Similar findings were observed *in vitro* using myeloid cell lines where overexpression of *LMO2* arrested cells in an immature blood cell state (Visvader et al., 1997). Translational clinical applications, such as stem cell regeneration and cancer treatment, can benefit from a better understanding of how these haematopoietic transcriptional factors are regulated. One approach is to further elucidate molecular mechanisms controlling haematopoiesis in embryonic models. Recently, it has been reported that the assembly

of the transcriptional complex comprising of Lmo2, Lbd1, Scl, and Gata1/2 involves the NAD salvage pathway (Figure 3.3) (Morishima et al., 2019), discussed below.

The NAD salvage pathway during haematopoiesis

The NAD salvage pathway is the process that maintains NAD concentration – an essential metabolite for several intracellular processes in many organisms, from bacteria to humans (Gazzaniga et al., 2009). The NAD salvage pathway is efficient in recycling NAD by-products using a sequence of enzymes (Figure 3.3) (Conlon & Ford, 2022). First, a dimeric type II nicotinamide phosphoribosyltransferase (NAMPT), the rate-limiting enzyme of the NAD pathway (Wang et al., 2006), converts nicotinamide to nicotinamide mononucleotide (NMN). Second, nicotinamide mononucleotide adenyltransferase (NMNAT) converts NMN to NAD. NAD is classically involved in metabolic oxidative reactions such as glycolysis in the cytoplasm and the electron transport chain in the mitochondria (Canto et al., 2015). Recently, it has gained prominence for its role as an important co-factor of poly(ADP-ribose) polymerases (PARPs) and silent information regulators (Sirtuins) (Conlon & Ford, 2022; Imai, 2009; Imai, 2016). PARPs are one of the most abundant proteins in the nucleus with roles in DNA repair, apoptosis, and regulating gene expression. Sirtuins are deacetylases that post-translationally modify and regulate protein activity (Chalkiadaki & Guarente, 2015). PARPs and Sirtuins consume NAD and release nicotinamide as a by-product. Therefore, the reconstitution of NAD by the NAD salvage pathway is critical to ensure the proper function of PARP and Sirtuins.

A recent report has shown that NAD is indispensable for haematopoiesis (Morishima et al., 2019). First, Sirtuin-2 uses NAD as a co-factor to deacetylate LMO2 at two lysine residues, K74 and K78. LMO2 undergoes conformational change thus permitting the docking of LDB1, SCL, and GATA1/2 (Figure 3.3). Together, the complex switches on a blood-related transcriptional program, including the expression of *gata*, *klf*, and *kdrl*.

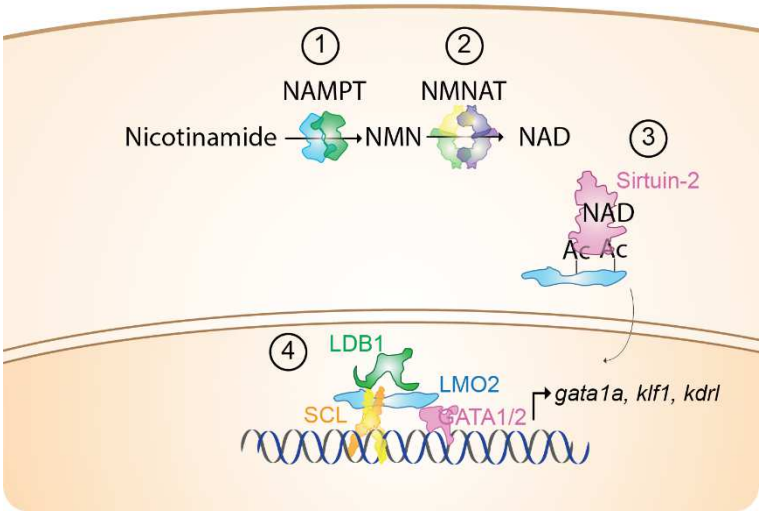

Figure 3.3 The NAD salvage pathway recycles NAD as a cofactor for Sirtuin-2 that deacetylates LMO2 for the assembly of haematopoietic complex.
The NAD salvage pathway restores NAD levels in cells by (1) NAMPT first converting nicotinamide to nicotinamide mononucleotide (NMN). (2) Then NMN adenyltransferase (NMNAT) converts NMN to NAD. (3) Then NAD serves as a co-factor for Sirtuin-2 that deacetylates LMO2. (4) Then LMO2 acts as a scaffold for LDB1, SCL, and GATA1/2, and together, they form a transcription factor complex for blood stem cell specification by turning on *gata1*, *klf1*, and *kdrl*. The diagram is based on the proposed mechanism by Morishima et al. (2019).

Morishima et al. (2019) have provided evidence of how NAMPT and Sirtuin-2 are involved during aberrant and embryonic haematopoiesis. First, they showed that leukemic cell proliferation can be reduced by using a specific Sirtuin-2 inhibitor, AC-93253, (Zhang et al., 2009) or using FK866 treatment that blocks NAMPT. Then, in zebrafish embryos, the morpholino knockdown of *sirtuin-2* or *nampta* caused a decrease in the blood cell population in the zebrafish blood islands (Morishima et al., 2019). The blood count in these zebrafish morphant embryos can be reconstituted by the overexpression of a deacetylation-mimic LMO2 mutant. This was further supported by quantifying changes in the expression of blood-related genes *gata1a* and *klf1* and the hemangioblast/endothelial cell gene *kdrl* by qRT-PCR. These findings by Morishima et al. (2019) suggest that the progression of haematopoiesis can be stalled by blocking Sirtuin-2 or by depleting NAD by blocking NAMPT. Interestingly, while all three genes were significantly decreased in *nampta* morphants, only *kdrl* expression was significantly rescued by overexpression of deacetylation-mimic LMO2 mutant and not *gata1a* and *klf1*. This discrepancy in the changes in the expression of the *gata1a*, *klf1*, and *kdrl* upon *nampta* knockdown and subsequent rescue with LMO2 warrants further investigation into how Nampta regulates zebrafish embryonic haematopoiesis.

Due to genomic duplication in teleost fish (Postlethwait et al., 2000), zebrafish have two Nampt homologues, Nampta and Namptb (Fang et al., 2015). While both homologues are present during zebrafish development, as shown using *in situ* hybridization experiments, developmental defects are observed only upon morpholino-mediated knockdown of *nampta* and not of *namptb* (Fang et al., 2015). Furthermore, protein sequence alignment data showed that *nampta* sequence is more closely conserved to human and mouse NAMPT than *namptb* (Fang et al., 2015). The authors suggested that Namptb may have evolved a divergent function in supporting water-breathing adaptation in fish or it may act redundantly to Nampta. Additionally, Morishima et al. (2019) knockdown *nampta* using splice-site morpholinos and observed a reduction in blood cell population and similar developmental abnormalities as Fang et al. (2015). Hence, previous findings suggest that Nampta, and not Namptb, may be the essential homologue in maintaining NAD levels in zebrafish embryos, specifically during haematopoiesis.

A later study reported that Nampta acts as a cytokine in muscle regeneration of zebrafish, independent of Nampta's NAD function (Ratnayake et al., 2021). *nampta* was detected to be upregulated in macrophages during muscle injury by single-cell RNA sequencing. Ratnayake et al. (2021) proposed that Nampta may be secreted and may bind to C-C motif chemokine receptor type 5 on muscle stem cells to trigger muscle stem cell proliferation. They generated *nampta* mutants and showed that the mutants had impaired muscle regeneration after injury. Surprisingly, the *nampta* mutants are wild-type and viable (Ratnayake et al., 2021) unlike *nampta* morphants, which are malformed and embryonically lethal (Fang et al., 2015; Morishima et al., 2019). Ratnayake et al. (2021) reported that their CRISPR/Cas9-generated *nampta* mutants had an indel in genomic exon-2 that produced three altered amino acid sequences followed by a premature stop codon. The mutant transcript was reduced compared to the wild-type transcript, which is indicative of an activated non-sense mediated decay pathway. The authors concluded that upon *nampta* loss-of-function, Namptb provided sufficient NAD but did not have Nampta signalling domain and, therefore, cannot induce muscle repair. However, it is not clear whether Namptb is additionally upregulated to genetically compensate for *nampta* loss-of-function.

While Nampta may function in different physiological contexts, as supported by previous studies highlighting mouse and human NAMPT's dual function as an enzyme

and as a signalling molecule (Camp et al., 2015; Imai, 2009; Revollo et al., 2007), the inconsistency in the phenotypes of *nampta* morphants (Fang et al., 2015; Morishima et al., 2019) and of *nampta* mutants (Ratnayake et al., 2021) challenges whether Nampta regulates zebrafish haematopoiesis. The difference in observed phenotypes may be due to the disparity between the two loss-of-function approaches – either by transient knockdown using morpholino or by stable knockout lines using CRISPR/Cas9.

Therefore, in this chapter, I aim to re-examine the role of Nampta during haematopoiesis by addressing the discrepancy in the phenotypes resulting from different *nampta* loss-of-function approaches. Here, I will address two possible explanations. First, *nampta* morpholinos may have an off-target toxic effect (Stainier et al., 2017); therefore, the observed phenotypes are unrelated to *nampta* knockdown. Second, the *nampta* mutants have a non-sense mutation that activates the non-sense mediated decay pathway; therefore, Nampta homologues, such as Namptb, function redundantly by genetic compensation (El-Brolosy et al., 2019; Ma & Chen, 2020; Ma et al., 2019) to buffer fluctuations in NAD levels. To address these two cases, first, I established a stable *nampta* mutant knockout line that recapitulates the effect of morpholino reported by Morishima et al. (2019) using the CRISPR/Cas9 mutagenesis approach (Figure 3.4-3.8). Second, I compared the two loss-of-function approaches, morpholinos and CRISPR/Cas9, by assaying their effects on zebrafish embryonic development and the blood cell population. Surprisingly, *nampta* mutants are viable and fertile in contrast to *nampta* morphants (Figure 3.9). While both *nampta* mutants and morphants have mRNA containing premature stop codon, *namptb* expression level did not significantly change in either loss-of-function approach compared to wild-type (Figure 3.10). Nonetheless, both *nampta* loss-of-function approaches cause a decrease in the erythroid maturation gene *klf1* and endothelial receptor *kdrl* expression, but not in the expression of the erythroid specification gene *gata1a* or the myeloid genes *mpx*, *lcp1*, and *mpeg1.1* (Figure 3.11-3.12). Furthermore, the lateral plate mesoderm cell population, precursor cells to cardio, kidney, and hemato-vascular cells, was not affected in *nampta* mutants, suggesting that the lowered expression of haematopoietic markers is not due to a decrease in mesodermal cell population earlier in development, but could be due to a decrease of the hemangioblast cell population (Figure 3.13). The current findings suggest that Nampta provides additional NAD for the assembly of Lmo2/Scl transcriptional complex for the lateral plate mesodermal cell

commitment to hemangioblast and additionally supports in maintaining the blood cell population. Overall, the findings suggest that Nampta is dispensable for zebrafish viability and haematopoiesis.

Results

nampta mutants have no obvious phenotypes in contrast to *nampta* morphants

Currently, there is a discrepancy between the phenotypes reported upon *nampta* loss-of-function in previous studies, which may be due to different loss-of-function approaches. Recently, it is recommended to use promoter-less or whole gene deletions to avoid genetic compensations when knocking-out genes for loss-of-function analysis (El-Brolosy et al., 2019; Ma & Chen, 2020; Ma et al., 2019; Tessadori et al., 2020). However, here, I first address the previously reported blood-related abnormalities when *nampta* exon-2 is spliced-out using *nampta* morpholinos. Therefore, I generated zebrafish *nampta* mutant lines using CRISPR/Cas9 that mimics the exon-skipping effect of morpholinos published by Morishima et al. (2019). The following describes how I established the homozygous *nampta* mutant line.

The splice-site *nampta* morpholino binds at the 5' end of exon-2 in the mRNA causing exon-2 to be spliced-out (Figure 3.4A) (Morishima et al., 2019); therefore, I designed gRNAs that target the *nampta* gene locus at exon-2. The resulting homozygous *nampta* mutant line had a 47 bp deletion spanning the 3' end of exon-2 and the 5' end of intron-2, thus deleting the 5' splice-site consensus sequence (Figure 3.4B). This *nampta* mutant allele was designated as *nampta*^{t10pm}. Interestingly, while the deletion of the 5' splice-site of intron-2 should cause splicing-in of intron-2, the resulting full-length *nampta*^{t10pm} transcript was shorter than the wild-type transcript (Figure 3.4C) because it lacked exon-2 – similar to the *nampta* morphant transcript (Figure 3.4D-F). The mutation may have deleted exon-splicing enhancers (Sharpe and Cooper, 2015), resulting in the spliceosome not recognizing exon-2. Therefore, the results suggest that *nampta* morphants and *nampta*^{t10pm} mutants have the same mature mRNA, except that *nampta* morphants still retain a substantial amount of wild-type *nampta* mRNA (Figure 3.4E).

Importantly, the CRISPR/Cas9 system has been reported to have off-target effects (Zhang et al., 2015). Therefore, to ensure similar genetic background between

mutants and wild-type controls including potential off-target genomic alterations by the CRISPR/Cas9 mechanism, the crispant and the following generation of mutant lines were backcrossed to wildtype *nampta* lines (Port et al., 2020), and *nampta* wild-type and *nampta*^{t10pm} mutants embryos originating from the same P0 crispant line were compared in all the subsequent experiments (Figure 3.5). Briefly, transgenic *draculin:eGFP* embryos were injected with Cas9 + gRNA (Figure 3.4A) to establish an P0 line, which was then reared to adulthood (Figure 3.5). These were backcrossed to the *draculin:eGFP* line to produce heterozygous F1 from which the *nampta*^{t10pm} line was selected. F1 generation was backcrossed to *draculin:eGFP* lines. Then heterozygous F2 fish were in-crossed to produce F3 homozygous mutant *nampta*$^{t10pm/t10pm}$ and wild-type *nampta*$^{+/+}$. F3 lines and subsequent generations were used for the following experiments with F3 *nampta*$^{+/+}$ lines serving as wild-type *nampta* cousin controls.

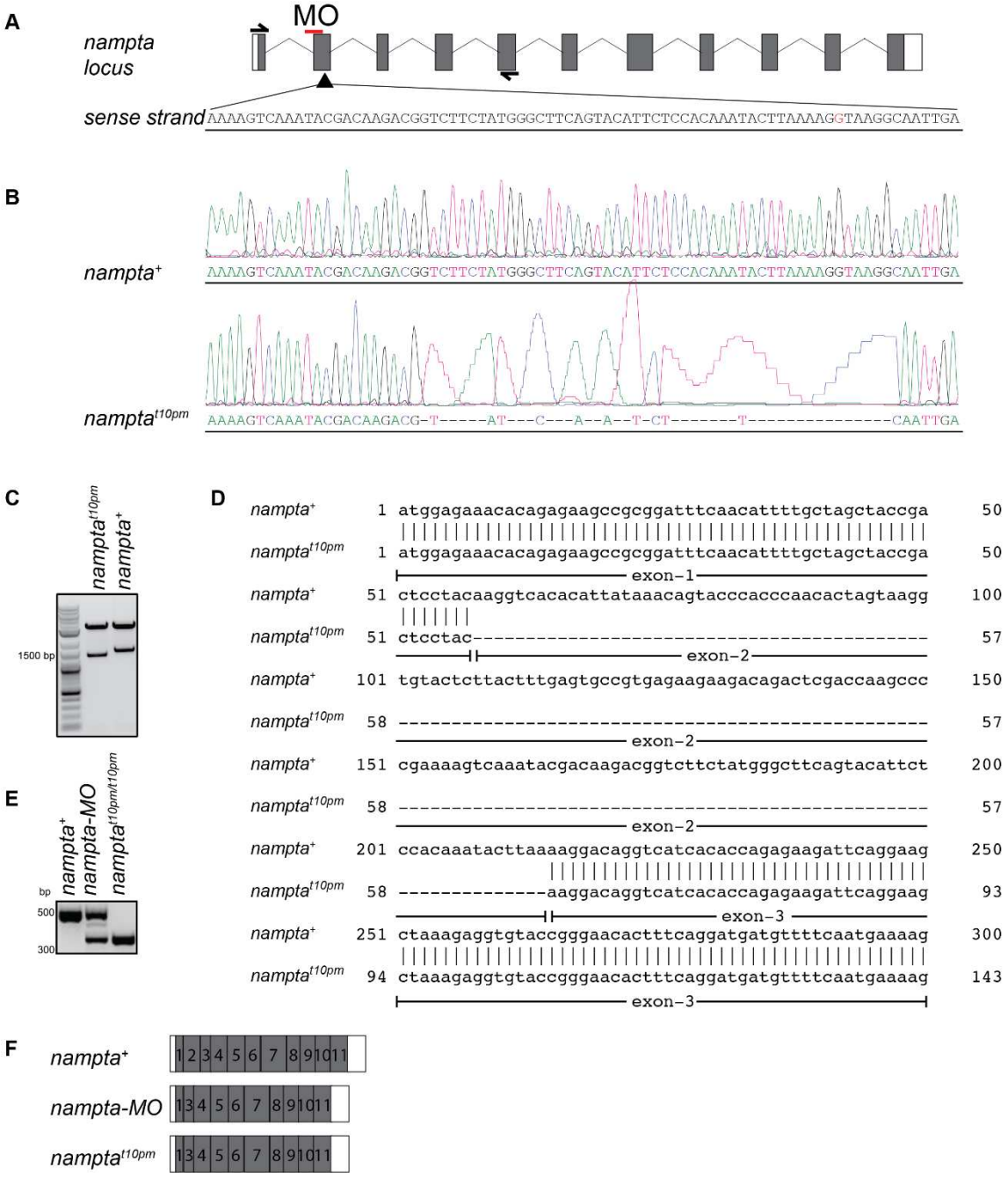

Figure 3.4 *nampta*^{t10pm} mutant line mature mRNA is the same as expected splice-site morphant transcript.

A) Schematic represents *nampta* locus. Grey bars represent exons; white bars represent UTRs, and thin black lines represent introns. Arrowhead marks sgRNA annealing site on *nampta* gene locus for CRISPR/Cas9 mutagenesis. The red bar indicates the morpholino (MO) binding site at the 3' splice site of the intron-1 and exon-2 splice junction on *nampta* pre-mRNA. Half arrows represent the primer annealing site used to amplify and sequence *nampta* mature mRNA, starting from exon-1 to exon-5. Inlet represents a short segment of exon-2 sense strand including 5' splice site 'G' in red between exon-2 and intron-2. **B)** DNA sequence alignment of wild-type *nampta* and *nampta*^{t10pm} with 47 bp indel. **C)** Cloning of wild-type *nampta*$^{+}$ and *nampta*^{t10pm} into *pCS2(+)* vectors and subsequent restriction enzyme digest. **D)** Alignment of cloned wild-type *nampta*$^{+}$ and *nampta*^{t10pm} in (C) show that exon-2 is absent in *nampta*^{t10pm} mutant transcript. **E)** PCR products amplified from wild-type

nampta, *nampta* morphants (*nampta-MO*), and *nampta*$^{t10pm/t10pm}$ cDNA using primers shown in (A). **F)** Schematic of *nampta* wild-type mature mRNA aligned to *nampta* morphant and *nampta*^{t10pm} mutant mature mRNA. Exons are in grey boxes and UTRs in white boxes. Exon-2 is spliced out in both loss-of-function approaches.

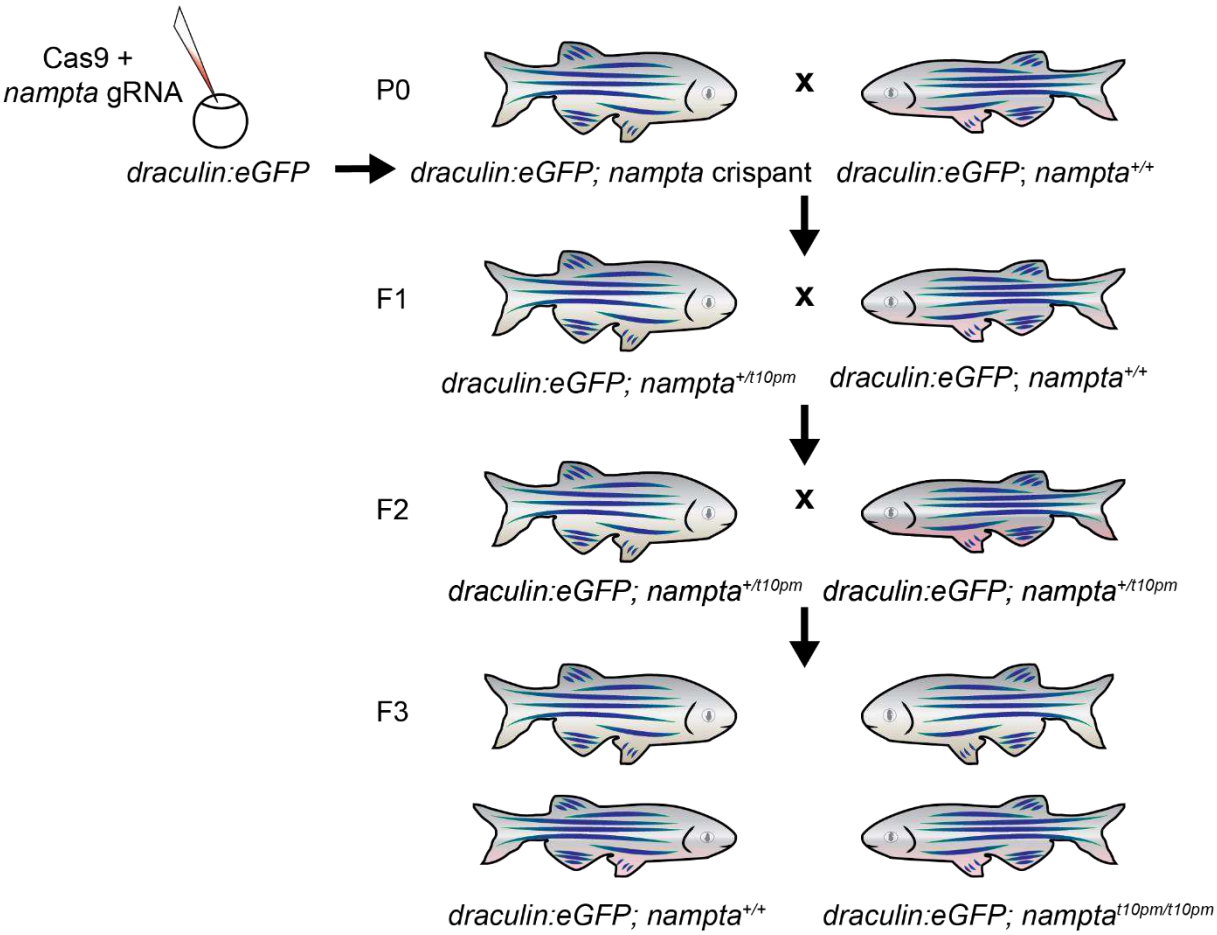

Figure 3.5 Homozygous *nampta*^{t10pm} mutant lines and negative control wild-type *nampta* siblings are from the same crispant background.
To generate homozygous *nampta*^{t10pm} mutant lines using CRISPR/Cas9, *draculin:eGFP* embryos were injected (triangle with red tip) with Cas9 and gRNA targeting exon-2 of the *nampta* gene as shown in Figure 3.4. *nampta* crispants that survived to adulthood are P0. These were backcrossed to *draculin:eGFP* fish, and heterozygous mutant progenies were raised to adulthood (F1). Of these, *nampta*^{t10pm} mutant allele had exon-2 absent in the mature transcript. F1 was backcrossed to *draculin:eGFP* to further eliminate off-target mutations. F2 fish were in-crossed to establish homozygous *nampta*^{t10pm} mutant lines (F3). To control for CRISPR/Cas9 off-target effect, F3 homozygous for the *nampta* wild-type allele *nampta*$^{+}$, were also raised to serve as wild-type cousin controls, thus maintaining a similar genetic background inherited from P0 *nampta* crispants. Adult male zebrafish are marked with pink fins.

Next, to further assess the nature of *nampta*$^{t10pm/t10pm}$ mutation, I determined what is the resulting protein product of the *nampta*^{t10pm} mutation. Nampta is reported to have enzymatic and cytokine functions (Camp et al., 2015; Imai, 2009; Revollo et al., 2007). NAD recycled by Nampta is reported to be indispensable for haematopoiesis

in zebrafish (Morishima et al., 2019). To determine if the NAPRTase domain is absent in *nampta*^{t10pm}, the predicted mutant protein was first determined *in silico* (Figure 3.6). Wild-type Nampta contains 493 amino acid residues and has 2 subdomains (The UniProt Consortium, 2022). The first is a domain of unknown function from N11 to I117, and the second is a domain belonging to the family of nicotinate phosphoribosyltransferase family (NAPRTase) from Y189-G466 (Figure 3.6A). The full-length wild-type Nampta protein product as predicted by NCBI is illustrated in Figure 3.6B using Expasy (Duvaud et al., 2021). Three translational products were predicted from 3 possible starting codon frames (Figure 3.6C). In mutants and morphants lacking exon-2, translation from the canonical start-site AUG results in a premature stop codon, and the Nampta mutant protein product has 96 residues, including aberrant amino acids (Figure 3.6C'). There are also predicted products from alternative start codons, such as short protein fragments in Figure 3.6C'' and another with the NAPRTase domain in Figure 3.6C'''.

Figure 3.6 *In silico* prediction of Nampta^{t10pm} mutant protein product.
A) Schematic of Nampta protein. Nampta contains a domain of unknown function (DUF) N-terminally and an enzymatic domain belonging to the Nicotinate phosphoribosyltransferase family (NAPRTase) C-terminally. **B)** The wild-type Nampta amino acid sequence as represented in Expasy (Duvaud et al., 2021) and **C'-C''')** the three predicted Nampta^{t10pm} mutant protein products. Open reading frames are highlighted in red, and residues in red letters are putative start codons marked by Expasy. The NAPRTase domain is underlined with black in B and C'''. Translation from canonical AUG in mutants results in a truncated product and insertion of aberrant residues, underlined in green in (C').

To assess whether the NAD enzymatic domain is present or absent in mutant embryos, *nampta*$^{+/+}$ and *nampta*$^{t10pm/t10pm}$ embryos were analysed by Western blot

using a commercially available monoclonal antibody that binds to a well-conserved region in the NAPRTase domain in human and mouse NAMPT (Cell Signalling) (Figure 3.7). This region is also present in zebrafish Nampta but not Namptb. Nampta has 493 residues, and the predicted molecular weight is 54 kDa. There was a band of approximately 49 kDa detected in the protein extracts from *nampta*$^{+/+}$ embryos but not in *nampta*$^{t10pm/t10pm}$ embryos (Figure 3.8A). An additional band at 15 kDa was detected in the wild-type sample, which could be degraded Nampta. This suggests that *nampta*$^{t10pm/t10pm}$ mutant protein product does not contain the NAPRTase domain. Therefore, this suggests that NAPRTase domain is not translated from an alternative starting codon as predicted in Figure 3.6C'''.

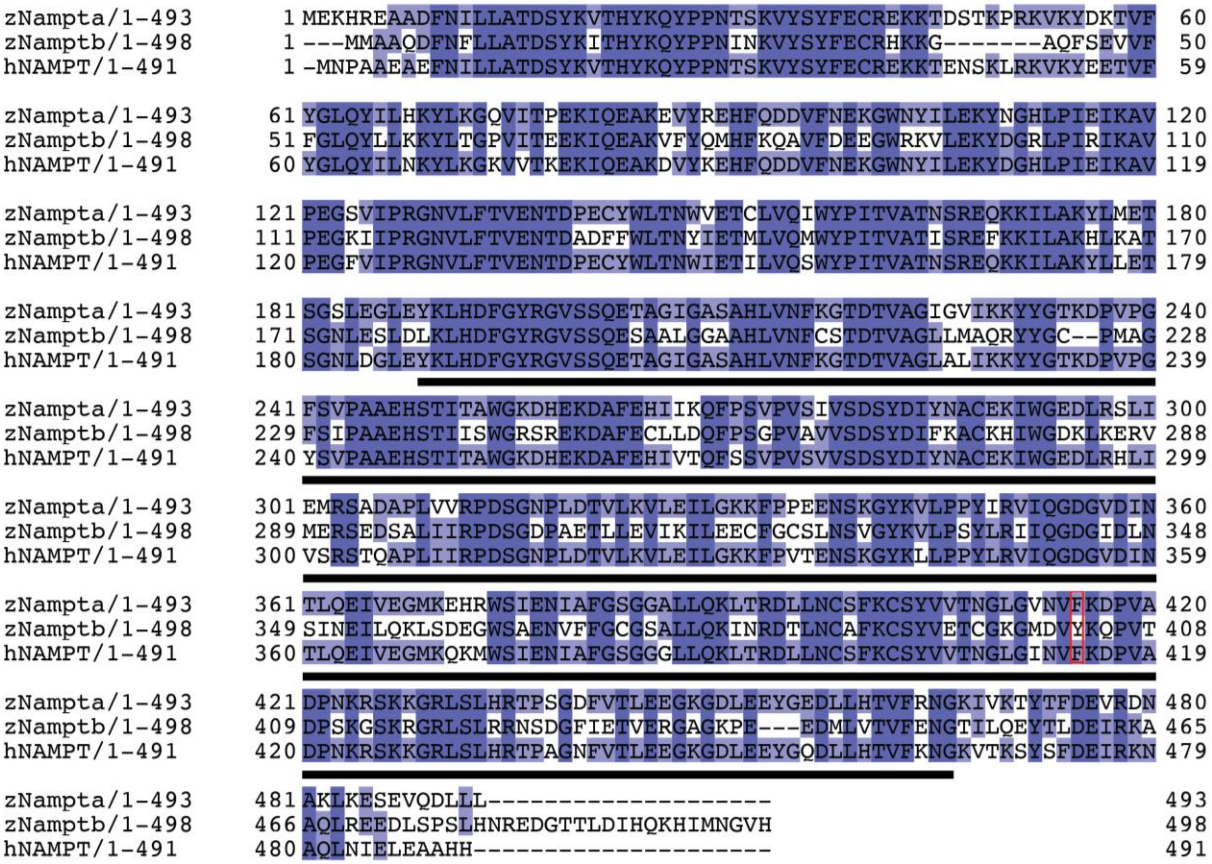

Figure 3.7 Alignment of zebrafish Nampta, Namptb, and human NAMPT.
The colour scheme represents percentage identity across all three homologues using Jalview (Waterhouse et al., 2009) in which white - no similarity, light blue - 2/3 are identical, and dark blue - 3/3 are identical. The commercial antibody used in Figure 3.8A was raised against a synthetic peptide surrounding amino acid F419 in human NAMPT, outlined in red. NAPRTase domain is underlined in black.

To further assay that the *nampta*^{t10pm} transcript is translated from the canonical start-site AUG resulting to 96 aa protein product (Figure 3.8B) as predicted *in silico* in Figure 3.6C', I designed fluorescently-tagged wild-type and mutant Nampta constructs

(Figure 3.8C). Then the resulting fusion proteins were assayed using Western blot (Figure 3.8D). Since the enzymatic domain is C-terminally located, the fluorescent constructs were designed with mCherry (25 kDa) fused at the N-terminus of Nampta (Svoboda *et al.*, 2019) with a FLAG tag as a linker sequence (Figure 3.8C). The predicted size of mCherry-FLAG-Nampta^{+} is 83 kDa and of mCherry-FLAG-Nampta^{t10pm} is 38 kDa. Western blot results showed that full-length *mCherry-FLAG-nampta*$^{+}$ was translated to a protein detected between 75-100 kDa, and the *mCherry-FLAG-nampta*^{t10pm} was translated to a protein detected at 40-50 kDa. This is consistent with the predicted length of mCherry-Nampta^{+} and mCherry-Nampta^{t10pm}. The results suggest that *nampta*^{t10pm} transcript is translated from the canonical AUG, resulting in a truncated protein product.

Intriguingly, the mCherry-FLAG-Nampta^{t10pm} band intensity was weaker than the mCherry-FLAG-Nampta^{+} band. Based on the Coomassie gel staining as the loading control, an equal amount of protein extracts was loaded per lane (Figure 3.8D). To further verify if this weak band is related to a weak fluorescent signal, I directly visualised the fluorescently-tagged constructs using confocal microscopy. In addition, eGFP-STOP-Nampta^{+} with a stop codon after eGFP was co-injected and served as an injection control (Figure 3.8C). The mCherry-FLAG-Nampta^{t10pm} fluorescent signal intensity was weaker than mCherry-FLAG-Nampta^{+} (Figure 3.8E), and eGFP-STOP-Nampta^{+} is comparable in all embryos. Together, these findings suggest that either the mutant construct was not translated as well as the wild-type construct, or that the mutant protein was not as stable as the wild-type protein and was readily degraded.

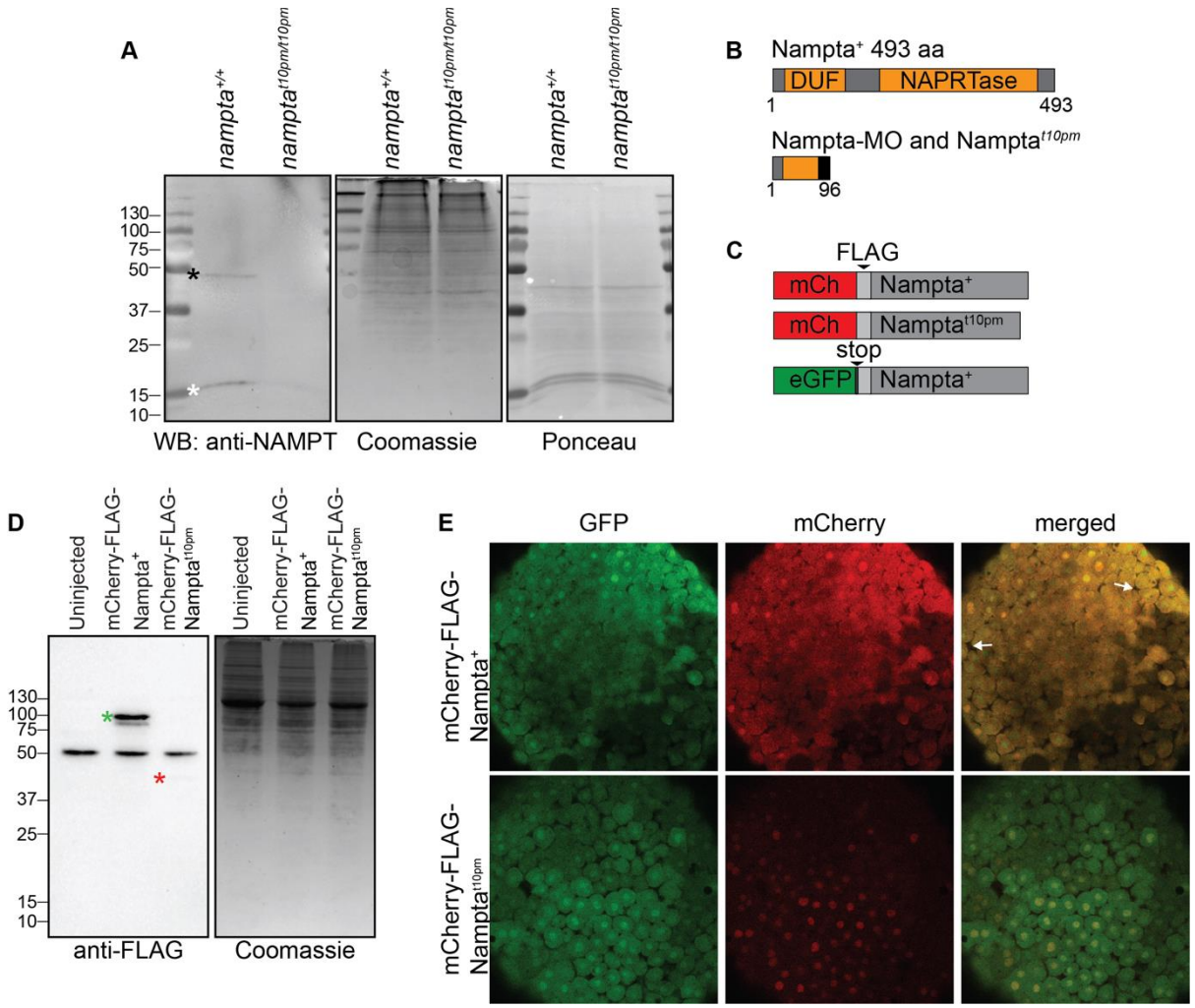

Figure 3.8 Nampta^{t10pm} mutant product is truncated and lacks the NAPRTase domain.
A) Western blot of *nampta*$^{+/+}$ and *nampta*$^{t10pm/t10pm}$ embryos at 5 dpf using anti-NAMPT antibody. Coomassie staining of the gel and Ponceau red staining of the membrane serve as loading controls. The asterisks indicate full-length wild-type Nampta (black) and possibly degraded Nampta (white). Western blot result is from one experimental trial. **B)** Schematic of wild-type Nampta (Nampta^{+}) and truncated Nampta in morphant and mutant. **C)** Schematic of the fluorescently-tagged Nampta, including eGFP-STOP-Nampta^{+} as injection control in (E). mCh – mCherry. **D)** Western blot analysis of fluorescently-tagged Nampta. Embryos were injected at the one-cell stage and deyolked at the sphere stage. Samples were run in SDS-PAGE, then blotted onto a PVDF membrane, and then probed with anti-FLAG antibody. Coomassie staining of the gel served as loading control. Wild-type Nampta is marked with a green asterisk, and mutant Nampta^{t10pm} is marked with a red asterisk. **E)** Embryos were co-injected with wild-type or mutant *mCherry-FLAG-nampta* and *eGFP-stop-nampta*$^{+}$ at the one-cell stage and imaged using a confocal microscope at the sphere stage. Note, that the two Western blots were performed once.

With well-characterised *nampta*^{t10pm} mutant lines, I then compared the phenotypes resulting from the two loss-of-function approaches. Since morphants and mutants were both lacking exon-2, in theory, their phenotypes should be the same.

Intriguingly, homozygous *nampta*$^{t10pm/t10pm}$ exhibited a wild-type phenotype similar to wild-type embryos *nampta*$^{+/+}$ at 1 dpf (Figure 3.9A). These mutants reached adulthood and were fertile (data not shown). This is consistent with the *nampta* mutant reported by Ratnayake et al. (2021). In contrast, morpholino-injected *nampta*$^{t10pm/t10pm}$ and *nampta*$^{+/+}$ embryos exhibited maldevelopment (Figure 3.9A). *nampta* morphants exhibited mild to severe phenotypes (Figure 3.9A-B). Mild morphant phenotypes had smaller eyes and heads, enlarged inner vacuolated cells in the notochord, and disorganised somites that lacked the typically well-defined chevron shape observed in their uninjected siblings. The yolk extension also appeared damaged. In moderate phenotypes, further reduction in head size and curved spinal structures led to a shortening of the body axis. Moreover, time-lapse imaging showed that there is substantial yolk leakage in severe cases, and the embryos lost integrity and disintegrated as the yolk burst before 100% epiboly (Figure 3.9C). Since *nampta*$^{t10pm/t10pm}$ and *nampta*$^{+/+}$ were similarly affected, regardless of their genetic background (Figure 3.9B), this suggests that the aberrant *nampta* morphant phenotype is caused by an off-target effect of the morpholino.

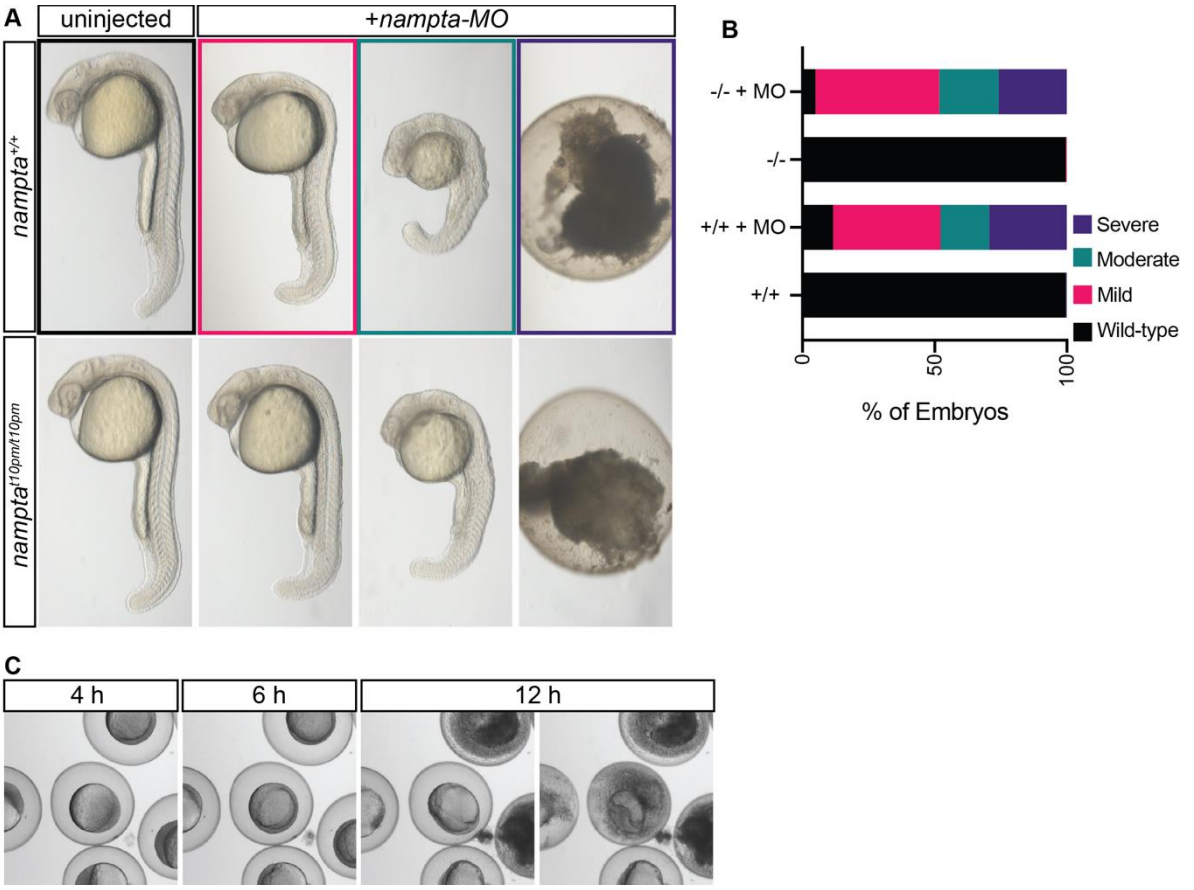

Figure 3.9 *nampta* morpholino has an off-target effect that leads to the maldevelopment of wild-type and mutant *nampta* embryos.
A) Phenotypes of *nampta*$^{+/+}$ and *nampta*$^{t10pm/t10pm}$ injected with *nampta* morpholino (*nampta-MO*). **B)** Distribution of the phenotypes of *nampta*$^{+/+}$ (+/+) and *nampta*$^{t10pm/t10pm}$ (-/-) embryos injected with *nampta* morpholino (MO). Results are a combination of four experimental trials. +/+, n = 366; +/+ + MO, n = 232; -/-, n = 351, and -/- + MO, n = 201. **C)** Time-lapse imaging of embryos with severe phenotypes injected with *nampta* morpholino between 4-12 hours post fertilization.

Next, I investigated whether the wild-type phenotype of *nampta*$^{t10pm/t10pm}$ is due to genetic compensation by Namptb. Recall that premature stop codons in the mature mRNA that are processed by the non-sense mediated decay pathway were reported to trigger transcriptional adaptation, which is the upregulation of homologous genes to buffer against loss-of-function (El-Brolosy et al., 2019; Ma et al., 2019). Here, I find that the Nampta^{t10pm} is truncated, and that mCherry-FLAG-Nampta^{t10pm} protein level is less than mCherry-FLAG-Nampta^{+} (Figure 3.8D), which suggest that either the mutant *nampta*^{t10pm} mRNA is degraded or not well-translated, or that the protein is degraded. If *nampta*^{t10pm} mRNA is degraded, transcriptional adaptation could take place, and Nampta homologues, such as Namptb, are upregulated to buffer against the reduction in NAD upon *nampta* loss-of-function in both approaches. However, while transcriptional adaptation was not observed in null mutants or upon knockdown of gene

function by start-site morpholinos (El-Brolosy et al., 2019), to the best of my knowledge, it is currently unknown whether mutant transcripts caused by splice-site morpholinos can also trigger the non-sense mediated decay pathway.

To investigate whether transcriptional adaptation takes place in embryos containing *nampta*^{t10pm} transcripts, *namptb* expression was quantified using qRT-PCR in uninjected *nampta*$^{+/+}$ and *nampta*$^{t10pm/t10pm}$ embryos and morpholino-injected siblings from both lines. If *namptb* expression is elevated in *nampta*$^{t10pm/t10pm}$, this indicates that transcriptional activation could rescue the *nampta* loss-of-function phenotype in *nampta*$^{t10pm/t10pm}$. However, there was no significant difference between *namptb* transcript levels in *nampta*$^{+/+}$ and *nampta*$^{t10pm/t10pm}$ (mean difference (Δ) = 0.25, p > 0.9999) (Figure 3.10A). This suggests that Namptb does not genetically compensate for *nampta* loss-of-function in mutants. Surprisingly, morpholino injections caused a mild reduction of *namptb* expression in *nampta*$^{+/+}$ and *nampta*$^{t10pm/t10pm}$ compared to uninjected *nampta*$^{+/+}$ embryos (p = 0.1810, p = 0.1342, respectively). The reason for this reduction in *namptb* expression is unclear. One possibility is that the developmental abnormalities in morphants are the result of an off-target effect causing the down-regulation of *namptb*.

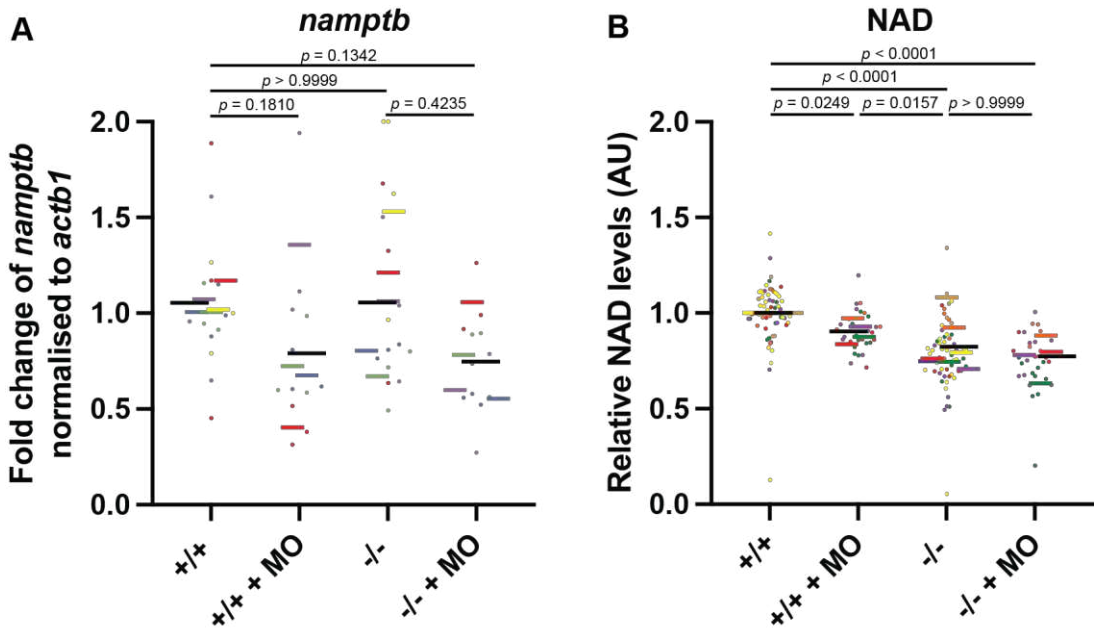

Figure 3.10 Nampta morphants and mutants have reduced NAD levels without genetic compensation by Namptb.
Wild-type *nampta*$^{+/+}$ (+/+) and mutant *nampta*$^{t10pm/t10pm}$ (-/-) embryos were injected with *nampta* morpholino (MO). **A)** Embryos were assayed at 1 dpf for *namptb* expression by qRT-PCR, and the fold change was calculated using $2^{-\Delta\Delta Ct}$ (Livak & Schmittgen, 2001). Data are represented as a scatter dot plot. Each coloured line represents the average from separate experimental trial days with black line representing the average from all trials, and each point representing one biological sample of ten embryos pooled for RNA extraction. **B)** NAD levels relative to uninjected *nampta*$^{+/+}$ are represented as scatter dot plot. Each coloured line represents the average from separate experimental trial days with black line representing the average from all trials, and each point represents individual embryos. For statistical analysis in (A-B), Kruskal-Wallis non-parametric test was applied, followed by Dunn's multiple comparison test to determine the *p*-value using Prism (GraphPad Software).

If *namptb* expression is lower in *nampta* morphants, this could lead to a reduction of NAD in the morphant embryos, which may account for *nampta* morphant maldevelopment. Additionally, it is also possible that currently uncharacterised Nampta homologues could genetically compensate for Nampta in mutants and produce NAD to reach NAD levels similar to wild-type embryos. For example, *nampta* mRNA sequence input in Blast (NCBI, 1988) results in several uncharacterised sequences aligning to *nampta* (data not shown). Therefore, to assess how NAD concentration is affected in the mutants and the morphants, the NAD levels of individual embryos from the four genetic backgrounds were compared (Figure 3.10B). I found that the NAD levels of *nampta*$^{+/+}$ morphants, uninjected *nampta*$^{t10pm/t10pm}$ embryos, and *nampta*$^{t10pm/t10pm}$ morphants were significantly lower than the NAD of uninjected *nampta*$^{+/+}$ embryos ($\Delta = 0.10$, $p = 0.0294$; $\Delta = 0.18$, $p < 0.0001$; $\Delta = 0.23$, $p < 0.0001$,

respectively). Additionally, uninjected *nampta*$^{t10pm/t10pm}$ NAD levels were significantly lower than the NAD levels of *nampta*$^{+/+}$ morphants (Δ = 0.08, p = 0.0157), suggesting a stronger NAD reduction in mutants than in morphants. Overall, while it is inconclusive whether there is additional compensation by other genes homologous to *nampta*, NAD levels are reduced in *nampta* morphants and mutants. Additionally, the morpholino injections did not cause further reduction of NAD levels in mutant *nampta*. This suggests that the reduction in NAD levels in morphants and mutants is caused specifically by *nampta* loss-of-function and not an off-target effect of the morpholino.

Together, the present results provide evidence that the *nampta*^{t10pm} is a non-sense mutation with a truncation upstream of the NAPRTase domain, thus causing a reduction in NAD levels. These results demonstrate that embryos are viable even with lower NAD upon *nampta* loss-of-function. This is consistent with the phenotypes of *nampta* mutants reported by Ratnayake et al. (2021), and therefore, the aberrant morphant phenotype in Figure 3.9A and Morishima et al. (2019) may be due to morpholino toxicity.

Previous experimental evidence linking haematopoiesis and Nampta in zebrafish is based on *nampta* morphant data (Morishima et al., 2019), yet the present findings suggest that the morpholino has off-target effects causing developmental defects unrelated to Nampta function. This suggests that the zebrafish viability, and perhaps blood development, are independent of Nampta; however, I cannot fully exclude that Nampta has no effect on haematopoiesis. It is yet to be determined whether the haematopoiesis is specifically dependent on NAD recycled by Nampta. Therefore, in the next section, I present how Nampta may precisely regulate the progression of haematopoiesis.

nampta loss-of-function causes a decrease in the expression level of blood and endothelial gene markers

Recall that deacetylation of Lmo2 by NAD-dependent Sirtuin-2 is essential for the assembly of haematopoietic transcription complex Lmo2/Lbd1/Scl/Gata1/2 (Figure 3.3) (Davidson & Zon, 2004; Morishima et al., 2019). In zebrafish, Lmo2 and Scl form a complex to convert non-axial mesoderm into hemangioblasts, expressing the blood transcription marker *gata2a* and the vascular endothelial receptor *kdrl*, which is indicative of hemangioblast bipotency (Davidson & Zon, 2004; Gering et al., 2003).

The expression of *gata1a* concurrent with down-regulation of *kdrl* expression in a subset of *scl*$^{+}$ cells converts hemangioblast to blood progenitor cells (Gering et al., 1998; Patterson et al., 2007), but in the absence of *gata1a*, the hemangioblast differentiate into endothelial cells (Gering et al., 2003). To re-examine Nampta's role in the progression of primitive haematopoiesis starting from hemangioblast specification and to more committed cells such as primitive erythrocytes, the expression of the endothelial marker *kdrl*, the erythroid-specific transcription factor *gata1a* (Rhodes et al., 2005), and the transcription factor *klf1* that binds to the beta-globin promoter for erythrocyte maturation (Kulkeaw & Sugiyama, 2012; Oates et al., 2001) were measured in uninjected *nampta*$^{+/+}$ and *nampta*$^{t10pm/t10pm}$ and in *nampta*$^{+/+}$ and *nampta*$^{t10pm/t10pm}$ morphants embryos at 1 dpf by qRT-PCR (Figure 3.11A-C). If Nampta regulates hemangioblasts specification, the expression of all 3 genes is expected to decrease upon *nampta* loss-of-function. If Nampta has a role later in haematopoiesis such as regulating the erythrocyte commitment and/or maturation, then *gata1a*, *klf1*, or both are expected to decrease upon *nampta* loss-of-function.

First, *kdrl* expression was significantly reduced in *nampta*$^{+/+}$ morphants (Δ = 0.25, p = 0.0005), in uninjected *nampta*$^{t10pm/t10pm}$ mutants (Δ = 0.23, p = 0.0007), and in *nampta*$^{t10pm/t10pm}$ morphants (Δ = 0.18, p = 0.0159) compared to uninjected *nampta*$^{+/+}$ (Figure 3.11A). This suggests that there is a reduction in hemangioblast population upon *nampta* loss-of-function. However, since *kdrl* is also expressed in endothelial cells, the possibility that *nampta* loss-of-function specifically causes the reduction of endothelial cells cannot be excluded. Interestingly, the reduction in either hemangioblasts or endothelial cells is not embryonically lethal, suggesting that sufficient NAD is remaining for some cells to undergo haematopoiesis.

Next, compared to uninjected *nampta*$^{+/+}$, *gata1a* expression was significantly reduced in *nampta*$^{+/+}$ morphants (Δ = 0.30, p = 0.0223), unaffected in uninjected *nampta*$^{t10pm/t10pm}$ mutants (Δ = 0.06, p > 0.9999), and mildly reduced in *nampta*$^{t10pm/t10pm}$ morphants (Δ = 0.20, p = 0.1172) (Figure 3.11B). In contrast to the reduction in *kdrl* expression upon *nampta* loss-of-function in both approaches, *gata1a* expression is only affected in morphants, suggesting that the morpholino has an off-target effect, which down-regulates *gata1a*. This also suggests that the loss of *nampta* does not impair the commitment of hemangioblast to erythroid cell lineage.

Finally, *klf1* expression was significantly reduced in *nampta*$^{+/+}$ morphants (Δ = 0.40, p = 0.0001), in uninjected *nampta*$^{t10pm/t10pm}$ mutants (Δ = 0.23, p = 0.0211), and

in *nampta*$^{t10pm/t10pm}$ morphants (Δ = 0.30, p = 0.0009) compared to uninjected *nampta*$^{+/+}$ (Figure 3.11C). The decrease in *klf1* expression suggests a reduction in erythrocyte maturation upon *nampta* loss-of-function.

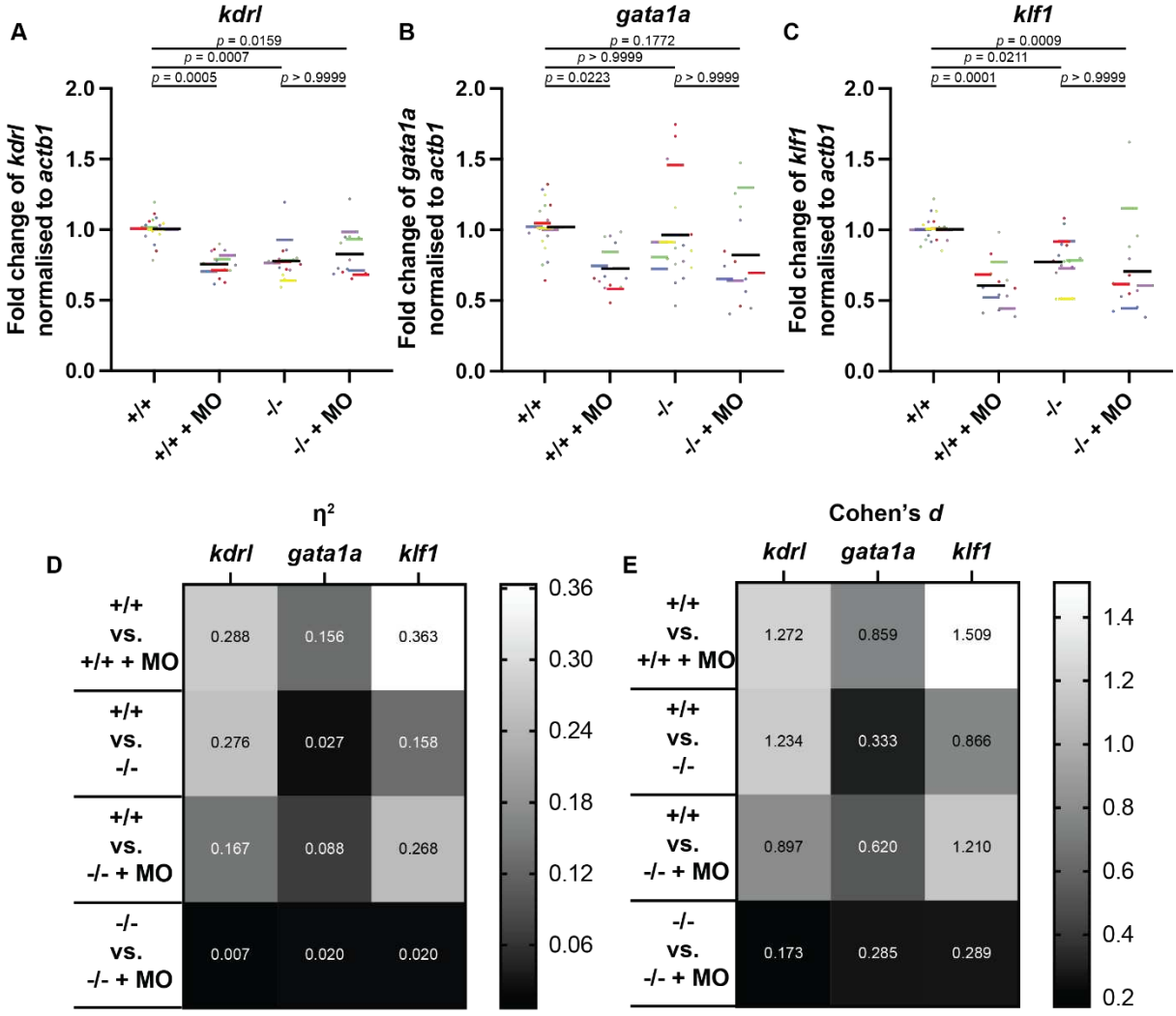

Figure 3.11 Hemangioblast/endothelial- and erythrocyte maturation marker expressions are reduced upon *nampta* loss-of-function.
nampta$^{+/+}$ (+/+) and *nampta*$^{t10pm/t10pm}$ (-/-) embryos were injected with *nampta* morpholino (MO). Embryos were assayed at 1 dpf for the expression of **A)** hemangioblast/endothelial marker *kdrl* and erythrocyte markers **B)** *gata1a* and **C)** *klf1* by qRT-PCR. The fold change was calculated using $2^{-\Delta\Delta Ct}$ (Livak & Schmittgen, 2001). Data are represented as scatter dot plot. Each coloured line represents the average from separate experimental trial days with black line representing the average from all trials, and each point represents one biological sample of ten embryos pooled for RNA extraction. For statistical analysis, Kruskal-Wallis non-parametric test was applied, followed by Dunn's multiple comparison test to determine the *p*-value using Prism (GraphPad Software). **D)** The effect size for Kruskal-Wallis multiple comparison test to compare each group is represented as eta squared (η^2). 0.01 - 0.6 is a small effect, 0.6 - 0.14 is a medium effect, and >0.14 is a large effect. **E)** The equivalent Cohen's *d* for each η^2 is provided.

Moreover, to facilitate comparison between the impact of the two loss-of-function approaches, the effect size, which represents how substantial is the difference between two populations, was quantified and represented as eta squared η^2 for the non-parametric Kruskal-Wallis test combined with Dunn's multiple comparison test (Figure 3.11D) (see Materials and Methods for further explanation). The equivalent Cohen's *d* to each η^2 is also shown (Figure 3.11E). I found that the effect size of the fold change in *kdrl* expression level in *nampta*$^{+/+}$ morphants and uninjected *nampta*$^{t10pm/t10pm}$ to uninjected *nampta*$^{+/+}$ were similar (η^2 = 0.288, η^2 = 0.276, respectively). However, the effect size of the fold change in *gata1a* expression level of both *nampta*$^{+/+}$ and *nampta*$^{t10pm/t10pm}$ morphants to uninjected *nampta*$^{+/+}$ (η^2 = 0.156, η^2 = 0.088, respectively) were greater than the effect size of uninjected *nampta*$^{t10pm/t10pm}$ to uninjected *nampta*$^{+/+}$ (η^2 = 0.027). The comparison of the effect sizes further suggests that the morpholino may reduce *gata1a* expression independent of *nampta* loss-of-function. Similarly, the effect size of the fold change in the expression level of *klf1* in *nampta*$^{+/+}$ and *nampta*$^{t10pm/t10pm}$ morphants to uninjected *nampta*$^{+/+}$ (η^2 = 0.363, η^2 = 0.268, respectively) were greater than that of uninjected *nampta*$^{t10pm/t10pm}$ to uninjected *nampta*$^{+/+}$ (η^2 = 0.158). These results also suggest that the morpholino causes a further decrease in *klf1* expression compared to the levels in stable mutant lines. However, the difference in effect size of the fold change in *gata1a* and *klf1* between uninjected *nampta*$^{t10pm/t10pm}$ and *nampta*$^{t10pm/t10pm}$ morphants is small (η^2 = 0.020 for both) (Figure 3.11D). This suggests that the morpholino does not cause a significant change in erythroid marker expression in *nampta* mutants.

The combined results of the effect sizes and mean difference suggest that the *nampta* morpholino has an off-target effect on *gata1a* and *klf1* expression but not on *kdrl*. This is in line with the results in Morishima et al. (2019) that, in *nampta* morphants, *kdrl* expression was significantly rescued by injection of deacetylation-mimic LMO2 mutant but not *gata1a* and *klf1* expression.

Overall, the present findings suggest that Nampta differentially regulates *gata1a*, *klf1*, and *kdrl*. *nampta* loss-of-function in stable mutant lines caused a significant decrease in the expression of *klf1* and *kdrl*, but not *gata1a*. If we then consider the expression of these genes as representative of the population of the cells that express them, we can then assume that *nampta* loss-of-function has varying effects on each cell type. First, based on the reduction of *kdrl* upon *nampta* loss-of-

function (Figure 3.11A), Nampta may support the maintenance of hemangioblast cell and/or endothelial cell populations. Second, based on the reduction of *klf1* and unaffected *gata1a* (Figure 3.11B-C), Nampta may have a role in erythrocyte maturation but no role in the erythroid cell commitment.

To determine further whether other blood cell types are affected upon *nampta* loss-of-function, additional blood cell markers were quantified by qRT-PCR. Specifically, fold change in expression of well-established leukocyte markers were quantified, such as *mpx* for granulocytes such as neutrophils (Davidson & Zon, 2004; Renshaw et al., 2006) and *lcp1* and *macrophage expressed 1* (*mpeg1.1*) for macrophages (Davidson & Zon, 2004; Ferrero et al., 2020; Kell et al., 2018) (Figure 3.1). I found that there was no significant change in the expression of all leukocyte markers between uninjected *nampta*$^{+/+}$ and uninjected *nampta*$^{t10pm/t10pm}$ or morphants (Figure 3.12A-C), except a significant increase in *mpx* in *nampta*$^{+/+}$ morphants (Δ = 1.8, p = 0.0127) (Figure 3.12A). Overall, this is in line with the unaffected *gata1a* expression (Figure 3.11B). Together, this indicates that the erythroid and myeloid populations are not strongly affected by *nampta* loss-of-function in zebrafish. However, it is not known whether the hemangioblast or endothelial cell population is affected upon *nampta* loss-of-function.

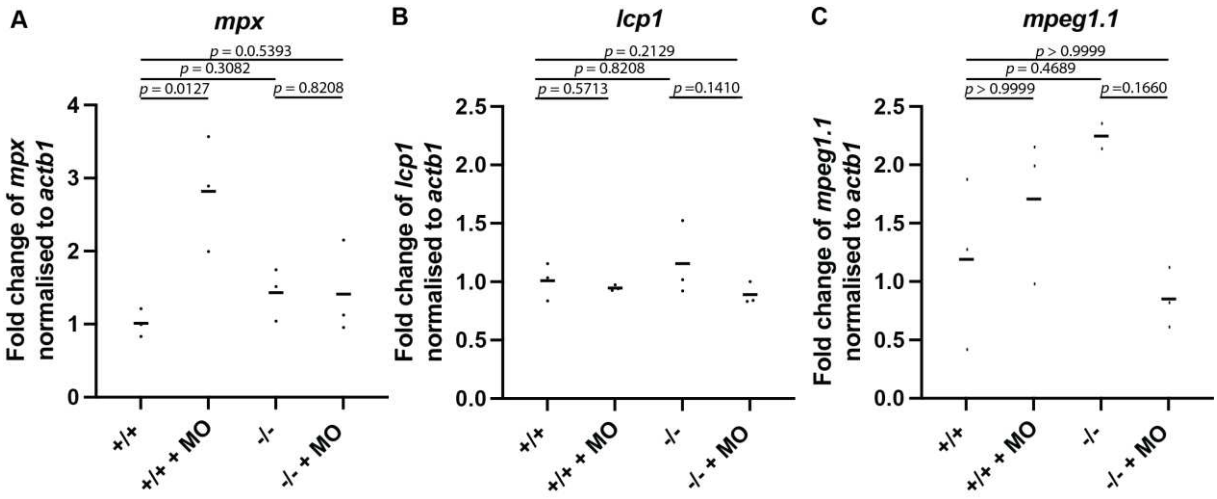

Figure 3.12 Myeloid gene markers expression levels are unaffected in either *nampta* loss-of-function approach.
nampta$^{+/+}$ (+/+) and mutant *nampta*$^{t10pm/t10pm}$ (-/-) embryos were injected with *nampta* morpholino (MO). Embryos were assayed at 1 dpf for the expression of **A)** granulocyte marker *mpx* and **B-C)** macrophage markers *lcp1* and *mpeg1.1* by qRT-PCR. The fold change was calculated using $2^{-\Delta\Delta Ct}$ Livak and Schmittgen (2001). Data are represented as scatter dot plot with the horizontal line representing the average from one experimental trial. Each point represents one biological sample of ten embryos pooled for RNA extraction. For statistical analysis, Kruskal-Wallis non-parametric test was applied, followed by Dunn's multiple comparison test to determine the *p*-value using Prism (GraphPad Software).

NAD-dependent Sirtuin-2 deacetylation of Lmo2 is essential for docking of additional haematopoietic transcription factors (Morishima et al., 2019) for specification of a subset of cells in the lateral plate mesoderm to become hemangioblast. This coincides with *nampta* expression at the onset of gastrulation (Figure 3.1), suggesting that Nampta may specify lateral plate mesodermal cell population or earlier precursor cells. In theory, this could explain the decrease in *kdrl* expression observed upon *nampta* loss-of-function. To this end, the *draculin:eGFP* fish line that stably expresses GFP under the *draculin* promoter as a marker for presumptive lateral plate mesodermal cells (Mosimann et al., 2015) was used to establish P0 (Figure 3.2B, Figure 3.5). To determine whether the lateral plate mesodermal cell population is affected in *nampta* loss-of-function, *draculin:eGFP* positive cells were quantified in both uninjected *nampta*$^{+/+}$ and uninjected *nampta*$^{t10pm/t10pm}$ by FACS (Figure 3.13). The cell suspension protocol for 1 dpf zebrafish embryos was optimised from Bresciani et al. (2018) (see Materials and Methods). To set a baseline for GFP^{-} cells, embryos from non-transgenic lines were used as controls (Figure 3.13A). Cells detected above this baseline represent GFP^{+} cells. For example, in embryos from *draculin:eGFP* lines, 9.83% of measured cells are GFP^{+} (Figure 3.13B). With this, I found that *nampta*$^{+/+}$ and

nampta$^{t10pm/t10pm}$ embryos had similar GFP$^+$ cell populations (Figure 3.13C-D). This suggests that the reduction in NAD upon *nampta* loss-of-function has no effect on the lateral plate mesodermal cell population. Together with the findings that there is a reduction in *kdrl* and *klf* expression but not *gata1a*, *mpx*, *lcp1*, and *mpeg1.1* upon *nampta* loss-of-function, the results suggests that *nampta* loss-of-function has a specific effect on endothelial cell population and erythrocytes specification.

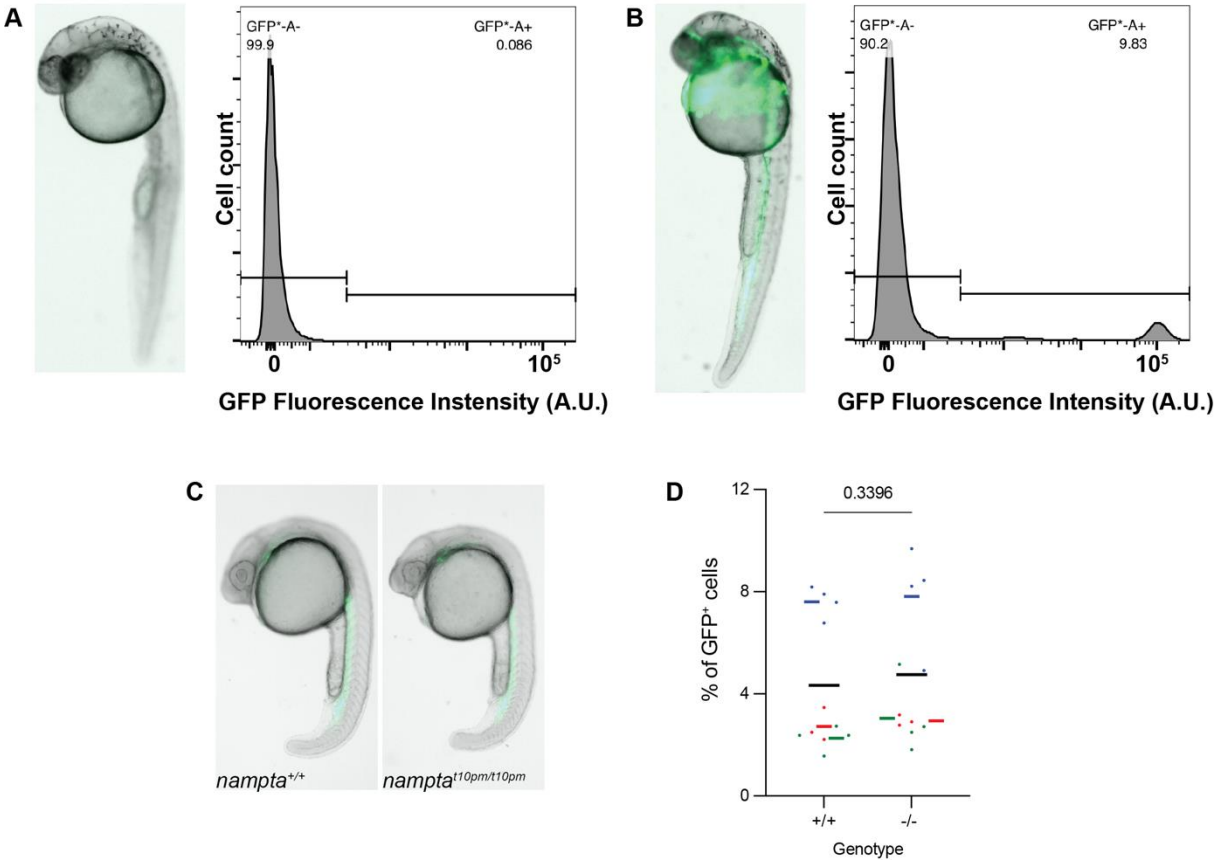

Figure 3.13 *nampta*$^{+/+}$ and *nampta*$^{t10pm/t10pm}$ embryos have comparable *draculin:eGFP* positive cell population.
To quantify the population of lateral plate mesodermal cells, transgenic *draculin:eGFP* zebrafish embryos were homogenized, and the GFP$^+$ cells were quantified using fluorescence activated cell sorting (FACS). **A)** Embryos without transgenic eGFP were used as cut-off for GFP$^-$ cells. A.U. – arbitrary unit. **B)** Example of FACS read-out of GFP$^+$ cells in *draculin:eGFP* embryos that are detected above the baseline cut-off set in (A). **C)** Images of *nampta*$^{+/+}$ (+/+) and *nampta*$^{t10pm/t10pm}$ (-/-) embryos in *draculin:eGFP* background (green) before homogenization and quantification of GFP$^+$ cells by FACS. **D)** Quantification of GFP$^+$ cells are represented as scatter dot plot with each coloured line representing the average from separate experimental trial day and each point representing one embryo. Black bar is the mean of all trials. For statistical analysis, Mann-Whitney test was applied to determine the *p*-value using Prism (GraphPad Software).

Discussion

In vertebrates and some invertebrates, embryonic development and animal survival throughout adulthood are dependent upon haematopoiesis for the production of blood cells (Grigorian & Hartenstein, 2013; Jagannathan-Bogdan & Zon, 2013). The process of haematopoiesis involves an intricate interplay of signalling molecules and transcription factors (Davidson & Zon, 2004; Hromas et al., 1992). The NAD-dependent assembly of Lmo2, Scl, and Gata1/2 is at the top of the transcriptional hierarchy of blood development (El Omari et al., 2011; Morishima et al., 2019). In this chapter, I analysed the extent of the contribution of Nampta, one of two Nampt homologues in the zebrafish, to the NAD levels necessary for haematopoiesis. The main motivation was to address the discrepancy between the phenotypes of the zebrafish embryos resulting from two different loss-of-function approaches in two separate reports – either by transient knockdown using morpholinos (Morishima et al., 2019) or by generation of stable mutant line using CRISPR/Cas9 (Ratnayake et al., 2021). First, I have generated and characterised the *nampta*^{t10pm} mutant lines in which exon-2 is spliced-out similar to the effect of previously published splice-site morpholinos (Morishima et al., 2019) (Figure 3.4). These are non-sense loss-of-function mutants with reduced NAD levels and no strong evidence of transcriptional adaptation by upregulation of *namptb* expression (Figure 3.10). Furthermore, these *nampta*^{t10pm} mutant lines are viable, have no observable developmental malformation (Figure 3.9), and have similar lateral plate mesodermal cell population as wild-type *nampta* lines (Figure 3.13). However, injections of *nampta* morpholino caused developmental defects similar to previously reported morphant phenotypes, suggesting an unspecific toxic effect of the morpholino. Analysis of blood and endothelial gene markers in *nampta*$^{t10pm/t10pm}$ mutants suggests that Nampta has a supporting role during haematopoiesis, such as a role in erythrocyte commitment and in maintaining hemangioblast and/or endothelial cell population (Figure 3.11). Overall, the NAD recycled by other Nampt homologues, such as Namptb, seems to be sufficient for haematopoiesis and for the viability of the zebrafish embryo.

nampta morpholino has off-target effects

The present findings have demonstrated that the splice-site *nampta* morpholinos from Morishima et al. (2019) have off-target effects. Since the *nampta*^{t10pm} mutants and *nampta* morphants have the same mature mRNA (Figure 3.4F), the

predicted phenotype would be the same in both *nampta* loss-of-function approaches. However, here, I have shown that *nampta* morphants exhibit developmental defects, while *nampta* mutants are wild-type and viable (Figure 3.9). Comparison of both loss-of-function approaches in the same embryo demonstrates that the morpholino can induce developmental defects in wild-type and mutant *nampta* embryos. In addition, there is a significant decrease in *gata1a* expression and a further decrease in *klf1* expression in *nampta* morphants compared to *nampta* mutants (Figure 3.11). The results suggest that the morpholino off-target effects are independent of *nampta* knockdown and may be independent of Lmo2 deacetylation. This is in line with the findings that injection of deacetylation-mimic LMO2 mutant did not significantly rescue *gata1a* or *klf1* expression (Morishima et al., 2019), while *kdrl* expression was rescued to the wild-type level. It is yet to be determined whether the off-target effects can be reduced by co-injection of *p53* morpholino as recommended by Stainier et al. (2017).

Such discrepancies between gene knockdown (morpholinos) and gene knockout (stable mutants) are observed for several genes and are currently debated in the zebrafish research community (Sztal & Stainier, 2020). The advent of facilitated reverse genetic screens revealed poor correlations between the stable mutants and transient morpholino knockdown (Kok et al., 2015). It was reported that approximately 10 of 20 stable mutant lines did not have the same phenotype as the corresponding morpholino (Kok et al., 2015). There are two explanations for these discrepancies.

First, El-Brolosy et al. (2019) presented a novel mechanism called transcriptional adaptation that explains how the nature of the mutation may determine whether or not genetic compensation occurs. Their work has shown that activation of the non-sense mediated decay pathway by the presence of premature termination codons in mutant mRNAs can signal for upregulation of homologous genes to buffer against the deleterious mutations. The milder phenotypes in mutants compared to morpholino knockdown are indications of genetic compensation (Rossi et al., 2015). For example, stable *Efl7* non-sense mutant lines are genetically compensated by the upregulation of *emilin* gene family that contains the same functional domain as *Efl7*. In contrast, complete deletion of the locus, deletion of transcriptional start site, or translation blocking morpholino do not have non-sense mRNAs with premature termination codons and, therefore, do not activate transcriptional adaptation (El-Brolosy et al., 2019). Moreover, whether splice-site morpholino causing non-sense

mutant mRNA can activate non-sense mediated decay pathway and transcriptional adaptation was previously unknown, but here, I have shown that *namptb* expression was not upregulated in splice-site morphants (Figure 3.10).

However, transcriptional adaptation does not occur in the presence of every non-sense mutant allele. That is, transcriptional adaptation may be gene- and allele-specific (El-Brolosy et al., 2019; Ma & Chen, 2020; Ma et al., 2019; Sztal & Stainier, 2020). For example, it is reported that transcriptional adaptation only occurred in mutant *capn3a* alleles in which at least 90% of the non-sense mutant mRNA is degraded (Ma et al., 2019). Therefore, for some genes, a sufficient amount of degraded mutant transcript must be produced by non-sense mediated decay pathway for transcriptional adaptation to take place. Additionally, the upregulation of homologous genes requires sequence similarity to either the exon or intron of the mutant allele (Sztal & Stainier, 2020). In this study, I provide additional evidence that suggest that not all genes with non-sense mutations can be genetically compensated by transcriptional adaptation through upregulation of homologous genes. Non-sense mutant *nampta*^{t10pm} did not have significant increase in *namptb* expression (Figure 3.10A), indicating that Namptb does not genetically compensate for the loss of Nampta, hence, the reduction of NAD levels in *nampta* mutants. Whether other genes with sequence similarity and functional domains to Nampta are upregulated is yet to be examined.

The second explanation for the discrepancy between morpholino and stable mutant phenotypes is that morpholinos can have off-target effects. The findings in this study have demonstrated that *nampta* morpholinos have off-target effects causing developmental defects, while *nampta* mutants that mimic the morphant mRNA are phenotypically wild-type. This observation is consistent with previous studies that also compared mutant and morphant results for other genes of interest and found that the morpholinos had off-target effects. For example, morpholino-mediated knockdown of the *prrx1a* gene was reported to cause incorrect heart-looping in zebrafish compared to control morpholinos (Ocaña et al., 2017). In contrast, later studies reported that zebrafish had normal heart-looping despite complete locus deletion of *prrx1a* and knockout of *prrx1* homologues (Tessadori et al., 2020). It was expected that since the complete deletion of the *prrx1a* coding region does not give rise to a mutant mRNA with premature termination codons and does not activate transcriptional adaptation,

the null mutants, just like the morphants, would show incorrect heart looping. However, only the *prrx1a* morpholino caused the heart-looping defect. Additional investigation revealed that the *prrx1a* morpholino affected heart-looping-related genes whose expression is before the onset of *prrx1a*. Tessadori et al. (2020) concluded that the initially reported *prrx1a* morpholino phenotypes in Ocaña et al. (2017) were due to morpholino off-target effects that may be upstream and independent of Prrx1 function.

Overall, these gene-specific findings have emphasized the need for a new gold standard when investigating a gene's function. This includes carefully comparing mutants and morphants and verifying the nature of the mutation. Specifically, it is recommended to follow the current guidelines when using morpholinos provided by Stainier *et al*. (2017) and to generate full-locus knockout or promoter-less mutants (El-Brolosy et al., 2019; Tessadori et al., 2020). However, additional caution must be taken when deleting large regions in case that the locus of the gene-of-interest has other genetic activities and regulates other genes (Suzzi et al., 2021).

Nampta is not critical for zebrafish viability

The *nampta* mutants presented in this study are viable, fertile, and phenotypically wild-type (Figure 3.9). While this finding is inconsistent with *nampta* morphant phenotypes that have developmental abnormalities (Morishima et al., 2019), it is line with the wild-type phenotypes of *nampta* mutants reported by Ratnayake et al. (2021), although the reported mutant alleles are different. It is yet to be determined whether the *nampta*^{t10pm} mutant allele causes impaired muscle regeneration similar to the findings of Ratnayake et al. (2021).

The viability of homozygous *nampta* mutants is also in line with the viability of *NAMPT* heterozygous mice (Revollo et al., 2007). *NAMPT* heterozygous mice are morphologically wild-type, and only homozygous *NAMPT* mutant mice are embryonically lethal (Revollo et al., 2007). In that sense, the functional *NAMPT* allelic copies are reduced by half in both heterozygous mutant *NAMPT* mice (Revollo et al., 2007) and homozygous mutant *nampta* zebrafish, since zebrafish have an additional homologue, *namptb* (Fang et al., 2015). Thus, zebrafish with a double knockout of *nampta* and *namptb* may be embryonically lethal. Altogether, based on zebrafish (Ratnayake et al., 2021) and mouse studies (Revollo et al., 2007), organisms with half the copies of NAMPT are viable.

It is important to note that while Nampta or Namptb alone may provide sufficient NAD for the viability of the zebrafish, each paralog may have evolved to have specific functions. For example, *namptb* is expressed from the one-cell stage, while *nampta* is expressed around the blastula stage (Papatheodorou et al., 2020). Therefore, in line with previous reports, Namptb may be sufficient to maintain NAD levels, and Nampta functions as a cytokine for muscle regeneration (Ratnayake et al., 2021) and redundantly maintains NAD levels. While in humans and in mice, there is only one NAMPT paralog, and this single NAMPT functions to recycle NAD, acts as a signalling molecule to bind to Toll-like receptor 4 in lung endothelial cells during inflammation (Camp et al., 2015; Hong et al., 2008), and is secreted by macrophages to stimulate muscle stem cell proliferation (Ratnayake et al., 2021). Conversely, in *NAMPT* heterozygous mice, there is a 66% reduction in NAD levels in their pancreatic cells but not in their liver cells (Revollo et al., 2007). Therefore, it could be that the distribution of NAD, as well as, the intracellular localisation of Nampta or Namptb could determine how and which tissues are affected. One evidence of NAD localisation for differential gene regulation is that, on the one hand, in cultured mouse adipose cells, NMNAT-1 is present in the nucleus to produce NAD for activation of PARP-1, which inhibits fat cell development (adipogenesis) (Ryu et al., 2018; Trefely & Wellen, 2018). On the other hand, NMNAT-2 is present in the cytosol to produce NAD for cellular metabolism and limits NMN availability in cells and NMNAT-1 production of NAD in the nucleus, thus indirectly promoting adipogenesis. Similar to NMNAT localisation in cultured mouse adipose cells, Nampta and Namptb may be specifically localised intracellularly and have evolved specific physiological roles, including in haematopoiesis.

Nampta may support erythrocyte specification and endothelial cell population

NAD is an essential cofactor in deacetylating Lmo2, which is a critical step for assembling blood transcription factors, including Lbd1, Scl, and Gata1/2 (Morishima et al., 2019). The authors have shown that in zebrafish, knockdown of *nampta* using morpholino down-regulates expression of blood-related genes *kdrl*, *klf1*, and *gata1a*. Here, I have found *nampta* loss-of-function had varying effects on the expression of different blood-related genes. First, I found that the expression of erythrocyte maturation marker *klf1* was reduced but not the expression of erythroid marker *gata1a*, suggesting that *nampta* loss-of-function has no effect on the establishment of erythroid lineage, but has an effect on the erythrocyte maturation (Figure 3.11). This is

inconsistent with previous findings that both genes are affected by the reduction of NAD and, consequently, a reduction in LMO2 acetylation (Morishima et al., 2019). One explanation could be that NAD produced by Namptb is sufficient for the assembly of Lmo2 and Scl to initiate *gata1a* expression. If zebrafish Gata1 and Gata2 can regulate their own expression and each other's expression such as in the mouse (Kobayashi et al., 2001; Moriguchi & Yamamoto, 2014; Suzuki et al., 2013), then upon reduction in Lmo2 associated blood transcription complex in *nampta* mutants, Gata1a could upregulate its own expression to reach erythroid cell count similar to wild-type embryos (Figure 3.14). In contrast, *klf1* expression could be more dependent on the NAD-dependent assembly of the Lmo2/Scl/Gata1a transcription complex, and Klf1 may not autoregulate its expression (Figure 3.14), hence the lower *klf1* expression in *nampta* mutants. Together, this suggests that there is a decrease in the number of mature erythrocytes but not in erythroid stem cells. To test this hypothesis, the expression of other erythrocyte-related genes such as *haemoglobin alpha embryonic-1* (*hbae1*) and *haemoglobin beta embryonic-1.1* (*hbbe1.1*) (Gore et al., 2018; Kulkeaw & Sugiyama, 2012) could be measured in *nampta*$^{t10pm/t10pm}$.

Moreover, I found that the leukocyte markers *mpx*, *lcp1*, and *mpeg1.1* were also not significantly reduced in the *nampta* mutants (Figure 3.12). With this finding, together with unaffected *gata1a* expression, it further suggests that the reduction in the NAD levels did not affect the establishment of primitive HSCs and the commitment of HSCs to the erythroid and myeloid lineage. This is inconsistent with the expected impairment of haematopoiesis and lowered expression of blood-related genes upon reduction of NAD-dependent deacetylation of Lmo2 (Morishima et al., 2019).

Conversely, I found that *kdrl* marker was significantly reduced in *nampta* mutants (Figure 3.11A). This could have different interpretations. One possible explanation could be that *kdrl* expression is also more dependent on the NAD-dependent assembly of Lmo2/Scl multiprotein complex than other transcription factors. Another interpretation could be that the hemangioblast and/or endothelial cell population may be reduced. To determine if the lower *kdrl* expression is due to a decrease in hemangioblast or endothelial cell populations, one possible experiment would be to determine at which time point is there a lower *kdrl* expression between *nampta*^{t10pm} mutants and wild-type embryos, such that a lower expression of *kdrl* during

early somitogenesis would indicate a lower hemangioblast population, and that at later stages would indicate a reduction in endothelial cell population only.

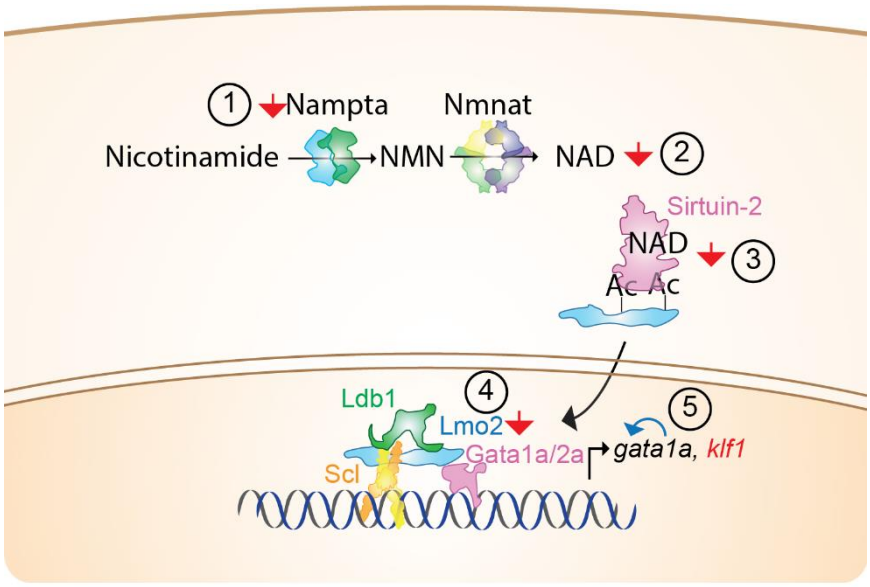

Figure 3.14 Gata1a may autoregulate to maintain erythroid specification upon *nampta* loss-of-function.
(1) Upon *nampta* loss-of-function, (2) NAD levels are reduced, and (3) there could be a reduction in deacetylated Lmo2, based on the model by Morishima et al. (2019). (4) Nonetheless, there may be sufficient NAD for the assembly of the blood transcription complex to initiate expression of *gata1a* for erythroid commitment and *klf1* for erythrocyte specification. (5) Gata1a can autoregulate its expression (blue arrow) to increase *gata1a* transcript levels in *nampta* mutants to levels in wild-type. However, Klf1 may not autoregulate, and therefore, a reduction in assembled blood transcription complex may lead to a reduction in *klf1* expression (in red).

A hypothetical decrease in hemangioblast population would not correlate with the current findings that the expressions of erythroid and myeloid cell gene markers are unaffected upon *nampta* loss-of-function. One possible explanation could be that, as a response to the reduced hemangioblast cell population, hemangioblast differentiation to the endothelial precursor cell may be sacrificed by down-regulating *kdrl* in hemangioblasts to reach wild-type HSC count (Figure 3.15). Previous studies have shown that hemangioblast *scl*$^{+}$ cells down-regulate *kdrl* expression and upregulate *gata1a* for blood cell commitment and vice versa for vascular endothelium commitment (Dooley et al., 2005; Gering et al., 1998; Gering et al., 2003). In line with this hypothesis, BMP signalling may be the switch for hemangioblast specification to either blood or endothelial cell. For example, knockdown of BMP signalling decreased the expression of another erythrocyte differentiation marker *hba1* and increased the level of endothelial precursor cell differentiation marker *aplnr* in *Xenopus* (Myers &

Krieg, 2013). This shift in hemangioblast cell fate to either blood or endothelial cell was not observed upon inhibition of other blood-related pathways such as Wnt, Notch, or FGF. Whether BMP signalling can regulate the expression of *hba1*, *aplnr*, and other blood- and endothelial-related gene markers to mediate hemangioblast cell specification in zebrafish and other organisms is yet to be investigated. One example of blood-related genes requiring BMP signalling is *gata1a*, whose expression is absent in *bmp2b* mutants (Mullins et al., 1996). Another future experiment is to quantify blood and endothelial cell population using transgenic backgrounds such as *fli*:*GFP* for endothelial cells (Lawson & Weinstein, 2002) and *gata1a*:*GFP* (Galloway et al., 2005) and *c-myb*:*GFP* (Bonkhofer et al., 2019) for haematopoietic stem cell and progenitor cells in the dorsal aorta in *nampta*^{t10pm} mutant embryos compared to wild-type embryos. These can be quantified using FACS or confocal microscopy (Esain et al., 2016).

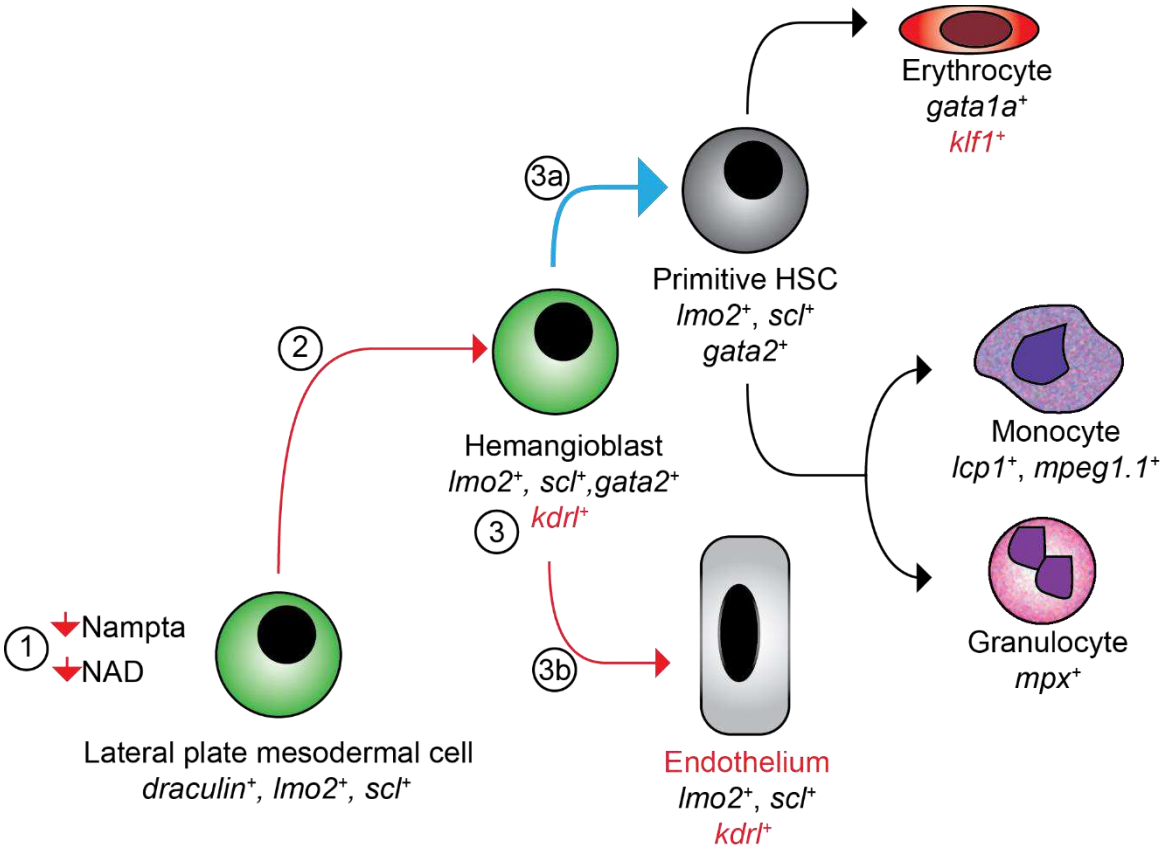

Figure 3.15 Proposed switch in hemangioblast specification towards HSC and away from endothelial commitment.
(1) *nampta* mutants have lower NAD levels, which could lead to (2) a reduction in the assembly of Lmo2/Scl oligomeric complex required for hemangioblast specification (red arrow). (3) To compensate for a decrease in hemangioblast population, *kdrl* expression could be down-regulated to tip the balance of hemangioblast differentiation towards (3a) primitive blood cell lineage (blue arrow) and (3b) away from endothelial cell lineage (red arrow). Genes whose expressions are lower in *nampta* mutants are in red.

To conclude, in this chapter, I demonstrated that Nampta, one of two Nampt homologues in the NAD salvage pathway in zebrafish, may support the endothelial cell population and erythrocyte maturation, but Nampta is not essential for haematopoiesis and the viability of the zebrafish. Here, I have only tested the effect of *nampta* loss-of-function on the expression of blood-related genes at 1 dpf, when blood circulation begins. At this point, it remains unclear if Nampta affects hemangioblast and/or endothelial cell population and the maturation of myeloid cells. These *nampta*^{t10pm} mutants can be used to further dissect Nampta contribution at the different stages of primitive and definitive haematopoiesis. Furthermore, this work emphasizes the need to further examine how transcriptional adaptation functions for other genes and in other transient knockdown approaches. Finally, similar to Chapter 2, it further emphasizes the need for a new gold standard for loss-of-function analysis.

Main Conclusion

A conserved set of signalling pathways orchestrates embryogenesis across the animal kingdom. How the molecular components of the shared signalling repertoire function in a species-specific manner is unresolved. In this dissertation, I aimed to understand how ancestral signalling pathways, BMP and NAD salvage pathway, specifically function to regulate two main processes during zebrafish embryogenesis, dorsal-ventral patterning and haematopoiesis, respectively. To extensively dissect the signalling pathways, I used classical approaches such as gain-of-function and loss-of-function analyses combined with cutting-edge tools such as CRISPR/Cas9 and *in toto* imaging using light sheet microscopy.

First, in Pomreinke et al. (2017) (Appendix A) and follow-up experiments presented in Chapter 1 of this dissertation, we determined that zebrafish dorsal-ventral patterning is achieved by a graded source-sink mechanism between diffusible BMP and Chordin with additional refinement by Sizzled and Tolloid. I also demonstrate that ADMP may have a biphasic effect, which can be due to being a weaker activator of BMP signalling. Our approach was to measure pSmad1/5/9 in respective mutants and to visualise fluorescent fusion constructs in ectopic settings. A future step is to use our fluorescent constructs to establish transgenic lines to visualise the interplay of BMP and its regulators in endogenous settings. Combined with the membrane-tethered nanobodies (Mörsdorf & Müller, 2019) and *in toto* imaging, we can further define the role of BMP diffusion during normal development and other biological contexts such as regeneration and secondary axis formation (Shih & Fraser, 1996). From an evolutionary standpoint, we have yet to determine whether diffusion is conserved across BMP homologues in the zebrafish and in other species.

Second, in collaboration with the lab of Grigory Genikhovich (Knabl et al. (2022), Appendix C), we determined that a previously uncharacterised Zswim5 can modulate BMP signalling in *Nematostella vectensis* and zebrafish, thus demonstrating the extent of the evolutionary conservation of genes that can modulate BMP signalling between anthozoa cnidarians and bilaterians. The precise upstream and downstream molecular wiring of Zswims in these sister groups is yet to be elucidated to further understand the evolutionary relationship of cnidarians and bilaterians (Genikhovich & Technau, 2017).

Third, I determined Nampta, one of two Nampt homologues in the zebrafish, is not essential for haematopoiesis and the zebrafish viability, but may support the maturation of blood cells and the maintenance of endothelial cell population. The new *nampta*^{t10pm} mutant lines combined with the improved tissue dissociation protocol for FACS presented here could be used to further dissect Nampta's role in haematopoiesis, as well as, to identify other Nampta-dependent embryonic processes.

To conclude, this dissertation provides a better understanding of how evolutionarily conserved signalling pathways may function specifically in the zebrafish. Understanding species-specific properties of signalling pathways could also be taken into consideration when designing and testing pharmaceutical reagents. From an evolutionary standpoint, these findings in zebrafish embryos may provide additional missing pieces to solve the puzzling question of embryogenesis and provide a different perspective on how signalling pathways could evolve in other branches of the animal kingdom.

Materials and Methods

General

Zebrafish embryos handling

Live embryos were kept in embryo medium containing 250 mg/L Instant Ocean sea salt mix (Aquarium Systems) and 1 mg/L methylene blue at 28°C. Prior to fixation, embryos were dechorionated with 1 mg/mL of Pronase (Roche, Cat. No. 11459643001).

Hotshot DNA extraction

100 µL of NaOH (50 mM) was added to either fin-clipping or embryo samples. Samples were heated at 95°C for 20 min, then 10 µL Tris-HCl (1 M, pH 8) was added (Meeker et al., 2007).

Microinjection

Injection mixes were prepared containing the respective reagents such as mRNA or morpholinos (see sections below) and with 0.1% phenol red (Sigma, Cat. No. P0209). Embryos were injected at the one-cell stage with 1 nL injection volume, unless otherwise stated.

In vitro transcription

mRNAs for microinjection were prepared as the following. *pCS2(+)* vectors were linearized by restriction digest with NotI-HF (New England Biolabs, Cat. No. R3189), then transcribed using SP6 mMessage mMachine kits (Thermo Fischer Scientific, Cat. No. AM1340), and the mRNAs were purified using RNeasy Mini kits (Qiagen, Cat. No. 74104) following the manufacturer's instruction.

Wide-field imaging of zebrafish embryos

Zebrafish embryos at 1 dpf were anesthetized and mounted in 2% methylcellulose in embryo medium and imaged with AxioZoom V16 (Zeiss) with PlanNeoFluar Z with 1x/0.25 objective.

Immunostainings

To visualise pSmad1/5/9 at different developmental stages, wild-type TE embryos were collected, dechorionated at the one-cell stage, and incubated at 28°C before fixation (Pomreinke et al. (2017), Appendix A). Embryos were fixed at different developmental stages in 4% formaldehyde (Roth, Cat. No. 4979.1) in PBS and stored overnight at 4°C on a shaker. Embryos were dehydrated sequentially with 30%, 50%, and 70% methanol in PBS and stored in 100% methanol at -20°C for a minimum of 2 h. The following immunostaining steps were performed using *In Situ* Pro hybridization robot (Abimed/Intavis). "Embryos were re-hydrated with 70%, 50%, and 30% methanol in PBS for 10 min each. The embryos were then washed eight times with PBS with 0.1% Tween (Fisher, Cat. No. BP337-500) (PBST) for 15 min and blocked twice with blocking solution (10% fetal bovine serum and 1% DMSO in PBST) for 1 hr, and incubated with 1:100 anti-pSmad1/5/8 antibody (Cell Signaling Technology, Cat. No. 9511) for 4 hr. Embryos were washed with blocking solution for 15 min, washed seven times with PBST, blocked with blocking solution for 1 hr, incubated with 1:500 Alexa 488-coupled goat anti-rabbit secondary antibody (Life Technologies, Cat. No. A11008) for 4 hr, and washed similarly to the procedure after primary antibody application. Embryos were then counterstained with DAPI solution (0.2 µg/mL in PBST) for 1 hr and washed with PBST" (Pomreinke et al. (2017), Appendix A).

To compare the BMP signalling gradient in the absence of Chordin (Pomreinke et al. (2017), Appendix A), Sizzled, or Tolloid, embryos from heterozygous *chordin*^{tt250}, *sizzled*^{tm305}, or *tolloid*^{tm124a} in-cross were collected, fixed at shield stage, and immunostained with anti-pSmad1/5/9 antibody (Cell Signaling Technology, Cat. No. 13820) with the similar procedure as described above, based on Pomreinke et al., 2017. One exception is that *chordin* mutants were first permeabilized with ice-cold acetone, see Pomreinke et al. (2017), Appendix A. After imaging, embryos were identified as wild-type, heterozygous, or homozygous mutant embryos by genotyping using PCR amplification as described below.

Genotyping of mutants

Hotshot DNA extraction was performed as described above. Genotyping assays for the *chordin*^{tt250} and *sizzled*^{tm305} lines were designed by ZIRC (2008). Genotyping assay for *tolloid*^{tm124a} is from Connors et al. (1999).

chordin^{tt250}:
Forward primer: 5'-TTCGTTTGGAGGACAACTCG-3'
Reverse primer: 5'-AACTCAGCAGCAGAAGTCAATTC-3'
PCR cycler program: 94°C for 3 min, 39 cycles of 94°C for 30 s, 55°C for 40 s, and 72°C for 30 s; and a final extension at 72°C for 5 min
Restriction digest: MspI (New England Biolabs, Cat. No. R0106) for 2 h
The PCR product size is 325 bp. The *chordin*^{tt250} mutation abolishes the MspI restriction enzyme recognition site. Therefore, the wild-type allele is cleaved to DNA fragments of 259 bp and 66 bp, and the mutant allele is undigested.

sizzled^{tm305}:
Forward primer: 5'-CCTCGATCTGACGACTTGAGGA-3'
Reverse primer: 5'-GCCAGTTCTAAATCATGAGCTACAC-3'
PCR cycler program: 94°C for 3 min, 39 cycles of 94°C for 30 s, 55°C for 40 s, and 72°C for 30 s; and a final extension at 72°C for 5 min
Restriction digest: TaqαI (New England Biolabs, Cat. No. R0149) for 2 h
The PCR product size is 300 bp. The *sizzled*^{tm305} mutation abolishes the TaqαI restriction enzyme recognition site. Therefore, the wild-type allele is cleaved to DNA fragments of 210 bp and 90 bp, and the mutant allele is undigested.

tolloid^{tm124a}:
Forward primer: 5'-TGTGTCAAGCATAAAGACTGG-3'
Reverse primer: 5'-TCTTCTCAATGAAAGTCACGC-3'
PCR cycler program: 94°C for 3 min, 39 cycles of 94°C for 30 s, 58°C for 40 s, and 72°C for 30 s; and a final extension at 72°C for 5 min
Restriction digest: MspI (New England Biolabs, Cat. No. R0106) for 2 h
The PCR product size is 218 bp. The *tolloid*^{tm124a} mutation abolishes the MspI restriction enzyme recognition site. Therefore, the wild-type allele is cleaved to DNA fragments of 143 bp and 76 bp, and the mutant allele is undigested.

Light sheet microscopy

pSmad1/5/9 immunostainings were visualised using *in toto* imaging similar to Pomreinke et al. (2017) (Appendix A), with the exception that the *sizzled*^{tm305}, *tolloid*^{tm124a}, and their respective control embryos were imaged from angles 0°, 90°, 180°, and 270°.

Generation of admp mutants

To generate *admp* mutants, three crRNAs that target exon-1 of the *admp* gene were designed using Integrated DNA Technologies (IDT) pre-designed program with PAM sequence in red and were designated by the manufacturer as:
Dr.Cas9.ADMP.1.AA: 5'-CGGGTTTTTCAACGAGCTGGAGG-3'
Dr.Cas9.ADMP.1.AB: 5'-TGCTCGAGGGAAACACGGTCCGG-3'
Dr.Cas9.ADMP.1.AC: 5'-AACACCATCGCTGATGTCGACGG-3'.

To prepare the CRISPR/Cas9 injection mix, I adopted the protocol from IDT. Alt-R crRNAs for ADMP were resuspended in 100 µL of IDTE buffer to make a 20 µM stock. The ADMP-gRNA-mix was made from 1 µL of each crRNA and 3 µL of tracrRNA (100 µM), mixed with 94 µL of Duplex buffer (IDT), and heated at 95°C for 5 min, then let to cool at room temperature. The Cas9 was diluted to 0.5 µg/µL with Cas9 working buffer that was freshly prepared prior to use. Cas9 working buffer consisted of 20 mM HEPES and 150 mM KCl in H_2O. The final injection mix was made up of 3 µL of ADMP-gRNA-mix and 3 µL Cas9 (0.5 µg/µL) and then was slightly dyed by mixing with a pipet tip dipped in phenol red to minimize further dilution of the gRNA-Cas9 solution. The embryos were injected with 3 nL injection volume.

To determine whether Cas9 has modified the target locus, DNA was extracted following Hotshot DNA extraction as described above, and then the region of interest was amplified by PCR with forward primer: 5'-TGGCTGTTCTCCAGTCAATC-3' and reverse primer: 5'-CGCATTAATAAAAGTCAGTTTTTG-3' and thermocycler program of 94°C for 3 min, 35 cycles of 94°C for 30 s, 56°C for 30 s, 72°C for 30 s, and a final elongation step at 72°C for 5 min. Then a denaturing and reannealing step was done by heating the samples at 95°C for 5 min, then cooled down to 85°C at -2°C per second, and then cooled down to 25°C at -0.1°C per second until 4°C. The PCR product solutions were then split into two tubes, and one half was treated with T7

endonuclease I with NEBuffer™ 2 (New England Biolabs, Cat. No. M0302), and the other half was treated only with the buffer. Surviving siblings of genotyped embryos were raised to adulthood. Stable *admp* mutant lines have a large deletion and can be genotyped using the same primers used for testing *admp* gRNA effectiveness in injected embryos.

Transplantation of embryonic cells

For transplantation experiments, donor embryos from H2A.F/Z-GFP (Pauls et al., 2001), referred to as H2A:GFP throughout the text, were injected with mRNA of either 5 pg *admp*, 250 pg *admp*, or 5 pg *bmp2b*. Host embryos from wild-type TE fish lines were injected with 1 nL injection mix containing 0.08 mM *bmp2b* morpholino: 5'-CGCGGACCACGGCGACCATGATC-3' (Lele, Bakkers, et al., 2001). Embryos were dechorionated at the high stage. At the sphere stage, cells were transplanted using glass needles with an inner tip diameter of 80 µm by Gary H. Soh. After transplantation, the embryos were let to recover in Ringer's solution (116 mM NaCl, 2.8 mM KCl, 1 mM $CaCl_2$, and 5 mM HEPES) (Soh et al., 2020) for 15 min and then placed at 28°C. At 30 or 60 min after transplantation, the embryos were fixed in ice-cold 4% formaldehyde (Roth, Cat. No. 4979.1) in PBS.

Double-immunostaining of pSmad1/5/9 and GFP

Embryos were double-immunostained using a mixture of two primary antibodies: 1:100 dilution of pSmad1/5/9 (Cell Signaling Technology, Cat. No. 13820 and 1:100 dilution of anti-GFP antibody (Aves Labs, Cat. No. GFP-1020), following the same procedure described above. After the washing steps, the embryos were incubated in a mixture of two secondary antibodies: 1:500 Alexa 488-coupled goat anti-rabbit secondary antibody (Life Technologies, Cat. No. A11008) and 1:500 dilution of Alexa Fluor 568-conjugated anti-chicken IgY (abcam, Cat. No. 175477). Embryos were stained with 1:5000 dilution of 1 mg/mL DAPI stock for 1 h at room temperature then washed 3 times for 10 min with PBST.

Image acquisition and analysis

For imaging, embryos were mounted into 1.5 mm glass capillary (Zeiss) using 1% low melting agarose NuSieve GTG agarose (Lonza, Cat. No. 50080) at 40°C and oriented perpendicular to the glass capillary using a dissection needle, hence the

animal pole points towards the objective camera. The samples were imaged from the animal pole to the margin as z-stacks using Lightsheet Z.1 microscope (Zeiss) with a W Plan-Apochromat 20x/1.0 objective, and maximum intensity projections were generated with ZEN software (Zeiss). pSmad1/5/9 intensity was measured 200 µm from the centre of the GFP signal using Fiji (Schindelin et al., 2012) with line profile tool, and the 'plot profile' function was applied. The lowest signal was used as background, which was subtracted from the gradient profiles. The data were plotted using Prism (GraphPad Software).

Generation of fluorescent BMP, Chordin, and Sizzled

Please see Pomreinke et al. (2017), Appendix A.

Generation of fluorescent ADMP

The constructs were generated by Katherine W. Rogers following the touchdown PCR protocol by Korbie & Mattick, 2008. All constructs contained the consensus Kozak sequence GCCACC 5' of the start codon and were inserted into EcoRI and XbaI sites of the *pCS2(+)* vector. To generate ADMP-sfGFP and ADMP-Dendra2, sequences encoding sfGFP or Dendra2 flanked by LGDPPVAT linkers were inserted either 11 amino acids (Plouhinec et al., 2013), 5 amino acids (Willot et al., 2002), or 1 amino acid downstream of ADMP's Furin cleavage site. The FLAG tag was inserted immediately downstream of the first linker.

Phenotyping of admp overexpression

Embryos were injected at one-cell as described above with *admp* mRNA and fluorescent constructs at different concentrations as indicated in each figure legend. Phenotypic categories to score the embryos are based on Willot et al. (2002), Lele, Nowak, et al. (2001), and Kishimoto et al. (1997).

Preparation of extracellularly enriched fractions for Western blotting

Please see Pomreinke et al. (2017), Appendix A.

Chapter 2

Cloning of zzswim-5

Total RNA was extracted from ten pooled embryos at 50%, 75% epiboly, or 1 dpf using TRIzol™ (Invitrogen, Cat. No. 15596018), and the samples were homogenized with a battery-operated pestle motor mixer. cDNA was generated from 500 ng of RNA using SuperScript™ III First-Strand Synthesis SuperMix for qRT-PCR (Thermo Fisher Scientific, Cat no. 11752-050).

zzswim5 was successfully amplified from cDNA of embryos at 75% epiboly using forward primer 5'- ATGGCGGAGGGACGTGGA-3' and reverse primer 5'-TTAACCGAAACGTTCCCGTACCA-3' and KOD Hot Start DNA polymerase (Novagen, Cat. No. 71086) with thermocycler program: 95°C for 2 min, 39 cycles of 95°C for 20 s, 65°C for 10 s, 70°C for 1.5 min, and final extension at 70°C for 5 min. The PCR product was extended using forward and reverse primers: 5'-TTCTTTTTGCAGGATCCCATCGATGCCACCATGGCGGAGGGACGTGGA-3' and 5'-TAGAGGCTCGAGAGGCCTTGAATTCTTAACCGAAACGTTCCCGTACCA-3', then cloned into ClaI and EcoRI sites of *pCS2(+)* vector with Kanamycin resistance using Gibson assembly (New England Biolabs GmbH, Cat. No. E2611). During troubleshooting, Q5 High-Fidelity DNA polymerase (New England BioLabs, Cat. No. M0491) was also used, but sequencing results indicated that the cloned *zzswim5* product amplified from KOD best aligned with *zzswim5* sequence NM_001144819-1.

Characterisation of nvZwim4-6 and zZswim5

Embryos were injected, and the phenotypes were also scored at 1 dpf. The embryos imaged at 1 dpf as described in the Materials and Methods, General section. *pCS2-nvZswim4-6* was provided by Genikhovich lab.

Characterisation of zzswim5 morpholinos

Morpholinos were ordered from Gene Tools, LLC. The three morpholinos were tested to knockdown zZswim5 (Accession no. ENSDART00000078305.6): *zzwim5-MO-1*: 5'-GTCCCTCCGCCATGACAACCAAATA-3', *zzswim5-MO-2*: 5'-AGAGAAATGGAGAGTGCCTCACCTT-3', and *zzswim5-MO-3*: 5'-AGCCCCTGAGAGACAAATGCACTTG-3'. *zzwim5-MO-1* is a translational blocker.

zzswim5-MO-2 binds to the splice junction between exon-3 and intron-3. *zzswim5-MO-3* binds to the splice junction between exon-1 and intron-1. *p53-MO* was previously reported by Robu et al. (2007) with sequence 5'-GCGCCATTGCTTTGCAAGAATTG-3'.

Immunostaining of embryos

Embryos were injected either with 480 pg of *nvzswim4-6*, 80 pg of *zzswim5*, or 150 mM of *zzswim5-MO1*. To quantify the pSmad1/5/9 gradient of *nvZswim4-6*- and *zzswim5*-injected embryos, embryos were fixed and immunostained with anti-pSmad1/5/9 antibody (Cell Signalling Technology, Cat. No. 13820) following the immunostaining procedure from Chapter 1 and in Pomreinke et al. (2017), Appendix A.

Fluorescence in situ hybridization of embryos

Embryos were injected at the one-cell stage and dechorionated at the sphere stage. Damaged embryos were removed. Embryos were fixed following the same procedure as in Pomreinke et al. (2017) and stored in 100% methanol at -20°C for at least 2 h. The fluorescence *in situ* hybridization protocol and reagents used are based on Thisse and Thisse (2008) and Almuedo-Castillo et al. (2018). The fixed embryos were rehydrated step-wise at 75%, 50%, and 25% methanol in PBST for 5 min each, then washed 4 times with PBST for 5 min. The proteinase K step was skipped because the embryos are less than 1 dpf. Embryos were incubated at 70°C in 1 mL of hybridization mix (50% deionized formamide, 5x SSC, 0.1% Tween 20, 50 µg/mL of heparin, and 500 µg/mL of RNase-free tRNA adjusted to pH 6.0 by adding citric acid), 2 times for 1 h. The embryos were then incubated with 150 ng of DIG-labelled *sizzled* and *admp* probes in hybridization solution overnight at 70°C. The probes were generously provided by Katherine W. Rogers. On the following day, the embryos were quickly washed with hybridization mix B (hybridization mix without heparin and tRNA) at 70°C. Then the embryos were washed at 70°C with 75%, 50%, and 25% hybridization mix B in 2x SSC for 15 min each and then 3 times with 2x SSC for 15 min, using *In Situ* Pro hybridization robot (Abimed/Intavis). Then the embryos were washed 3 times with 100% 0.2x SSC at 70°C for 15 min, then at room temperature with 75%, 50%, and 25% 0.2x SSC in PBST and 2x with PBST for 15 min. The embryos were transferred to a 48-well dish with 300 µL of blocking solution (2% blocking reagent

(Roche, Cat. No. 11096176001) in 1x maleic washing buffer (150 mM maleic acid, 100 mM NaCl, 0.1% Tween 20; pH 7.5)) and incubated for 2 h at room temperature on a shaker. Then the blocking solution was removed and replaced with 200 µL 1:500 Anti-Digoxigenin-POD (Roche, Cat. No. 11207733910) in blocking solution for overnight incubation at 4°C, kept in the dark on a shaker. On the following day, embryos were washed briefly with PBST, then washed 8 times with PBST for 15 min using the *In Situ* Pro hybridization robot. To develop the signal, the samples were taken out of the robot and incubated in amplification buffer (TSA Plus Cyanine 3 System, Perkin Elmer, Cat. Not. NEL744001KT) for 15 min and then in 100 µL 1:75 Cy3-TSA in 1x amplification buffer for 35 min for embryos treated with *sizzled* probes and 45 min for embryos with *admp* probes. The staining solution was discarded, and the embryos were washed with PBST, first briefly, then 2x for 15 min at room temperature. The samples were washed 4 times with 100% methanol and then stored at -20°C until the imaging step.

Image acquisition

In toto imaging of pSmad1/5/9 immunostained embryos were imaged using Lightsheet Z.1 (Zeiss) following the procedure described in Materials and Methods, Chapter 1 and Pomreinke et al. (2017), Appendix A and projected into 2D maps, with the exception that the embryos were imaged from angles 0°, 90°, 180°, and 270°. Other pSmad1/5/9 immunostained embryos were imaged from the animal pole to the margin using Lightsheet Z.1 (Zeiss), and the maximum intensity projections were quantified.

Before imaging, fluorescence *in situ* hybridization samples were rehydrated with 75%, 50%, and 25% with methanol in PBST and washed 8 times with PBST for 10 min each. For *in situ* images in Figure 2.9 C-D, embryos were mounted in 1% low melting agarose and oriented animal down on glass-bottom Petri dishes (MatTek Corporation), then imaged from the animal pole to margin using LSM 780 NLO system (Zeiss) with an LD LCI Plan-Apochromat 25x/0.8 Imm Korr DIC. For *in situ* images in Figure 2.12, embryos were mounted and imaged from the animal pole using Lightsheet Z.1 (Zeiss). Maximum intensity projections were generated with ZEN software (Zeiss).

For time-lapse imaging, ten embryos were placed in embryo medium without methylene blue. The embryos were imaged for 20 h every 10 min with ACQUIFER Imaging Machine (DITABIS AG) following the same settings described in Capek et al. (2023).

Image analysis

For image analysis, the 3D-to-2D projections and maximum intensity projections of pSmad1/5/9 immunostaining and *in situ* hybridization images were analysed using Fiji following a similar procedure as described in Pomreinke et al. (2017), Appendix A. In brief, embryos were oriented with the ventral side to the left. Then the embryo images were traced using manual polygon selections and masked to remove the signal outside the animal cap. A rectangle profile around the embryo was used combined with the 'Plot Profile' function to quantify the average intensity starting from the ventral to the dorsal side. The background signal of the embryos was determined by the lowest value in all samples per experimental trial and was subtracted from the raw data to generate final values for the gradient profile. The data were plotted using Prism (GraphPad Software).

Chapter 3

Generation of nampta^{t10pm} mutant

draculin:eGFP zebrafish embryos were collected 5 min after they were laid and were injected at the one-cell stage with CRISPR/Cas9 mixture containing Cas9 protein and crRNA targeting *nampta* exon-2 sequence 5'-ACGACAAGACGGTCTTCTATGGG-3' (100 mM stock concentration) (IDT). At 1 dpf, injected embryos were assayed for mutagenesis by amplifying the region of interest followed by T7 endonuclease I assay. For PCR amplification, the forward primer 5'-CTTTCATTGCAGGTCACACATT-3' and reverse primer 5'-GCTGGAACAAACAGTGGTGTTA-3' were used with the following thermocycler program: an initial denaturation step at 94°C for 3 min, 35 cycles of 94°C for 30 s, 56°C for 30 s, 72°C for 30 s, and a final elongation step at 72°C for 5 min. Then the PCR products were denatured and reannealed by heating at 95°C for 5 min, cooled down to 85°C at -2°C per second, and then cooled down to 25°C at -0.1°C per second until 4°C. The PCR product solutions were split into two tubes. One half was treated with T7 endonuclease I with NEBuffer™ 2 (New England Biolabs, Cat. No. M0302), and the other half was only treated with the buffer. PCR amplicons were loaded into 2% agarose gel electrophoresis.

To understand the effect of the deletion in the mature mRNA transcript, RNA was extracted from *nampta*$^{+/+}$, *nampta*$^{t10pm/t10pm}$, and morphant embryos using TRIzol™ (Invitrogen, Cat. No. 15596018), and cDNA was synthesized using SuperScript III First-Strand Synthesis SuperMix for qRT-PCR (Thermo Fischer Scientific, Cat. No. 11752-050). Primers flanking exon-1 and exon-5 were used for PCR amplification as previously described by Morishima et al. (2019) with forward primer 5'-AGAGAAGCCGCGGATTTCAA-3' and reverse primer 5'-CTCCAGTCCTTCCAGGCTTC-3'.

Cloning of nampta wild-type and mutant alleles

To compare the wild-type and mutant *nampta* full length transcripts, the *nampta* alleles were amplified from cDNA of *nampta*$^{+/+}$ and *nampta*$^{t10pm/t10pm}$ embryos at 1 dpf using primers binding to the 5' and 3' end of *nampta*, with forward primer 5'-CCATCGATTCGAATTCATGGAGAAACACAGAGAAGCC-3' and reverse primer 5'-ACTCACTATAGTTCTAGATCAGAGCAGCAGATCCTGC-3' and with KOD Hot Start DNA polymerase (Novagen, Cat. No. 71086) and with the thermocycler program of 95°C for 2 min, 35 cycles of 95°C for 20 s, 60°C for 10 s, 70°C for 40 s, and a final elongation step at 70°C for 10 min. The PCR products were gel-purified with Wizard kit (Promega, Cat. No. A9281). The PCR amplification and gel-purification steps were repeated to increase PCR product concentration. Then the product was topocloned using Zero Blunt™ TOPO™ PCR cloning Kit (Thermo Fischer Scientific, Cat. No. K280002) following the manufacturer's instructions and subsequently sequenced.

Rearing and maintenance of nampta$^{+/+}$ and *nampta*$^{t10pm/t10pm}$ *fish lines*

The remaining CRISPR-Cas9 + gRNA injected embryos were raised to adulthood as P0 and screened for germline transmission of mutation by backcrossing to *draculin:eGFP* zebrafish lines (Mosimann et al., 2015), thus generating stable heterozygous mutant F1 lines (Figure 3.5). To genotype adult fish, the same PCR protocol described above in *Generation of nampta*^{t10pm} *mutant* section can be followed.

To further reduce potential off-target mutations, F1 heterozygous *nampta*^{t10pm} fish was backcrossed to *draculin:eGFP* (Port et al., 2020) to produce F2 heterozygous *nampta*^{t10pm} (Figure 3.5). F2 fish were in-crossed to generate homozygous *nampta*^{t10pm} lines (F3). To control for remaining potential off-target mutations, wild-type *nampta*

siblings (F3) resulting from F2 in-crossed were also raised to use as wild-type cousin controls. Note that the lines were designated as *nampta*$^{t\#}$, following the ZFIN Zebrafish nomenclature convention in which fish lines generated in Tuebingen contain the superscript 't' followed by a unique identifier number (ZFIN, 2022).

Alignment of zebrafish Nampta, Namptb, and human NAMPT

The protein sequences Nampta (XP_002661386.1), Namptb (NP_997833.2), and human NAMPT (NP_005797.1) were aligned using Clustal Omega in Jalview version 2.11.2.6 (Waterhouse et al., 2009), and the percentage identity option was used to set the colour scheme.

Generation of fluorescently-tagged Nampta

To compare wild-type Nampta and Nampta^{t10pm} protein products, fluorescent constructs were designed for Western blot assay. All constructs contain the consensus Kozak sequence GCCACC 5' of the start codon and were inserted between EcoRI and XbaI sites of the *pCS2(+)* vector with Kanamycin resistance using Gibson assembly (New England BioLabs, Cat. No. E2611S). To generate fluorescent wild-type and mutant *nampta*, the sequence coding for mCherry was placed in the N-terminal end after the start codon of *nampta*, followed by a *FLAG* tag sequence as a linker. For *eGFP-stop-nampta*$^{+}$, there was a stop codon between the *GFP* and *FLAG* tag sequence.

Live imaging of embryos injected with fluorescently-tagged nampta

Embryos were co-injected with *eGFP-STOP-nampta*$^{+}$ (50-100 pg) and either *mCherry-nampta*$^{+}$ (77.5 pg) or *mCherry-nampta*^{t10pm} (77 pg) with 2 nL injection volume at the one-cell stage. The embryos were dechorionated at high-stage. At the sphere stage, embryos were mounted in 1% low melting agarose and oriented animal down on glass-bottom Petri dishes (MatTek Corporation), then imaged approximately 30 µm deep from the animal pole using LSM 780 NLO system (Zeiss) with an LD LCI Plan-Apochromat 25x/0.8 Imm Korr DIC.

Preparation of protein samples to detect endogenous and fluorescently-tagged Nampta

To detect endogenous Nampta protein, ten embryos at 5 dpf were pooled and snap-frozen in liquid nitrogen. The embryos were homogenized using 100 µL ice-cold cell lysis solution (500 µL Pierce® RIPA buffer (Thermo Fisher Scientific, Cat. No. 89900), half of cOmplete Mini EDTA-free Protease inhibitor (Roche, Cat. No. 11836170001), and 5 mM EDTA) for 1 min with battery-operated pestle motor mixer. The samples were then incubated for 1 h on a tube rotator at 4°C and subsequently centrifuged at 8000 x g for 10 min at 4°C. The supernatant was discarded, and SDS loading buffer was added onto the pellet fraction, which was then heated at 95°C for 10 min, and then stored at -20°C until use. 25 µL of the samples in loading buffer were loaded into SDS-PAGE.

To analyse fluorescently-tagged Nampta^{+} and Nampta^{t10pm} using Western blot, TE wild-type embryos were injected with 369 pg in 3 nL injection volume of either *mCherry-nampta*$^{+}$ or *mCherry-nampta*^{t10pm} mRNA at the one-cell stage. At the sphere stage, the embryos were manually deyolked as previously described (Müller et al., 2012). 25 animal caps were snap-frozen in liquid nitrogen. Then SDS loading buffer was added to the samples, which were then heated at 95°C for 10 min, and stored at -20°C until use.

Western blot

Protein samples were loaded and resolved by SDS-PAGE using 12% polyacrylamide gels. Proteins were then transferred onto PVDF membranes using Mixed Molecular Weight program in the Trans-Blot Turbo Transfer system (Bio-Rad, Cat. No. 170-4272). Membranes were blocked with 5% non-fat milk (Roth, Cat. No. T145.2) in PBST for 1-2 h at room temperature.

To detect endogenous Nampta in 5 dpf embryos, the membrane was incubated with anti-Nampt antibody (Cell Signaling Technology, D7V5J) at 1:1000 dilution in 5% non-fat milk in PBST and placed on a shaker at 4°C overnight. Then the membrane was washed, and HRP-coupled goat anti-rabbit secondary antibody (Jackson ImmunoResearch, Cat. No. 111-035-003) was used at 1:25000 dilution in 5% non-fat milk in PBST for 3 h at room temperature. Chemiluminescence detection was

performed using SuperSignal™ West Dura Extended Duration Substrate (Thermo Fisher Scientific, Cat. No. 34075) and imaged with a chemiluminescence imaging system (ChemiDoc™ MP, Bio-Rad).

To detect FLAG-tagged fluorescent Nampta constructs, the membrane was incubated with anti-FLAG antibody (Sigma, Cat. No. F3165) at 1:2000 dilution in 5% non-fat milk in PBST and placed on a shaker at 4°C overnight. Then the membrane was washed, and HRP-coupled donkey anti-mouse (Jackson ImmunoResearch, Cat. No. 715-035-150) was used as a secondary antibody at 1:25000 dilution in 5% non-fat milk in PBST. Chemiluminescence detection and imaging protocol were the same as above.

Injection of nampta morpholino

nampta$^{+/+}$ and *nampta*$^{t10pm/t10pm}$ embryos were injected with 150 µM of *nampta* morpholino 5'-TGTGTGACCTGCAATGAAAGAAAGA-3' (Morishima et al., 2019) with an injection volume of 1.5 nL.

Live imaging of embryos

Embryos were imaged with AxioZoom (Zeiss) and ACQUIFER Imaging Machine (DITABIS AG) as described in Materials and Methods, General section and Chapter 2, respectively.

Measurement of NAD levels

Individual embryos with intact chorions at 1 dpf were placed in a 1 mL Eppendorf tube and homogenized with a battery-operated pestle motor mixer. Then the homogenized tissue was rinsed off from the pestle with 150 µL of PBS. To measure NAD levels, 50 µL of homogenized tissue and 50 µL of NAD/NADH-Glo™ Assay master mix (Promega, Cat. No. G9071), prepared following the manufacturer's instructions, were combined and mixed in white 96 well-plates (LUMITRAC, Cat. No. 655075) and then incubated for 45 min at room temperature. The luminescence was measured using a plate reader (BioTek: gen5). The NAD levels were quantified as the ratio of luminescence measured from each embryo to the average luminescence of *nampta*$^{+/+}$ embryos for each experimental trial.

Quantitative reverse transcription PCR

RNA was extracted from ten pooled embryos using either TRIzol™ (Invitrogen, Cat. No. 15596018) or NucleoZol (Macherey-Nagel) following the manufacturer's instructions and homogenized with a battery-operated pestle motor mixer. If necessary, additional RNA clean-up was performed by acid precipitation. Briefly, 500 µL H_2O was added to precipitated RNA, then 50 µL of 3 M sodium acetate (pH 5.3) and 10 µg of GlycoBlue™ Coprecipitant (Thermo Fisher Scientific, Cat. No. AM9516) were mixed well into the RNA solution. Then 500 µL of room temperature isopropanol was added to the solution. The samples were mixed well and then incubated at room temperature for 20 min. Subsequently, the samples were centrifuged at 12 000 x g at 4°C for 10 min. The RNA pellet was washed 2 times with 500 µL of ice-cold 70% ethanol. The RNA pellet was air-dried for 15 min at room temperature and at 65°C for 1 min to remove excess alcohol. The RNA pellet was dissolved in 15 µL of nuclease-free H_2O.

cDNA was generated from 500 ng of RNA using SuperScript™ III First-Strand Synthesis SuperMix for qRT-PCR (Thermo Fisher Scientific, Cat No. 11752-050) following the manufacturer's instructions. Then 4 µL of 1:5 diluted cDNA was mixed with qRT-PCR reaction master mix (10 µL Platinum® SYBR® Green qRT-PCR SuperMix-UDG (Thermo Fisher Scientific, Cat. No. 11733046), 0.4 µL of 10 µM forward primer and 0.4 µL of 10 µM reverse primer for gene-of-interest listed in Supplementary Table 1, and 5.2 µL of nuclease-free H_2O). Then the qRT-PCR thermocycler setting was set to 50°C for 2 min, 95°C for 2 min, then 40 cycles of 95°C for 15 s, 60°C for 30 s, plate read, and final melting curve from 55°C to 95°C with increment of 0.5°C for 5 s and plate read using CFX Connect™ Real-Time System (Bio-Rad). Note that two qRT-PCR trials were performed blindly by Maria Langegger and Christine Gottschalk.

Supplementary Table 1. Primers for qRT-PCR.
To measure the fold change in blood-related marker gene and *namptb* expression normalised to *actb1*, as a housekeeping gene, the following primer pairs were used for qRT-PCR. F – forward primer, R – reverse primer. Primers for *mpx*, *lcp1*, *mpeg1.1*, and *namptb* were designed by inputting the accession numbers in Primer-Blast (NCBI, 1988).

Primer name	Sequence 5' to 3'	Reference
actb1_F	GCTGTTTTCCCCTCCATTGTT	Morishima et al. (2019)
actb1_R	TCCCATGCCAACCATCACT	
gata1a_F	ACTCCTCTGAGCCTTCTCGT	
gata1a_R	GACTTGGCGAACTGGACTGT	
kdrl_F	CTGGTGGAGAGGCTAGGAGA	
kdrl_R	TGATCGGGATGTAGTGCTTTC	
klf1_F	CTCCGTACACACACAGGTGAAA	
klf1_R	ACTCATACGGCTTCTGTCCG	
mpx_F	GTTCACCACCAAACAGAAAACAG	NM_212779.2
mpx_R	ATGCCACCATCACCAGTCTC	
lcp1_F	GCCCTTCACCATACAGGAGA	NM_131320.3
lcp1_R	CGCCGATGTTCACCACG	
mpeg1.1_ F	GTTACAGCACGGGTTCAAGTCC	NM_212737.1
mpeg1.1_ R	GGCGTCAGCGATTTCTTCTGC	
namptb_ F	ACAGACTCTTATAAGATTACCCACTAC	NM_212668.2
namptb_ R	GGCCATCATATTTCTCTAAAACTTTCC	

To analyse the changes in gene expression, I calculated the fold change of each gene normalised to *act1b* using $2^{-\Delta\Delta Ct}$ by Livak and Schmittgen (2001).

Quantification of draculin:eGFP cells by fluorescent activated cell sorting (FACS)

To compare the *draculin:eGFP*$^{+}$ cell populations, *nampta*$^{+/+}$ and *nampta*$^{t10pm/t10pm}$ embryos in *draculin:eGFP* background were prepared for FACS. To dissociate embryos at 1 dpf, the protocol from Bresciani et al. (2018) was adapted. Ten dechorionated embryos were pooled and placed into 1.5 mL Eppendorf tubes and washed with 1 mL of 1x PBS. A dissociation mix (250 µL of 0.25% trypsin-EDTA (Sigma, T4049) and 250 µL Liberase™ (1mg/mL) (Roche, Cat. No. 05466202001)) was pre-heated at 30°C and then added to the embryos. Embryos were mechanically dissociated via harsh pipetting, first with P1000, and then with P200 for 5-10 min until the solution looked homogeneous. The reaction was stopped with a mixture of 360 µL Gibco™ DMEM (Cat. No. 11960-044) and 10% FBS (Biochrom, Cat. No. S0415) that was preheated at 30°C. Samples were centrifuged for 5 min at 700 g at room temperature, washed, and resuspended with 1 mL 1x PBS and centrifuged 5 min at

700 g. The supernatant was discarded, and the pellet was resuspended in 1 mL 1x PBS and filtered through a cell strainer with 30 µM mesh. GFP^+ cells were quantified using BD FACSMelody™ Cell sorter (BD Biosciences). Live healthy cells' profile was gated from unhealthy cells based on their internal complexity using side scatter (SSC-A) versus the measured cell size using with forward scatter (FSC-A). To ensure that only singlets are measured, the live cells' profile were further gated based on the correlation of cell height (FSC-H) vs cell area (FSC-A) using the forward scatter optical detector. To set a baseline of GFP^- cells, embryos from non-transgenic lines were used as negative controls.

Data analysis

Results of the NAD level and qRT-PCR measurements were plotted using Prism (GraphPad Software). To calculate the *p*-value and *z*-statistics, the Kruskal-Wallis (KW) non-parametric test combined with Dunn's multiple comparison test function was used. For example, Supplementary Table 2 shows the resulting *p*-value and *z*-statistics for *kdrl*.

Supplementary Table 2. An example of the results from Dunn's multiple comparison test.
nampta$^{+/+}$ (+/+) and *nampta*$^{t10pm/t10pm}$ (-/-) embryos were injected with *nampta* morpholino (MO). Then, for the statistical analysis of the fold change of the target gene expression normalised to *actb1* expression between different treatments, the *p*-value and *z*-statistics were quantified using Prism (GraphPad Software). The values presented are for *kdrl* with the total number of values as 54.

Dunn's multiple comparison test	**Adjusted *p*-value**	***Z***
+/+ vs. +/+ + MO	0.0005	3.943
+/+ vs. -/-	0.0007	3.859
+/+ vs. -/- + MO	0.0159	3.007
-/- vs. -/- + MO	>0.9999	0.6319

To determine the effect size between two specific groups for the Kruskal-Wallis test, the effect size is quantified in terms of eta squared (η^2) (Kassambara, 2023). η^2 and the equivalent Cohen's *d* were determined by entering the *z*-statistic from Prism into an effect size calculator by Lenhard and Lenhard (2016). For example, with the '*z*' test option, the *z*-value of 3.943 (Supplementary Table 2) and the total sample size of 54 were entered, and the resulting η^2 was 0.288 with an equivalent Cohen's *d* of 1.272 (Figure 3.11D-E). The results were then plotted in Prism.

Reference List

Affolter, M., Marty, T., Vigano, M. A., & Jazwinska, A. (2001). Nuclear interpretation of Dpp signaling in *Drosophila*. *EMBO J, 20*(13), 3298-3305. https://doi.org/10.1093/emboj/20.13.3298

Alhathal, N., Maddirevula, S., Coskun, S., Alali, H., Assoum, M., Morris, T., Deek, H. A., Hamed, S. A., Alsuhaibani, S., Mirdawi, A., Ewida, N., Al-Qahtani, M., Ibrahim, N., Abdulwahab, F., Altaweel, W., Dasouki, M. J., Assiri, A., Qabbaj, W., & Alkuraya, F. S. (2020). A genomics approach to male infertility. *Genet Med, 22*(12), 1967-1975. https://doi.org/10.1038/s41436-020-0916-0

Almuedo-Castillo, M., Bläßle, A., Morsdorf, D., Marcon, L., Soh, G. H., Rogers, K. W., Schier, A. F., & Muller, P. (2018). Scale-invariant patterning by size-dependent inhibition of Nodal signalling. *Nat Cell Biol, 20*(9), 1032-1042. https://doi.org/10.1038/s41556-018-0155-7

Anderson, K. V., & Nusslein-Volhard, C. (1984). Information for the dorsal-ventral pattern of the *Drosophila* embryo is stored as maternal mRNA. *Nature, 311*(5983), 223-227. https://doi.org/10.1038/311223a0

Anderson, K. V., Schneider, D. S., Morisato, D., Jin, Y., & Ferguson, E. L. (1992). Extracellular morphogens in *Drosophila* embryonic dorsal-ventral patterning. *Cold Spring Harb Symp Quant Biol, 57*, 409-417. https://doi.org/10.1101/sqb.1992.057.01.046

Arnone, M., Konantz, M., Hanns, P., Paczulla Stanger, A. M., Bertels, S., Godavarthy, P. S., Christopeit, M., & Lengerke, C. (2020). Acute myeloid leukemia stem cells: The challenges of phenotypic heterogeneity. *Cancers (Basel), 12*(12). https://doi.org/10.3390/cancers12123742

Basilicata, M. F., & Keller Valsecchi, C. I. (2021). The good, the bad, and the ugly: Evolutionary and pathological aspects of gene dosage alterations. *PLoS Genet, 17*(12), e1009906. https://doi.org/10.1371/journal.pgen.1009906

Belele, C. L., English, M. A., Chahal, J., Burnetti, A., Finckbeiner, S. M., Gibney, G., Kirby, M., Sood, R., & Liu, P. P. (2009). Differential requirement for Gata1 DNA binding and transactivation between primitive and definitive stages of hematopoiesis in zebrafish. *Blood, 114*(25), 5162-5172. https://doi.org/10.1182/blood-2009-05-224709

Ben-Zvi, D., Shilo, B. Z., Fainsod, A., & Barkai, N. (2008). Scaling of the BMP activation gradient in *Xenopus* embryos. *Nature, 453*(7199), 1205-1211. https://doi.org/10.1038/nature07059

Bennett, J. T., Joubin, K., Cheng, S., Aanstad, P., Herwig, R., Clark, M., Lehrach, H., & Schier, A. F. (2007). Nodal signaling activates differentiation genes during zebrafish gastrulation. *Dev Biol, 304*(2), 525-540. https://doi.org/10.1016/j.ydbio.2007.01.012

Bertrand, J. Y., Chi, N. C., Santoso, B., Teng, S., Stainier, D. Y., & Traver, D. (2010). Haematopoietic stem cells derive directly from aortic endothelium during development. *Nature, 464*(7285), 108-111. https://doi.org/10.1038/nature08738

Bertrand, J. Y., Kim, A. D., Violette, E. P., Stachura, D. L., Cisson, J. L., & Traver, D. (2007). Definitive hematopoiesis initiates through a committed erythromyeloid progenitor in the zebrafish embryo. *Development, 134*(23), 4147-4156. https://doi.org/10.1242/dev.012385

Bier, E. (2008). Intriguing extracellular regulation of BMP signaling. *Dev Cell, 15*(2), 176-177. https://doi.org/10.1016/j.devcel.2008.07.012

Bier, E., & De Robertis, E. M. (2015). BMP gradients: A paradigm for morphogen-mediated developmental patterning. *Science, 348*(6242), aaa5838. https://doi.org/10.1126/science.aaa5838

Bijakowski, C., Vadon-Le Goff, S., Delolme, F., Bourhis, J. M., Lecorche, P., Ruggiero, F., Becker-Pauly, C., Yiallouros, I., Stoocker, W., Dive, V., Hulmes, D. J. S., & Moali, C. (2012). Sizzled is unique among Secreted Frizzled-related proteins for its ability to specifically inhibit Bone Morphogenetic Protein-1 (BMP-1)/Tolloid-like proteinases. *Journal of Biological Chemistry, 287*(40), 33581-33593. https://doi.org/10.1074/jbc.M112.380816

Bläßle, A., & Müller, P. (2015). PyFDAP: automated analysis of fluorescence decay after photoconversion (FDAP) experiments. *Bioinformatics, 31*(6), 972-974. https://doi.org/10.1093/bioinformatics/btu735

Boatman, S., Barrett, F., Satishchandran, S., Jing, L., Shestopalov, I., & Zon, L. I. (2013). Assaying hematopoiesis using zebrafish. *Blood Cells Mol Dis, 51*(4), 271-276. https://doi.org/10.1016/j.bcmd.2013.07.009

Bonkhofer, F., Rispoli, R., Pinheiro, P., Krecsmarik, M., Schneider-Swales, J., Tsang, I. H. C., de Bruijn, M., Monteiro, R., Peterkin, T., & Patient, R. (2019). Blood stem cell-forming haemogenic endothelium in zebrafish derives from arterial endothelium. *Nat Commun, 10*(1), 3577. https://doi.org/10.1038/s41467-019-11423-2

Bradford, Y. M., Van Slyke, C.E., Ruzicka, L., Singer, A., Eagle, A., Fashena, D., Howe, D.G., Frazer, K., Martin, R., Paddock, H., Pich, C., Ramachandran, S., Westerfield, M. (2022). *ZFIN*. University of Oregon. http://zfin.org/

Bresciani, E., Broadbridge, E., & Liu, P. P. (2018). An efficient dissociation protocol for generation of single cell suspension from zebrafish embryos and larvae. *MethodsX, 5*, 1287-1290. https://doi.org/10.1016/j.mex.2018.10.009

Briscoe, J., & Small, S. (2015). Morphogen rules: design principles of gradient-mediated embryo patterning. *Development, 142*(23), 3996-4009. https://doi.org/10.1242/dev.129452

Camp, S. M., Ceco, E., Evenoski, C. L., Danilov, S. M., Zhou, T., Chiang, E. T., Moreno-Vinasco, L., Mapes, B., Zhao, J., Gursoy, G., Brown, M. E., Adyshev, D. M., Siddiqui, S. S., Quijada, H., Sammani, S., Letsiou, E., Saadat, L., Yousef, M., Wang, T., Liang, J., & Garcia, J. G. (2015). Unique Toll-Like Receptor 4 activation by NAMPT/PBEF induces NFκB signaling and inflammatory lung injury. *Sci Rep, 5*, 13135. https://doi.org/10.1038/srep13135

Canto, C., Menzies, K. J., & Auwerx, J. (2015). NAD(+) metabolism and the control of energy homeostasis: a balancing act between mtochondria and the nucleus. *Cell Metab, 22*(1), 31-53. https://doi.org/10.1016/j.cmet.2015.05.023

Capek, D., Safroshkin, M., Morales-Navarrete, H., Toulany, N., Arutyunov, G., Kurzbach, A., Bihler, J., Hagauer, J., Kick, S., Jones, F., Jordan, B., & Muller, P. (2023). EmbryoNet: using deep learning to link embryonic phenotypes to signaling pathways. *Nat Methods, 20*(6), 815-823. https://doi.org/10.1038/s41592-023-01873-4

Carisey, A., Stroud, M., Tsang, R., & Ballestrem, C. (2011). Fluorescence recovery after photobleaching. *Methods Mol Biol, 769*, 387-402. https://doi.org/10.1007/978-1-61779-207-6_26

Chalkiadaki, A., & Guarente, L. (2015). The multifaceted functions of sirtuins in cancer. *Nat Rev Cancer, 15*(10), 608-624. https://doi.org/10.1038/nrc3985

Chudakov, D. M., Lukyanov, S., & Lukyanov, K. A. (2007). Using photoactivatable fluorescent protein Dendra2 to track protein movement. *Biotechniques, 42*(5), 553, 555, 557 passim. https://doi.org/10.2144/000112470

Conlon, N., & Ford, D. (2022). A systems-approach to NAD+ restoration. *Biochem Pharmacol, 198*, 114946. https://doi.org/10.1016/j.bcp.2022.114946

Connors, S. A., Trout, J., Ekker, M., & Mullins, M. C. (1999). The role of tolloid/mini fin in dorsoventral pattern formation of the zebrafish embryo. *Development, 126*(14), 3119-3130. https://doi.org/10.1242/dev.126.14.3119

Constam, D. B. (2014). Regulation of TGFβ and related signals by precursor processing. *Semin Cell Dev Biol, 32*, 85-97. https://doi.org/10.1016/j.semcdb.2014.01.008

Cui, Y., Hackenmiller, R., Berg, L., Jean, F., Nakayama, T., Thomas, G., & Christian, J. L. (2001). The activity and signaling range of mature BMP-4 is regulated by sequential cleavage at two sites within the prodomain of the precursor. *Genes Dev, 15*(21), 2797-2802. https://doi.org/10.1101/gad.940001

Cui, Y., Jean, F., Thomas, G., & Christian, J. L. (1998). BMP-4 is proteolytically activated by furin and/or PC6 during vertebrate embryonic development. *EMBO J, 17*(16), 4735-4743. https://doi.org/10.1093/emboj/17.16.4735

Daetwyler, S., & Huisken, J. (2016). Fast Fluorescence Microscopy with Light Sheets. *Biol Bull, 231*(1), 14-25. https://doi.org/10.1086/689588

Dalcq, A. (1938). *Form and causality in early development*. Cambridge University Press. https://books.google.de/books?id=xdw5AAAAMAAJ

Dale, L., Evans, W., & Goodman, S. A. (2002). Xolloid-related: a novel BMP1/Tolloid-related metalloprotease is expressed during early *Xenopus* development. *Mech Dev, 119*(2), 177-190. https://doi.org/10.1016/s0925-4773(02)00359-3

Dale, L., Howes, G., Price, B. M., & Smith, J. C. (1992). Bone morphogenetic protein 4: a ventralizing factor in early *Xenopus* development. *Development, 115*(2), 573-585. https://doi.org/10.1242/dev.115.2.573

Davidson, A. J., & Zon, L. I. (2004). The 'definitive' (and 'primitive') guide to zebrafish hematopoiesis. *Oncogene, 23*(43), 7233-7246. https://doi.org/10.1038/sj.onc.1207943

De Robertis, E. M., & Sasai, Y. (1996). A common plan for dorsoventral patterning in Bilateria. *Nature, 380*(6569), 37-40. https://doi.org/10.1038/380037a0

Decotto, E., & Ferguson, E. L. (2001). A positive role for short gastrulation in modulating BMP signaling during dorsoventral patterning in the *Drosophila* embryo. *Development, 128*(19), 3831-3841. https://doi.org/10.1242/dev.128.19.3831

Dee, C. T., Hirst, C. S., Shih, Y. H., Tripathi, V. B., Patient, R. K., & Scotting, P. J. (2008). Sox3 regulates both neural fate and differentiation in the zebrafish ectoderm. *Dev Biol, 320*(1), 289-301. https://doi.org/10.1016/j.ydbio.2008.05.542

Deignan, L., Pinheiro, M. T., Sutcliffe, C., Saunders, A., Wilcockson, S. G., Zeef, L. A., Donaldson, I. J., & Ashe, H. L. (2016). Regulation of the BMP Signaling-Responsive Transcriptional Network in the *Drosophila* Embryo. *PLoS Genet, 12*(7), e1006164. https://doi.org/10.1371/journal.pgen.1006164

Detrich, H. W., 3rd, Kieran, M. W., Chan, F. Y., Barone, L. M., Yee, K., Rundstadler, J. A., Pratt, S., Ransom, D., & Zon, L. I. (1995). Intraembryonic hematopoietic cell migration during vertebrate development. *Proc Natl Acad Sci U S A, 92*(23), 10713-10717. https://doi.org/10.1073/pnas.92.23.10713

Dick, A., Hild, M., Bauer, H., Imai, Y., Maifeld, H., Schier, A. F., Talbot, W. S., Bouwmeester, T., & Hammerschmidt, M. (2000). Essential role of Bmp7 (*snailhouse*) and its prodomain in dorsoventral patterning of the zebrafish embryo. *Development, 127*(2), 343-354. https://doi.org/10.1242/dev.127.2.343

Dobrzycki, T., Mahony, C. B., Krecsmarik, M., Koyunlar, C., Rispoli, R., Peulen-Zink, J., Gussinklo, K., Fedlaoui, B., de Pater, E., Patient, R., & Monteiro, R. (2020). Deletion of a conserved Gata2 enhancer impairs haemogenic endothelium programming and adult Zebrafish haematopoiesis. *Commun Biol, 3*(1), 71. https://doi.org/10.1038/s42003-020-0798-3

Dooley, K. A., Davidson, A. J., & Zon, L. I. (2005). Zebrafish *scl* functions independently in hematopoietic and endothelial development. *Dev Biol, 277*(2), 522-536. https://doi.org/10.1016/j.ydbio.2004.09.004

Driever, W., & Nusslein-Volhard, C. (1988). The bicoid protein determines position in the *Drosophila* embryo in a concentration-dependent manner. *Cell, 54*(1), 95-104. https://doi.org/10.1016/0092-8674(88)90183-3

Dutko, J. A., & Mullins, M. C. (2011). SnapShot: BMP signaling in development. *Cell, 145*(4), 636, 636 e631-632. https://doi.org/10.1016/j.cell.2011.05.001

Duvaud, S., Gabella, C., Lisacek, F., Stockinger, H., Ioannidis, V., & Durinx, C. (2021). Expasy, the Swiss Bioinformatics Resource Portal, as designed by its users. *Nucleic Acids Research, 49*(W1), W216-W227. https://doi.org/10.1093/nar/gkab225

Dzierzak, E., & Bigas, A. (2018). Blood development: Hematopoietic stem cell dependence and independence. *Cell Stem Cell, 22*(5), 639-651. https://doi.org/10.1016/j.stem.2018.04.015

El Omari, K., Hoosdally, S. J., Tuladhar, K., Karia, D., Vyas, P., Patient, R., Porcher, C., & Mancini, E. J. (2011). Structure of the leukemia oncogene LMO2: implications for the assembly of a hematopoietic transcription factor complex. *Blood, 117*(7), 2146-2156. https://doi.org/10.1182/blood-2010-07-293357

El-Brolosy, M. A., Kontarakis, Z., Rossi, A., Kuenne, C., Gunther, S., Fukuda, N., Kikhi, K., Boezio, G. L. M., Takacs, C. M., Lai, S. L., Fukuda, R., Gerri, C., Giraldez, A. J., & Stainier, D. Y. R. (2019). Genetic compensation triggered by mutant mRNA degradation. *Nature, 568*(7751), 193-197. https://doi.org/10.1038/s41586-019-1064-z

Eldar, A., Dorfman, R., Weiss, D., Ashe, H., Shilo, B. Z., & Barkai, N. (2002). Robustness of the BMP morphogen gradient in *Drosophila* embryonic patterning. *Nature, 419*(6904), 304-308. https://doi.org/10.1038/nature01061

Esain, V., Cortes, M., & North, T. E. (2016). Enumerating hematopoietic stem and progenitor cells in zebrafish embryos. *Methods Mol Biol, 1451*, 191-206. https://doi.org/10.1007/978-1-4939-3771-4_13

Evanko, D. (2006). Training GFP to fold. *Nat Methods, 3*(2), 76. https://doi.org/10.1038/nmeth0206-76

Fang, C., Guan, L., Zhong, Z., Gan, X., & He, S. (2015). Analysis of the nicotinamide phosphoribosyltransferase family provides insight into vertebrate adaptation to different oxygen levels during the water-to-land transition. *FEBS J, 282*(15), 2858-2878. https://doi.org/10.1111/febs.13327

Ferguson, E. L., & Anderson, K. V. (1991). Dorsal-ventral pattern formation in the *Drosophila* embryo: the role of zygotically active genes. *Curr Top Dev Biol, 25*, 17-43. https://doi.org/10.1016/s0070-2153(08)60410-x

Ferguson, E. L., & Anderson, K. V. (1992a). *decapentaplegic* acts as a morphogen to organize dorsal-ventral pattern in the *Drosophila* embryo. *Cell, 71*(3), 451-461. https://doi.org/10.1016/0092-8674(92)90514-d

Ferguson, E. L., & Anderson, K. V. (1992b). Localized enhancement and repression of the activity of the TGF-β family member, *decapentaplegic*, is necessary for dorsal-ventral pattern formation in the *Drosophila* embryo. *Development, 114*(3), 583-597. https://www.ncbi.nlm.nih.gov/pubmed/1618130

Ferrero, G., Gomez, E., Lyer, S., Rovira, M., Miserocchi, M., Langenau, D. M., Bertrand, J. Y., & Wittamer, V. (2020). The *macrophage-expressed gene* (*mpeg*) 1 identifies a subpopulation of B cells in the adult zebrafish. *J Leukoc Biol, 107*(3), 431-443. https://doi.org/10.1002/JLB.1A1119-223R

Finnerty, J. R. (2003). The origins of axial patterning in the metazoa: how old is bilateral symmetry? *Int J Dev Biol, 47*(7-8), 523-529. http://www.ijdb.ehu.es/web/descarga/paper/14756328

Finnerty, J. R., Pang, K., Burton, P., Paulson, D., & Martindale, M. Q. (2004). Origins of bilateral symmetry: *Hox* and *dpp* expression in a sea anemone. *Science, 304*(5675), 1335-1337. https://doi.org/10.1126/science.1091946

Francois, P., Vonica, A., Brivanlou, A. H., & Siggia, E. D. (2009). Scaling of BMP gradients in *Xenopus* embryos. *Nature, 461*(7260), E1; discussion E2. https://doi.org/10.1038/nature08305

Francois, V., & Bier, E. (1995). *Xenopus chordin* and *Drosophila short gastrulation* genes encode homologous proteins functioning in dorsal-ventral axis formation. *Cell, 80*(1), 19-20. https://doi.org/10.1016/0092-8674(95)90446-8

Frank, P., & Bleakney, J. S. (1976). Histology and sexual reproduction of the anemone *Nematostella vectensis* Stephenson 1935. *Journal of Natural History, 10*, 441-449.

Galloway, J. L., Wingert, R. A., Thisse, C., Thisse, B., & Zon, L. I. (2005). Loss of Gata1 but not Gata2 converts erythropoiesis to myelopoiesis in zebrafish embryos. *Dev Cell, 8*(1), 109-116. https://doi.org/10.1016/j.devcel.2004.12.001

Gazzaniga, F., Stebbins, R., Chang, S. Z., McPeek, M. A., & Brenner, C. (2009). Microbial NAD metabolism: lessons from comparative genomics. *Microbiol Mol Biol Rev, 73*(3), 529-541, Table of Contents. https://doi.org/10.1128/MMBR.00042-08

Genikhovich, G., Fried, P., Prunster, M. M., Schinko, J. B., Gilles, A. F., Fredman, D., Meier, K., Iber, D., & Technau, U. (2015). Axis patterning by BMPs: Cnidarian network reveals evolutionary constraints. *Cell Rep, 10*(10), 1646-1654. https://doi.org/10.1016/j.celrep.2015.02.035

Genikhovich, G., & Technau, U. (2017). On the evolution of bilaterality. *Development, 144*(19), 3392-3404. https://doi.org/10.1242/dev.141507

Gering, M., Rodaway, A. R., Gottgens, B., Patient, R. K., & Green, A. R. (1998). The *SCL* gene specifies haemangioblast development from early mesoderm. *EMBO J, 17*(14), 4029-4045. https://doi.org/10.1093/emboj/17.14.4029

Gering, M., Yamada, Y., Rabbitts, T. H., & Patient, R. K. (2003). Lmo2 and Scl/Tal1 convert non-axial mesoderm into haemangioblasts which differentiate into endothelial cells in the absence of Gata1. *Development, 130*(25), 6187-6199. https://doi.org/10.1242/dev.00875

Gierer, A., & Meinhardt, H. (1972). A theory of biological pattern formation. *Kybernetik, 12*(1), 30-39. https://doi.org/10.1007/BF00289234

Gilbert, S. F. (2000). The generation of dorsal-ventral polarity. In *Developmental Biology* (6th ed.). Available from: https://www.ncbi.nlm.nih.gov/books/NBK10082/

Gilbert, S. F. (2003). *Developmental Biology* (7th ed.). Sinauer Associates Inc.

Gilbert, S. F., & Barresi, M. J. F. (2016). *Developmental Biology* (11th ed.). Sinauer Associates, Inc.

Glenn, N. O., Schumacher, J. A., Kim, H. J., Zhao, E. J., Skerniskyte, J., & Sumanas, S. (2014). Distinct regulation of the anterior and posterior *myeloperoxidase* expression by Etv2 and Gata1 during primitive granulopoiesis in zebrafish. *Dev Biol, 393*(1), 149-159. https://doi.org/10.1016/j.ydbio.2014.06.011

Gore, A. V., Pillay, L. M., Venero Galanternik, M., & Weinstein, B. M. (2018). The zebrafish: A fintastic model for hematopoietic development and disease. *Wiley Interdiscip Rev Dev Biol, 7*(3), e312. https://doi.org/10.1002/wdev.312

Gorfinkiel, N., & Martinez Arias, A. (2021). The cell in the age of the genomic revolution: Cell Regulatory Networks. *Cells Dev, 168*, 203720. https://doi.org/10.1016/j.cdev.2021.203720

Graf, T. (2002). Differentiation plasticity of hematopoietic cells. *Blood, 99*(9), 3089-3101. https://doi.org/10.1182/blood.v99.9.3089

Grigorian, M., & Hartenstein, V. (2013). Hematopoiesis and hematopoietic organs in arthropods. *Dev Genes Evol, 223*(1-2), 103-115. https://doi.org/10.1007/s00427-012-0428-2

Haffter, P., & Nusslein-Volhard, C. (1996). Large scale genetics in a small vertebrate, the zebrafish. *Int J Dev Biol, 40*(1), 221-227. http://www.ijdb.ehu.es/web/descarga/paper/8735932

Hammerschmidt, M., Pelegri, F., Mullins, M. C., Kane, D. A., van Eeden, F. J., Granato, M., Brand, M., Furutani-Seiki, M., Haffter, P., Heisenberg, C. P., Jiang, Y. J., Kelsh, R. N., Odenthal, J., Warga, R. M., & Nusslein-Volhard, C. (1996). *dino* and *mercedes*, two genes regulating dorsal development in the

zebrafish embryo. *Development, 123*, 95-102. https://doi.org/10.1242/dev.123.1.95

Harmansa, S., Alborelli, I., Bieli, D., Caussinus, E., & Affolter, M. (2017). A nanobody-based toolset to investigate the role of protein localization and dispersal in Drosophila. *Elife, 6*. https://doi.org/10.7554/eLife.22549

Harmansa, S., Hamaratoglu, F., Affolter, M., & Caussinus, E. (2015). Dpp spreading is required for medial but not for lateral wing disc growth. *Nature, 527*(7578), 317-322. https://doi.org/10.1038/nature15712

Hashiguchi, M., & Mullins, M. C. (2013). Anteroposterior and dorsoventral patterning are coordinated by an identical patterning clock. *Development, 140*(9), 1970-1980. https://doi.org/10.1242/dev.088104

He, X., Chen, W., Liu, Z., Yu, G., Chen, Y., Cai, Y. J., Sun, L., Xu, W., Zhong, L., Gao, C., Chen, J., Zhang, M., Yang, S., Yao, Y., Zhang, Z., Ma, F., Zhang, C. C., Lu, H. P., Yu, B., Cheng, T. L., Qiu, J., Sheng, Q., Zhou, H. M., Lv, Z. R., Yan, J., Zhou, Y., Qiu, Z., Cui, Z., Zhang, X., Meng, A., Sun, Q., & Yang, Y. (2020). Efficient and risk-reduced genome editing using double nicks enhanced by bacterial recombination factors in multiple species. *Nucleic Acids Res, 48*(10), e57. https://doi.org/10.1093/nar/gkaa195

Hemmati-Brivanlou, A., & Thomsen, G. H. (1995). Ventral mesodermal patterning in *Xenopus* embryos: expression patterns and activities of BMP-2 and BMP-4. *Dev Genet, 17*(1), 78-89. https://doi.org/10.1002/dvg.1020170109

Holley, S. A., & Ferguson, E. L. (1997). Fish are like flies are like frogs: conservation of dorsal-ventral patterning mechanisms. *Bioessays, 19*(4), 281-284. https://doi.org/10.1002/bies.950190404

Hong, S. B., Huang, Y., Moreno-Vinasco, L., Sammani, S., Moitra, J., Barnard, J. W., Ma, S. F., Mirzapoiazova, T., Evenoski, C., Reeves, R. R., Chiang, E. T., Lang, G. D., Husain, A. N., Dudek, S. M., Jacobson, J. R., Ye, S. Q., Lussier, Y. A., & Garcia, J. G. (2008). Essential role of pre-B-cell colony enhancing factor in ventilator-induced lung injury. *Am J Respir Crit Care Med, 178*(6), 605-617. https://doi.org/10.1164/rccm.200712-1822OC

Howe, K., Clark, M. D., Torroja, C. F., Torrance, J., Berthelot, C., Muffato, M., Collins, J. E., Humphray, S., McLaren, K., Matthews, L., McLaren, S., Sealy, I., Caccamo, M., Churcher, C., Scott, C., Barrett, J. C., Koch, R., Rauch, G. J., White, S., Chow, W., Kilian, B., Quintais, L. T., Guerra-Assuncao, J. A., Zhou, Y., Gu, Y., Yen, J., Vogel, J. H., Eyre, T., Redmond, S., Banerjee, R., Chi, J., Fu, B., Langley, E., Maguire, S. F., Laird, G. K., Lloyd, D., Kenyon, E., Donaldson, S., Sehra, H., Almeida-King, J., Loveland, J., Trevanion, S., Jones, M., Quail, M., Willey, D., Hunt, A., Burton, J., Sims, S., McLay, K., Plumb, B., Davis, J., Clee, C., Oliver, K., Clark, R., Riddle, C., Elliot, D., Threadgold, G., Harden, G., Ware, D., Begum, S., Mortimore, B., Kerry, G., Heath, P., Phillimore, B., Tracey, A., Corby, N., Dunn, M., Johnson, C., Wood, J., Clark, S., Pelan, S., Griffiths, G., Smith, M., Glithero, R., Howden, P., Barker, N., Lloyd, C., Stevens, C., Harley, J., Holt, K., Panagiotidis, G., Lovell,

J., Beasley, H., Henderson, C., Gordon, D., Auger, K., Wright, D., Collins, J., Raisen, C., Dyer, L., Leung, K., Robertson, L., Ambridge, K., Leongamornlert, D., McGuire, S., Gilderthorp, R., Griffiths, C., Manthravadi, D., Nichol, S., Barker, G., Whitehead, S., Kay, M., Brown, J., Murnane, C., Gray, E., Humphries, M., Sycamore, N., Barker, D., Saunders, D., Wallis, J., Babbage, A., Hammond, S., Mashreghi-Mohammadi, M., Barr, L., Martin, S., Wray, P., Ellington, A., Matthews, N., Ellwood, M., Woodmansey, R., Clark, G., Cooper, J., Tromans, A., Grafham, D., Skuce, C., Pandian, R., Andrews, R., Harrison, E., Kimberley, A., Garnett, J., Fosker, N., Hall, R., Garner, P., Kelly, D., Bird, C., Palmer, S., Gehring, I., Berger, A., Dooley, C. M., Ersan-Urun, Z., Eser, C., Geiger, H., Geisler, M., Karotki, L., Kirn, A., Konantz, J., Konantz, M., Oberlander, M., Rudolph-Geiger, S., Teucke, M., Lanz, C., Raddatz, G., Osoegawa, K., Zhu, B., Rapp, A., Widaa, S., Langford, C., Yang, F., Schuster, S. C., Carter, N. P., Harrow, J., Ning, Z., Herrero, J., Searle, S. M., Enright, A., Geisler, R., Plasterk, R. H., Lee, C., Westerfield, M., de Jong, P. J., Zon, L. I., Postlethwait, J. H., Nusslein-Volhard, C., Hubbard, T. J., Roest Crollius, H., Rogers, J., & Stemple, D. L. (2013). The zebrafish reference genome sequence and its relationship to the human genome. *Nature, 496*(7446), 498-503. https://doi.org/10.1038/nature12111

Hromas, R., Zon, L., & Friedman, A. D. (1992). Hematopoietic transcription regulators and the origins of leukemia. *Crit Rev Oncol Hematol, 12*(2), 167-190. https://doi.org/10.1016/1040-8428(92)90088-8

Huang, Z., Zhang, C., Chen, S., Ye, F., & Xing, X. H. (2013). Active inclusion bodies of acid phosphatase PhoC: aggregation induced by GFP fusion and activities modulated by linker flexibility. *Microb Cell Fact, 12*, 25. https://doi.org/10.1186/1475-2859-12-25

Huisken, J., & Stainier, D. Y. (2009). Selective plane illumination microscopy techniques in developmental biology. *Development, 136*(12), 1963-1975. https://doi.org/10.1242/dev.022426

Hume, D. A., Monkley, S. J., & Wainwright, B. J. (1995). Detection of *c-fms* protooncogene in early mouse embryos by whole mount in situ hybridization indicates roles for macrophages in tissue remodelling. *Br J Haematol, 90*(4), 939-942. https://doi.org/10.1111/j.1365-2141.1995.tb05220.x

Huning, L., & Kunkel, G. R. (2020). Two paralogous *znf143* genes in zebrafish encode transcriptional activator proteins with similar functions but expressed at different levels during early development. *BMC Mol Cell Biol, 21*(1), 3. https://doi.org/10.1186/s12860-020-0247-7

Imai, S. (2009). Nicotinamide phosphoribosyltransferase (Nampt): a link between NAD biology, metabolism, and diseases. *Curr Pharm Des, 15*(1), 20-28. https://doi.org/10.2174/138161209787185814

Imai, S. I. (2016). The NAD World 2.0: the importance of the inter-tissue communication mediated by NAMPT/NAD(+)/SIRT1 in mammalian aging and longevity control. *NPJ Syst Biol Appl, 2*, 16018. https://doi.org/10.1038/npjsba.2016.18

Inbal, A., Kim, S. H., Shin, J., & Solnica-Krezel, L. (2007). Six3 represses Nodal activity to establish early brain asymmetry in zebrafish. *Neuron, 55*(3), 407-415. https://doi.org/10.1016/j.neuron.2007.06.037

Inomata, H., Shibata, T., Haraguchi, T., & Sasai, Y. (2013). Scaling of dorsal-ventral patterning by embryo size-dependent degradation of Spemann's organizer signals. *Cell, 153*(6), 1296-1311. https://doi.org/10.1016/j.cell.2013.05.004

Irish, V. F., & Gelbart, W. M. (1987). The *decapentaplegic* gene is required for dorsal-ventral patterning of the *Drosophila* embryo. *Genes Dev, 1*(8), 868-879. https://doi.org/10.1101/gad.1.8.868

Itoh, K., Ossipova, O., & Sokol, S. Y. (2021). Pinhead antagonizes Admp to promote notochord formation. *iScience, 24*(6), 102520. https://doi.org/10.1016/j.isci.2021.102520

Jagannathan-Bogdan, M., & Zon, L. I. (2013). Hematopoiesis. *Development, 140*(12), 2463-2467. https://doi.org/10.1242/dev.083147

Jones, C. M., Armes, N., & Smith, J. C. (1996). Signalling by TGF-β family members: short-range effects of Xnr-2 and BMP-4 contrast with the long-range effects of activin. *Curr Biol, 6*(11), 1468-1475. https://doi.org/10.1016/s0960-9822(96)00751-8

Karlstrom, R. O., & Kane, D. A. (1996). A flipbook of zebrafish embryogenesis. *Development, 123*, 461. https://doi.org/10.1242/dev.123.1.461

Kassambara, A. (2023). *rstatix: Pipe-Friendly Framework for Basic Statistical Tests*. https://rdrr.io/cran/rstatix/man/kruskal_effsize.html

Kell, M. J., Riccio, R. E., Baumgartner, E. A., Compton, Z. J., Pecorin, P. J., Mitchell, T. A., Topczewski, J., & LeClair, E. E. (2018). Targeted deletion of the zebrafish actin-bundling protein L-plastin (*lcp1*). *PLoS One, 13*(1), e0190353. https://doi.org/10.1371/journal.pone.0190353

Keller, P. J., Schmidt, A. D., Wittbrodt, J., & Stelzer, E. H. (2008). Reconstruction of zebrafish early embryonic development by scanned light sheet microscopy. *Science, 322*(5904), 1065-1069. https://doi.org/10.1126/science.1162493

Kimmel, C. B., Ballard, W. W., Kimmel, S. R., Ullmann, B., & Schilling, T. F. (1995). Stages of embryonic development of the zebrafish. *Dev Dyn, 203*(3), 253-310. https://doi.org/10.1002/aja.1002030302

Kishimoto, Y., Lee, K. H., Zon, L., Hammerschmidt, M., & Schulte-Merker, S. (1997). The molecular nature of zebrafish *swirl*: BMP2 function is essential during early dorsoventral patterning. *Development, 124*(22), 4457-4466. https://www.ncbi.nlm.nih.gov/pubmed/9409664

Knabl, P., Schauer, A., Pomreinke, A. P., Zimmermann, B., Rogers, K. W., Müller, P., & Genikhovich, G. (2022). Analysis of SMAD1/5 target genes in a sea

anemone reveals ZSWIM4-6 as a novel BMP signaling modulator. *bioRxiv*, 2022.2006.2003.494682. https://doi.org/10.1101/2022.06.03.494682

Kobayashi, M., Nishikawa, K., & Yamamoto, M. (2001). Hematopoietic regulatory domain of *gata1* gene is positively regulated by GATA1 protein in zebrafish embryos. *Development, 128*(12), 2341-2350. https://doi.org/10.1242/dev.128.12.2341

Kok, F. O., Shin, M., Ni, C. W., Gupta, A., Grosse, A. S., van Impel, A., Kirchmaier, B. C., Peterson-Maduro, J., Kourkoulis, G., Male, I., DeSantis, D. F., Sheppard-Tindell, S., Ebarasi, L., Betsholtz, C., Schulte-Merker, S., Wolfe, S. A., & Lawson, N. D. (2015). Reverse genetic screening reveals poor correlation between morpholino-induced and mutant phenotypes in zebrafish. *Dev Cell, 32*(1), 97-108. https://doi.org/10.1016/j.devcel.2014.11.018

Kondo, M. (2007). Bone morphogenetic proteins in the early development of zebrafish. *FEBS J, 274*(12), 2960-2967. https://doi.org/10.1111/j.1742-4658.2007.05838.x

Korbie, D. J., & Mattick, J. S. (2008). Touchdown PCR for increased specificity and sensitivity in PCR amplification. *Nat Protoc, 3*(9), 1452-1456. https://doi.org/10.1038/nprot.2008.133

Kulkeaw, K., & Sugiyama, D. (2012). Zebrafish erythropoiesis and the utility of fish as models of anemia. *Stem Cell Res Ther, 3*(6), 55. https://doi.org/10.1186/scrt146

Lacaud, G., & Kouskoff, V. (2017). Hemangioblast, hemogenic endothelium, and primitive versus definitive hematopoiesis. *Exp Hematol, 49*, 19-24. https://doi.org/10.1016/j.exphem.2016.12.009

Lawrence, P. A. (1966). Gradients in the insect segment: The orientation of hairs in the milkweed bug *Oncopeltus Fasciatus*. *The Journal of Experimental Biology, 44*(3). https://doi.org/10.1242/jeb.44.3.607

Lawson, N. D., & Weinstein, B. M. (2002). *In vivo* imaging of embryonic vascular development using transgenic zebrafish. *Dev Biol, 248*(2), 307-318. https://doi.org/10.1006/dbio.2002.0711

Lebedeva, T., Aman, A. J., Graf, T., Niedermoser, I., Zimmermann, B., Kraus, Y., Schatka, M., Demilly, A., Technau, U., & Genikhovich, G. (2021). Cnidarian-bilaterian comparison reveals the ancestral regulatory logic of the β-catenin dependent axial patterning. *Nat Commun, 12*(1), 4032. https://doi.org/10.1038/s41467-021-24346-8

Leclere, L., & Rentzsch, F. (2014). RGM regulates BMP-mediated secondary axis formation in the sea anemone *Nematostella vectensis*. *Cell Rep, 9*(5), 1921-1930. https://doi.org/10.1016/j.celrep.2014.11.009

Lee, H. X., Ambrosio, A. L., Reversade, B., & De Robertis, E. M. (2006). Embryonic dorsal-ventral signaling: secreted Frizzled-related proteins as inhibitors of

tolloid proteinases. *Cell, 124*(1), 147-159. https://doi.org/10.1016/j.cell.2005.12.018

Lee, R. T., Zhao, Z., & Ingham, P. W. (2016). Hedgehog signalling. *Development, 143*(3), 367-372. https://doi.org/10.1242/dev.120154

Lele, Z., Bakkers, J., & Hammerschmidt, M. (2001). Morpholino phenocopies of the *swirl*, *snailhouse*, *somitabun*, *minifin*, *silberblick*, and *pipetail* mutations. *Genesis, 30*(3), 190-194. https://doi.org/10.1002/gene.1063

Lele, Z., Nowak, M., & Hammerschmidt, M. (2001). Zebrafish *admp* is required to restrict the size of the organizer and to promote posterior and ventral development. *Dev Dyn, 222*(4), 681-687. https://doi.org/10.1002/dvdy.1222

Lenhard, W., & Lenhard, A. (2016). *Computation of effect sizes*. Psychometrica. Retrieved August 24, 2022 from https://www.psychometrica.de/effect_size.html

Li, Y., Wu, Y., Zhou, J., Zhang, H., Zhang, Y., Ma, H., Jiang, X., & Shi, Q. (2021). A recurrent *ZSWIM7* mutation causes male infertility resulting from decreased meiotic recombination. *Hum Reprod, 36*(5), 1436-1445. https://doi.org/10.1093/humrep/deab046

Liang, D., Chang, J. R., Chin, A. J., Smith, A., Kelly, C., Weinberg, E. S., & Ge, R. (2001). The role of vascular endothelial growth factor (VEGF) in vasculogenesis, angiogenesis, and hematopoiesis in zebrafish development. *Mech Dev, 108*(1-2), 29-43. https://doi.org/10.1016/s0925-4773(01)00468-3

Liao, W., Bisgrove, B. W., Sawyer, H., Hug, B., Bell, B., Peters, K., Grunwald, D. J., & Stainier, D. Y. (1997). The zebrafish gene *cloche* acts upstream of a *flk-1* homologue to regulate endothelial cell differentiation. *Development, 124*(2), 381-389. https://doi.org/10.1242/dev.124.2.381

Little, S. C., & Mullins, M. C. (2006). Extracellular modulation of BMP activity in patterning the dorsoventral axis. *Birth Defects Res C Embryo Today, 78*(3), 224-242. https://doi.org/10.1002/bdrc.20079

Livak, K. J., & Schmittgen, T. D. (2001). Analysis of relative gene expression data using real-time quantitative PCR and the 2-ΔΔCt method. *Methods, 25*(4), 402-408. https://doi.org/10.1006/meth.2001.1262

Lyons, S. E., Lawson, N. D., Lei, L., Bennett, P. E., Weinstein, B. M., & Liu, P. P. (2002). A nonsense mutation in zebrafish *gata1* causes the bloodless phenotype in *vlad* tepes. *Proc Natl Acad Sci U S A, 99*(8), 5454-5459. https://doi.org/10.1073/pnas.082695299

Ma, Z., & Chen, J. (2020). Premature termination codon-bearing mRNA mediates genetic compensation response. *Zebrafish*. https://doi.org/10.1089/zeb.2019.1824

Ma, Z., Zhu, P., Shi, H., Guo, L., Zhang, Q., Chen, Y., Chen, S., Zhang, Z., Peng, J., & Chen, J. (2019). PTC-bearing mRNA elicits a genetic compensation response via Upf3a and COMPASS components. *Nature, 568*(7751), 259-263. https://doi.org/10.1038/s41586-019-1057-y

Makarova, K. S., Aravind, L., & Koonin, E. V. (2002). SWIM, a novel Zn-chelating domain present in bacteria, archaea and eukaryotes. *Trends Biochem Sci, 27*(8), 384-386. https://doi.org/10.1016/s0968-0004(02)02140-0

McGlacken-Byrne, S. M., Le Quesne Stabej, P., Del Valle, I., Ocaka, L., Gagunashvili, A., Crespo, B., Moreno, N., James, C., Bacchelli, C., Dattani, M. T., Williams, H. J., Kelberman, D., Achermann, J. C., & Conway, G. S. (2022). ZSWIM7 Is associated with human female meiosis and familial primary ovarian insufficiency. *J Clin Endocrinol Metab, 107*(1), e254-e263. https://doi.org/10.1210/clinem/dgab597

Mead, P. E., Deconinck, A. E., Huber, T. L., Orkin, S. H., & Zon, L. I. (2001). Primitive erythropoiesis in the *Xenopus* embryo: the synergistic role of LMO-2, SCL and GATA-binding proteins. *Development, 128*(12), 2301-2308. https://doi.org/10.1242/dev.128.12.2301

Meeker, N. D., Hutchinson, S. A., Ho, L., & Trede, N. S. (2007). Method for isolation of PCR-ready genomic DNA from zebrafish tissues. *Biotechniques, 43*(5), 610, 612, 614. https://doi.org/10.2144/000112619

Meinhardt, H. (2015). Dorsoventral patterning by the Chordin-BMP pathway: a unified model from a pattern-formation perspective for *Drosophila*, vertebrates, sea urchins and *Nematostella*. *Dev Biol, 405*(1), 137-148. https://doi.org/10.1016/j.ydbio.2015.05.025

Meinhardt, H., & Roth, S. (2002). Developmental biology: sharp peaks from shallow sources. *Nature, 419*(6904), 261-262. https://doi.org/10.1038/419261a

Miller-Bertoglio, V. E., Fisher, S., Sanchez, A., Mullins, M. C., & Halpern, M. E. (1997). Differential regulation of chordin expression domains in mutant zebrafish. *Dev Biol, 192*(2), 537-550. https://doi.org/10.1006/dbio.1997.8788

Montecinos-Franjola, F., Bauer, B. L., Mears, J. A., & Ramachandran, R. (2020). GFP fluorescence tagging alters dynamin-related protein 1 oligomerization dynamics and creates disassembly-refractory puncta to mediate mitochondrial fission. *Sci Rep, 10*(1), 14777. https://doi.org/10.1038/s41598-020-71655-x

Morgan, T. H. (1898). Experimental studies of the regeneration of *Planaria maculata*. *Roux's archives of developmental biology 7*, 364-397.

Morgan, T. H. (1904). An Analysis of the Phenomena of Organic 'Polarity'. *Science, 20*(518), 742-748. https://doi.org/10.1126/science.20.518.742

Moriguchi, T., & Yamamoto, M. (2014). A regulatory network governing *Gata1* and *Gata2* gene transcription orchestrates erythroid lineage differentiation. *Int J Hematol, 100*(5), 417-424. https://doi.org/10.1007/s12185-014-1568-0

Morishima, T., Krahl, A. C., Nasri, M., Xu, Y., Aghaallaei, N., Findik, B., Klimiankou, M., Ritter, M., Hartmann, M. D., Gloeckner, C. J., Stefanczyk, S., Lindner, C., Oswald, B., Bernhard, R., Hahnel, K., Hermanutz-Klein, U., Ebinger, M., Handgretinger, R., Casadei, N., Welte, K., Andre, M., Müller, P., Bajoghli, B., & Skokowa, J. (2019). LMO2 activation by deacetylation is indispensable for hematopoiesis and T-ALL leukemogenesis. *Blood, 134*(14), 1159-1175. https://doi.org/10.1182/blood.2019000095

Moriyama, Y., & De Robertis, E. M. (2018). Embryonic regeneration by relocalization of the Spemann organizer during twinning in *Xenopus*. *Proc Natl Acad Sci U S A, 115*(21), E4815-E4822. https://doi.org/10.1073/pnas.1802749115

Mörsdorf, D. (2019). *Quantifying and perturbing the movement of extracellular proteins in zebrafish embryos* [Cumulative, University of Tuebingen]. Tuebingen.

Mörsdorf, D., & Müller, P. (2019). Tuning protein diffusivity with membrane tethers. *Biochemistry, 58*(3), 177-181. https://doi.org/10.1021/acs.biochem.8b01150

Mosimann, C., Panakova, D., Werdich, A. A., Musso, G., Burger, A., Lawson, K. L., Carr, L. A., Nevis, K. R., Sabeh, M. K., Zhou, Y., Davidson, A. J., DiBiase, A., Burns, C. E., Burns, C. G., MacRae, C. A., & Zon, L. I. (2015). Chamber identity programs drive early functional partitioning of the heart. *Nat Commun, 6*, 8146. https://doi.org/10.1038/ncomms9146

Müller, P., Rogers, K. W., Jordan, B. M., Lee, J. S., Robson, D., Ramanathan, S., & Schier, A. F. (2012). Differential diffusivity of Nodal and Lefty underlies a reaction-diffusion patterning system. *Science, 336*(6082), 721-724. https://doi.org/10.1126/science.1221920

Müller, P., Rogers, K. W., Yu, S. R., Brand, M., & Schier, A. F. (2013). Morphogen transport. *Development, 140*(8), 1621-1638. https://doi.org/10.1242/dev.083519

Mullins, M. C. (1998). Holy Tolloido: Tolloid cleaves SOG/Chordin to free DPP/BMPs. *Trends Genet, 14*(4), 127-129. https://doi.org/10.1016/s0168-9525(98)01431-0

Mullins, M. C. (2006). Tolloid gets Sizzled competing with Chordin. *Dev Cell, 10*(2), 154-156. https://doi.org/10.1016/j.devcel.2006.01.009

Mullins, M. C., Hammerschmidt, M., Haffter, P., & Nusslein-Volhard, C. (1994). Large-scale mutagenesis in the zebrafish: in search of genes controlling development in a vertebrate. *Curr Biol, 4*(3), 189-202. https://doi.org/10.1016/s0960-9822(00)00048-8

Mullins, M. C., Hammerschmidt, M., Kane, D. A., Odenthal, J., Brand, M., van Eeden, F. J., Furutani-Seiki, M., Granato, M., Haffter, P., Heisenberg, C. P., Jiang, Y. J., Kelsh, R. N., & Nusslein-Volhard, C. (1996). Genes establishing dorsoventral pattern formation in the zebrafish embryo: the ventral specifying genes. *Development, 123*, 81-93. https://doi.org/10.1242/dev.123.1.81

Muraoka, O., Shimizu, T., Yabe, T., Nojima, H., Bae, Y. K., Hashimoto, H., & Hibi, M. (2006). Sizzled controls dorso-ventral polarity by repressing cleavage of the Chordin protein. *Nat Cell Biol, 8*(4), 329-338. https://doi.org/10.1038/ncb1379

Murayama, E., Kissa, K., Zapata, A., Mordelet, E., Briolat, V., Lin, H. F., Handin, R. I., & Herbomel, P. (2006). Tracing hematopoietic precursor migration to successive hematopoietic organs during zebrafish development. *Immunity, 25*(6), 963-975. https://doi.org/10.1016/j.immuni.2006.10.015

Musser, J. M., Schippers, K. J., Nickel, M., Mizzon, G., Kohn, A. B., Pape, C., Ronchi, P., Papadopoulos, N., Tarashansky, A. J., Hammel, J. U., Wolf, F., Liang, C., Hernandez-Plaza, A., Cantalapiedra, C. P., Achim, K., Schieber, N. L., Pan, L., Ruperti, F., Francis, W. R., Vargas, S., Kling, S., Renkert, M., Polikarpov, M., Bourenkov, G., Feuda, R., Gaspar, I., Burkhardt, P., Wang, B., Bork, P., Beck, M., Schneider, T. R., Kreshuk, A., Worheide, G., Huerta-Cepas, J., Schwab, Y., Moroz, L. L., & Arendt, D. (2021). Profiling cellular diversity in sponges informs animal cell type and nervous system evolution. *Science, 374*(6568), 717-723. https://doi.org/10.1126/science.abj2949

Myers, C. T., & Krieg, P. A. (2013). BMP-mediated specification of the erythroid lineage suppresses endothelial development in blood island precursors. *Blood, 122*(24), 3929-3939. https://doi.org/10.1182/blood-2013-03-490045

Nakanishi, N., Renfer, E., Technau, U., & Rentzsch, F. (2012). Nervous systems of the sea anemone *Nematostella vectensis* are generated by ectoderm and endoderm and shaped by distinct mechanisms. *Development, 139*(2), 347-357. https://doi.org/10.1242/dev.071902

NCBI. (1988). *National Center for Biotechnology Information*. National Library of Medicine (US), National Center for Biotechnology Information;. https://www.ncbi.nlm.nih.gov/

Nellen, D., Burke, R., Struhl, G., & Basler, K. (1996). Direct and long-range action of a DPP morphogen gradient. *Cell, 85*(3), 357-368. https://doi.org/10.1016/s0092-8674(00)81114-9

Nerlov, C., Querfurth, E., Kulessa, H., & Graf, T. (2000). GATA-1 interacts with the myeloid PU.1 transcription factor and represses PU.1-dependent transcription. *Blood, 95*(8), 2543-2551. https://www.ncbi.nlm.nih.gov/pubmed/10753833

Ng, X. W., Sampath, K., & Wohland, T. (2018). Fluorescence Correlation and Cross-Correlation Spectroscopy in Zebrafish. *Methods Mol Biol, 1863*, 67-105. https://doi.org/10.1007/978-1-4939-8772-6_5

Niehrs, C. (2010). On growth and form: a Cartesian coordinate system of Wnt and BMP signaling specifies bilaterian body axes. *Development, 137*(6), 845-857. https://doi.org/10.1242/dev.039651

Nusslein-Volhard, C. (2022). The *Toll* gene in *Drosophila* pattern formation. *Trends Genet, 38*(3), 231-245. https://doi.org/10.1016/j.tig.2021.09.006

Nusslein-Volhard, C., & Wieschaus, E. (1980). Mutations affecting segment number and polarity in *Drosophila*. *Nature, 287*(5785), 795-801. https://doi.org/10.1038/287795a0

Oates, A. C., Pratt, S. J., Vail, B., Yan, Y., Ho, R. K., Johnson, S. L., Postlethwait, J. H., & Zon, L. I. (2001). The zebrafish *klf* gene family. *Blood, 98*(6), 1792-1801. https://doi.org/10.1182/blood.v98.6.1792

Ocaña, O. H., Coskun, H., Minguillon, C., Murawala, P., Tanaka, E. M., Galceran, J., Munoz-Chapuli, R., & Nieto, M. A. (2017). A right-handed signalling pathway drives heart looping in vertebrates. *Nature, 549*(7670), 86-90. https://doi.org/10.1038/nature23454

Oelgeschlager, M., Kuroda, H., Reversade, B., & De Robertis, E. M. (2003). Chordin is required for the Spemann organizer transplantation phenomenon in *Xenopus* embryos. *Dev Cell, 4*(2), 219-230. https://doi.org/10.1016/s1534-5807(02)00404-5

Palis, J., & Yoder, M. C. (2001). Yolk-sac hematopoiesis: the first blood cells of mouse and man. *Exp Hematol, 29*(8), 927-936. https://doi.org/10.1016/s0301-472x(01)00669-5

Papatheodorou, I., Moreno, P., Manning, J., Fuentes, A. M.-P., George, N., Fexova, S., Fonseca, N. A., Füllgrabe, A., Green, M., Huang, N., Huerta, L., Iqbal, H., Jianu, M., Mohammed, S., Zhao, L., Jarnuczak, A. F., Jupp, S., Marioni, J., Meyer, K., Petryszak, R., Prada Medina, C. A., Talavera-López, C., Teichmann, S., Vizcaino, J. A., & Brazma, A. (2020). Expression Atlas update: from tissues to single cells. *Nucleic Acids Research, 48*(D1), D77-D83. https://doi.org/10.1093/nar/gkz947

Parichy, D. M. (2015). Advancing biology through a deeper understanding of zebrafish ecology and evolution. *Elife, 4*. https://doi.org/10.7554/eLife.05635

Patterson, L. J., Gering, M., Eckfeldt, C. E., Green, A. R., Verfaillie, C. M., Ekker, S. C., & Patient, R. (2007). The transcription factors Scl and Lmo2 act together during development of the hemangioblast in zebrafish. *Blood, 109*(6), 2389-2398. https://doi.org/10.1182/blood-2006-02-003087

Pauls, S., Geldmacher-Voss, B., & Campos-Ortega, J. A. (2001). A zebrafish histone variant H2A.F/Z and a transgenic H2A.F/Z:GFP fusion protein for in vivo studies of embryonic development. *Dev Genes Evol, 211*(12), 603-610. https://doi.org/10.1007/s00427-001-0196-x

Pedelacq, J. D., Cabantous, S., Tran, T., Terwilliger, T. C., & Waldo, G. S. (2006). Engineering and characterization of a superfolder green fluorescent protein. *Nat Biotechnol, 24*(1), 79-88. https://doi.org/10.1038/nbt1172

Pera, E. M., Ikeda, A., Eivers, E., & De Robertis, E. M. (2003). Integration of IGF, FGF, and anti-BMP signals via Smad1 phosphorylation in neural induction. *Genes Dev, 17*(24), 3023-3028. https://doi.org/10.1101/gad.1153603

Piccolo, S., Agius, E., Lu, B., Goodman, S., Dale, L., & De Robertis, E. M. (1997). Cleavage of Chordin by Xolloid metalloprotease suggests a role for proteolytic processing in the regulation of Spemann organizer activity. *Cell, 91*(3), 407-416. https://doi.org/10.1016/s0092-8674(00)80424-9

Piccolo, S., Sasai, Y., Lu, B., & De Robertis, E. M. (1996). Dorsoventral patterning in *Xenopus*: inhibition of ventral signals by direct binding of Chordin to BMP-4. *Cell, 86*(4), 589-598. https://doi.org/10.1016/s0092-8674(00)80132-4

Plouhinec, J. L., Zakin, L., Moriyama, Y., & De Robertis, E. M. (2013). Chordin forms a self-organizing morphogen gradient in the extracellular space between ectoderm and mesoderm in the *Xenopus* embryo. *Proc Natl Acad Sci U S A, 110*(51), 20372-20379. https://doi.org/10.1073/pnas.1319745110

Pomreinke, A. P., Soh, G. H., Rogers, K. W., Bergmann, J. K., Bläßle, A. J., & Müller, P. (2017). Dynamics of BMP signaling and distribution during zebrafish dorsal-ventral patterning. *Elife, 6*. https://doi.org/10.7554/eLife.25861

Port, F., Strein, C., Stricker, M., Rauscher, B., Heigwer, F., Zhou, J., Beyersdorffer, C., Frei, J., Hess, A., Kern, K., Lange, L., Langner, N., Malamud, R., Pavlovic, B., Radecke, K., Schmitt, L., Voos, L., Valentini, E., & Boutros, M. (2020). A large-scale resource for tissue-specific CRISPR mutagenesis in *Drosophila*. *Elife, 9*. https://doi.org/10.7554/eLife.53865

Postlethwait, J. H., Woods, I. G., Ngo-Hazelett, P., Yan, Y. L., Kelly, P. D., Chu, F., Huang, H., Hill-Force, A., & Talbot, W. S. (2000). Zebrafish comparative genomics and the origins of vertebrate chromosomes. *Genome Res, 10*(12), 1890-1902. https://doi.org/10.1101/gr.164800

Potapov, V., & Ong, J. L. (2017). Examining sources of error in PCR by single-molecule sequencing. *PLoS One, 12*(1), e0169774. https://doi.org/10.1371/journal.pone.0169774

Rabbitts, T. H. (1994). Chromosomal translocations in human cancer. *Nature, 372*(6502), 143-149. https://doi.org/10.1038/372143a0

Ramel, M. C., & Hill, C. S. (2012). Spatial regulation of BMP activity. *FEBS Lett, 586*(14), 1929-1941. https://doi.org/10.1016/j.febslet.2012.02.035

Ramel, M. C., & Hill, C. S. (2013). The ventral to dorsal BMP activity gradient in the early zebrafish embryo is determined by graded expression of BMP ligands. *Dev Biol, 378*(2), 170-182. https://doi.org/10.1016/j.ydbio.2013.03.003

Ratnayake, D., Nguyen, P. D., Rossello, F. J., Wimmer, V. C., Tan, J. L., Galvis, L. A., Julier, Z., Wood, A. J., Boudier, T., Isiaku, A. I., Berger, S., Oorschot, V., Sonntag, C., Rogers, K. L., Marcelle, C., Lieschke, G. J., Martino, M. M., Bakkers, J., & Currie, P. D. (2021). Macrophages provide a transient muscle

stem cell niche via NAMPT secretion. *Nature, 591*(7849), 281-287. https://doi.org/10.1038/s41586-021-03199-7

Reber-Muller, S., Streitwolf-Engel, R., Yanze, N., Schmid, V., Stierwald, M., Erb, M., & Seipel, K. (2006). BMP2/4 and BMP5-8 in jellyfish development and transdifferentiation. *Int J Dev Biol, 50*(4), 377-384. https://doi.org/10.1387/ijdb.052085sr

Rekhtman, N., Radparvar, F., Evans, T., & Skoultchi, A. I. (1999). Direct interaction of hematopoietic transcription factors PU.1 and GATA-1: functional antagonism in erythroid cells. *Genes Dev, 13*(11), 1398-1411. https://doi.org/10.1101/gad.13.11.1398

Renshaw, S. A., Loynes, C. A., Trushell, D. M., Elworthy, S., Ingham, P. W., & Whyte, M. K. (2006). A transgenic zebrafish model of neutrophilic inflammation. *Blood, 108*(13), 3976-3978. https://doi.org/10.1182/blood-2006-05-024075

Rentzsch, F., Anton, R., Saina, M., Hammerschmidt, M., Holstein, T. W., & Technau, U. (2006). Asymmetric expression of the BMP antagonists *chordin* and *gremlin* in the sea anemone *Nematostella vectensis*: implications for the evolution of axial patterning. *Dev Biol, 296*(2), 375-387. https://doi.org/10.1016/j.ydbio.2006.06.003

Rentzsch, F., Bakkers, J., Kramer, C., & Hammerschmidt, M. (2004). Fgf signaling induces posterior neuroectoderm independently of Bmp signaling inhibition. *Dev Dyn, 231*(4), 750-757. https://doi.org/10.1002/dvdy.20244

Rentzsch, F., Guder, C., Vocke, D., Hobmayer, B., & Holstein, T. W. (2007). An ancient chordin-like gene in organizer formation of Hydra. *Proc Natl Acad Sci U S A, 104*(9), 3249-3254. https://doi.org/10.1073/pnas.0604501104

Reversade, B., & De Robertis, E. M. (2005). Regulation of ADMP and BMP2/4/7 at opposite embryonic poles generates a self-regulating morphogenetic field. *Cell, 123*(6), 1147-1160. https://doi.org/10.1016/j.cell.2005.08.047

Revollo, J. R., Korner, A., Mills, K. F., Satoh, A., Wang, T., Garten, A., Dasgupta, B., Sasaki, Y., Wolberger, C., Townsend, R. R., Milbrandt, J., Kiess, W., & Imai, S. (2007). Nampt/PBEF/Visfatin regulates insulin secretion in β cells as a systemic NAD biosynthetic enzyme. *Cell Metab, 6*(5), 363-375. https://doi.org/10.1016/j.cmet.2007.09.003

Rhodes, J., Hagen, A., Hsu, K., Deng, M., Liu, T. X., Look, A. T., & Kanki, J. P. (2005). Interplay of Pu.1 and Gata1 determines myelo-erythroid progenitor cell fate in zebrafish. *Dev Cell, 8*(1), 97-108. https://doi.org/10.1016/j.devcel.2004.11.014

Ritchie, H. (2022). *How many species are there?* OurWorldInData.org. https://ourworldindata.org/how-many-species-are-there

Robertson, A. L., Avagyan, S., Gansner, J. M., & Zon, L. I. (2016). Understanding the regulation of vertebrate hematopoiesis and blood disorders - big lessons from a small fish. *FEBS Lett, 590*(22), 4016-4033. https://doi.org/10.1002/1873-3468.12415

Robu, M. E., Larson, J. D., Nasevicius, A., Beiraghi, S., Brenner, C., Farber, S. A., & Ekker, S. C. (2007). p53 activation by knockdown technologies. *PLoS Genet, 3*(5), e78. https://doi.org/10.1371/journal.pgen.0030078

Rogers, K. W., Bläßle, A., Schier, A. F., & Muller, P. (2015). Measuring protein stability in living zebrafish embryos using fluorescence decay after photoconversion (FDAP). *J Vis Exp*(95), 52266. https://doi.org/10.3791/52266

Rogers, K. W., & Müller, P. (2019). Nodal and BMP dispersal during early zebrafish development. *Dev Biol, 447*(1), 14-23. https://doi.org/10.1016/j.ydbio.2018.04.002

Rogers, K. W., & Schier, A. F. (2011). Morphogen gradients: from generation to interpretation. *Annu Rev Cell Dev Biol, 27*, 377-407. https://doi.org/10.1146/annurev-cellbio-092910-154148

Ross, J. J., Shimmi, O., Vilmos, P., Petryk, A., Kim, H., Gaudenz, K., Hermanson, S., Ekker, S. C., O'Connor, M. B., & Marsh, J. L. (2001). Twisted gastrulation is a conserved extracellular BMP antagonist. *Nature, 410*(6827), 479-483. https://doi.org/10.1038/35068578

Rossi, A., Kontarakis, Z., Gerri, C., Nolte, H., Holper, S., Kruger, M., & Stainier, D. Y. (2015). Genetic compensation induced by deleterious mutations but not gene knockdowns. *Nature, 524*(7564), 230-233. https://doi.org/10.1038/nature14580

Roth, S., Stein, D., & Nusslein-Volhard, C. (1989). A gradient of nuclear localization of the *dorsal* protein determines dorsoventral pattern in the *Drosophila* embryo. *Cell, 59*(6), 1189-1202. https://doi.org/10.1016/0092-8674(89)90774-5

Ryan, J. F., & Baxevanis, A. D. (2007). Hox, Wnt, and the evolution of the primary body axis: insights from the early-divergent phyla. *Biol Direct, 2*, 37. https://doi.org/10.1186/1745-6150-2-37

Ryu, K. W., Nandu, T., Kim, J., Challa, S., DeBerardinis, R. J., & Kraus, W. L. (2018). Metabolic regulation of transcription through compartmentalized NAD(+) biosynthesis. *Science, 360*(6389). https://doi.org/10.1126/science.aan5780

Saina, M., Genikhovich, G., Renfer, E., & Technau, U. (2009). BMPs and Chordin regulate patterning of the directive axis in a sea anemone. *Proc Natl Acad Sci U S A, 106*(44), 18592-18597. https://doi.org/10.1073/pnas.0900151106

Sander, K. (1960). Analyse des ooplasmatischen Reaktionssystems von *Euscelis plejebus* Fall (Cicadina) durch Isolieren und Kombinieren von Keimteilen. II. Mitteilung: Die Differenzierungsleistungen nach Verlagern von

Hinterpolmaterial *Wilhelm Roux' Archiv fur Entwicklungsmechanik der Organismen, 151*(5), 660-707. https://doi.org/10.1007/BF00577816

Sasai, Y., Lu, B., Steinbeisser, H., Geissert, D., Gont, L. K., & De Robertis, E. M. (1994). *Xenopus* chordin: a novel dorsalizing factor activated by organizer-specific homeobox genes. *Cell, 79*(5), 779-790. https://doi.org/10.1016/0092-8674(94)90068-x

Schier, A. F., & Shen, M. M. (2000). Nodal signalling in vertebrate development. *Nature, 403*(6768), 385-389. https://doi.org/10.1038/35000126

Schier, A. F., & Talbot, W. S. (2005). Molecular genetics of axis formation in zebrafish. *Annu Rev Genet, 39*, 561-613. https://doi.org/10.1146/annurev.genet.37.110801.143752

Schierwater, B., & DeSalle, R. (2018). Placozoa. *Curr Biol, 28*(3), R97-R98. https://doi.org/10.1016/j.cub.2017.11.042

Schindelin, J., Arganda-Carreras, I., Frise, E., Kaynig, V., Longair, M., Pietzsch, T., Preibisch, S., Rueden, C., Saalfeld, S., Schmid, B., Tinevez, J. Y., White, D. J., Hartenstein, V., Eliceiri, K., Tomancak, P., & Cardona, A. (2012). Fiji: an open-source platform for biological-image analysis. *Nat Methods, 9*(7), 676-682. https://doi.org/10.1038/nmeth.2019

Schmid, B., Shah, G., Scherf, N., Weber, M., Thierbach, K., Campos, C. P., Roeder, I., Aanstad, P., & Huisken, J. (2013). High-speed panoramic light-sheet microscopy reveals global endodermal cell dynamics. *Nat Commun, 4*, 2207. https://doi.org/10.1038/ncomms3207

Schmidt, J., Francois, V., Bier, E., & Kimelman, D. (1995). *Drosophila short gastrulation* induces an ectopic axis in *Xenopus*: evidence for conserved mechanisms of dorsal-ventral patterning. *Development, 121*(12), 4319-4328. https://doi.org/10.1242/dev.121.12.4319

Schulte-Merker, S., Lee, K. J., McMahon, A. P., & Hammerschmidt, M. (1997). The zebrafish organizer requires *chordino*. *Nature, 387*(6636), 862-863. https://doi.org/10.1038/43092

Scuderi, A., & Letsou, A. (2005). Amnioserosa is required for dorsal closure in *Drosophila*. *Dev Dyn, 232*(3), 791-800. https://doi.org/10.1002/dvdy.20306

Sewell, H., Tanaka, T., El Omari, K., Mancini, E. J., Cruz, A., Fernandez-Fuentes, N., Chambers, J., & Rabbitts, T. H. (2014). Conformational flexibility of the oncogenic protein LMO2 primes the formation of the multi-protein transcription complex. *Sci Rep, 4*, 3643. https://doi.org/10.1038/srep03643

Shalaby, F., Rossant, J., Yamaguchi, T. P., Gertsenstein, M., Wu, X. F., Breitman, M. L., & Schuh, A. C. (1995). Failure of blood-island formation and vasculogenesis in Flk-1-deficient mice. *Nature, 376*(6535), 62-66. https://doi.org/10.1038/376062a0

Sharpe, J. (2019). Wolpert's French Flag: what's the problem? *Development, 146*(24). https://doi.org/10.1242/dev.185967

Shih, J., & Fraser, S. E. (1996). Characterizing the zebrafish organizer: microsurgical analysis at the early-shield stage. *Development, 122*(4), 1313-1322. https://doi.org/10.1242/dev.122.4.1313

Shimmi, O., & O'Connor, M. B. (2003). Physical properties of Tld, Sog, Tsg and Dpp protein interactions are predicted to help create a sharp boundary in Bmp signals during dorsoventral patterning of the *Drosophila* embryo. *Development, 130*(19), 4673-4682. https://doi.org/10.1242/dev.00684

Siatecka, M., & Bieker, J. J. (2011). The multifunctional role of EKLF/KLF1 during erythropoiesis. *Blood, 118*(8), 2044-2054. https://doi.org/10.1182/blood-2011-03-331371

Smith, J. D., Hing, A. V., Clarke, C. M., Johnson, N. M., Perez, F. A., Park, S. S., Horst, J. A., Mecham, B., Maves, L., Nickerson, D. A., University of Washington Center for Mendelian, G., & Cunningham, M. L. (2014). Exome sequencing identifies a recurrent de novo *ZSWIM6* mutation associated with acromelic frontonasal dysostosis. *Am J Hum Genet, 95*(2), 235-240. https://doi.org/10.1016/j.ajhg.2014.07.008

Soh, G. H. (2020). *Germ layer patterning via morphogen crosstalk* [Cumulative, University of Tuebingen]. Tuebingen.

Soh, G. H., Pomreinke, A. P., & Müller, P. (2020). Integration of Nodal and BMP signaling by mutual signaling effector antagonism. *Cell Rep, 31*(1), 107487. https://doi.org/10.1016/j.celrep.2020.03.051

Soto, R. A., Najia, M. A. T., Hachimi, M., Frame, J. M., Yette, G. A., Lummertz da Rocha, E., Stankunas, K., Daley, G. Q., & North, T. E. (2021). Sequential regulation of hemogenic fate and hematopoietic stem and progenitor cell formation from arterial endothelium by Ezh1/2. *Stem Cell Reports, 16*(7), 1718-1734. https://doi.org/10.1016/j.stemcr.2021.05.014

Spemann, H. (1918). Über die Determination der ersten Organanlagen des Amphibienembryo, IV. *Arch. f. Entw.mech., 43*, 448-555.

Stachura, D. L., & Traver, D. (2016). Cellular dissection of zebrafish hematopoiesis. *Methods Cell Biol, 133*, 11-53. https://doi.org/10.1016/bs.mcb.2016.03.022

Stainier, D. Y. R., Raz, E., Lawson, N. D., Ekker, S. C., Burdine, R. D., Eisen, J. S., Ingham, P. W., Schulte-Merker, S., Yelon, D., Weinstein, B. M., Mullins, M. C., Wilson, S. W., Ramakrishnan, L., Amacher, S. L., Neuhauss, S. C. F., Meng, A., Mochizuki, N., Panula, P., & Moens, C. B. (2017). Guidelines for morpholino use in zebrafish. *PLoS Genet, 13*(10), e1007000. https://doi.org/10.1371/journal.pgen.1007000

Steinmetz, P. R. H., Aman, A., Kraus, J. E. M., & Technau, U. (2017). Gut-like ectodermal tissue in a sea anemone challenges germ layer homology. *Nat Ecol Evol, 1*(10), 1535-1542. https://doi.org/10.1038/s41559-017-0285-5

Stevens, M. L., Chaturvedi, P., Rankin, S. A., Macdonald, M., Jagannathan, S., Yukawa, M., Barski, A., & Zorn, A. M. (2017). Genomic integration of Wnt/β-catenin and BMP/Smad1 signaling coordinates foregut and hindgut transcriptional programs. *Development, 144*(7), 1283-1295. https://doi.org/10.1242/dev.145789

Steward, R., Zusman, S. B., Huang, L. H., & Schedl, P. (1988). The dorsal protein is distributed in a gradient in early *Drosophila* embryos. *Cell, 55*(3), 487-495. https://doi.org/10.1016/0092-8674(88)90035-9

Stumpf, H. F. (1966). Mechanism by which cells estimate their location within the body. *Nature, 212*(5060), 430-431. https://doi.org/10.1038/212430a0

Suzuki, M., Kobayashi-Osaki, M., Tsutsumi, S., Pan, X., Ohmori, S., Takai, J., Moriguchi, T., Ohneda, O., Ohneda, K., Shimizu, R., Kanki, Y., Kodama, T., Aburatani, H., & Yamamoto, M. (2013). GATA factor switching from GATA2 to GATA1 contributes to erythroid differentiation. *Genes Cells, 18*(11), 921-933. https://doi.org/10.1111/gtc.12086

Suzzi, S., Ahrendt, R., Hans, S., Semenova, S. A., Chekuru, A., Wirsching, P., Kroehne, V., Bilican, S., Sayed, S., Winkler, S., Spiess, S., Machate, A., Kaslin, J., Panula, P., & Brand, M. (2021). Deletion of *lrrk2* causes early developmental abnormalities and age-dependent increase of monoamine catabolism in the zebrafish brain. *PLoS Genet, 17*(9), e1009794. https://doi.org/10.1371/journal.pgen.1009794

Sztal, T. E., & Stainier, D. Y. R. (2020). Transcriptional adaptation: a mechanism underlying genetic robustness. *Development, 147*(15). https://doi.org/10.1242/dev.186452

Tessadori, F., de Bakker, D. E. M., Barske, L., Nelson, N., Algra, H. A., Willekers, S., Nichols, J. T., Crump, J. G., & Bakkers, J. (2020). Zebrafish *prrx1a* mutants have normal hearts. *Nature, 585*(7826), E14-E16. https://doi.org/10.1038/s41586-020-2674-1

The UniProt Consortium. (2022). UniProt: the Universal Protein Knowledgebase in 2023. *Nucleic Acids Research, 51*(D1), D523-D531. https://doi.org/10.1093/nar/gkac1052

Thisse, B., Pflumio, S., Fürthauer, M., Loppin, B., Heyer, V., Degrave, A., Woehl, R., Lux, A., Steffan, T., Charbonnier, X. Q., & Thisse, C. (2001). *Expression of the zebrafish genome during embryogenesis (NIH R01 RR15402)*. ZFIN Direct Data Submission. http://zfin.org

Thisse, C., & Thisse, B. (2008). High-resolution in situ hybridization to whole-mount zebrafish embryos. *Nat Protoc, 3*(1), 59-69. https://doi.org/10.1038/nprot.2007.514

Tirosh-Finkel, L., Zeisel, A., Brodt-Ivenshitz, M., Shamai, A., Yao, Z., Seger, R., Domany, E., & Tzahor, E. (2010). BMP-mediated inhibition of FGF signaling promotes cardiomyocyte differentiation of anterior heart field progenitors. *Development, 137*(18), 2989-3000. https://doi.org/10.1242/dev.051649

Trefely, S., & Wellen, K. E. (2018). Metabolite regulates differentiation. *Science, 360*(6389), 603-604. https://doi.org/10.1126/science.aat6663

Tripic, T., Deng, W., Cheng, Y., Zhang, Y., Vakoc, C. R., Gregory, G. D., Hardison, R. C., & Blobel, G. A. (2009). SCL and associated proteins distinguish active from repressive GATA transcription factor complexes. *Blood, 113*(10), 2191-2201. https://doi.org/10.1182/blood-2008-07-169417

Tuazon, F. B., Wang, X., Andrade, J. L., Umulis, D., & Mullins, M. C. (2020). Proteolytic restriction of chordin range underlies BMP gradient formation. *Cell Rep, 32*(7), 108039. https://doi.org/10.1016/j.celrep.2020.108039

Tucker, J. A., Mintzer, K. A., & Mullins, M. C. (2008). The BMP signaling gradient patterns dorsoventral tissues in a temporally progressive manner along the anteroposterior axis. *Dev Cell, 14*(1), 108-119. https://doi.org/10.1016/j.devcel.2007.11.004

Turing, A. M. (1952). The chemical basis of morphogenesis. 1953. *Bull Math Biol, 52*(1-2), 153-197; discussion 119-152. https://doi.org/10.1007/BF02459572

Valet, M., Siggia, E. D., & Brivanlou, A. H. (2022). Mechanical regulation of early vertebrate embryogenesis. *Nat Rev Mol Cell Biol, 23*(3), 169-184. https://doi.org/10.1038/s41580-021-00424-z

Visvader, J. E., Mao, X., Fujiwara, Y., Hahm, K., & Orkin, S. H. (1997). The LIM-domain binding protein Ldb1 and its partner LMO2 act as negative regulators of erythroid differentiation. *Proc Natl Acad Sci U S A, 94*(25), 13707-13712. https://doi.org/10.1073/pnas.94.25.13707

Vogeli, K. M., Jin, S. W., Martin, G. R., & Stainier, D. Y. (2006). A common progenitor for haematopoietic and endothelial lineages in the zebrafish gastrula. *Nature, 443*(7109), 337-339. https://doi.org/10.1038/nature05045

von Ubisch, L. (1953). *Entwicklungsprobleme*. Fischer.

Wagner, D. S., & Mullins, M. C. (2002). Modulation of BMP activity in dorsal-ventral pattern formation by the Chordin and Ogon antagonists. *Dev Biol, 245*(1), 109-123. https://doi.org/10.1006/dbio.2002.0614

Wang, T., Zhang, X., Bheda, P., Revollo, J. R., Imai, S., & Wolberger, C. (2006). Structure of Nampt/PBEF/visfatin, a mammalian NAD+ biosynthetic enzyme. *Nat Struct Mol Biol, 13*(7), 661-662. https://doi.org/10.1038/nsmb1114

Waterhouse, A. M., Procter, J. B., Martin, D. M., Clamp, M., & Barton, G. J. (2009). Jalview Version 2 - a multiple sequence alignment editor and analysis

workbench. *Bioinformatics, 25*(9), 1189-1191. https://doi.org/10.1093/bioinformatics/btp033

Wattrus, S. J., & Zon, L. I. (2018). Stem cell safe harbor: the hematopoietic stem cell niche in zebrafish. *Blood Adv, 2*(21), 3063-3069. https://doi.org/10.1182/bloodadvances.2018021725

Weiss, M. J., & Orkin, S. H. (1995). Transcription factor GATA-1 permits survival and maturation of erythroid precursors by preventing apoptosis. *Proc Natl Acad Sci U S A, 92*(21), 9623-9627. https://doi.org/10.1073/pnas.92.21.9623

Whelan, N. V., Kocot, K. M., Moroz, T. P., Mukherjee, K., Williams, P., Paulay, G., Moroz, L. L., & Halanych, K. M. (2017). Ctenophore relationships and their placement as the sister group to all other animals. *Nat Ecol Evol, 1*(11), 1737-1746. https://doi.org/10.1038/s41559-017-0331-3

Wieschaus, E., & Nusslein-Volhard, C. (2016). The Heidelberg Screen for pattern mutants of *Drosophila*: A personal account. *Annu Rev Cell Dev Biol, 32*, 1-46. https://doi.org/10.1146/annurev-cellbio-113015-023138

Willot, V., Mathieu, J., Lu, Y., Schmid, B., Sidi, S., Yan, Y. L., Postlethwait, J. H., Mullins, M., Rosa, F., & Peyrieras, N. (2002). Cooperative action of ADMP- and BMP-mediated pathways in regulating cell fates in the zebrafish gastrula. *Dev Biol, 241*(1), 59-78. https://doi.org/10.1006/dbio.2001.0494

Wolpert, L. (1968). The French flag problem: A contribution to the discussion on pattern development and regeneration. In A. P. Company (Ed.), *Towards a Theoretical Biology, Vol. 1, (ed. C. H. Waddington)*.

Wolpert, L. (1969). Positional information and the spatial pattern of cellular differentiation. *J Theor Biol, 25*(1), 1-47. https://doi.org/10.1016/s0022-5193(69)80016-0

Xiao, X., Yu, X., Zhang, Z., Zhao, Y., Jiang, Y., Li, Z., Yang, Y., & Zhu, C. (2018). Transcranial brain atlas. *Sci Adv, 4*(9), eaar6904. https://doi.org/10.1126/sciadv.aar6904

Xu, P. F., Houssin, N., Ferri-Lagneau, K. F., Thisse, B., & Thisse, C. (2014). Construction of a vertebrate embryo from two opposing morphogen gradients. *Science, 344*(6179), 87-89. https://doi.org/10.1126/science.1248252

Xue, Y., Gao, S., & Liu, F. (2015). Genome-wide analysis of the zebrafish Klf family identifies two genes important for erythroid maturation. *Dev Biol, 403*(2), 115-127. https://doi.org/10.1016/j.ydbio.2015.05.015

Xue, Y., Zheng, X., Huang, L., Xu, P., Ma, Y., Min, Z., Tao, Q., Tao, Y., & Meng, A. (2014). Organizer-derived Bmp2 is required for the formation of a correct Bmp activity gradient during embryonic development. *Nat Commun, 5*, 3766. https://doi.org/10.1038/ncomms4766

Yabe, T., Shimizu, T., Muraoka, O., Bae, Y. K., Hirata, T., Nojima, H., Kawakami, A., Hirano, T., & Hibi, M. (2003). Ogon/Secreted Frizzled functions as a negative feedback regulator of Bmp signaling. *Development, 130*(12), 2705-2716. https://doi.org/10.1242/dev.00506

Yamada, Y., Warren, A. J., Dobson, C., Forster, A., Pannell, R., & Rabbitts, T. H. (1998). The T cell leukemia LIM protein Lmo2 is necessary for adult mouse hematopoiesis. *Proc Natl Acad Sci U S A, 95*(7), 3890-3895. https://doi.org/10.1073/pnas.95.7.3890

Yan, Y., Ning, G., Li, L., Liu, J., Yang, S., Cao, Y., & Wang, Q. (2019). The BMP ligand Pinhead together with Admp supports the robustness of embryonic patterning. *Sci Adv, 5*(12), eaau6455. https://doi.org/10.1126/sciadv.aau6455

Zebrafish Issue. (1996). Zebrafish Issue. *Development, 123*(1), 1-461. https://doi.org/10.1242/dev.123

Zeiss. *ZEISS Lightsheet Z.1*. Retrieved 13. June. 2018 from https://asset-downloads.zeiss.com/catalogs/download/mic/1ef55a85-bffe-4ffe-906c-0fea10482ed6/EN_product-info_Lightsheet-Z.1_rel-2.3.pdf

ZFIN. *Zebrafish Information Network*. http://zfin.org/

ZFIN. (2022). *ZFIN Zebrafish Nomenclature Conventions*. Retrieved June 14th, 2023 from https://zfin.org/

Zhang, P., Behre, G., Pan, J., Iwama, A., Wara-Aswapati, N., Radomska, H. S., Auron, P. E., Tenen, D. G., & Sun, Z. (1999). Negative cross-talk between hematopoietic regulators: GATA proteins repress PU.1. *Proc Natl Acad Sci U S A, 96*(15), 8705-8710. https://doi.org/10.1073/pnas.96.15.8705

Zhang, P., Zhang, X., Iwama, A., Yu, C., Smith, K. A., Mueller, B. U., Narravula, S., Torbett, B. E., Orkin, S. H., & Tenen, D. G. (2000). PU.1 inhibits GATA-1 function and erythroid differentiation by blocking GATA-1 DNA binding. *Blood, 96*(8), 2641-2648. https://www.ncbi.nlm.nih.gov/pubmed/11023493

Zhang, X. H., Tee, L. Y., Wang, X. G., Huang, Q. S., & Yang, S. H. (2015). Off-target effects in CRISPR/Cas9-mediated genome engineering. *Mol Ther Nucleic Acids, 4*(11), e264. https://doi.org/10.1038/mtna.2015.37

Zhang, Y., Au, Q., Zhang, M., Barber, J. R., Ng, S. C., & Zhang, B. (2009). Identification of a small molecule SIRT2 inhibitor with selective tumor cytotoxicity. *Biochem Biophys Res Commun, 386*(4), 729-733. https://doi.org/10.1016/j.bbrc.2009.06.113

Zhu, H., Traver, D., Davidson, A. J., Dibiase, A., Thisse, C., Thisse, B., Nimer, S., & Zon, L. I. (2005). Regulation of the *lmo2* promoter during hematopoietic and vascular development in zebrafish. *Dev Biol, 281*(2), 256-269. https://doi.org/10.1016/j.ydbio.2005.01.034

Zinski, J., Bu, Y., Wang, X., Dou, W., Umulis, D., & Mullins, M. C. (2017). Systems biology derived source-sink mechanism of BMP gradient formation. *Elife, 6*. https://doi.org/10.7554/eLife.22199

Zinski, J., Tajer, B., & Mullins, M. C. (2018). TGF-β family signaling in early vertebrate development. *Cold Spring Harb Perspect Biol, 10*(6). https://doi.org/10.1101/cshperspect.a033274

Zinski, J., Tuazon, F., Huang, Y., Mullins, M., & Umulis, D. (2019). Imaging and quantification of p-Smad1/5 in zebrafish blastula and gastrula Embryos. *Methods Mol Biol, 1891*, 135-154. https://doi.org/10.1007/978-1-4939-8904-1_10

ZIRC. (2008). *Zebrafish International Resource Center*. http://zebrafish.org

Appendices

A. Pomreinke, A. P., Soh, G. H., Rogers, K. W., Bergmann, J. K., Bläßle, A. J., & Müller, P. (2017). Dynamics of BMP signaling and distribution during zebrafish dorsal-ventral patterning. *eLife, 6*. https://doi.org/10.7554/eLife.25861

B. Soh, G. H., Pomreinke, A. P., & Müller, P. (2020). Integration of Nodal and BMP signaling by mutual signaling effector antagonism. *Cell Rep, 31*(1), 107487. https://doi.org/10.1016/j.celrep.2020.03.051

C. Knabl, P., Schauer, A., Pomreinke, A. P., Zimmermann, B., Rogers, K. W., Müller, P., & Genikhovich, G. (2022). Analysis of SMAD1/5 target genes in a sea anemone reveals ZSWIM4-6 as a novel BMP signaling modulator. *bioRxiv*, 2022.2006.2003.494682. https://doi.org/10.1101/2022.06.03.494682

eLIFE elifesciences.org

Appendix A RESEARCH ARTICLE

Dynamics of BMP signaling and distribution during zebrafish dorsal-ventral patterning

Autumn P Pomreinke†, Gary H Soh†, Katherine W Rogers†, Jennifer K Bergmann, Alexander J Bläßle, Patrick Müller*

Systems Biology of Development Group, Friedrich Miescher Laboratory of the Max Planck Society, Tübingen, Germany

Abstract During vertebrate embryogenesis, dorsal-ventral patterning is controlled by the BMP/Chordin activator/inhibitor system. BMP induces ventral fates, whereas Chordin inhibits BMP signaling on the dorsal side. Several theories can explain how the distributions of BMP and Chordin are regulated to achieve patterning, but the assumptions regarding activator/inhibitor diffusion and stability differ between models. Notably, 'shuttling' models in which the BMP distribution is modulated by a Chordin-mediated increase in BMP diffusivity have gained recent prominence. Here, we directly test five major models by measuring the biophysical properties of fluorescently tagged BMP2b and Chordin in zebrafish embryos. We found that BMP2b and Chordin diffuse and rapidly form extracellular protein gradients, Chordin does not modulate the diffusivity or distribution of BMP2b, and Chordin is not required to establish peak levels of BMP signaling. Our findings challenge current self-regulating reaction-diffusion and shuttling models and provide support for a graded source-sink mechanism underlying zebrafish dorsal-ventral patterning.
DOI: https://doi.org/10.7554/eLife.25861.001

***For correspondence:** pmueller@tuebingen.mpg.de

†These authors contributed equally to this work

Competing interests: The authors declare that no competing interests exist.

Funding: See page 27

Received: 08 February 2017
Accepted: 30 August 2017
Published: 31 August 2017

Reviewing editor: Deborah Yelon, University of California, San Diego, United States

Introduction

The dorsal-ventral axis is one of the earliest coordinate systems established during animal development and divides the embryo into dorsal (back) and ventral (belly) territories. This axis forms under the influence of the BMP/Chordin patterning system. The activator BMP induces the formation of ventral tissues, and BMP signaling is antagonized on the dorsal side by the inhibitor Chordin. There are currently several disparate models that can explain how BMP signaling is restricted to the ventral side (***Ben-Zvi et al., 2008***; ***Barkai and Ben-Zvi, 2009***; ***Francois et al., 2009***; ***Ben-Zvi et al., 2011b***; ***Inomata et al., 2013***; ***Ramel and Hill, 2013***; ***Ben-Zvi et al., 2014***), but the underlying biophysical assumptions have not been fully tested.

In the 'Graded source-sink + mobile BMP model' (Model 1), BMP is produced in a graded, ventrally biased source, and signaling from diffusing BMP is antagonized by binding to its inhibitor Chordin (***Figure 1—figure supplement 1***, ***Table 1***). Chordin (Chd) diffuses from a localized source on the opposing dorsal side and therefore provides a 'sink' that inactivates BMP molecules diffusing through the embryo, helping to shape the signaling distribution into a gradient that peaks ventrally. The distributions of *bmp* and *chd* mRNA in developing embryos are consistent with this idea – initially nearly uniform *bmp* expression refines to a ventrally biased gradient over time (***Ramel and Hill, 2013***; ***Zinski et al., 2017***), and *chd* expression is restricted to the dorsal region (***Miller-Bertoglio et al., 1997***).

Similar to Model 1, BMP signaling activity in the 'Graded source-sink + immobile BMP model' (Model 2, ***Figure 1—figure supplement 1***, ***Table 1***) is also restricted by the inhibitor Chordin diffusing from the dorsal side. However, Model 2 assumes that BMP does not diffuse (***Ramel and Hill,***

eLife digest Animals start life as clumps of cells that ultimately give rise to complex structures and organs. Over a century of research has revealed a small number of proteins that are crucial for complex structures to form from these clumps, including one protein called BMP. Different levels of BMP instruct cells to give rise to different tissues. In zebrafish, BMP is more abundant on one side of the embryo than the other. This gradient in BMP levels causes different tissues to form at distinct positions and helps coordinate embryo development.

Several theories have been proposed to explain how the BMP gradient is established. They all suggest that a second protein – Chordin – plays an important role in influencing how cells sense the BMP gradient by blocking BMP's activity. However, the exact role of Chordin in the formation of the BMP gradient is disputed. To address this, Pomreinke, Soh, Rogers et al. directly tested five theories of how BMP and Chordin molecules spread through embryos.

The experiments used microscopy to track the movements of fluorescent versions of both molecules in zebrafish embryos. The measurements contradict one theory stating that BMP does not move, and another in which Chordin increases the mobility of BMP. Pomreinke, Soh, Rogers et al. also found that embryos that lack Chordin have increased BMP signaling levels only on the side where Chordin is normally made but not on the opposite side where BMP is made, ruling out several of the theories. The findings are most consistent with the idea that the BMP gradient forms mainly as a result of higher production of BMP on one side of the embryo combined with movement of BMP away from where it is made. Chordin produced at the opposite end of the embryo helps to ensure that only the correct cells receive instructions from BMP.

In the future, two approaches could further clarify how the BMP gradient is formed. First, better techniques to directly observe the BMP gradient in normally developing embryos would be useful. Second, new theories that take into account additional players other than BMP and Chordin might help explain some features of development that current theories cannot address. Uncovering the mechanisms that control the formation of BMP gradients will improve our understanding of how clumps of cells can develop into animals.

DOI: https://doi.org/10.7554/eLife.25861.002

2013) and that it binds to Chordin with weaker affinity than in Model 1 (see Materials and methods). Proponents have argued that the similarities between the graded *bmp* mRNA distribution, signaling gradient, and target gene expression indicate negligible BMP diffusion during patterning (***Ramel and Hill, 2013***). Consistent with this, BMP4 was unable to induce long-range signaling in *Xenopus* experiments (***Jones et al., 1996***), although BMP target genes are induced outside of BMP-expressing clones in zebrafish (***Xu et al., 2014***). However, measuring the diffusivity of BMP *in vivo* is the most direct way to determine whether BMP is mobile (***Kicheva et al., 2007***; ***Zinski et al., 2017***).

Although these two relatively simple models are generally supported by biological observations, they do not take into account other regulators known to be crucial for dorsal-ventral patterning, such as the BMP-like ligand ADMP, and Sizzled, an inhibitor of the Chordin protease Tolloid/Xlr. Three models described below include these important dorsal-ventral regulators in addition to BMP and Chordin and have also been shown to explain scale-invariant patterning, a phenomenon in which embryos adjust their tissue proportions to differently sized patterning fields.

The recent 'Long-range accumulation and feedback model' (Model 3, ***Figure 1—figure supplement 1***, ***Table 1***) postulates that BMP and Chordin have equally high mobility, but that dorsal-ventral patterning is controlled by differences in BMP and Chordin protein stability (***Inomata et al., 2013***). In this model, BMP and ADMP induce the secreted, highly diffusible and stable Chordin protease inhibitor Sizzled. This protects Chordin from proteolysis and promotes its expansion towards the ventral side. Over time the resulting inhibition of BMP signaling leads to decreased Sizzled production, destabilizing Chordin and relieving inhibition of BMP. In this way, an appropriate balance between ventral BMP and dorsal Chordin levels can be established even in differently sized embryos.

In the 'Self-regulating reaction-diffusion model' (Model 4, ***Figure 1—figure supplement 1***, ***Table 1***), BMP and Chordin both have low diffusivities and equivalent protein stabilities. Interactions with highly mobile ADMP and Sizzled in two coupled reaction-diffusion networks eventually result in

Table 1. Summary of model assumptions, predictions, and experimental findings.
Model assumptions or predictions that are consistent with the experimental findings (gray) are highlighted in green. NA: no testable model assumptions or predictions.

	Model 1 Graded source-sink (mobile BMP)	Model 2 Graded source-sink (immobile BMP)	Model 3 Long-range accumulation and feedback	Model 4 Self-regulating reaction-diffusion system	Model 5 Shuttling	Experimental findings
Diffusivity of BMP and Chordin	D(BMP) > 0 D(BMP) < D(Chd)	D(BMP) ≈ 0 D(Chd) high	D(BMP) ≈ D(Chd) High	D(BMP) ≈ D(Chd) Low	D(BMP) << D(Chd)	D(BMP) ≤ D(Chd) (≈2 and 6 μm^2/s)
Effect of Chordin on BMP diffusivity	No effect	No effect	No effect	No effect	Chd enhances BMP diffusion	No effect
Half-life of BMP and Chordin	τ(BMP) ≈ τ(Chd)	Unconstrained	τ(BMP) >> τ(Chd)	τ(BMP) ≈ τ(Chd)	τ(BMP) > τ(Chd)*	τ(BMP) ≈ τ(Chd) (130 and 120 min)
pSmad gradient formation kinetics	Progressive rise ventrally, always low dorsally	Progressive rise ventrally, always low dorsally	Initially high dorsally and ventrally	Progressive rise ventrally, always low dorsally	Progressive rise ventrally, always low dorsally	Progressive rise ventrally, always low dorsally
Ventral pSmad peak decreased in the absence of Chordin?	No	No	No	No	Yes	No
Dorso-lateral pSmad expansion in the absence of Chordin?	Yes	Yes	Yes	No	Yes	Yes
Diffusivity of Sizzled relative to BMP/Chordin	NA	NA	D(ADMP) & D(Szl) ≈ D(BMP) & D (Chd)	D(ADMP) & D (Szl) >> D(BMP) & D (Chd)	NA	D(Szl) ≈ D(BMP) & D(Chd) (≈10, 2, and 6 μm^2/s)

*The simplified shuttling model without ADMP presented here is based on the experimentally measured clearance rate constants of BMP and Chordin; the full model for scale-invariant patterning including ADMP (***Ben-Zvi et al., 2008***) assumes a lower stability of Chordin due to Xlr-mediated degradation.
DOI: https://doi.org/10.7554/eLife.25861.003

the restriction of BMP signaling activity on the ventral side, assuming an initial dorsal Chordin or ventral BMP bias (***Francois et al., 2009***). Such a system self-regulates even with noisy initial conditions and could provide robustness during embryogenesis – e.g., the ability of developing organisms to withstand noise in gene expression or fluctuating environmental conditions – that can be difficult to explain with other models.

Finally, the prominent 'Shuttling model' (Model 5, ***Figure 1—figure supplement 1***, ***Table 1***) postulates that Chordin not only acts as an inhibitor of BMP, but also modulates the mobility and distribution of BMP protein (***Ben-Zvi et al., 2008***; ***Barkai and Ben-Zvi, 2009***; ***Ben-Zvi et al., 2011b***; ***Ben-Zvi et al., 2014***). In this model, BMP is poorly diffusive, Chordin is highly diffusive, and BMP mobility increases when bound to Chordin. Cleavage of the BMP/Chordin complex by the uniformly distributed protease Tolloid/Xlr combined with a flux of Chordin from the dorsal side is thought to 'shuttle' BMP towards the ventral side by facilitated diffusion over time. In this way, Chordin is responsible for the accumulation of BMP protein on the ventral side, and actively helps establish the subsequent ventral BMP signaling peak.

These five conflicting models postulate different diffusion (no diffusion, equal diffusion, differential diffusion, facilitated diffusion) and stability properties of BMP and Chordin proteins (***Table 1***, ***Figure 1—figure supplement 1***). However, these biophysical properties have not been fully measured experimentally, in part due to the lack of reagents and techniques to detect active BMP and Chordin in living vertebrate embryos. To test the biophysical tenets of these models, we developed active BMP and Chordin fluorescent fusion proteins, and used a combination of mathematical modeling and quantitative experiments to determine how BMP2b and Chordin gradients form. Additionally, we tested the distinct predictions that the five models make about how BMP signaling changes in the absence of Chordin. We found that (i) BMP2b and Chordin proteins have similar stabilities, (ii) both BMP2b and Chordin diffuse and form gradients in the extracellular space, and (iii) Chordin does not significantly facilitate BMP2b diffusion or play an active role in establishing peak ventral BMP signaling levels. Together, our results are most consistent with dorsal-ventral patterning mediated by Model 1, the 'Graded source-sink + mobile BMP' model.

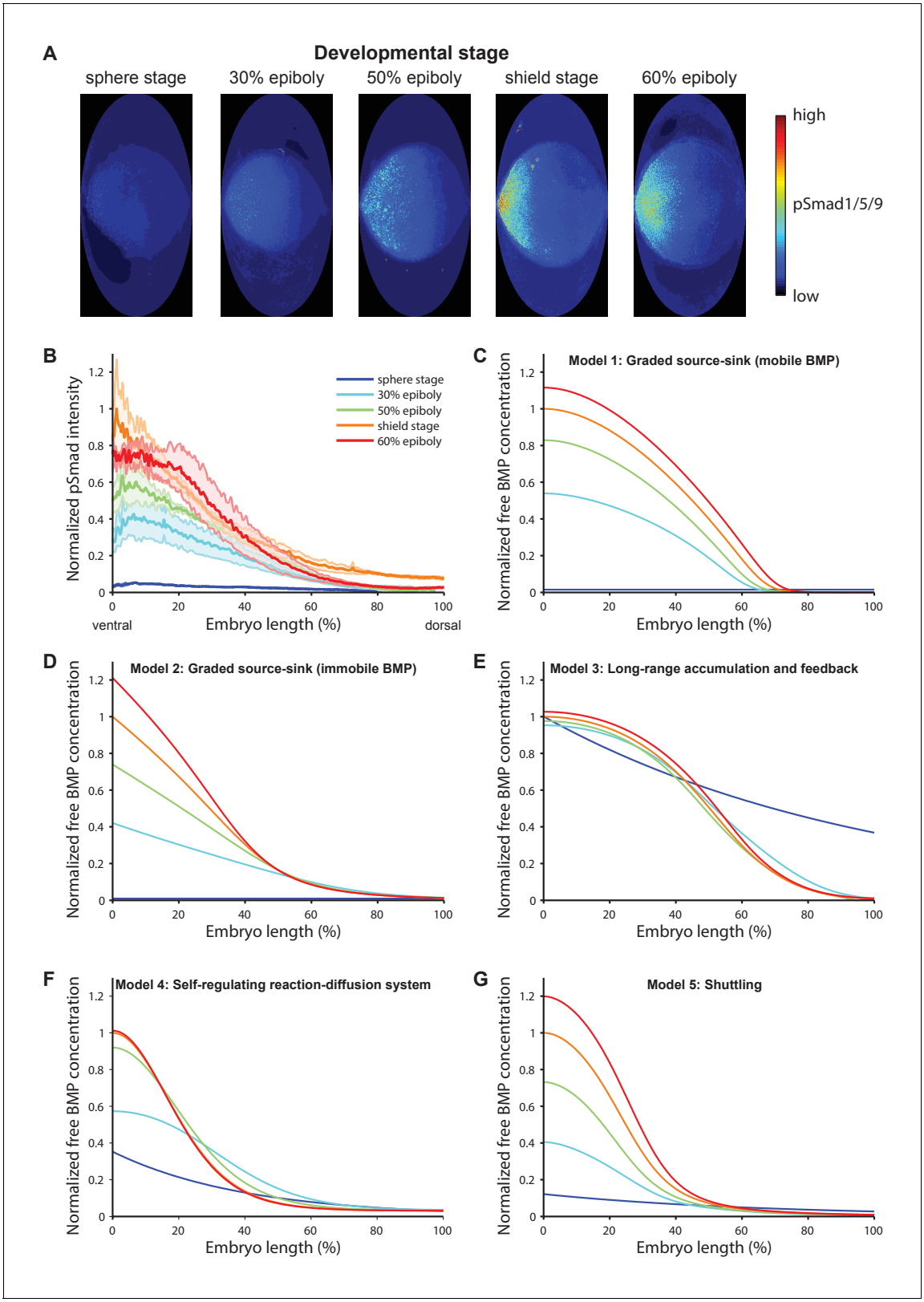

Figure 1. BMP signaling (pSmad1/5/9) gradient formation and simulations of five major dorsal-ventral patterning models over relevant zebrafish developmental stages (3 hr). (**A**) Two-dimensional Hammer-Aitoff projections (2D maps) of pSmad1/5/9-immunostained individual wild type zebrafish embryos at different developmental stages. Embryos were imaged using light sheet microscopy (see Materials and methods for details). (**B**) Quantification of ventral-to-dorsal average pSmad1/5/9 distributions in one-dimensional projections of 2D maps generated for embryos at different

Figure 1 continued on next page

Figure 1 continued

developmental stages (n = 3 for each stage) as in (**A**). Error bars denote standard error. (**C–G**) Gradient formation kinetics simulated for Models 1–5 at relevant zebrafish developmental stages.

DOI: https://doi.org/10.7554/eLife.25861.004

The following figure supplement is available for figure 1:

Figure supplement 1. Mathematical formulation of five major models of BMP/Chordin-mediated dorsal-ventral patterning.

DOI: https://doi.org/10.7554/eLife.25861.005

Results

Chordin does not actively establish peak ventral BMP signaling

BMP signaling induces phosphorylation and nuclear localization of the transcriptional effectors Smad1/5/9 (***Schier and Talbot, 2005***). To quantitatively measure BMP signaling activity during early dorsal-ventral patterning, we imaged pSmad1/5/9-immunostained zebrafish embryos fixed at different developmental stages using *in toto* light sheet microscopy, converted pSmad1/5/9 signaling activities into information-compressed two-dimensional maps (***Schmid et al., 2013***), and quantified pSmad1/5/9 intensities along the ventral-dorsal axis (***Figure 1A***, Materials and methods). Over the course of approximately 3 hr during early zebrafish development, BMP signaling rapidly shifts from a low-level near-uniform distribution to a gradient with peak levels on the ventral side (***Figure 1A+B***, ***Videos 1–5***) (***Tucker et al., 2008***), similar to changes in the distribution of *bmp2b* mRNA over time (***Ramel and Hill, 2013***; ***Zinski et al., 2017***). We simulated pSmad1/5/9 gradient formation kinetics predicted by each of the five models over a similar time period (***Figure 1C–G***). Our measurements are consistent with the gradient kinetics predicted by Models 1, 2, 4, and 5, whereas the dynamics predicted by Model 3 do not resemble the experimentally observed distributions.

All five major models of BMP/Chordin-mediated dorsal-ventral patterning qualitatively explain the formation of a ventral signaling peak, but they assign different roles to the inhibitor Chordin (***Figure 2A–E***, ***Table 1***, and ***Figure 1—figure supplement 1***). Models 1 and 2 assume that a flux of the inhibitor Chordin from the dorsal side restricts the range of BMP signaling activity throughout the embryo. They thus predict that in the absence of Chordin, BMP signaling should be expanded throughout the embryo with a small increase in the peak levels on the ventral side (***Figure 2A+B***). Model 3 adds an additional regulatory layer: Here, the abundance of Chordin is regulated by feedback interactions that modify its stability and affect ventral BMP signaling levels (***Figure 1—figure supplement 1***). Similar to Models 1 and 2, Model 3 also predicts that in the absence of Chordin, BMP signaling should be expanded throughout the embryo (***Figure 2C***).

In Model 4, two reaction-diffusion systems involving BMP/Sizzled and Chordin/ADMP are coupled. In a completely homogenous field of cells with no initial expression biases, this self-organizing system would give rise to both ventral and dorsal BMP peaks (***Francois et al., 2009***). To achieve a single ventral BMP peak, an initial dorsal Chordin or ventral BMP bias is required (see Materials and methods). Under these conditions, the initial advantage in BMP signaling on the ventral side is amplified by autoregulation of BMP production. Since Chordin inhibits the autoregulation of BMP production, the absence of Chordin leads to a more pronounced ventral BMP peak but has no effect in the rest of the embryo (***Figure 2D***). Model 4 thus predicts that in the absence of Chordin, pSmad1/5/9 levels would be increased on the ventral but not the dorsal side.

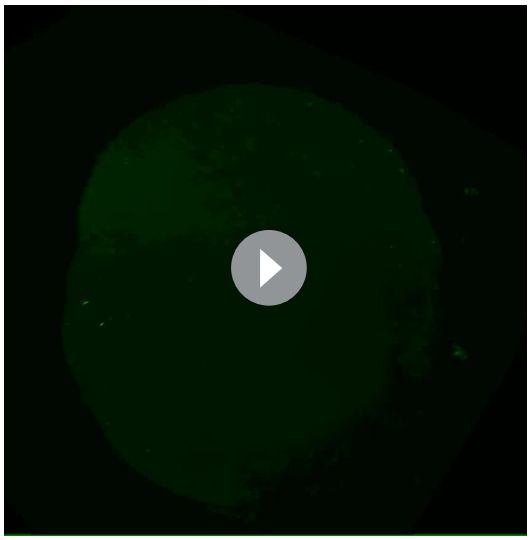

Video 1. 3D reconstruction of pSmad1/5/9 localization in a wild type sphere stage zebrafish embryo imaged by light sheet microscopy.

DOI: https://doi.org/10.7554/eLife.25861.006

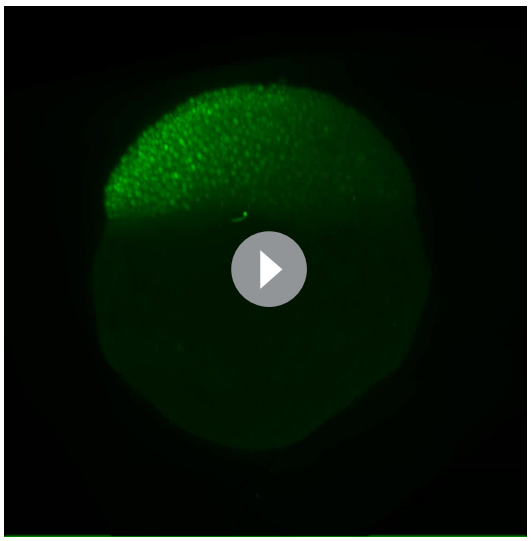

Video 2. 3D reconstruction of pSmad1/5/9 localization in a wild type 30% epiboly stage zebrafish embryo imaged by light sheet microscopy.
DOI: https://doi.org/10.7554/eLife.25861.007

Video 3. 3D reconstruction of pSmad1/5/9 localization in a wild type 50% epiboly stage zebrafish embryo imaged by light sheet microscopy.
DOI: https://doi.org/10.7554/eLife.25861.008

In contrast to Models 1–4, Model 5 assigns a more active role to Chordin in promoting the ventral BMP signaling peak. This model proposes that Chordin activity results in *increased* BMP signaling ventrally: Chordin increases ventral BMP levels by binding to and physically moving BMP protein towards the ventral side. This model therefore predicts that in embryos lacking Chordin, BMP signaling should be lower on the ventral side compared to wild type embryos (***Figure 2E***).

To experimentally test these predictions, we quantitatively measured BMP signaling activity in fixed *chordin*$^{-/-}$ zebrafish embryos (***Video 6***) and their wild type siblings using pSmad1/5/9 immunostaining and *in toto* light sheet microscopy. Strikingly, BMP signaling was increased in dorso-lateral domains in *chordin*$^{-/-}$ mutants compared to wild type embryos, but BMP signaling on the

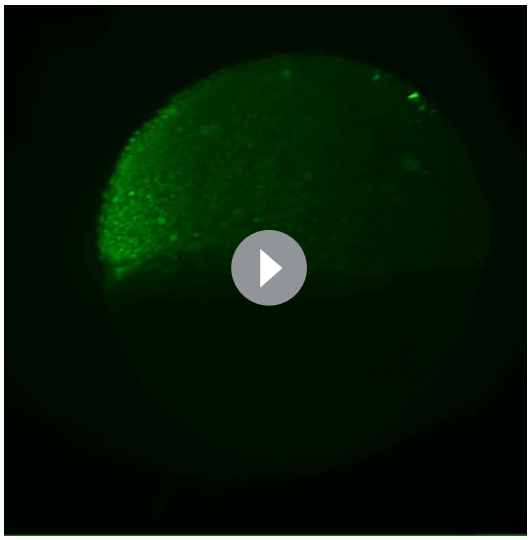

Video 4. 3D reconstruction of pSmad1/5/9 localization in a wild type shield stage zebrafish embryo imaged by light sheet microscopy.
DOI: https://doi.org/10.7554/eLife.25861.009

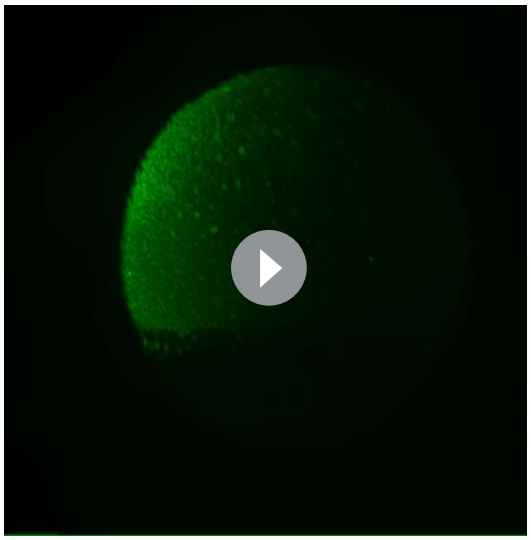

Video 5. 3D reconstruction of pSmad1/5/9 localization in a wild type 60% epiboly stage zebrafish embryo imaged by light sheet microscopy.
DOI: https://doi.org/10.7554/eLife.25861.010

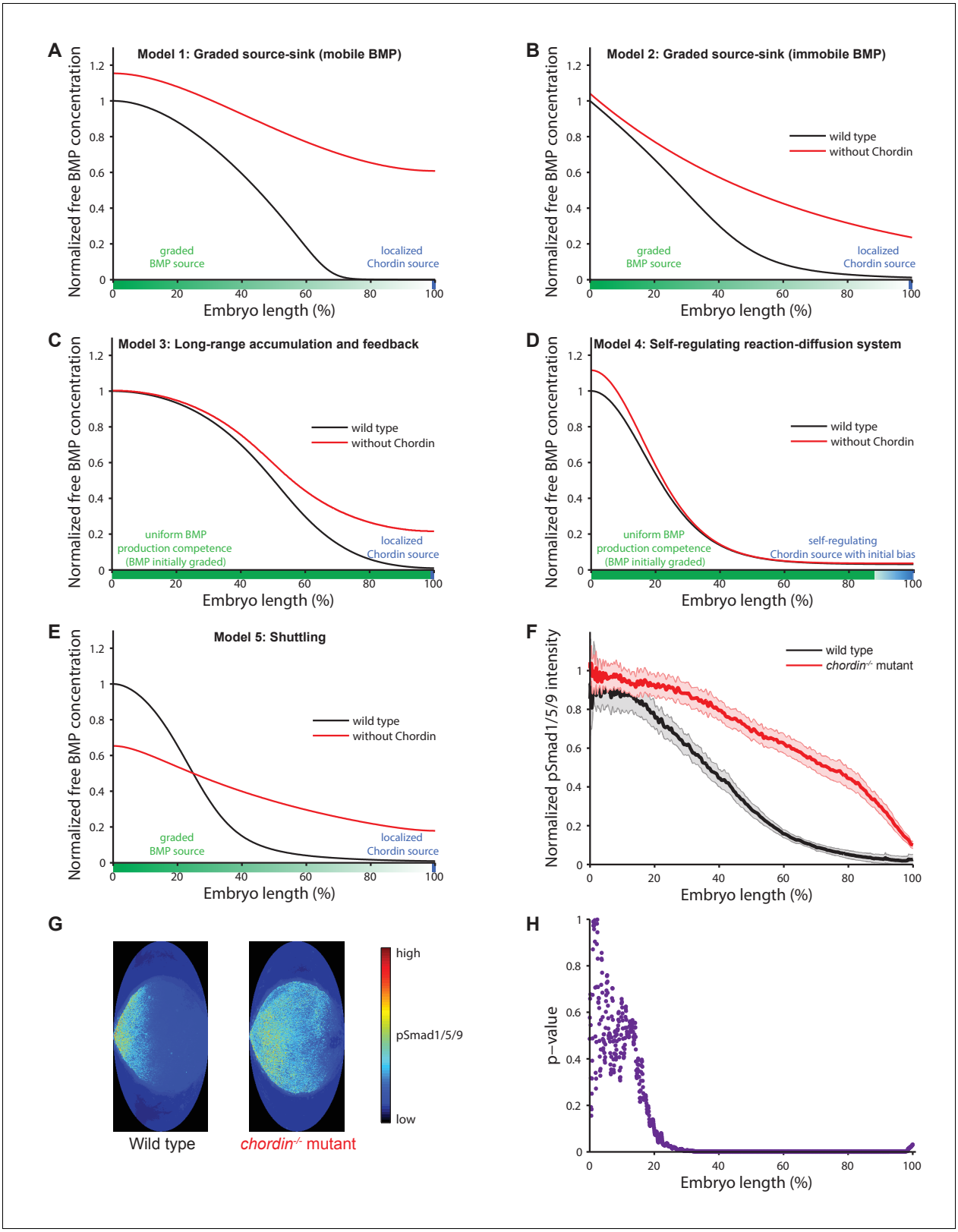

Figure 2. Theoretical predictions for the influence of the inhibitor Chordin on the BMP signaling gradient and experimental test. (**A–E**) Simulations of BMP distributions in five major models of dorsal-ventral patterning in the presence (black) or absence (red) of Chordin. The BMP and Chordin sources are indicated below each graph in green and blue, respectively. Note that the spatial production rates in Models 3 and 4 are modulated over time by feedback. (**F–G**) Quantification of average pSmad1/5/9 distributions in wild type (black) and *chordin*$^{-/-}$ (red) embryos using one-dimensional

Figure 2 continued on next page

Figure 2 continued

projections of 2D maps. Wild type n = 7, *chordin*$^{-/-}$ mutants n = 10. Error bars denote standard error. (**H**) p-values (unpaired two-tailed t-test assuming equal variance) calculated as a function of space between pSmad1/5/9 distributions in wild type and *chordin*$^{-/-}$ embryos shown in (**F**) indicate no significant difference of pSmad1/5/9 on the ventral side but a dramatic expansion into dorsal-lateral domains.

DOI: https://doi.org/10.7554/eLife.25861.011

ventral side was not significantly affected (***Figure 2F–H***), consistent with the predictions from Models 1–3 and observations in *Xenopus* and zebrafish embryos (***Plouhinec et al., 2013***; ***Zinski et al., 2017***), but not with the BMP signaling distributions predicted by Models 4 and 5 (***Table 1***).

BMP and Chordin fluorescent fusion proteins diffuse and rapidly form gradients *in vivo*

In order to understand the underlying basis of BMP/Chordin distribution and directly test the biophysical assumptions of the five dorsal-ventral patterning models, we developed fluorescent fusion proteins. We fused superfolder-GFP (sfGFP [***Pédelacq et al., 2006***]) and the photoconvertible protein Dendra2 (***Gurskaya et al., 2006***) to zebrafish Chordin and BMP2b, the major BMP ligand regulating zebrafish dorsal-ventral patterning (***Kishimoto et al., 1997***; ***Xu et al., 2014***). Basing our design on previously established fusions with small peptide tags (***Cui et al., 1998***; ***Degnin et al., 2004***; ***Sopory et al., 2006***), we inserted fluorescent proteins to label the mature signaling domains, and obtained fusion proteins that are processed similarly and have similar biological activity as untagged versions or constructs fused to small FLAG tags (***Figure 3A–E***, ***Figure 3—figure supplement 1***). Indeed, *BMP2b* mutants (*swr*$^{-/-}$, which are normally severely dorsalized [***Kishimoto et al., 1997***]) can be rescued by injection of mRNA encoding BMP2b-Dendra2 or BMP2b-sfGFP at levels equivalent to untagged BMP2b (***Figure 3C***). In these experiments, the injected mRNA should be uniformly distributed, highlighting the important role of Chordin or other antagonists in shaping the graded BMP signaling distribution.

To measure the kinetics of BMP and Chordin protein gradient formation, we expressed BMP2b-sfGFP and Chordin-sfGFP from local sources in wild type zebrafish embryos (***Müller et al., 2012***) and imaged the distribution profiles over time using light sheet microscopy (***Figure 3F–I***). Importantly, in previous experiments it has been demonstrated that BMP2b clones generated in a similar manner can recapitulate BMP signaling comparable to that observed along the dorsal-ventral axis (***Xu et al., 2014***). Strikingly, both BMP2b-sfGFP and Chordin-sfGFP are secreted and diffuse in the extracellular space (***Figure 3F+G***, ***Videos 7+8***), in contrast to the proposal of Model 2 that only Chordin – but not BMP – diffuses (***Ramel and Hill, 2013***) (***Table 1***) and the absence of long-range BMP4 signaling in *Xenopus* (***Jones et al., 1996***). Both BMP2b-sfGFP and Chordin-sfGFP rapidly establish concentration gradients over the course of one hour (***Figure 3H+I***), consistent with the rapid patterning of the dorsal-ventral axis during zebrafish development.

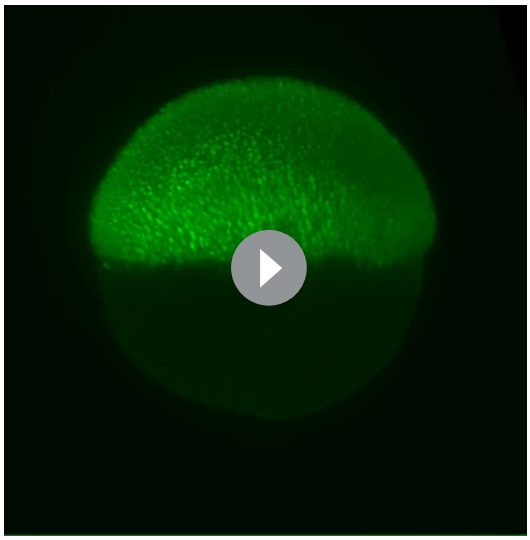

Video 6. 3D reconstruction of pSmad1/5/9 localization in a *chordin*$^{-/-}$ shield stage zebrafish embryo imaged by light sheet microscopy.

DOI: https://doi.org/10.7554/eLife.25861.012

BMP and Chordin fluorescent fusion proteins have similar stabilities *in vivo*

The gradient formed by Chordin-sfGFP has a moderately longer range than the one formed by BMP2b-sfGFP. For example, 60 min post-transplantation the BMP2b-sfGFP signal drops to 50% of the maximal concentration at a distance of 30–40 µm, whereas the gradient formed by Chordin-sfGFP reaches 50% of its maximal concentration at a distance of 50–60 µm from the source boundary at this time point (***Figure 3H+I***). This

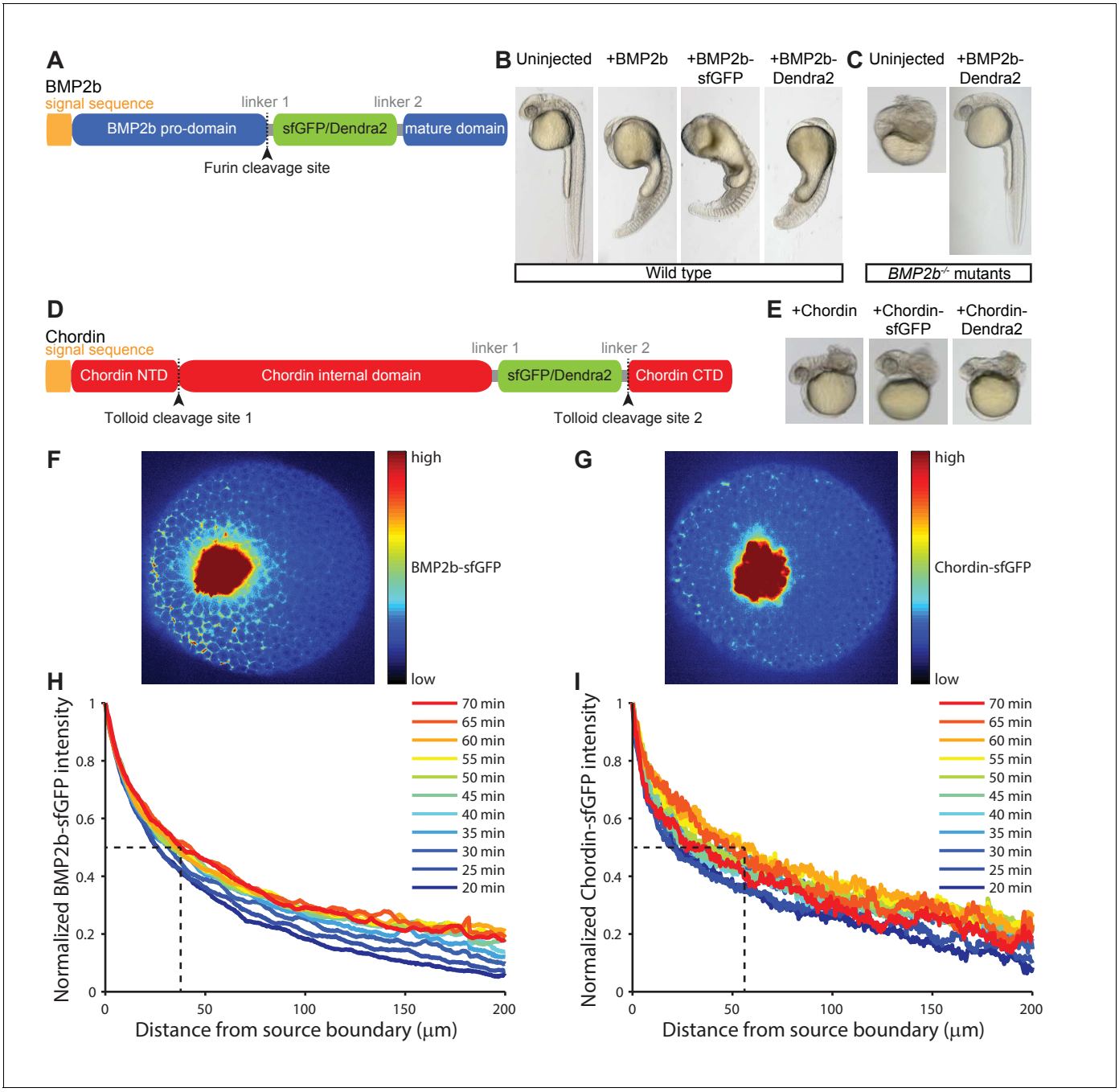

Figure 3. Gradient formation kinetics of fluorescently tagged BMP and Chordin. (**A**) Schematic of BMP2b-sfGFP and -Dendra2 fusion constructs. (**B**) Fluorescent BMP2b fusion constructs can induce ventralization, a BMP-overexpression phenotype (***Kishimoto et al., 1997***). mRNA amounts equimolar to 2 pg of *BMP2b* mRNA were injected at the one-cell stage, and images were taken 30 hr post-fertilization (hpf). (**C**) Rescue of a *BMP2b* mutant (*swr*$^{-/-}$) with BMP2b-Dendra2. 2.74 pg of BMP2b-Dendra2-encoding mRNA were injected at the one-cell stage, and images were taken at 30 hpf. In a separate experiment with 1 pg of BMP2b-sfGFP-encoding mRNA, 20% (9/44) of all injected *swr*$^{-/-}$ mutants were rescued, 16% (7/44) were ventralized, and 64% (28/44) were dorsalized. (**D**) Schematic of Chordin-sfGFP and -Dendra2 fusion constructs. (**E**) Fluorescent Chordin constructs can induce dorsalization, a *Chordin*-overexpression phenotype. mRNA amounts equimolar to 30 pg of *Chordin* mRNA were injected into wild type embryos at the one-cell stage, and images were taken at 30 hpf. F + G) Light sheet microscopy images of BMP- and Chordin-sfGFP gradients forming from a local source in live zebrafish embryos. Approximately 50–75 cells expressing *BMP2b-sfGFP* (**F**) or *Chordin-sfGFP* (**G**) were transplanted into host embryos at sphere stage (see Materials and methods for details). The images show gradient formation in single optical slices approximately 20 min after transplantation. H + I) Quantification of BMP2b-sfGFP (**H**) and Chordin-sfGFP (**I**) gradient formation kinetics from a local source (BMP2b-sfGFP: n = 8; Chordin-sfGFP: n = 5). Dashed lines indicate the distance at which the protein distributions drop to 50% of their maximal concentration 60 min post-transplantation.

Figure 3 continued on next page

Figure 3 continued

DOI: https://doi.org/10.7554/eLife.25861.013

The following figure supplements are available for figure 3:

Figure supplement 1. Detailed characterization of fluorescently tagged BMP2b and Chordin.

DOI: https://doi.org/10.7554/eLife.25861.014

Figure supplement 2. Modeling of BMP and Chordin gradient formation kinetics and comparison to measured gradients.

DOI: https://doi.org/10.7554/eLife.25861.015

suggests that stability or diffusivity might differ between these proteins (***Müller and Schier, 2011***; ***Müller et al., 2013***). Importantly, Models 3 and 5 assume that BMP is more stable than Chordin, whereas the other models assume either similar or unconstrained stabilities (***Table 1***).

To distinguish between these possibilities, we first determined protein stability in living zebrafish embryos using a Fluorescence Decrease After Photoconversion (FDAP) assay (***Müller et al., 2012***; ***Bläßle and Müller, 2015***; ***Rogers et al., 2015***). We expressed BMP2b and Chordin fused to the green-to-red photoconvertible protein Dendra2 uniformly in zebrafish embryos, used brief UV exposure to convert the signal from green to red to generate a pulsed protein pool, and monitored the decrease in extracellular red fluorescence over time (***Figure 4A+B***). For BMP2b-Dendra2, we found a clearance rate constant of $k_1 = (8.9 \pm 0.1) \times 10^{-5}$/s (half-life 130 min, ***Figure 4A***). For Chordin-Dendra2, we measured a similar clearance rate constant of $k_1 = (9.6 \pm 0.3) \times 10^{-5}$/s (half-life 120 min, ***Figure 4B***). The similar clearance rate constants suggest that differential protein stabilities cannot account for the different protein distributions of BMP2b and Chordin. Importantly, these results are inconsistent with the differential protein stabilities predicted by Models 3 and 5 (***Table 1***).

Diffusivity of BMP and Chordin fluorescent fusion proteins *in vivo*

Our finding that BMP2b- and Chordin-Dendra2 fusions have similar stabilities (***Figure 4A+B***) suggests that differences in diffusivity could account for the slight differences in gradient formation kinetics. Indeed, when we fitted a gradient formation model based on local production, uniform diffusion, and clearance constrained with our measured protein half-lives in a realistic three-dimensional zebrafish embryo-like geometry (***Müller et al., 2012***) to the measured protein distributions, we obtained the best agreement between model and data with lower diffusivity of BMP2b (4 μm^2/s) compared to Chordin (6 μm^2/s) (***Figure 3—figure supplement 2A+B***).

Importantly, the five models assume distinct BMP and Chordin diffusion properties (***Table 1***, ***Figure 1—figure supplement 1***), from no BMP diffusion (Model 2) to substantially higher Chordin

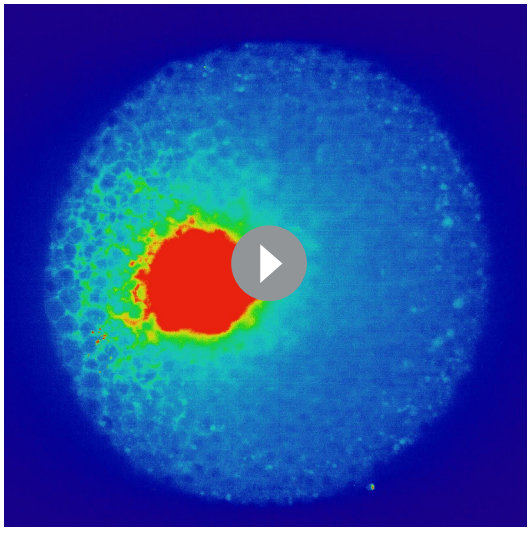

Video 7. Gradient formation in a dome stage wild type embryo with a BMP2b-sfGFP clone.

DOI: https://doi.org/10.7554/eLife.25861.016

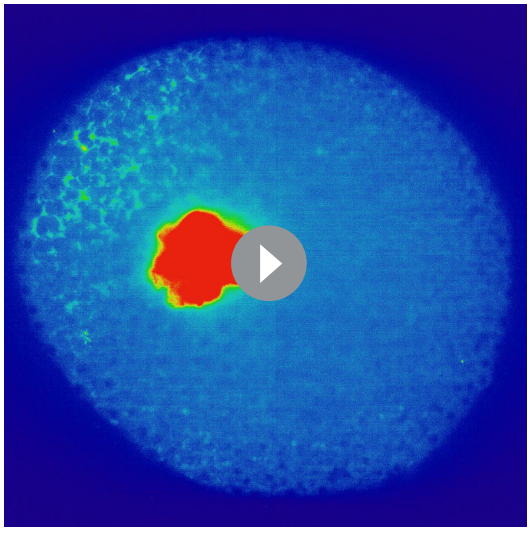

Video 8. Gradient formation in a dome stage wild type embryo with a Chordin-sfGFP clone.

DOI: https://doi.org/10.7554/eLife.25861.017

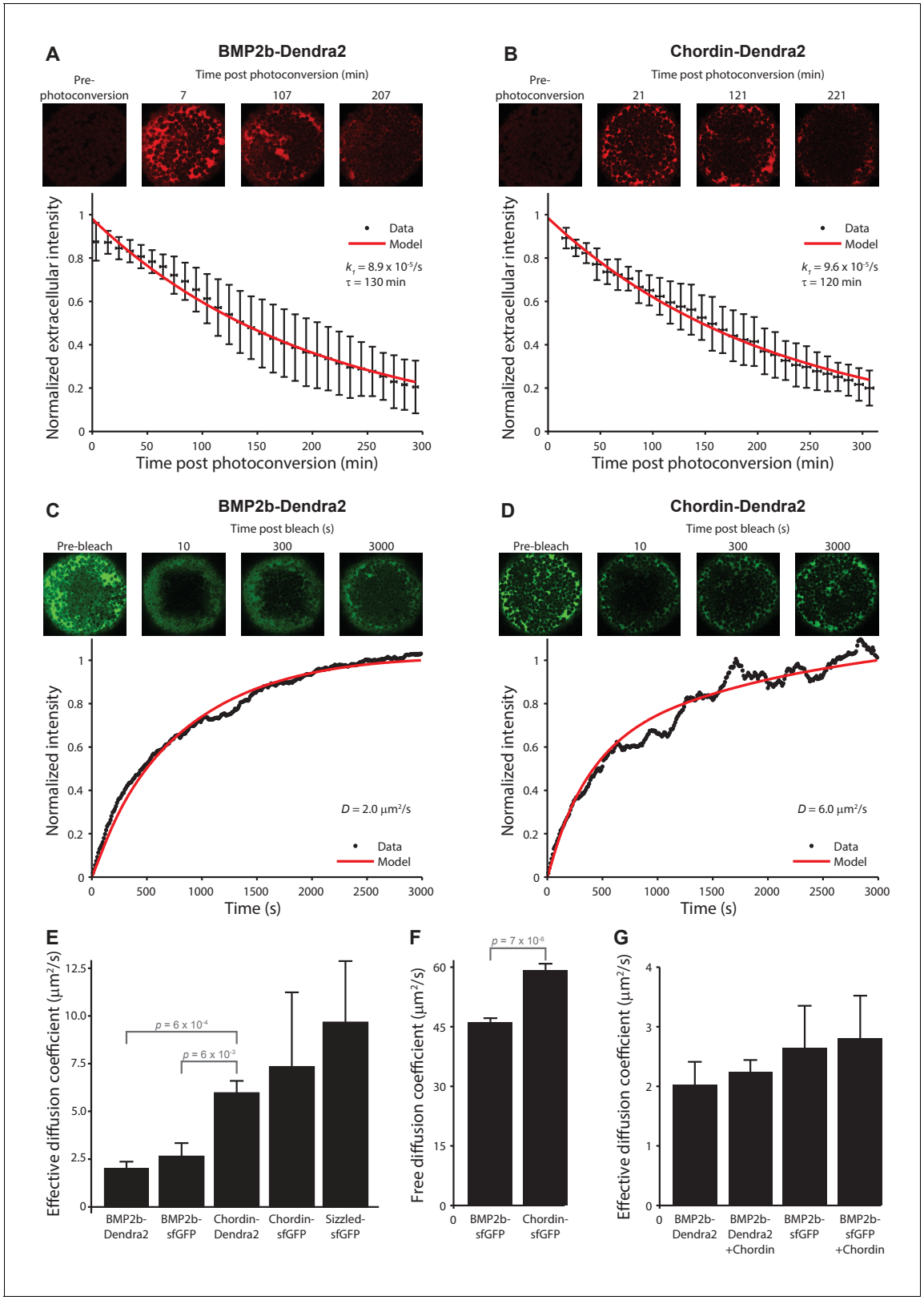

Figure 4. Biophysical measurements of BMP and Chordin protein stability and diffusivity. A + B) FDAP protein stability measurements for BMP2b-Dendra2 (**A**) and Chordin-Dendra2 (**B**). Error bars denote standard deviation. BMP2b-Dendra2: n = 22; Chordin-Dendra2: n = 6. C + D) FRAP effective protein diffusivity measurements for BMP2b-Dendra2 (**C**) and Chordin-Dendra2 (**D**). Data and fits from single experiments are shown. (**E**) Bar chart of the average effective diffusion coefficients from FRAP experiments. Error bars denote standard error. BMP2b-Dendra2: n = 6; BMP2b-sfGFP: n = 8;

Figure 4 continued on next page

Figure 4 continued

Chordin-Dendra2: n = 8; Chordin-sfGFP: n = 6; Sizzled-sfGFP: n = 12. (**F**) Free diffusion coefficients of BMP2b-sfGFP and Chordin-sfGFP measured by Fluorescence Correlation Spectroscopy (FCS) in a diffraction-limited spot within the zebrafish embryonic extracellular space far away from cell membranes (see Materials and methods for details). Error bars denote standard error. BMP2b-sfGFP: n = 17 measurements from 4 embryos; Chordin-sfGFP: n = 19 measurements from 5 embryos. (**G**) Negligible influence of Chordin on BMP2b effective diffusion. Untagged Chordin was co-expressed with BMP2b-Dendra2 (n = 8) or BMP2b-sfGFP (n = 9) in zebrafish embryos subjected to FRAP measurements at blastula stages. The data shown for BMP2b-Dendra2 and BMP2b-sfGFP FRAP experiments without co-expressed *Chordin* is identical to the data shown in (**E**). p-values (unpaired two-tailed t-test assuming equal variance) are shown for statistically significant ($p<0.05$) data sets.

DOI: https://doi.org/10.7554/eLife.25861.018

The following figure supplement is available for figure 4:

Figure supplement 1. Characterization of Sizzled diffusion and its role in gradient formation.

DOI: https://doi.org/10.7554/eLife.25861.019

mobility compared to BMP (Model 5). To directly test these predictions, we determined the effective diffusivities of fluorescently tagged BMP2b and Chordin moving through developing zebrafish embryos. We used a Fluorescence Recovery After Photobleaching (FRAP) assay (***Müller et al., 2012***) that measures the dynamics of re-appearance of fluorescence in a bleached region in embryos uniformly expressing fluorescent fusion proteins (***Figure 4C–E***). We found effective diffusion coefficients of 2–3 $\mu m^2/s$ for BMPs (BMP2b-Dendra2: 2.0 ± 0.4 $\mu m^2/s$; BMP2b-sfGFP: 2.6 ± 0.7 $\mu m^2/s$ (similar to [***Zinski et al., 2017***]) and of 6–7 $\mu m^2/s$ for Chordin (Chordin-Dendra2: 6.0 ± 0.7 $\mu m^2/s$; Chordin-sfGFP: 7.3 ± 3.9 $\mu m^2/s$), indicating that slight differences in diffusivities could underlie the differences in protein distributions. This idea is further supported by the agreement between gradients simulated with the measured diffusivities and clearance rate constants and our experimentally determined protein gradients (***Figure 3—figure supplement 2E–H***). The measured diffusion coefficients are most consistent with Models 1 and 4, which assume either similarly low diffusivities (Model 4) or that BMP has a moderately lower diffusion coefficient than Chordin (Model 1, ***Table 1***). As observed in the BMP2b-sfGFP gradient formation experiment (***Figure 3F–I***), our FRAP data demonstrate that BMP2b-sfGFP is mobile *in vivo*, inconsistent with Model 2.

Strikingly, local diffusion measurements in very small extracellular volumes far away from cell surfaces using Fluorescence Correlation Spectroscopy (FCS) assays showed that BMP2b-sfGFP (free diffusion coefficient: D_f = 46 ± 1 $\mu m^2/s$) and Chordin-sfGFP (free diffusion coefficient: D_f = 59 ± 2 $\mu m^2/$

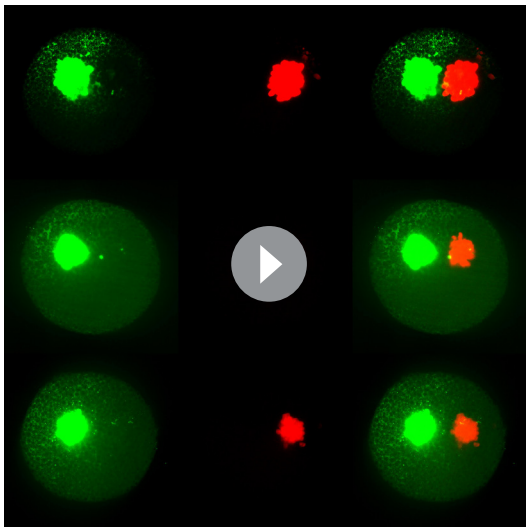

Video 9. Gradient formation in three representative dome stage wild type embryos with BMP2b-sfGFP clones (green) next to clones labeled with Alexa 546-coupled dextran (red).

DOI: https://doi.org/10.7554/eLife.25861.021

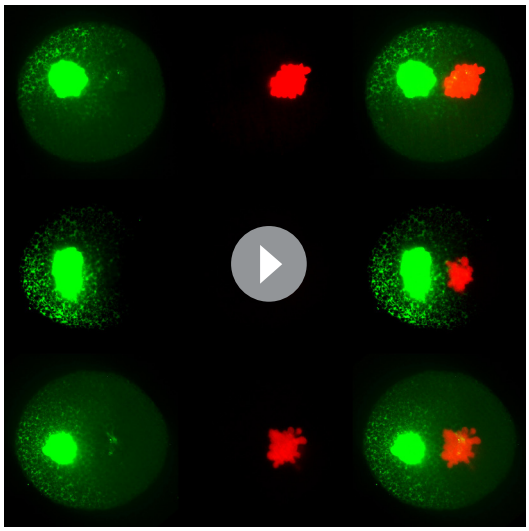

Video 10. Gradient formation in three representative dome stage wild type embryos with BMP2b-sfGFP clones (green) next to *chordin*-expressing clones labeled with Alexa 546-coupled dextran (red).

DOI: https://doi.org/10.7554/eLife.25861.022

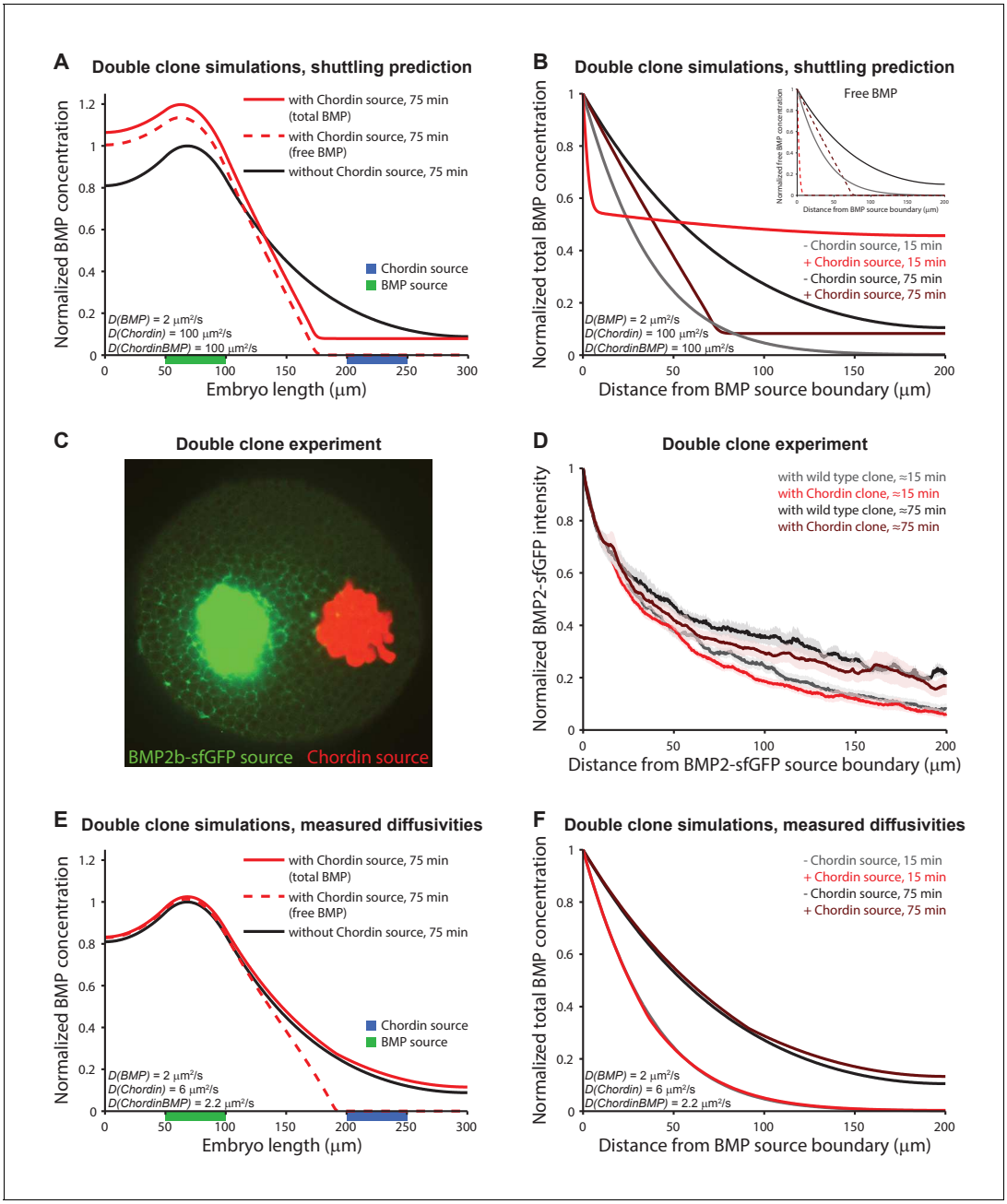

Figure 5. Testing shuttling of BMP2b predicted by Model 5. (**A**) One-dimensional model of two clones expressing BMP (green) or Chordin (blue) with D_{BMP} = 2 μm^2/s, D_{Chd} = 100 μm^2/s, and D_{ChdBMP} = 100 μm^2/s. BMP levels increase over time due to constant production. In the presence of Chordin, the BMP gradient is deflected away from the Chordin source indicative of shuttling (compare black and red lines). Solid lines show total BMP levels (i.e. BMP + ChdBMP in the presence of Chordin), and dashed line shows free BMP levels. (**B**) BMP gradients to the right of the BMP-expressing clone re-normalized to the BMP concentration at the source boundary to demonstrate that the range of BMP is decreased between the two clones in the presence of Chordin. The main panel shows total BMP levels (i.e., BMP + ChdBMP in the presence of Chordin), and the inset shows free BMP levels (dashed lines). (**C**) Experimental test of the predictions in (**A**) and (**B**). Clones of cells expressing BMP2b-sfGFP (green) were generated by transplanting approximately 50–75 cells from a donor embryo into wild type hosts at sphere stage (see Materials and methods for details). Another clone of cells (red) was transplanted next to the BMP2b-sfGFP-expressing clone shortly after. The red clone is marked by the presence of fluorescent Alexa 546-coupled dextran. Cells from red-labeled clones either contained only Alexa 546-coupled dextran (***Video 9***) or Alexa-546-coupled dextran and ectopic *chordin* mRNA (***Video 10***). 15–20 min after transplantation of the clones, embryos were imaged using light sheet microscopy. The image shows gradient formation in a single optical slice approximately 20 min after transplantation. (**D**) Quantification of average BMP2b-sfGFP gradients at ~15 min or ~75 min after transplantation in embryos generated as in (**C**) with (red/brown) or without (black/gray) ectopic Chordin sources. Error bars denote standard error. n = 8 for each condition. (**E**) One-dimensional simulation of two clones expressing BMP (green) or Chordin (blue) with the experimentally measured diffusion coefficients D_{BMP} = 2 μm^2/s, D_{Chd} = 6 μm^2/s, and D_{ChdBMP} = 2.2 μm^2/s. BMP levels increase over time due to constant production.

Figure 5 continued on next page

Figure 5 continued

Solid lines show total BMP levels (i.e. BMP + ChdBMP in the presence of Chordin), and the dashed line shows free BMP levels. Only the distribution of free BMP is affected as a consequence of Chordin binding, and the gradient of total BMP is not deflected away from the Chordin source (compare solid black and red lines). (**F**) Gradients of total BMP levels to the right of the BMP expressing clone simulated with the experimentally measured diffusion coefficients (D_{BMP} = 2 μm^2/s, D_{Chd} = 6 μm^2/s, and D_{ChdBMP} = 2.2 μm^2/s) and renormalized to the concentration at the boundary show that the range of BMP is not decreased between the two clones in the presence of Chordin.

DOI: https://doi.org/10.7554/eLife.25861.020

s) are highly mobile over short spatial and temporal scales (***Figure 4F***), whereas their diffusivities are reduced at the global scale when they move across a field of cells (***Figure 4E***). We hypothesize that the difference between effective diffusivities (measured by FRAP) and local diffusivities (measured by FCS) is due to binding to immobile extracellular molecules, which could serve as diffusion regulators that hinder the mobility of BMP2b and Chordin, similar to what has been proposed for other developmental signals such as Nodal and FGF (***Müller et al., 2012***; ***Müller et al., 2013***).

Sizzled, BMP, and Chordin diffusivities are within the same order of magnitude

Models 3 and 4 assign important roles to the secreted proteins ADMP and Sizzled in regulating BMP signaling and distribution. Model 3 postulates diffusivities of ADMP and Sizzled equivalent to BMP and Chordin, whereas Model 4 requires approximately 25-fold higher diffusivities of ADMP and Sizzled compared to BMP and Chordin (***Table 1***). To measure the diffusivities of ADMP and Sizzled and test these assumptions, we developed fluorescent ADMP and Sizzled fusion proteins (see Materials and methods). Whereas Sizzled fusion proteins had activity comparable to untagged Sizzled (***Figure 4—figure supplement 1A–C***), ADMP fusions with sfGFP or FLAG tags inserted 2, 5, or 11 amino acids after the Furin cleavage site were much less active than untagged ADMP (data not shown), and could therefore not be used for diffusion measurements. Using FRAP, we measured an effective diffusion coefficient of 9.7 ± 3.2 μm^2/s for Sizzled-sfGFP (***Figure 4E***, ***Figure 4—figure supplement 1D***). This measurement is consistent with Model 3, but not Model 4, the latter of which requires much higher Sizzled mobility (***Table 1***).

When parameterized with these measured diffusion coefficients and over a ~100-fold range of ADMP diffusion coefficients, Model 3 can form ventral-dorsal gradients over relevant time scales (***Figure 4—figure supplement 1F–J***), but the kinetics of gradient formation do not reflect the measurements of pSmad1/5/9 distribution profiles in ***Figure 1A+B***. Moreover, the relatively minor difference between BMP/Chordin and Sizzled diffusivity is not compatible with the 25-fold differential required for Model 4 (***Figure 4—figure supplement 1K–P***).

Chordin does not regulate BMP protein diffusivity or distribution

Model 5 (Shuttling) postulates that highly diffusive Chordin enhances the mobility of poorly diffusive BMPs (***Ben-Zvi et al., 2008***). In this model, Chordin is secreted dorsally, binds to relatively immobile BMP, and creates a highly mobile BMP/Chordin complex. This complex then diffuses until Chordin is cleaved by a protease (Xlr), rendering BMP immobile again (***Figure 1—figure supplement 1***). To investigate whether Chordin is not only an inhibitor of BMP, but also enhances BMP diffusivity, we increased Chordin levels and measured the effective diffusivity of fluorescent BMP2b. In embryos overexpressing Chordin, we did not observe a significant change in the effective diffusivity of fluorescently tagged BMP2b compared to embryos that did not overexpress Chordin (BMP2b-Dendra2 + Chordin: 2.2 ± 0.2 μm^2/s; BMP2b-sfGFP + Chordin: 2.8 ± 0.7 μm^2/s; ***Figure 4G***). The ability of Chordin to enhance the diffusivity of BMP, a major tenet of Model 5, is therefore not supported by FRAP data.

Model 5 also predicts that Chordin alters the distribution of BMP protein. Over time, the shuttling of BMP by Chordin causes BMP to accumulate away from the Chordin source, resulting in an opposing peak of BMP. Our observation that Chordin does not affect the diffusivity of BMP challenges this view (***Figure 4G***). However, to directly test whether a Chordin source can alter BMP distribution (***Figure 5A+B***), we juxtaposed clones of BMP2b-sfGFP-producing cells with clones of cells secreting untagged Chordin and imaged the formation of the BMP2b-sfGFP gradient over time using light sheet fluorescence microscopy (***Figure 5C+D***, ***Videos 9–10***). Model 5 predicts a steeper BMP2b-

sfGFP gradient in the presence of an adjacent Chordin-producing clone compared to a wild type clone (***Figure 5A+B***). Although BMP2b-sfGFP gradients tend to be slightly steeper in the presence of a neighboring Chordin-expressing clone compared to a non-Chordin-expressing clone (***Figure 5D***), this minor change is unlikely to account for the formation of a ventral peak in BMP signaling during the short time (hours) required to complete dorsal-ventral patterning (***Figure 1A+B***). We also failed to observe significant redistribution of BMP in simulations of adjacent BMP and Chordin clones using our measured diffusion coefficients and half-lives (***Figure 5E+F***). This suggests that shuttling of BMP2b by Chordin is not relevant for the early aspects of dorsal-ventral patterning in zebrafish embryos.

Discussion

The BMP signaling gradient patterns the dorsal-ventral axis during animal development. Five major models can explain how a ventral peak of BMP signaling forms, but the biophysical assumptions underlying these models differ widely (***Table 1***). After experimentally examining these assumptions, our findings lead to four main conclusions. First, Chordin does not play an active role in generating BMP signaling peaks, but only globally inhibits BMP (***Figure 2***). This is consistent with graded source-sink-type models (e.g. Models 1 and 2) and Model 3, but inconsistent with Models 4 and 5 (***Table 1***). Interestingly, BMP signaling in the absence of Chordin is not raised on the extreme dorsal side, indicating that other extracellular inhibitors such as Follistatin or Noggin (***Umulis et al., 2009***) or inhibitors of *bmp* expression (***Koos and Ho, 1999***; ***Leung et al., 2003***; ***Ramel and Hill, 2013***) that were not included in the tested models might further restrict BMP signaling in these regions. Second, BMP2b and Chordin both diffuse in the extracellular space (***Figure 3F–I***), challenging models involving immobile BMP (Model 2). Third, fluorescently tagged BMP2b and Chordin have similarly high local diffusivities (***Figure 4F***), but on a global scale they move much more slowly through the embryo (***Figure 4E***). These findings rule out Models 2, 3, and 5, but are consistent with Models 1 and 4. Fourth, Chordin does not significantly affect BMP2b diffusion or protein distribution in zebrafish embryos (***Figure 4G***, ***Figure 5***), undermining shuttling models in this developmental context. Instead, our data are most consistent with Model 1, the graded source-sink model of BMP/Chordin-mediated dorsal-ventral patterning during early zebrafish development. Our conclusions are also consistent with a recent complementary study (***Zinski et al., 2017***).

Notably, shuttling models (e.g. Model 5) have gained prominence in many developmental contexts including scale-invariant patterning (***Ben-Zvi et al., 2008***; ***Barkai and Ben-Zvi, 2009***; ***Francois et al., 2009***; ***Plouhinec and De Robertis, 2009***; ***Ben-Zvi and Barkai, 2010***; ***Ben-Zvi et al., 2011a***; ***Haskel-Ittah et al., 2012***), but the fundamental tenet, that is, whether putative shuttles such as Chordin change the diffusivity and distribution of signals such as BMP, has not been directly examined. Alternative models that do not invoke Chordin-dependent facilitated BMP diffusion (Model 4) (***Francois et al., 2009***) or that postulate differential protein stability (Model 3) (***Inomata et al., 2013***) can also explain scale-invariant patterning. Our data do not provide strong evidence for shuttling of BMP2b at time scales relevant for dorsal-ventral patterning during early zebrafish embryogenesis: We failed to observe a significant modulation of BMP2b-sfGFP or BMP2b-Dendra2 diffusivity or distribution by Chordin (***Figure 4G***, ***Figure 5***). It is, however, possible that other BMPs (e.g. BMP4, BMP7, ADMP) are shuttled by interactions with Chordin and its protease Tolloid/Xlr. Indeed, *tolloid* mutants display a mild patterning defect of the ventral tail fin (***Connors et al., 1999***) that might reflect a requirement for the ventral accumulation of a weakly active, dorsally expressed BMP ligand such as ADMP (***Dickmeis et al., 2001***; ***Lele et al., 2001***).

The graded source-sink model (Model 1) that is best supported by our data describes a system in which the graded, ventrally biased distribution of *bmp* mRNA and the dorsally localized *chd* mRNA distribution produce opposing sources of extracellular, diffusing BMP and Chordin protein, which together generate the BMP signaling gradient required for proper dorsal-ventral patterning. Notably, this model fails to take other known dorsal-ventral regulators into account (e.g., ADMP, Sizzled, Follistatin, Noggin). Furthermore, approximately one third of *bmp2b* and *chordin* mutant embryos can be rescued by apparently uniform *bmp* and *chordin* expression, respectively (***Kishimoto et al., 1997***; ***Fisher and Halpern, 1999***) (***Figure 3C***), arguing against a strong requirement for concurrent opposing BMP and Chordin sources as long as one component of the system is biased (i.e. ventrally biased *bmp2b* expression with uniform Chordin, or dorsally biased *chordin* expression with uniform

BMP). Thus, further adjustments to the basic Model 1 will be required to fully describe dorsal-ventral patterning.

Although our results support a role for BMP diffusion in dorsal-ventral patterning, the necessity of signal diffusion for developmental patterning has recently been challenged by several studies (**Brankatschk and Dickson, 2006**; **Roy and Kornberg, 2011**; **Alexandre et al., 2014**; **Dominici et al., 2017**; **Varadarajan et al., 2017**). It will be interesting to determine whether BMP diffusion is indeed required for proper patterning using emerging nanobody-mediated diffusion perturbations (**Harmansa et al., 2015**) or optogenetics-based cell-autonomous modulation of signaling range (**Sako et al., 2016**).

Materials and methods

Immunostainings

To visualize pSmad1/5/9, wild type TE embryos were dechorionated at the one-cell stage using 1 mg/ml of Pronase (Roche, Cat. No. 11 459 643 001). Dechorionated embryos were incubated at 28°C and fixed at different developmental stages in 4% formaldehyde (Roth) in PBS overnight at 4°C on a shaker. Embryos were then stored in 100% methanol at −20°C for at least 2 hr. All subsequent steps were carried out at room temperature. Embryos were re-hydrated with 70%, 50%, and 30% methanol in PBS for 10 min each. The embryos were then washed eight times with PBST (0.1% Tween) for 15 min and blocked twice with blocking solution (10% fetal bovine serum and 1% DMSO in PBST) for 1 hr, and incubated with 1:100 anti-pSmad1/5/9 antibody (Cell Signaling Technology, Cat. No. 9511) for 4 hr. Embryos were washed with blocking solution for 15 min, washed seven times with PBST, blocked with blocking solution for 1 hr, incubated with 1:500 Alexa 488-coupled goat anti-rabbit secondary antibody (Life Technologies, Cat. No. A11008) for 4 hr, and washed similarly to the procedure after primary antibody application. Embryos were then counterstained with DAPI solution (0.2 µg/ml in PBST) for 1 hr and washed with PBST. Immunostainings were performed using an In situ Pro hybridization robot (Abimed/Intavis).

To analyze pSmad1/5/9 distributions in the absence of Chordin, embryos from one pair of *chordin*^{tt250} (**Hammerschmidt et al., 1996**) heterozygous parents were collected, fixed, immunostained with anti-pSmad1/5/9 antibody (Cell Signaling Technology, Cat. No. 13820S) as above, and imaged simultaneously to minimize differences between samples. Embryos were treated as described above, except that progeny from *chordin*$^{+/-}$ incrosses were first permeabilized with ice-cold acetone at −20°C for 7 min before the re-hydration step. After imaging and DNA extraction (**Meeker et al., 2007**), progeny from the *chordin*^{tt250} heterozygote incross were identified as wild type, heterozygous, or homozygous mutant embryos by PCR amplification using the forward primer 5'-TTCG TTTGGAGGACAACTCG-3' and the reverse primer 5'-AACTCAGCAGCAGAAGTCAATTC-3' with an initial denaturation step of 94°C for 3 min; 39 cycles of 94°C for 30 s, 55°C for 40 s, and 72°C for 30 s; and a final extension at 72°C for 5 min with subsequent digestion with MspI (New England Biolabs, Cat. No. R0106) for 2 hr. The genotyping assay for the *chordin*^{tt250} line was designed by the Zebrafish International Resource Center (ZIRC) staff and downloaded from the ZIRC website at http://zebrafish.org.

Generation of fluorescent BMP2b fusions

All constructs were generated by PCR-based methods (**Horton et al., 1990**), contain the consensus Kozak sequence *gccacc* 5' of the start codon, and were inserted into the EcoRI and XhoI sites of the pCS2(+) vector. To generate BMP2b-sfGFP and BMP2b-Dendra2, sequences encoding sfGFP or Dendra2 flanked by LGDPPVAT linkers were inserted two amino acids downstream of the BMP2b Furin cleavage site. Sequences encoding the FLAG tag DYKDDDDK were inserted between the first linker and sfGFP or Dendra2 to generate BMP2b-sfGFP-FLAG and BMP2b-Dendra2-FLAG. To generate BMP2b-FLAG, the FLAG tag was inserted between two LGDPPVAT linkers two amino acids downstream of the BMP2b Furin cleavage site.

Generation of fluorescent Chordin fusions

All constructs were generated by PCR-based methods (**Horton et al., 1990**) and contain the consensus Kozak sequence *gccacc* 5' of the start codon. Chordin was inserted into the ClaI site of pCS2(+).

All other Chordin-containing constructs were inserted into the EcoRI and XbaI sites of the pCS2(+) vector. To generate Chordin-sfGFP and BMP2b-Dendra2, sequences encoding sfGFP or Dendra2 flanked by LGDPPVAT linkers were inserted immediately 5' of the Tolloid cleavage site 2. To generate Chordin-FLAG, sequences encoding the FLAG tag DYKDDDDK were inserted immediately 5' of the Tolloid cleavage site 2 without additional linkers. To generate Chordin-sfGFP-FLAG and Chordin-Dendra2-FLAG, sequences encoding the FLAG tag were inserted between the first linker and sfGFP or Dendra2 of Chordin-sfGFP and Chordin-Dendra2 constructs.

Generation of fluorescent Sizzled fusions

All Sizzled constructs were generated by PCR-based methods (**Horton et al., 1990**), contain the consensus Kozak sequence *gccacc* 5' of the start codon, and were inserted into the EcoRI and XbaI sites of the pCS2(+) vector. To generate Sizzled-sfGFP, sequences encoding sfGFP with an N-terminal LGLG linker were fused to the C-terminus of Sizzled. Sequences encoding the FLAG tag DYKDDDDK were inserted between the LGLG linker and sfGFP to generate Sizzled-sfGFP-FLAG. To generate Sizzled-FLAG, the FLAG tag was fused to the C-terminus of Sizzled separated by an LGLG linker.

mRNA *in vitro* synthesis

mRNA was generated using SP6 mMessage mMachine kits (Thermo Fisher) after vector linearization with NotI-HF (New England Biolabs, Cat. No. R3189). mRNA was purified using LiCl precipitation or Qiagen RNeasy kits following the manufacturers' instructions.

Phenotypic analysis

Scoring of ventralization and dorsalization was executed as previously described (**Mullins et al., 1996**; **Kishimoto et al., 1997**). Embryos were injected at the one- to two-cell stage with equimolar amounts of *BMP2b* (1 pg), *BMP2b-sfGFP* (1.49 pg), and *BMP2b-Dendra2* (1.47 pg) mRNA to assess ventralizing activity. At 1 day post-fertilization, BMP2b-injected embryos were classified as weakly ventralized (V1) to strongly ventralized (V4). V1 embryos have reduced eyes but a prominent head. V2 embryos have no eyes, reduction of the head, and expansion of posterior structures such as somites and tail. V3 embryos completely lack head structures and exhibit a further expanded tail and enlarged blood islands. Finally, V4 embryos lack most structures except for a short, protruding, and expanded tail.

To assess dorsalizing activity of the Chordin constructs, embryos were injected with equimolar amounts of *Chordin* (30 pg), *Chordin-sfGFP* (37 pg), *Chordin-Dendra2* (37 pg), and *Chordin-FLAG* mRNA (30 pg). Embryos were scored at 1 day post-fertilization and classified as weakly dorsalized (C1) to strongly dorsalized (C5) (**Kishimoto et al., 1997**). C1 embryos lack the ventral tail fin. C2 embryos have a further loss of ventral structures, such as the ventral tail vein, and a bent tail. C3 embryos exhibit a tail that is shortened and twisted. C4 embryos have observable head structures and develop eyes with twisting of the posterior structures above the yolk. C5 embryos are fully dorsalized and frequently lyse (**Mullins et al., 1996**; **Kishimoto et al., 1997**).

Rescue of *BMP2b* ($swr^{-/-}$) mutants

Injection of *BMP2b* mRNA can rescue *BMP2b* mutants (**Kishimoto et al., 1997**). To investigate whether tagged BMP2b constructs can rescue $swr^{tc300-/-}$ mutants (**Mullins et al., 1996**), the rescuing amount of *BMP2b* mRNA was first determined (1.8 pg), and equimolar amounts of mRNA encoding fluorescent fusion constructs were subsequently injected into the progeny of heterozygous $swr^{+/-}$ mutant incrosses. Embryos with wild type morphology at 24 hpf were anesthetized and mounted in 2% methylcellulose for imaging with an AxioZoom V16 (ZEISS) microscope at 30–33 hpf. To genotype embryos following DNA extraction (**Meeker et al., 2007**), PCR was performed to amplify a BMP2b fragment with the forward primer 5'-AAAAGCCGAGGAGAAAGCAC-3' and the reverse primer 5'-AGTCCTTCATTGGGGAGATTGTTC-3', and the following thermocycling parameters: An initial denaturation step of 94°C for 3 min; 39 cycles of 94°C for 30 s, 58°C for 40 s, and 72°C for 40 s; and a final extension at 72°C for 5 min. PCR amplicons were subsequently digested with HaeIII (New England Biolabs, Cat. No. R0108) at 37°C for 2 hr. The genotyping assay for the

swr^{tc300} line was designed by the Zebrafish International Resource Center (ZIRC) staff and downloaded from the ZIRC website at http://zebrafish.org.

Preparation of extracellularly enriched fractions for western blotting

Extracellularly enriched and cellular fractions from manually deyolked embryos between sphere and dome stage were obtained as described previously (**Müller et al., 2012**). mRNAs encoding FLAG-tagged constructs were injected at the one- or two-cell stage at equimolar amounts (*BMP2b-FLAG*: 444 pg, *BMP2b-sfGFP-FLAG*: 638 pg, *BMP2b-Dendra2-FLAG*: 630 pg; and *Chordin-FLAG*: 500 pg, *Chordin-sfGFP-FLAG*: 620 pg, *Chordin-Dendra2-FLAG*: 615 pg). For protein samples with BMP2b constructs, fractions from approximately 19 embryos were loaded and resolved by SDS-PAGE using 12% polyacrylamide gels. For protein samples with Chordin constructs, fractions from approximately 17–18 embryos were loaded and resolved in 8% polyacrylamide gels. Proteins were subsequently transferred onto PVDF membranes using a Trans-Blot Turbo Transfer System (Bio-Rad, Cat. No. 170–4272). Membranes were blocked with 5% non-fat milk (Roth, Cat. No. T145.2) in PBST (0.1% Tween) and incubated with anti-FLAG antibody (Sigma, Cat. No. F3165) at a concentration of 1:2000 in non-fat milk in PBST at 4°C overnight. HRP-coupled donkey anti-mouse secondary antibody (Jackson ImmunoResearch, Cat. No. 715-035-150) was used at concentration of 1:25,000 for 3 hr at room temperature. Chemiluminescence was detected using SuperSignal West Dura Extended Duration Substrate (Thermo Fisher, Cat. No. 34075) and imaged with a chemiluminescence imaging system (Fusion Solo, Vilber Lourmat).

Transplantations

To generate clonal sources secreting BMP2b-sfGFP, Chordin-sfGFP, and untagged Chordin (**Figures 3** and **5**), approximately 50–75 cells were transplanted from sphere stage wild type TE donor embryos expressing these constructs into uninjected, sphere stage sibling hosts (similar to [**Müller et al., 2012**]). Transplantations were carried out in 1 x Ringer's buffer. Cells were explanted from donors, extruded briefly into the buffer to wash away cellular debris and extracellular fluorescent protein, and then transplanted into host embryos.

Donor embryos were dechorionated with 1 mg/ml Pronase (Roche, Cat. No. 11 459 643 001) and injected with 1–2 nl injection mix at the one-cell stage. Sibling host embryos were dechorionated together with donors at the one-cell stage, and all embryos were incubated at 28°C until transplantation. Unfertilized or injured embryos were discarded.

For single (**Figure 3**) and double (**Figure 5**) transplantation experiments, BMP2b-sfGFP and Chordin-sfGFP donors were injected with 500 pg mRNA (**Figure 3—figure supplement 1F–H**).

For double transplantation experiments (**Figure 5**), embryos received one transplantation from a donor expressing BMP2b-sfGFP and a second transplantation from a donor injected at the one-cell stage with either 50 pg Alexa 546-coupled dextran (10 kDa, Molecular Probes, Cat. No. D22911) or 1000 pg Chordin mRNA + 50 pg Alexa 546-coupled dextran. Alexa 546-coupled dextran was used to mark the location of the second clone.

2–10 min post-transplantation, embryos were mounted in 1% low-melting NuSieve GTG agarose (Lonza, Cat. No. 50080) dissolved in embryo medium (250 mg/l Instant Ocean salt dissolved in reverse osmosis water). Embryos were immersed in 40°C molten low melting point agarose, pulled into 1.5 mm glass capillary tubes (ZEISS), and positioned with the animal pole perpendicular to the capillary using a metal probe. Agarose tubes were then suspended in embryo medium, and imaged at room temperature using a ZEISS Lightsheet Z.1 microscope (see *Light sheet microscopy* section for further imaging details).

Light sheet microscopy

Fluorescence images in **Figures 1**, **2**, **3** and **5**, and **Figure 3—figure supplement 1** were obtained using a Lightsheet Z.1 microscope (ZEISS). For fixed, immunostained embryos, samples were mounted into a glass capillary sample holder in 1% low-melting NuSieve GTG agarose (Lonza, Cat. No. 50080) in embryo medium with 0.2 µm dark red fluorescent FluoSpheres (Life Technologies, Cat. No. F8807) diluted 1:200,000 from a 2% solids stock. Embryos were imaged at 0°, 45°, 180° and 225° angles (**Schmid et al., 2013**) using identical imaging conditions. For 3D reconstruction, an interactive bead-based registration algorithm was used to determine the threshold that most accurately

selects the beads (**Preibisch et al., 2010**). Reconstructed images were converted to 8-bit format using ImageJ, and Imaris software (Bitplane) was used for 3D data visualization and video generation. The videos were cropped using Avidemux 2.6.

To visualize the entire embryo in a single image, reconstructed images were first converted to 16-bit files using ImageJ, and equirectangular 2D map projections were then generated (**Schmid et al., 2013**). The 2D maps were re-aligned into Hammer-Aitoff projections using Hugin panorama photo stitcher software (http://hugin.sourceforge.net) to orient the peak of pSmad1/5/9 intensity to the ventral pole (left in **Figure 1** panels) and the trough of pSmad1/5/9 intensity to the dorsal pole (right in **Figure 1** panels). For gradient quantifications in **Figure 1A+B** and **Figure 2F–H**, the embryo proper was masked using manual polygon selections in Fiji (**Schindelin et al., 2012**) in order to exclude signal from the yolk syncytial layer and yolk. The 'Plot Profile' function in Fiji was then applied to the entire masked image to determine ventral-to-dorsal gradients. The background signal of immunostained embryos was determined by finding the lowest value in the profiles of sphere stage embryos (**Figure 1A+B**) and the lowest value in the profiles of *chordin*$^{-/-}$ embryos (**Figure 2F+G**), respectively. These background values were subtracted from the data sets, and the profiles were normalized to the highest value in each data series. The mean and standard error of the normalized data sets was then calculated piece-wise for every point along the ventral-to-dorsal profile.

For transplantation experiments in **Figures 3** and **5**, imaging began 5 to 20 min post-transplantation and continued for approximately 1 hr (see *Transplantation* section for further details). The following imaging conditions were used:

- W Plan-Apochromat 20 x objective, 0.5 x zoom
- dual side light sheets
- 488 nm laser (100 mW) at 6% power (for sfGFP-containing constructs)
- 561 nm laser (20 mW) at 5% power (for double transplantations only; to detect Alexa 546 signal)
- separate exposure to 488/561 nm lasers (in double transplantation experiments only) to avoid cross-talk
- exposure time: 250 ms
- average light sheet thickness: 6.4 µm
- 3 µm intervals between z-slices; 60 slices per embryo (≈180 µm total)
- 5 min intervals between imaging

Gradients were quantified using maximum intensity projections of 15 z-slices similar to the approach in (**Müller et al., 2012**). A rectangular region of interest abutting the clone with a fixed height of 86.34 µm (corresponding to 189 pixels) and varying widths depending on embryo length was drawn in Fiji (**Schindelin et al., 2012**), and the average intensity in 0.457 µm strips was calculated from the maximum intensity projections. Background intensity resulting from autofluorescence was measured similarly in uninjected embryos (for single transplantation experiments, n = 4) or in uninjected embryos transplanted with a clone of cells containing Alexa 546-coupled dextran (for double transplantation experiments, n = 2). A single value for background subtraction was determined by calculating the average of the intensity profile values. After subtracting the background value from the experimental intensity profiles, the data was normalized to the value closest to the clonal source boundary. This approach allows for the comparison of the relative gradient range, which is independent of constant production rates. We assume constant production rates over the relatively short time scales of observation (≈80 min).

Embryos with low signal-to-noise ratios were excluded from analysis.

Fluorescence decrease after photoconversion (FDAP) experiments

FDAP experiments were carried out as described in (**Müller et al., 2012**; **Rogers et al., 2015**). Embryos were injected at the one-cell stage with either 60 pg *BMP2b-Dendra2* mRNA + 0.5 ng Alexa 488-dextran (3 kDa, Molecular Probes) or 150 pg *Chordin-Dendra2* mRNA + 0.5 ng Alexa 488-dextran. To assess background fluorescence, embryos were injected with 0.5 ng Alexa 488-dextran only. Embryos were mounted in 1% low melting point agarose in glass-bottom Petri dishes (MatTek Corporation) covered with embryo medium to hydrate the agarose during imaging.

FDAP experiments were performed using an LSM 780 (ZEISS) confocal microscope. Pre-conversion and post-conversion images were acquired using an LD C-Apochromat 40x/1.1 NA water

immersion objective. A single pre-photoconversion image was first acquired for each sample followed by photoconversion and multiposition time-lapse imaging with 10 min intervals for approximately 300 min. For photoconversion, embryos were illuminated with a Sola SE II LED lamp at 100% power for 30 s through a C-Apochromat 10x/0.45 NA objective and an AHF F36-500 UV filter cube. For both pre- and post-conversion images, Alexa 488 was excited using a 488 nm Argon laser, and a DPSS 561 nm laser was used to excite photoconverted Dendra2. The emission signal between 494–576 nm (Alexa 488) and 578–696 nm (photoconverted Dendra2) was collected using a 32 channel GaAsP QUASAR detector array. Embryos that produced only low levels of photoconverted Dendra2 signal or whose position shifted significantly over time as well as embryos with non-uniform signal distribution or embryos that died were excluded from analysis. Sample numbers: n = 22 for BMP2b-Dendra2 (with n = 17 background embryos); n = 6 for Chordin-Dendra2 (with n = 1 background embryo).

All experiments were analyzed using PyFDAP (**Bläßle and Müller, 2015**; **Rogers et al., 2015**), version 1.1.2. PyFDAP extracts the extracellular and intracellular photoconverted Dendra2 signal by masking the Alexa 488 signal, and fits the resulting average intensities with a linear decay model. The ordinary differential equation describing linear protein decay is given by

$$\frac{dc}{dt} = -k_1 c$$

where c is the concentration of the protein and k_1 is its clearance rate constant. We assume that Dendra2 signal is directly proportional to the protein concentration. The analytical solution of this equation is given by

$$c(t) = c_0 e^{-k_1 t} + y_0$$

where $c_0 + y_0$ is the protein's concentration at $t = 0$, and y_0 is the protein's concentration at $t = \infty$. The half-life τ of the protein can then be calculated as

$$\tau = \ln(2)/k$$

PyFDAP estimates a lower bound for y_0 by computing the maximum relative effect of photobleaching $F_{i,r}$. For each background data set, the strongest influence of photobleaching was computed by taking the minimum over all differences of background intensity $B_{j,r}$ and background noise N_i, and the difference between pre-conversion background intensity $B_{\mathrm{pre},i,r}$ and noise level. Here, r denotes the region under consideration, i.e. extracellular, intracellular, or the entire imaging slice; i indicates the ith data set, and j counts the background data sets. The average over all b background data sets was then taken to arrive at the mean effect of photobleaching. The factor

$$F_{i,r} = \frac{1}{b}\sum_{j=1}^{b} \min_t \left(\frac{B_{j,r}(t) - N_i}{B_{\mathrm{pre}_{j,r}} - N_i} \right)$$

was used to scale the pre-conversion intensity of the FDAP data set according to

$$y_{0_{i,r}} \geq F_{i,r}\left(I_{\mathrm{pre}_{i,r}} - N_i\right) + N_i$$

This lower bound was then used to constrain a Nelder-Mead simplex algorithm when minimizing

$$SSD = \sum_n (\bar{I}(t_n) - c(t_n))^2$$

Fluorescence recovery after photobleaching (FRAP) experiments

FRAP experiments and data analysis were carried out as previously described (**Müller et al., 2012**; **Müller et al., 2013**) using an LSM 780 NLO confocal microscope (ZEISS) and an LD LCI Plan-Apochromat 25x water immersion objective. Embryos were injected at the one-cell stage with 30 pg of mRNA encoding BMP2b-sfGFP, 60 pg of mRNA encoding BMP2b-Dendra2, 60 pg of mRNA encoding Chordin-sfGFP, 120 pg of mRNA encoding Chordin-Dendra2, or 30 pg of mRNA encoding Sizzled-sfGFP. To analyze the effect of Chordin on BMP2b diffusion, embryos were injected at the one-cell stage with 30 pg of mRNA encoding BMP2b-sfGFP plus 60 or 200 pg of mRNA encoding

Chordin, or 60 pg of mRNA encoding BMP2b-Dendra2 plus 200 pg of mRNA encoding Chordin. Embryos were mounted in 1% low-melting point agarose in glass-bottom Petri dishes (MatTek Corporation) covered with embryo medium to hydrate the agarose during imaging. Embryos with low or non-uniform fluorescence and embryos that died or whose position shifted significantly over time were excluded from analysis.

For FRAP data analysis, the fits of a model with uniform production, diffusion, and clearance were constrained with the clearance rate constants of BMP2b-Dendra2 and Chordin-Dendra2 fusions measured by FDAP in the present study (BMP2b-Dendra2: $k_1 = 8.9 \times 10^{-5}$/s; Chordin-Dendra2: $k_1 = 9.6 \times 10^{-5}$/s). Sizzled-sfGFP fits were constrained with the clearance constant measured for BMP2b-Dendra2 assuming similar protein stability. As shown previously, the estimation of diffusion coefficients does not sensitively depend on the values of clearance rate constants if the time scales of observation (here: 50 min) and protein stability (here: approximately 120 min) are similar (***Müller et al., 2012***).

Fluorescence correlation spectroscopy (FCS) experiments

The FCS experiments were done using an LD C-Apochromat 40x/1.1 NA water immersion objective on an LSM 780 NLO confocal microscope (ZEISS). Embryos were injected at the one-cell stage with 30 pg of mRNA encoding BMP2b-sfGFP or 60 pg of mRNA encoding Chordin-sfGFP. Embryos were mounted in 1% low-melting point agarose in glass-bottom Petri dishes (MatTek Corporation) and covered with embryo medium to hydrate the agarose during imaging. The fluorophores (sfGFP, Alexa 488) were excited using an Argon 488 nm laser, and the emission light between 494 and 542 nm was collected using a 32-channel GaAsP QUASAR detector array. Before each FCS experiment, the pinhole was aligned and set to 1 Airy unit, and the instrument was calibrated using a solution of 40 nM Alexa 488 dye (Thermo Fisher) in water. For each FCS sample, fluorescence fluctuations were measured for 10 s with 10 repeats, and any irregularities in the 100 s count trace resulting from cellular movements were excluded from analysis.

Auto-correlation curves for Alexa 488 were freely fitted to determine the structural parameter as well as the diffusion time, the triplet state fraction, and the triplet state relaxation time of Alexa 488 for every experiment. The auto-correlation curves for BMP2b-sfGFP and Chordin-sfGFP were fitted with a fixed structural parameter, fixed triplet state fraction, and fixed triplet relaxation time determined from the Alexa 488 calibration measurements. The curves were fitted using ZEISS ZEN Pro software with a one-component 'free diffusion with triplet state correction' model. The first 10^{-6} seconds lag time for the correlation curve was excluded in the fitting (***Yu et al., 2009***; ***Müller et al., 2013***). The diffusion coefficient was then calculated by comparing the diffusion time of BMP2b-sfGFP and Chordin-sfGFP with Alexa 488 (reference diffusion coefficient: 435 μm^2/s [***Petrásek and Schwille, 2008***]).

Since the values of the triplet state fraction and the triplet state relaxation time of sfGFP are unknown and not necessarily identical to those of Alexa 488, we also freely fitted the autocorrelation curves for BMP2b-sfGFP and Chordin-sfGFP with the experimentally measured structural parameter as the only constraint, and determined free diffusion coefficients of $D = 35 \pm 2$ μm^2/s for BMP2b-sfGFP (n = 17 measurements from 4 embryos) and $D = 50 \pm 3$ μm^2/s for Chordin-sfGFP (n = 19 measurements from 5 embryos), within a deviation of approximately 20–30% compared to the diffusion coefficients determined by constraining the fits with a fixed structural parameter, fixed triplet state fraction, and fixed triplet relaxation time ($D = 46 \pm 1$ μm^2/s for BMP2b-sfGFP, and $D = 59 \pm 2$ μm^2/s for Chordin-sfGFP; values reported in ***Figure 4***). The similar diffusion coefficients determined by differently constrained fits indicate that the diffusion time measured in our experiments does not sensitively depend on the values of the triplet state fraction and triplet state relaxation time.

Mathematical modeling of BMP2b-sfGFP and Chordin-sfGFP gradient formation

The geometry of the zebrafish blastoderm was approximated by the complement of two spheres with a columnar subdomain placed off-center to represent the signal source region with the same parameters as described in ***Müller et al. (2012)***. Gradient formation was simulated with the source-diffusion-sink model

$$\frac{\partial c}{\partial t} = D\nabla^2 c - k_1 c + \delta_s k_2$$

with

$$\delta_s = \begin{cases} 1 & \text{in the source} \\ 0 & \text{otherwise} \end{cases}$$

For ***Figure 3—figure supplement 2***, the experimental data were fitted with solutions from a 50 × 50 parameter grid spanning all possible combinations of 50 diffusion coefficients (logarithmically spaced from 0.1 $\mu m^2/s$ to 50 $\mu m^2/s$) and 50 clearance rate constants (logarithmically spaced from 1 × 10^{-5}/s to 5 × 10^{-4}).

Simulations of previous models

The finite element method was used for all numerical simulations. All geometries are one-dimensional representations of embryos. The solution at each time step in the discretized geometries was determined using a sparse LU factorization algorithm (UMFPACK), and the time stepping was computed using a backward Euler step method (Comsol Multiphysics). Simulations in ***Figure 1C–E,G*** (Models 1, 2, 3, and 5) were executed for a total of 10080 s (i.e., for approximately 3 hr from sphere to shield stage during zebrafish embryogenesis [***Kimmel et al., 1995***]) and read out every 2520 s (i.e., approximately every 42 min at relevant zebrafish stages). The simulation in ***Figure 1F*** (Model 4) was executed for a total of 20 time steps near steady state and read out at every fifth time step.

The following model descriptions comprise the complete wild type systems. For simulations of *chordin* mutants, the Chordin flux was set to 0 (Models 1, 2, 3, and 5), or the Chordin-dependent terms were removed from the equations and the initial concentration of Chordin was set to 0 (Model 4). To focus on the role of Chordin in regulating BMP signaling and distribution, we did not include other negative regulators of BMP such as Noggin and Follistatin (***Umulis et al., 2009***). For the interpretation of the simulations, we assume that the distribution of free BMPs is correlated with BMP signaling and the distribution of pSmad1/5/9.

To facilitate comparison of the models, the distribution profiles of free BMP are shown as a function of relative embryo length, and the solutions were normalized to the ventral-most free BMP concentration at shield stage (i.e., at t = 7560 s for Models 1, 2, 3, and 5, and at t = 15 for Model 4) in wild type simulations.

Model 1: Graded source-sink (mobile BMP)

In the graded source-sink model, the BMP source $\rho_{BMP}(x)$ was modeled after the known distribution of *bmp2b* mRNA between sphere stage and 30% epiboly (***Ramel and Hill, 2013***). The model does not include autoregulation of BMP production since positive feedback only appears to be important for later stages of development (***Ramel and Hill, 2013***; ***Zinski et al., 2017***). Chordin binds BMP irreversibly and acts as a sink. The model was simulated using the following equations:

$$\frac{\partial[\mathrm{BMP}]}{\partial t} = D_{\mathrm{BMP}}\nabla^2[\mathrm{BMP}] - \kappa[\mathrm{Chd}][\mathrm{BMP}] - \lambda_{\mathrm{BMP}}[\mathrm{BMP}] + \rho_{\mathrm{BMP}}(x)$$

$$\frac{\partial[\mathrm{Chd}]}{\partial t} = D_{\mathrm{Chd}}\nabla^2[\mathrm{Chd}] - \kappa[\mathrm{Chd}][\mathrm{BMP}] - \lambda_{\mathrm{Chd}}[\mathrm{Chd}]$$

$$\frac{\partial[\mathrm{ChdBMP}]}{\partial t} = D_{\mathrm{ChdBMP}}\nabla^2[\mathrm{ChdBMP}] + \kappa[\mathrm{Chd}][\mathrm{BMP}] - \lambda_{\mathrm{Chd}}[\mathrm{ChdBMP}]$$

Embryo geometry and boundary conditions

Embryo length: 300 × 10^{-6} m (300 µm, the typical length of the zebrafish blastoderm)
Constant Chordin flux from the dorsal boundary: 5 × 10^{-14} mol/(m^2•s)
No-flux boundary condition for all other species on both ventral and dorsal boundaries

Parameter values

D_{BMP} = 2 $\mu m^2/s$ (measured in the present study)
D_{Chd} = 7 $\mu m^2/s$ (measured in the present study)
D_{ChdBMP} = 7 $\mu m^2/s$

λ_{BMP} = 8.9 × 10^{-5}/s (measured in the present study)
λ_{Chd} = 9.6 × 10^{-5}/s (measured in the present study)
κ = 400 × 10^{3} m^3/(mol•s)
$\rho_{BMP}(x)$ = 0.57 × 10^{-9} × e^{-5000x} mol/m^3 (accounting for the inhomogeneous ventrally peaking distribution of *bmp2b* mRNA in zebrafish embryos)

Initial conditions

BMP initial concentration: 2.85 × 10^{-8} mol/m^3 everywhere (one-twentieth of the concentration used for *Xenopus* frogs in [***Inomata et al., 2013***])
Chordin initial concentration: 0 mol/m^3 everywhere
Chordin-BMP complex initial concentration: 0 mol/m^3 everywhere

Model 2: Graded source-sink (immobile BMP)

As for Model 1, the graded source-sink model (immobile BMP) was modeled without autoregulation of BMP production since positive feedback only appears to be important for later stages of development (***Ramel and Hill, 2013***; ***Zinski et al., 2017***). Here κ, which reflects the binding between Chordin and BMP, is smaller than in Model 1 to obtain a realistic-free BMP distribution; using the same value for κ as in Model 1 creates an unrealistically steep free BMP gradient. The model was simulated using the following equations:

$$\frac{\partial[\mathrm{BMP}]}{\partial t} = -\kappa[\mathrm{Chd}][\mathrm{BMP}] - \lambda_{\mathrm{BMP}}[\mathrm{BMP}] + \rho_{\mathrm{BMP}}(x)$$

$$\frac{\partial[\mathrm{Chd}]}{\partial t} = D_{\mathrm{Chd}}\nabla^2[\mathrm{Chd}] - \kappa[\mathrm{Chd}][\mathrm{BMP}] - \lambda_{\mathrm{Chd}}[\mathrm{Chd}]$$

$$\frac{\partial[\mathrm{ChdBMP}]}{\partial t} = D_{\mathrm{ChdBMP}}\nabla^2[\mathrm{ChdBMP}] + \kappa[\mathrm{Chd}][\mathrm{BMP}] - \lambda_{\mathrm{Chd}}[\mathrm{ChdBMP}]$$

Embryo geometry and boundary conditions

Embryo length: 300 × 10^{-6} m (300 µm, the typical length of a zebrafish blastoderm)
Constant Chordin flux from the dorsal boundary: 5 × 10^{-14} mol/(m^2•s)
No-flux boundary condition for all other species on both ventral and dorsal boundaries

Parameter values

D_{Chd} = 7 μm^2/s (measured in the present study)
D_{ChdBMP} = 7 μm^2/s
λ_{BMP} = 8.9 × 10^{-5}/s (measured in the present study)
λ_{Chd} = 9.6 × 10^{-5}/s (measured in the present study)
κ = 4 × 10^{3} m^3/(mol•s)
$\rho_{BMP}(x)$ = 0.57 × 10^{-9} × e^{-5000x} mol/m^3 (accounting for the inhomogenous ventrally peaking distribution of *bmp2b* mRNA in zebrafish embryos)

Initial conditions

BMP initial concentration: 2.85 × 10^{-8} mol/m^3 everywhere (one-twentieth of the concentration used for *Xenopus* frogs in [***Inomata et al., 2013***]).
Chordin initial concentration: 0 mol/m^3 everywhere
Chordin-BMP complex initial concentration: 0 mol/m^3 everywhere

Model 3: Long-range accumulation and feedback

The model was developed for frog embryogenesis. For the simulations in the present study the equations, geometry, initial conditions, and parameters used were exactly as described in (***Inomata et al., 2013***):

$$\frac{\partial[\mathrm{BMP}]}{\partial t} = D\nabla^2[\mathrm{BMP}] + \frac{v_{\mathrm{BMP}}([\mathrm{ADMP}]+[\mathrm{BMP}])^{10}}{k_{\mathrm{BMP}}^{10}+([\mathrm{ADMP}]+[\mathrm{BMP}])^{10}} - \lambda_{\mathrm{BMP}}[\mathrm{BMP}]$$

$$+\frac{\lambda_{\mathrm{Chd}}[\mathrm{ChdBMP}]}{1+\frac{[\mathrm{Szl}]}{ki}+\frac{[\mathrm{Chd}]+[\mathrm{ChdBMP}]+[\mathrm{ChdADMP}]}{km}} - k[\mathrm{Chd}][\mathrm{BMP}]$$

$$\frac{\partial[\mathrm{Chd}]}{\partial t} = D\nabla^2[\mathrm{Chd}] + \frac{v_{\mathrm{Chd}}k_{\mathrm{Chd}}^{10}}{k_{\mathrm{Chd}}^{10}+([\mathrm{ADMP}]+[\mathrm{BMP}])^{10}} - \frac{\lambda_{\mathrm{Chd}}[\mathrm{Chd}]}{1+\frac{[\mathrm{Szl}]}{ki}+\frac{[\mathrm{Chd}]+[\mathrm{ChdBMP}]+[\mathrm{ChdADMP}]}{km}}$$

$$-k[\mathrm{Chd}][\mathrm{BMP}] - k[\mathrm{Chd}][\mathrm{ADMP}]$$

$$\frac{\partial[\mathrm{ADMP}]}{\partial t} = D\nabla^2[\mathrm{ADMP}] + \frac{v_{\mathrm{ADMP}}k_{\mathrm{ADMP}}^{10}}{k_{\mathrm{ADMP}}^{10}+([\mathrm{ADMP}]+[\mathrm{BMP}])^{10}} - \lambda_{\mathrm{BMP}}[\mathrm{ADMP}]$$

$$+\frac{\lambda_{\mathrm{Chd}}[\mathrm{ChdADMP}]}{1+\frac{[\mathrm{Szl}]}{ki}+\frac{[\mathrm{Chd}]+[\mathrm{ChdBMP}]+[\mathrm{ChdADMP}]}{km}} - k[\mathrm{Chd}][\mathrm{ADMP}]$$

$$\frac{\partial[\mathrm{Szl}]}{\partial t} = D\nabla^2[\mathrm{Szl}] + \frac{v_{\mathrm{Szl}}([\mathrm{ADMP}]+[\mathrm{BMP}])^{20}}{k_{\mathrm{Szl}}^{20}+([\mathrm{ADMP}]+[\mathrm{BMP}])^{20}} - \lambda_{\mathrm{Szl}}[\mathrm{Szl}]$$

$$\frac{\partial[\mathrm{ChdBMP}]}{\partial t} = D\nabla^2[\mathrm{ChdBMP}] - \frac{\lambda_{\mathrm{Chd}}[\mathrm{ChdBMP}]}{1+\frac{[\mathrm{Szl}]}{ki}+\frac{[\mathrm{Chd}]+[\mathrm{ChdBMP}]+[\mathrm{ChdADMP}]}{km}} + k[\mathrm{Chd}][\mathrm{BMP}]$$

$$\frac{\partial[\mathrm{ChdADMP}]}{\partial t} = D\nabla^2[\mathrm{ChdADMP}] - \frac{\lambda_{\mathrm{Chd}}[\mathrm{ChdADMP}]}{1+\frac{[\mathrm{Szl}]}{ki}+\frac{[\mathrm{Chd}]+[\mathrm{ChdBMP}]+[\mathrm{ChdADMP}]}{km}} + k[\mathrm{Chd}][\mathrm{ADMP}]$$

Embryo geometry and boundary conditions

Embryo length: 1000 × 10^{-6} m (1000 µm, the typical length of a frog embryo)
Constant Chordin flux from the dorsal boundary: 4.8 × 10^{-12} mol/(m^2•s)
No-flux boundary condition for all other species on both ventral and dorsal boundaries

Parameter values

km = 25 × 10^{-6} mol/m^3
ki = 25 × 10^{-6} mol/m^3
v_{Chd} = 5 × 10^{-10} mol/(m^3•s)
k_{Chd} = 7 × 10^{-8} mol/m^3
v_{BMP} = 1.4 × 10^{-10} mol/(m^3•s)
k_{BMP} = 3.5 × 10^{-7} mol/m^3
v_{Szl} = 100 × 10^{-6} mol/(m^3•s)
k_{Szl} = 1 × 10^{-6} mol/m^3
v_{ADMP} = 3.2 × 10^{-9} mol/(m^3•s)
k_{ADMP} = 3 × 10^{-8} mol/m^3
λ_{Chd} = 1 × 10^{-3}/s
λ_{BMP} = 2 × 10^{-4}/s
λ_{Szl} = 3.8 × 10^{-5}/s
D = 15 µm^2/s
k = 280 m^3/(mol•s)

Initial conditions

BMP initial concentration: 0.57 × 10^{-6} × e^{-1000x} mol/m^3 throughout the embryo (the amplitude of this distribution is the same as in [***Inomata et al., 2013***], but the initial BMP profile was modeled as a gradient instead of uniform)
Chordin initial concentration: 0 mol/m^3 everywhere

ADMP initial concentration: 0 mol/m^3 everywhere
Sizzled initial concentration: 0 mol/m^3 everywhere
Chordin-BMP complex initial concentration: 0 mol/m^3 everywhere
Chordin-AMP complex initial concentration: 0 mol/m^3 everywhere

For the simulations in ***Figure 4—figure supplement 1E–J***, all parameters were identical to the parameter values listed above except for *D*(BMP) = 3 µm^2/s, *D*(Chd) = 6 µm^2/s, *D*(ChdADMP) = 10 µm^2/s, and *D*(ChdBMP) = 10 µm^2/s. *D*(Sizzled) was set to 150 µm^2/s in ***Figure 4—figure supplement 1E***, and to 10 µm^2/s in ***Figure 4—figure supplement 1F–J***. *D*(ADMP) was varied from 0.1 µm^2/s to 150 µm^2/s as indicated in ***Figure 4—figure supplement 1E–J***.

Model 4: Self-regulating reaction-diffusion system

The non-dimensional model, geometry, initial conditions, and parameters used for the simulations were similar to the ones described in [***Francois et al., 2009***]:

$$\frac{\partial[\mathrm{BMP}]}{\partial t} = D_{\mathrm{BMP}}\nabla^2[\mathrm{BMP}] + \frac{[\mathrm{BMP}]^2}{(1+[\mathrm{Chd}])[\mathrm{Szl}]} - \mu_{\mathrm{BMP}}[\mathrm{BMP}] + \rho_{\mathrm{BMP}}$$

$$\frac{\partial[\mathrm{Chd}]}{\partial t} = D_{\mathrm{Chd}}\nabla^2[\mathrm{Chd}] + \frac{[\mathrm{Chd}]^2}{[\mathrm{ADMP}]} - \mu_{\mathrm{Chd}}[\mathrm{Chd}] + \rho_{\mathrm{Chd}}$$

$$\frac{\partial[\mathrm{ADMP}]}{\partial t} = D_{\mathrm{ADMP}}\nabla^2[\mathrm{ADMP}] + [\mathrm{Chd}]^2 - \mu_{\mathrm{ADMP}}[\mathrm{ADMP}]$$

$$\frac{\partial[\mathrm{Szl}]}{\partial t} = D_{\mathrm{Szl}}\nabla^2[\mathrm{Szl}] + [\mathrm{BMP}]^2 - \mu_{\mathrm{Szl}}[\mathrm{Szl}]$$

Embryo geometry and boundary conditions

Embryo length: 25
No-flux boundary conditions on the ventral and dorsal boundaries

Parameter values

$D_{Chd} = D_{BMP} = 6$
$\mu_{Chd} = \mu_{BMP} = 1.2$
$\rho_{Chd} = \rho_{BMP} = 0.1$
$\mu_{ADMP} = \mu_{Szl} = 1.5$
$D_{ADMP} = D_{Szl} = 150$

Initial conditions

BMP initial concentration: $\rho_{BMP} = e^{-0.1x}$
Chordin initial concentration of 1 from position 0 to 24 and Chordin initial concentration of 10 from 24 to 25 (i.e., the dorsal organizer) in the simulated embryo
ADMP initial concentration: 1 everywhere
Sizzled initial concentration: 1 everywhere

For the simulations in ***Figure 4—figure supplement 1K–P***, all parameters were identical to the parameter values listed above except for *D*(BMP) = 3 and *D*(Chd) = 6. *D*(Sizzled) was set to 150 in ***Figure 4—figure supplement 1K***, and to 10 in ***Figure 4—figure supplement 1L–P***. *D*(ADMP) was varied from 0.1 to 150 as indicated in ***Figure 4—figure supplement 1K–P***.

Model 5: Shuttling

For Model 5, a minimal transport model that excludes the effects of downstream patterning circuits was used to illustrate the biophysical aspects of shuttling (***Ben-Zvi et al., 2008***):

$$\frac{\partial[\mathrm{BMP}]}{\partial t} = D_{\mathrm{BMP}}\nabla^2[\mathrm{BMP}] - \kappa[\mathrm{Chd}][\mathrm{BMP}] + \lambda[\mathrm{Xlr}][\mathrm{ChdBMP}] - \lambda_{\mathrm{BMP}}[\mathrm{BMP}] + \rho_{\mathrm{BMP}}(x)$$

$$\frac{\partial[\mathrm{Chd}]}{\partial t} = D_{\mathrm{Chd}}\nabla^2[\mathrm{Chd}] - \kappa[\mathrm{Chd}][\mathrm{BMP}] - \lambda_{\mathrm{Chd}}[\mathrm{Chd}]$$

$$\frac{\partial[\mathrm{ChdBMP}]}{\partial t} = D_{\mathrm{ChdBMP}}\nabla^2[\mathrm{ChdBMP}] + \kappa[\mathrm{Chd}][\mathrm{BMP}] - \lambda[\mathrm{Xlr}][\mathrm{ChdBMP}] - \lambda_{\mathrm{Chd}}[\mathrm{ChdBMP}]$$

Embryo geometry and boundary conditions

Embryo length: 300×10^{-6} m (300 µm)
Constant Chordin flux from the dorsal boundary: 3×10^{-14} mol/(m^2•s)
No-flux boundary condition for all other species on both ventral and dorsal boundaries

Parameter values

D_{BMP} = 0.1 µm^2/s
D_{Chd} = 10 µm^2/s
D_{ChdBMP} = 10 µm^2/s
$\lambda_{BMP} = 8.9 \times 10^{-5}$/s (measured in the present study)
$\lambda_{Chd} = 9.6 \times 10^{-5}$/s (measured in the present study)
$\kappa = 100 \times 10^3$ m^3/(mol•s)
$\lambda = \kappa$
[Xlr] = 2×10^{-8} mol/m^3
$\rho_{BMP}(x) = 0.57 \times 10^{-10} \times e^{-5000x}$ mol/m^3 (accounting for the inhomogeneous ventrally peaking distribution of *bmp2b* mRNA in zebrafish embryos)

Initial conditions

BMP initial concentration: $0.57 \times 10^{-7} \times e^{-5000x}$ mol/m^3 throughout the embryo
Chordin initial concentration: 0 mol/m^3 everywhere
Chordin-BMP complex initial concentration: 0 mol/m^3 everywhere

Shuttling simulations of adjacent BMP and Chordin clones shown in *Figure 5*

The one-dimensional simulations in ***Figure 5*** were executed similarly to the ones described above and solved at 15 and 75 min for comparison to the zebrafish embryo double transplantation experiments. The solutions in ***Figure 5A*** and ***Figure 5E*** were normalized to the highest free BMP concentration in the simulation without the Chordin source, and the solutions in ***Figure 5B*** and ***Figure 5F*** were normalized to the free BMP concentration at the BMP source boundary (at 100 µm) for each condition to facilitate comparison between the gradient ranges.

The double transplantation experiments were modeled using the following equations:

$$\frac{\partial[\mathrm{BMP}]}{\partial t} = D_{\mathrm{BMP}}\nabla^2[\mathrm{BMP}] - \lambda_{\mathrm{BMP}}[\mathrm{BMP}] - \kappa[\mathrm{Chd}][\mathrm{BMP}] + \lambda[\mathrm{Xlr}][\mathrm{ChdBMP}] + \delta_{\mathrm{BMP}}\eta_{\mathrm{BMP}}$$

$$\frac{\partial[\mathrm{Chd}]}{\partial t} = D_{\mathrm{Chd}}\nabla^2[\mathrm{Chd}] - \kappa[\mathrm{Chd}][\mathrm{BMP}] + \delta_{\mathrm{Chd}}\eta_{\mathrm{Chd}}$$

$$\frac{\partial[\mathrm{ChdBMP}]}{\partial t} = D_{\mathrm{ChdBMP}}\nabla^2[\mathrm{ChdBMP}] + \kappa[\mathrm{Chd}][\mathrm{BMP}] - \lambda[\mathrm{Xlr}][\mathrm{ChdBMP}]$$

with

$$\delta_{\mathrm{BMP}} = \begin{cases} 1 \text{ in the BMP source} \\ 0 \text{ otherwise} \end{cases}$$

and

$$\delta_{\mathrm{Chd}} = \begin{cases} 1 \text{ in the Chordin source} \\ 0 \text{ otherwise} \end{cases}$$

Embryo geometry and boundary conditions

Embryo length: 300×10^{-6} m (300 µm)
BMP source: between 50 and 100 µm from the left boundary
Chordin source: between 200 and 250 µm from the left boundary
No-flux boundary conditions on the left and right boundaries

Parameter values for simulations of shuttling predictions (***Figure 5A+B***)

D_{BMP} = 2 µm^2/s (measured in the present study)
λ_{BMP} = 0.0001/s (similar to measurements in the present study)
η_{BMP} = 5×10^{-5} mol/(m^3•s)
η_{Chd} = 5×10^{-5} mol/(m^3•s)
D_{Chd} = 100 µm^2/s
$D_{ChdBMP} = D_{Chd}$
$\kappa = 10 \times 10^3$ m^3/(mol•s)
$\lambda = \kappa$
[Xlr] = 2×10^{-7} mol/m^3

Parameter values for simulations with experimentally measured diffusivities (***Figure 5E+F***)

D_{BMP} = 2 µm^2/s (measured in the present study)
λ_{BMP} = 0.0001/s (similar to measurements in the present study)
η_{BMP} = 5×10^{-5} mol/(m^3•s)
η_{Chd} = 5×10^{-5} mol/(m^3•s)
D_{Chd} = 6 µm^2/s (measured in the present study)
D_{ChdBMP} = 2.2 µm^2/s (measured in the present study)
$\kappa = 10 \times 10^3$ m^3/(mol s)
$\lambda = \kappa$
[Xlr] = 2×10^{-7} mol/m^3

Initial conditions

BMP initial concentration: 0 mol/m^3 everywhere
Chordin initial concentration: 0 mol/m^3 everywhere
Chordin-BMP complex initial concentration: 0 mol/m^3 everywhere

Acknowledgements

We are grateful to Hans Meinhardt for valuable discussions of BMP/Chordin-mediated dorsal-ventral patterning mechanisms. We thank Edgar Herrera and Luciano Marcon for support with immunostainings, light sheet microscopy, data reconstruction, and helpful discussions. We acknowledge Matteo Pilz and Sarah Keim for technical assistance. This work was supported by the Max Planck Society and a Human Frontier Science Program (HFSP) Career Development Award to PM.

Additional information

Funding

Funder	Grant reference number	Author
Max-Planck-Gesellschaft		Patrick Müller
Human Frontier Science Program	Career Development Award (CDA00031/2013-C)	Patrick Müller

The funders had no role in study design, data collection and interpretation, or the decision to submit the work for publication.

Author contributions

Autumn P Pomreinke, Gary H Soh, Data curation, Formal analysis, Investigation, Visualization, Methodology, Writing—review and editing; Katherine W Rogers, Conceptualization, Resources, Data curation, Formal analysis, Investigation, Visualization, Methodology, Writing—review and editing; Jennifer K Bergmann, Resources, Data curation, Formal analysis, Investigation, Visualization; Alexander J Bläßle, Data curation, Software, Formal analysis, Investigation, Visualization, Methodology, Writing—review and editing; Patrick Müller, Conceptualization, Resources, Data curation, Software, Formal analysis, Supervision, Funding acquisition, Validation, Investigation, Visualization, Methodology, Writing—original draft, Project administration, Writing—review and editing

Author ORCIDs

Katherine W Rogers, http://orcid.org/0000-0001-5700-2662
Patrick Müller, http://orcid.org/0000-0002-0702-6209

Decision letter and Author response

Decision letter https://doi.org/10.7554/eLife.25861.024
Author response https://doi.org/10.7554/eLife.25861.025

Additional files

Supplementary files

- Transparent reporting form

DOI: https://doi.org/10.7554/eLife.25861.023

References

Alexandre C, Baena-Lopez A, Vincent JP. 2014. Patterning and growth control by membrane-tethered Wingless. *Nature* **505**:180–185. DOI: https://doi.org/10.1038/nature12879, PMID: 24390349

Barkai N, Ben-Zvi D. 2009. 'Big frog, small frog'–maintaining proportions in embryonic development: delivered on 2 July 2008 at the 33rd FEBS Congress in Athens, Greece. *The FEBS Journal* **276**:1196–1207. DOI: https://doi.org/10.1111/j.1742-4658.2008.06854.x, PMID: 19175672

Ben-Zvi D, Shilo BZ, Fainsod A, Barkai N. 2008. Scaling of the BMP activation gradient in Xenopus embryos. *Nature* **453**:1205–1211. DOI: https://doi.org/10.1038/nature07059, PMID: 18580943

Ben-Zvi D, Barkai N. 2010. Scaling of morphogen gradients by an expansion-repression integral feedback control. *PNAS* **107**:6924–6929. DOI: https://doi.org/10.1073/pnas.0912734107, PMID: 20356830

Ben-Zvi D, Pyrowolakis G, Barkai N, Shilo BZ. 2011a. Expansion-repression mechanism for scaling the Dpp activation gradient in Drosophila wing imaginal discs. *Current Biology* **21**:1391–1396. DOI: https://doi.org/10.1016/j.cub.2011.07.015, PMID: 21835621

Ben-Zvi D, Shilo BZ, Barkai N. 2011b. Scaling of morphogen gradients. *Current Opinion in Genetics & Development* **21**:704–710. DOI: https://doi.org/10.1016/j.gde.2011.07.011, PMID: 21873045

Ben-Zvi D, Fainsod A, Shilo BZ, Barkai N. 2014. Scaling of dorsal-ventral patterning in the Xenopus laevis embryo. *BioEssays* **36**:151–156. DOI: https://doi.org/10.1002/bies.201300136, PMID: 24323952

Bläßle A, Müller P. 2015. PyFDAP: automated analysis of fluorescence decay after photoconversion (FDAP) experiments. *Bioinformatics* **31**:972–974. DOI: https://doi.org/10.1093/bioinformatics/btu735, PMID: 25380959

Brankatschk M, Dickson BJ. 2006. Netrins guide Drosophila commissural axons at short range. *Nature Neuroscience* **9**:188–194. DOI: https://doi.org/10.1038/nn1625, PMID: 16429137

Connors SA, Trout J, Ekker M, Mullins MC. 1999. The role of tolloid/mini fin in dorsoventral pattern formation of the zebrafish embryo. *Development* **126**:3119–3130. PMID: 10375503

Cui Y, Jean F, Thomas G, Christian JL. 1998. BMP-4 is proteolytically activated by furin and/or PC6 during vertebrate embryonic development. *The EMBO Journal* **17**:4735–4743. DOI: https://doi.org/10.1093/emboj/17.16.4735, PMID: 9707432

Degnin C, Jean F, Thomas G, Christian JL. 2004. Cleavages within the prodomain direct intracellular trafficking and degradation of mature bone morphogenetic protein-4. *Molecular Biology of the Cell* **15**:5012–5020. DOI: https://doi.org/10.1091/mbc.E04-08-0673, PMID: 15356272

Dickmeis T, Rastegar S, Aanstad P, Clark M, Fischer N, Korzh V, Strähle U. 2001. Expression of the anti-dorsalizing morphogenetic protein gene in the zebrafish embryo. *Development Genes and Evolution* **211**:568–572. DOI: https://doi.org/10.1007/s00427-001-0190-3, PMID: 11862464

Dominici C, Moreno-Bravo JA, Puiggros SR, Rappeneau Q, Rama N, Vieugue P, Bernet A, Mehlen P, Chédotal A. 2017. Floor-plate-derived netrin-1 is dispensable for commissural axon guidance. *Nature* **545**:350–354. DOI: https://doi.org/10.1038/nature22331, PMID: 28445456

Fisher S, Halpern ME. 1999. Patterning the zebrafish axial skeleton requires early chordin function. *Nature Genetics* **23**:442–446. DOI: https://doi.org/10.1038/70557, PMID: 10581032

Francois P, Vonica A, Brivanlou AH, Siggia ED. 2009. Scaling of BMP gradients in Xenopus embryos. *Nature* **461**: E1. DOI: https://doi.org/10.1038/nature08305, PMID: 19736667

Gurskaya NG, Verkhusha VV, Shcheglov AS, Staroverov DB, Chepurnykh TV, Fradkov AF, Lukyanov S, Lukyanov KA. 2006. Engineering of a monomeric green-to-red photoactivatable fluorescent protein induced by blue light. *Nature Biotechnology* **24**:461–465. DOI: https://doi.org/10.1038/nbt1191, PMID: 16550175

Hammerschmidt M, Pelegri F, Mullins MC, Kane DA, van Eeden FJ, Granato M, Brand M, Furutani-Seiki M, Haffter P, Heisenberg CP, Jiang YJ, Kelsh RN, Odenthal J, Warga RM, Nüsslein-Volhard C. 1996. dino and mercedes, two genes regulating dorsal development in the zebrafish embryo. *Development* **123**:95–102. PMID: 9007232

Harmansa S, Hamaratoglu F, Affolter M, Caussinus E. 2015. Dpp spreading is required for medial but not for lateral wing disc growth. *Nature* **527**:317–322. DOI: https://doi.org/10.1038/nature15712, PMID: 26550827

Haskel-Ittah M, Ben-Zvi D, Branski-Arieli M, Schejter ED, Shilo BZ, Barkai N. 2012. Self-organized shuttling: generating sharp dorsoventral polarity in the early Drosophila embryo. *Cell* **150**:1016–1028. DOI: https://doi.org/10.1016/j.cell.2012.06.044, PMID: 22939625

Horton RM, Cai ZL, Ho SN, Pease LR. 1990. Gene splicing by overlap extension: tailor-made genes using the polymerase chain reaction. *BioTechniques* **8**:528–535. DOI: https://doi.org/10.2144/000114017, PMID: 2357375

Inomata H, Shibata T, Haraguchi T, Sasai Y. 2013. Scaling of dorsal-ventral patterning by embryo size-dependent degradation of Spemann's organizer signals. *Cell* **153**:1296–1311. DOI: https://doi.org/10.1016/j.cell.2013.05.004, PMID: 23746842

Jones CM, Armes N, Smith JC. 1996. Signalling by TGF-beta family members: short-range effects of Xnr-2 and BMP-4 contrast with the long-range effects of activin. *Current Biology* **6**:1468–1475. DOI: https://doi.org/10.1016/S0960-9822(96)00751-8, PMID: 8939607

Kicheva A, Pantazis P, Bollenbach T, Kalaidzidis Y, Bittig T, Jülicher F, González-Gaitán M. 2007. Kinetics of morphogen gradient formation. *Science* **315**:521–525. DOI: https://doi.org/10.1126/science.1135774, PMID: 17255514

Kimmel CB, Ballard WW, Kimmel SR, Ullmann B, Schilling TF. 1995. Stages of embryonic development of the zebrafish. *Developmental Dynamics* **203**:253–310. DOI: https://doi.org/10.1002/aja.1002030302, PMID: 8589427

Kishimoto Y, Lee KH, Zon L, Hammerschmidt M, Schulte-Merker S. 1997. The molecular nature of zebrafish swirl: BMP2 function is essential during early dorsoventral patterning. *Development* **124**:4457–4466. PMID: 9409664

Koos DS, Ho RK. 1999. The nieuwkoid/dharma homeobox gene is essential for bmp2b repression in the zebrafish pregastrula. *Developmental Biology* **215**:190–207. DOI: https://doi.org/10.1006/dbio.1999.9479, PMID: 10545230

Lele Z, Nowak M, Hammerschmidt M. 2001. Zebrafish admp is required to restrict the size of the organizer and to promote posterior and ventral development. *Developmental Dynamics* **222**:681–687. DOI: https://doi.org/10.1002/dvdy.1222, PMID: 11748836

Leung T, Bischof J, Söll I, Niessing D, Zhang D, Ma J, Jäckle H, Driever W. 2003. bozozok directly represses bmp2b transcription and mediates the earliest dorsoventral asymmetry of bmp2b expression in zebrafish. *Development* **130**:3639–3649. DOI: https://doi.org/10.1242/dev.00558, PMID: 12835381

Meeker ND, Hutchinson SA, Ho L, Trede NS. 2007. Method for isolation of PCR-ready genomic DNA from zebrafish tissues. *BioTechniques* **43**:610–614. DOI: https://doi.org/10.2144/000112619, PMID: 18072590

Miller-Bertoglio VE, Fisher S, Sánchez A, Mullins MC, Halpern ME. 1997. Differential regulation of chordin expression domains in mutant zebrafish. *Developmental Biology* **192**:537–550. DOI: https://doi.org/10.1006/dbio.1997.8788, PMID: 9441687

Mullins MC, Hammerschmidt M, Kane DA, Odenthal J, Brand M, van Eeden FJ, Furutani-Seiki M, Granato M, Haffter P, Heisenberg CP, Jiang YJ, Kelsh RN, Nüsslein-Volhard C. 1996. Genes establishing dorsoventral pattern formation in the zebrafish embryo: the ventral specifying genes. *Development* **123**:81–93. PMID: 9007231

Müller P, Schier AF. 2011. Extracellular movement of signaling molecules. *Developmental Cell* **21**:145–158. DOI: https://doi.org/10.1016/j.devcel.2011.06.001, PMID: 21763615

Müller P, Rogers KW, Jordan BM, Lee JS, Robson D, Ramanathan S, Schier AF. 2012. Differential diffusivity of Nodal and Lefty underlies a reaction-diffusion patterning system. *Science* **336**:721–724. DOI: https://doi.org/10.1126/science.1221920, PMID: 22499809

Müller P, Rogers KW, Yu SR, Brand M, Schier AF. 2013. Morphogen transport. *Development* **140**:1621–1638. DOI: https://doi.org/10.1242/dev.083519, PMID: 23533171

Petrásek Z, Schwille P. 2008. Precise measurement of diffusion coefficients using scanning fluorescence correlation spectroscopy. *Biophysical Journal* **94**:1437–1448. DOI: https://doi.org/10.1529/biophysj.107.108811, PMID: 17933881

Plouhinec JL, De Robertis EM. 2009. Systems biology of the self-regulating morphogenetic gradient of the Xenopus gastrula. *Cold Spring Harbor Perspectives in Biology* **1**:a001701. DOI: https://doi.org/10.1101/cshperspect.a001701, PMID: 20066084

Plouhinec JL, Zakin L, Moriyama Y, De Robertis EM. 2013. Chordin forms a self-organizing morphogen gradient in the extracellular space between ectoderm and mesoderm in the Xenopus embryo. *PNAS* **110**:20372–20379. DOI: https://doi.org/10.1073/pnas.1319745110, PMID: 24284174

Preibisch S, Saalfeld S, Schindelin J, Tomancak P. 2010. Software for bead-based registration of selective plane illumination microscopy data. *Nature Methods* **7**:418–419. DOI: https://doi.org/10.1038/nmeth0610-418, PMID: 20508634

Pédelacq JD, Cabantous S, Tran T, Terwilliger TC, Waldo GS. 2006. Engineering and characterization of a superfolder green fluorescent protein. *Nature Biotechnology* **24**:79–88. DOI: https://doi.org/10.1038/nbt1172, PMID: 16369541

Ramel MC, Hill CS. 2013. The ventral to dorsal BMP activity gradient in the early zebrafish embryo is determined by graded expression of BMP ligands. *Developmental Biology* **378**:170–182. DOI: https://doi.org/10.1016/j.ydbio.2013.03.003, PMID: 23499658

Rogers KW, Blässle A, Schier AF, Müller P. 2015. Measuring protein stability in living zebrafish embryos using fluorescence decay after photoconversion (FDAP). *Journal of Visualized Experiments*:52266. DOI: https://doi.org/10.3791/52266, PMID: 25650549

Roy S, Kornberg TB. 2011. Direct delivery mechanisms of morphogen dispersion. *Science Signaling* **4**:pt8. DOI: https://doi.org/10.1126/scisignal.2002434, PMID: 22114143

Sako K, Pradhan SJ, Barone V, Inglés-Prieto Á, Müller P, Ruprecht V, Čapek D, Galande S, Janovjak H, Heisenberg CP. 2016. Optogenetic control of nodal signaling reveals a temporal pattern of nodal signaling regulating cell fate specification during gastrulation. *Cell Reports* **16**:866–877. DOI: https://doi.org/10.1016/j.celrep.2016.06.036, PMID: 27396324

Schier AF, Talbot WS. 2005. Molecular genetics of axis formation in zebrafish. *Annual Review of Genetics* **39**:561–613. DOI: https://doi.org/10.1146/annurev.genet.37.110801.143752, PMID: 16285872

Schindelin J, Arganda-Carreras I, Frise E, Kaynig V, Longair M, Pietzsch T, Preibisch S, Rueden C, Saalfeld S, Schmid B, Tinevez JY, White DJ, Hartenstein V, Eliceiri K, Tomancak P, Cardona A. 2012. Fiji: an open-source platform for biological-image analysis. *Nature Methods* **9**:676–682. DOI: https://doi.org/10.1038/nmeth.2019, PMID: 22743772

Schmid B, Shah G, Scherf N, Weber M, Thierbach K, Campos CP, Roeder I, Aanstad P, Huisken J. 2013. High-speed panoramic light-sheet microscopy reveals global endodermal cell dynamics. *Nature Communications* **4**:2207. DOI: https://doi.org/10.1038/ncomms3207, PMID: 23884240

Sopory S, Nelsen SM, Degnin C, Wong C, Christian JL. 2006. Regulation of bone morphogenetic protein-4 activity by sequence elements within the prodomain. *Journal of Biological Chemistry* **281**:34021–34031. DOI: https://doi.org/10.1074/jbc.M605330200, PMID: 16966322

Tucker JA, Mintzer KA, Mullins MC. 2008. The BMP signaling gradient patterns dorsoventral tissues in a temporally progressive manner along the anteroposterior axis. *Developmental Cell* **14**:108–119. DOI: https://doi.org/10.1016/j.devcel.2007.11.004, PMID: 18194657

Umulis D, O'Connor MB, Blair SS. 2009. The extracellular regulation of bone morphogenetic protein signaling. *Development* **136**:3715–3728. DOI: https://doi.org/10.1242/dev.031534, PMID: 19855014

Varadarajan SG, Kong JH, Phan KD, Kao TJ, Panaitof SC, Cardin J, Eltzschig H, Kania A, Novitch BG, Butler SJ. 2017. Netrin1 Produced by Neural Progenitors, Not Floor Plate Cells, Is Required for Axon Guidance in the Spinal Cord. *Neuron* **94**:790–799. DOI: https://doi.org/10.1016/j.neuron.2017.03.007, PMID: 28434801

Xu PF, Houssin N, Ferri-Lagneau KF, Thisse B, Thisse C. 2014. Construction of a vertebrate embryo from two opposing morphogen gradients. *Science* **344**:87–89. DOI: https://doi.org/10.1126/science.1248252, PMID: 24700857

Yu SR, Burkhardt M, Nowak M, Ries J, Petrásek Z, Scholpp S, Schwille P, Brand M. 2009. Fgf8 morphogen gradient forms by a source-sink mechanism with freely diffusing molecules. *Nature* **461**:533–536. DOI: https://doi.org/10.1038/nature08391, PMID: 19741606

Zinski J, Bu Y, Wang X, Dou W, Umulis D, Mullins M. 2017. Systems biology derived source-sink mechanism of BMP gradient formation. *eLife* **6**:e22199. DOI: https://doi.org/10.7554/eLife.22199, PMID: 28826472

eLIFE elifesciences.org

RESEARCH ARTICLE

Figures and figure supplements

Dynamics of BMP signaling and distribution during zebrafish dorsal-ventral patterning

Autumn P Pomreinke *et al*

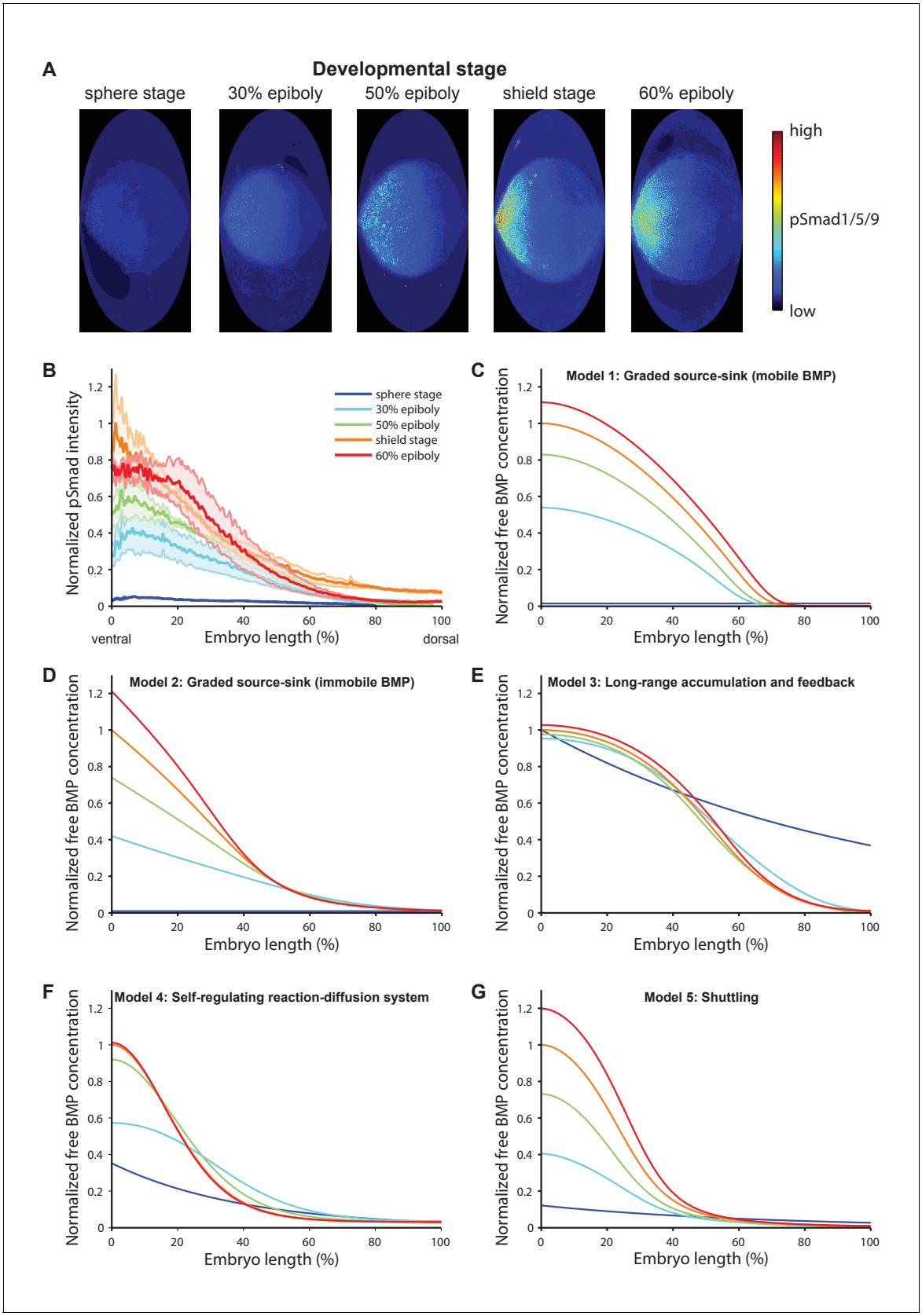

Figure 1. BMP signaling (pSmad1/5/9) gradient formation and simulations of five major dorsal-ventral patterning models over relevant zebrafish developmental stages (3 hr). (**A**) Two-dimensional Hammer-Aitoff projections (2D maps) of pSmad1/5/9-immunostained individual wild type zebrafish

Figure 1 continued on next page

Figure 1 continued

embryos at different developmental stages. Embryos were imaged using light sheet microscopy (see Materials and methods for details). (**B**) Quantification of ventral-to-dorsal average pSmad1/5/9 distributions in one-dimensional projections of 2D maps generated for embryos at different developmental stages (n = 3 for each stage) as in (**A**). Error bars denote standard error. (**C–G**) Gradient formation kinetics simulated for Models 1–5 at relevant zebrafish developmental stages.

DOI: https://doi.org/10.7554/eLife.25861.004

little to no diffusion
moderate diffusion
high diffusion

A Model 1: Graded source-sink (mobile BMP)

$$\frac{\partial[\mathrm{BMP}]}{\partial t} = D_{\mathrm{BMP}}\nabla^2[\mathrm{BMP}] - \kappa[\mathrm{Chd}][\mathrm{BMP}] - \lambda_{\mathrm{BMP}}[\mathrm{BMP}] + \rho_{\mathrm{BMP}}(x)$$

$$\frac{\partial[\mathrm{Chd}]}{\partial t} = D_{\mathrm{Chd}}\nabla^2[\mathrm{Chd}] - \kappa[\mathrm{Chd}][\mathrm{BMP}] - \lambda_{\mathrm{Chd}}[\mathrm{Chd}]$$

$$\frac{\partial[\mathrm{ChdBMP}]}{\partial t} = D_{\mathrm{ChdBMP}}\nabla^2[\mathrm{ChdBMP}] + \kappa[\mathrm{Chd}][\mathrm{BMP}] - \lambda_{\mathrm{Chd}}[\mathrm{ChdBMP}]$$

B Model 2: Graded source-sink (immobile BMP)

$$\frac{\partial[\mathrm{BMP}]}{\partial t} = -\kappa[\mathrm{Chd}][\mathrm{BMP}] - \lambda_{\mathrm{BMP}}[\mathrm{BMP}] + \rho_{\mathrm{BMP}}(x)$$

$$\frac{\partial[\mathrm{Chd}]}{\partial t} = D_{\mathrm{Chd}}\nabla^2[\mathrm{Chd}] - \kappa[\mathrm{Chd}][\mathrm{BMP}] - \lambda_{\mathrm{Chd}}[\mathrm{Chd}]$$

$$\frac{\partial[\mathrm{ChdBMP}]}{\partial t} = D_{\mathrm{ChdBMP}}\nabla^2[\mathrm{ChdBMP}] + \kappa[\mathrm{Chd}][\mathrm{BMP}] - \lambda_{\mathrm{Chd}}[\mathrm{ChdBMP}]$$

C Model 3: Long-range accumulation and feedback

$$\frac{\partial[\mathrm{BMP}]}{\partial t} = D\nabla^2[\mathrm{BMP}] + \frac{v_{\mathrm{BMP}}([\mathrm{ADMP}]+[\mathrm{BMP}])^{10}}{k_{\mathrm{BMP}}{}^{10} + ([\mathrm{ADMP}]+[\mathrm{BMP}])^{10}} - \lambda_{\mathrm{BMP}}[\mathrm{BMP}] + \frac{\lambda_{\mathrm{Chd}}[\mathrm{ChdBMP}]}{1 + \frac{[\mathrm{Szl}]}{ki} + \frac{[\mathrm{Chd}]+[\mathrm{ChdBMP}]+[\mathrm{ChdADMP}]}{km}} - k[\mathrm{Chd}][\mathrm{BMP}]$$

$$\frac{\partial[\mathrm{Chd}]}{\partial t} = D\nabla^2[\mathrm{Chd}] + \frac{v_{\mathrm{Chd}}k_{\mathrm{Chd}}{}^{10}}{k_{\mathrm{Chd}}{}^{10} + ([\mathrm{ADMP}]+[\mathrm{BMP}])^{10}} - \frac{\lambda_{\mathrm{Chd}}[\mathrm{Chd}]}{1 + \frac{[\mathrm{Szl}]}{ki} + \frac{[\mathrm{Chd}]+[\mathrm{ChdBMP}]+[\mathrm{ChdADMP}]}{km}} - k[\mathrm{Chd}][\mathrm{BMP}] - k[\mathrm{Chd}][\mathrm{ADMP}]$$

$$\frac{\partial[\mathrm{ADMP}]}{\partial t} = D\nabla^2[\mathrm{ADMP}] + \frac{v_{\mathrm{ADMP}}k_{\mathrm{ADMP}}{}^{10}}{k_{\mathrm{ADMP}}{}^{10} + ([\mathrm{ADMP}]+[\mathrm{BMP}])^{10}} - \lambda_{\mathrm{BMP}}[\mathrm{ADMP}] + \frac{\lambda_{\mathrm{Chd}}[\mathrm{ChdADMP}]}{1 + \frac{[\mathrm{Szl}]}{ki} + \frac{[\mathrm{Chd}]+[\mathrm{ChdBMP}]+[\mathrm{ChdADMP}]}{km}} - k[\mathrm{Chd}][\mathrm{ADMP}]$$

$$\frac{\partial[\mathrm{Szl}]}{\partial t} = D\nabla^2[\mathrm{Szl}] + \frac{v_{\mathrm{Szl}}([\mathrm{ADMP}]+[\mathrm{BMP}])^{20}}{k_{\mathrm{Szl}}{}^{20} + ([\mathrm{ADMP}]+[\mathrm{BMP}])^{20}} - \lambda_{\mathrm{Szl}}[\mathrm{Szl}]$$

$$\frac{\partial[\mathrm{ChdBMP}]}{\partial t} = D\nabla^2[\mathrm{ChdBMP}] - \frac{\lambda_{\mathrm{Chd}}[\mathrm{ChdBMP}]}{1 + \frac{[\mathrm{Szl}]}{ki} + \frac{[\mathrm{Chd}]+[\mathrm{ChdBMP}]+[\mathrm{ChdADMP}]}{km}} + k[\mathrm{Chd}][\mathrm{BMP}]$$

$$\frac{\partial[\mathrm{ChdADMP}]}{\partial t} = D\nabla^2[\mathrm{ChdADMP}] - \frac{\lambda_{\mathrm{Chd}}[\mathrm{ChdADMP}]}{1 + \frac{[\mathrm{Szl}]}{ki} + \frac{[\mathrm{Chd}]+[\mathrm{ChdBMP}]+[\mathrm{ChdADMP}]}{km}} + k[\mathrm{Chd}][\mathrm{ADMP}]$$

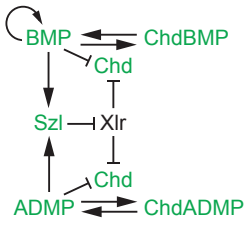

D Model 4: Self-regulating reaction-diffusion system

$$\frac{\partial[\mathrm{BMP}]}{\partial t} = D_{\mathrm{BMP}}\nabla^2[\mathrm{BMP}] + \frac{[\mathrm{BMP}]^2}{(1+[\mathrm{Chd}])[\mathrm{Szl}]} - \mu_{\mathrm{BMP}}[\mathrm{BMP}] + \rho_{\mathrm{BMP}}$$

$$\frac{\partial[\mathrm{Chd}]}{\partial t} = D_{\mathrm{Chd}}\nabla^2[\mathrm{Chd}] + \frac{[\mathrm{Chd}]^2}{[\mathrm{ADMP}]} - \mu_{\mathrm{Chd}}[\mathrm{Chd}] + \rho_{\mathrm{Chd}}$$

$$\frac{\partial[\mathrm{ADMP}]}{\partial t} = D_{\mathrm{ADMP}}\nabla^2[\mathrm{ADMP}] + [\mathrm{Chd}]^2 - \mu_{\mathrm{ADMP}}[\mathrm{ADMP}]$$

$$\frac{\partial[\mathrm{Szl}]}{\partial t} = D_{\mathrm{Szl}}\nabla^2[\mathrm{Szl}] + [\mathrm{BMP}]^2 - \mu_{\mathrm{Szl}}[\mathrm{Szl}]$$

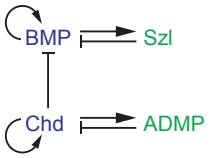

E Model 5: Shuttling

$$\frac{\partial[\mathrm{BMP}]}{\partial t} = D_{\mathrm{BMP}}\nabla^2[\mathrm{BMP}] - \kappa[\mathrm{Chd}][\mathrm{BMP}] + \lambda[\mathrm{Xlr}][\mathrm{ChdBMP}] - \lambda_{\mathrm{BMP}}[\mathrm{BMP}] + \rho_{\mathrm{BMP}}(x)$$

$$\frac{\partial[\mathrm{Chd}]}{\partial t} = D_{\mathrm{Chd}}\nabla^2[\mathrm{Chd}] - \kappa[\mathrm{Chd}][\mathrm{BMP}] - \lambda_{\mathrm{Chd}}[\mathrm{Chd}]$$

$$\frac{\partial[\mathrm{ChdBMP}]}{\partial t} = D_{\mathrm{ChdBMP}}\nabla^2[\mathrm{ChdBMP}] + \kappa[\mathrm{Chd}][\mathrm{BMP}] - \lambda[\mathrm{Xlr}][\mathrm{ChdBMP}] - \lambda_{\mathrm{Chd}}[\mathrm{ChdBMP}]$$

Figure 1—figure supplement 1. Mathematical formulation of five major models of BMP/Chordin-mediated dorsal-ventral patterning. See Materials and methods for details. Selected essential features of the models are illustrated on the right. (**A**) Model 1: Graded source-sink (mobile BMP). In this model, BMP diffuses from a ventrally biased graded source, and Chordin produced from the dorsal side inhibits BMP by irreversible binding. (**B**) Model 2: Graded source-sink (immobile BMP). In this model, BMP diffusion is negligible (D = 0 $\mu m^2/s$). The mechanism of restricting BMP signaling by Chordin irreversibly binding to BMP is the same as in Model 1, but with weaker binding kinetics. (**C**) Model 3: Long-range accumulation and feedback. Model and parameters were adapted from (***Inomata et al., 2013***). (**D**) Model 4: Self-regulating reaction-diffusion system. Model and parameters were adapted

Figure 1—figure supplement 1 continued on next page

Figure 1—figure supplement 1 continued

from (***Francois et al., 2009***). (**E**) Model 5: Shuttling. A simplified model without feedback to purely illustrate the biophysical aspects of shuttling was adapted from (***Ben-Zvi et al., 2008***).

DOI: https://doi.org/10.7554/eLife.25861.005

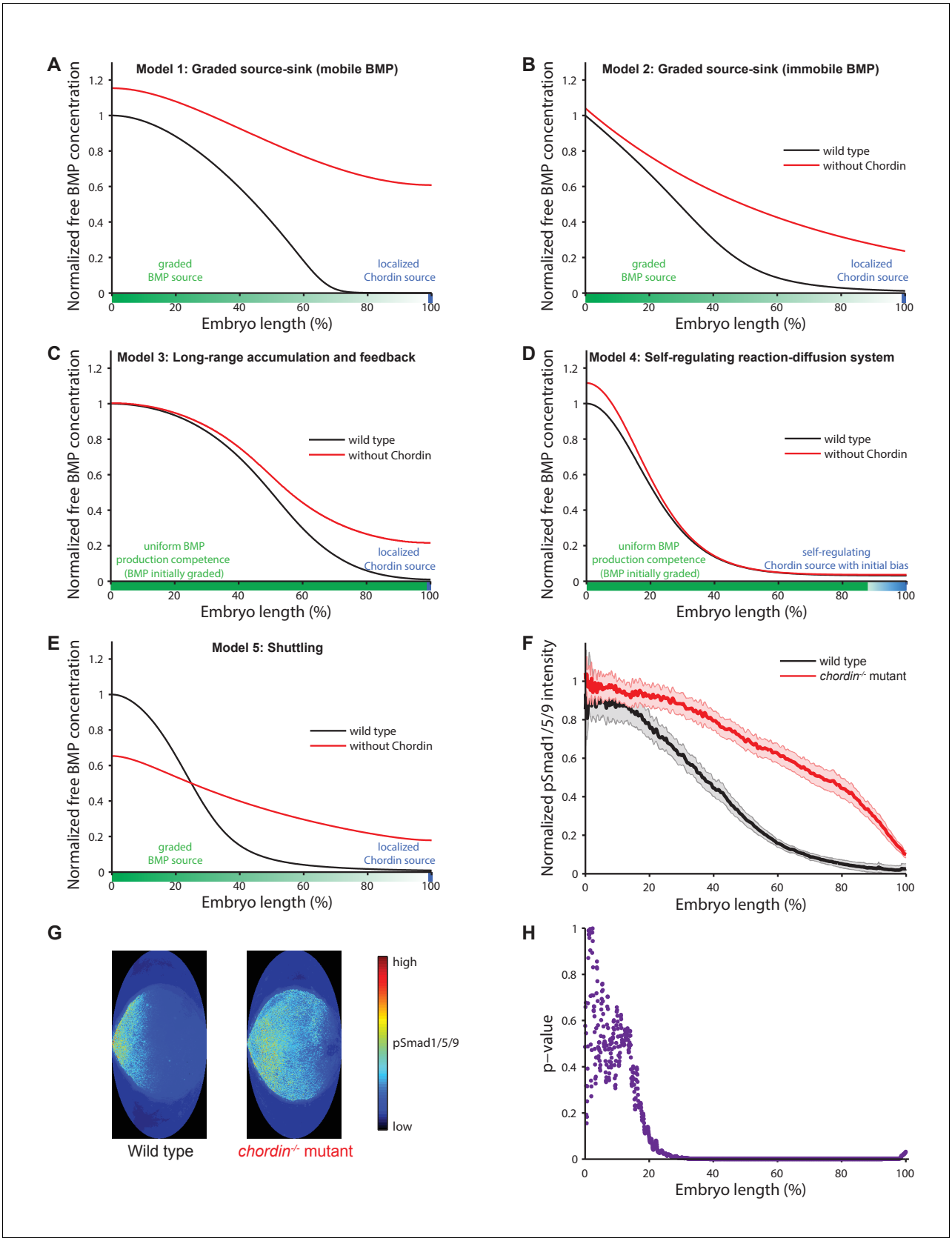

Figure 2. Theoretical predictions for the influence of the inhibitor Chordin on the BMP signaling gradient and experimental test. (**A–E**) Simulations of BMP distributions in five major models of dorsal-ventral patterning in the presence (black) or absence (red) of Chordin. The BMP and Chordin sources

Figure 2 continued on next page

Figure 2 continued

are indicated below each graph in green and blue, respectively. Note that the spatial production rates in Models 3 and 4 are modulated over time by feedback. (**F–G**) Quantification of average pSmad1/5/9 distributions in wild type (black) and *chordin*$^{-/-}$ (red) embryos using one-dimensional projections of 2D maps. Wild type n = 7, *chordin*$^{-/-}$ mutants n = 10. Error bars denote standard error. (**H**) p-values (unpaired two-tailed t-test assuming equal variance) calculated as a function of space between pSmad1/5/9 distributions in wild type and *chordin*$^{-/-}$ embryos shown in (**F**) indicate no significant difference of pSmad1/5/9 on the ventral side but a dramatic expansion into dorsal-lateral domains.

DOI: https://doi.org/10.7554/eLife.25861.011

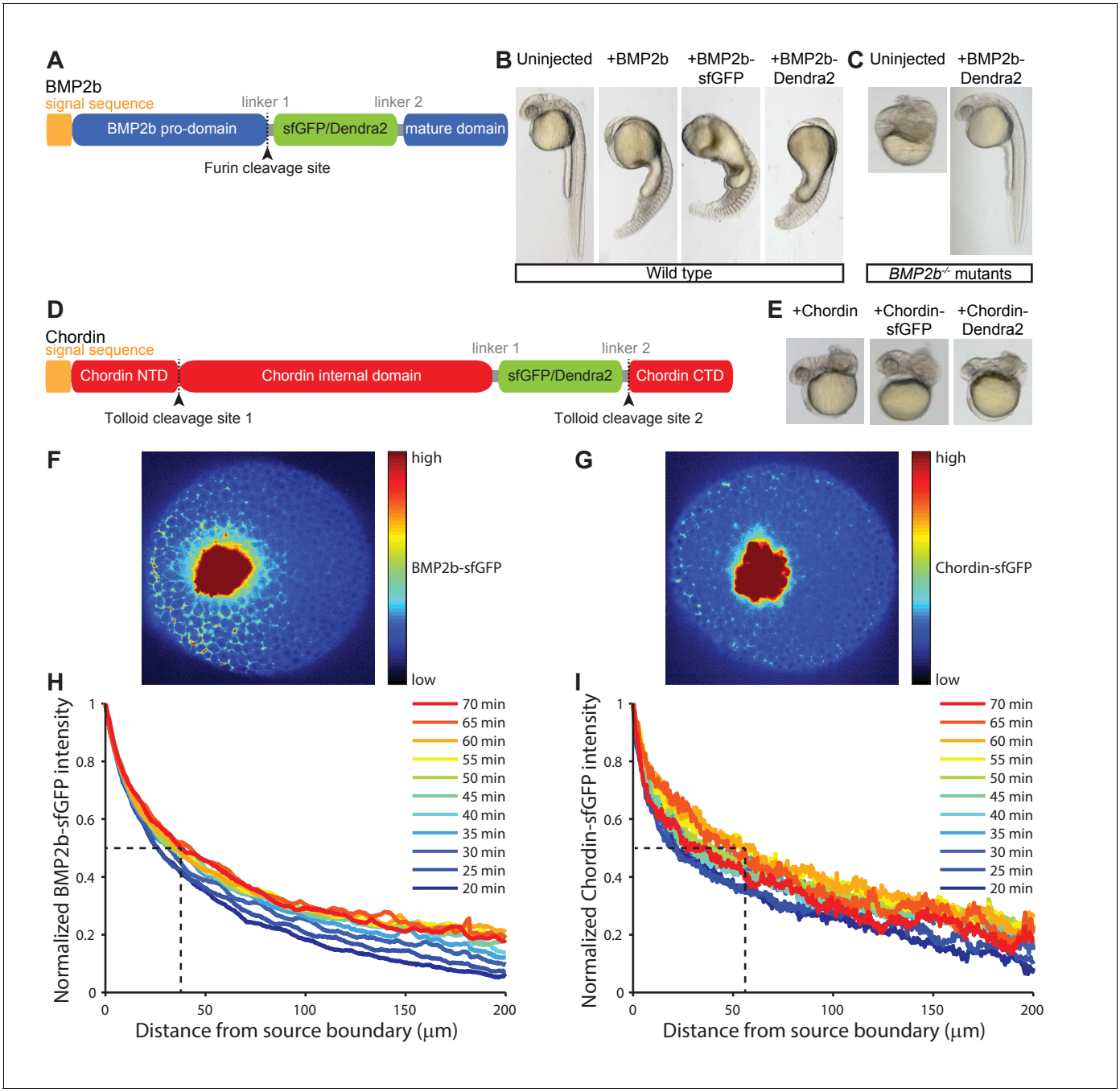

Figure 3. Gradient formation kinetics of fluorescently tagged BMP and Chordin. (**A**) Schematic of BMP2b-sfGFP and -Dendra2 fusion constructs. (**B**) Fluorescent BMP2b fusion constructs can induce ventralization, a BMP-overexpression phenotype (***Kishimoto et al., 1997***). mRNA amounts equimolar to 2 pg of *BMP2b* mRNA were injected at the one-cell stage, and images were taken 30 hr post-fertilization (hpf). (**C**) Rescue of a *BMP2b* mutant ($swr^{-/-}$) with BMP2b-Dendra2. 2.74 pg of BMP2b-Dendra2-encoding mRNA were injected at the one-cell stage, and images were taken at 30 hpf. In a separate experiment with 1 pg of BMP2b-sfGFP-encoding mRNA, 20% (9/44) of all injected $swr^{-/-}$ mutants were rescued, 16% (7/44) were ventralized, and 64% (28/44) were dorsalized. (**D**) Schematic of Chordin-sfGFP and -Dendra2 fusion constructs. (**E**) Fluorescent Chordin constructs can induce dorsalization, a *Chordin*-overexpression phenotype. mRNA amounts equimolar to 30 pg of *Chordin* mRNA were injected into wild type embryos at the one-cell stage, and images were taken at 30 hpf. F + G) Light sheet microscopy images of BMP- and Chordin-sfGFP gradients forming from a local source in live zebrafish embryos. Approximately 50–75 cells expressing *BMP2b-sfGFP* (**F**) or *Chordin-sfGFP* (**G**) were transplanted into host embryos at sphere stage (see Materials and methods for details). The images show gradient formation in single optical slices approximately 20 min after transplantation. H + I) Quantification of BMP2b-sfGFP (**H**) and Chordin-sfGFP (**I**) gradient formation kinetics from a local source (BMP2b-sfGFP: n = 8;

Figure 3 continued on next page

Figure 3 continued

Chordin-sfGFP: n = 5). Dashed lines indicate the distance at which the protein distributions drop to 50% of their maximal concentration 60 min post-transplantation.

DOI: https://doi.org/10.7554/eLife.25861.013

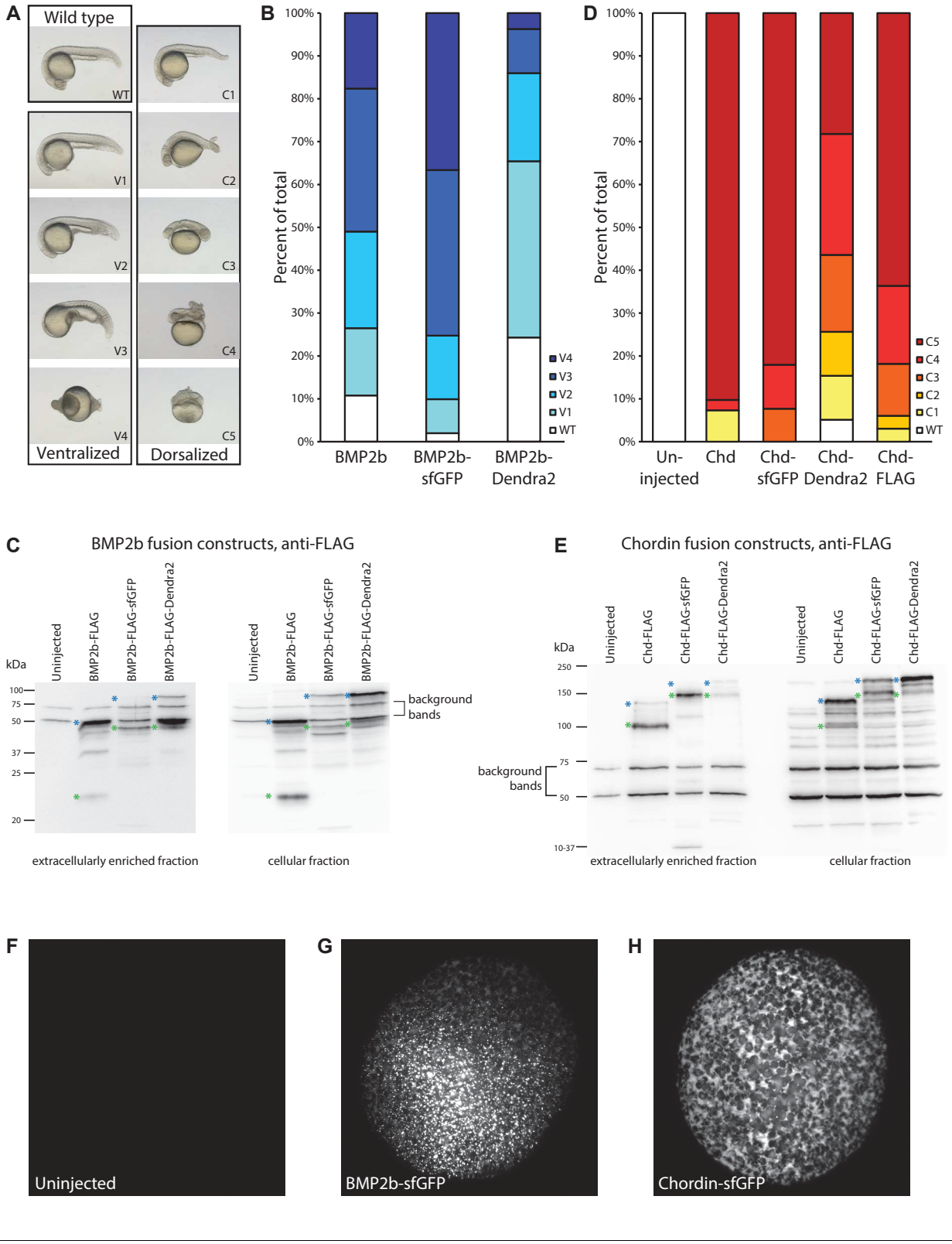

Figure 3—figure supplement 1. Detailed characterization of fluorescently tagged BMP2b and Chordin. (**A**) Ventralized and dorsalized phenotypes at 24 hr post-fertilization (hpf) were categorized using established classification schemes (***Mullins et al., 1996***; ***Kishimoto et al., 1997***). (**B**) Embryos were

Figure 3—figure supplement 1 continued on next page

Figure 3—figure supplement 1 continued

injected with equimolar amounts of mRNA encoding BMP2b (1 pg, n = 102), BMP2b-sfGFP (1.49 pg, n = 101), and BMP2b-Dendra2 (1.47 pg, n = 107) at the one-cell stage. BMP2b-sfGFP induced stronger ventralization, and BMP2b-Dendra2 induced weaker ventralization compared to untagged BMP2b. (**C**) To determine whether the differences in the degree of ventralization (**B**) are due to changes in protein activity or protein levels, extracellularly enriched extracts were obtained from zebrafish embryos injected with mRNA amounts equimolar to 444 pg BMP2b-FLAG-encoding mRNA. Levels and processing of FLAG-tagged BMP ligands were assessed using anti-FLAG western blots. Green asterisks to the left of a band indicate properly processed mature BMP2b ligand; blue asterisks indicate unprocessed full-length pro-protein. Similar to FLAG-tagged BMP2b, FLAG-tagged BMP2b-sfGFP and -Dendra2 are properly processed and mostly secreted as mature ligands into the extracellular space. BMP2b-sfGFP-FLAG protein levels are higher compared to FLAG-tagged BMP2b, possibly owing to the rapid folding kinetics of sfGFP (***Pédelacq et al., 2006***); in contrast, BMP2b-Dendra2-FLAG levels are lower. The correlation between protein levels and activity (**B**) suggests that the fluorescent BMP2b constructs are equivalent to untagged BMP2b in inducing downstream signaling responses. (**D**) Phenotype distributions at 24 hpf. Zebrafish embryos were injected at the one-cell stage with equimolar amounts of mRNA encoding Chordin (30 pg, n = 41), Chordin-sfGFP (37 pg, n = 39), Chordin-Dendra2 (37 pg, n = 39), and Chordin-FLAG (30 pg, n = 33) (uninjected: n = 49). (**E**) Extracellularly enriched fractions were obtained from zebrafish embryos injected with mRNA equimolar to 500 pg of Chordin-FLAG-encoding mRNA. Levels and processing of FLAG-tagged Chordin constructs were assessed using anti-FLAG western blots. Green asterisks indicate properly processed mature Chordin; blue asterisks indicate unprocessed full-length protein. Similar to the correlation between BMP2b construct levels and ventralization activity, the dorsalization activity of Chordin constructs (**D**) is correlated with protein levels. (**F–H**) Distribution of BMP2b/Chordin-sfGFP in transplantation donors similar to those used in experiments shown in ***Figures 3*** and ***5*** . Embryos were injected at the one-cell stage with 500 pg BMP2b-sfGFP- (**G**) or 1000 pg Chordin-sfGFP- (**H**) encoding mRNA (compare to uninjected embryo (**F**)). Embryos were imaged using light sheet microscopy at sphere stage (5–5.5 hpf), when transplantations were carried out in the experiments shown in ***Figures 3*** and ***5***. Maximum intensity projections are shown.

DOI: https://doi.org/10.7554/eLife.25861.014

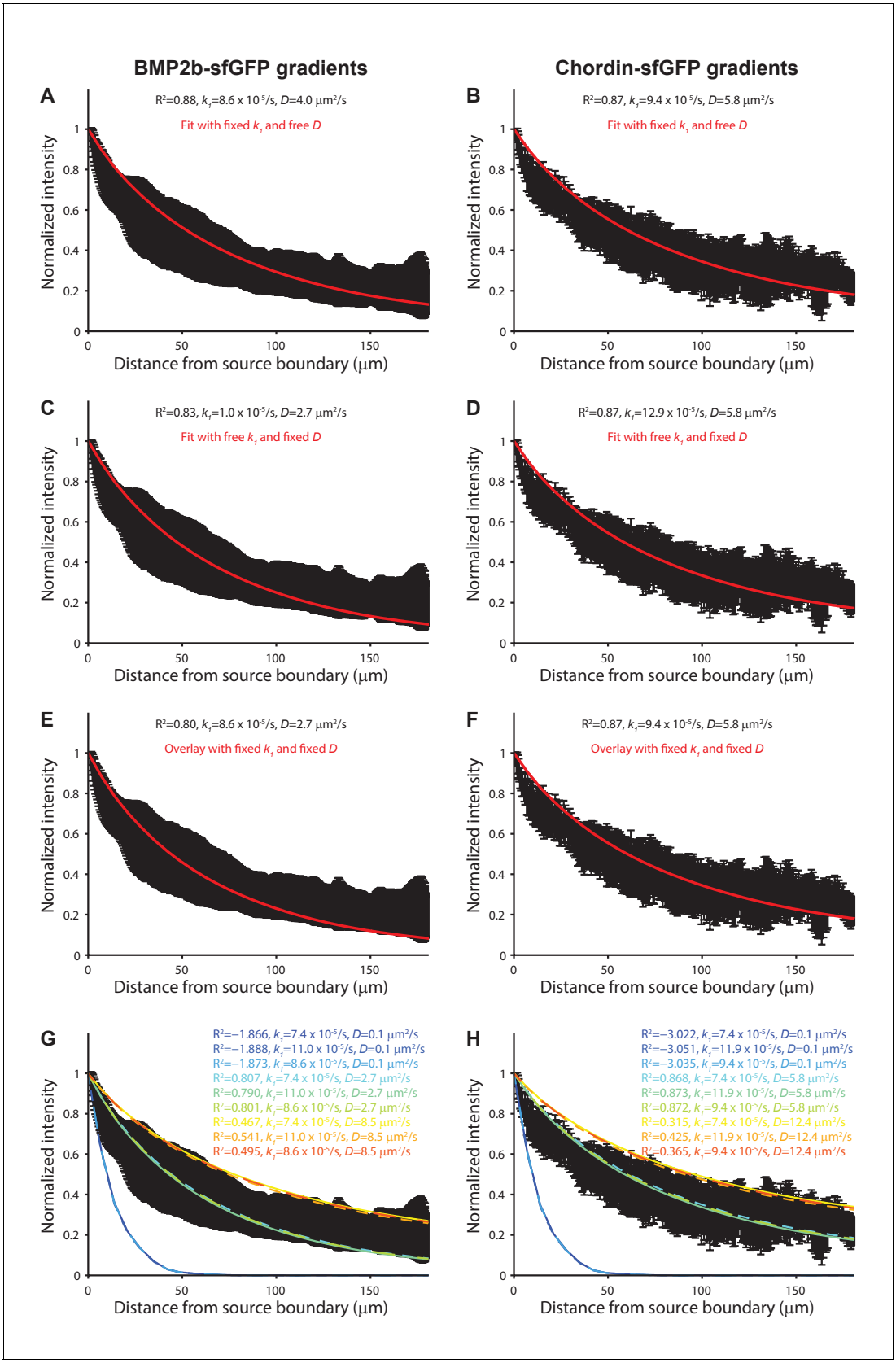

Figure 3—figure supplement 2. Modeling of BMP and Chordin gradient formation kinetics and comparison to measured gradients. Gradient simulations were executed in a three-dimensional embryo-like geometry with a local production source and uniform diffusion and clearance as in

Figure 3—figure supplement 2 continued on next page

Figure 3—figure supplement 2 continued

(***Müller et al., 2012***). Gradient formation was simulated for 70 min and compared to gradients measured in vivo ≈70–75 min post-transplantation. A 50 by 50 logarithmically spaced parameter grid was simulated for diffusion coefficients (*D*) ranging from 0.1 to 50 $\mu m^2/s$ and clearance rate constants (k_1) ranging from to $1 \times 10^{-5}/s$ to $5 \times 10^{-4}/s$. The fits in (**A**) and (**B**) were constrained with the measured clearance rate constants of BMP2b-Dendra2 and Chordin-Dendra2 and fitted with *D* as the free parameter. The fits in (**C**) and (**D**) were constrained with the measured diffusion coefficients of fluorescent BMP2b and Chordin constructs and fitted with k_1 as the free parameter. The data in (**E**) and (**F**) was overlaid with simulations using the measured *D* and k_1 values. (**G–H**) Sensitivity analysis of gradient simulations with all combinations of measured *D* and k_1 values as well as *D* and k_1 values three standard deviations above and below the measured averages (rainbow colors) overlaid with the experimental data (black). R^2 values indicate the goodness of the fit. Error bars denote standard deviation.

DOI: https://doi.org/10.7554/eLife.25861.015

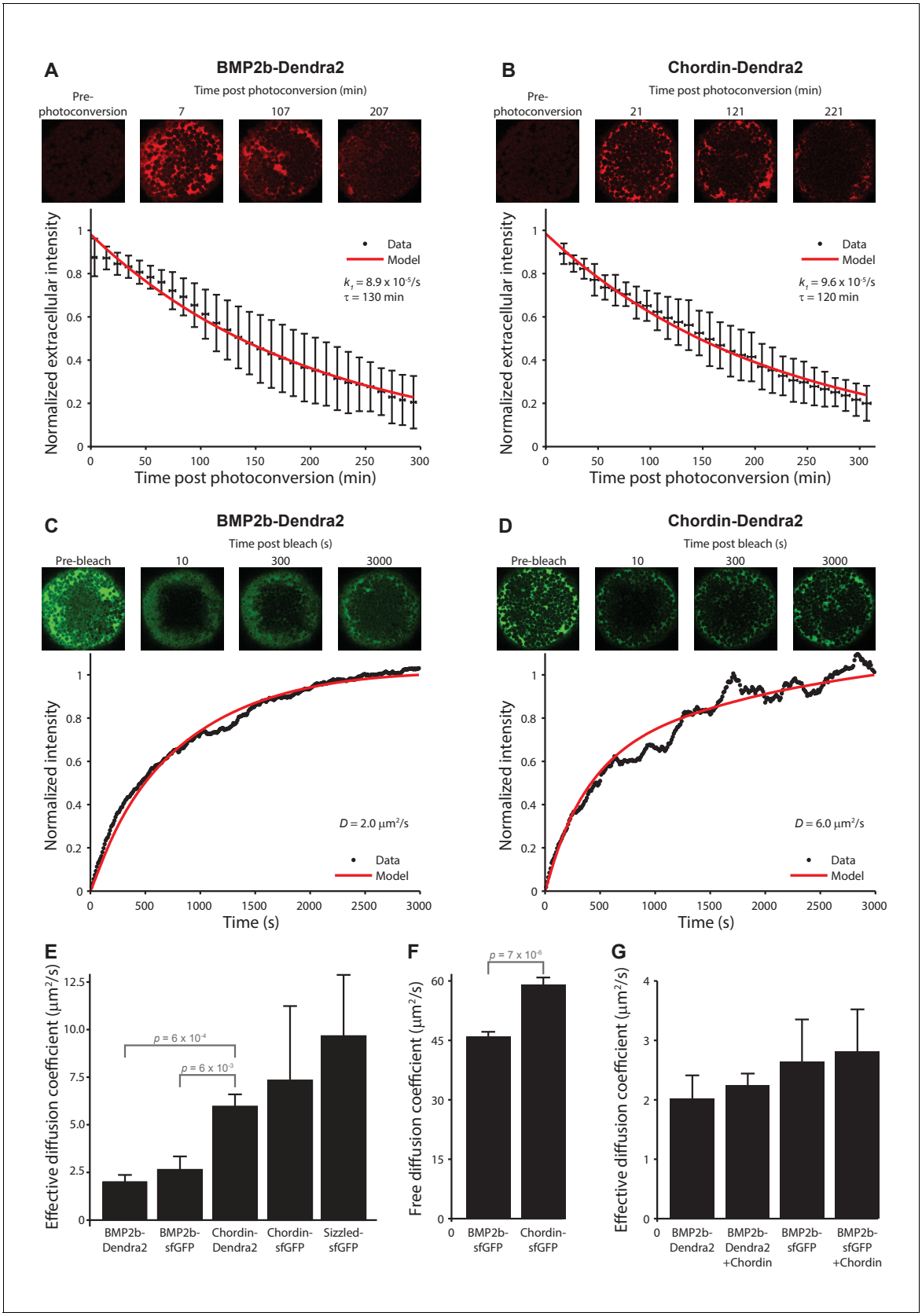

Figure 4. Biophysical measurements of BMP and Chordin protein stability and diffusivity. A + B) FDAP protein stability measurements for BMP2b-Dendra2 (**A**) and Chordin-Dendra2 (**B**). Error bars denote standard deviation. BMP2b-Dendra2: n = 22; Chordin-Dendra2: n = 6. C + D) FRAP effective

Figure 4 continued on next page

Figure 4 continued

protein diffusivity measurements for BMP2b-Dendra2 (**C**) and Chordin-Dendra2 (**D**). Data and fits from single experiments are shown. (**E**) Bar chart of the average effective diffusion coefficients from FRAP experiments. Error bars denote standard error. BMP2b-Dendra2: n = 6; BMP2b-sfGFP: n = 8; Chordin-Dendra2: n = 8; Chordin-sfGFP: n = 6; Sizzled-sfGFP: n = 12. (**F**) Free diffusion coefficients of BMP2b-sfGFP and Chordin-sfGFP measured by Fluorescence Correlation Spectroscopy (FCS) in a diffraction-limited spot within the zebrafish embryonic extracellular space far away from cell membranes (see Materials and methods for details). Error bars denote standard error. BMP2b-sfGFP: n = 17 measurements from 4 embryos; Chordin-sfGFP: n = 19 measurements from 5 embryos. (**G**) Negligible influence of Chordin on BMP2b effective diffusion. Untagged Chordin was co-expressed with BMP2b-Dendra2 (n = 8) or BMP2b-sfGFP (n = 9) in zebrafish embryos subjected to FRAP measurements at blastula stages. The data shown for BMP2b-Dendra2 and BMP2b-sfGFP FRAP experiments without co-expressed *Chordin* is identical to the data shown in (**E**). p-values (unpaired two-tailed t-test assuming equal variance) are shown for statistically significant ($p<0.05$) data sets.

DOI: https://doi.org/10.7554/eLife.25861.018

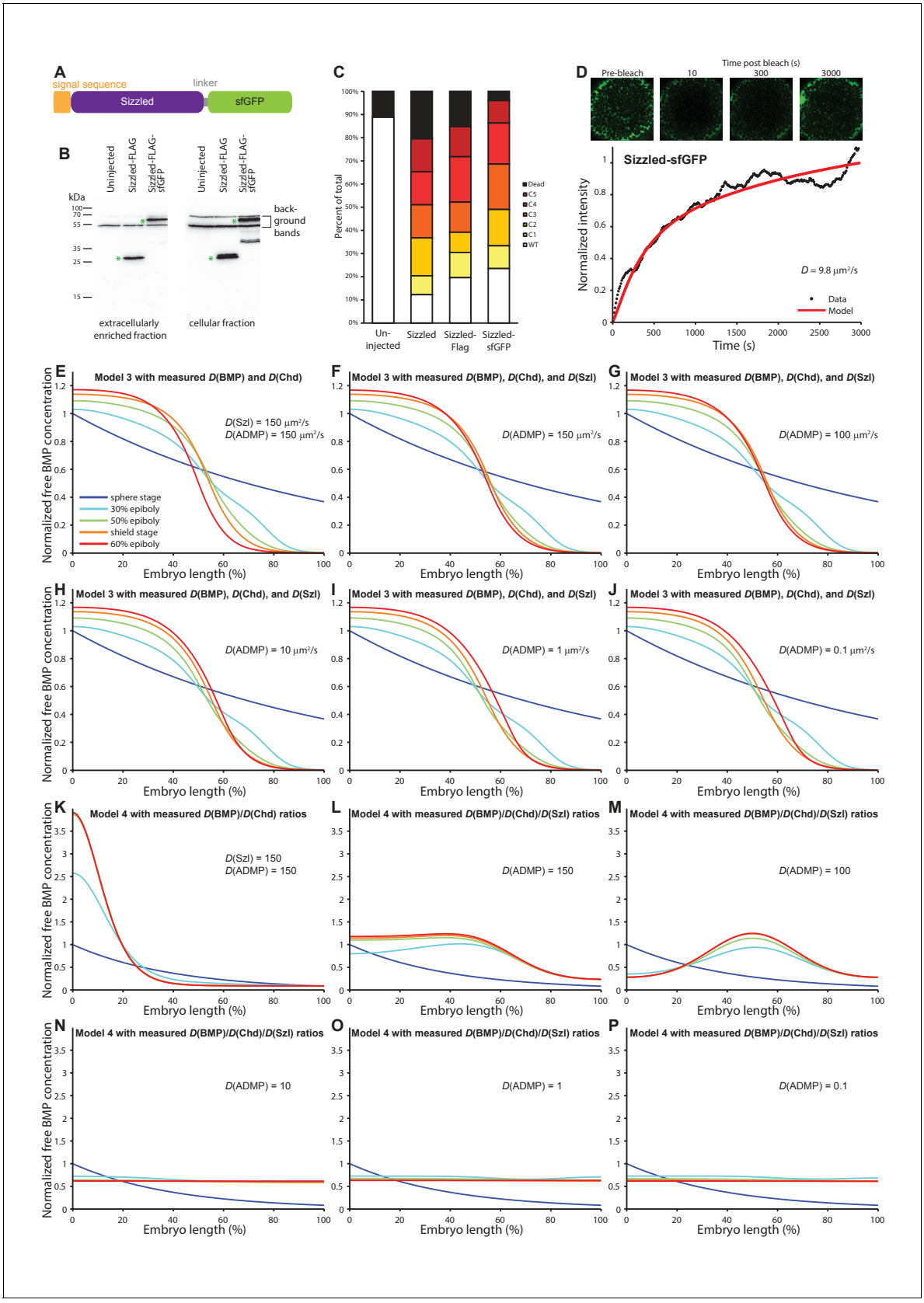

Figure 4—figure supplement 1. Characterization of Sizzled diffusion and its role in gradient formation. (**A**) Schematic of the Sizzled-sfGFP fusion protein. (**B**) Anti-FLAG western blot analysis of Sizzled-sfGFP. Green asterisks indicate full-length Sizzled fusions. (**C**) Characterization of phenotypes

Figure 4—figure supplement 1 continued on next page

Figure 4—figure supplement 1 continued

after overexpression of Sizzled fusion proteins (mRNA injections at the one-cell stage equivalent to 1 pg *sizzled* mRNA; uninjected n = 45, Sizzled n = 49, Sizzled-FLAG n = 46, Sizzled-sfGFP n = 51). (**D**) FRAP analysis of Sizzled-sfGFP effective diffusion (D = 9.7 ± 3.2 $\mu m^2/s$, n = 12). Data and fit from a single experiment is shown. (**E–J**) Simulations of Model 3 using the effective diffusion coefficients of BMP2b and Chordin measured here instead of the previously assumed value D = 15 $\mu m^2/s$ (***Inomata et al., 2013***). The diffusion coefficient of Sizzled was set to 150 $\mu m^2/s$ in (**E**) and to the measured value of 10 $\mu m^2/s$ in (**F–J**). ADMP diffusivity was varied from 0.1 $\mu m^2/s$ to 150 $\mu m^2/s$ as indicated in (**E–J**). Gradients form over time, but the gradient evolution profiles are not consistent with the pSmad1/5/9 distribution measurements in ***Figure 1B***. (**K–P**) Simulations of Model 4 using the ratio of effective BMP/Chordin diffusion coefficients (i.e. Chordin is approximately two to three times more diffusive than BMP; D(BMP) = 3, D(Chordin) = 6) measured here. The diffusion coefficient of Sizzled was set to 150 in (**K**) as in (***Francois et al., 2009***) and to 10 in (**L–P**), reflecting the ~3 fold higher measured diffusivity of Sizzled compared to BMP2b. ADMP diffusivity was varied from 0.1 to 150 (***Francois et al., 2009***) as indicated in (**K–P**). With 50-fold higher diffusion coefficients for ADMP and Sizzled compared to BMP (**K**) gradients peaking on the ventral side form over time, but with realistic diffusion ratios relevant gradients do not form (**L–P**).

DOI: https://doi.org/10.7554/eLife.25861.019

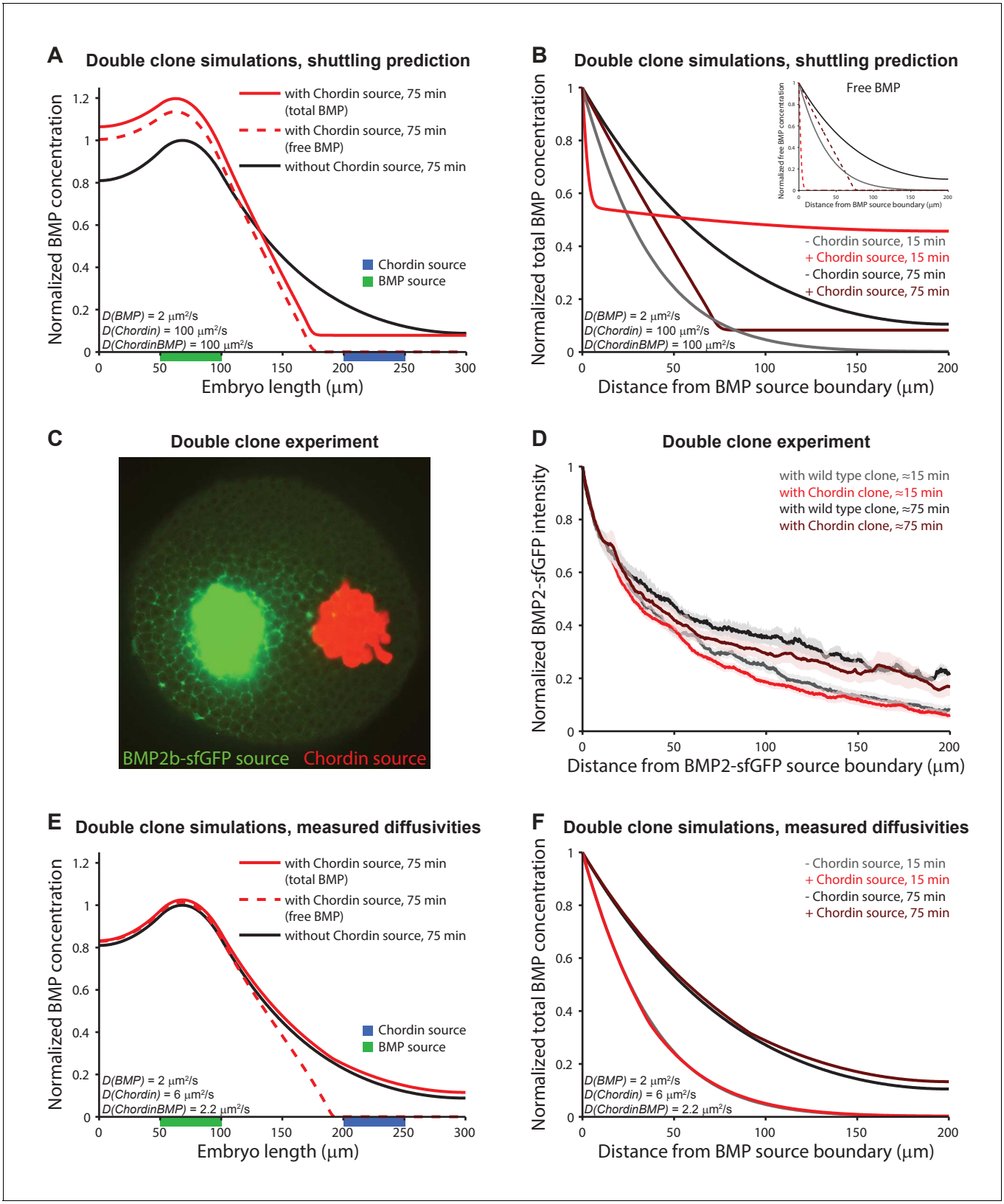

Figure 5. Testing shuttling of BMP2b predicted by Model 5. (**A**) One-dimensional model of two clones expressing BMP (green) or Chordin (blue) with D_{BMP} = 2 μm^2/s, D_{Chd} = 100 μm^2/s, and D_{ChdBMP} = 100 μm^2/s. BMP levels increase over time due to constant production. In the presence of Chordin, the BMP gradient is deflected away from the Chordin source indicative of shuttling (compare black and red lines). Solid lines show total BMP levels (i.e.

Figure 5 continued on next page

Figure 5 continued

BMP + ChdBMP in the presence of Chordin), and dashed line shows free BMP levels. (**B**) BMP gradients to the right of the BMP-expressing clone re-normalized to the BMP concentration at the source boundary to demonstrate that the range of BMP is decreased between the two clones in the presence of Chordin. The main panel shows total BMP levels (i.e., BMP + ChdBMP in the presence of Chordin), and the inset shows free BMP levels (dashed lines). (**C**) Experimental test of the predictions in (**A**) and (**B**). Clones of cells expressing BMP2b-sfGFP (green) were generated by transplanting approximately 50–75 cells from a donor embryo into wild type hosts at sphere stage (see Materials and methods for details). Another clone of cells (red) was transplanted next to the BMP2b-sfGFP-expressing clone shortly after. The red clone is marked by the presence of fluorescent Alexa 546-coupled dextran. Cells from red-labeled clones either contained only Alexa 546-coupled dextran (***Video 9***) or Alexa-546-coupled dextran and ectopic *chordin* mRNA (***Video 10***). 15–20 min after transplantation of the clones, embryos were imaged using light sheet microscopy. The image shows gradient formation in a single optical slice approximately 20 min after transplantation. (**D**) Quantification of average BMP2b-sfGFP gradients at ~15 min or ~75 min after transplantation in embryos generated as in (**C**) with (red/brown) or without (black/gray) ectopic Chordin sources. Error bars denote standard error. n = 8 for each condition. (**E**) One-dimensional simulation of two clones expressing BMP (green) or Chordin (blue) with the experimentally measured diffusion coefficients D_{BMP} = 2 $\mu m^2/s$, D_{Chd} = 6 $\mu m^2/s$, and D_{ChdBMP} = 2.2 $\mu m^2/s$. BMP levels increase over time due to constant production. Solid lines show total BMP levels (i.e. BMP + ChdBMP in the presence of Chordin), and the dashed line shows free BMP levels. Only the distribution of free BMP is affected as a consequence of Chordin binding, and the gradient of total BMP is not deflected away from the Chordin source (compare solid black and red lines). (**F**) Gradients of total BMP levels to the right of the BMP expressing clone simulated with the experimentally measured diffusion coefficients (D_{BMP} = 2 $\mu m^2/s$, D_{Chd} = 6 $\mu m^2/s$, and D_{ChdBMP} = 2.2 $\mu m^2/s$) and renormalized to the concentration at the boundary show that the range of BMP is not decreased between the two clones in the presence of Chordin.

DOI: https://doi.org/10.7554/eLife.25861.020

Article

Cell Reports

Integration of Nodal and BMP Signaling by Mutual Signaling Effector Antagonism

Graphical Abstract

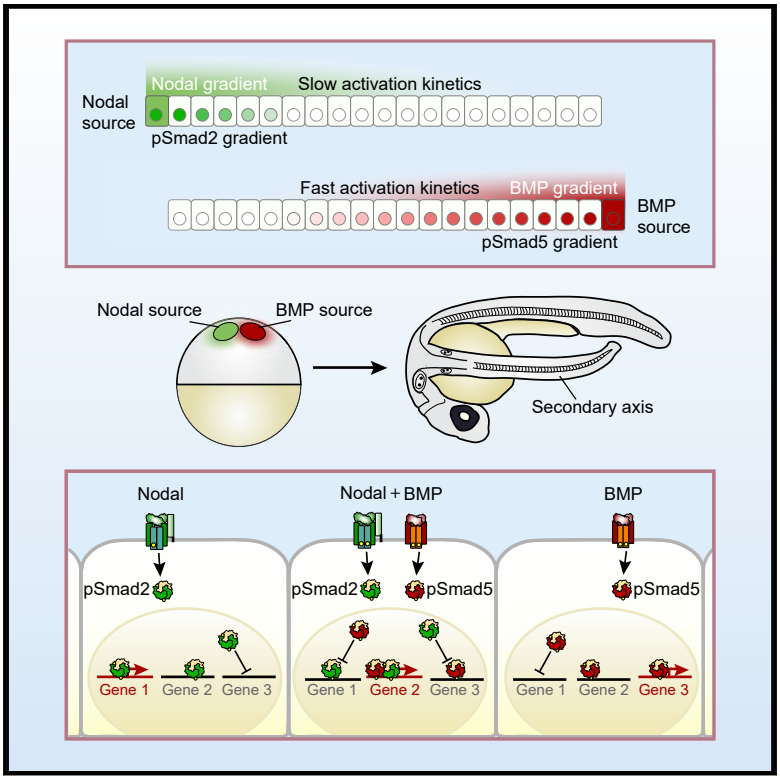

Highlights

- Nodal induces pSmad at a shorter range than BMP due to slower activation kinetics
- Different ratios of active Smad2 and Smad5 can induce different embryonic structures
- Smad2 and Smad5 inhibit each other or act synergistically to induce specific cell fates

Authors

Gary Huiming Soh,
Autumn Penecilla Pomreinke,
Patrick Müller

Correspondence

patrick.mueller@tuebingen.mpg.de

In Brief

Juxtaposed Nodal and BMP sources can induce the formation of a secondary axis in zebrafish embryos. Soh et al. analyze the input-output relationships in this patterning system and find that differential signaling kinetics lead to different activity ranges of Nodal and BMP, which are crucial for secondary axis formation.

Soh et al., 2020, Cell Reports *31*, 107487
April 7, 2020
https://doi.org/10.1016/j.celrep.2020.03.051

CellPress

Cell Reports
Article

Integration of Nodal and BMP Signaling by Mutual Signaling Effector Antagonism

Gary Huiming Soh,[1] Autumn Penecilla Pomreinke,[1] and Patrick Müller[1,2,3,*]
[1]Systems Biology of Development Group, Friedrich Miescher Laboratory of the Max Planck Society, Max-Planck-Ring 9, 72076 Tübingen, Germany
[2]Modeling Tumorigenesis Group, Translational Oncology Division, Eberhard Karls University Tübingen, Otfried-Müller-Straße 10, 72076 Tübingen, Germany
[3]Lead Contact
*Correspondence: patrick.mueller@tuebingen.mpg.de
https://doi.org/10.1016/j.celrep.2020.03.051

SUMMARY

Opposing sources of bone morphogenetic protein (BMP) and Nodal signaling molecules are sufficient to induce the formation of a full axis in zebrafish embryos. To address how these signals orchestrate patterning, we transplant sources of fluorescently tagged Nodal and BMP into zebrafish embryos, robustly inducing the formation of secondary axes. Nodal and BMP signal non-cell-autonomously and form similar protein gradients in this context, but the signaling range of Nodal (pSmad2) is shorter than the BMP range (pSmad5). This yields a localized region of pSmad2 activity around the Nodal source, overlapping with a broad domain of pSmad5 activity across the embryo. Cell fates induced in various regions stereotypically correlate with pSmad2-to-pSmad5 ratios and can even be induced BMP- and Nodal-independently with different ratios of constitutively active Smad2 and Smad5. Strikingly, we find that Smad2 and Smad5 antagonize each other for specific cell fates, providing a mechanism for how cells integrate and discriminate between overlapping signals during development.

INTRODUCTION

During development, cells need to know their location and fate in order to form an embryo. The required positional information can be conveyed by gradients of secreted signaling molecules that diffuse from a localized source to induce exposure-dependent cell responses (reviewed in Müller et al., 2013; Rogers and Schier, 2011). The earliest cell-fate decisions during vertebrate development are controlled by the signaling molecules Nodal and BMP, which form orthogonal overlapping activity gradients in zebrafish embryos (Figure 1A). Nodal induces the formation of the germ layers, which are subdivided into ventral and dorsal territories by BMP signaling (reviewed in Rogers and Müller, 2019). Nodal and BMP are secreted transforming growth factor β (TGF-β) superfamily ligands (Zhou et al., 1993; Wozney et al., 1988), which signal through a hetero-tetrameric complex composed of ligand-specific serine/threonine kinase receptors (Wrana et al., 1992) as well as co-receptors (Shen and Schier, 2000). Nodal signaling leads to the phosphorylation of the latent cytoplasmic signaling effectors Smad2/3, whereas BMP signaling causes the phosphorylation of Smad1/5/8. These pSmads then accumulate in the nucleus, where they regulate the expression of target genes (Heldin et al., 1997).

During zebrafish germ-layer patterning, the two Nodals Squint and Cyclops are produced at the embryonic margin and induce endoderm and mesoderm formation at a distance from the source (Bisgrove et al., 2017; Montague and Schier, 2017; Pelliccia et al., 2017; Chen and Schier, 2001; Feldman et al., 1998). Fgf8, a Nodal target gene, further extends the range of mesoderm (van Boxtel et al., 2018; van Boxtel et al., 2015; Mathieu et al., 2004; Rodaway et al., 1999). At the same time, the two BMPs Bmp2b and Bmp7 are produced predominantly on the ventral side to control dorsal-ventral patterning (Pomreinke et al., 2017; Zinski et al., 2017; Ramel and Hill, 2013). Bmp2b and Bmp7 form heterodimers, and homodimers of Bmp2b and Bmp7 alone do not elicit signaling (Little and Mullins, 2009). Additionally, Bmp2b is produced in the dorsal organizer to moderate the production of Chordin, a BMP inhibitory protein (Xue et al., 2014).

Strikingly, Nodal and BMP signaling together are sufficient to trigger all processes required to form an embryo. This was spectacularly demonstrated by generating ectopic juxtaposed sources of Nodal and BMP to induce a secondary embryonic axis in zebrafish (Figure 1A) (Xu et al., 2014). The ratio of Nodal to BMP signaling was suggested to be the determining factor in specifying the necessary cell fates for the embryonic axis. Nodal by itself creates axial structures, high Nodal-to-BMP ratios induce posterior head structures, low Nodal-to-BMP ratios organize the tail, and intermediate ratios generate the middle trunk (Fauny et al., 2009). However, it is unknown how Nodal and BMP gradients form, it is currently debated whether Nodal and BMP signal over long distances (Rogers and Müller, 2019; Pomreinke et al., 2017; Zinski et al., 2017; van Boxtel et al., 2015; Ramel and Hill, 2013; Müller et al., 2012; Chen and Schier, 2001), and the molecular mechanisms that allow cells to respond to different ratios of Nodal and BMP signaling are unclear.

To address these questions, we transplanted sources expressing fluorescently tagged Nodal and BMP into zebrafish embryos and generated secondary axes with high efficiency. Interestingly, Nodal and BMP formed protein gradients with similar shape and

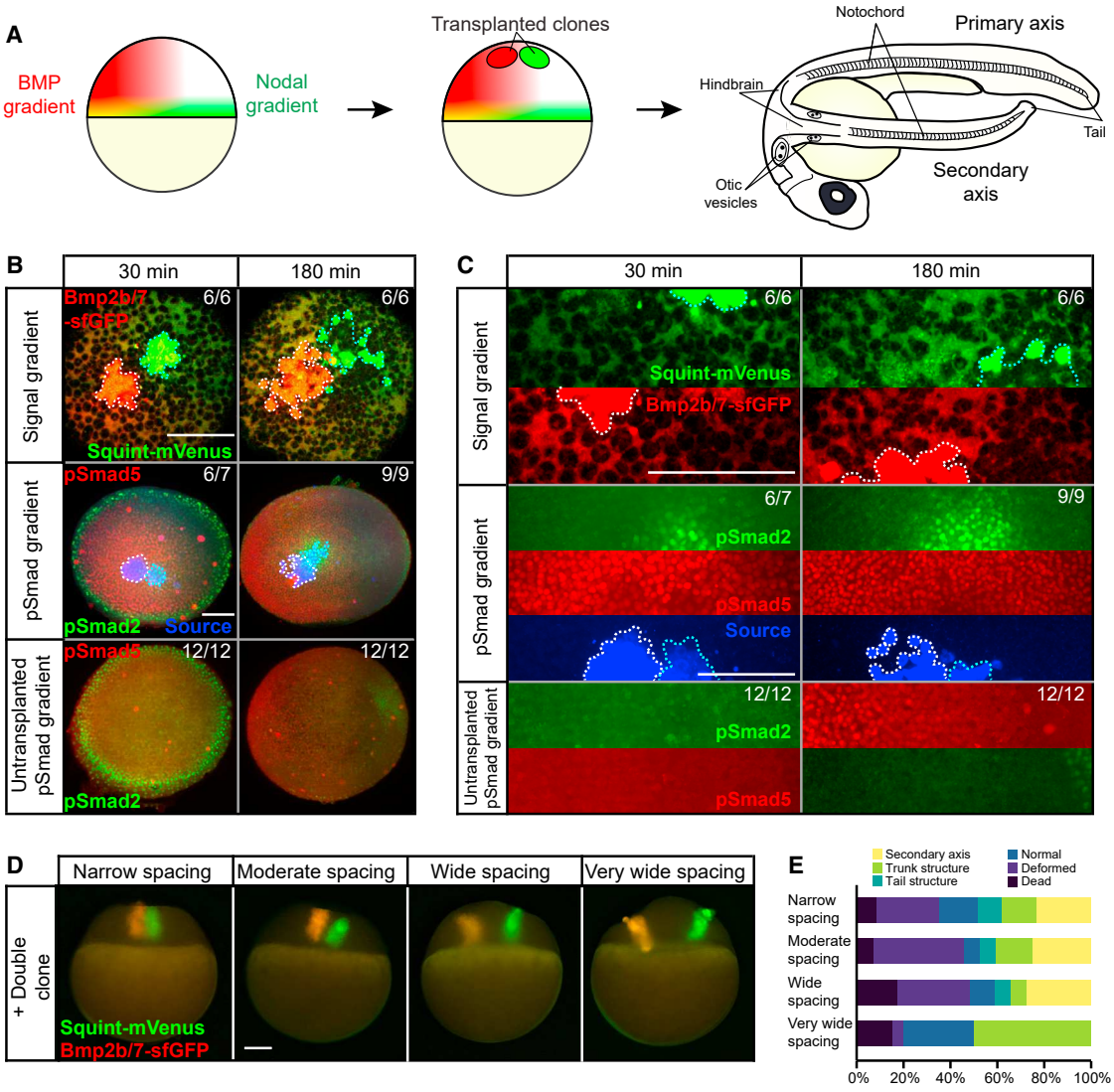

Figure 1. Secondary Axis Inducing Nodal and BMP Double Clones Produce a Localized Region of pSmad2 Activity Overlapping with a Broad Domain of pSmad5 Activity

(A) Nodal and BMP form orthogonal overlapping gradients in zebrafish embryos. Transplanting ectopic sources of Nodal and BMP induces the formation of a secondary axis, which contains both anterior and posterior structures such as the hindbrain, otic vesicles, notochord, and tail.

(B) Double clones of Bmp2b/7-sfGFP and Squint-mVenus imaged 30 min and 180 min post-transplantation. The first row depicts confocal microscopy images of Bmp2b/7-sfGFP (red) and Squint-mVenus (green). The second row shows light-sheet microscopy images of embryos immunostained with anti-pSmad2 (green) or anti-pSmad5 (red) antibodies as well as a cross-reactive anti-GFP antibody to detect Bmp2b/7-sfGFP and Squint-mVenus (blue). The third row shows comparable wild-type embryos. Nodal clones are traced in cyan and BMP clones are traced in white. Scale bar, 150 μm.

(C) Higher magnification of images shown in (B) with separate fluorescent channels. Scale bar, 150 μm.

(D) Images showing Nodal/BMP double clones with different spacings of transplanted cells taken immediately after transplantation. Scale bar, 150 μm.

(E) Nodal/BMP double clones were transplanted with different spacings into blastula-stage zebrafish embryos: narrow (~0 μm between clones, n = 60), moderate (40–50 μm between clones, n = 44), wide (120–150 μm between clones, n = 29), and very wide (>170 μm between clones, n = 20). Narrow to wide spacings support the formation of secondary axes, whereas secondary axis formation fails with extremely wide spacing between Nodal and BMP clones. Quantification was performed at 24 h post-transplantation.

amplitude in these secondary axis formation assays, but BMP had a long signaling range whereas Nodal induced pSmad signaling only locally around the transplanted clone. We found that the difference in signaling ranges can be explained by differential signaling activities of BMP and Nodal. Strikingly, specific ratios of constitutively active Smad2 and Smad5 were also able to generate a variety of embryonic structures, showing that the organizing ability of different Nodal/BMP ratios is mediated by different ratios of Smad2 and Smad5. We discovered that Smad2 and Smad5 selectively antagonize each other for certain cell fates while acting synergistically for others, which allows cells to respond differently to varying Nodal/BMP ratios. This selective

mutual antagonism might represent a general mechanism for how cells integrate and discriminate between two overlapping signals during development.

RESULTS

BMP and Nodal Induce pSmad Signaling with Different Ranges

To visualize the organizing signaling gradients during secondary axis formation, we optimized a protocol to generate secondary axes by transplanting juxtaposed sources of fluorescently tagged Nodal and BMP into zebrafish embryos (Figure 1A). In contrast to the original blastomere injection approach (Xu et al., 2014), this method allows for precise control over the timing, placement, and spacing of Nodal- and BMP-producing sources. We tagged the signaling molecules with various fluorophores and tested different ratios of the fusion proteins to assess their efficiency in generating secondary axes after transplantation. Many combinations of fluorophores showed good activity in generating secondary axes (Table S1), similar to the previously reported efficiency using untagged Nodal and BMP (Xu et al., 2014). Interestingly, both zebrafish Nodals (Squint and Cyclops) were able to generate secondary axes (only Cyclops was used in the previous work of Xu et al., 2014), albeit at different amounts of the injected mRNAs. Although mCherry-tagged versions also induced secondary axes, the required relative molar amounts differed drastically from those of the untagged versions (Table S1). In contrast, mVenus- and sfGFP-labeled Nodal and BMP had similar activity as the untagged versions (Figure S1). Furthermore, immunoblots of extracellular extracts showed that the fusion proteins were properly processed without releasing free fluorophores (Figure S1). We therefore decided to use Squint-mVenus and a 1:1 mixture of Bmp2b-sfGFP plus Bmp7-sfGFP (Bmp2b/7-sfGFP) for all subsequent axis-induction assays.

By generating localized sources of Squint-mVenus and Bmp2b/7-sfGFP, we found that these signaling molecules formed extracellular protein gradients within 30 min (Figures 1B and 1C). The gradients remained largely unchanged over the following 2 h (Figures 1B and 1C), similar to previous descriptions of Bmp2b-sfGFP and Squint-GFP gradient formation (Pomreinke et al., 2017; Müller et al., 2012). Interestingly, at 30 min post-transplantation, Nodal signaling (as assessed by pSmad2 induction; Figures 1B and 1C) was mostly limited to regions near the Nodal source, whereas BMP signaling (as assessed by pSmad5 induction; Figures 1B and 1C) had already spread extensively across the embryo. At 180 min, the pSmad2 signal was extended but still largely restricted to regions near the Nodal source, whereas pSmad5 remained more widely distributed (Figures 1B and 1C).

The wide and flat distribution of BMP signaling implied that the previously postulated close juxtaposition of opposing Nodal and BMP clones (Xu et al., 2014) might not be necessary for secondary axis induction and that localized Nodal signaling might be sufficient as long as there is some additional BMP signaling in the embryo. To test this prediction, we varied the spacing between Nodal and BMP sources and found that secondary axes could be generated for a wide range of different spacings (Figures 1D and 1E). The formation of secondary axes only failed when we placed the Nodal source much farther away from the BMP source than the range spanned by the pSmad5 gradient (~220 μm; Figure 1E). These results suggest that the BMP source generates a much more extensive signaling gradient than the Nodal source, even though the extracellular distributions of Nodal and BMP appear to be similar.

Secondary Axis Formation Does Not Depend on Relay Signaling

It had previously been suggested that secondary axis formation requires relay signaling through endogenous TGF-β superfamily ligands (de Olivera-Melo et al., 2018; Xu et al., 2014). To test this idea and measure signaling kinetics in the absence of endogenous signals, we transplanted clones secreting BMP and Nodal into wild-type and mutant zebrafish embryos that lack the endogenous signaling molecules. We first transplanted clones secreting zebrafish BMP into wild-type embryos and compared the induction kinetics of pSmad5 to *MZswr* (maternal-zygotic *swirl*$^{-/-}$ mutant) embryos that had received *MZswr* clones ectopically producing BMP. *MZswr* embryos lack functional Bmp2b (Schmid et al., 2000; Kishimoto et al., 1997) and are ideally suited to analyze the kinetics of pSmad5 induction in the absence of endogenous BMP signaling during embryonic development. Local BMP sources in wild-type embryos caused ventralization (Figure 2A, middle left), indicative of increased BMP activity in the entire embryo. The ubiquitous induction of BMP signaling was corroborated by the effects of small BMP clones in *MZswr* embryos (Figure 2A, middle right) that were well rescued except for tail defects, indicating that the BMP clone indeed induced long-range signaling. Consistent with these phenotypes, BMP clones induced signaling rapidly, and pSmad5 signal filled up the entire field in both wild-type and *MZswr* embryos (Figures 2B, 2C, S2, and S3A). The ability of the BMP source to induce pSmad5 signaling in *MZswr* embryos demonstrates that a relay through the induction of endogenous *bmp2b* is not required. Strikingly, local BMP juxtaposed to Nodal clones even induced secondary axes in *MZswr* embryos (Figure 2A, bottom right), indicating that BMP can work non-cell-autonomously and without relay signaling in this context.

To test the role of potential relays and quantify the dynamics of Nodal signaling, we transplanted cells producing Squint-mVenus into wild-type or *MZsqt;cyc* mutant host embryos (clones transplanted into *MZsqt;cyc* host embryos were *MZsqt;cyc* mutant as well). *MZsqt;cyc* mutants lack all maternal and zygotic Nodal ligands (Feldman et al., 1998) and serve as a background to analyze Nodal signaling in the absence of endogenous Nodal signals. Squint-mVenus clones in wild-type and *MZsqt;cyc* embryos generated ectopic axial trunk structures (Figure 2D, middle). Strikingly, Nodal and BMP double clones were able to generate a secondary axis with anterior mesodermal structures such as anterior somites (Figure 2D, bottom right, blue arrowhead), which are normally absent in Nodal-deficient *MZsqt;cyc* embryos (Figure 2D, top right, cyan arrowhead). The primary axis in these embryos lacked anterior mesodermal structures (Figure 2D, bottom right), as is expected for *MZsqt;cyc* embryos (Feldman et al., 1998).

In agreement with the restricted effect of anterior mesoderm rescue, pSmad2 staining was found locally around the Nodal

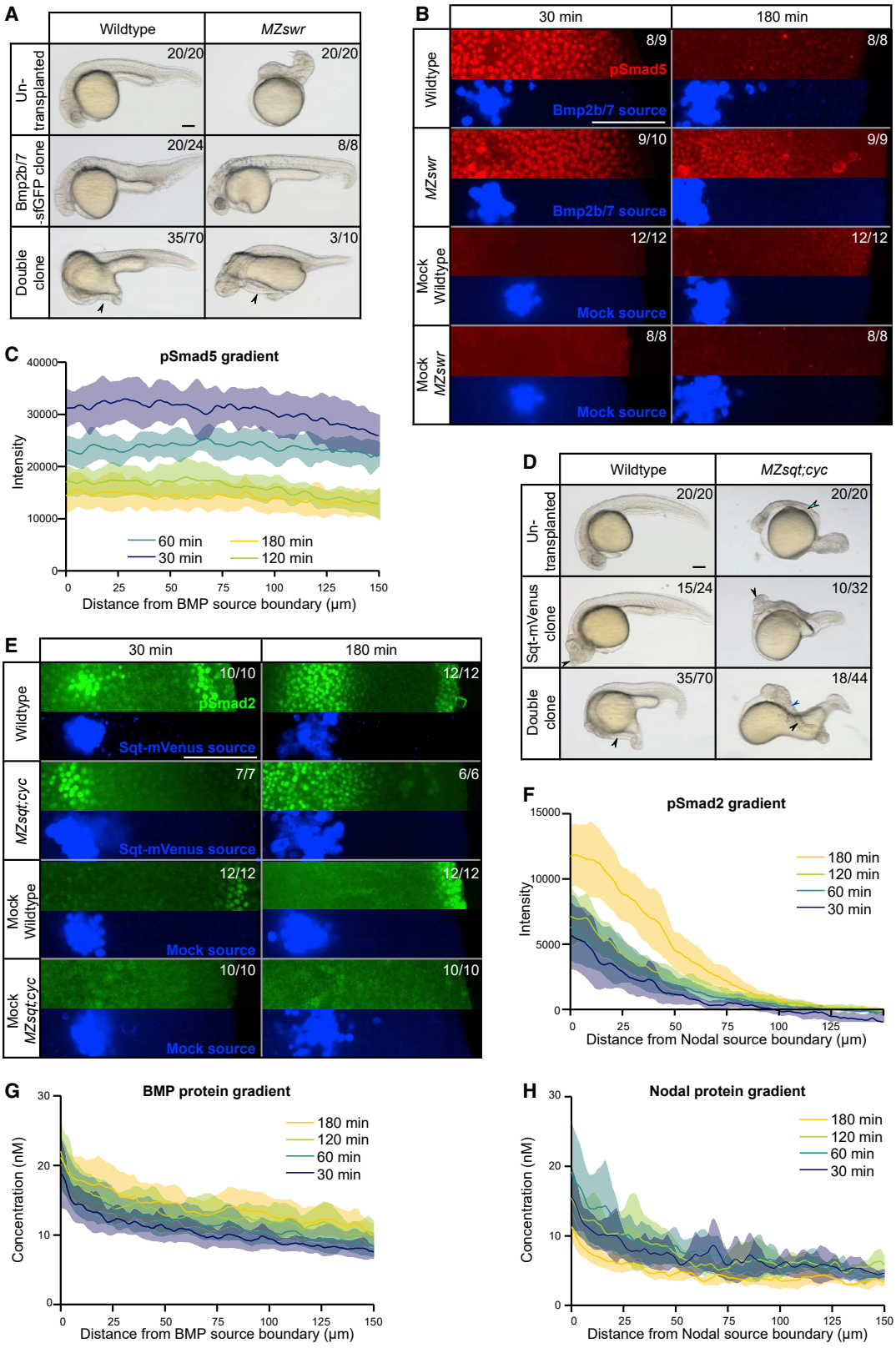

(legend on next page)

clones (Figure 2E). pSmad2 signal in *MZsqt;cyc* embryos extended up to several cell diameters away from the clone (Figures 2E and S3B), demonstrating that Nodal acts non-cell autonomously and without the need for a relay-based mechanism in this context as well. However, the range of Nodal-induced pSmad2 was significantly shorter than the range of BMP-induced pSmad5 (Figures 2C, 2F, and S3B). Importantly, untagged Squint and Bmp2b/7 generated a similarly large difference in the spatial ranges of Nodal and BMP signaling (Figures S2A and S2B), ruling out the possibility that the fluorescent tags are causal for the range differences.

Nodal and BMP Have Different Signaling Ranges despite Similar Ligand Distributions

Our finding that secondary axis formation is independent of relay signaling and purely relies on exogenously supplied signals provides an ideal system to test whether differences in signal gradient formation kinetics can explain the different signaling activity ranges. To relate the signal gradients to the signaling ranges, we developed a method to quantify the absolute concentrations of labeled Nodal and BMP in living zebrafish embryos based on their fluorescence intensities. We first purified recombinant sfGFP and mVenus proteins and established calibration curves relating the molar concentrations to their fluorescence intensities (Figure S4). We then used these calibration curves to determine the concentrations of fluorescently tagged Nodal and BMP expressed from local sources in zebrafish embryos. We found that the BMP gradient spanned a concentration range from 20 nM to 7 nM over 150 μm at 30 min post-transplantation (Figure 2G). At this time point, the pSmad5 gradient was similarly broad (Figure 2C), even when 5-fold less *bmp2b/7-sfGFP* mRNA was used (Figure S2C). Interestingly, although the concentration of BMP slightly increased over time (Figure 2G), most likely due to a larger effect of BMP production compared to its degradation, pSmad5 intensity concomitantly decreased (Figures 2C, S2A, and S2C). The decrease in pSmad5 intensity was also observed in *chordin* morphants (Figure S2D), arguing against the possibility of BMP signaling dampening by this major BMP antagonist (Fisher and Halpern, 1999; Blader et al., 1997; Schulte-Merker et al., 1997) in this context. In contrast, other Chordin-independent BMP-feedback inhibitors such as Bambia and Smad7 might be responsible for the down-regulation of BMP signaling over time (Pogoda and Meyer, 2002; Tsang et al., 2000).

The Squint-mVenus gradient produced from a localized clone formed with similar concentration distributions and dynamics as the BMP protein gradient at early time points but sharply dropped by 180 min post-transplantation (Figure 2H), possibly due to unstable mRNA, decreased translation, reduced secretion, or rapid internalization. In contrast to the drop in the Nodal gradient amplitude (Figure 2H), the levels of pSmad2 increased over time (Figure 2F).

Together, these results show that although Nodal and BMP form similar proteins distributions, their respective pSmad gradients are radically different, similar to the distinct distributions of pSmads induced by endogenous signaling molecules (Figure S2E). Therefore, the drastic differences in the pSmad gradients cannot be explained by the small differences in the amount of secreted Nodal and BMP proteins or by their similar effective diffusion coefficients (~3 $\mu m^2/s$) (Bläßle et al., 2018; Pomreinke et al., 2017; Zinski et al., 2017; Müller et al., 2012).

Different Signaling Ranges Arise from Differences in Signaling Activity

Nodal signaling is antagonized by the feedback-induced Nodal inhibitors Lefty1 and Lefty2 during early zebrafish development (Rogers and Müller, 2019; Rogers et al., 2017; Agathon et al., 2001; Meno et al., 1999; Thisse and Thisse, 1999). To test whether the shorter signaling range of Nodal compared to BMP is due to inhibition by Lefty1 or Lefty2, we assessed signaling in Squint-mVenus clone experiments in which both the donor and the recipient embryo were *MZlefty1;lefty2* double mutants lacking all maternal and zygotic Lefty activity (Rogers et al., 2017). Interestingly, in the absence of Lefty antagonism, the pSmad2 signal was extended (Figures S2F and S3C) but still much shorter than the range of pSmad5 induced by BMP clones

Figure 2. Nodal and BMP Form Similar Protein Gradients but Have Different Signaling Ranges during Secondary Axis Formation

(A) Bmp2b/7-sfGFP as well as Squint-mVenus and Bmp2b/7-sfGFP double clones in wild-type or maternal-zygotic *swirl* mutant (*MZswr*) embryos at 1 day post-transplantation, with untransplanted embryos for comparison. The arrowheads point to ectopic secondary axes. Scale bar, 150 μm.

(B) Bmp2b/7-sfGFP clones compared to uninjected mock clones 30 min and 180 min post-transplantation in wild-type or *MZswr* embryos. Embryos were immunostained with anti-pSmad5 (red) and anti-GFP (blue) antibodies. Mock sources were labeled with cascade blue-dextran (blue). Scale bar, 150 μm.

(C) pSmad5 distributions in embryos with single Bmp2b/7-sfGFP clones in *MZswr* embryos at 30 min (n = 9), 60 min (n = 8), 120 min (n = 10), and 180 min (n = 9) post-transplantation. Shaded regions indicate 95% confidence intervals around the mean (lines). Scale bar, 150 μm.

(D) Squint-mVenus as well as Squint-mVenus and Bmp2b/7-sfGFP double clones in wild-type or maternal-zygotic *squint* and *cyclops* double mutant (*MZsqt;cyc*) embryos 1 day post-transplantation, with untransplanted embryos for comparison. The arrowheads point to ectopic structures or secondary axes. Scale bar, 150 μm.

(E) Squint-mVenus clones compared to uninjected mock clones 30 min and 180 min post-transplantation in wild-type or *MZsqt;cyc* embryos. Embryos were immunostained with anti-pSmad2 (green) and anti-GFP (blue) antibodies. Mock sources were labeled with cascade blue-dextran (blue). Scale bar, 150 μm.

(F) pSmad2 distributions in embryos with single Squint-mVenus clones in wild-type embryos at 30, 60, 120, and 180 min post-transplantation (n = 11 each). Shaded regions indicate 95% confidence intervals around the mean (lines).

(G) BMP protein gradients in wild-type embryos with single Bmp2b/7-sfGFP clones at 30, 60, 120, and 180 min post-transplantation. The same embryos were imaged throughout the time course (n = 14). Fluorescence intensity was converted to concentration based on a calibration curve using recombinant sfGFP imaged with the same microscope settings. Shaded regions indicate 95% confidence intervals around the mean (lines).

(H) Nodal protein gradients in wild-type embryos with single Squint-mVenus clones at 30, 60, 120, and 180 min post-transplantation. The same embryos were imaged throughout the time course (n = 12). Fluorescence intensity was converted to concentration based on a calibration curve using recombinant mVenus imaged with the same microscope settings. Shaded regions indicate 95% confidence intervals around the mean (lines).

See also Figures S2–S4.

(compare to Figure 2C). These results show that signaling range modulation by Lefty cannot explain the drastic difference between Nodal distribution and signaling in this context.

We therefore hypothesized that the different signaling ranges (pSmad5 and pSmad2) from similar input gradients (BMP and Nodal) might result from different signaling activation kinetics. According to the law of mass action and Hill kinetics, signals with higher sensitivity can induce activation faster, leading to a longer signaling range, whereas signals with low sensitivity might require extended exposure until activation is induced in a threshold-type manner, leading to a shorter signaling range (Michaelis et al., 2011). To test this idea, we took advantage of the recent discovery that a single source of mouse BMP4 can generate a secondary zebrafish axis (de Olivera-Melo et al., 2018), which suggested the possibility that mouse BMP4 might carry both BMP and Nodal signal activities with different ranges. Previous experiments were carried out with commercial preparations of recombinant mouse BMP4 (de Olivera-Melo et al., 2018), but we found that a single source of mRNA encoding mouse BMP4 can also induce secondary axes in zebrafish embryos (Figure 3A), ruling out the possibility that potential contaminations of commercial mouse BMP4 with other TGF-β superfamily ligands are responsible for secondary axis formation.

To assess the plausibility that a single source of mouse BMP4 might generate different pSmad distributions, we developed a mathematical model based on Hill kinetics that we parameterized with the diffusion coefficient and protein half-life previously measured for zebrafish BMP (Pomreinke et al., 2017; Zinski et al., 2017) (Figure 3B). In this model, the differential readout of the mouse BMP4 gradient by pSmad5 and pSmad2 is dependent on a single parameter, i.e., the steepness of the pSmad activation term (k_d for pSmad5, k_e for pSmad2) that convolves the affinity of the BMP4 ligand for the BMP and Nodal receptors as well as the pSmad activation kinetics (Figure 3B). Simulations with smaller k_d compared to k_e values predicted that pSmad2 should be activated close to the mouse BMP4 source, whereas pSmad5 should have a wider range (Figure 3B).

In agreement with this model prediction, we found that pSmad2 and pSmad5 were indeed activated at different ranges by mouse BMP4. Local sources of mouse BMP4 in zebrafish embryos induced locally restricted pSmad2 but widespread pSmad5 (Figures 3C and 3D), providing further support that opposing sources of Nodal and BMP are not strictly needed for secondary axis formation. To rule out the possibility that pSmad2 activation is due to indirect induction of endogenous Nodal signals (de Olivera-Melo et al., 2018), we generated clones expressing mouse *bmp4* in Nodal-deficient *MZsqt;cyc* mutant zebrafish embryos. We found that mouse BMP4 can indeed directly induce both pSmad2 and pSmad5 non-cell-autonomously (Figures 3E and 3F). Together, these results support our model that the exact same signal gradient can induce signaling effector activation at different ranges solely due to differences in signaling activity.

Our model implies that the action range of a signaling molecule with high signaling activity should be limited by its diffusion coefficient, whereas the action range of a signaling molecule with low signaling activity should be limited by its signaling activity rather than its diffusivity. To test this prediction, we sought to artificially reduce the diffusion coefficients of Nodal and BMP and measure how this affects their signaling ranges. We perturbed the protein distributions of Nodal and BMP using morphotraps, transmembrane proteins with extracellularly facing anti-GFP nanobodies that can drastically reduce the diffusivity of extracellular proteins tagged with GFP derivatives (Mörsdorf and Müller, 2019; Almuedo-Castillo et al., 2018; Harmansa et al., 2017). The protein distributions of Bmp2b/7-sfGFP and Squint-mVenus expressed from localized sources were strongly restricted in the presence of the morphotrap (Figure 3G). The sharp Bmp2b/7-sfGFP distribution led to a strongly restricted pSmad5 signal around the clone, whereas the already narrow range of pSmad2 was only marginally affected when the Squint-mVenus distribution was perturbed (Figures 3G and S2G). These findings provide additional support for our model that BMP has a longer signaling range than Nodal due to its higher signaling activity.

Strikingly, morphotrap-mediated range-restricted Nodal and BMP still supported the formation of secondary axes when the clones were closely juxtaposed (~0 μm between clones), whereas secondary axes could no longer be induced when the clones were far apart (>120–150 μm) from each other (Figure 3H, top). To test whether the long-range activity of Nodal or BMP is required in this context, we next perturbed the ranges of Nodal or BMP individually. Interestingly, morphotrap-mediated range restriction of Nodal was without consequence for narrowly or widely spaced clones (Figure 3H, middle), whereas secondary axis formation was abrogated when range-restricted BMP clones were placed far away from normal Nodal clones (Figure 3H, bottom). These results show that differences in the Nodal and BMP signaling ranges are functionally relevant for the formation of secondary axes. We note, however, that in normal embryos BMPs do not form a discrete source but are expressed in a broad domain, which gives rise to a broad signaling domain of pSmad5. Nodal by contrast is localized to the margin in a much more restricted domain, and pSmad2 is likewise activated in a much more restricted domain (reviewed in Rogers and Müller, 2019).

In conclusion, we showed that Nodal and BMP can induce signaling with different ranges, differential signaling activity can explain the differences in signaling ranges, and differential signaling ranges are relevant for secondary axis formation.

Different Structures Can Be Induced by Specific Amounts of Active Smad2 and Smad5

Our results suggest that the formation of a secondary axis requires a broad distribution of BMP and highly localized Nodal signaling. However, in addition to the spatial distributions, the relative signaling levels may also important for secondary axis formation (Fauny et al., 2009). By varying the relative levels of BMP and Nodal, we found that it is the ratio of Nodal to BMP rather than the absolute signaling level that determines whether a secondary axis can form. Lowering Nodal levels with respect to BMP levels precluded secondary axis induction (Figure S5A), whereas a commensurate reduction in both Nodal and BMP levels restored secondary axis formation (Figure S5A), correlating with a specific distribution of pSmad2 to pSmad5 ratios (Figures S5B and S5C).

To test whether the observed pSmad2-to-pSmad5 signaling effector ratio is causal for secondary axis induction, we

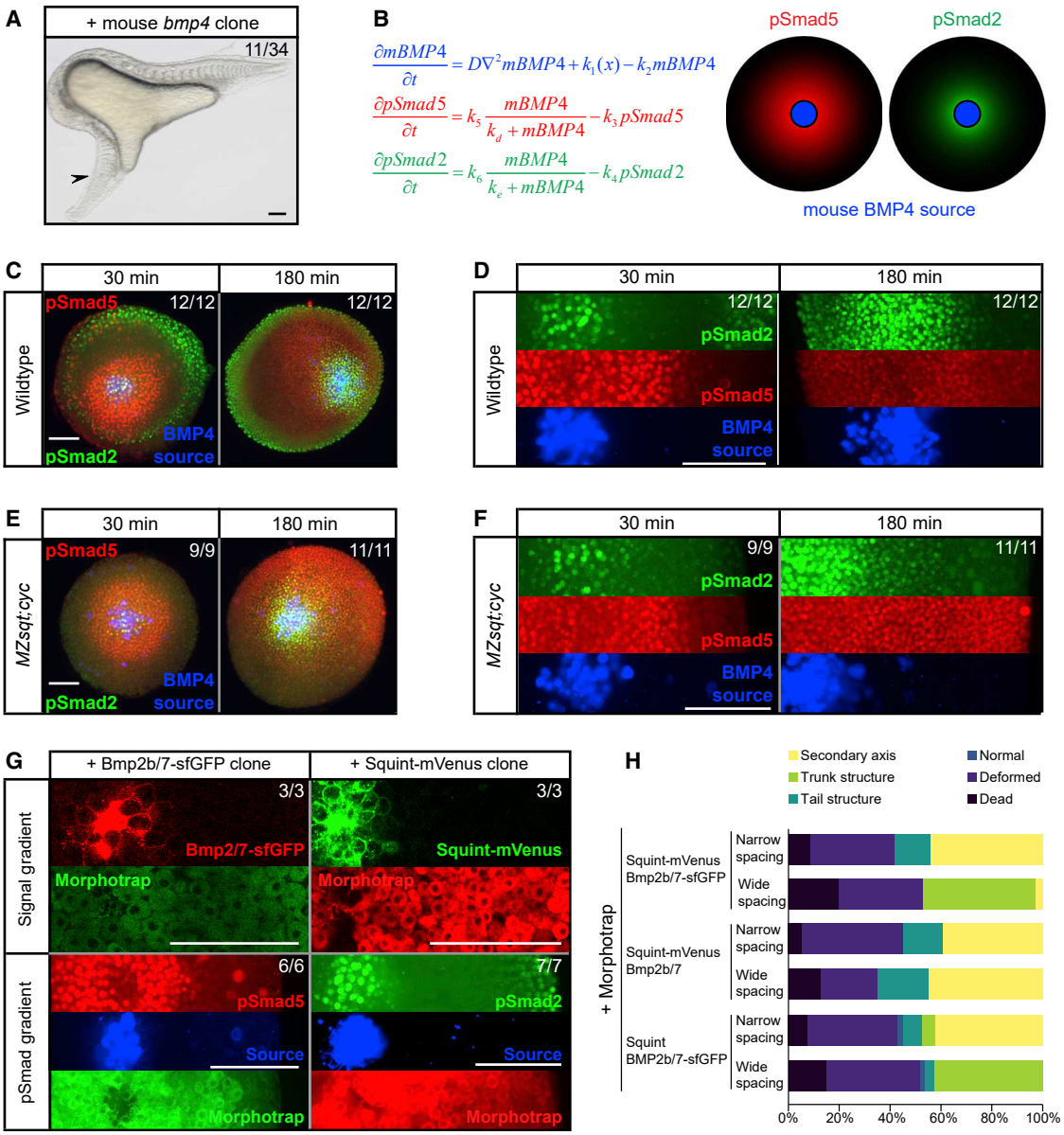

Figure 3. Different BMP and Nodal Signaling Ranges Arise from Differential Signaling Activation Kinetics

(A) Single clones expressing mouse *BMP4* (mBMP4) induce the formation of a secondary axis in zebrafish embryos (arrowhead). Scale bar, 150 μm.

(B) Mathematical modeling shows that a difference in signaling activation kinetics could explain how a single gradient of mBMP4 induces pSmad5 and pSmad2 at different ranges.

(C) Wild-type zebrafish embryos with clones expressing *mBMP4* 30 min and 180 min post-transplantation immunostained with anti-pSmad5 (red) and anti-pSmad2 (green) antibodies. The clones were labeled with cascade blue-dextran (blue). Scale bars, 150 μm.

(D) Higher magnification of images shown in (C) with separated fluorescent channels. Scale bar, 150 μm.

(E) *MZsqt;cyc* embryos with clones expressing *mBMP4* 30 min and 180 min post-transplantation immunostained with anti-pSmad5 (red) and anti-pSmad2 (green) antibodies. The clones were labeled with cascade blue-dextran (blue). Scale bars, 150 μm.

(F) Higher magnification of images shown in (E) with separated fluorescent channels. Scale bar, 150 μm.

(G) Zebrafish Bmp2b/7-sfGFP and Squint-mVenus clones in morphotrap-expressing wild-type embryos 30 min post-transplantation. Scale bar, 150 μm.

(H) Double clones with fluorescently tagged or untagged zebrafish Nodal and BMP and with narrow or wide spacing were generated in morphotrap-expressing embryos. The frequency of the different structures induced by the clones was assessed 24 h post-transplantation.

generated embryos in which we activated specific ratios of Smads in a localized region independently of the extracellular signaling molecules. By exchanging the three C-terminal serines with aspartates, we generated constitutively active Smad2 (Smad2-CA) and Smad5 (Smad5-CA) signaling effectors, which can activate the transcription of their respective target genes

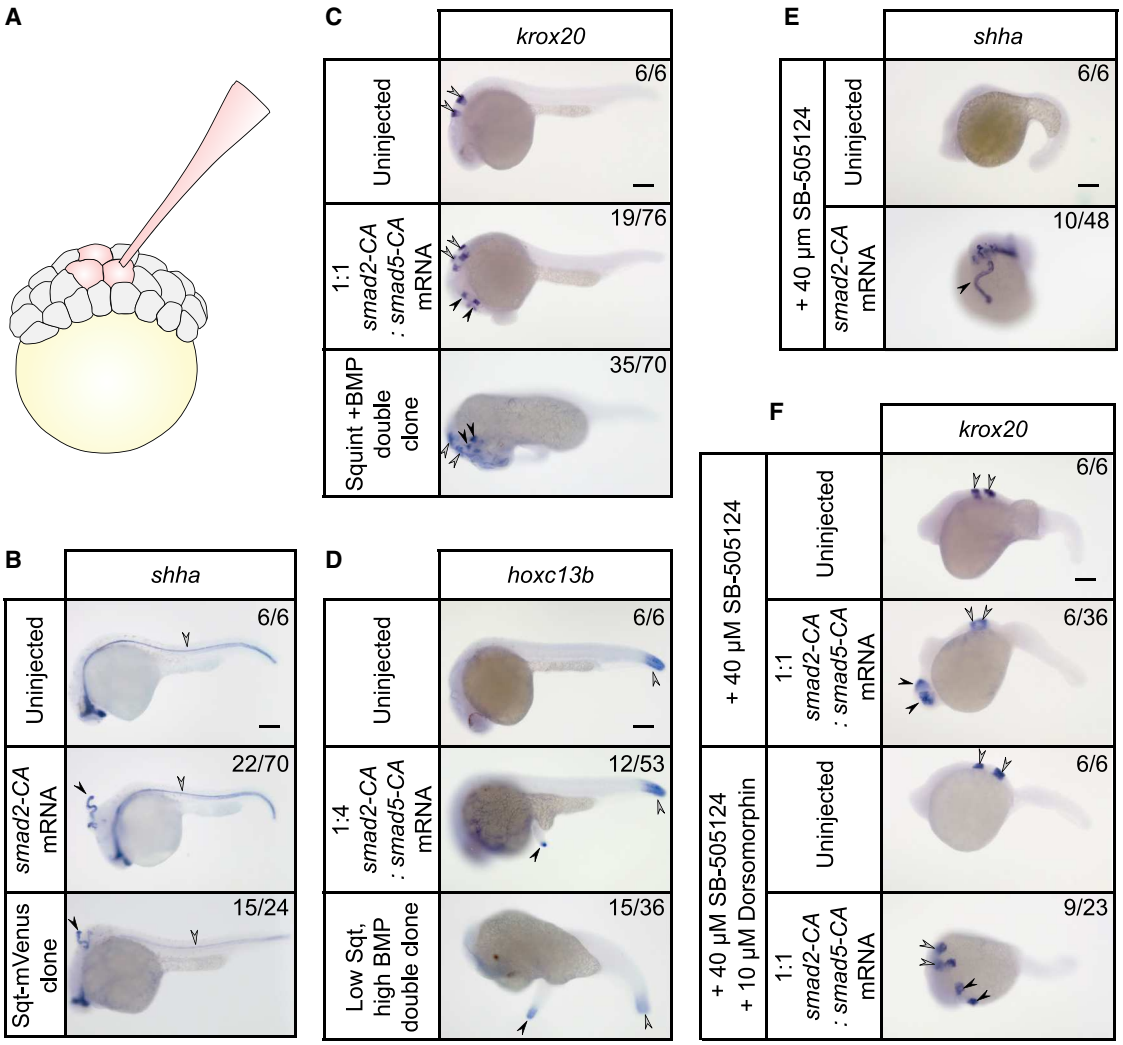

Figure 4. Ectopic Expression of Different Amounts of *smad2-CA* and *smad5-CA* mRNA Generates Distinct Embryonic Structures

(A) Ectopic structures were generated by injecting three adjacent blastomeres in 64- to 128-cell-stage embryos.

(B) The floorplate marker *shha* is expressed throughout the axis (gray arrowhead) of wild-type embryos 24 h post-fertilization (hpf). Injection of *smad2-CA* mRNA into animal pole blastomeres results in the formation of an ectopic axial structure (black arrowhead) that expresses *shha*, similar to the results with a *squint-mVenus*-expressing clone.

(C) *krox20* is expressed as a pair in rhombomeres 3 and 5 in the hindbrain (gray arrowhead) of wild-type embryos at 24 hpf. Injection of *smad2-CA* and *smad5-CA* mRNA in animal pole blastomeres results in the formation of anterior trunk structures with paired *krox20* expression (black arrowhead), similar to the outcome with a *squint-mVenus* and *bmp2b/7-sfGFP*-expressing double clone.

(D) *hoxc13b* is expressed in the tail tip (gray arrowhead) in wild-type embryos at 24 hpf. Injection of *smad2-CA* and four times more *smad5-CA* mRNA into animal pole blastomeres results in the formation of a tail structure expressing *hoxc13b* (black arrowhead), similar to the outcome with a double clone expressing low *squint-mVenus* and high *bmp2b/7-sfGFP* (Figure S5).

(E) *shha* is not expressed in embryos exposed to the Nodal receptor inhibitor SB-505124. Injection of *smad2-CA* mRNA into animal pole blastomeres results in ectopic *shha*-positive axial structures despite Nodal receptor inhibition.

(F) *krox20* remains expressed (gray arrowheads) in embryos exposed to SB-505124. Injection of *smad2-CA* and *smad5-CA* mRNA into animal pole blastomeres stage results in the formation of anterior trunk structures with paired *krox20* expression (black arrowheads). Nodal and BMP receptor inhibition by combined exposure to SB-505124 and Dorsomorphin generates embryos with reduced tails compared to the treatment with SB-505124 alone, but *krox20* expression persists (gray arrowhead). Injection of *smad2-CA* and *smad5-CA* mRNA into animal pole blastomeres results in the formation of anterior trunk structures with paired *krox20* expression (black arrowhead) despite Nodal and BMP receptor inhibition. Scale bar in all images, 150 µm.

(Figure S6). We found that expression of *smad2-CA* and *smad5-CA* in a localized region (Figure 4A) can generate various ectopic embryonic structures. Injecting *smad2-CA* alone generated an ectopic trunk structure containing axial tissues expressing the floorplate marker *shha* (Krauss et al., 1993) (Figure 4B, black arrowhead), just like in the case of an ectopic source of Nodal (Figure 4B) (Fauny et al., 2009). When we injected *smad2-CA* mixed with increasing amounts of *smad5-CA* mRNA (Figures

4C and 4D), structures expressing more ventral genes were induced, similar to previous findings in which the extracellular signaling molecules Nodal and BMP instead of the active signaling effectors were used (Fauny et al., 2009). Using Smad2-CA and Smad5-CA in a 1:1 ratio led to the induction of an ectopic structure with paired *krox20* expression, similar to the secondary axis generated by Nodal and BMP double clones (Figure 4C). *krox20* is expressed in rhombomeres 3 and 5 of the hindbrain (Ghosh et al., 2018), indicating that the ectopic structure represents an anterior trunk (Figure 4C). 4-fold more Smad5-CA over Smad2-CA can generate ectopic tail structures (Figure 4D) expressing the tail tip marker *hoxc13b* (Fauny et al., 2009). The induction of these structures was robust to the absence of endogenous Nodal and BMP signaling. Embryos expressing *smad2-CA* that were exposed to 40 μM of SB-505124, which fully inhibits signaling from the upstream Nodal receptor (Almuedo-Castillo et al., 2018; Rogers et al., 2017; Hagos and Dougan, 2007), were still able to generate ectopic trunk structures expressing *shha* (Figure 4E). Furthermore, embryos expressing *smad2-CA* and *smad5-CA* that were exposed to 40 μM of SB-505124 and 10 μM of the BMP receptor inhibitor Dorsomorphin were also able to generate anterior trunk structures expressing *krox20* (Figure 4F).

Since the inductive capabilities of constitutively active Smad2 and Smad5 are similar to those of the upstream signaling molecules Nodal and BMP, we conclude that the organizing activities of Nodal and BMP are mediated by specific amounts and ratios of active Smad2 and Smad5.

Selective Mutual Antagonism of Active Smad2 and Smad5 Yields Specific Responses to Different Signaling Ratios

We found that different ectopic structures can be induced by specific ratios of Smad2 and Smad5. To determine how the induction of these structures is related to the activation of target genes, we injected embryos with different ratios of Smad2-CA and Smad5-CA and assessed the expression of Nodal and BMP target genes with representative endogenous expression domains (Figure 5A). *gsc* is induced by Nodal signaling and a marker of axial mesoderm (Bennett et al., 2007; Gritsman et al., 1999) but only expressed at the dorsal margin (despite pSmad2 activity throughout the margin), suggesting that it is induced by high pSmad2 and low pSmad5 levels; *foxi1* is a BMP target gene and an epidermal marker that is expressed on the ventral side but appears to be excluded from the ventral margin at shield stage (Hans et al., 2007) (although pSmad5 signaling is also present at the ventral margin), suggesting that is induced by high pSmad5 and low pSmad2 levels; and *eve1* is expressed in the ventral margin (where both pSmad2 and pSmad5 are active) and a marker for ventral mesoderm, suggesting that it is induced by high pSmad2 and high pSmad5 levels. Interestingly, we found that Smad2-CA and Smad5-CA antagonized each other for the induction of *gsc* and *foxi1*, whereas *eve1* showed a biphasic sensitivity to these signaling effectors. Smad2-dependent *gsc* expression was suppressed by high levels of Smad5-CA compared to Smad2-CA (Figure 5B), whereas Smad5-dependent *foxi1* expression was inhibited by high Smad2-CA levels (Figure 5C). Strikingly, *eve1* was induced synergistically by both Smad2-CA and Smad5-CA at a moderate amount of Smad2-CA (Figure 5D). In contrast, high amounts of Smad2-CA led to reduced *eve1* expression (Figure 5D), consistent with the absence of dorsal *eve1* expression (Joly et al., 1993) where Nodal signaling is active over a long period of time (van Boxtel et al., 2018; Dubrulle et al., 2015). These results suggest that the selective mutual antagonism of Smad2 and Smad5 allows cells to respond specifically to different ratios of Smad2 and Smad5.

Our selective mutual antagonism mechanism predicted specific expression patterns of *gsc*, *foxi1*, and *eve1* in the Nodal/BMP double clone secondary axis formation assay. *gsc* is induced by high Smad2 activity and suppressed by Smad5 activity (Figure 5B) and should therefore be expressed near the Nodal source opposite to the BMP clone, *foxi1* is induced by high Smad5 activity and suppressed by Smad2 activity (Figure 5C) and should therefore be expressed near the BMP source opposite to the Nodal clone, and *eve1* has a biphasic activation profile (Figure 5D) and should therefore be expressed in a complex pattern. To test these predictions, we subjected embryos carrying Nodal/BMP double clones to *in situ* hybridization with various probes followed by pSmad2 and pSmad5 immunostaining (Figure 5E). In agreement with the predictions of our selective mutual antagonism model, we found that *gsc* was expressed in the presence of pSmad2, but not when pSmad2 overlapped with pSmad5 (Figure 5E). In contrast, *foxi1* was expressed in regions of pSmad5 activity, but expression was reduced when pSmad5 overlapped with pSmad2 (Figure 5E). Strikingly, *eve1* was expressed in the predicted complex domain; *eve1* was induced where pSmad2 overlapped with pSmad5, but it was not detected at the highest pSmad2 activity in the overlapping region (Figure 5E).

In conclusion, we found that the organizing activities of Nodal and BMP are mediated by specific amounts of active Smad2 and Smad5, whose selective mutual antagonism allows cells to respond specifically to different Nodal/BMP input ratios.

DISCUSSION

Understanding the dynamics of axis formation during early vertebrate development has largely been hampered by the lack of tools to relate the input from signaling gradients to the patterning output in terms of signaling effector activation and target gene expression. Transgenic animals expressing fluorescent fusions of the relevant signaling molecules under the control of endogenous regulatory elements are currently not available, and the timing and amplitudes of signaling gradients cannot be easily manipulated with good spatiotemporal control. Here, we used our optimized secondary zebrafish axis induction assay as an experimentally tractable model system to understand signaling input-output relationships and to decipher how Nodal and BMP signaling are integrated to form a secondary embryo.

Using active fluorescent fusions of Nodal and BMP expressed from clonal sources, we found that the signaling molecules form similar protein gradients of comparable shape and amplitude in zebrafish embryos. The similar protein gradients are in stark contrast to the differential distributions of the signaling effectors. The Nodal source generates a localized pSmad2 gradient that is overlaid by a broader pSmad5

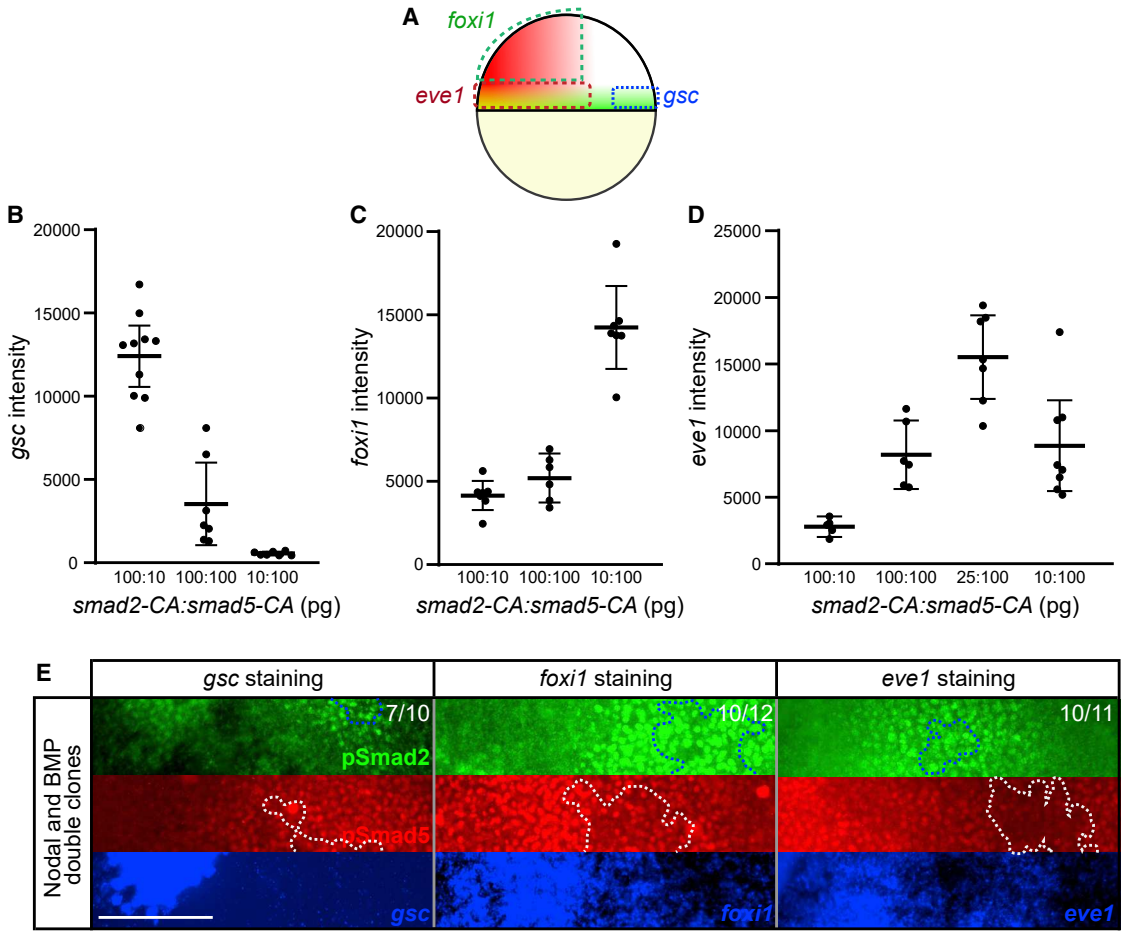

Figure 5. Mutual Antagonism of Smad2 and Smad5 for Specific Cell Fates

(A) *gsc* is expressed at the dorsal margin (Stachel et al., 1993), while *foxi1* is expressed on the ventral side but excluded from the margin (Dal-Pra et al., 2006), and *eve1* is expressed at the ventral margin (Joly et al., 1993) where Nodal and BMP signaling overlap (Figure 1A).

(B) Average *gsc* fluorescence *in situ* hybridization (FISH) intensity in 6-hpf embryos that were injected with the indicated *smad2-CA* and *smad5-CA* mRNA amounts at the one-cell stage (n = 10, 7, and 7).

(C) Average *foxi1* FISH intensity in 6-hpf embryos that were injected with the indicated *smad2-CA* and *smad5-CA* mRNA amounts at the one-cell stage (n = 7, 6, and 7).

(D) Average *eve1* FISH intensity of 6-hpf embryos that were injected with the indicated *smad2-CA* and *smad5-CA* mRNA amounts at the one-cell stage (n = 5, 6, 7, and 8).

(E) Embryos with Nodal and BMP double clones subjected to FISH with *gsc* (left, blue), *foxi1* (middle, blue), or *eve1* (right, blue) probes followed by pSmad2 (green) and pSmad5 (red) immunostaining. Blue dotted lines trace Nodal clones, and white dotted lines trace BMP clones. Scale bar, 150 μm. Error bars indicate 95% confidence intervals around the mean (horizontal lines) in (B)–(D).

gradient induced by the BMP source. Taking advantage of the dual BMP/Nodal activity of mouse BMP4, we experimentally confirmed the prediction of our model that different signaling ranges of a single protein gradient can be explained by differences in signaling activity. In addition to differences in diffusion/clearance-based signal dispersal (Rogers and Müller, 2019), differences in signaling activity might therefore represent an additional knob to tune the ranges of signaling molecules and may play a role in restricting Nodal signaling to the margin. Consistent with this hypothesis, similar differences in TGF-β superfamily signaling dynamics were recently identified in cultured cells (Miller et al., 2019; Yoney et al., 2018). For example, Activin exogenously added to mouse embryonic stem cells was found to activate Smad2 rapidly and had a long signaling range, whereas BMP4 activated Smad1 more slowly and had a shorter signaling range (Yoney et al., 2018). In agreement with law of mass action considerations (Michaelis et al., 2011), it may thus be a general feature of developmental signaling systems that ligands that rapidly activate their effectors have a longer range, whereas ligands that slowly activate their effectors have a shorter range.

The difference in Nodal and BMP signaling ranges arises due to differences in signaling activation kinetics and yields a field of various positional information values in terms of pSmad2-to-pSmad5 ratios. Previous work has shown that ectopic expression of different amounts of Nodal and BMP induces the

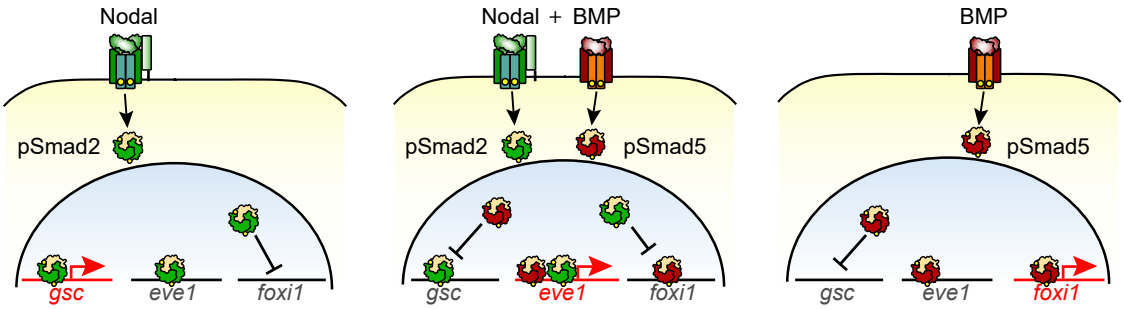

Figure 6. Selective Mutual Antagonism of pSmad2 and pSmad5 Allows Cells to Respond to Different Ratios of Nodal and BMP Signaling

Schematic of a parsimonious model explaining the present findings. The antagonism of pSmad2 and pSmad5 to *foxi1* and *gsc* induction, respectively, allows cells with both high pSmad2 and pSmad5 to express *eve1* without expressing *foxi1* or *gsc*. The activation and inhibition arrows are an abstraction, and the underlying mechanisms may be direct or indirect.

formation of specific embryonic structures (Fauny et al., 2009). Here, we found that ectopic expression of different amounts of constitutively active Smads is sufficient to generate these structures, indicating that varying ratios of Smads are the major factors that confer the inductive capabilities of Nodal and BMP. Mutual antagonism as well as limited synergism between activated Smad2 and Smad5 can lead to distinct combinations of target gene expression sets that correlate with their spatial expression domains (Figures 5 and 6), and an important future goal will be to decipher the molecular mechanism by which pSmad ratios are integrated at the level of signaling or at target gene promotors (Figure 6).

Similar cases of mutual antagonism also exist for other signaling pairs, such as Bicoid and Caudal (reviewed in Briscoe and Small, 2015). However, since Bicoid represses Caudal translation via direct binding to *caudal* mRNA (Niessing et al., 2002), their mutual antagonism is not selective. The selective antagonism mechanism might be needed for Nodal and BMP because they form overlapping orthogonal gradients (reviewed in Rogers and Müller, 2019) instead of anti-parallel gradients. The overlapping nature of the Nodal and BMP gradients leads to an area with both high pSmad2 and pSmad5 activity, areas with either high pSmad2 or high pSmad5 alone, as well as areas without pSmad2 or pSmad5. However, cell fates in areas with high pSmad2 alone or high pSmad5 alone are different from those in areas with both high pSmad2 and high pSmad5. Therefore, the selective antagonism mechanism not only allows cells to sense the ratio of Nodal and BMP but also can work when these gradients extensively overlap at the ventral margin. It is possible that similarly easily implemented mechanisms might generally be involved in the interpretation of other overlapping gradients.

In summary, we used the Nodal/BMP-mediated secondary axis formation assay as a model system to understand how the integration of signaling gradients leads to the activation of signaling effectors and subsequent patterning. In this context, we found that Nodal and BMP activate effector Smads non-cell autonomously and induce signaling at different spatial ranges due to differences in their signaling activities. This yields a field of positional information values in terms of differential signaling effector ratios. Varying ratios of constitutively active Smads can induce different embryonic structures, and selective mutual antagonism of activated Smad2 and Smad5 allows cells to respond to different ratios of Nodal and BMP signaling. It is tempting to speculate that, similar to the Yamanaka factors that can convert differentiated cells into pluripotent cells (Takahashi and Yamanaka, 2006), it might be possible in the future to use the inductive properties of different ratios of constitutively active Smads to induce the formation of desired embryonic structures from pluripotent stem cells for regenerative medicine.

STAR★METHODS

Detailed methods are provided in the online version of this paper and include the following:

- KEY RESOURCES TABLE
- LEAD CONTACT AND MATERIALS AVAILABILITY
- EXPERIMENTAL MODEL AND SUBJECT DETAILS
  - Zebrafish lines
- METHOD DETAILS
  - Plasmids and *in vitro* synthesis of RNA
  - Recombinant proteins
  - Immunoblotting
  - Injections and transplantations
  - Combined whole-mount immunofluorescence and *in situ* hybridization
  - Light-sheet microscopy
  - Confocal microscopy
- QUANTIFICATION AND STATISTICAL ANALYSIS
  - Image analysis
  - Mathematical modeling
- DATA AND CODE AVAILABILITY

SUPPLEMENTAL INFORMATION

Supplemental Information can be found online at https://doi.org/10.1016/j.celrep.2020.03.051.

ACKNOWLEDGMENTS

We thank Katherine Rogers and Daniel Čapek for helpful discussions and Jelena Raspopovic for providing the pCS2-mBMP4 plasmid. This work was

supported by the Max Planck Society and the ERC Starting Grant *QUANTPATTERN* (Grant Agreement No. 637840).

AUTHOR CONTRIBUTIONS

Conceptualization, G.H.S. and P.M.; Methodology, G.H.S. and P.M.; Investigation, G.H.S. and A.P.P.; Writing – Original Draft, G.H.S. and P.M.; Writing – Review & Editing, G.H.S., A.P.P., and P.M.; Funding Acquisition, P.M.; Resources, P.M.; Supervision, P.M.

DECLARATION OF INTERESTS

The authors declare no competing interests.

Received: September 5, 2019
Revised: November 26, 2019
Accepted: March 16, 2020
Published: April 7, 2020

REFERENCES

Agathon, A., Thisse, B., and Thisse, C. (2001). Morpholino knock-down of antivin1 and antivin2 upregulates nodal signaling. Genesis *30*, 178–182.

Almuedo-Castillo, M., Bläßle, A., Mörsdorf, D., Marcon, L., Soh, G.H., Rogers, K.W., Schier, A.F., and Müller, P. (2018). Scale-invariant patterning by size-dependent inhibition of Nodal signalling. Nat. Cell Biol. *20*, 1032–1042.

Bennett, J.T., Joubin, K., Cheng, S., Aanstad, P., Herwig, R., Clark, M., Lehrach, H., and Schier, A.F. (2007). Nodal signaling activates differentiation genes during zebrafish gastrulation. Dev. Biol. *304*, 525–540.

Bisgrove, B.W., Su, Y.C., and Yost, H.J. (2017). Maternal Gdf3 is an obligatory cofactor in Nodal signaling for embryonic axis formation in zebrafish. eLife *6*, e28534.

Blader, P., Rastegar, S., Fischer, N., and Strähle, U. (1997). Cleavage of the BMP-4 antagonist chordin by zebrafish tolloid. Science *278*, 1937–1940.

Bläßle, A., Soh, G., Braun, T., Mörsdorf, D., Preiß, H., Jordan, B.M., and Müller, P. (2018). Quantitative diffusion measurements using the open-source software PyFRAP. Nat. Commun. *9*, 1582.

Briscoe, J., and Small, S. (2015). Morphogen rules: design principles of gradient-mediated embryo patterning. Development *142*, 3996–4009.

Chen, Y., and Schier, A.F. (2001). The zebrafish Nodal signal Squint functions as a morphogen. Nature *411*, 607–610.

Ciruna, B., Weidinger, G., Knaut, H., Thisse, B., Thisse, C., Raz, E., and Schier, A.F. (2002). Production of maternal-zygotic mutant zebrafish by germ-line replacement. Proc. Natl. Acad. Sci. USA *99*, 14919–14924.

Dal-Pra, S., Fürthauer, M., Van-Celst, J., Thisse, B., and Thisse, C. (2006). Noggin1 and Follistatin-like2 function redundantly to Chordin to antagonize BMP activity. Dev. Biol. *298*, 514–526.

de Olivera-Melo, M., Xu, P.F., Houssin, N., Thisse, B., and Thisse, C. (2018). Generation of ectopic morphogen gradients in the zebrafish blastula. Methods Mol. Biol. *1863*, 125–141.

Dubrulle, J., Jordan, B.M., Akhmetova, L., Farrell, J.A., Kim, S.H., Solnica-Krezel, L., and Schier, A.F. (2015). Response to Nodal morphogen gradient is determined by the kinetics of target gene induction. eLife *4*, e05042.

Fauny, J.D., Thisse, B., and Thisse, C. (2009). The entire zebrafish blastula-gastrula margin acts as an organizer dependent on the ratio of Nodal to BMP activity. Development *136*, 3811–3819.

Feldman, B., Gates, M.A., Egan, E.S., Dougan, S.T., Rennebeck, G., Sirotkin, H.I., Schier, A.F., and Talbot, W.S. (1998). Zebrafish organizer development and germ-layer formation require nodal-related signals. Nature *395*, 181–185.

Fisher, S., and Halpern, M.E. (1999). Patterning the zebrafish axial skeleton requires early chordin function. Nat. Genet. *23*, 442–446.

Ghosh, P., Maurer, J.M., and Sagerström, C.G. (2018). Analysis of novel caudal hindbrain genes reveals different regulatory logic for gene expression in rhombomere 4 versus 5/6 in embryonic zebrafish. Neural Dev. *13*, 13.

Gritsman, K., Zhang, J., Cheng, S., Heckscher, E., Talbot, W.S., and Schier, A.F. (1999). The EGF-CFC protein one-eyed pinhead is essential for nodal signaling. Cell *97*, 121–132.

Hagos, E.G., and Dougan, S.T. (2007). Time-dependent patterning of the mesoderm and endoderm by Nodal signals in zebrafish. BMC Dev. Biol. *7*, 22.

Hans, S., Christison, J., Liu, D., and Westerfield, M. (2007). Fgf-dependent otic induction requires competence provided by Foxi1 and Dlx3b. BMC Dev. Biol. *7*, 5.

Harmansa, S., Alborelli, I., Bieli, D., Caussinus, E., and Affolter, M. (2017). A nanobody-based toolset to investigate the role of protein localization and dispersal in Drosophila. eLife *6*, e22549.

Hawley, S.H., Wünnenberg-Stapleton, K., Hashimoto, C., Laurent, M.N., Watabe, T., Blumberg, B.W., and Cho, K.W. (1995). Disruption of BMP signals in embryonic Xenopus ectoderm leads to direct neural induction. Genes Dev. *9*, 2923–2935.

Heldin, C.H., Miyazono, K., and ten Dijke, P. (1997). TGF-β signalling from cell membrane to nucleus through SMAD proteins. Nature *390*, 465–471.

Joly, J.S., Joly, C., Schulte-Merker, S., Boulekbache, H., and Condamine, H. (1993). The ventral and posterior expression of the zebrafish homeobox gene eve1 is perturbed in dorsalized and mutant embryos. Development *119*, 1261–1275.

Kishimoto, Y., Lee, K.H., Zon, L., Hammerschmidt, M., and Schulte-Merker, S. (1997). The molecular nature of zebrafish swirl: BMP2 function is essential during early dorsoventral patterning. Development *124*, 4457–4466.

Krauss, S., Concordet, J.P., and Ingham, P.W. (1993). A functionally conserved homolog of the Drosophila segment polarity gene hh is expressed in tissues with polarizing activity in zebrafish embryos. Cell *75*, 1431–1444.

Lambert, T.J. (2019). FPbase: a community-editable fluorescent protein database. Nat. Methods *16*, 277–278.

Little, S.C., and Mullins, M.C. (2009). Bone morphogenetic protein heterodimers assemble heteromeric type I receptor complexes to pattern the dorsoventral axis. Nat. Cell Biol. *11*, 637–643.

Liu, G., Amin, S., Okuhama, N.N., Liao, G., and Mingle, L.A. (2006). A quantitative evaluation of peroxidase inhibitors for tyramide signal amplification mediated cytochemistry and histochemistry. Histochem. Cell Biol. *126*, 283–291.

Mathieu, J., Griffin, K., Herbomel, P., Dickmeis, T., Strähle, U., Kimelman, D., Rosa, F.M., and Peyriéras, N. (2004). Nodal and Fgf pathways interact through a positive regulatory loop and synergize to maintain mesodermal cell populations. Development *131*, 629–641.

Meno, C., Gritsman, K., Ohishi, S., Ohfuji, Y., Heckscher, E., Mochida, K., Shimono, A., Kondoh, H., Talbot, W.S., Robertson, E.J., et al. (1999). Mouse Lefty2 and zebrafish antivin are feedback inhibitors of nodal signaling during vertebrate gastrulation. Mol. Cell *4*, 287–298.

Michaelis, L., Menten, M.L., Johnson, K.A., and Goody, R.S. (2011). The original Michaelis constant: translation of the 1913 Michaelis-Menten paper. Biochemistry *50*, 8264–8269.

Miller, D.S.J., Schmierer, B., and Hill, C.S. (2019). TGF-β family ligands exhibit distinct signalling dynamics that are driven by receptor localisation. J. Cell Sci. *132*, jcs234039.

Montague, T.G., and Schier, A.F. (2017). Vg1-Nodal heterodimers are the endogenous inducers of mesendoderm. eLife *6*, e28183.

Mörsdorf, D., and Müller, P. (2019). Tuning protein diffusivity with membrane tethers. Biochemistry *58*, 177–181.

Müller, P., Rogers, K.W., Jordan, B.M., Lee, J.S., Robson, D., Ramanathan, S., and Schier, A.F. (2012). Differential diffusivity of Nodal and Lefty underlies a reaction-diffusion patterning system. Science *336*, 721–724.

Müller, P., Rogers, K.W., Yu, S.R., Brand, M., and Schier, A.F. (2013). Morphogen transport. Development *140*, 1621–1638.

Mullins, M.C., Hammerschmidt, M., Kane, D.A., Odenthal, J., Brand, M., van Eeden, F.J., Furutani-Seiki, M., Granato, M., Haffter, P., Heisenberg, C.P.,

et al. (1996). Genes establishing dorsoventral pattern formation in the zebrafish embryo: the ventral specifying genes. Development *123*, 81–93.

Nagai, T., Ibata, K., Park, E.S., Kubota, M., Mikoshiba, K., and Miyawaki, A. (2002). A variant of yellow fluorescent protein with fast and efficient maturation for cell-biological applications. Nat. Biotechnol. *20*, 87–90.

Niessing, D., Blanke, S., and Jäckle, H. (2002). Bicoid associates with the 5′-cap-bound complex of caudal mRNA and represses translation. Genes Dev. *16*, 2576–2582.

Pédelacq, J.D., Cabantous, S., Tran, T., Terwilliger, T.C., and Waldo, G.S. (2006). Engineering and characterization of a superfolder green fluorescent protein. Nat. Biotechnol. *24*, 79–88.

Pelliccia, J.L., Jindal, G.A., and Burdine, R.D. (2017). Gdf3 is required for robust Nodal signaling during germ layer formation and left-right patterning. eLife *6*, e28635.

Pogoda, H.M., and Meyer, D. (2002). Zebrafish Smad7 is regulated by Smad3 and BMP signals. Dev. Dyn. *224*, 334–349.

Pomreinke, A.P., Soh, G.H., Rogers, K.W., Bergmann, J.K., Bläßle, A.J., and Müller, P. (2017). Dynamics of BMP signaling and distribution during zebrafish dorsal-ventral patterning. eLife *6*, 25861.

Ramel, M.C., and Hill, C.S. (2013). The ventral to dorsal BMP activity gradient in the early zebrafish embryo is determined by graded expression of BMP ligands. Dev. Biol. *378*, 170–182.

Rodaway, A., Takeda, H., Koshida, S., Broadbent, J., Price, B., Smith, J.C., Patient, R., and Holder, N. (1999). Induction of the mesendoderm in the zebrafish germ ring by yolk cell-derived TGF-β family signals and discrimination of mesoderm and endoderm by FGF. Development *126*, 3067–3078.

Rogers, K.W., and Müller, P. (2019). Nodal and BMP dispersal during early zebrafish development. Dev. Biol. *447*, 14–23.

Rogers, K.W., and Schier, A.F. (2011). Morphogen gradients: from generation to interpretation. Annu. Rev. Cell Dev. Biol. *27*, 377–407.

Rogers, K.W., Blässle, A., Schier, A.F., and Müller, P. (2015). Measuring protein stability in living zebrafish embryos using fluorescence decay after photoconversion (FDAP). J. Vis. Exp. *95*, 52266.

Rogers, K.W., Lord, N.D., Gagnon, J.A., Pauli, A., Zimmerman, S., Aksel, D.C., Reyon, D., Tsai, S.Q., Joung, J.K., and Schier, A.F. (2017). Nodal patterning without Lefty inhibitory feedback is functional but fragile. eLife *6*, 28785.

Samarkina, O.N., Popova, A.G., Gvozdik, E.Y., Chkalina, A.V., Zvyagin, I.V., Rylova, Y.V., Rudenko, N.V., Lusta, K.A., Kelmanson, I.V., Gorokhovatsky, A.Y., and Vinokurov, L.M. (2009). Universal and rapid method for purification of GFP-like proteins by the ethanol extraction. Protein Expr. Purif. *65*, 108–113.

Sampath, K., Rubinstein, A.L., Cheng, A.M., Liang, J.O., Fekany, K., Solnica-Krezel, L., Korzh, V., Halpern, M.E., and Wright, C.V. (1998). Induction of the zebrafish ventral brain and floorplate requires cyclops/nodal signalling. Nature *395*, 185–189.

Schindelin, J., Arganda-Carreras, I., Frise, E., Kaynig, V., Longair, M., Pietzsch, T., Preibisch, S., Rueden, C., Saalfeld, S., Schmid, B., et al. (2012). Fiji: an open-source platform for biological-image analysis. Nat. Methods *9*, 676–682.

Schmid, B., Fürthauer, M., Connors, S.A., Trout, J., Thisse, B., Thisse, C., and Mullins, M.C. (2000). Equivalent genetic roles for bmp7/snailhouse and bmp2b/swirl in dorsoventral pattern formation. Development *127*, 957–967.

Schulte-Merker, S., Lee, K.J., McMahon, A.P., and Hammerschmidt, M. (1997). The zebrafish organizer requires chordino. Nature *387*, 862–863.

Shen, M.M., and Schier, A.F. (2000). The EGF-CFC gene family in vertebrate development. Trends Genet. *16*, 303–309.

Stachel, S.E., Grunwald, D.J., and Myers, P.Z. (1993). Lithium perturbation and goosecoid expression identify a dorsal specification pathway in the pregastrula zebrafish. Development *117*, 1261–1274.

Takahashi, K., and Yamanaka, S. (2006). Induction of pluripotent stem cells from mouse embryonic and adult fibroblast cultures by defined factors. Cell *126*, 663–676.

Thisse, C., and Thisse, B. (1999). Antivin, a novel and divergent member of the TGFbeta superfamily, negatively regulates mesoderm induction. Development *126*, 229–240.

Thisse, C., and Thisse, B. (2008). High-resolution in situ hybridization to whole-mount zebrafish embryos. Nat. Protoc. *3*, 59–69.

Tsang, M., Kim, R., de Caestecker, M.P., Kudoh, T., Roberts, A.B., and Dawid, I.B. (2000). Zebrafish nma is involved in TGFbeta family signaling. Genesis *28*, 47–57.

van Boxtel, A.L., Chesebro, J.E., Heliot, C., Ramel, M.C., Stone, R.K., and Hill, C.S. (2015). A temporal window for signal activation dictates the dimensions of a Nodal signaling domain. Dev. Cell *35*, 175–185.

van Boxtel, A.L., Economou, A.D., Heliot, C., and Hill, C.S. (2018). Long-range signaling activation and local inhibition separate the mesoderm and endoderm lineages. Dev. Cell *44*, 179–191.e5.

Wozney, J.M., Rosen, V., Celeste, A.J., Mitsock, L.M., Whitters, M.J., Kriz, R.W., Hewick, R.M., and Wang, E.A. (1988). Novel regulators of bone formation: molecular clones and activities. Science *242*, 1528–1534.

Wrana, J.L., Attisano, L., Cárcamo, J., Zentella, A., Doody, J., Laiho, M., Wang, X.F., and Massagué, J. (1992). TGF β signals through a heteromeric protein kinase receptor complex. Cell *71*, 1003–1014.

Xu, P.F., Houssin, N., Ferri-Lagneau, K.F., Thisse, B., and Thisse, C. (2014). Construction of a vertebrate embryo from two opposing morphogen gradients. Science *344*, 87–89.

Xue, Y., Zheng, X., Huang, L., Xu, P., Ma, Y., Min, Z., Tao, Q., Tao, Y., and Meng, A. (2014). Organizer-derived Bmp2 is required for the formation of a correct Bmp activity gradient during embryonic development. Nat. Commun. *5*, 3766.

Yoney, A., Etoc, F., Ruzo, A., Carroll, T., Metzger, J.J., Martyn, I., Li, S., Kirst, C., Siggia, E.D., and Brivanlou, A.H. (2018). WNT signaling memory is required for ACTIVIN to function as a morphogen in human gastruloids. eLife *7*, e38279.

Zhou, X., Sasaki, H., Lowe, L., Hogan, B.L., and Kuehn, M.R. (1993). Nodal is a novel TGF-β-like gene expressed in the mouse node during gastrulation. Nature *361*, 543–547.

Zinski, J., Bu, Y., Wang, X., Dou, W., Umulis, D., and Mullins, M.C. (2017). Systems biology derived source-sink mechanism of BMP gradient formation. eLife *6*, e22199.

STAR★METHODS

KEY RESOURCES TABLE

REAGENT or RESOURCE	SOURCE	IDENTIFIER
Antibodies		
Rabbit monoclonal anti-phospho-Smad2/Smad3	Cell Signaling Technology	Cat#8828; RRID:AB_2631089
Rabbit monoclonal anti-phospho-Smad1/Smad5/Smad9	Cell Signaling Technology	Cat#13820S; RRID:AB_2493181
Goat anti-rabbit horseradish peroxidase	Jackson ImmunoResearch	Cat#111-035-003; RRID:AB_2313567
Anti-digoxigenin alkaline phosphatase Fab fragments	Roche Diagnostics	Cat#32871920
Anti-digoxigenin horseradish peroxidase Fab fragments	Sigma-Aldrich	Cat#11207733910
Chicken polyclonal anti-GFP	Aves Labs	Cat#GFP-1020; RRID:AB_10000240
Goat anti-rabbit Alexa647	Invitrogen	Cat#A21245; RRID:AB_141775
Goat anti-chicken Alexa568	Abcam	Cat#ab175477
Goat anti-chicken DyLight405	Agrisera	Cat#AS16 3624
Rabbit anti-GFP	Life Technologies	Cat#A11122; RRID:AB_221569
Bacterial Strains		
One Shot TOP10 chemically competent *E. coli*	Life Technologies	Cat#C4040
Chemicals and Recombinant Proteins		
Dorsomorphin	Abcam	Cat#ab120843
SB-505124	Sigma-Aldrich	Cat#S4696-5MG
Cascade Blue dextran, 10 kDa, anionic, lysine fixable	Thermo Fisher Scientific	Cat#D1976
Pronase	Roche	Cat#11459643001
Critical Commercial Assays		
TSA plus fluorescein system	Perkin Elmer	Cat#NEL741001KT
RNeasy kit	QIAGEN	Cat#74104
Pierce protein concentrator PES, 10K MWCO, 5-20 ml	Thermo Fisher Scientific	Cat#88528
SuperSignal West Dura extended duration substrate	Thermo Fisher Scientific	Cat#34075
Q5® site-directed mutagenesis kit	New England Biolabs	Cat#E0554S
Zero Blunt TOPO PCR cloning kit	Thermo Fisher Scientific	Cat#K2800J10
SP6 mMessage mMachine transcription kit	Thermo Fisher Scientific	Cat#AM1340
DIG RNA labeling mix	Sigma-Aldrich	Cat#11277073910
Experimental Models: Organisms/Strains		
Zebrafish: *sqt*^{cz35}	Feldman et al., 1998	N/A
Zebrafish: *cyc*^{m294}	Sampath et al., 1998	N/A
Zebrafish: *swr*^{tc300a}	Mullins et al., 1996	N/A
Zebrafish: *lefty1*^{a145}	Rogers et al., 2017	N/A
Zebrafish: *lefty2*^{a146}	Rogers et al., 2017	N/A
Oligonucleotides		
eve1_For: CTGGTTCCAGAACCGGAGA	This paper	N/A
eve1_Rev: GGAAAGCATATGTACATGGGTTTGTAT	This paper	N/A
foxi1_For: GTCGAGCCAGCAGACCAG	This paper	N/A
foxi1_Rev: CTGTTGTTGTGCGATGCTG	This paper	N/A
shha_For: ATACTGGCGTCCTGTTACGC	This paper	N/A
shha_Rev: ACATTTCCTGACACCTTGCCT	This paper	N/A
krox20_For: CAAACCCTTCCAGTGTCGGA	This paper	N/A
krox20_Rev: GACCCGCGTTAGTCACTTCA	This paper	N/A
hoxc13b_For: AAGCCGAGATGAACGGCTAC	This paper	N/A
hoxc13b_Rev:ACACAAACAGTTTAATATTGGGGGA	This paper	N/A
smad2-CA_For: TCGATTCGAATTCGCCACCATGTCCTCCATCTTGCCTTTCAC	This paper	N/A

(*Continued on next page*)

Continued

REAGENT or RESOURCE	SOURCE	IDENTIFIER
smad2-CA_Rev: ACTATAGTTCTAGATTAGTCCATGTCATCGCAGCGTACGGAGGG	This paper	N/A
smad5_For: GCGCGAATTCGCCACCATGACCTCCATGTCTAGTCTG	This paper	N/A
smad5_Rev: GCGCTCTAGATTACGAGACAGAAGAGATGGG	This paper	N/A
smad5-CA_For: GACGTCGACTAATCTAGAACTATAGTG	This paper	N/A
smad5-CA_Rev: ATCGATGGGGTTCAGAGG	This paper	N/A
Recombinant DNA		
pCS2-Bmp2b-sfGFP	Pomreinke et al., 2017	N/A
pCS2-Bmp7-sfGFP	This paper	N/A
pCS2-Bmp2b-mCherry	This paper	N/A
pCS2-Squint-mVenus	This paper	N/A
pCS2-Squint-mCherry	This paper	N/A
pCS2-Cyclops-mVenus	This paper	N/A
pCS2-Cyclops-mCherry	This paper	N/A
pCS2-Smad2-CA	This paper	N/A
pCS2-Smad5-CA	This paper	N/A
pCS2-mouseBMP4	This paper	N/A
pCRII-eve1	This paper	N/A
pCRII-foxi1	This paper	N/A
pCRII-shha	This paper	N/A
pCRII-hoxc13b	This paper	N/A
pCRII-krox20	This paper	N/A
pCS2-gsc	Müller et al., 2012	N/A
pCS2-sox32	Müller et al., 2012	N/A
pBAD-sfGFP	Pédelacq et al., 2006	Addgene Plasmid #54519; RRID:Addgene_54519
pBAD-mVenus	Nagai et al., 2002	Addgene Plasmid #54845; RRID:Addgene_54845
Software and Algorithms		
Fiji	Schindelin et al., 2012	https://fiji.sc/
Prism	GraphPad Software	https://www.graphpad.com/scientific-software/prism/
COMSOL Multiphysics 3.5a	COMSOL, Inc.	https://www.comsol.com/

LEAD CONTACT AND MATERIALS AVAILABILITY

All reagents generated in this study are available without restriction from the Lead Contact, Patrick Müller (patrick.mueller@tuebingen.mpg.de).

EXPERIMENTAL MODEL AND SUBJECT DETAILS

Zebrafish lines

Zebrafish husbandry was executed in accordance with the guidelines of the State of Baden-Württemberg (Germany) and approved by the Regierungspräsidium Tübingen (35/9185.46-5, 35/9185.81-5). The TE strain was used for experiments with wild-type zebrafish embryos. Maternal-zygotic double-homozygous *sqt*^{cz35} (Feldman et al., 1998) and *cyc*^{m294} (Sampath et al., 1998) mutants (*MZsqt;cyc*) as well as maternal-zygotic *swr*^{tc300a} (Mullins et al., 1996) (*MZswr*) mutants were generated by germline replacement (Ciruna et al., 2002). Maternal-zygotic double-homozygous *lefty1*^{a145};*lefty2*^{a146} mutants (*MZlefty1;lefty2*) were generated using a rescue approach with 4.8 μM of the Nodal inhibitor SB-505124 (Rogers et al., 2017).

METHOD DETAILS

Plasmids and *in vitro* synthesis of RNA

All plasmids for *in vitro* synthesis of mRNA were generated by inserting the sequence of interest into the EcoRI and XhoI sites of the *pCS2(+)* vector, containing the consensus Kozak sequence GCCACC directly in front of the start codon (Müller et al., 2012).

To generate pCS2-Bmp7-sfGFP, sequences encoding sfGFP flanked by LGDPPVAT linkers were inserted two amino acids downstream of the RSVR Furin cleavage site (Hawley et al., 1995). pCS2-Bmp2b-sfGFP was described previously (Pomreinke et al., 2017). pCS2-Bmp2b-mCherry was derived from pCS2-Bmp2b-sfGFP by exchanging the sfGFP-coding sequence with mCherry-encoding sequences. pCS2-Squint-mVenus and pCS2-Squint-mCherry were derived from pCS2-Squint-GFP (Müller et al., 2012) by exchanging the GFP-coding sequence with mVenus- and mCherry-encoding sequences, respectively. pCS2-Cyclops-mVenus and pCS2-Cyclops-mCherry were derived from pCS2-Cyclops-GFP (Müller et al., 2012) by exchanging the GFP-coding sequence with mVenus- and mCherry-encoding sequences, respectively.

Constitutively active Smads were generated by replacing the three C-terminal serine codons with aspartate codons. Smad5 was cloned from zebrafish shield-stage cDNA into the *pCS2(+)* vector with the primers GCGCGAATTCGCCACCATGACCTCCATGTC TAGTCTG and GCGCTCTAGATTACGAGACAGAAGAGATGGG. The Q5 site-directed mutagenesis kit (New-England Biolabs) was then used to replace the C-terminal serine codons with the primers GACGTCGACTAATCTAGAACTATAGTG and ATCGATGGGGTT CAGAGG. Smad2-CA was directly amplified and modified from zebrafish shield-stage cDNA with the primers TCGATTC GAATTCGCCACCATGTCCTCCATCTTGCCTTTCAC and ACTATAGTTCTAGATTAGTCCATGTCATCGCAGCGTACGGAGGG. The amplicon was cloned into the *pCS2(+)* vector.

mRNA for microinjection was generated using the SP6 mMessage mMachine kit (Thermo Fisher Scientific) according to the manufacturer's instructions after plasmid linearization with NotI-HF (New England Biolabs, Cat#R3189).

Plasmids containing sequence fragments of *eve1*, *foxi1*, *shha*, *krox20* and *hoxc13b* were generated using Zero Blunt TOPO PCR Cloning (Invitrogen, Thermo Fisher Scientific) and the following primers: CTGGTTCCAGAACCGGAGA and GGAAAGCATATGTA CATGGGTTTGTAT for *eve1*, GTCGAGCCAGCAGACCAG and CTGTTGTTGTGCGATGCTG for *foxi1*, ATACTGGCGTCCTGTTACGC and ACATTTCCTGACACCTTGCCT for *shha*, CAAACCCTTCCAGTGTCGGA and GACCCGCGTTAGTCACTTCA for *krox20*, AAGCCGAGATGAACGGCTAC and ACACAAACAGTTTAATATTGGGGGA for *hoxc13b*. For *foxi1,* shield-stage cDNA was used as a template, whereas genomic DNA was used as a template for *eve1*, *shha*, *krox20* and *hoxc13b*. Linear fragments for *eve1*, *foxi1*, *shha*, *krox20* and *hoxc13b* were produced by PCR with M13 forward and M13 reverse primers. To generate templates for *gsc* and *sox32* probes, plasmids were linearized with EcoRI and NotI (New England Biolabs) respectively (Müller et al., 2012). RNA probes for *in situ* hybridization were synthesized from these linearized plasmids using SP6 or T7 polymerase and DIG-modified ribonucleotides (Roche). RNA probes were purified using RNeasy kits (QIAGEN).

Recombinant proteins

sfGFP and mVenus were expressed in One Shot TOP10 *E. coli* using the plasmids pBAD-sfGFP (Addgene plasmid #54519 (Pédelacq et al., 2006)) and pBAD-mVenus (Addgene plasmid #54845 (Nagai et al., 2002)) after overnight induction with 10 mg/ml arabinose at 16°C. The fluorescent proteins were then purified by ethanol extraction as previously described (Samarkina et al., 2009). Briefly, *E. coli* cells were lysed by sonication in 20 mM Tris–HCl, 150 mM NaCl, 5 mM EDTA, pH 7.8, and sodium chloride and ammonium sulfate were added to the lysate to a final concentration of 0.41 M and 2.63 M, respectively. 1.2 volumes of 96% ethanol were then added to the lysate, and the mixture was vigorously shaken. After centrifugation, the fluorescent proteins became partitioned into the upper organic phase. The upper phase was recovered, and 0.25 volumes of n-Butanol were added. The mixture was then centrifuged, causing the fluorescent proteins to be partitioned into the lower aqueous phase from which they were recovered. The purified fluorescent proteins were then concentrated and buffer-exchanged into phosphate buffered saline (PBS) via ultrafiltration with Pierce protein concentrators (10K MWCO, Thermo Fisher Scientific). Fluorescent proteins were quantified using a Nanodrop 1000 (Thermo Fisher Scientific) by measuring their absorption spectra. The concentration was calculated according to the Beer–Lambert law using the measured peak absorption and the molar extinction coefficients taken from FPbase (Lambert, 2019).

Immunoblotting

Extra- and intracellularly enriched embryo extracts were prepared as described previously (Pomreinke et al., 2017; Müller et al., 2012). Protein samples were resolved on 12% polyacrylamide gels and transferred to polyvinylidene fluoride membranes using a semi-dry blotting system (Bio-Rad). The blots were blocked in 5% low fat milk in PBS containing 0.1% Tween 20 (PBST) for 1 hour, before being incubated overnight at 4°C with a dilution of 1:5000 rabbit anti-GFP antibody (Life Technologies) in 1% low fat milk in PBST. The blots were washed 3 times for 10 min each with PBST and then incubated for 1 h at room temperature with a dilution of 1:5000 goat anti-rabbit horseradish peroxidase (Jackson ImmunoResearch) in 1% low fat milk in PBST. Finally, the blots were washed 3 times for 10 min each with PBST, and the signal was developed with SuperSignal West Dura extended duration substrate (Thermo Fisher Scientific) for imaging with a chemiluminescence imaging system (Fusion 483 Solo, Vilber Lourmat).

Injections and transplantations

For transplantation experiments, embryos were dechorionated using 0.1 mg/ml Pronase (Roche) in 5 mL embryo medium and rinsed in embryo medium to remove the Pronase (Rogers et al., 2015). Embryos were then injected with 2 nL of injection mix at the 1- or 2-cell stage and incubated at 28°C until transplantation. Unfertilized or injured embryos were discarded. Transplantation was done when the embryos reached sphere stage. A cylinder of cells, approximately 80 μm in diameter and 100 μm in length, was transplanted from sphere-stage donor embryos expressing *squint-mVenus* or *bmp2b-sfGFP* + *bmp7-sfGFP* (termed *bmp2b/7-sfGFP* in the following) into uninjected sphere-stage sibling hosts. Combinations of 100 pg *squint-mVenus* mRNA or 100 pg + 100 pg *bmp2b/7-sfGFP* mRNA were used for most experiments, except for Figure S5, where 20 pg *squint-mVenus* mRNA along with 20 pg + 20 pg *bmp2b/7-sfGFP* mRNA and 20 pg *squint-mVenus* mRNA along with 100 pg + 100 pg *bmp2b/7-sfGFP* mRNA were additionally used. For transplantations with mouse BMP4, 40 pg of *mouse bmp4* mRNA was used. Cells for mock transplantations and those with mouse BMP4 were additionally labeled by injecting 100 pg of 10 kDa cascade blue-dextran (Thermo Fisher Scientific) at the one-cell stage. Following transplantation, the embryos were placed in Ringer's solution (116 mM NaCl, 2.8 mM KCl, 1 mM $CaCl_2$, 5 mM HEPES) for 15 min to recover and then incubated at 28°C until further processing.

To test the activity of constitutively active Smads, different amounts of *smad2-CA* or *smad5-CA* mRNA as detailed in the figures were injected into one-cell stage embryos, which were dechorionated at shield stage before fixation.

For the generation of ectopic structures with constitutively active Smads, embryos were dechorionated. Three adjacent blastomeres in embryos at the 64-cell stage were then injected with 20 pg *smad2-CA*, 20 pg *smad2-CA* + 20 pg *smad5-CA*, or 20 pg *smad2-CA* + 80 pg *smad5-CA* mRNA per blastomere. For Nodal and BMP receptor inhibition, 40 μM of SB-505124 (Sigma-Aldrich) and 10 μM of Dorsomorphin (Abcam) were used, respectively.

Combined whole-mount immunofluorescence and *in situ* hybridization

Embryos were fixed in 4% formaldehyde in PBS overnight at 4°C, dehydrated in 100% methanol and stored at −20°C until further processing. Chromogenic *in situ* hybridization was carried out as described before (Thisse and Thisse, 2008). Fluorescent *in situ* hybridization (FISH) was executed as described before (Almuedo-Castillo et al., 2018). If immunostainings were subsequently done, embryos were also incubated with 20 mM HCl for 25 min to inactivate the horse radish peroxidase (Liu et al., 2006).

For whole-mount immunostainings, embryos were washed three times with PBST and then permeabilized with cold acetone at −20°C for 20 min. Blocking and antibody incubations were performed in 10% FBS in PBST, and all washes were done with PBST. To carry out the dual pSmad2 and pSmad5 stainings, embryos were first blocked and then incubated with a 1:5000 dilution of a rabbit anti-pSmad2 antibody (Cell Signaling Technology) at 4°C overnight followed by 8 washes for 15 min each. The samples were then blocked and incubated with 1:500 goat anti-rabbit horseradish peroxidase (Jackson ImmunoResearch) at 4°C overnight followed by 8 washes for 15 min each. The signal was detected with TSA fluorescein at a dilution of 1:75 in amplification buffer (Perkin Elmer) for 45 min at room temperature followed by three washes for 5 min each. The embryos were then incubated with methanol for 3 h, washed three times for 10 min, blocked and incubated with a 1:100 dilution of a rabbit anti-pSmad5 antibody (Cell Signaling Technology) and a 1:200 dilution of chicken anti-GFP antibody (Aves Labs) at 4°C overnight. The samples were washed 8 times for 15 min each, blocked and incubated with 1:100 anti-rabbit Alexa647 IgG and 1:200 anti-chicken Alexa 568 IgG (in cases where no *in situ* hybridization was carried out) or anti-chicken DyLight 405 IgG (for combined *in situ* hybridization) at 4°C overnight. The embryos were finally washed 8 times for 15 min each and imaged immediately afterward using a light-sheet microscope.

Light-sheet microscopy

Fluorescence images of fixed samples were obtained using a Lightsheet Z.1 microscope (ZEISS). Samples were mounted in 1% low-melting agarose (Lonza, Cat#50080) in embryo medium using a size 3 glass capillary sample holder (ZEISS) and a needle to orient the embryos. The samples were imaged as a series of z stacks with the following objectives and imaging conditions: W Plan-Apochromat 20 × objective, 0.5 × zoom, separate exposure, 80 ms exposure time, 6.4 μm average light-sheet thickness, 10 μm intervals between z-slices. For samples stained by *in situ* hybridization alone, a 488 nm laser (100 mW) was used at 6% power for *foxi1*, 1% power for *gsc*, 8% power for *eve1*. For samples with double pSmad staining, a 488 nm laser (100 mW) was used at 1% power, a 561 nm laser (20 mW) at 5% power, and a 638 nm laser (75 mW) at 8% power. For samples with *in situ* hybridization signals and double pSmad staining, a 561 nm laser (20 mW) was used at 5% power, and a 405 nm laser (20 mW) was used at 10% power in addition to the other three lasers. Images were acquired with 1920 pixels × 1920 pixels (877.13 μm × 811.13 μm) dimensions.

Confocal microscopy

Live imaging of embryos was executed on an LSM 780 NLO confocal microscope (ZEISS) using an LD C-Apochromat 40 × / 1.1 NA water immersion objective. Embryos were mounted in 1% low-melting point agarose in glass bottom Petri dishes (MatTek Corporation) and covered with embryo medium. Embryos were maintained at 28°C during the experiments using a heated chamber and imaged 30, 60, 120 and 180 min post-transplantation. The fluorophores were excited with a 50 mW argon laser. sfGFP was excited at 488 nm with 16% laser power, and mVenus was excited at 514 nm with 35% power. The emission was collected as a multispectral image using a 32-channel GaAsP QUASAR array. Images were acquired with 512 × 512 pixels (425.10 × 425.10 μm) dimensions. The multispectral image was then converted into a single channel image by linear unmixing using ZEN Black (ZEISS) (Figure S2H).

QUANTIFICATION AND STATISTICAL ANALYSIS

Image analysis

Fiji was used for all image analyses (Schindelin et al., 2012). Nodal and BMP gradients were quantified similar to previous approaches (Pomreinke et al., 2017; Müller et al., 2012). A median filter of 1 pixel radius was applied to the images for denoising. This was followed by a maximum intensity projection of 14 z-slices.

Nodal, BMP, pSmad2 and pSmad5 gradients were quantified in a rectangular 66 μm wide and 150 μm long region. The "*plot profile*" function in Fiji was used, which averages the data along the width. Background levels were determined by measuring the average intensity from untransplanted embryos, and the background was subtracted from the gradient profiles. Prism (GraphPad Software) was used for data plotting. All error bars indicate 95% confidence intervals.

The pSmad ratio images were generated by first subtracting background intensities from each channel separately followed by a Gaussian blur with a sigma of 10. The Gaussian blur was performed to visualize an area of pSmad2 or pSmad5 activity instead of specific nuclei and to minimize aberrantly high ratios resulting from division by very low pSmad5 intensities. After Gaussian blurring, the pSmad2 channel was divided by the pSmad5 channel to generate the final image.

To determine the target gene response with varying amounts of Smad2-CA + Smad5-CA, the average intensity in a central circular region with half of the embryo radius was measured.

Mathematical modeling

The finite element method was used for two-dimensional numerical simulations of differential signaling activation kinetics from a single input gradient. The zebrafish animal pole was modeled as a circle with a radius of 300 μm, and the mouse *BMP4* (mBMP4) expressing clone was placed concentrically into the embryo disc with a radius of 10 μm. mBMP4 gradient formation was simulated using the following partial differentiation equation:

$$\frac{\partial mBMP4}{\partial t} = D\nabla^2 mBMP4 + k_1(x) - k_2 mBMP4$$

where $D = 3\ \mu m^2/s$ represents the diffusion coefficient of mBMP4 (based on measurements of zebrafish Bmp2b (Pomreinke et al., 2017; Zinski et al., 2017)), $k_1 = 1/s$ represents the spatially restricted production rate constant of mBMP4 exclusively within the clone, and $k_2 = 10^{-4}/s$ (based on measurements of zebrafish Bmp2b (Pomreinke et al., 2017)) represents the spatially uniform clearance rate constant.

The readout of the resulting mBMP4 gradient by pSmad5 and pSmad2 was modeled as

$$\frac{\partial pSmad5}{\partial t} = k_5 \frac{mBMP4}{k_d + mBMP4} - k_3 pSmad5$$

$$\frac{\partial pSmad2}{\partial t} = k_6 \frac{mBMP4}{k_e + mBMP4} - k_4 pSmad2$$

where $k_3 = k_4 = 10^{-4}/s$ represent the degradation rate constants of the pSmads and $k_5 = k_6 = 1/s$ represent their production rate constants. $k_d = 100$ and $k_e = 10^6$ represent the different signaling thresholds that activate pSmad5 and pSmad2, respectively.

The solution at each time step in the discretized geometry was determined using a sparse LU factorization algorithm (UMFPACK), and the time stepping was computed using a backward Euler step method (COMSOL Multiphysics 3.5a). Simulations were executed for a total of 7200 s.

While D and k_2 are based on directly measured quantities, the values for k_1, k_3, k_4, k_5, k_6, k_d and k_e have not been experimentally determined. k_1, k_5 and k_6 control the amplitude of the gradients – but not their shape – and were therefore set to an arbitrary value of 1/s. Equal values of k_3 and k_4 were chosen to reflect the timescale of gradient formation. A large difference between k_d and k_e values was chosen to illustrate that a single signaling molecule gradient can generate vastly different activity gradients based on differential signaling kinetics.

DATA AND CODE AVAILABILITY

The raw images and data used in this work are available from the Lead Contact upon request.

Cell Reports, Volume *31*

Supplemental Information

Integration of Nodal and BMP Signaling by Mutual Signaling Effector Antagonism

Gary Huiming Soh, Autumn Penecilla Pomreinke, and Patrick Müller

Table S1, Related to Figure 1.

Nodal		BMP		Ratio of Nodal to BMP mRNA	Secondary axis formation rate (%)	n
Amount (pg)	Construct	Amount (pg)	Construct			
66	Squint	132	Bmp2b/7	0.50	40	45
100	Squint-mVenus	200	Bmp2b/7-sfGFP	0.50	50	70
400	Cyclops-mVenus	40	Bmp2b/7-sfGFP	10.00	20	69
200	Squint-mCherry	2200	Bmp2b/7-sfGFP	0.09	26	66
1200	Squint-GFP	250	Bmp2b-mCherry	4.80	24	72
100	Cyclops-mCherry	800	Bmp2b-sfGFP	0.13	14	50

Secondary axis formation efficiency of different fluorescently tagged Nodal and BMP fusions. Embryos received donor cells injected with various amounts of fluorescently tagged Nodal- and BMP-encoding mRNA. The percentage of embryos with secondary axes was assessed at 24 h post-transplantation.

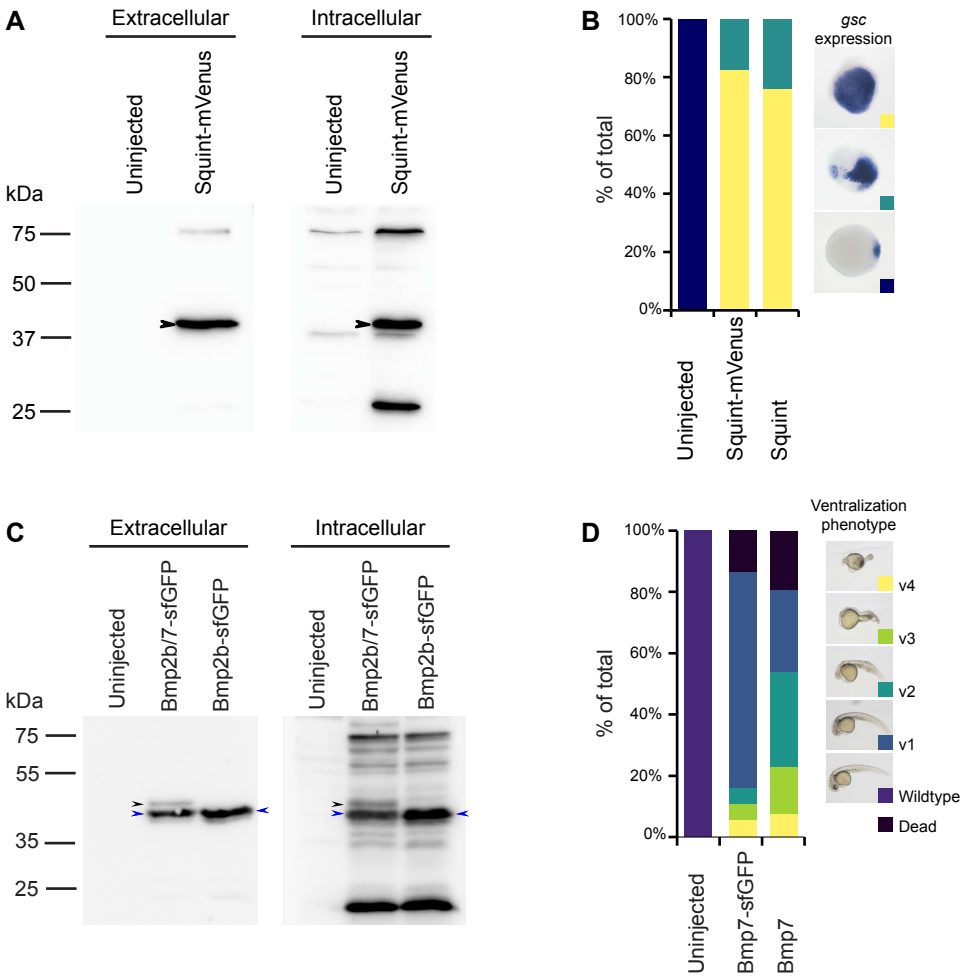

Figure S1. Characterization of Squint-mVenus and Bmp7-sfGFP, Related to Figure 1. (A) Extra- and intracellularly enriched extracts were obtained from uninjected zebrafish embryos or embryos injected with 200 pg *squint-mVenus* mRNA. The extracts were subjected to immunoblotting with anti-GFP antibodies (Müller et al., 2012). The arrowheads point to the band representing processed mature Squint-mVenus. Note that no free mVenus protein (size ≈25 kDa) was detected in the extracellularly enriched extracts. **(B)** Zebrafish embryos were injected with equimolar amounts of mRNA encoding Squint (1 pg, n=23) and Squint-mVenus (1.48 pg, n=25) at the one-cell stage. Embryos were then fixed, stained for the expression of the Nodal target gene *gsc* by whole-mount *in situ* hybridization and classified based on the staining extent. Squint and Squint-mVenus have a similar specific activity to induce *gsc* expression. **(C)** Extra- and intracellularly enriched extracts were obtained from uninjected zebrafish embryos and embryos injected with 150 pg *bmp7-sfGFP* + *bmp2b-sfGFP* or 200 pg *bmp2b-sfGFP* mRNA. The extracts were subjected to immunoblotting with anti-GFP antibodies. *bmp2b-sfGFP* mRNA was used as a control that had previously been shown to be properly processed (Pomreinke et al., 2017). The arrowheads point to the bands representing processed mature Bmp2b-sfGFP (blue arrow) and Bmp7-sfGFP (black arrow). Note that no free sfGFP protein (size ≈25 kDa) was detected in the extracellularly enriched extracts. **(D)** Zebrafish embryos were injected with equimolar amounts of mRNA encoding Bmp7 (9 pg, n=102) and Bmp7-sfGFP (11 pg, n=107) at the one-cell stage. Ventralization phenotypes at 24 h post-fertilization were categorized using established classification schemes (Pomreinke et al., 2017; Mullins et al., 1996).

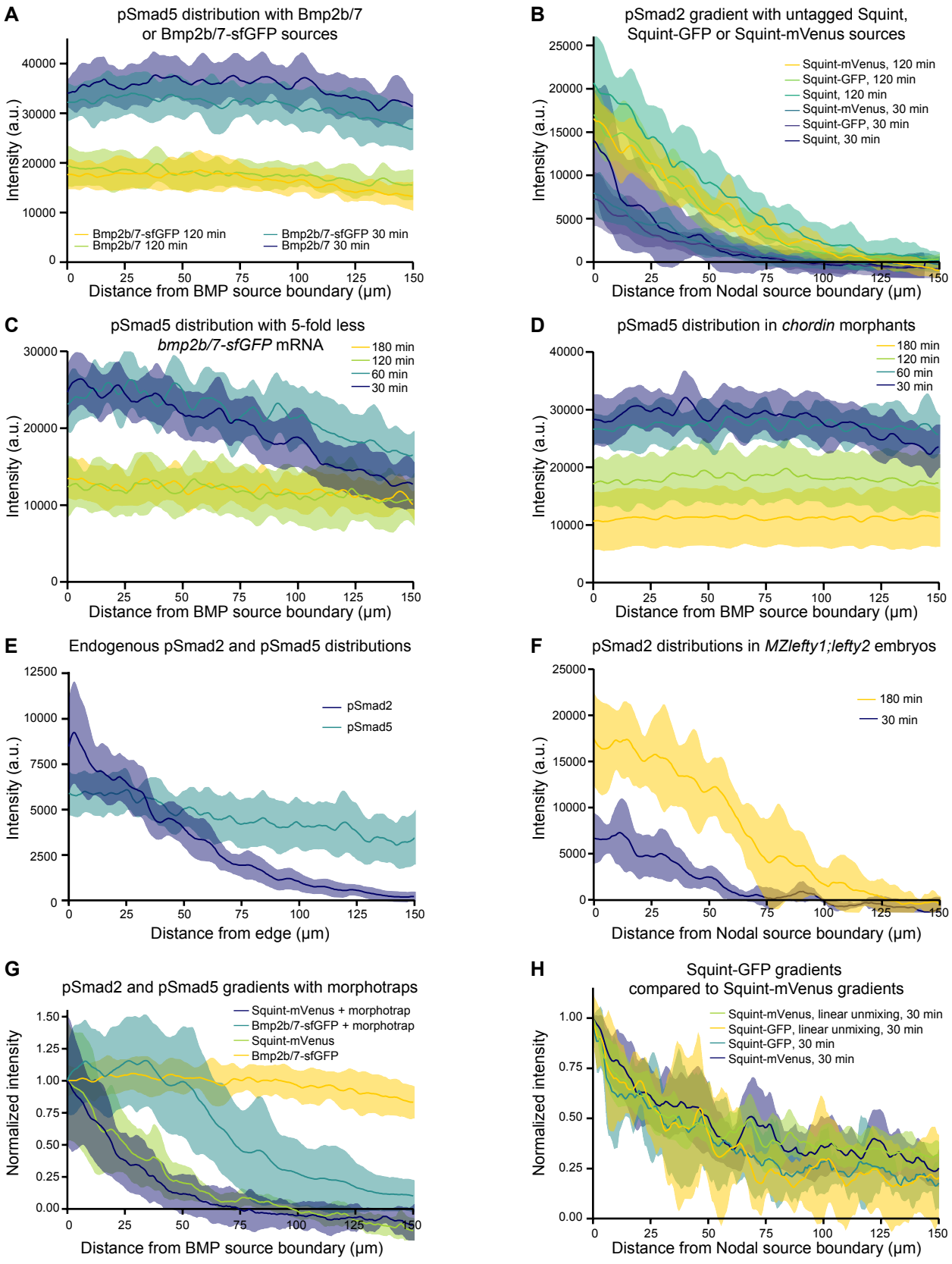

Figure S2. Quantification of endogenous and ectopic signaling distributions, Related to Figure 2. (A) Spatiotemporal pSmad5 distributions for single clones of untagged Bmp2b/7 and Bmp2b/7-sfGFP at 30 min (n[Bmp2b/7]=9, n[Bmp2b/7-sfGFP]=9) and 120 min (n[Bmp2b/7]=11, n[Bmp2b/7-sfGFP]=10) post-transplantation. **(B)** Spatiotemporal pSmad2 distributions for single clones of untagged Squint, Squint-GFP or Squint-mVenus at 30 min (n[Squint]=6, n[Squint-GFP]=8, n[Squint-mVenus]=9) and 120 min (n[Squint]=8, n[Squint-GFP]=10, n[Squint-mVenus]=9) post-transplantation. **(C)** Spatiotemporal pSmad5 distributions at 30 (n=12), 60 (n=9), 120 (n=8) and 180 (n=12) min post-transplantation in embryos with single Bmp2b/7-sfGFP clones that carried five times less *bmp2b/7-sfGFP* mRNA than the clones shown in Figure 2C. **(D)** Spatiotemporal pSmad5 distributions in embryos with single Bmp2b/7-sfGFP clones in *chordin* morphants at 30 (n=9), 60 (n=8), 120 (n=9) and 180 (n=10) min post-transplantation. **(E)** Distribution of endogenous pSmad5 along the ventral-dorsal axis (n=10), and endogenous pSmad2 signal along the vegetal-animal axis (n=12) in wildtype embryos at 50% epiboly. **(F)** pSmad2 distributions in *MZlefty1;lefty2* embryos with single Squint-mVenus clones at 30 and 180 min post-transplantation (n=6 each). **(G)** Normalized pSmad2 and pSmad5 gradients induced by Squint-mVenus and Bmp2b/7-sfGFP clones with or without morphotraps expressed in the host embryo (n[Squint-mVenus+morphotrap]=7, n[Bmp2b/7-sfGFP+morphotrap]=6, n[Squint-mVenus]=11, n[Bmp2b/7-sfGFP]=9). **(H)** Nodal protein gradients in embryos with single Squint-GFP (n=4) or Squint-mVenus (n=12) clones at 30 min post-transplantation, with or without linear unmixing. In all panels, the shaded regions represent 95% confidence intervals around the mean (lines).

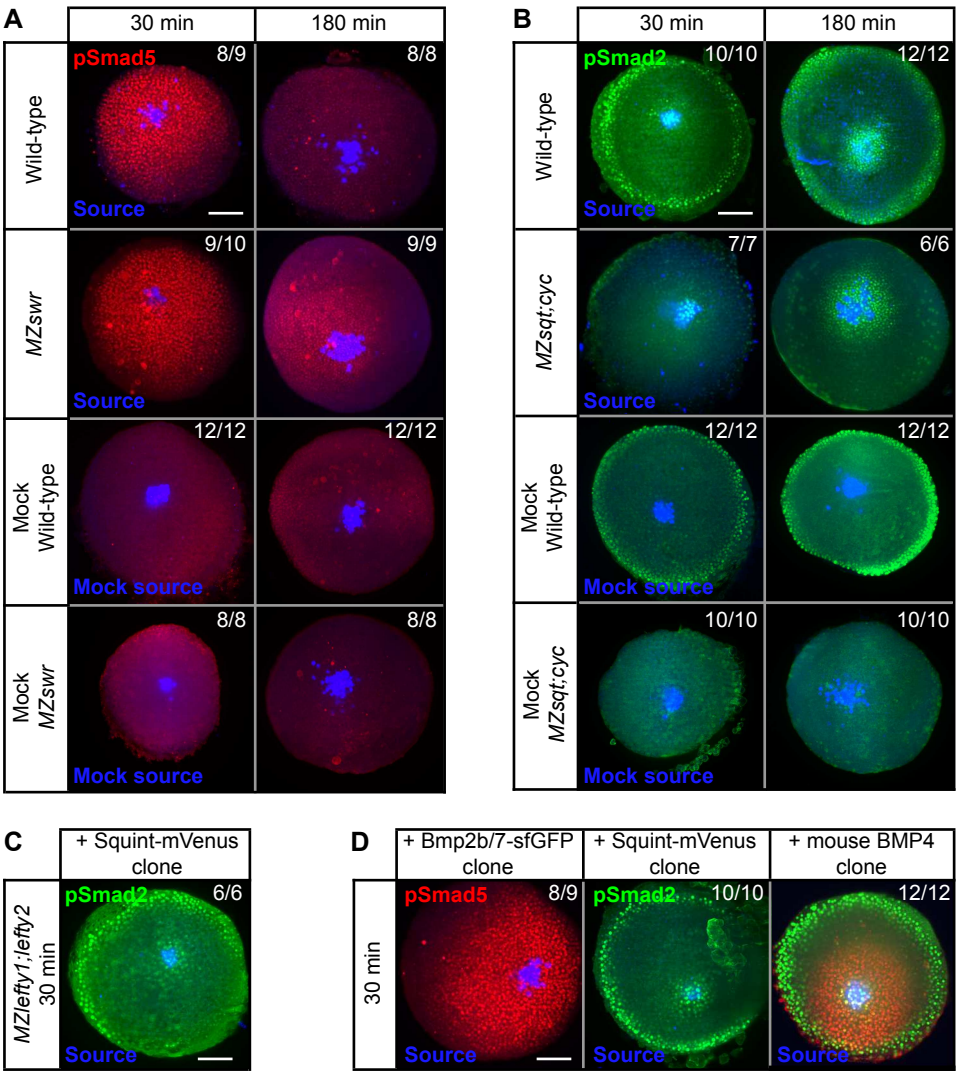

Figure S3. Comparison of pSmad5 and pSmad2 ranges in whole-embryo views, Related to Figure 2. (A) Whole-embryo views of Bmp2b/7-sfGFP clones 30 min and 180 min post-transplantation in wild-type or *MZswr* embryos compared to uninjected mock sources transplanted into wild-type or *MZswr* embryos. Embryos were immunostained with anti-pSmad5 (red) and anti-GFP (blue) antibodies. Mock sources were labeled with cascade blue-dextran (blue). Scale bar: 150 µm. **(B)** Whole-embryo views of Squint-mVenus clones 30 min and 180 min post-transplantation in wild-type or *MZsqt;cyc* embryos compared to uninjected mock sources transplanted into wild-type or *MZsqt;cyc* embryos. Embryos were immunostained with anti-pSmad2 (green) and anti-GFP (blue) antibodies. Mock sources were labeled with cascade blue-dextran (blue). Scale bar: 150 µm. **(C)** Whole-embryo views of Squint-mVenus clones derived from *MZlefty1;lefty2* donor embryos in *MZlefty1;lefty2* host embryos 30 min after transplantation. Embryos were immunostained with anti-pSmad2 (green) and anti-GFP (blue) antibodies. Scale bar: 150 µm. **(D)** Whole-embryo views of wildtype embryos with clones expressing *bmp2b/7-sfGFP*, *squint-mVenus* or mouse *bmp4*. Embryos were fixed 30 min post-transplantation and immunostained with anti-pSmad2 (green) or anti-pSmad5 (red) antibodies. Bmp2b/7-sfGFP and Squint-mVenus were stained with anti-GFP (blue) antibodies, and transplanted mouse *bmp4*-expressing cells were pre-labeled with cascade blue-dextran (blue). Scale bar: 150 µm.

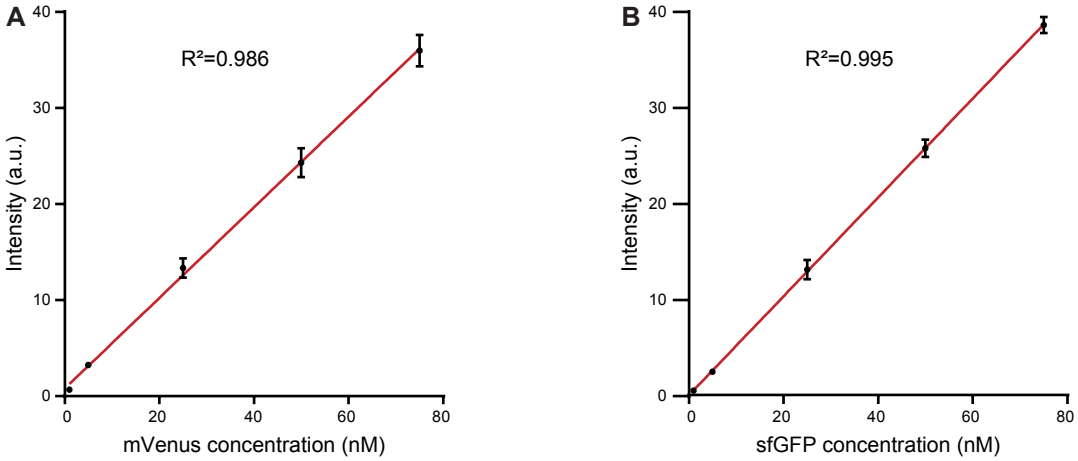

Figure S4. Calibration curves for recombinant mVenus and sfGFP to relate fluorescence intensities to concentrations, Related to Figure 2. (A,B) Calibration curves were generated for (A) recombinant mVenus (n[1 nM]=11, n[5 nM]=11, n[25 nM]=11, n[50 nM]=10, n[75 nM]=11) and (B) recombinant sfGFP (n[1 nM]=11, n[5 nM]=11, n[25 nM]=11, n[50 nM]=10, n[75 nM]=10) by applying increasing concentrations of the proteins onto a coverslip, mounting the sample on a confocal microscope, and imaging with the same settings as those that were used to image zebrafish embryos. The error bars in both graphs represent 95% confidence intervals around the mean (black dots). The red lines are linear fits that match the data with the indicated R^2 values.

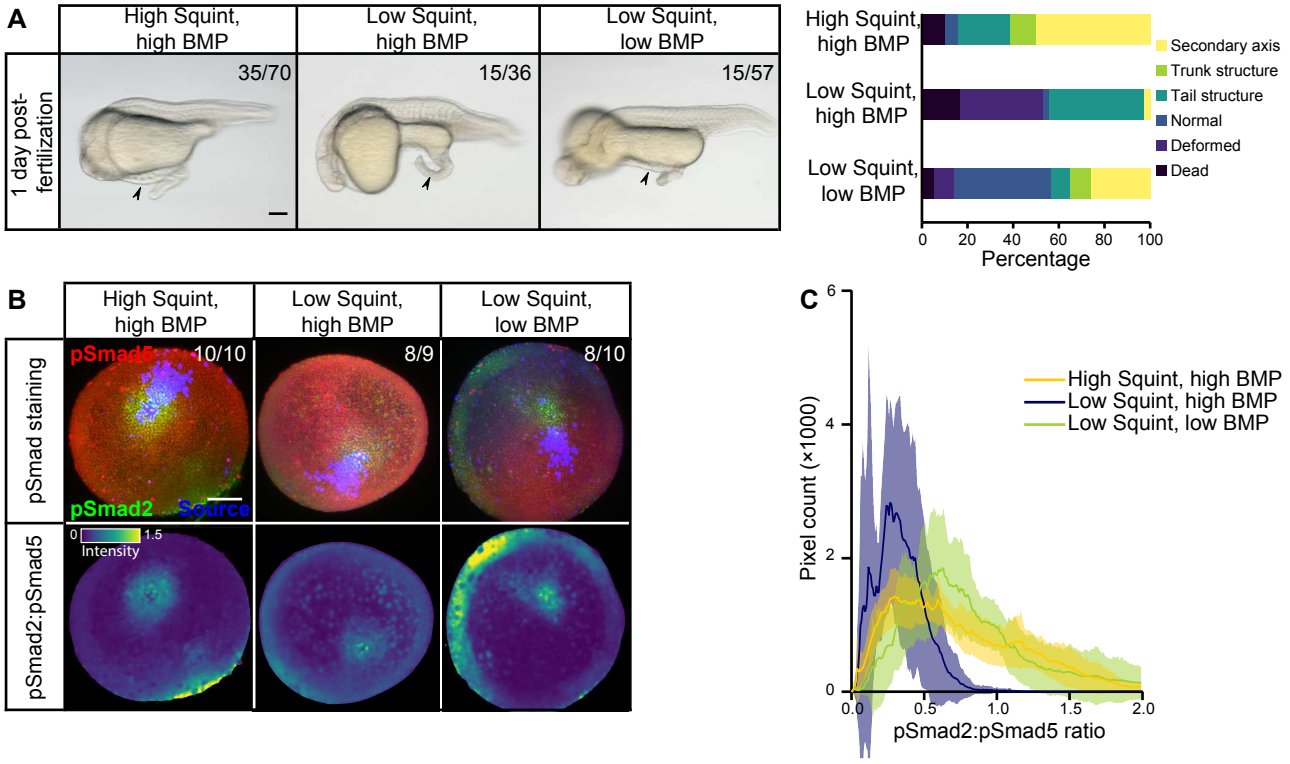

Figure S5. Nodal:BMP signaling ratios, rather than absolute signaling levels, underlie secondary axis formation, Related to Figure 4. (A) Embryonic phenotypes at 24 h post-transplantation and frequency of different structures induced by clones expressing various amounts of Bmp2b/7-sfGFP and Squint-mVenus. High Squint, high BMP: 100 pg *squint-mVenus* mRNA and 100 pg + 100 pg *bmp2b/7-sfGFP* mRNA (n=70); Low Squint, high BMP: 20 pg *squint-mVenus* mRNA and 100 pg + 100 pg *bmp2b/7-sfGFP* mRNA (n=36); Low Squint, low BMP: 20 pg *squint-mVenus* mRNA and 20 pg + 20 pg *bmp2b/7-sfGFP* mRNA (n=5). The arrowheads point to secondary axes or ectopic structures. Scale bar: 150 µm. **(B)** Double clones with various amounts of Bmp2b/7-sfGFP and Squint-mVenus generated as in (A), but immunostained for pSmad2 and pSmad5 at early gastrula stages. The lower panel shows the pSmad2:pSmad5 ratios. Scale bar: 150 µm. **(C)** Histogram of pSmad2:pSmad5 ratios from the pSmad2-positive region induced by Nodal clones in embryos generated as in (B). High Squint, high BMP: n=10; Low Squint, high BMP: n=6; Low Squint, low BMP: n=6. The shaded regions indicate 95% confidence intervals around the mean (lines).

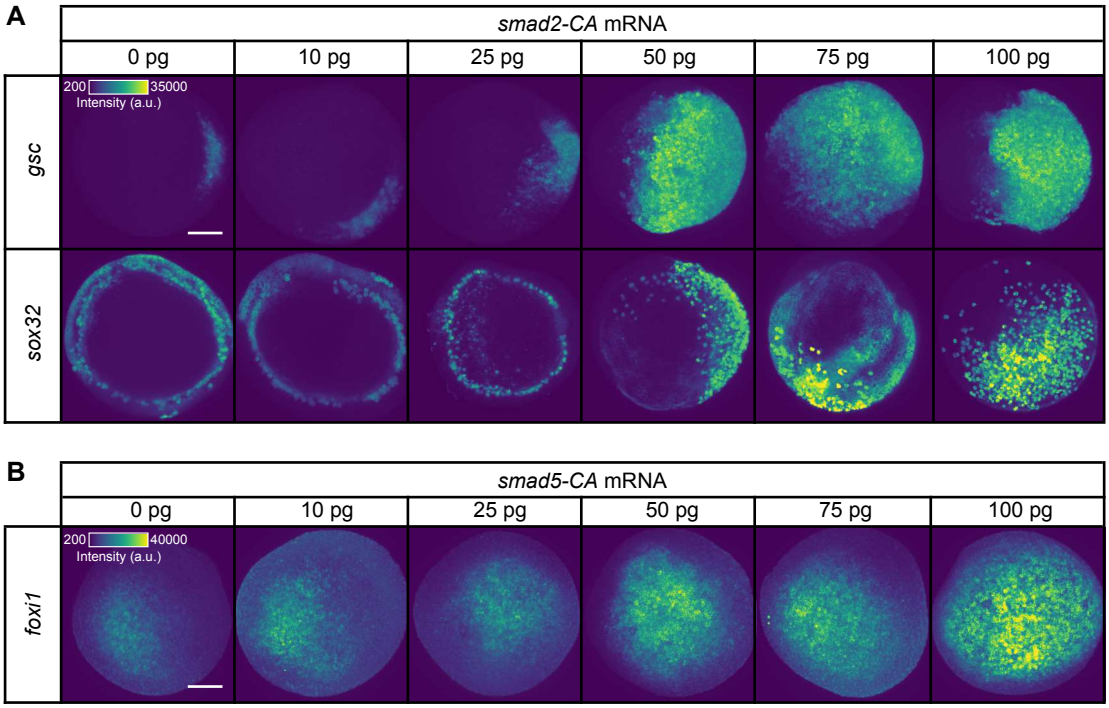

Figure S6. Constitutively active Smad2-CA and Smad5-CA activate Nodal and BMP target genes in a dose-dependent manner, Related to Figure 5. (A) Embryos were injected with increasing amounts of *smad2-CA* mRNA, and the expression of the Nodal target genes *gsc* (n[0 pg]=7, n[10 pg]=7, n[25 pg]=10, n[50 pg]=3, n[75 pg]=10, n[100 pg]=6) and *sox32* (n[0 pg]=7, n[10 pg]=7, n[25 pg]=9, n[50 pg]=5, n[75 pg]=10, n[100 pg]=7) was assessed by fluorescence *in situ* hybridization (FISH). Each experimental group gave rise to similar expression patterns. Scale bar: 150 µm. (B) Embryos were injected with increasing amounts of *smad5-CA* mRNA, and the expression of the BMP target gene *foxi1* (n[0 pg]=7, n[10 pg]=8, n[25 pg]=9, n[50 pg]=6, n[75 pg]=9, n[100 pg]=7) was assessed by FISH. Each experimental group gave rise to similar expression patterns. Scale bar: 150 µm.

Appendix C

Analysis of SMAD1/5 target genes in a sea anemone reveals ZSWIM4-6 as a novel BMP signaling modulator

Paul Knabl[1,2§], Alexandra Schauer[1,5§], Autumn Penecilla Pomreinke[3], Bob Zimmermann[1], Katherine W. Rogers[3,6], Patrick Müller[3,4], Grigory Genikhovich[1*]

[1] Department of Neurosciences and Developmental Biology, University of Vienna, Austria
[2] Vienna Doctoral School of Ecology and Evolution (VDSEE), University of Vienna, Austria
[3] Friedrich Miescher Laboratory of the Max Planck Society, Germany
[4] University of Konstanz, Germany
[5] Present address: Institute of Science and Technology Austria, Austria
[6] Present address: Division of Developmental Biology, Eunice Kennedy Shriver National Institute of Child Health and Human Development, NIH, USA

§ These authors contributed equally to the study
*Corresponding author: grigory.genikhovich@univie.ac.at

Abstract

BMP signaling has a conserved function in patterning the dorsal-ventral body axis in Bilateria and the directive axis in anthozoan cnidarians. So far, cnidarian studies have focused on the role of different BMP signaling network components in regulating pSMAD1/5 gradient formation. Much less is known about the target genes downstream of BMP signaling. To address this, we generated a genome-wide list of direct pSMAD1/5 target genes in the anthozoan *Nematostella vectensis*, several of which were conserved in *Drosophila* and *Xenopus*. Our ChIP-Seq analysis revealed that many of the regulatory molecules with documented bilaterally symmetric expression in *Nematostella* are directly controlled by BMP signaling. Among the so far uncharacterized BMP-dependent transcription factors and signaling molecules we identified several, whose bilaterally symmetric expression may be indicative of their involvement in secondary axis patterning. One of these molecules, *zswim4-6*, encodes a novel nuclear modulator of the pSMAD1/5 gradient potentially promoting BMP-dependent gene repression. Strikingly, overexpression of the zebrafish homologue *zswim5* suggests that its effect on the pSMAD1/5 gradient is conserved between anthozoan Cnidaria and Bilateria.

Introduction

The clade Bilateria unites animals with bilaterally symmetric body plans that are determined by two orthogonally oriented body axes, termed the anterior-posterior (A-P) axis and the dorsal-ventral (D-V) axis. These body axes form a Cartesian coordinate system, in which the location of different morphological structures is specified by gradients of morphogen signaling (Niehrs, 2010). Notably, bilaterality is also observed in representatives of a single animal clade outside of Bilateria: their evolutionary sister group Cnidaria (Berking, 2007; Finnerty et al., 2004). Common to all cnidarians is the formation of an oral-aboral (O-A) body axis which is patterned by Wnt/β-catenin signaling (Kraus et al., 2016; Lebedeva et al., 2021; Lee et al., 2007; Marlow et al., 2013; Momose et al., 2008; Momose and Houliston, 2007; Wikramanayake et al., 2003). However, in contrast to Medusozoa (jellyfish and hydroids), Anthozoa (sea anemones and corals) have an additional secondary, “directive” body axis (Fig. 1A), which is patterned by bone morphogenetic protein (BMP, Fig. 1B) signaling (Finnerty et al., 2004; Saina et al., 2009). BMP signaling has also been shown to regulate patterning of the D-V axis in Bilateria (Arendt and Nubler-Jung, 1997; Holley et al., 1995; Kozmikova et al., 2013; Lapraz et al., 2009; Özuak et al., 2014; van der Zee et al., 2006), however, it remains unclear whether this second, BMP-dependent body axis was a feature of the last common cnidarian-bilaterian ancestor and lost in Medusozoa, or whether it evolved independently in anthozoan Cnidaria and in Bilateria (Genikhovich and Technau, 2017). To address this fundamental evolutionary question, we need to gain a better understanding of how the directive axis is established and patterned.

In contrast to Bilateria, where the D-V axis and the A-P axis usually form simultaneously and very early during development, the directive body axis of the sea anemone *Nematostella vectensis* appears only at gastrula stage (Matus et al., 2006a; Matus et al., 2006b; Rentzsch et al., 2006), while the O-A axis is maternally determined (Lee et al., 2007). The expression of the core components of the BMP signaling network *bmp2/4* and *chordin* is initially controlled by β-catenin signaling and radially symmetric (Kirillova et al., 2018; Kraus et al., 2016; Rentzsch et al., 2006). During gastrulation, the embryo undergoes a BMP signaling-dependent symmetry break establishing the directive axis at a molecular level (Rentzsch et al., 2006; Saina et al., 2009), with a BMP signaling activity gradient forming as revealed by antibody staining against phosphorylated SMAD1/5 (pSMAD1/5) (Fig. 1C-D) (Genikhovich et al., 2015; Leclère and Rentzsch, 2014). Each end of the directive axis expresses a set of BMP ligands and BMP antagonists: *bmp2/4* and *bmp5-8* are transcribed on the low-BMP signaling activity side of the directive axis together with the antagonist *chordin*, while the BMP ligand *gdf5-like* (*gdf5-l*) and the BMP antagonist *gremlin* are expressed on the high-BMP signaling activity side (Genikhovich et al., 2015; Rentzsch et al., 2006). The pSMAD1/5 gradient is maintained by the genetic interactions between these molecules, with Chordin likely acting as a shuttle for BMP2/4/BMP5-8 and Gremlin serving as a primary GDF5-like antagonist (Genikhovich et al., 2015). Another essential player in this network is the *repulsive guidance molecule (rgm)*, which is necessary for the maintenance of the low-BMP signaling side of the directive axis (Leclère and Rentzsch, 2014).

The graded BMP signaling activity is essential for the patterning of the endoderm and the formation of the so-called mesenteries, gastrodermal folds compartmentalizing the endoderm of the late planula into eight distinct chambers as demonstrated by knockdown (KD) experiments

(Genikhovich et al., 2015; Leclère and Rentzsch, 2014). More specifically, complete abolishment of the BMP signaling gradient by KD of *bmp2/4*, *bmp5-8* or *chordin* results in embryos which are not only molecularly, but also morphologically radialized, failing to form any mesenteries (Genikhovich et al., 2015; Leclère and Rentzsch, 2014). In line with this, KD of *gdf5-l* or *gremlin* alter the profile of the BMP signaling gradient, and also lead to abnormal mesentery formation (Genikhovich et al., 2015).

Despite these important insights over the last decades, our knowledge of BMP-dependent directive axis patterning mechanisms, in particular regarding effector molecules linking BMP signaling and subsequent morphological bilaterality in *Nematostella* remains incomplete, precluding proper comparison of anthozoan directive and bilaterian D-V axis patterning. To address this, we performed a genome-wide search for direct BMP signaling targets at two developmental stages in *Nematostella* using ChIP-Seq with an αpSMAD1/5 antibody. We demonstrate that regulatory genes, including many with previously documented bilaterally symmetric expression, are overrepresented among direct BMP signaling targets. We also identify multiple previously uncharacterized transcription factors and signaling molecules, whose bilaterally symmetric expression suggests that these direct BMP signaling targets may be involved in the patterning of the directive axis and in endoderm compartmentalization. Several of these seem to be shared between *Nematostella*, *Drosophila*, and *Xenopus* as shown by comparison of pSMAD1/5 ChIP-Seq targets at similar developmental stages. Among the targets with maximum ChIP enrichment, we find *zswim4-6*, a gene encoding a so far uncharacterized zinc-finger protein with a SWIM domain (ZSWIM4-6), whose paralogs are also pSMAD1/5 targets in the frog. Functional analyses show that *Nematostella* ZSWIM4-6 can modulate the shape of the pSMAD1/5 gradient and appears to promote BMP signaling-mediated gene repression. Overexpression of the zebrafish paralogue *zswim5* revealed similar effects on the BMP signaling gradient in *Danio rerio*, indicating that the function of ZSWIM4-6 may be conserved in Bilateria.

Results

Identification of BMP signaling targets in *Nematostella*

Staining with an antibody recognizing the transcriptionally active phosphorylated form of SMAD1/5 (pSMAD1/5) demonstrates that BMP signaling activity is highly dynamic during early development in *Nematostella*. In the early *Nematostella* gastrula, nuclear pSMAD1/5 can be detected in a radially symmetric domain around the blastopore (Fig. 1D panel ii). Subsequently, it becomes restricted to one side of the gastrula (Fig. 1D panels iii-iv) in a symmetry breaking process, which has been shown to depend on BMP signaling itself (Saina et al., 2009). The resulting BMP gradient is crucial for the formation of the directive axis. The gradient, however, disappears by late planula, when the general patterning of the directive axis is complete, and the BMP signaling activity is confined to the mesenteries, and to eight stripes following the mesenteries in the ectoderm and merging in pairs to surround the future tentacle buds and ending in a circumoral ring (Fig. 1D panels v-vi, Supplementary video 1).

Although the role of BMP signaling in symmetry breaking and compartmentalization of the *Nematostella* endoderm has been well described, insight regarding direct targets of BMP signaling during these fundamental developmental processes is currently lacking. To generate a genome-wide list of direct BMP signaling targets in *Nematostella*, we performed ChIP-Seq using an anti-pSMAD1/5 antibody at two developmental stages: late gastrula, when BMP signaling forms a gradient along the directive axis (Fig. 1D panel iii), and late planula (4 d) when the mesenteries have formed and BMP signaling is confined to the mesenteries and to stripes of cells in the body wall ectoderm following the mesenteries (Fig. 1D panel vi). We found 68 direct pSMAD1/5 target genes at late gastrula stage and 208 in 4d planulae, 24 of which were bound by pSMAD1/5 at both developmental stages (Fig. 1E). MEME-ChIP analysis (Ma et al., 2014) of the sequences occupied by pSMAD1/5 showed that the BMP response element (BRE) sequence, a vertebrate SMAD1/5 binding motif, was enriched at many of the bound sites (Fig. 1E). Most genes identified as pSMAD1/5 targets at both stages carry a BRE motif (22/24), with 13 additional gastrula-specific targets and 20 additional 4d planula-specific targets containing a BRE site. Next, we manually annotated pSMAD1/5 targets using reciprocal best BLAST hits and found among them many key regulatory genes whose dependence on BMP signaling has previously been documented in *Nematostella* (Genikhovich et al., 2015; Leclère and Rentzsch, 2014; Saina et al., 2009). These included *gbx*, *hoxB*, *hoxD* and *hoxE* - i.e. genes shown to play a central role in the subdivision of the directive axis into mesenterial chambers and specifying the fate of each mesenterial chamber (He et al., 2018) - as well as the BMP signaling regulators *chordin*, *gremlin* and *rgm* (Genikhovich et al., 2015; Leclère and Rentzsch, 2014; Saina et al., 2009). Intriguingly, none of the BMP ligand-coding genes, i.e. *bmp2/4*, *bmp5-8* or *gdf5-like*, was found as a direct BMP signaling target (Supplementary Data 1).

To expand this analysis and gain insight into the response of the 252 newly found putative direct pSMAD1/5 target genes to abolished or reduced BMP signaling, we injected previously characterized antisense morpholino oligonucleotides against *bmp2/4* and *gdf5-like* (Genikhovich et al., 2015; Saina et al., 2009), as well as a standard control morpholino, and analyzed by RNA-Seq whether the pSMAD1/5 target genes were differentially expressed upon *gdf5-like* or *bmp2/4* KD (Supplementary Fig. 1, Supplementary Data 1). 139 direct pSMAD1/5 target genes were among the genes differentially expressed in the KD ($p_{adj} \leq 0.05$), 64 of which showed more than a two-fold change in expression upon BMP2/4 and/or GDF5-like KD (Supplementary Data 1). The transcriptional response of the previously described downstream targets of BMP signaling confirmed previous *in situ* hybridization analysis, i.e. *chordin* and *rgm* were upregulated while *gbx*, *hox* genes and *gremlin* were downregulated in our RNA-Seq datasets confirming their specificity. Notably, out of 55 pSMAD1/5 target genes with BRE motifs, 37 (67.3%) were shown to be differentially expressed upon BMP2/4 and/or GDF5-like KD.

To gain insight into the function of pSMAD1/5 target genes in *Nematostella*, we roughly categorized them according to the putative function of their bilaterian homologs. We found that the fraction of transcription factors and signaling molecules was strongly increased among the direct BMP signaling targets at both developmental stages in comparison to 100 randomly selected genes from the *Nematostella* genome (Fig. 1F-G). This suggests that direct downstream targets of BMP signaling constitute a second tier of a regulatory cascade governing patterning and morphogenesis of the *Nematostella* gastrula and planula.

Since we were particularly interested in identifying new players in the BMP-dependent regulation of the directive axis, we characterized the expression domain of a subset of pSMAD1/5 targets with so far unknown expression patterns and validated the expression of several previously described pSMAD1/5 targets using whole mount *in situ* hybridization (WISH). In accordance with a potential role in the directive axis regulation, we found several of the newly identified pSMAD1/5 targets to be bilaterally expressed (e.g. *otxB*, *tbx2/3*, *tbx20.1*, *p63*, *dusp1*, *bmprII*, *c-ski*, *morn*, *pik, zswim4-6*) (Fig. 2), further motivating the investigation of their function in directive axis patterning.

Conservation of direct BMP signaling targets between Anthozoa and Bilateria

To identify BMP signaling targets conserved between Anthozoa and Bilateria, we compared *Nematostella* pSMAD1/5 targets with available ChIP-Seq data from two bilaterians. In *Drosophila melanogaster*, pMAD targets were identified at two developmental time points (2 and 3 h after fertilization) (Deignan et al., 2016), and in *Xenopus laevis*, SMAD1 targets were found post-gastrulation (NF20 stage) (Stevens et al., 2017). In a 3-way comparison of *Nematostella* (*Nve*), fly (*Dme*), and frog (*Xla*), putative orthologs were identified using best reciprocal BLAST hits based on the bit score. We found 103 direct BMP signaling targets that were conserved between at least two organisms, of which four were shared by all three species (Fig. 3E). Anchoring the analysis on *Nematostella* indicates that several of the targets, which are shared between only two species in a strict 3-way comparison, can be assigned to all three species thus increasing the number of common targets to nine (*meis, gata, hoxB, tbx2/3, nkain, irx, zfp36l1, ptc, tp53bp2)*. Among the shared targets, conserved transcription factors (TFs) and signaling molecules (SMs) are enriched compared to genes with other functions (69/103). Multiple Hox genes are direct targets of BMP signaling in embryos of *Nematostella* (*hoxB, hoxD, hoxE*), fly (*dfd, pb, antp*) and frog (*hox3-7/9-11/13, hoxa1-2, hoxb1-9, hoxc3-6/8-12, hoxd1/3/4/8-11/13*); however, the orthology of the cnidarian and bilaterian Hox genes is currently unclear, due to the likely independent diversification of the “anterior” and “non-anterior” Hox genes in these two sister clades (Chourrout et al., 2006; Genikhovich and Technau, 2017).

zswim4-6 – a previously uncharacterized, asymmetrically expressed gene encoding a nuclear protein

One of the highest enrichment levels in our ChIP-Seq was detected for *zswim4-6* – a pSMAD1/5 target shared between *Nematostella* and *Xenopus* (Fig. 3). This gene encodes a zinc-finger containing protein with a SWIM-domain clustering together with ZSWIM4/5/6 of zebrafish (*Danio rerio*) and mouse (*Mus musculus*) (Fig. 4A). *Zswim4-6* starts to be expressed at the early gastrula stage around the blastopore (Fig. 4B-C’), concomitant with the onset of BMP signaling activity. At late gastrula, when a symmetry break in the BMP signaling activity establishes the directive axis, *zswim4-6* expression becomes restricted to the ectoderm and endoderm on one side of it (Fig. 4D-D’). Double *in situ* hybridization of *chd* and *zswim4-6* shows that *zswim4-6* is expressed opposite to *chd*, i.e. on the side of high pSMAD1/5 activity (Fig. 4E-E’), suggesting that BMP signaling activates *zswim4-6* expression. At late planula stage, *zswim4-6* expression is confined to the eight mesenteries (Fig. 4F-F’). Taken together, *in situ* hybridization analysis showed that

the *zswim4-6* expression domain followed the dynamic changes in pSMAD1/5 activity (compare Fig. 1D and Fig. 4B-F').

Sequence analysis of the deduced ZSWIM4-6 protein revealed a potential N-terminal nuclear localization signal (NLS). To analyze the intracellular localization of ZSWIM4-6, we mosaically overexpressed an EGFP-tagged version of ZSWIM4-6 in F0 transgenic animals under the control of the ubiquitously active *EF1α* promoter (Kraus et al., 2016; Steinmetz et al., 2017). We compared the intracellular localization of the tagged wild type form to a truncated version of ZSWIM4-6 (ZSWIM4-6ΔNLS-EGFP), where the first 24 bases coding for the putative NLS were replaced by a start codon. Full-length ZSWIM4-6-EGFP was enriched in the cell nuclei (Fig. 4G), while the truncated version of ZSWIM4-6 lacking the NLS remained cytoplasmic, similar to the EGFP signal in transgenic animals overexpressing only cytoplasmic EGFP (Fig. 4H-I). Nuclear localization of ZSWIM4-6 could be confirmed by microinjection of *zswim4-6-EGFP* mRNA (Fig. 4J-L). Strikingly, the nuclear fluorescent signal of ZSWIM4-6-EGFP, which is weak but clearly visible at the blastula stage (Fig. 4J), progressively decreases and is barely detectable at 24 hpf (Fig. 4K). In contrast, injection of mRNA encoding cytoplasmic EGFP results in a strong fluorescent signal lasting for several days (Fig. 4L). Currently, the dynamics of the endogenous ZSWIM4-6 protein, as well as the mechanism behind this fast turnover after overexpression are unclear.

To analyze the function of BMP signaling in establishing the *zswim4-6* expression domain, we performed KDs of several components of the BMP signaling network (Fig. 5A). Previous studies have shown that the KDs of *bmp2/4* and *chd* suppress BMP signaling activity and abolish the pSMAD1/5 gradient (Genikhovich et al., 2015; Leclère and Rentzsch, 2014). A KD of another BMP ligand, GDF5-like, reduces BMP signaling activity, although a shallow BMP signaling gradient is preserved, while the knockdown of the BMP inhibitor Gremlin results in an expansion of the nuclear pSMAD1/5 gradient (Genikhovich et al., 2015). In line with the proposed role of BMP signaling in activating *zswim4-6* expression, the KDs of *bmp2/4* and *chd* led to a loss of *zswim4-6* expression (Fig. 5B-D', Supplementary Data 1). In contrast, KD of *gdf5-like* and *gremlin* did not strongly affect *zswim4-6* expression (Fig. 5E-F', Supplementary Data 1), suggesting that *zswim4-6* expression might either be robust towards milder alterations in pSMAD1/5 levels, or specifically depend on the BMP2/4-mediated, but not GDF5-like-mediated BMP signaling, or both.

To address these two possibilities in more detail, we first tested the response of *zswim4-6* to reduced levels of BMP signaling. We injected *Nematostella* embryos with different concentrations of BMP2/4MO starting with 50 µM and going up to the regular BMP2/4MO working concentration of 300 µM in steps of 50 µM, and stained these embryos with probes against *zswim4-6* and *bmp2/4*. Strikingly, within individual embryos, the response to the different concentrations of the BMP2/4MO was binary: either *zswim4-6* and *bmp2/4* expression appeared normal, or it was lost (*zswim4-6*) or radialized (*bmp2-4*), while intermediate phenotypes were never observed (Supplementary Fig. 2). However, the proportion of the embryos showing radialized bmp2/4 and abolished zswim4-6 expression increased depending on the amount of injected BMP2/4MO. This independently confirms an earlier observation of the binary effect of injecting iteratively decreasing concentrations of BMP2/4MO on mesentery formation (Leclère and Rentzsch, 2014). In their hands, the embryos either developed 8 or 0 mesenteries, but never some number in

between, and the fraction of the embryos without mesenteries grew along with the increasing BMP2/4MO concentration. These results suggest that alterations in the BMP2/4-mediated signaling may not change the shape of the BMP signaling gradient, to which *zswim4-6* expression could be more or less robust, but rather define whether there is a BMP signaling gradient or not.

Since differential ligand selectivity of the BMP receptors was another possible explanation for the *zswim4-6* dependence on BMP2/4 but not on GDF5-like, we analyzed the expression of *zswim4-6* upon suppression of each of the two *Nematostella* BMP Type I receptors (*alk2* and *alk3/6*), and a single BMP Type II receptor (BMPRII) (Supplementary Fig. 3). We suppressed Alk2, Alk3/6 and BMPRII either by microinjecting mRNA of the dominant-negative version of each of these receptors, in which the intracellular kinase domain was replaced by EGFP, or by shRNA-mediated RNAi (Fig. 5G). In both assays, *zswim4-6* expression appears to be stronger affected by the Alk3/6 suppression than by the Alk2 suppression, and is nearly abolished by the combined Alk3/6/Alk2 KD (Fig. 5G-K, M-P). In contrast, it is largely unaffected by BMP Type II receptor suppression (Fig. 5G, L, Q). Thus, currently, our data favor the hypothesis that *zswim4-6* expression is regulated by BMP2/4-mediated signaling, which appears to be preferentially transduced by the Alk3/6 receptor or, possibly by the Alk3/6/Alk2 heterodimer, as it has been recently reported in fish (Tajer et al., 2021). Surprisingly, it also appears that the suppression of BMPRII during early *Nematostella* development can be compensated for - likely by another Type II TGFβ receptor molecule.

ZSWIM4-6 is a modulator of BMP-dependent patterning

Given that *zswim4-6* expression is bilaterally symmetric and highly dependent on BMP signaling in *Nematostella*, we wanted to see whether *zswim4-6* itself contributes to the patterning of the directive axis. To this end, we performed KD of *zswim4-6* activity using a translation-blocking morpholino targeting *zswim4-6* (Supplementary Fig. 4).

Analysis of the overall morphology at late planula stage showed that *zswim4-6* KD leads to defects in endoderm compartmentalization. In control morphants, eight mesenteries reach all the way to the pharynx, and the primary polyp has four tentacles (Fig. 6A-A''). In contrast, in ZSWIM4-6MO, the mesenterial chamber expressing HoxE protein fails to reach the pharynx resulting in the fusion of the two neighboring mesenterial segments (Fig. 6B-B'). Consequently, *zswim4-6* morphant primary polyps form only three instead of the typical four tentacles (Fig. 6B''). Endoderm segmentation defects have previously been observed in *Nematostella* larvae with defects in pSMAD1/5 gradient formation, as well as in *Hox* gene activity (Genikhovich et al., 2015; He et al., 2018; Leclère and Rentzsch, 2014), and, based on its expression domain, *zswim4-6* may be involved in either of these two processes. However, in contrast to the *HoxE* mutants, which also have characteristic three-tentacle primary polyps due to the loss of the *HoxE*-expressing mesenterial chamber and the fusion of the *HoxD*-expressing mesenterial chambers capable of forming a tentacle (He et al., 2018), the affected pair of mesenteries is not lost in the *zswim4-6* morphants, and *HoxE* is detectable (Fig, 6B'). Therefore, we concentrated on analyzing the molecular role of *zswim4-6* in the BMP signaling network.

First, we assessed whether the pSMAD1/5 gradient is affected upon *zswim4-6* KD. To this end, we performed anti-pSMAD1/5 immunostainings in 2d planulae and quantified pSMAD1/5 levels along the directive axis. We found that the gradient profile of pSMAD1/5 in the endoderm was flattened in *zswim4-6* morphants compared to controls, and that peak levels of pSMAD1/5 activity were not reached. pSMAD1/5 activity in the ectoderm was, however, strongly elevated upon *zswim4-6* KD (Fig. 6C-C', D-D'). To corroborate this, we then analyzed the pSMAD1/5 gradient in embryos microinjected with *zswim4-6-EGFP* mRNA. Due to the fast turnover of ZSWIM4-6-EGFP (see Fig. 4J-L), we quantified the gradient at the earliest possible stage after the symmetry break, i.e. at late gastrula. *zswim4-6* mRNA overexpression did not result in significant changes in the shape of the pSMAD1/5 gradient in the endoderm, however, ectodermal pSMAD1/5 levels were significantly reduced in the area where BMP signaling is normally strongest (Fig. 6E-E', F-F').

We then evaluated how KD of *zswim4-6* affected the transcription of markers expressed on the low BMP and high BMP signaling ends of the directive axis. First, we looked at *bmp2/4* and *chd* - the two key regulators of pSMAD1/5 gradient formation in *Nematostella*, whose expression is repressed by high levels of BMP signaling (Genikhovich et al., 2015; Leclère and Rentzsch, 2014; Saina et al., 2009). The *bmp2/4* and *chd* expression domains were expanded in *zswim4-6* morphants compared to controls (Fig. 6G-H'), which was especially evident in the ectodermal expansion of *chd*. Similarly, the *chd* expression domain was expanded in mosaic F0 *zswim4-6* knockouts generated by CRISPR/Cas9 to corroborate our morpholino KD results (Supplementary Fig. 5). This is striking as pSMAD1/5 stainings (Fig. 6C-D') suggest that BMP signaling is stronger in the ectoderm of the morphants, therefore one could expect a reduction rather than an expansion of the *chordin* expression domain. Next, we looked at the markers of the high BMP signaling end: *zswim4-6*, *gdf5-like*, and *grm,* which are positively regulated by BMP signaling. The KD of *zswim4-6* translation resulted in a strong upregulation of *zswim4-6* transcription, especially in the ectoderm, suggesting that ZSWIM4-6 might either act as its own transcriptional repressor or that *zswim4-6* transcription reacts to the increased ectodermal pSMAD1/5 (Fig. 6I-I'). The expression of *gdf5-like* was largely unaffected (Fig. 6J-J'), while expression of *grm* was expanded in the ectoderm (Fig. 6K-K'), which reflects the flattening of the endodermal and the expansion of the ectodermal pSMAD1/5 gradient in the morphants (Fig. 6C-D').

The overexpression of *zswim4-6-EGFP* by mRNA injection resulted in largely reciprocal effects on gene expression compared to morpholino-mediated KD, although less pronounced. As expected from the analysis of the morphants, *zswim4-6-egfp* overexpression resulted in a mild reduction of the expression domains of *bmp2/4* and *chd* (Fig. 6L-M'). Moreover, the otherwise very sharp border of the *chd* expression domain appeared diffuse (Fig. 6M'). *In situ* hybridization with the *zswim4-6* probe detected exogenous *zswim4-6* throughout the injected embryo (Fig. 6N-N'). Not much change was observed in the *gdf5-like* expression (Fig. 6O-O'), while *grm* was slightly reduced (Fig. 6P-P'), which also reflects the behavior of the pSMAD1/5 gradient (Fig. 6F-F'). Taken together, in the absence of ZSWIM4-6, changes in the expression of genes expressed on the high pSMAD1/5 side (*gdf5-like*, *grm*) appear to mimic the changes in the levels and range of the BMP signaling gradient. In contrast, genes repressed by BMP signaling and expressed on the low BMP signaling side of the directive axis (*bmp2/4*, *chd*) seem to expand their expression domains in the absence of ZSWIM4-6 despite the increase in pSMAD1/5 levels. One possible

explanation for this observation is that BMP signaling-mediated gene repression is less effective in the absence of *ZSWIM4-6*.

If ZSWIM4-6 is indeed involved in the transcriptional repression of the pSMAD1/5 targets, we would expect to find ZSWIM4-6 bound to pSMAD1/5 binding sites at the genes repressed by BMP signaling, but not at the genes activated by BMP signaling. Due to the lack of an αZSWIM4-6 antibody and fast ZSWIM4-6-EGFP turnover in mRNA-injected embryos (Fig. 4J-K), we microinjected *EF1α::ZSWIM4-6-EGFP* plasmid (Fig. 4G) to perform αGFP-ChIP on mosaic F0 embryos, where *zswim4-6-egfp* is transcribed under control of a ubiquitously active promoter in a small fraction of cells in each embryo. Since the amount of chromatin that could be immunoprecipitated in such an experimental setup was very low, we were limited to selecting one negatively regulated direct BMP target and one positively regulated direct BMP target for the subsequent qPCR analysis. We chose pSMAD1/5 sites in the regulatory regions of the negatively regulated direct BMP target *chordin* and the positively regulated direct BMP target *gremlin*, and checked by qPCR whether they were bound by ZSWIM4-6-EGFP. Binding to the *Intergenic region IntA* (Schwaiger et al., 2021; Schwaiger et al., 2014) was used as a normalization control. The pSMAD1/5 binding site-containing region at the *gremlin* locus was similarly depleted in wild type and in *EF1α::ZSWIM4-6-EGFP* injected embryos upon αGFP-ChIP (0.35-fold enrichment and 0.27-fold enrichment respectively; insignificant according to the two-tailed t-test; P=0.496). On the other hand, the pSMAD1/5 binding site-containing region at the *chordin* locus was 1.82-fold enriched upon αGFP-ChIP in *EF1α::ZSWIM4-6-EGFP* embryos and 0.15-fold enriched (significant according to the two-tailed t-test; P=0.00032) in wild type embryos (Fig. 6Q). Thus, the enrichment of the pSMAD1/5 binding site-containing region at the *gremlin* locus in *EF1α::ZSWIM4-6-EGFP* embryos in comparison to the wild type embryos was 0.87-fold. In stark contrast, the enrichment of the pSMAD1/5 binding site-containing region at the *chordin* locus in *EF1α::ZSWIM4-6-EGFP* embryos in relation to wild type embryos was 12.13-fold. This suggests an interaction of ZSWIM4-6 with the pSMAD1/5 binding site of the *chordin* regulatory region, but not of the *gremlin* regulatory region, and supports the hypothesis that ZSWIM4-6 might act as a co-repressor for pSMAD1/5 targets.

Our comparison of evolutionary conserved pSMAD1/5 ChIP targets showed that the *Nematostella zswim4-6* homolog *zswim5* is a direct BMP target also in *Xenopus* (Fig. 3C), but its function as a modulator of vertebrate BMP signaling has not been addressed. To determine whether vertebrate ZSWIM5 also influences BMP-mediated patterning, we assessed the effect of *zswim5* overexpression in zebrafish embryos. Injection of increasing amounts of zebrafish *zswim5* mRNA into zebrafish embryos at the one-cell stage caused increasingly severe developmental defects (Fig. 7A-F”). These defects included shortened and twisted tails as well as disorganized head structures and partially resemble loss-of-function mutants of the BMP pathway, such as the *bmp2* mutant *swirl* (Kishimoto et al., 1997; Nguyen et al., 1998). *zswim5* overexpression also led to a dampening of the ventrally-peaking BMP signaling gradient in early gastrulation-stage zebrafish embryos, as detected by pSMAD1/5/9 immunofluorescence (Fig. 7G). The reduced amplitude of ventral BMP signaling caused by *zswim5* overexpression in zebrafish mirrors the decrease in pSMAD1/5 levels observed in the *Nematostella* ectoderm upon overexpression of *zswim4-6* (Fig. 6E-F’). Together, this suggests that the function of ZSWIM4-6 as a BMP signaling modulator has likely been conserved in evolution since before the cnidarian-bilaterian split.

Discussion

BMP signaling governs the expression of a second tier of developmental regulators

BMP signaling regulates the patterning of the anthozoan directive axis and the bilaterian D-V axis; however, the extent of conservation of downstream target genes between Bilateria and Cnidaria involved in the axial patterning has been largely unknown. In our αpSMAD1/5-ChIP-Seq in *Nematostella*, we identified putative direct targets of BMP signaling during the establishment of the directive axis in the late gastrula and in the fully compartmentalized 4d planula, providing new insights into the genetic program responsible for directive axis patterning. Functional annotation of the identified targets highlights an abundance of transcription factors (TFs) and signaling molecules (SMs) (Fig. 1F), suggesting that BMP signaling largely regulates a second tier of regulators rather than structural genes at the two stages we assayed. TFs and SMs were also prominent among the differentially expressed target genes upon knockdown of the BMP ligands BMP2/4 and GDF5-like (Fig. 1F), and among the targets with an identifiable BMP response element (BRE) (Katagiri et al., 2002). The presence of multiple members of Wnt, MAPK, Hedgehog, and Notch signaling pathways among the BMP signaling targets points at a high degree of coordination between different signal transduction cascades necessary to generate a properly organized embryo. Comparison of the *Nematostella* pSMAD1/5 targets with the available ChIP-seq data of the frog *Xenopus* (Stevens et al., 2017) and the fly *Drosophila* (Deignan et al., 2016), shows that BMP targets shared between Anthozoa and Bilateria are also mainly TFs and SMs.

Several molecules of the BMP pathway in Bilateria are known to be directly regulated by BMP signaling (Fig. 3C), (Deignan et al., 2016; Genander et al., 2014; Greenfeld et al., 2021; Rogers et al., 2020; Stevens et al., 2017). Likewise, pSMAD1/5 in *Nematostella* directly controls the transcription of multiple BMP network components (*chd, grm, bmprII, rgm, smad1/5, smad4*) and other associated regulators (*e2f4, morn, tob2, c-ski, tld1-like, bmp1-like, dusp1, dusp7*) that have not been characterized yet. Curiously, unlike *Xenopus bmp2, -4, -5, -7,* and *gdf2, -6, -9,* and *-10*, or *Drosophila dpp* (Deignan et al., 2016; Stevens et al., 2017), the promoters of *Nematostella* BMP-encoding genes do not appear to be directly bound by pSMAD1/5. Our ChIP-Seq data suggest that BMP signaling-dependent repression of *Nematostella bmp2/4* and *bmp5-8,* and BMP signaling-dependent activation of *gdf5-like* (Genikhovich et al., 2015) is indirect, but the link between the pSMAD1/5 activity and the transcriptional regulation of BMPs is still unknown.

Staggered expression of Hox genes in *Nematostella* is directly controlled by BMP signaling

Bilateral body symmetry in *Nematostella* is manifested in the anatomy of the mesenteries subdividing the endoderm along the second body axis of the animal. In *Nematostella,* endodermal *hox* genes and *gbx* are expressed in staggered domains along the directive axis, and their expression boundaries exactly correspond to the positions of the emerging mesenteries (Ryan et al., 2007). This staggered endodermal *hox* and *gbx* expression is lost when BMP signaling is

suppressed (Genikhovich et al., 2015). Recent loss-of-function analyses showed that RNAi of *hoxE*, *hoxD*, *hoxB* or *gbx* led to the loss of the pairs of mesenteries corresponding to the expression boundaries of the knocked down genes, while the knockdown of the putative co-factor of all Hox proteins, *Pbx*, resulted in the loss of all mesenteries (He et al., 2018) phenocopying the loss of BMP signaling (Genikhovich et al., 2015; Leclère and Rentzsch, 2014; Saina et al., 2009). Our ChIP-Seq analysis showed that the endodermal BMP-dependent staggered expression of *hox* genes and *gbx* is directly controlled by nuclear pSMAD1/5. In the future, it will be of great interest to test whether the loss of the mesenteries upon *BMP2/4*, *BMP5-8*, or *Chd* KD is only correlated with or actually caused by the resulting simultaneous suppression of all the staggered endodermal *hox* genes and *gbx* in the absence of BMP signaling (Genikhovich et al., 2015; He et al., 2018).

The question of whether Hox-dependent axial patterning was a feature of the cnidarian-bilaterian ancestor or evolved independently in Cnidaria and Bilateria remains debated. Different authors used different *hox* genes to homologize the different cnidarian body axes to the bilaterian ones (Arendt et al., 2016; DuBuc et al., 2018; Finnerty et al., 2004). The unclear orthology of cnidarian *hox* genes (Chourrout et al., 2006), as well as the staggered expression along a cnidarian body axis patterned by BMP signaling rather than along the one regulated by Wnt and FGF, as in Bilateria, allowed us to suggest that the involvement of staggered *hox* genes in axial patterning in anthozoans and bilaterians is probably convergent (Genikhovich et al., 2015; Genikhovich and Technau, 2017). This, however, does not exclude the possibility that regulation of some specific *hox* genes by BMP signaling was indeed conserved since before the cnidarian-bilaterian split. We find several *hox* genes as conserved direct BMP targets in *Xenopus* and *Drosophila*, and BMP-dependent regulation of *hox* expression has been reported in these models. For instance, in *Xenopus,* during the specification of the hindgut, direct pSMAD1/β-catenin interactions control the expression of *hoxa11*, *hoxb4* and *hoxd1* (Stevens et al., 2017), and in *Drosophila*, a BMP-Hox gene regulatory network mutually regulating *decapentaplegic*, *labial* and *deformed* was shown to be involved in the head morphogenesis (Stultz et al., 2012). Another indication in favor of the ancient origin of the BMP control over Hox-dependent processes is our finding that the gene encoding the TALE class homeodomain transcription factor Meis is among the ChIP targets conserved between *Nematostella*, *Xenopus* and *Drosophila*. Meis, together with another TALE class transcription factor Pbx, forms a trimeric complex essential for the Hox and Parahox function in the bilaterian anterior-posterior axis patterning (Merabet and Galliot, 2015). Hox proteins were also shown to directly interact with Meis/Pbx in *Nematostella* (Hudry et al., 2014). This interaction appears to be crucial for the function of *Nematostella* Hox proteins since *Pbx* KD resulted in the loss of all eight mesenteries (He et al., 2018), phenocopying the “no *hox*, no *gbx*” state of the endoderm with suppressed BMP signaling.

Roles of BMP signaling during neurogenesis

In protostome and deuterostome Bilateria with centralized nervous systems, one of the key roles of BMP signaling is repression of neuroectoderm formation. In contrast, cnidarians possess diffuse nervous systems with certain local neural accumulations, which, however, cannot be considered ganglia or brains (Arendt et al., 2016; Kelava et al., 2015; Martin-Duran and Hejnol,

2021). There is no indication that the onset of nervous system development in *Nematostella* is affected by BMP signaling. The expression of neuronal terminal differentiation genes starts already at the blastula stage (Richards and Rentzsch, 2014), which is before the onset of detectable BMP signaling. During subsequent development, neurons continue to form in both germ layers in a radially symmetric manner (Nakanishi et al., 2012), regulated by Wnt, MAPK and Notch signaling (Layden et al., 2016; Layden and Martindale, 2014; Richards and Rentzsch, 2014; Richards and Rentzsch, 2015; Watanabe et al., 2014). The only known exception to this is the population of GLWamide+ neurons. They arise on the *bmp2/4*-expressing side of the directive axis (area of minimal BMP signaling) under control of the atonal-related protein Arp6 (neuroD), which is the only *Nematostella Arp* gene with a bilaterally symmetric expression (Watanabe et al., 2014). Our ChIP and RNA-Seq data showed that *Arp6* is directly suppressed by BMP. *Arp6*, however, is not the only *Nematostella* BMP target gene, whose bilaterian orthologs are implicated in the regulation of neuronal development. We also find *isl*, *irx*, *lmx, ashB, hmx3, atoh7,* and *soxC* - a *Sox4/Sox11* ortholog (the latter is also a BMP target in *Xenopus*) (Bergsland et al., 2006; Doucet-Beaupre et al., 2015; Liang et al., 2011; Miesfeld et al., 2020; Rodriguez-Seguel et al., 2009; Stevens et al., 2017; Tomita et al., 2000; Wang et al., 2004). Similarly, among the ChIP targets we find orthologs of the “canonical” bilaterian axon guidance molecules such as *rgm*, *ephrin B*, and *netrin* (Lai Wing Sun et al., 2011; Niederkofler et al., 2004; Williams et al., 2003); however, it remains unclear whether these molecules are involved in the regulation of neural development in *Nematostella* or have a different function. In Bilateria, these proteins are expressed in various non-neural contexts. For example, RGM was shown to act as a potentiator of BMP signaling in *Nematostella* and in Bilateria (Leclère and Rentzsch, 2014; Mueller, 2015), and Netrin was demonstrated to inhibit BMP signaling (Abdullah et al., 2021).

Nematostella ZSWIM4-6 as a potential conveyor of the BMP signaling-mediated gene repression

One of the most enriched pSMAD1/5 ChIP-targets in *Nematostella* was *zswim4-6*. Members of the zinc-finger family with SWIM domain were found in Archaea, prokaryotes and eukaryotes, and they were suggested to be capable of interacting with other proteins or DNA (Makarova et al., 2002). *Nematostella zswim4-6* gene activity follows the dynamics of BMP signaling. ZSWIM4-6 is a nuclear protein, whose paralogs, ZSWIM4, -/5, and -/6 proteins are conserved in Bilateria. To-date, several studies have linked ZSWIM4/5/6 with vertebrate neurogenesis and forebrain development. For instance, in the mouse, the paralogues *zswim4-6* were found to be expressed in the forebrain with distinct spatiotemporal patterns (Chang et al., 2020; Chang et al., 2021). *Zswim6* knockout mice display abnormal striatal neuron morphology and motor function (Tischfield et al., 2017). Additionally, *zswim4* mutations frequently occur in patients with acute myelogenous leukemia (Walter et al., 2012), while *zswim6* mutations in mammals associate with acromelic frontonasal dysostosis (a rare disease characterized by craniofacial, brain and limb malformations), and schizophrenia (Smith et al., 2014; Tischfield et al., 2017). Interestingly, *zswim4/5* in the frog embryo and *zswim4/6* in transit-amplifying mouse hair follicle cells are also direct targets of BMP signaling (Genander et al., 2014; Stevens et al., 2017). This suggests that *zswim4*-6 is a conserved downstream target of BMP signaling and may contribute to BMP

signaling-dependent patterning events in various contexts. However, the function of zswim4-6 homologs during early embryogenesis has remained largely unexplored.

Here we provide evidence that *Nematostella zswim*4-6 acts as a feedback regulator of the shape of the BMP signaling gradient, and its loss of function results in defects in tissue compartmentalization. While the extracellular signaling network setting up the pSMAD1/5 gradient along the directive axis in *Nematostella* has been addressed before (Genikhovich et al., 2015; Leclère and Rentzsch, 2014; Saina et al., 2009), our study provides the first example of a nuclear protein modulating the pSMAD1/5 gradient in a non-bilaterian organism. Strikingly, overexpression of a *Danio rerio zswim4-6* paralog, *zswim5*, significantly dampened pSMAD1/5 levels in zebrafish, and the embryos displayed dose-dependent developmental defects with increasing amounts of injected *zswim5* mRNA. This recapitulated the effect of *zswim4-6* overexpression on the pSMAD1/5 gradient in *Nematostella*, indicating that ZSWIM4-6 proteins may play a conserved role in modulating the pSMAD1/5 gradient in Bilateria and Anthozoa.

Analysis of the transcriptional response to *zswim4-6* KD showed that the genes known to be negatively regulated by BMP signaling were de-repressed in spite of the increased levels of nuclear pSMAD1/5, while the genes positively regulated by BMP signaling were barely affected. This allowed us to hypothesize that ZSWIM4-6 promotes BMP-mediated transcriptional repression, while positively regulated BMP targets react to changes in the pSMAD1/5 gradient and do not become repressed by ZSWIM4-6. In line with this, our ChIP analysis of EGFP-tagged *Nematostella* ZSWIM4-6 showed that ZSWIM4-6 can directly bind to the pSMAD1/5 binding site in the upstream regulatory region of at least one gene, *chordin*, which is directly repressed by BMP signaling, but not to the upstream regulatory region of *gremlin*, which, unlike *chordin*, is directly activated by BMP signaling. In the future, the generation of a tagged ZSWIM4-6 transgenic line followed by ChIP-Seq will clarify at the genome-wide scale whether or not ZSWIM4-6 directly acts exclusively on genes repressed by BMP signaling.

zswim4-6 is selectively activated by BMP2-4 but not by GDF5-like

KD of distinct *Nematostella* BMP ligands showed that not all perturbations lead to a similar reduction in the *zswim4-6* expression domain. While KD of BMP2/4 and its putative shuttle Chordin abolished *zswim4-6* expression, the effect of GDF5-like KD on *zswim4-6* was minimal, despite a striking reduction in the pSMAD1/5 levels caused by GDF5lMO injection (Genikhovich et al., 2015). We see two possible explanations for this phenomenon: i) it can reflect the different levels of reduction of pSMAD1/5 signaling intensity upon BMP2/4 and GDF5-like KD; ii) it can indicate different receptor or binding co-factor preferences for different BMP ligands. Our attempts to gradually reduce BMP signaling by injecting different concentrations of BMP2/4MO confirmed an earlier observation (Leclère and Rentzsch, 2014) that these perturbations result in binary response: the embryos appear either normal (normal pSMAD1/5 gradient and normal marker gene expression at early planula, 8 mesenteries at late planula), or completely radialized (abolished pSMAD1/5gradient, radialized *bmp2/4* expression, 0 mesenteries at late planula). In contrast, GDF5-like morphants display an intermediate phenotype with a shallow pSMAD1/5 gradient at early planula and 4 mesenteries at late planula (Genikhovich et al., 2015). This

suggests that, in spite of converging at the point of SMAD1/5 phosphorylation, BMP2/4-mediated and GDF5-like-mediated signaling may differ by their mode of action, which can be achieved, for instance, by different BMP ligands having different receptor preferences.

In vitro and *in vivo* studies showed that in Bilateria, different BMPs elicit combinatorial, non-redundant responses (Chen et al., 2013; Klumpe et al., 2022) displaying complex, promiscuous binding to various BMP and Activin receptors (Klumpe et al., 2022; Mueller and Nickel, 2012; Nickel and Mueller, 2019; Su et al., 2022). In different contexts, different ligands show distinct receptor preferences. For example, the protein precursor of the *Drosophila* BMP5-8 paralog Glass bottom boat can be proteolytically processed into a long and a short isoform, which have different developmental functions and preferentially signal via different Type II BMP receptors (Anderson and Wharton, 2017). In mammalian cell culture and biosensor assays, BMP2 and BMP4 were shown to bind and signal via Type I BMPR receptors Alk3 and Alk6, while GDF5 preferentially bound Alk6 (Heinecke et al., 2009; Nickel and Mueller, 2019). Strikingly, GDF5 could be mutated to mimic the binding preferences of BMP2, however, the binding of GDF5 and BMP2 to the same set of receptors elicited different, and in some cases opposite, cellular responses, which suggests the presence of some yet unknown co-factors involved in signal transduction (Klammert et al., 2015). In contrast, in vivo, the mammalian BMP5-8 paralogs BMP6 and BMP7 seem to be able to signal only through Alk2, although they bind Alk3 with a 30-fold higher affinity in vitro (Nickel and Mueller, 2019). Recent evidence from zebrafish suggests that Alk3/6 and Alk2 (zebrafish has two *alk3*, two *alk6* and one *alk2* gene) are non-redundant. At physiological expression levels, BMP2 and BMP7 homodimers do not appear to signal at all during D-V patterning; however, BMP2/7 heterodimers signal very effectively and require both Alk3 and Alk2 Type I receptors for signaling (Tajer et al., 2021). In our hands, shRNA-mediated KD and overexpression of the dominant-negative forms of *Nematostella* Alk2 and Alk3/6 also suggested their non-redundant roles. *Zswim4-6* expression was not affected by Alk2 KD, but became weaker upon Alk3/6 KD and abolished upon simultaneous Alk2/Alk3/6 KD. In contrast, BMPR-II appeared to be expendable for this signaling interaction, suggesting that its loss of function might be compensated by a different Type II receptor. In summary, in *Nematostella*, BMP2/4-mediated signaling, but not GDF5-like-mediated signaling, regulates *zswim4-6* expression. It appears that this selective action of different BMP ligands takes place at the level of the ligand-receptor interaction. Our experiments suggest that BMP2/4 (or rather a putative BMP2/4/BMP5-8 heterodimer) requires Alk3/6 or a combination of Alk3/6 and Alk2 but not Alk2 alone to regulate *zswim4/6*.

Conclusion

In this paper we present evidence showing that in the sea anemone *Nematostella vectensis*, BMP signaling directly controls the expression of a number of previously characterized and many novel regulators of their bilaterally symmetric body plan. We show that *gbx* and all the *hox* genes, previously shown to control the regionalization of the secondary body axis of *Nematostella,* are under direct BMP regulation. In our dataset, we identified BMP target genes conserved between Cnidaria and Bilateria, among which we found a novel modulator of BMP signaling, the putative transcriptional repressor *zswim4-6*, whose expression is tightly controlled by BMP2/4- but not by

GDF5-like-mediated BMP signaling. Our paper provides a valuable resource for future studies of BMP signaling in Cnidaria and Bilateria and offers the first glimpse into the fascinating area of control of BMP ligand/receptor selectivity in a bilaterally symmetric non-bilaterian.

Materials and Methods

Animal husbandry and microinjection

Adult *Nematostella vectensis* polyps were kept in the dark at 18 °C in *Nematostella* medium (16‰ artificial seawater, NM) and induced for spawning in a 25 °C incubator with 10 h of constant illumination. Egg packages were fertilized for 30 min, de-jellied in 3% L-cysteine/NM and washed 6 times with NM. Microinjection was carried out under a Nikon TS100F Microscope, using an Eppendorf Femtojet and Narishige micromanipulators as described in (Renfer and Technau, 2017).

Adult TE zebrafish were kept in accordance with the guidelines of the State of Baden-Württemberg (Germany) and approved by the Regierungspräsidium Tübingen (35/9185.46–5, 35/9185.81–5). Zebrafish embryos were maintained at 28℃ in embryo medium (250 mg/l Instant Ocean salt in reverse osmosis water adjusted to pH 7 with $NaHCO_3$). Microinjections were carried out using PV820 Pneumatic PicoPumps (World Precision Instruments), M-152 micromanipulators (Narishige) and 1B100f-4 capillaries (World Precision Instruments) shaped with P-1000 micropipette puller (Sutter Instrument Company).

Transgenesis, gene overexpression and knockdown

The full-length sequence of *Nematostella zswim4-6* was isolated by RACE-PCR. Native *zswim4-6* (EF1α*::zswim4-6-egfp*) and a truncated version lacking the first 24 bases coding for the NLS (*EF1α::zswim4-6Δnls-egfp)* were cloned into *AscI* and *SbfI* sites in the *Nematostella* transgenesis vector, downstream of the ubiquitously active *EF1α* promoter, and *I-SceI* meganuclease-mediated transgenesis was performed as specified (Renfer and Technau, 2017). For mRNA synthesis, the *EF1α* promoter was removed by digestion with PacI and AscI, the ends were blunted, and the plasmid re-ligated, which placed *zswim4-6* directly downstream of the SP6 promoter. Capped mRNA was synthesized using an SP6 mMessage mMachine Transcription Kit (Life Technologies) and purified with the Invitrogen MEGAclear Transcription Clean-Up Kit (Ambion). For overexpression, 150ng/µl mRNA of *ZSWIM4-6-EGFP* or *EGFP* control were injected. *zswim4-6* knockout animals were generated using the IDT CRISPR/Cas9 (Alt-R CRISPR-Cas9 crRNA:tracrRNA) gRNA system. Genotyping of F0 mosaic mutants after *in situ* hybridization was performed as described in (Lebedeva et al., 2021). Target sequence for gRNAs and genotyping primers are listed in the Supplementary Table 1. Dominant-negative BMP receptors were generated by removing the C-terminal serine-threonine kinase domains of Alk2, Alk3/6 and BMPRII and replacing them with the *EGFP* coding sequence. mRNAs of dominant-negative receptors and *EGFP* control were injected at 60ng/µl (Supplementary Table 2).

The zebrafish *zswim5* cDNA was cloned into the pCS2+ vector as follows. RNA was obtained from 75% epiboly-stage embryos using TRIzol (Invitrogen) and reverse-transcribed into cDNA using SuperScript III First-Strand Synthesis SuperMix (Invitrogen). *zswim5* was then amplified from cDNA using the primers ATGGCGGAGGGACGTGGA and TTAACCGAAACGTTCCCGTACCA followed by the addition of ClaI and EcoRI restriction sites using the primers TTCTTTTTGCAGGATCCCATCGATGCCACCATGGCGGAGGGACGTGGA and TAGAGGCTCGAGAGGCCTTGAATTCTTAACCGAAACGTTCCCGTACCA. The resulting amplicon was cloned into pCS2+ using ClaI and EcoRI (NEB) digestion and Gibson assembly (NEB). To generate mRNA, the pCS2-zswim5 plasmid was linearized with NotI-HF (NEB) and purified using a Wizard SV Gel and PCR Clean-up System (Promega). mRNA was generated from linearized plasmid using an SP6 mMessage mMachine Transcription Kit (Thermo Fisher Scientific) and column-purified using an RNeasy Mini Kit (Qiagen). mRNA concentration was quantified using an Implen NanoPhotometer NP80. For phenotype assessment, TE wild-type zebrafish embryos were injected through the chorion at the one-cell stage with 20, 40, 80, or 210 pg *zswim5* mRNA. Unfertilized and damaged embryos were removed approximately 1.3 h post-injection, and embryos were incubated at 28°C. At 1 day post-fertilization, embryos were scored based on gross morphology visible through the chorion. Representative embryos were immobilized with MESAB, dechorionated manually, and imaged in 2% methylcellulose on an Axio Zoom V16 microscope (ZEISS).

KD of *bmp2/4*, *chordin*, *gremlin* and *gdf5-l* in *Nematostella* were performed using previously published morpholino oligonucleotides (Supplementary Tables 3-4) as described (Genikhovich et al., 2015; Saina et al., 2009). The activity of the new translation-blocking ZSWIM4/6MO (5' CCGTCCATAGCTTGTACTGATCGAC) was tested by co-injecting morpholino with mRNA containing the *mCherry* coding sequence preceded by either wildtype or 5-mismatch ZSWIM4/6MO recognition sequence in frame with mCherry (Supplementary Fig. 4). Approximately 4pL (Renfer and Technau, 2017) of 500µM solutions of GrmMO and GDF5-lMO, and 300 µM solutions of BMP2/4MO, ChdMO and ZSWIM4/6MO were injected, unless indicated differently.

shRNA-mediated BMP receptor KD were carried out as described (Karabulut et al., 2019) using injection or electroporation of 800ng/µl shRNA for *alk2*, *alk3/6* and *bmprII* (Supplementary Table 5). shRNA against *mOrange* was used as control in all KD. To determine KD specificity, two non-overlapping shRNAs were tested for each gene and efficiencies were estimated by *in situ* hybridization and qPCR (Supplementary Table 6). qPCR normalization was performed using primers against GADPH.

Chromatin immunoprecipitation and RNA-Seq

Processing of *Nematostella* embryos of two developmental stages, namely late gastrula and late planula, for ChIP was performed as described previously (Kreslavsky et al., 2017; Schwaiger et al., 2014). Input DNA was taken aside after chromatin shearing and pre-blocking with Protein-G sepharose beads. Immunoprecipitation was performed overnight at 4°C using 300µg of chromatin per reaction and polyclonal rabbit anti-Phospho-Smad1 (Ser463/465)/Smad5 (Ser463/465)/Smad8 (Ser426/428) (Cell Signaling, #9511; 1:1000). Pulldown of the

immunoprecipitated chromatin using protein-G sepharose beads and elution were performed as described (Schwaiger et al., 2014). Libraries for sequencing of the input and immunoprecipitated DNA were prepared using the NEBNext Ultra End Repair/dA-Tailing Module kit and NEBNextUltraLigation Module with subsequent PCR amplification using KAPA Real Time Library Amplification Kit. 50 bp PE Illumina HiSeq2500 sequencing was performed by the Vienna BioCenter Core Facilities.

Raw reads were trimmed using trimmomatic v0.32 (Bolger et al., 2014) using the paired end mode and the ILLUMINACLIP option, specifying TruSeq3-PE as the target adaptors, seed mismatches at 2, a palindrome clip threshold of 30 and a simple clip threshold of 10. Additionally, the leading and trailing quality threshold were 5, and reads under a length of 36 were filtered out. Trimmed reads were aligned to the *Nematostella vectensis* genome (Putnam et al., 2007) using the "mem" algorithm and default settings. Alignments were then for conversion to bedpe format using the samtools v1.3.1 (Li et al., 2009) name sort and fixmate utilities. Bedtools (Quinlan and Hall, 2010) was used to convert to bedpe. Peak calling was performed using a modified version of peakzilla (Bardet et al., 2011) ("peakzilla_qnorm_patched.py") which used quantile normalization for peak height. Peaks were merged across lanes using a custom script ("join_peaks.py") using a maximum distance of 100 bp. Joined peaks were then annotated using a custom script ("associate_genes.py"). Gene model assignment was then manually curated to discard wrong gene models. A filter was applied ("final_filter.py") which required the peaks to have an enrichment score of at least 10 and have an overall score of at least 80. Motif analysis was done using the MEME-ChIP pipeline (Machanick and Bailey, 2011) with the anr model, a window range of 5-30, number of motifs 10, DREME e-value threshold of 0.05, centrimo score and evalue thresholds of 5 and 10, respectively, against the JASPAR 2018 core motif database. Custom scripts mentioned above can be found in the following github repository: https://github.com/nijibabulu/chip_tools.

For RNA-seq, total RNA was extracted from 2 dpf embryos with TRIZOL (Invitrogen) according to the manufacturer's protocol. Poly-A-enriched mRNA library preparation (Lexogen) and 50 bp SE Illumina HiSeq2500 sequencing was performed by the Vienna BioCenter Core Facilities. The number of the sequenced biological replicates is shown in the Supplementary Fig. 1. The reads were aligned with STAR (Dobin et al., 2013) to the *Nematostella vectensis* genome (Putnam et al., 2007) using the ENCODE standard options, with the exception that --alignIntronMax was set to 100 kb. Hits to the NVE gene models v2.0 (https://figshare.com/articles/Nematostella_vectensis_transcriptome_and_gene_models_v2_0/807696), were quantified with featureCounts (Liao et al., 2014), and differential expression analysis was performed with DeSeq2 (Love et al., 2014). Expression changes in genes with the adjusted p-value < 0.05 were considered significant. No additional expression fold change cutoff was imposed. Putative transcription factors (TF) and secreted molecules (SignalP) were identified using INTERPROSCAN (Madeira et al., 2019).

Low input ChIP

EGFP-IP was performed on *EF1α::zswim4-6-egfp* F0 transgenic *Nematostella* 30 hpf. 4000-6000 embryos were used per replicate. Embryos were washed 2x with NM, 2x with ice-cold 1xPBS and collected in a 2 ml tube. They were fixed in 1 part of 50 mM HEPES pH 8, 1 mM EDTA pH 8, 0.5

mM EGTA pH 8, 100 mM NaCl and 3 parts of 1x PBS and 2% methanol-free formaldehyde (Sigma) for 15 min at RT on an overhead rotator. The fixative was removed and exchanged with 125 mM glycine in PBS for 10 min and the embryos were washed 3x with PBS. For long-term storage, embryos were equilibrated in HEG buffer (50 mM HEPES pH 7.5, 1 mM EDTA, 20% glycerol), as much liquid as possible was removed, and embryos were snap-frozen in liquid nitrogen and stored at –80°. Before sonication, embryos were thawed on ice and resuspended in 1ml E1 buffer (50 mM HEPES pH 7.5, 140 mM NaCl, 1 mM EDTA, 10% glycerol, 0.5% NP40, 0.25% Triton X-100, 1 mM PMSF, 1x Complete Protease Inhibitor (Roche), 1 mM DTT) and homogenized in a 1 ml dounce homogenizer with a tight pestle for 5 min directly on ice. The homogenate was centrifuged twice for 10 min at 4°C 1500 g, the supernatant was discarded and both pellets were resuspended in 130 µl lysis buffer (50 mM HEPES pH 7.5, 500 mM NaCl, 1 mM EDTA, 0.1% SDS, 0.5% N-Laurylsarcosine sodium, 0.3% Triton X-100, 0.1% sodium deoxycholate, 1 mM PMSF and 1x Complete Protease Inhibitor) and incubated in lysis buffer for 30min. The samples were sonicated in 130µl glass tubes in a Covaris S220 with following settings: for 20 s repeated 4 times: peak power=175, duty factor=20, cycles/burts=200; with pausing steps (peak power=2.5, duty factor=0.1, cycles/burts=5;) for 9 s in between each treatment.

After sonication, the sample was transferred to a low-bind Eppendorf tube and centrifuged at 4°C for 10 min at 16000 g. For the input fraction, 15 µl of the sample were taken aside and stored at -20°C. For the IP, the rest of the sample was filled up to 1ml with dilution buffer (10 mM Tris/HCl pH 7.5; 150 mM NaCl; 0.5 mM EDTA). GFP-Trap MA beads (Chromotek) were prepared according to the manufacturer's instructions and incubated with the sample at 4°C overnight under rotation. The samples were washed 1x with dilution buffer, 1x with high salt dilution buffer (500 mM NaCl), again with dilution buffer and eluted twice with 50 µl 0.2 M glycine pH 2.5 within 5 min under pipetting. The eluates were immediately neutralized using 20 µl 1 M Tris pH 8. The IP fractions were filled up to 200 µl with MiliQ water, and the input fractions were filled up to 200µl with dilution buffer and incubated with 4µl of 10 mg/ml RNase A for 30 min at 37°C. Then 10 mM EDTA pH 8.0, 180 mM NaCl and 100µg/ml Proteinase K were added and incubated overnight at 65°C. The samples were purified using a Qiagen PCR Purification Kit. The IP fraction was eluted in 40 µl elution buffer, and the input fraction was eluted in 100 µl. The regulatory regions identified by pSMAD1/5 ChIP-Seq of *chordin* and *gremlin* were tested for enrichment by qPCR. Primers against the intergenic region A (*IntA*, scaffold_96:609598-609697) were used for normalization.

Orthology analysis

The *Nematostella* proteome was downloaded from a public repository https://doi.org/10.6084/m9.figshare.807696.v2. The proteome from *Drosophila melanogaster* version BDGP6, corresponding to that used in Deignan et al. 2016, was downloaded from FlyBase (Larkin et al., 2021). The *Xenopus laevis* proteome version 9.1, corresponding to that used in (Stevens et al., 2017), was downloaded from the JGI genome browser (Nordberg et al., 2014). Orthology links between all proteomes were inferred using NCBI blastp (Altschul et al., 1990), requiring an e-value of at most 1e-5. Reciprocal best blast hits were determined using the bit score as the metric. For *X. laevis*, the genome suffix (.S or .L) was ignored, and only genes with BLAST hits in all species were considered (Fig. 3). The resulting hits were filtered for genes found

as pSMAD1/5 targets in this study and in *Drosophila* and *Xenopus* analyses (Deignan et al., 2016; Stevens et al., 2017).

In situ hybridization

Fragments for preparing in situ probes were amplified by PCR on ss cDNA (Supplementary Table 7) and cloned. *In situ* hybridization was carried out as described previously (Lebedeva et al., 2021), with minor changes. *Nematostella* embryos were fixed for 1 h in 4% PFA/PTW (1x PBS, 0.1% Tween 20) at room temperature. Permeabilization was performed for 20 min in 10 µg/ml Proteinase K/PTW. 4d planulae were incubated for 40min in 1U/µl RNAseT1 in 2xSSC at 37°C after the initial 2xSSC wash and before the 0.075xSSC washes.

Phylogenetic analysis

Protein sequences of ZSWIM4-6 and related proteins (Supplementary Data 2) were aligned with MUSCLE using MegaX (Kumar et al., 2018) and trimmed with TrimAl 1.3 using an Automated 1 setting (Capella-Gutierrez et al., 2009). A maximum likelihood tree (JTTDCMut+F+G4, bootstrap 100) was calculated using IQTREE (Trifinopoulos et al., 2016).

Antibody staining and pSMAD1/5 quantification

Immunostainings in *Nematostella* were performed according to Leclère and Rentzsch (2014) with minor changes. Embryos were fixed for 2min in ice-cold 2.5% glutaraldehyde/3.7% formaldehyde/PTX (1x PBS, 0.3% Triton-X), then transferred to ice-cold 3.7% FA/PTX and fixed at 4°C for 1 h. The samples were washed 5x with PTX, incubated in ice-cold methanol for 8 min, and washed 3x with PTX. After 2 h in the blocking solution containing 5% heat-inactivated sheep serum/95% PTX-BSA (PTX-BSA = 1% BSA/PTX), the samples were incubated overnight with the primary antibody (rabbit αpSMAD1/5/9 (Cell Signaling, #13820; 1:200) or rat αNvHoxE antibody (1:500)) in blocking solution. Embryos were then washed 5x with PTX, blocked for 2 h in blocking solution and incubated overnight with secondary antibody (goat α-rabbit IgG-Alexa568 or goat α-rabbit IgG-Alexa633) and DAPI (1:1000) in blocking solution. After the secondary antibody staining, the samples were washed 5x with PTX, mounted in Vectashield (VectorLabs), and imaged under Leica SP5X or Leica SP8 confocal microscopes. pSMAD1/5 staining intensities were quantified as described in Genikhovich et al., 2015. Control MO and ZSWIM4-6MO embryos, as well as *zswim4-6* mRNA and *egfp* injected embryos were stained with αpSMAD1/5 and DAPI and 16-bit images of single confocal sections of oral views were collected. The intensities of the pSMAD1/5 staining of the nuclei were measured in a 180° arc of from 0 to π using Fiji (Schindelin et al., 2012). Measurements in the endodermal and the ectodermal body wall were performed separately. The nuclei were selected in the DAPI channel and measured in the pSMAD1/5 channel, starting in the middle of the domain where the pSMAD1/5 signal is strongest and moving towards the position on the opposite side of the embryo. Every nucleus in each embryo was assigned a coordinate along the 0 to π arc by dividing the sequential number of each nucleus by the total number of analyzed nuclei in that particular embryo. αpSMAD1/5 staining intensities were then depicted as a function of the relative position of the nucleus.

TE wild type zebrafish embryos were dechorionated using Pronase and injected at the one-cell stage with 20-210 pg *zswim5* mRNA (80 pg mRNA was injected for the quantification). Unfertilized and damaged embryos were removed ~1.5 h post-injection, and embryos were incubated at 28°C. At 50% epiboly embryos were fixed in cold 4% formaldehyde diluted in PBS. Uninjected embryos reached 50% epiboly 30-45 min before injected siblings. Fixed embryos were stored at 4°C overnight, washed with PBST, transferred to methanol (three PBST washes followed by three methanol washes), and stored at -20°C for at least 2 h. Embryos were then washed 4-5 times with PBST, blocked in FBS-PBST (10% FBS, 1% DMSO, 0.1% Tween-20 in PBS) for at least 1 h and then incubated in 1:100 anti-pSmad1/5/9 (Cell Signaling, #13820) in FBS-PBST at 4°C overnight. After 5-7 PBST washes over a period of 2-6 h, embryos were incubated again in FBS-PBST for at least 1 h and then transferred to 1:500 goat-anti-rabbit-Alexa488 (Life Technologies, A11008) and 1:1000 DRAQ7 (Invitrogen, D15105) overnight at 4°C. Embryos were washed 5-7 times with PBST over a period of 2-6 h and stored at 4°C overnight. pSmad1/5/9 immunofluorescence and DRAQ7 nuclear signal were imaged on a Lightsheet Z.1 microscope (ZEISS). Briefly, embryos were mounted in 1% low melting point agarose and imaged in water using a 20× objective. Embryos were oriented with the animal pole toward the imaging objective, and 50-90 z-slices with 7 µm between each slice were acquired. Quantification was performed on maximum intensity projections. Images were manually rotated in Fiji with the ventral side to the left, an ROI was manually drawn around each embryo to exclude non-embryo background, and the ventral-to-dorsal intensity profile was determined by calculating the average intensity in each column of pixels (pixel size: 0.457 µm × 0.457 µm). The profiles were binned and normalized to % length to account for embryo-to-embryo variability in length (Rogers et al., 2020). For background subtraction, intensities measured as described above in four randomly oriented controls not exposed to the primary antibody were subtracted from intensity profiles.

Acknowledgements

This work was funded by the Austrian Science Foundation (FWF) grants P26962-B21 and P32705-B to G.G. and by the European Research Council (ERC) grants 637840 (*QUANTPATTERN*) and 863952 (*ACE-OF-SPACE*) to P.M.. We thank Michaela Schwaiger, Taras Kreslavsky, Hiromi Tagoh and Patricio Ferrer Murguia for their help with the ChIP protocol, Matthias Richter and Christian Hofer for their assistance with *in situ* analyses, Catrin Weiler for the assistance in cloning zebrafish *zswim5*, David Mörsdorf for critically reading the manuscript, and the Core Facility for Cell Imaging and Ultrastructure Research of the University of Vienna for access to the confocal microscope.

Author contributions

A.S. and P.K. performed the majority of *Nematostella* experiments, analyzed data and wrote the paper. B.Z. performed the bioinformatic analyses. P.M. designed and supervised the zebrafish experiments. A.P. carried out pilot zebrafish experiments, and K.W.R. generated the data and

analyses shown in Fig. 7. G.G. conceived the study, performed experiments, analyzed data and wrote the paper. All authors edited the paper.

Data availability

All the sequencing data are available at NCBI as an SRA project PRJNA820593.

Competing interests

The authors declare no competing interests

References

Abdullah, A., Herdenberg, C. and Hedman, H. (2021). Netrin-1 functions as a suppressor of bone morphogenetic protein (BMP) signaling. *Sci Rep* **11**, 8585.

Altschul, S. F., Gish, W., Miller, W., Myers, E. W. and Lipman, D. J. (1990). Basic local alignment search tool. *Journal of molecular biology* **215**, 403-410.

Anderson, E. N. and Wharton, K. A. (2017). Alternative cleavage of the bone morphogenetic protein (BMP), Gbb, produces ligands with distinct developmental functions and receptor preferences. *The Journal of biological chemistry* **292**, 19160-19178.

Arendt, D. and Nubler-Jung, K. (1997). Dorsal or ventral: similarities in fate maps and gastrulation patterns in annelids, arthropods and chordates. *Mechanisms of development* **61**, 7-21.

Arendt, D., Tosches, M. A. and Marlow, H. (2016). From nerve net to nerve ring, nerve cord and brain--evolution of the nervous system. *Nat Rev Neurosci* **17**, 61-72.

Bardet, A. F., He, Q., Zeitlinger, J. and Stark, A. (2011). A computational pipeline for comparative ChIP-seq analyses. *Nat Protoc* **7**, 45-61.

Bergsland, M., Werme, M., Malewicz, M., Perlmann, T. and Muhr, J. (2006). The establishment of neuronal properties is controlled by Sox4 and Sox11. *Genes & development* **20**, 3475-3486.

Berking, S. (2007). Generation of bilateral symmetry in Anthozoa: a model. *J Theor Biol* **246**, 477-490.

Bolger, A. M., Lohse, M. and Usadel, B. (2014). Trimmomatic: a flexible trimmer for Illumina sequence data. *Bioinformatics* **30**, 2114-2120.

Capella-Gutierrez, S., Silla-Martinez, J. M. and Gabaldon, T. (2009). trimAl: a tool for automated alignment trimming in large-scale phylogenetic analyses. *Bioinformatics* **25**, 1972-1973.

Chang, C. C., Kuo, H. Y., Chen, S. Y., Lin, W. T., Lu, K. M., Saito, T. and Liu, F. C. (2020). Developmental characterization of Zswim5 expression in the progenitor domains and tangential migration pathways of cortical interneurons in the mouse forebrain. *The Journal of comparative neurology* **528**, 2404-2419.

---- (2021). Developmental Characterization of Schizophrenia-Associated Gene Zswim6 in Mouse Forebrain. *Front Neuroanat* **15**, 669631.

Chen, H., Brady Ridgway, J., Sai, T., Lai, J., Warming, S., Chen, H., Roose-Girma, M., Zhang, G., Shou, W. and Yan, M. (2013). Context-dependent signaling defines roles of BMP9 and BMP10 in embryonic and postnatal development. *Proceedings of the National Academy of Sciences of the United States of America* **110**, 11887-11892.

Chourrout, D., Delsuc, F., Chourrout, P., Edvardsen, R. B., Rentzsch, F., Renfer, E., Jensen, M. F., Zhu, B., de Jong, P., Steele, R. E., et al. (2006). Minimal ProtoHox cluster inferred from bilaterian and cnidarian Hox complements. *Nature* **442**, 684-687.

Deignan, L., Pinheiro, M. T., Sutcliffe, C., Saunders, A., Wilcockson, S. G., Zeef, L. A., Donaldson, I. J. and Ashe, H. L. (2016). Regulation of the BMP Signaling-Responsive Transcriptional Network in the Drosophila Embryo. *PLoS genetics* **12**, e1006164.

Dobin, A., Davis, C. A., Schlesinger, F., Drenkow, J., Zaleski, C., Jha, S., Batut, P., Chaisson, M. and Gingeras, T. R. (2013). STAR: ultrafast universal RNA-seq aligner. *Bioinformatics* **29**, 15-21.

Doucet-Beaupre, H., Ang, S. L. and Levesque, M. (2015). Cell fate determination, neuronal maintenance and disease state: The emerging role of transcription factors Lmx1a and Lmx1b. *FEBS letters* **589**, 3727-3738.

DuBuc, T. Q., Stephenson, T. B., Rock, A. Q. and Martindale, M. Q. (2018). Hox and Wnt pattern the primary body axis of an anthozoan cnidarian before gastrulation. *Nat Commun* **9**, 2007.

Finnerty, J. R., Pang, K., Burton, P., Paulson, D. and Martindale, M. Q. (2004). Origins of bilateral symmetry: Hox and dpp expression in a sea anemone. *Science (New York, N.Y* **304**, 1335-1337.

Genander, M., Cook, P. J., Ramskold, D., Keyes, B. E., Mertz, A. F., Sandberg, R. and Fuchs, E. (2014). BMP signaling and its pSMAD1/5 target genes differentially regulate hair follicle stem cell lineages. *Cell Stem Cell* **15**, 619-633.

Genikhovich, G., Fried, P., Prünster, M. M., Schinko, J. B., Gilles, A. F., Meier, K., Iber, D. and Technau, U. (2015). Axis patterning by BMPs: cnidarian network reveals evolutionary constraints. *Cell Rep* **10**, 1646–1654.

Genikhovich, G. and Technau, U. (2017). On the evolution of bilaterality. *Development (Cambridge, England)* **144**, 3392-3404.

Greenfeld, H., Lin, J. and Mullins, M. C. (2021). The BMP signaling gradient is interpreted through concentration thresholds in dorsal-ventral axial patterning. *PLoS biology* **19**, e3001059.

He, S., Del Viso, F., Chen, C. Y., Ikmi, A., Kroesen, A. E. and Gibson, M. C. (2018). An axial Hox code controls tissue segmentation and body patterning in Nematostella vectensis. *Science (New York, N.Y* **361**, 1377-1380.

Heinecke, K., Seher, A., Schmitz, W., Mueller, T. D., Sebald, W. and Nickel, J. (2009). Receptor oligomerization and beyond: a case study in bone morphogenetic proteins. *BMC biology* **7**, 59.

Holley, S. A., Jackson, P. D., Sasai, Y., Lu, B., De Robertis, E. M., Hoffmann, F. M. and Ferguson, E. L. (1995). A conserved system for dorsal-ventral patterning in insects and vertebrates involving sog and chordin. *Nature* **376**, 249-253.

Hudry, B., Thomas-Chollier, M., Volovik, Y., Duffraisse, M., Dard, A., Frank, D., Technau, U. and Merabet, S. (2014). Molecular insights into the origin of the Hox-TALE patterning system. *Elife* **3**, e01939.

Karabulut, A., He, S., Chen, C. Y., McKinney, S. A. and Gibson, M. C. (2019). Electroporation of short hairpin RNAs for rapid and efficient gene knockdown in the starlet sea anemone, Nematostella vectensis. *Developmental biology* **448**, 7-15.

Katagiri, T., Imada, M., Yanai, T., Suda, T., Takahashi, N. and Kamijo, R. (2002). Identification of a BMP-responsive element in Id1, the gene for inhibition of myogenesis. *Genes Cells* **7**, 949-960.

Kelava, I., Rentzsch, F. and Technau, U. (2015). Evolution of eumetazoan nervous systems: insights from cnidarians. *Philosophical transactions of the Royal Society of London* **370**.

Kirillova, A., Genikhovich, G., Pukhlyakova, E., Demilly, A., Kraus, Y. and Technau, U. (2018). Germ-layer commitment and axis formation in sea anemone embryonic cell aggregates. *Proceedings of the National Academy of Sciences* **115**, 1813-1818.

Kishimoto, Y., Lee, K. H., Zon, L., Hammerschmidt, M. and Schulte-Merker, S. (1997). The molecular nature of zebrafish swirl: BMP2 function is essential during early dorsoventral patterning. *Development (Cambridge, England)* **124**, 4457-4466.

Klammert, U., Mueller, T. D., Hellmann, T. V., Wuerzler, K. K., Kotzsch, A., Schliermann, A., Schmitz, W., Kuebler, A. C., Sebald, W. and Nickel, J. (2015). GDF-5 can act as a context-dependent BMP-2 antagonist. *BMC biology* **13**, 77.

Klumpe, H. E., Langley, M. A., Linton, J. M., Su, C. J., Antebi, Y. E. and Elowitz, M. B. (2022). The context-dependent, combinatorial logic of BMP signaling. *Cell Syst* **13**, 388-407 e310.

Kozmikova, I., Candiani, S., Fabian, P., Gurska, D. and Kozmik, Z. (2013). Essential role of Bmp signaling and its positive feedback loop in the early cell fate evolution of chordates. *Developmental biology* **382**, 538-554.

Kraus, Y., Aman, A., Technau, U. and Genikhovich, G. (2016). Pre-bilaterian origin of the blastoporal axial organizer. *Nat Commun* **7**, 11694.

Kreslavsky, T., Vilagos, B., Tagoh, H., Poliakova, D. K., Schwickert, T. A., Wohner, M., Jaritz, M., Weiss, S., Taneja, R., Rossner, M. J., et al. (2017). Essential role for the transcription factor Bhlhe41 in regulating the development, self-renewal and BCR repertoire of B-1a cells. *Nat Immunol* **18**, 442-455.

Kumar, S., Stecher, G., Li, M., Knyaz, C. and Tamura, K. (2018). MEGA X: Molecular Evolutionary Genetics Analysis across Computing Platforms. *Molecular biology and evolution* **35**, 1547-1549.

Lai Wing Sun, K., Correia, J. P. and Kennedy, T. E. (2011). Netrins: versatile extracellular cues with diverse functions. *Development (Cambridge, England)* **138**, 2153-2169.

Lapraz, F., Besnardeau, L. and Lepage, T. (2009). Patterning of the dorsal-ventral axis in echinoderms: insights into the evolution of the BMP-chordin signaling network. *PLoS biology* **7**, e1000248.

Larkin, A., Marygold, S. J., Antonazzo, G., Attrill, H., Dos Santos, G., Garapati, P. V., Goodman, J. L., Gramates, L. S., Millburn, G., Strelets, V. B., et al. (2021). FlyBase: updates to the Drosophila melanogaster knowledge base. *Nucleic acids research* **49**, D899-D907.

Layden, M. J., Johnston, H., Amiel, A. R., Havrilak, J., Steinworth, B., Chock, T., Rottinger, E. and Martindale, M. Q. (2016). MAPK signaling is necessary for neurogenesis in Nematostella vectensis. *BMC biology* **14**, 61.

Layden, M. J. and Martindale, M. Q. (2014). Non-canonical Notch signaling represents an ancestral mechanism to regulate neural differentiation. *Evodevo* **5**, 30.

Lebedeva, T., Aman, A. J., Graf, T., Niedermoser, I., Zimmermann, B., Kraus, Y., Schatka, M., Demilly, A., Technau, U. and Genikhovich, G. (2021). Cnidarian-bilaterian comparison reveals the ancestral regulatory logic of the β-catenin dependent axial patterning. *Nat Commun* **12**, 4032.

Leclère, L. and Rentzsch, F. (2014). RGM Regulates BMP-Mediated Secondary Axis Formation in the Sea Anemone Nematostella vectensis. *Cell Rep* **9**, 1-10.

Lee, P. N., Kumburegama, S., Marlow, H. Q., Martindale, M. Q. and Wikramanayake, A. H. (2007). Asymmetric developmental potential along the animal-vegetal axis in the anthozoan cnidarian, Nematostella vectensis, is mediated by Dishevelled. *Developmental biology* **310**, 169-186.

Li, H., Handsaker, B., Wysoker, A., Fennell, T., Ruan, J., Homer, N., Marth, G., Abecasis, G., Durbin, R. and Genome Project Data Processing, S. (2009). The Sequence Alignment/Map format and SAMtools. *Bioinformatics* **25**, 2078-2079.

Liang, X., Song, M. R., Xu, Z., Lanuza, G. M., Liu, Y., Zhuang, T., Chen, Y., Pfaff, S. L., Evans, S. M. and Sun, Y. (2011). Isl1 is required for multiple aspects of motor neuron development. *Mol Cell Neurosci* **47**, 215-222.

Liao, Y., Smyth, G. K. and Shi, W. (2014). featureCounts: an efficient general purpose program for assigning sequence reads to genomic features. *Bioinformatics* **30**, 923-930.

Love, M. I., Huber, W. and Anders, S. (2014). Moderated estimation of fold change and dispersion for RNA-seq data with DESeq2. *Genome biology* **15**, 550.

Ma, W., Noble, W. S. and Bailey, T. L. (2014). Motif-based analysis of large nucleotide data sets using MEME-ChIP. *Nat Protoc* **9**, 1428-1450.

Machanick, P. and Bailey, T. L. (2011). MEME-ChIP: motif analysis of large DNA datasets. *Bioinformatics* **27**, 1696-1697.

Madeira, F., Park, Y. M., Lee, J., Buso, N., Gur, T., Madhusoodanan, N., Basutkar, P., Tivey, A. R. N., Potter, S. C., Finn, R. D., et al. (2019). The EMBL-EBI search and sequence analysis tools APIs in 2019. *Nucleic acids research* **47**, W636-w641.

Makarova, K. S., Aravind, L. and Koonin, E. V. (2002). SWIM, a novel Zn-chelating domain present in bacteria, archaea and eukaryotes. *Trends in biochemical sciences* **27**, 384-386.

Marlow, H., Matus, D. Q. and Martindale, M. Q. (2013). Ectopic activation of the canonical wnt signaling pathway affects ectodermal patterning along the primary axis during larval development in the anthozoan Nematostella vectensis. *Developmental biology* **380**, 324-334.

Martin-Duran, J. M. and Hejnol, A. (2021). A developmental perspective on the evolution of the nervous system. *Developmental biology* **475**, 181-192.

Matus, D. Q., Pang, K., Marlow, H., Dunn, C. W., Thomsen, G. H. and Martindale, M. Q. (2006a). Molecular evidence for deep evolutionary roots of bilaterality in animal development. *Proceedings of the National Academy of Sciences of the United States of America* **103**, 11195-11200.

Matus, D. Q., Thomsen, G. H. and Martindale, M. Q. (2006b). Dorso/ventral genes are asymmetrically expressed and involved in germ-layer demarcation during cnidarian gastrulation. *Current biology : CB* **16**, 499-505.

Merabet, S. and Galliot, B. (2015). The TALE face of Hox proteins in animal evolution. *Front Genet* **6**, 267.

Miesfeld, J. B., Ghiasvand, N. M., Marsh-Armstrong, B., Marsh-Armstrong, N., Miller, E. B., Zhang, P., Manna, S. K., Zawadzki, R. J., Brown, N. L. and Glaser, T. (2020). The Atoh7 remote enhancer provides transcriptional robustness during retinal ganglion cell development. *Proceedings of the National Academy of Sciences of the United States of America* **117**, 21690-21700.

Momose, T., Derelle, R. and Houliston, E. (2008). A maternally localised Wnt ligand required for axial patterning in the cnidarian Clytia hemisphaerica. *Development (Cambridge, England)* **135**, 2105-2113.

Momose, T. and Houliston, E. (2007). Two oppositely localised frizzled RNAs as axis determinants in a cnidarian embryo. *PLoS biology* **5**, e70.

Mueller, T. D. (2015). RGM co-receptors add complexity to BMP signaling. *Nature structural & molecular biology* **22**, 439-440.

Mueller, T. D. and Nickel, J. (2012). Promiscuity and specificity in BMP receptor activation. *FEBS letters* **586**, 1846-1859.

Nakanishi, N., Renfer, E., Technau, U. and Rentzsch, F. (2012). Nervous systems of the sea anemone Nematostella vectensis are generated by ectoderm and endoderm and shaped by distinct mechanisms. *Development (Cambridge, England)* **139**, 347-357.

Nguyen, V. H., Schmid, B., Trout, J., Connors, S. A., Ekker, M. and Mullins, M. C. (1998). Ventral and lateral regions of the zebrafish gastrula, including the neural crest

progenitors, are established by a bmp2b/swirl pathway of genes. *Developmental biology* **199**, 93-110.

Nickel, J. and Mueller, T. D. (2019). Specification of BMP Signaling. *Cells* **8**.

Niederkofler, V., Salie, R., Sigrist, M. and Arber, S. (2004). Repulsive guidance molecule (RGM) gene function is required for neural tube closure but not retinal topography in the mouse visual system. *J Neurosci* **24**, 808-818.

Niehrs, C. (2010). On growth and form: a Cartesian coordinate system of Wnt and BMP signaling specifies bilaterian body axes. *Development (Cambridge, England)* **137**, 845-857.

Nordberg, H., Cantor, M., Dusheyko, S., Hua, S., Poliakov, A., Shabalov, I., Smirnova, T., Grigoriev, I. V. and Dubchak, I. (2014). The genome portal of the Department of Energy Joint Genome Institute: 2014 updates. *Nucleic acids research* **42**, D26-31.

Özuak, O., Buchta, T., Roth, S. and Lynch, J. A. (2014). Dorsoventral polarity of the Nasonia embryo primarily relies on a BMP gradient formed without input from Toll. *Curr Biol* **24**, 2393-2398.

Putnam, N. H., Srivastava, M., Hellsten, U., Dirks, B., Chapman, J., Salamov, A., Terry, A., Shapiro, H., Lindquist, E., Kapitonov, V. V., et al. (2007). Sea anemone genome reveals ancestral eumetazoan gene repertoire and genomic organization. *Science (New York, N.Y* **317**, 86-94.

Quinlan, A. R. and Hall, I. M. (2010). BEDTools: a flexible suite of utilities for comparing genomic features. *Bioinformatics* **26**, 841-842.

Renfer, E. and Technau, U. (2017). Meganuclease-assisted generation of stable transgenics in the sea anemone Nematostella vectensis. *Nat Protoc* **12**, 1844-1854.

Rentzsch, F., Anton, R., Saina, M., Hammerschmidt, M., Holstein, T. W. and Technau, U. (2006). Asymmetric expression of the BMP antagonists chordin and gremlin in the sea anemone Nematostella vectensis: implications for the evolution of axial patterning. *Developmental biology* **296**, 375-387.

Richards, G. S. and Rentzsch, F. (2014). Transgenic analysis of a SoxB gene reveals neural progenitor cells in the cnidarian Nematostella vectensis. *Development (Cambridge, England)* **141**, 4681-4689.

---- (2015). Regulation of Nematostella neural progenitors by SoxB, Notch and bHLH genes. *Development (Cambridge, England)* **142**, 3332-3342.

Rodriguez-Seguel, E., Alarcon, P. and Gomez-Skarmeta, J. L. (2009). The Xenopus Irx genes are essential for neural patterning and define the border between prethalamus and thalamus through mutual antagonism with the anterior repressors Fezf and Arx. *Developmental biology* **329**, 258-268.

Rogers, K. W., ElGamacy, M., Jordan, B. M. and Muller, P. (2020). Optogenetic investigation of BMP target gene expression diversity. *Elife* **9**, e58641.

Ryan, J. F., Mazza, M. E., Pang, K., Matus, D. Q., Baxevanis, A. D., Martindale, M. Q. and Finnerty, J. R. (2007). Pre-bilaterian origins of the Hox cluster and the Hox code: evidence from the sea anemone, Nematostella vectensis. *PLoS ONE* **2**, e153.

Saina, M., Genikhovich, G., Renfer, E. and Technau, U. (2009). BMPs and chordin regulate patterning of the directive axis in a sea anemone. *Proceedings of the National Academy of Sciences of the United States of America* **106**, 18592-18597.

Schindelin, J., Arganda-Carreras, I., Frise, E., Kaynig, V., Longair, M., Pietzsch, T., Preibisch, S., Rueden, C., Saalfeld, S., Schmid, B., et al. (2012). Fiji: an open-source platform for biological-image analysis. *Nat Methods* **9**, 676-682.

Schwaiger, M., Andrikou, C., Dnyansagar, R., Ferrer Murguia, P., Paganos, P., Voronov, D., Zimmermann, B., Lebedeva, T., Schmidt, H., Genikhovich, G., et al. (2021). An ancestral Wnt-Brachyury feedback loop and recruitment of mesoderm-determining target

genes revealed by comparative Brachyury target screens. https://www.researchsquare.com/article/rs-753399/v1.

Schwaiger, M., Schönauer, A., Rendeiro, A. F., Pribitzer, C., Schauer, A., Gilles, A. F., Schinko, J. B., Renfer, E., Fredman, D. and Technau, U. (2014). Evolutionary conservation of the eumetazoan gene regulatory landscape. *Genome research* **24**, 639-650.

Smith, J. D., Hing, A. V., Clarke, C. M., Johnson, N. M., Perez, F. A., Park, S. S., Horst, J. A., Mecham, B., Maves, L., Nickerson, D. A., et al. (2014). Exome sequencing identifies a recurrent de novo ZSWIM6 mutation associated with acromelic frontonasal dysostosis. *Am J Hum Genet* **95**, 235-240.

Steinmetz, P. R., Aman, A., Kraus, J. E. M. and Technau, U. (2017). Gut-like ectodermal tissue in a sea anemone challenges germ layer homology. *Nature Ecology & Evolution* **1**, 1535–1542.

Stevens, M. L., Chaturvedi, P., Rankin, S. A., Macdonald, M., Jagannathan, S., Yukawa, M., Barski, A. and Zorn, A. M. (2017). Genomic integration of Wnt/beta-catenin and BMP/Smad1 signaling coordinates foregut and hindgut transcriptional programs. *Development (Cambridge, England)* **144**, 1283-1295.

Stultz, B. G., Park, S. Y., Mortin, M. A., Kennison, J. A. and Hursh, D. A. (2012). Hox proteins coordinate peripodial decapentaplegic expression to direct adult head morphogenesis in Drosophila. *Developmental biology* **369**, 362-376.

Su, C. J., Murugan, A., Linton, J. M., Yeluri, A., Bois, J., Klumpe, H., Langley, M. A., Antebi, Y. E. and Elowitz, M. B. (2022). Ligand-receptor promiscuity enables cellular addressing. *Cell Syst* **13**, 408-425 e412.

Tajer, B., Dutko, J. A., Little, S. C. and Mullins, M. C. (2021). BMP heterodimers signal via distinct type I receptor class functions. *Proceedings of the National Academy of Sciences of the United States of America* **118**.

Tischfield, D. J., Saraswat, D. K., Furash, A., Fowler, S. C., Fuccillo, M. V. and Anderson, S. A. (2017). Loss of the neurodevelopmental gene Zswim6 alters striatal morphology and motor regulation. *Neurobiol Dis* **103**, 174-183.

Tomita, K., Moriyoshi, K., Nakanishi, S., Guillemot, F. and Kageyama, R. (2000). Mammalian achaete-scute and atonal homologs regulate neuronal versus glial fate determination in the central nervous system. *The EMBO journal* **19**, 5460-5472.

Trifinopoulos, J., Nguyen, L. T., von Haeseler, A. and Minh, B. Q. (2016). W-IQ-TREE: a fast online phylogenetic tool for maximum likelihood analysis. *Nucleic acids research* **44**, W232-235.

van der Zee, M., Stockhammer, O., von Levetzow, C., Nunes da Fonseca, R. and Roth, S. (2006). Sog/Chordin is required for ventral-to-dorsal Dpp/BMP transport and head formation in a short germ insect. *Proceedings of the National Academy of Sciences of the United States of America* **103**, 16307-16312.

Walter, M. J., Shen, D., Ding, L., Shao, J., Koboldt, D. C., Chen, K., Larson, D. E., McLellan, M. D., Dooling, D., Abbott, R., et al. (2012). Clonal architecture of secondary acute myeloid leukemia. *N Engl J Med* **366**, 1090-1098.

Wang, W., Grimmer, J. F., Van De Water, T. R. and Lufkin, T. (2004). Hmx2 and Hmx3 homeobox genes direct development of the murine inner ear and hypothalamus and can be functionally replaced by Drosophila Hmx. *Developmental cell* **7**, 439-453.

Watanabe, H., Kuhn, A., Fushiki, M., Agata, K., Ozbek, S., Fujisawa, T. and Holstein, T. W. (2014). Sequential actions of beta-catenin and Bmp pattern the oral nerve net in Nematostella vectensis. *Nat Commun* **5**, 5536.

Wikramanayake, A. H., Hong, M., Lee, P. N., Pang, K., Byrum, C. A., Bince, J. M., Xu, R. and Martindale, M. Q. (2003). An ancient role for nuclear beta-catenin in the evolution of axial polarity and germ layer segregation. *Nature* **426**, 446-450.

Williams, S. E., Mann, F., Erskine, L., Sakurai, T., Wei, S., Rossi, D. J., Gale, N. W., Holt, C. E., Mason, C. A. and Henkemeyer, M. (2003). Ephrin-B2 and EphB1 mediate retinal axon divergence at the optic chiasm. *Neuron* **39**, 919-935.

Figures

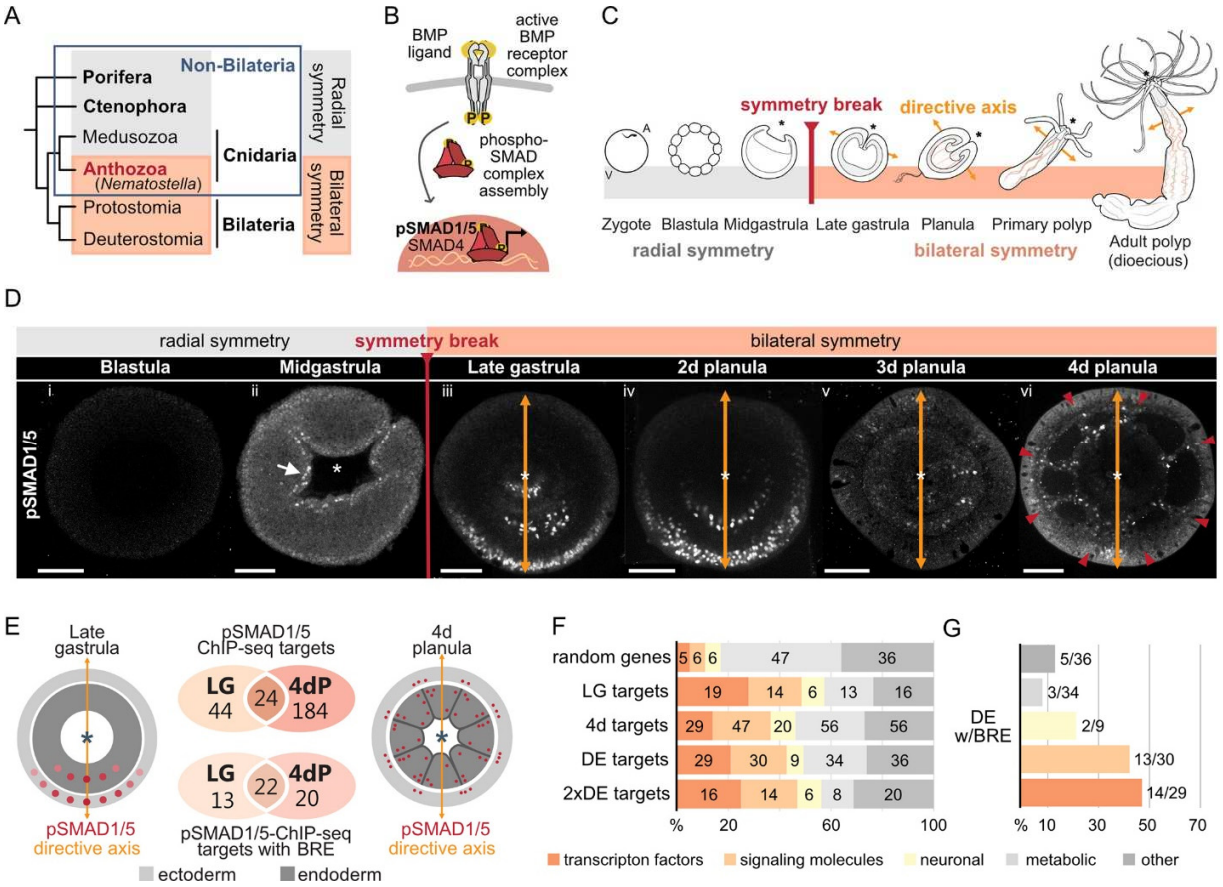

Figure 1. Bilateral body symmetry of the non-bilaterian sea anemone *Nematostella* is BMP signaling-dependent. (A) Bilateral body symmetry is observed in Bilateria and in anthozoan Cnidaria. (B) BMP signaling is initiated by BMP ligands binding to BMP receptors that trigger phosphorylation, assembly, and nuclear translocation of a pSMAD1/5/SMAD4 complex to regulate gene expression. (C) A BMP signaling-dependent symmetry break at late gastrula stage results in the formation of the secondary (directive) body axis in the sea anemone *Nematostella*. (D) BMP signaling dynamics during *Nematostella* development. No pSMAD1/5 is detectable in the blastula (Di). Nuclear pSMAD1/5 is localized in the blastopore lip of midgastrula (Dii), forms a gradient along the directive axis in the late gastrula (Diii) and 2d planula (Div). By day 3, the gradient progressively disperses (Dv), and the signaling activity shifts to the eight forming endodermal mesenteries (Dvi) and to the ectodermal stripes vis-à-vis the mesenteries (arrowheads). Images Dii-Dvi show oral views (asterisks). Scale bars 50 µm. (E) Comparison of the direct BMP signaling targets at late gastrula (LG) and 4d planula (4dP) shows little overlap. Schemes show oral views of a late gastrula and a 4d planula with red spots indicating the position of pSMAD1/5-positive nuclei in the ectoderm (light-grey) and endoderm (dark-grey). (F) Transcription factors, signaling molecules, and neuronal genes are overrepresented among the pSMAD1/5 targets compared to the functional distribution of 100 random genes. LG – late gastrula targets, 4dP – 4d planula targets, DE – pSMAD1/5 ChIP targets differentially expressed

in BMP2/4 and/or GDF5-like morphants (padj ≤ 0.05), 2xDE targets - pSMAD1/5 ChIP targets differentially expressed in BMP2/4 and/or GDF5-like morphants (padj ≤ 0.05) showing ≥2-fold change in expression. (G) Fractions of each functional category of the differentially expressed pSMAD1/5 target genes (see panel F) containing BRE.

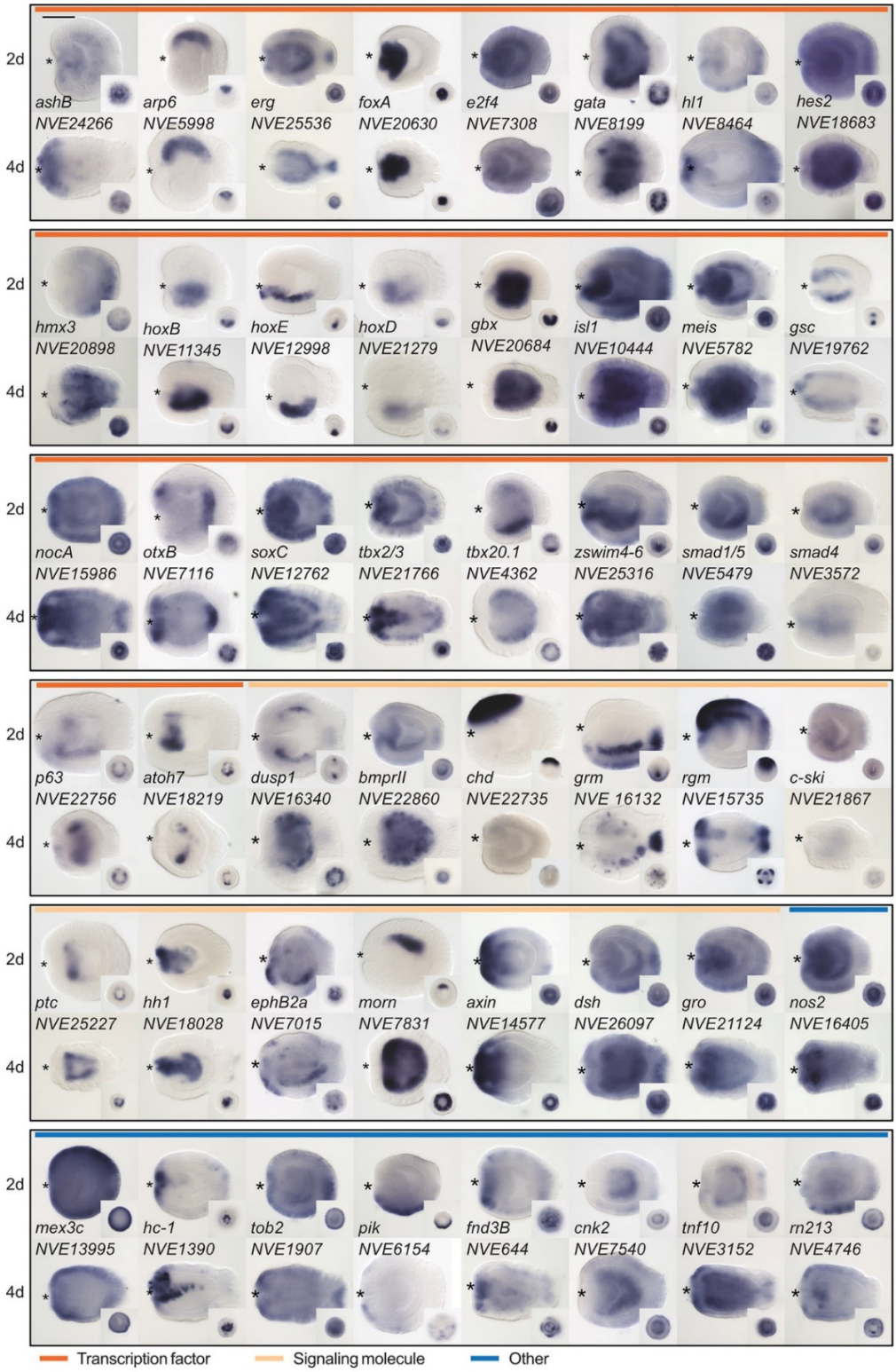

Figure 2. Expression patterns of a selection of the direct targets of BMP signaling in 2d and 4d planulae. In lateral views, the oral end is marked with an asterisk, inlets show oral views. Scale bar represents 100 µm.

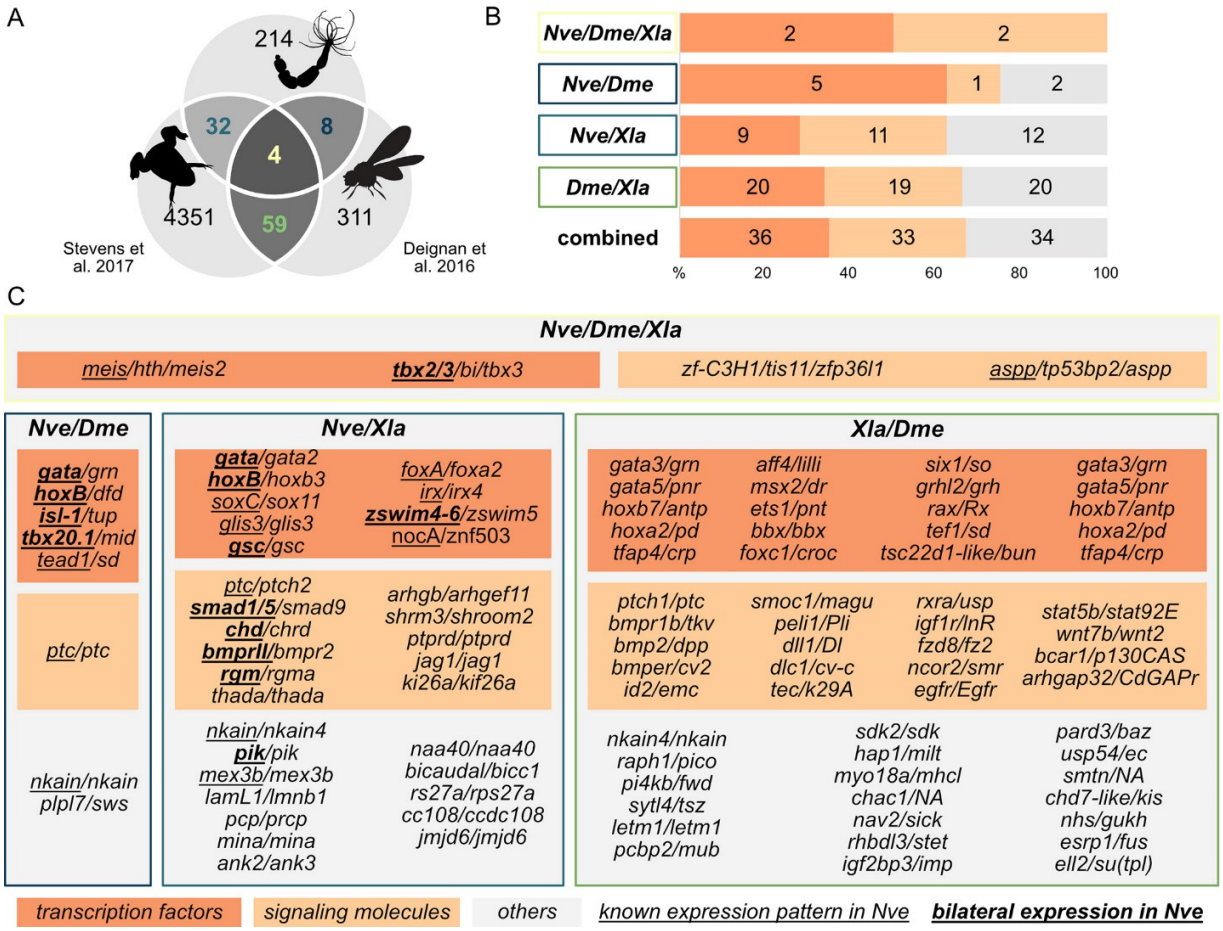

Figure 3. *Nematostella* and Bilateria share BMP signaling targets, which predominantly encode transcription factors and signaling molecules. (A) Overlap of BMP signaling targets at comparable embryonic stages in the 3-way comparison of *Nematostella*, *Drosophila* (Deignan et al., 2016) and *Xenopus* (Stevens et al., 2017). Orthology links were deduced by NCBI BLASTP of the respective proteomes with a cut-off e-value ≤1e-5, and reciprocal best BLAST hits were determined using the bit score. (B) Transcription factors and signaling molecules represent more than 60% of pSMAD1/5 targets shared between *Nematostella* (*Nve*), fly (*Dme*), and frog (*Xla*). (C) Gene names of orthologous targets shared between *Nematostella*, fly and frog. For targets shared with *Nematostella*, genes with known expression patterns in the embryo are underlined, genes expressed asymmetrically along the directive axis are underlined and bold.

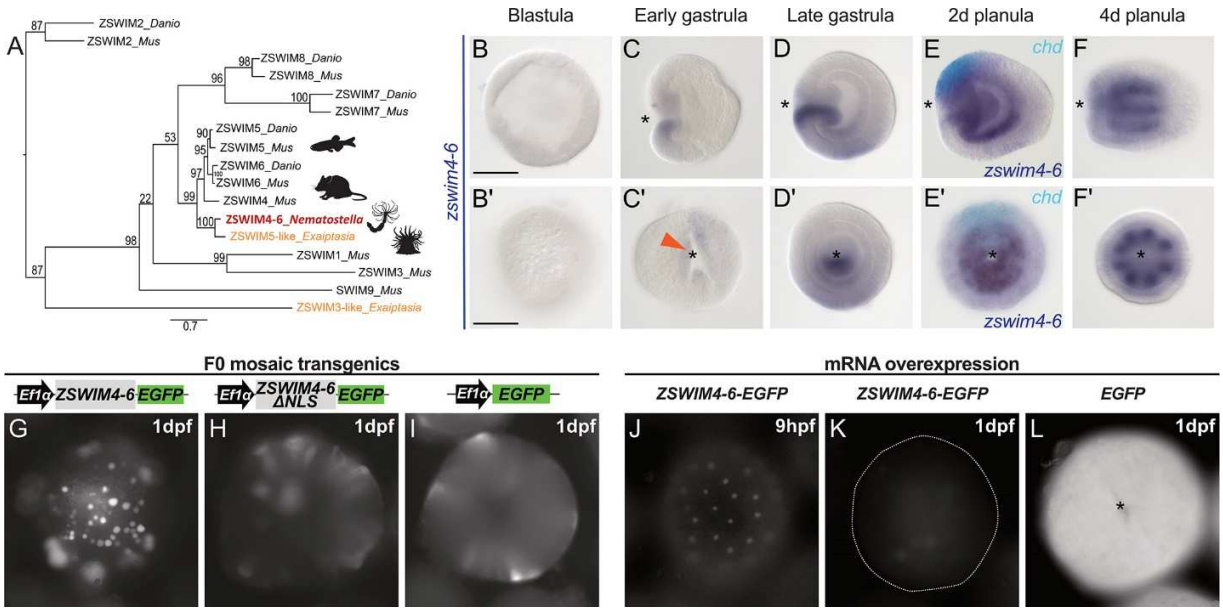

Figure 4. *zswim4-6* is a target of BMP signaling with bilaterally symmetric expression, and encodes a nuclear protein. (A) Maximum likelihood phylogeny shows that *Nematostella* ZSWIM4-6 clusters with ZSWIM4/5/6 from zebrafish and mouse. (B-F') *Nematostella zswim4-6* expression follows the dynamic BMP signaling domain (see Fig. 1D for comparison). Double ISH shows *zswim4-6* and *chd* transcripts localize to the opposite sides of the directive axis. (G-I) Mosaic expression of ZSWIM4-6-EGFP under the control of the ubiquitously active *EF1α* promoter in F0 transgenic animals demonstrates that ZSWIM4-6 is a nuclear protein. Full-length ZSWIM4-6-EGFP is translocated into the nuclei (G), while ZSWIM4-6ΔNLS-EGFP missing the predicted NLS remains cytoplasmic (H), similar to the EGFP control (I). Exposure time was the same in all images. (J-L) Microinjection of *ZSWIM4-6-EGFP* mRNA results in a weak EGFP signal detectable in the nuclei of the early blastula (J), which progressively disappears towards late gastrula (K). EGFP translated from *EGFP* mRNA remains readily detectable (L). To visualize the weak signal in (J-K), the exposure had to be increased in comparison to (L). Asterisks mark the oral side; scale bars 100 µm.

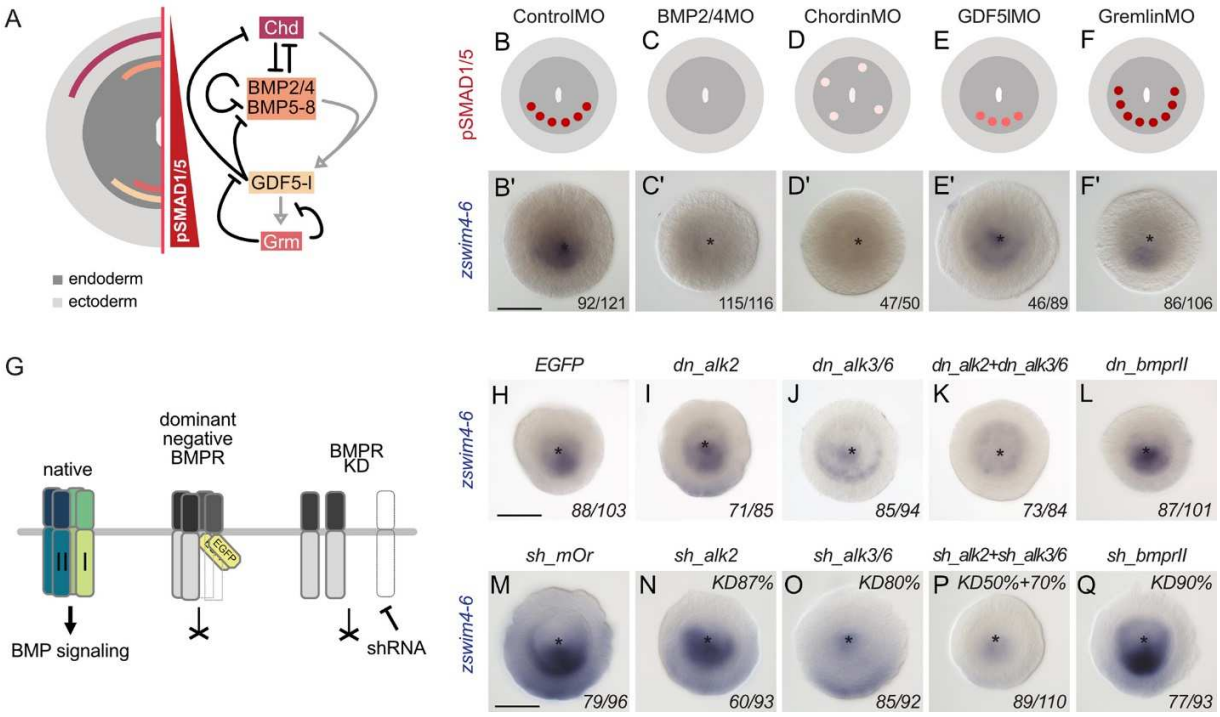

Figure 5. *zswim4-6* expression is regulated by BMP2/4 but not by GDF5-like signaling, and preferentially via the BMPRI receptor ALK3/6. (A) Expression domains and putative interactions of the BMP network components in 2d embryos (based on Genikhovich et al., 2015). (B-F') Effect of the KD of the individual BMP signaling components on nuclear pSMAD1/5 and on *zswim4-6* expression. *zswim4-6* expression is abolished upon KD of *bmp2/4* and *chordin*, but not in KD of *gdf5-l* and *gremlin*. Sketches in B-F show that the gradient is lost upon BMP2/4 and Chd KD, reduced upon GDF5-like KD and expanded upon Gremlin KD (based on Genikhovich et al., 2015). (G) Overview of the expected effect of the dominant negative BMP receptor (Ser/Thr-kinase domain replaced with EGFP) overexpression and BMP receptor RNAi on BMP signaling. (H-L) *zswim4-6* expression is reduced upon overexpression of the dominant negative Type I BMP receptor dn_Alk3/6 and combined overexpression of dn_Alk2 and dn_Alk3/6 but remains unchanged in dn_Alk2 alone and dominant negative Type II BMP receptor dn_BMPRII. (M-Q) Expression of *zswim4-6* is reduced upon KD of the Type I BMP receptor Alk3/6 and combined KD of Alk2 and Alk3/6 but unaffected upon KD of Alk2 and BMPRII. Asterisks mark the oral side. Scale bars correspond to 100 µm. The numbers in the bottom right corner indicate the ratio of embryos displaying the phenotype shown in the image to the total number of embryos treated and stained as indicated in the figure.

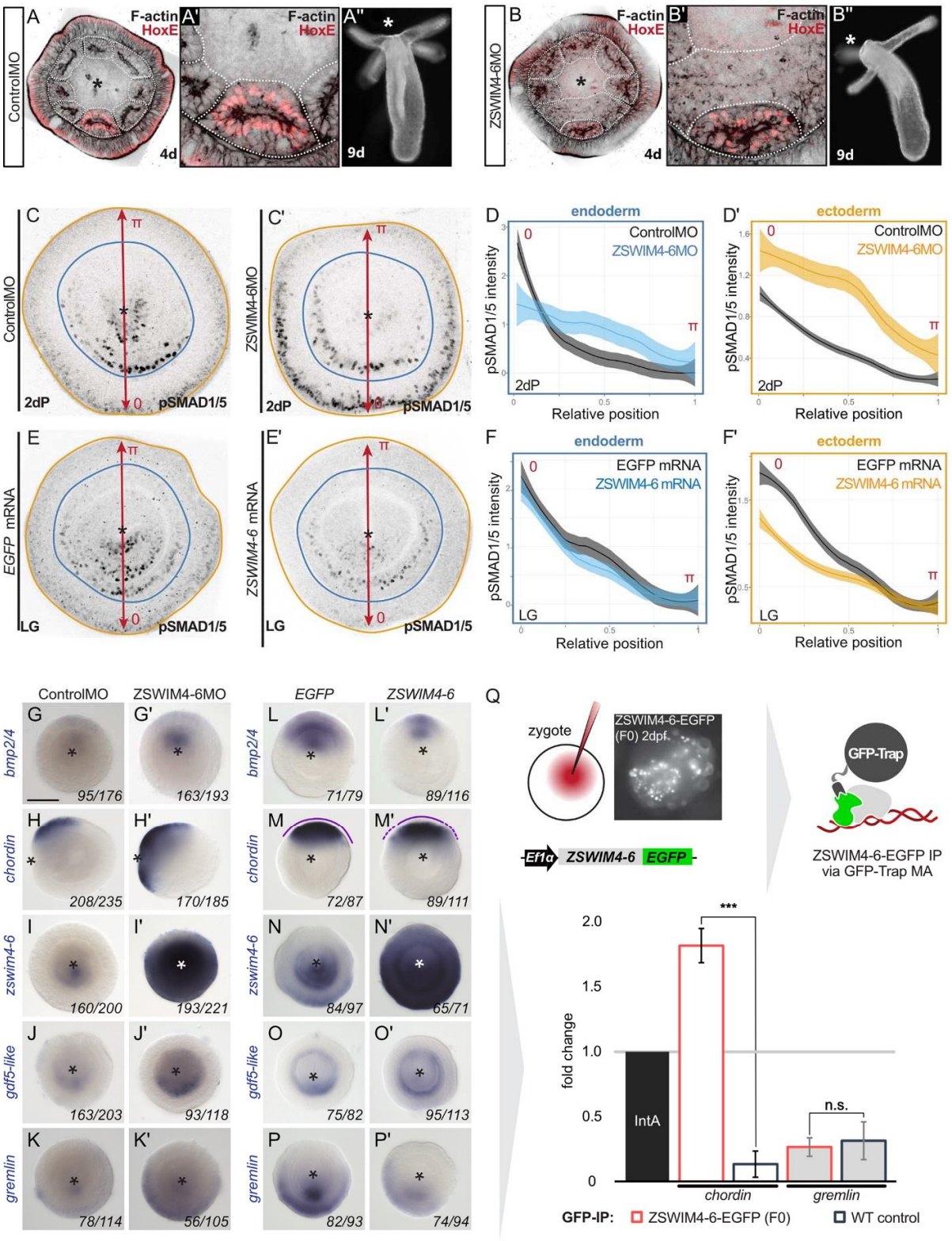

Figure 6. ZSWIM4-6 is a modulator of BMP signaling that appears to act as transcriptional repressor. (A-B) Morpholino KD of *zswim4-6* results in patterning defects. In the 4d planula, the

HoxE-positive mesenterial chamber does not reach the pharynx, which leads to the fusion of neighboring chambers (compare A, A' with B, B'). This results in the formation of three instead of four tentacles in the 9d polyp (compare A'' with B''). (C-F') Immunofluorescence and quantification of relative nuclear anti-pSMAD1/5 staining intensities in 2d ZSWIM4-6 morphants (C-D') and upon *zswim4-6* mRNA overexpression in the late gastrula (E-F'). Intensity measurements are plotted as a function of the relative position of each nucleus in the endoderm or in the ectoderm along a 180° arc from 0 (high signaling side) to π (low signaling side). The measurements from Control MO embryos (n=32) and ZSWIM4-6MO embryos (n=33), as well as *egfp* mRNA embryos (n=24) and *zswim4-6* mRNA embryos (n=26) are described by a LOESS smoothed curve (solid line) with a 99% confidence interval for the mean (shade). For visualization purposes, the intensity values were normalized to the upper quantile value among all replicates and conditions of each control-experiment pair. (G-K') Expression of *zswim4-6* and BMP network components in the 2d planula upon morpholino KD of *zswim4-6*; All images except for H and H' show oral views; (L-P') Expression of *zswim4-6* and BMP network components in late gastrula (30 h) upon *zswim4-6* mRNA injection; oral views, purple dashed line marks the loss of a sharp boundary of *chd* expression. Asterisks mark the oral side. (Q) ChIP with GFP-Trap detects ZSWIM4-6-EGFP fusion protein in the vicinity of the pSMAD1/5 binding site in the upstream regulatory region of *chordin* but not of *gremlin*.

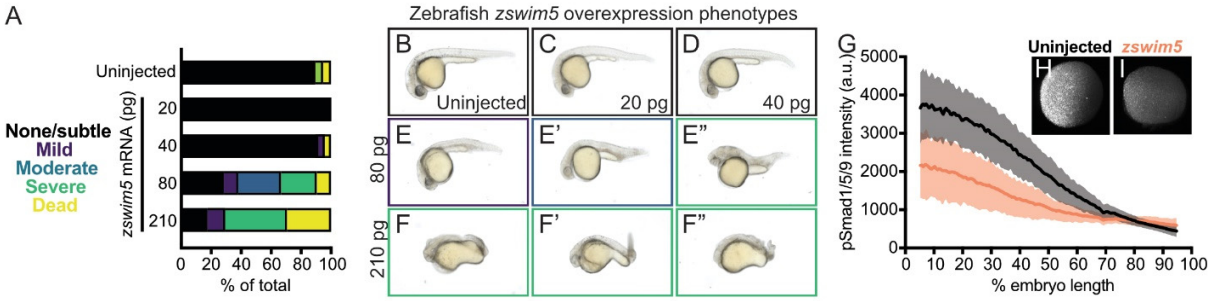

Figure 7. *Zswim5* overexpression dampens BMP signaling and causes developmental defects in zebrafish. (A-F") Wild type zebrafish embryos were left uninjected (B) or injected at the one-cell stage with 20, 40, 80, or 210 pg *zswim5* mRNA. (A) Phenotype quantification at 1 day post-fertilization (dpf) shows increasingly severe developmental defects at higher amounts of mRNA. A representative selection was imaged at 1 dpf (B-F''). Multiple embryos are shown for 80 (E-E") and 210 (F-F") pg to illustrate the variety of defects. Number of embryos - Uninjected: 19, 20 pg: 20, 40 pg: 24, 80 pg: 21, 210 pg: 17. (G-I) Embryos were injected with 80 pg *zswim5* mRNA or left uninjected and fixed at 50% epiboly (early gastrulation). BMP signaling levels were assessed using pSmad1/5/9 immunostaining. Animal pole views are shown with ventral on the left. (G) Quantification of immunofluorescence reveals lower amplitude BMP signaling gradients in *zswim5*-overexpressing embryos (I) compared to uninjected controls (H). Average background-subtracted intensity with standard deviation is plotted. Number of embryos - Uninjected: 8, *zswim5*-injected: 8.

Supplemental Information

Analysis of SMAD1/5 target genes in a sea anemone reveals ZSWIM4-6 as a novel BMP signaling modulator.

Paul Knabl, Alexandra Schauer, Autumn Pomreinke, Bob Zimmermann, Katherine W. Rogers, Patrick Müller, Grigory Genikhovich.

Contents

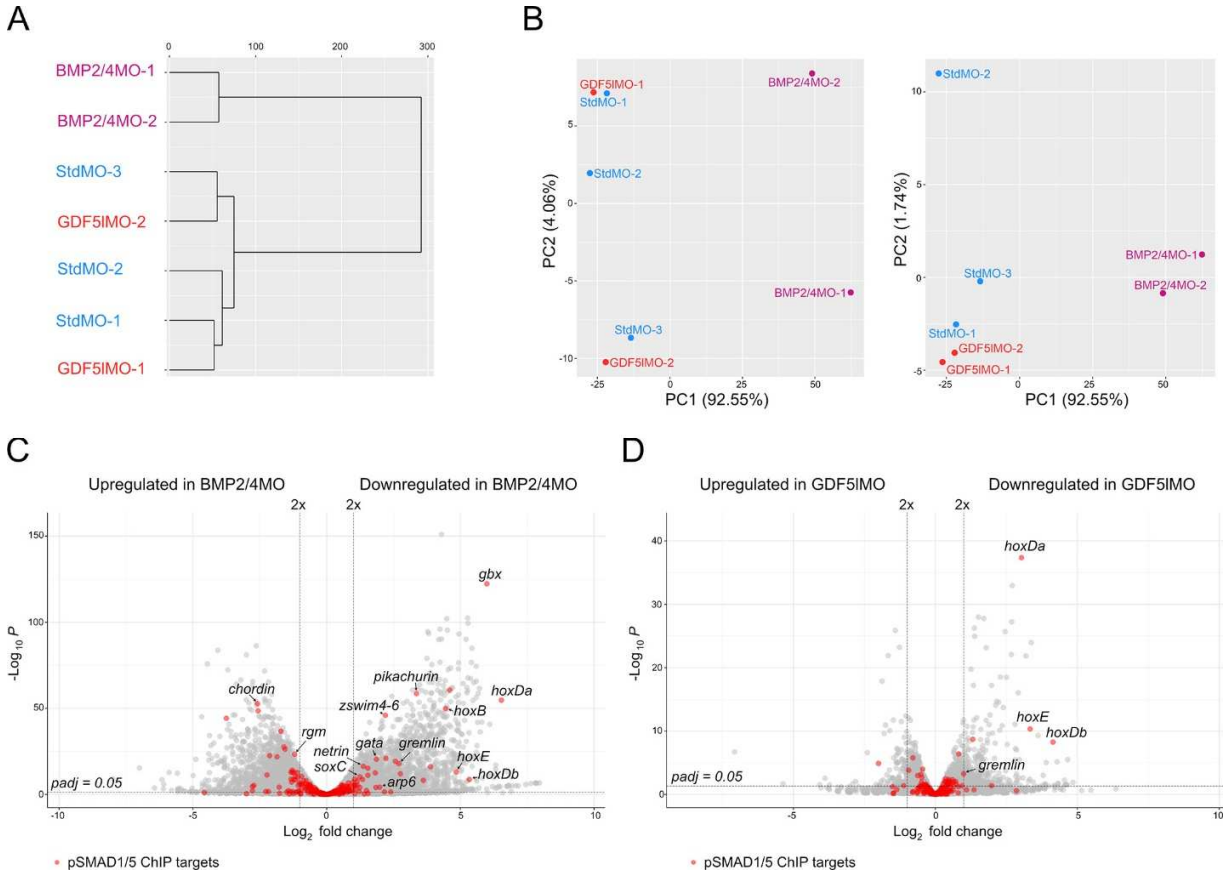

Supplementary Fig 1 – Transcriptomic comparison of BMP2/4, GDF5-l and control morphants and differential expression of pSMAD1/5 ChIP targets upon different knockdowns. (A) In the cluster dendrogram and (B) principal component analysis, replicates of GDF5–lMO (red) and StdMO (blue) transcriptomes group together, while the transcriptome of BMP2/4MO (magenta) is separated. (C-D) Volcano plots highlight differentially expressed pSMAD1/5 ChIP targets (red) in (C) BMP2/4 morphants and (D) GDF5-l morphants ($p_{adj} \leq 0.05$).

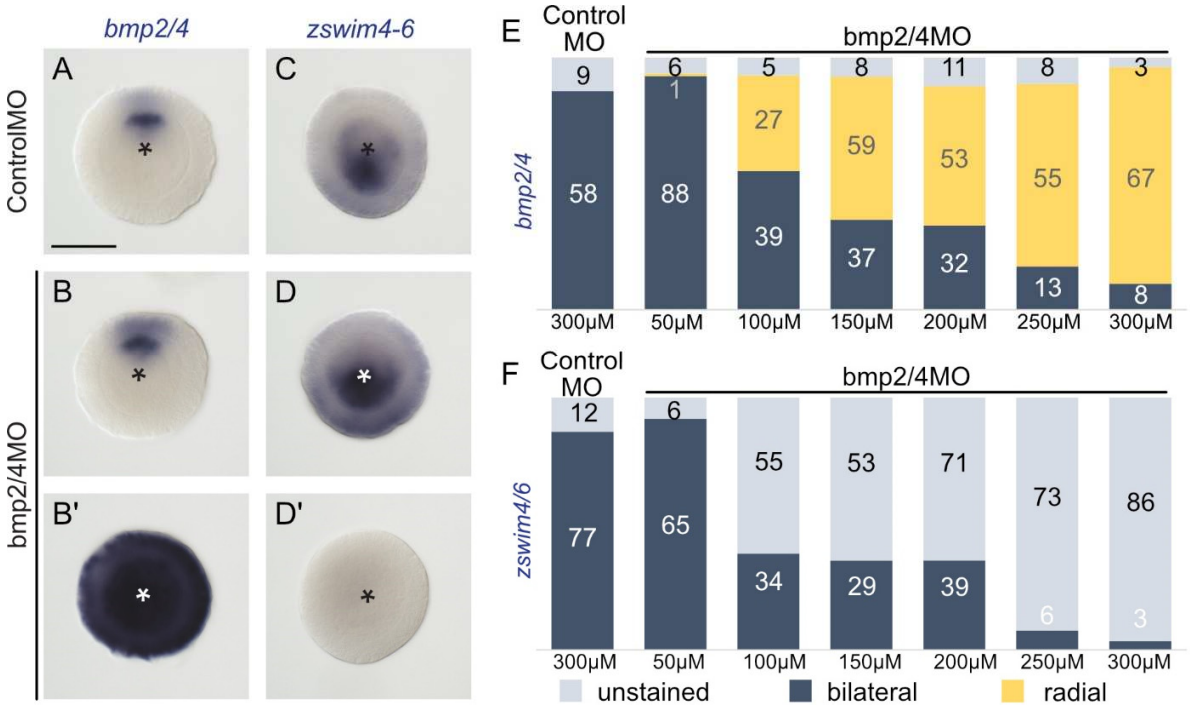

Supplementary Fig. 2 – Knockdown of *bmp2/4* using different concentrations of bmp2/4 morpholino results in either normal, bilaterally symmetric expression or complete radialization but no intermediate phenotypes. (A) In the 2d planula normal bmp2/4 expression is confined to a narrow stripe on one side of the directive axis. Injection of different concentrations of bmp2/4MO results in either (B) no change of the normal expression pattern or (B') complete radialization. (C) *zswim4/6* is expressed asymmetrically, on the opposite side of the directive axis. Different concentrations of bmp2/4MO result in either (D) normal *zswim4-6* expression or (D') suppression of *zswim4-6*. (E) With the injection of increasing concentrations of *bmp2/4* morpholino, the number of embryos displaying a complete radialization of *bmp2/4* expression increases and (F) the number of embryos expressing *zswim4-6* decreases.

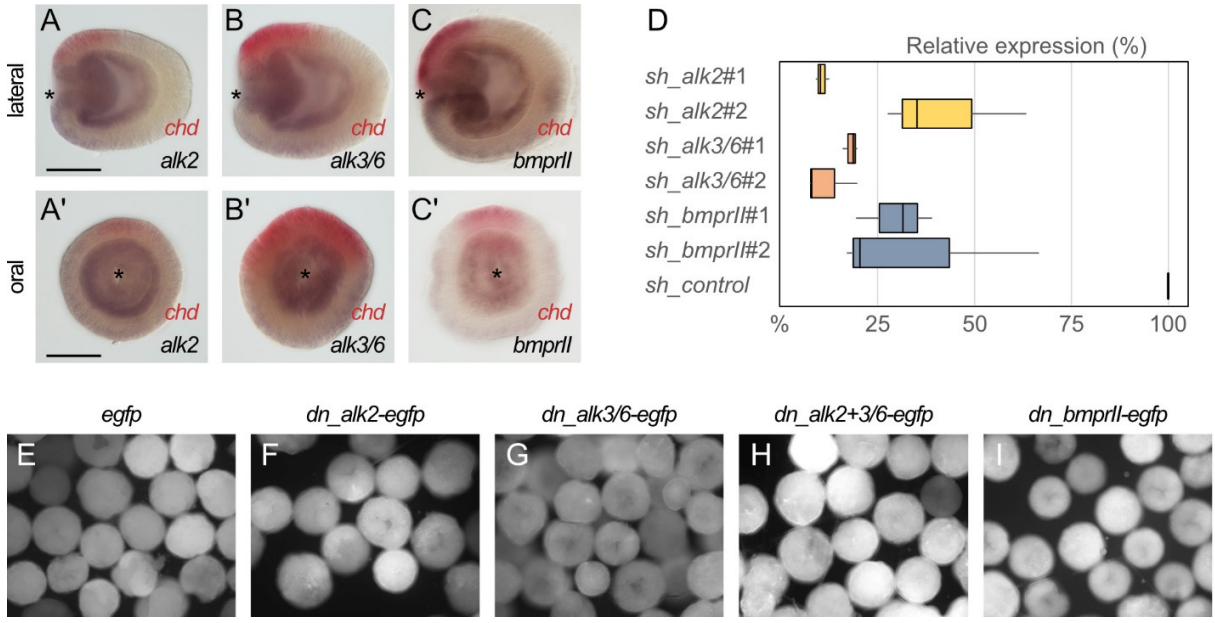

Supplementary Fig. 3 – Expression of BMP receptors, efficiencies of RNAi mediated knockdowns and overexpression of dominant negative (dn) receptor constructs. Expression of BMP receptors (A-A') *alk2*, (B-B') *alk3/6* and (C-C') *bmprII* is broadly detectable in endoderm with stronger expression on the high-BMP signaling activity side of the directive axis, opposite to *chordin* (red). (D) qPCR quantification of KD efficiencies for BMP receptor shRNAs. (E-I) EGFP signal in late gastrula embryos injected with (E) *egfp* mRNA and (F-I) mRNA of dominant-negative BMP receptor constructs. Asterisks mark the oral side, scale bars correspond to 100 µm.

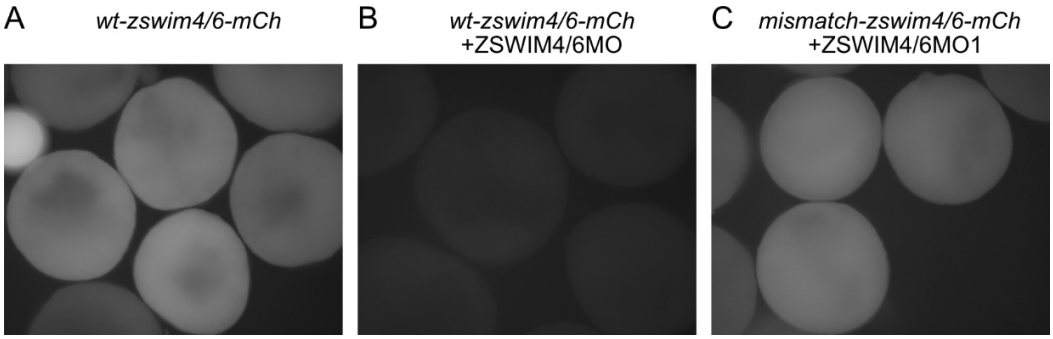

Supplementary Fig. 4 – Testing ZSWIM4/6 morpholino specificity. (A) Fluorescent signal in embryos injected with mRNA coding for the ZSWIM4/6 recognition sequence fused to the mCherry (*wt-zswim4/6-mCh*) coding sequence. (B) Co-injection with ZSWIM4/6 morpholino can suppress the translation of mRNAs containing the respective recognition sequence. (C) Translation of mRNA coding for the zswim4/6 recognition sequence carrying 5 mismatches and fused to mCherry (*mismatch-zswim4/6-mCh*) is no longer suppressed when co-injected with ZSWIM4/6 morpholino.

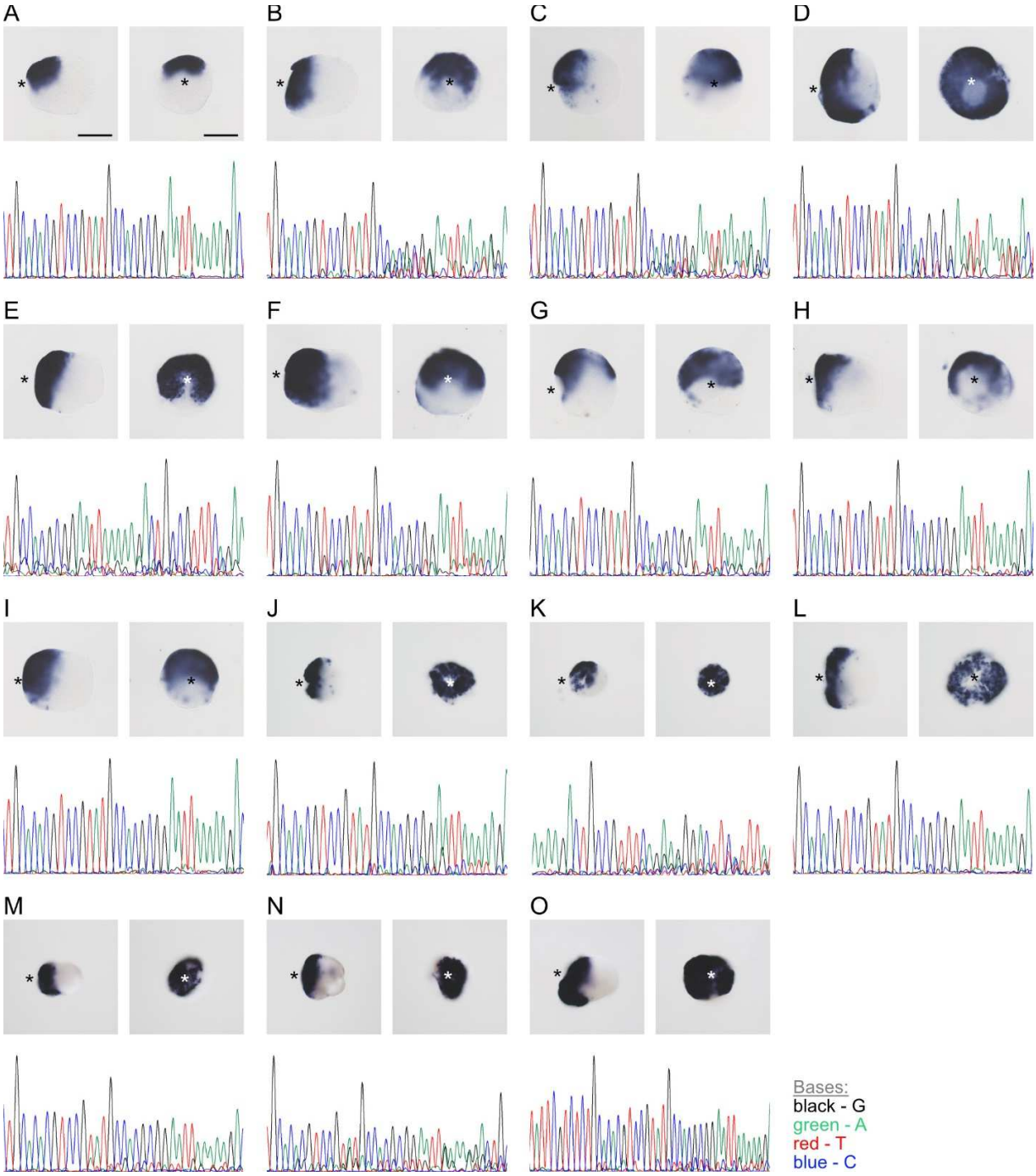

Supplementary Fig. 5 – CRISPR/Cas9 mediated mutagenesis of *zswim4-6* results in the expansion of *chordin* expression in mosaic mutants (F0). (A) Bilateral expression of *chordin* in wild type 2d planula and corresponding sequencing chromatogram of *zswim4-6* guide RNA target region. (B-O) expanded or radialized chordin expression in 2d mutant planulae injected with a single guide RNA (B-I) or two guide RNAs (J-O) targeting the SWIM zinc-finger domain. Corresponding sequencing chromatograms show variability in the target loci of mutant animals. Asterisks mark the oral side, scale bars represent 100µm.

Supplementary Table 1 - ZSWIM4-6 guide RNA sequences and sequencing primers

Name	Sequence
zswim4-6_g254	GCACACGTCCGTATGCCACGCGG
zswim4-6_g282	AAAAGACTGCCGTTTCAGAAGGG
zswim4-6_sqF	CTAGACCTAGCCGCGAAGTG
zswim4-6_sqR	TTTGCACCGACCGACTACAA

Supplementary Table 2 - Primers used for cloning dominant-negative BMP receptor fragments

Name	Sequence
Alk2F	ATGCCGCCTTCTTTTGCTATAACCCTTGT
Alk2swF	TGCCCATGTAATGAGGAAAGAGGTGGTGGTGGTAGTGTGA
Alk2swR	TCACACTACCACCACCACCTCTTTCCTCATTACATGGGCA
Alk3/6F	ATGGCTTTAGCCACCAAATCAACCATTTTC
Alk3/6swF	CGCATTAACTTTATAAGCTCTGGTGGTGGTGGTAGTGTGA
Alk3/6swR	TCACACTACCACCACCACCAGAGCTTATAAAGTTAATGCG
bmpRIIF	ATGTCTTGGATTTGGAGATTCC
bmpRIswF	TTCCCTGGACTTGAGCCAGGGTGGTGGTGGTAGTGTGA
bmpRIswR	TCACACTACCACCACCACCCTGGCTCAAGTCCAGGGAA

Supplementary Table 3 - Morpholino sequences

Name	MO sequence	Concentration	Reference
BMP2-4MO (DPPMO)	GTAAGAAACAGCGTAAGAGAAGCAT	300 µM	Saina et al., 2009; Genikhovich et al., 2015
ChdMO	GATCCACTCACCATCTTTGCGAGAC	300 µM	Saina et al., 2009; Genikhovich et al., 2015
GDF5lMO	AGGTTATTTAGCCTGACCTTGATCG	500 µM	Genikhovich et al., 2015
GrmMO	CTCAACAGCTTCTTCAATGATCCGT	500 µM	Genikhovich et al., 2015
ZSWIM4-6MO	CCGTCCATAGCTTGTACTGATCGAC	300 µM	this study
Control MO	CCTCTTACCTCAGTTACAATTTATA	500 µM	Genikhovich et al., 2015

Supplementary Table 4 - Primer sequences for MO specificity testing

Name	Sequence
wtZSWIM4-6MOmCh_F	GTCGATCAGTACAAGCTATGGACGGTGTGAGCAAGGGCGAG
misZSWIM4-6MOmCh_F	GTGGATCTGTAGAACCTATGGATGGTGTGAGCAAGGGCGAG

Supplementary Table 5 - Short hairpin RNA targets

Name	Target sequence
sh_alk2#1	GTGGCAAGCCTAATCTACA
sh_alk2#2	GGCATGACTTAGGACCAGT
sh_alk3/6#1	GGCCAAGTCACTCAAATGT
sh_alk3/6#2	GGAGAGGCGCATTAACTTT
sh_bmpRII#1	GTCGAGAGGACCCTTACTT
sh_bmpRII#2	GCTGGTACAGTCCAAGAAT

Supplementary Table 6 - qPCR primers

Name	forward	reverse
alk2q	TGTGTCGGAGGTGTGAACATC	TGTCTCTGTGCTGCAGGTTTG
alk3/6q	AGCGGAGGAAGAAGGCTATGA	TTCCTATGCACACTGGCAGG
bmpRIIq	TGGACGGGTCATGTGTCTTG	TAACGCAGTGTTCCCACCTC
Chd_genomic	tcaaaacaatagcaaagccaga	gcttgctgaccaaagacctc
Grm_genomic	ggcagccaatagctcttctg	gtcgatcgtcggaaagtagc
IntA_genomic	ttctgaatgaatgcggatga	ggatttctgctttgcgactc

Supplementary Table 7 - Primer sequences for in situ probes

NVE	Name	forward	reverse
NVE25316	*zswim4/6*	CGCATGCTCAGTCTGATCAC	CCAAGTCCTAGTCCGCTGAA
NVE15986	*nocA*	AGAAATCACCGTTGGCCCTA	CTGCTAGACTGAACAGGGCT
NVE6154	*pik*	GCATGCTGGACCTTTCTCAG	TCCATGACTGACGCTTTCCT
NVE20898	*hmx3*	tcacaggcttaaaacgtcgc	acctgctatttgacCTACACCA
NVE14226	*ephrin-b2*	AGCCCACAACACAATCAACA	aatcagcagggtgaaaatcg

NVE15989	*nocA*	AGAAATCACCGTTGGCCCTA	CTGCTAGACTGAACAGGGCT
NVE22756	*p63*	TGCCAACCACATCACAAGACA	GCTGATCACAGGGTTCCCAA
NVE18219	*atoh7*	GCCCAGTCAAAACCACCAAC	TGTCATTCAGTGTTTGGTGACG
NVE16340	*dusp1*	CCTACGCGGTGCAAACTTGT	AGGCGACTCTGCAGTTGGAA
NVE7831	*morn*	AGTGGTTCTAGTGGAGCGCAA	CGTGCACGTCACTAAACAACG
NVE13995	*mex3c*	GGGTCTTGTTGTCGGTCCTA	GCATACAGGGCAGACAGAGT
NVE6154	*pik*	GCATGCTGGACCTTTCTCAG	TCCATGACTGACGCTTTCCT
NVE644	*fnd3b*	AAGAGGAAGAAGGCCGAAGAGT	CTCCACTTACCGTGCTCTCATCT
NVE3152	*tnf10*	CATGCTGCTAACTCGGTGTG	CCGCCCAAAGAATCGAAGTG
NVE5866	*gsc*	TTTACGCCACAAAACGAGCG	ATTGACTCGCACATCTCGGG
NVE8464	*hl1*	CCAAGCTGGAAAAAGCGGAC	GTTCTCTGCTTGGGAAGCCT
NVE22860	*bmprII*	TGGACTTGAGCCAGCTAACA	TTGCTGACTTCTGGTTGTGC
NVE10444	*isl-1*	GAAGACGTACTGCAAGCGAG	TATGACTCGCGGACTCAGAC